

Cell

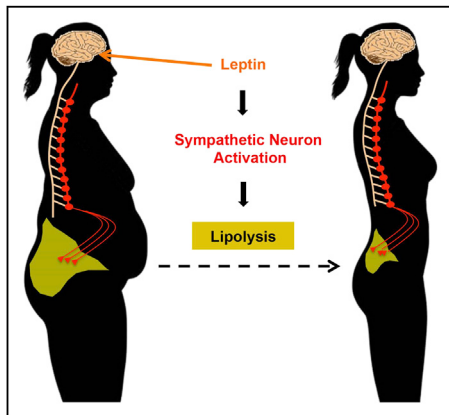
Volume 163
Number 1

September 24, 2015

www.cell.com



In This Issue



Fat on the Verge of a Nervous Breakdown

ZENG ET AL., PAGE 84

Leptin action in the brain stimulates sympathetic neurons that innervate fat deposits, forming neuro-adipose junctions that break down fat. Local optogenetic activation of these neuronal terminals promotes fat loss and could be used to circumvent central leptin resistance.

Building a Bigger Brain

POLLEN ET AL., PAGE 55

Radial glia in the ventricular and outer subventricular zones show molecular differences at the single-cell level, and transcriptomic analysis suggests that outer radial glia generate a self-sustaining proliferative niche that supports primate brain expansion during development of the cerebral cortex.

Looking Human

PRESCOTT ET AL., PAGE 68

Epigenome and transcriptome profiling from in-vitro-derived human and chimpanzee cranial neural crest cells allows for exploration of recent changes in the *cis*-regulatory landscape underlying human craniofacial evolution.

Microbiota on a Gastro-Tour

DEY ET AL., PAGE 95

A mouse model of short-term dietary changes, mimicking what happens when humans travel to places with different culinary traditions, reveals how a single food ingredient like turmeric can, in combination with microbially generated biomolecules, regulate host physiology.

Liquified Mitotic Forces

JIANG ET AL., PAGE 108

A protein associated with mitotic spindle transitions coalesces into a liquid droplet to promote microtubule polymerization and spindle assembly, suggesting that the biophysical properties associated with liquid demixing may shape the characteristics of a hypothesized but elusive spindle matrix.

When Stress Relief Gets Sticky

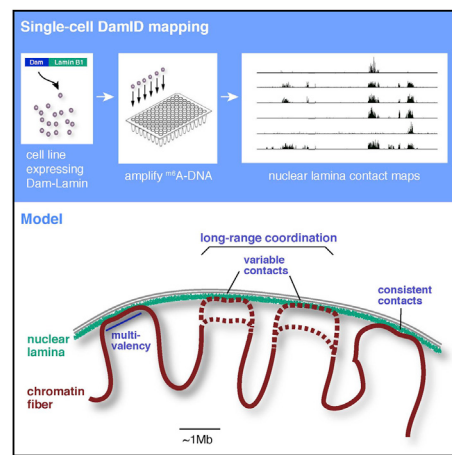
MOLLEIX ET AL., PAGE 123

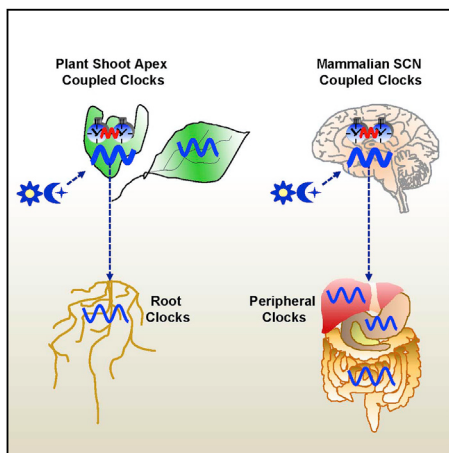
RNA binding proteins with low complexity sequence domains drive liquid phase separation to form stress granules within the cytoplasm; however, if the granules persist, pathological protein fibrillization results.

Nuclear Organization Cell by Cell

KIND ET AL., PAGE 134

Looking at chromosome-lamina interactions in single cells reveals cell-to-cell variation in interphase chromosome architecture and extensive intra-chromosomal coordination of nuclear lamina contacts.





Central Circadian Control for Plants

TAKAHASHI ET AL., PAGE 148

Plants harbor a clock in their shoot apex that functions like the mammalian suprachiasmatic nucleus, acting to couple and synchronize rhythms in distal organs.

Striking at the Heart of Triple-Negative Breast Cancer

WANG ET AL., PAGE 174

Triple-negative breast cancer's strong dependence on the transcriptional kinase CDK7, which drives expression of a cluster of cancer-promoting genes, suggests a potential new therapy.

Decoder Ring for Mutations in Cancer Signaling

CREIXELL ET AL., PAGE 187

CREIXELL ET AL., PAGE 202

Determining the residues that drive the specificity of kinases and of SH2 domains that bind phosphorylation sites paves the way for a systematic interpretation of mutations on signaling networks. Applying this approach to genomic variants in cancer reveals the many ways in which signaling networks can be rewired, including the creation or destruction of phosphorylation sites.

Monitoring Methylation Changes in Single Cells

STELZER ET AL., PAGE 218

A clever reporter system indicates DNA methylation status in single cells and how it changes over time *in vivo*.

The Silence of the Proviruses

YANG ET AL., PAGE 230

Proviral silencing is a characteristic of the pluripotent state, and the precise expression of endogenous retrovirus is critical for embryogenesis and development. Identification of cellular factors and mechanisms involved in retroviral repression in embryonic stem cells provides key insights into these processes.

Chromatin Architecture in the Brain

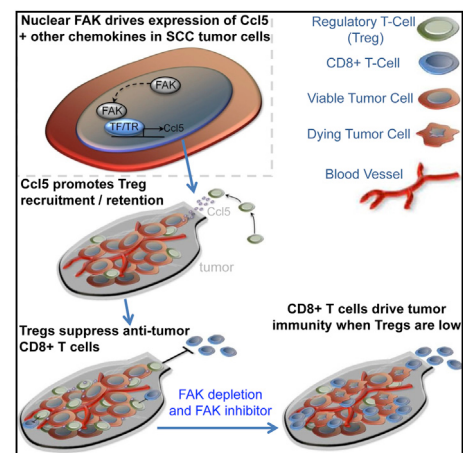
LINHOFF ET AL., PAGE 246

Interrogation of chromatin architecture at high resolution in complex tissues such as the brain is made possible through the combined analysis of epigenetic modifications, intranuclear localization of specific DNA sequences, and high-resolution segregation of nuclear compartments using advanced array tomography imaging.

The FAKts about Tregs in Cancer

SERRELS ET AL., PAGE 160

Nuclear Focal Adhesion Kinase or FAK regulates transcription of chemokines that drive recruitment of tumor-associated regulatory T cells to promote oncogenic growth by inhibiting cytotoxic CD8+ T cells. A FAK inhibitor helps to deplete Tregs and initiate anti-tumorigenic responses.



Taking a Healthy Interest in Translational Research

It is now readily possible to determine, often in exquisite detail, the ways in which a single cell or a single individual differs from another. Although we are rapidly figuring out how these cellular features are altered in disease states, pulling medical advances from this haystack of facts remains a challenge. Yet, the view from *Cell* on prospects for medical advancement in this era of integrated “omics” could be summed up in a single word: optimistic. From our daily engagement with researchers in pursuit of the most exciting scientific discoveries, we feel a palpable acceleration of interest and enthusiasm in translational work occurring within the community.

Cell has a key role in fostering this essential dialog between the research and medical fields, and we’re eager to continue pushing the boundaries of how we think about disease and its treatment. Papers that resonate with both communities come in many varieties, and you can find examples in our recent issues that include enhancing transplantation efficiency for stem cells derived from cord blood ([http://www.cell.com/cell/abstract/S0092-8674\(15\)00574-7](http://www.cell.com/cell/abstract/S0092-8674(15)00574-7)), using organoids for personalized drug screening ([http://www.cell.com/cell/abstract/S0092-8674\(15\)00373-6](http://www.cell.com/cell/abstract/S0092-8674(15)00373-6)), suggesting new combination treatments in cancer immunotherapy ([http://www.cell.com/cell/abstract/S0092-8674\(15\)01040-5](http://www.cell.com/cell/abstract/S0092-8674(15)01040-5) and [http://www.cell.com/cell/abstract/S0092-8674\(15\)01028-4](http://www.cell.com/cell/abstract/S0092-8674(15)01028-4)), and exploring antibody-based treatments for cachexia ([http://www.cell.com/cell/abstract/S0092-8674\(15\)01045-4](http://www.cell.com/cell/abstract/S0092-8674(15)01045-4)). Also as part of our commitment to the dialog across the medical-research divide, Cell Press has recently joined forces with The Lancet group of journals to support the launch of an exciting new open access journal, *EBioMedicine*, with the aim of creating a forum to bring a community of scientists and physicians together toward the shared goal of improving human health.

As we expand into more translational and clinical arenas, we need to educate ourselves about publication standards and concerns in more clinical fields while building our pool of qualified rigorous reviewers. For example, we find that many disease-oriented studies increasingly include testing of compounds or combination therapies in mouse models, and a major bottleneck for these efforts is to improve reproducibility and the success rate of new prospective treatments through the pre-clinical and clinical development pipeline. Glenn Merlino and colleagues on page 39 of this issue tackle this matter of improving the ability of pre-clinical models in cancer to predict successful outcomes in human trials and highlight new approaches. We are also observing an increasing number of studies crossing our transom that take advantage of patient samples and other human data to support a proposed target’s therapeutic potential. For these, we need to pay special attention to issues of consent and patient confidentiality and to the importance of study design and the use of appropriate statistics in assessing clinical data. Overall, the engagement of our community of researchers with the therapeutic development pipeline is robust and strengthening. With the accelerating pace at which new discoveries are informing new potential treatments, it is now possible to

envision a time in the not too distant future when a paper in *Cell* could include both basic insights and results from randomized human clinical trials.

In the world of translational research, a landmark event is governmental approval of a new drug or therapeutic, which directly impacts how a disease is treated and offers new hope for patients. To celebrate these achievements and help promote the conversation between basic scientists, pharma/biotech, and physicians, we’ve recently launched a new format called “Bench to Bedside.” On page 17, you will see our latest feature, which looks at Orkambi, a combination therapy that promotes the correct folding of the mutated channel that causes cystic fibrosis. Following its approval, it is expected that up to 50% of patients will benefit, marking a major milestone for a difficult-to-treat disease and highlighting protein folding as a medically targetable aspect of cell biology. All of this stems from the discovery more than 20 years ago that the disease is caused by mutations in a channel protein that impair its trafficking to the cell surface and promote its degradation ([http://www.cell.com/cell/abstract/S0092-8674\(90\)90148-8](http://www.cell.com/cell/abstract/S0092-8674(90)90148-8)).

For the bench researcher, Bench to Bedside will keep you abreast of exciting developments in new drugs and biologics. For the clinician, we aim to provide a succinct reference that conveys how the treatment works and the biological discoveries that made it possible. The timelines of key discoveries that feature in each Bench to Bedside hammer home the societal impact of sustained investment in research, and we hope that these will spark pride in what the research, pharma, and medical communities have together accomplished.

As a community, it is essential that we make clear to the public and to policymakers the ways in which basic and translational discoveries contribute to new treatments. On page 21 of this issue, Sanders Williams and colleagues present a Commentary that advocates for greater use of data mining and network analysis in assessing the individual and institutional contributions to recently approved treatments. They create a new bioinformatics tool, and using the example of ivacaftor (a component of Orkambi), they establish that the timeline of key discoveries in the cystic fibrosis field goes back nearly six decades and includes efforts from more than 2,000 researchers. The analyses also provide insight into the most influential researchers and institutions for a given breakthrough, offering quantifiable validation for why long-term thinking matters when it comes to research funding.

When *Cell* was founded four decades ago, the molecular biology revolution was exploding, powered by recombinant DNA technologies. This is when *Cell* established the roots that still nourish its pages today. Staying at the cutting edge ever since has led us in new areas, and today one of these areas that is rapidly expanding, powered by new omics technologies and mechanism-based drug development, is translational research. Being explicit in our advocacy and interest in translational work comes at the risk of some fearing that *Cell* “won’t like my paper because it doesn’t have a translational message.” We’ll stop you right there. For one, we’ve had a longstanding

interest in translational potential as one of the many elements considered when evaluating a study, and so this editorial perspective is not new. More to the point, conceptual impact—from whatever source or discipline—is our guiding principle, and we will continue to aggressively pursue and publish what is most exciting in basic biological research. Even as we remain

firmly grounded by our roots, we see in the current era a lifting of the fog between basic biological insight and clinical treatment that is making the shorelines of each visible to the other. This process will shape how these disciplines cross-pollinate, and as journal, we are dedicated to amplifying and enhancing the speed of this exchange.

The *Cell* editorial team

<http://dx.doi.org/10.1016/j.cell.2015.09.018>

Microbial Gardening

For many of us, salicylic acid may conjure up teenage memories of waking up to a huge pimple taking form on our face, just in time for picture day or the school dance. Perhaps fewer of us are aware that like many medicinal compounds, this acne-fighting molecule comes from plants. In fact, salicylic acid is a well-studied plant hormone that plays key roles in a variety of fundamental physiological processes, including growth, stress responses, and perhaps most notably, the plant's innate immune response to microbes. A new study now shows that salicylic acid also plays a key role in shaping the root microbiome (Lebeis et al., 2015).

Like us, plants have a complex relationship with the bacteria in their environment (Sloan and Lebeis, 2015). Exactly how host-microbiome communication is mediated is still unclear, but in animals, the host immune system closely regulates the community of microbes resident in the gut (Belkaid and Hand, 2014). Just as animals are exposed to a variety of bacteria through their guts, where nutrient absorption takes place, plants encounter a huge assortment of soil bacteria through their root systems. However, as is the case for the gut microbiome, only a limited selection of bacteria actually takes up residence in the roots (Lundberg et al., 2012; Bulgarelli et al., 2012).

A recent study from Jeff Dangl and colleagues now shows that plants cultivate the bacteria in their root systems, tending some and weeding out others (Lebeis et al., 2015). By using *Arabidopsis* mutants in which salicylic acid signaling was either disrupted or constitutive, the authors found that the phytohormone altered the bacterial communities colonizing the root. Remarkably, this shift reflected a phylum-level regulation rather than just changes in specific species of bacteria, suggesting that the overall structure of the root microbial community is controlled by salicylic acid. In further bacterial colonization experiments analogous to those carried out in germ-free animals, Lebeis et al. reconstructed a synthetic microbial community in sterile seedlings grown in artificial soil and showed that salicylic acid directly inhibits growth of some bacteria but promotes the growth of others. In fact, one type of bacteria carrying salicylate metabolism genes was able to grow on minimal media with salicylic acid as the only carbon source, suggesting that the plant hormone directly feeds its growth.

In addition to providing a potential entry point for improving crop production through microbiome modulation, the study raises broader questions about host-microbiome relationships. The finding that a single molecule can shape the taxonomic structure of the microbiome is intriguing; given that salicylic acid is so crucial for regulating systemic functions in plants, it will be interesting to see whether there will be analogous systemic mechanisms in animals.

Moreover, given that we ingest plants and that diet affects the gut microbiome (Faith et al., 2011), how might this relationship between plant compounds and bacteria play out inside us? Soil bacteria are remarkably effective at colonizing the gut in mice, outcompeting even gut bacteria from other organisms (Seedorf et al., 2014). Do soil-derived bacteria that have evolved to be responsive to plant innate immune hormones reside in our own gut? If so, what happens when we eat plants, thereby introducing the compounds that regu-



Arabidopsis plant growing in microbe-rich soil. (image from iStock.com/dra_schwartz).

late these bacteria into our bodies? What effects might this interaction in turn have on our own innate immune function and its regulation of the gut microbiome?

It should also be noted that aspirin, which has anti-inflammatory, anti-diabetic, and anti-cancer properties, converts to salicylic acid in the stomach. Although salicylic acid has been shown to activate AMPK, thereby increasing fat oxidation, its anti-diabetic effects are observed even in AMPK mutant mice (Hawley et al., 2012), suggesting an alternate mechanism. Given the effects of salicylic acid on the root microbiome, might some of its health consequences in animals be in part mediated through microbes in the gut? Ultimately, understanding the molecular mechanisms underlying host-microbiota communication will provide the framework for addressing important questions in human health and disease.

REFERENCES

Belkaid, Y., and Hand, T.W. (2014). *Cell* 157, 121–141.

Bulgarelli, D., Rott, M., Schlaepff, K., Ver Loren van Themaat, E., Ahmadinejad, N., Assenza, F., Rauf, P., Huettel, B., Reinhardt, R., Schmelzer, E., et al. (2012). *Nature* 488, 91–95.

Faith, J.J., McNulty, N.P., Rey, F.E., and Gordon, J.I. (2011). *Science* 333, 101–104.

Hawley, S.A., Fullerton, M.D., Ross, F.A., Schertzer, J.D., Chevtzoff, C., Walker, K.J., Peggie, M.W., Zivrova, D., Green, K.A., Mustard, K.J., et al. (2012). *Science* 336, 918–922.

Lebeis, S.L., Paredes, S.H., Lundberg, D.S., Breakfield, N., Gehring, J., McDonald, M., Malfatti, S., Glavina del Rio, T., Jones, C.D., Tringe, S.G., and Dangl, J.L. (2015). *Science* 349, 860–864.

Lundberg, D.S., Lebeis, S.L., Paredes, S.H., Yourstone, S., Gehring, J., Malfatti, S., Tremblay, J., Engelbrektson, A., Kunin, V., del Rio, T.G., et al. (2012). *Nature* 488, 86–90.

Seedorf, H., Griffin, N.W., Ridaura, V.K., Reyes, A., Cheng, J., Rey, F.E., Smith, M.I., Simon, G.M., Scheffrahn, R.H., Woebken, D., et al. (2014). *Cell* 159, 253–266.

Sloan, S.S., and Lebeis, S.L. (2015). *Curr. Opin. Plant Biol.* 26, 32–66.

Cindy Lu

Mendel, Mechanism, Models, Marketing, and More

James A. Birchler^{1,*}

¹Division of Biological Sciences, University of Missouri, Columbia, MO 65211, USA

*Correspondence: birchlerj@missouri.edu

<http://dx.doi.org/10.1016/j.cell.2015.09.008>

This year marks the 150th anniversary of the presentation by Gregor Mendel of his studies of plant hybridization to the Brunn Natural History Society. Their nature and meaning have been discussed many times. However, on this occasion, we reflect on the scientific enterprise and the perception of new discoveries.

Moche, Ming, and Mendel

Mendel sought and applied principles of probability to genetic ratios to develop a “law” describing the behavior of factors for plant characteristics over generations. It was known from horticultural and plant and animal domestication work at the time that hybrids would “revert” to grand-parental forms in their progeny. Mendel ([Mendel, 1866](#)) alluded to such findings in the Introduction to his seminal paper. Charles Darwin ([Darwin, 1868](#)) also noted “crossed forms of the first generation are generally nearly intermediate in character between the two parents, but in the next generation the offspring commonly revert to one or both of their grandparents and occasionally to more remote ancestors” in his 1868 book.

Indeed, it is potentially the case that “genetic ratios” were observed by many over the millennia. Walt Galinat ([Galinat, 1998](#)) noted that the Moche culture, who populated the coast of present day Peru centuries ago and who were renowned of their ceramic creativity, have among their many designs, images of four maize plants with different characteristics in 3:1 or 1:1 ratios. Did this indicate a familiarity with the basics of genetics? The skeptic would note that any difference among four plants will produce 3:1 and 1:1 ratios. But why four plants?

Whoever in China assembled the silkie chicken (*wu gu ji*) variety ([Dorshorst et al., 2010](#)) with its set of bizarre single gene characteristics

such as fluffy feathers, black skin and bones, blue earlobes, rose comb, polydactyly, feathered legs, and short tail feathers, first written about from the travels of Marco Polo around the time of the Ming Dynasty, but likely generated well before then, must have understood genetic ratios and how they operate in making combinations. No doubt there could be other examples. However, Mendel was the first to publish an attempt to attribute a significance or “law” to such ratios!

Some have questioned whether Mendel knew the actual significance of his work ([Endersby, 2007](#)) and that Correns, de Vries, and Tschermark, who discovered

similar findings in 1900, should rightfully be declared the fathers of genetics. Yet, Mendel did recognize a pattern where others did not; he recognized that there were factors following these patterns that determined characteristics of organisms; he tried to rationalize how inheritance in general could be explained by many such factors. While it might or might not be the case that the numerical classes of inherited characteristics were recognized before Mendel, to his credit he explicitly stated that the factors he studied were involved with inheritance. Indeed, this fact is apparently not necessarily intuitive as illustrated by those that went before him and did not recognize the significance of these patterns. Sophomore genetics students also illustrate this point. After many attempts by the author to explain the meaning of Mendel’s results, an exasperated student exclaimed during office hours: “Why does two piles of peas mean that a gene is involved?”

Menaces

One reason that Mendel’s work might have not met with wide acceptance is that it actually did not seem to explain much about how inheritance is realized in practice. We now know that his “factors” behave as they do because they reflect the mechanics of meiosis. Because of this realization, we automatically think in Mendelian terms with regard to the action of alleles and genes



Statue of Gregor Mendel at the St. Thomas Abbey in Brno, Czech Republic, where Mendel worked. Photo by James A. Birchler.

regardless of whether or how they affect the phenotype. But meiosis was not known at the time. And most traits that we typically examine are controlled by quantitative trait loci that are multigenic, semidominant to some degree, of small effect and variable in the extent with which they affect the phenotype. Mendel actually noted that some characteristics that he considered showed “the difference is of a ‘more or less’ nature...” and therefore he did not use them. He refers to the characters that he did use as “constant characters.” He notes that previous workers had described hybrids as often intermediate between the parents but he ascribes this to the random distribution of multiple characters that were independent of each other. The variation for quantitative characters is of low magnitude and multigenic; therefore, it is difficult to observe segregation ratios. Mendel rationalized this by suggesting that an astronomical number of progeny would be needed to see the reconstitution of a parental type. Indeed, in a broad sense, this is true.

Another feature of hybrids that potentially confounded the acceptance and appreciation of Mendel’s studies is the phenomenon of hybrid vigor or heterosis. Mendel actually noted the more robust nature of hybrids in his description of the dwarf versus normal sized pea plants. Darwin ([Darwin, 1876](#)) also examined this reaction of hybrids extensively and Mendel made no attempt to explain it, rightfully so.

The most famous example of results that stood in the way of acceptance was Mendel’s use of hawkweed (*Hieracium spp.*) in subsequent experiments to confirm his results with peas, beans, and other species ([Mendel, 1870](#)). Hawkweed exhibits very extensive variation in form and features that would have seemed to be an excellent system to investigate their behavior in hybrids and their progeny. However, the reason for this great variability is that hawkweed is clonally reproduced via the process of apomixis that bypasses meiosis but still produces seeds. New mutations or chromosomal abnormalities that arise in a clone are maintained. However, because they produce pollen and seeds, one would be tricked into believing hybrids could be made when in fact this would not be the case. Mendel thought he had suc-

ceeded in producing hybrids but they usually followed the “maternal” type indicating the presumed stable nature of the characters, which did not revert ([Endersby, 2007](#)). Ironically, this line of investigation was encouraged by the Swiss botanist, Carl Nageli ([Mendel, 1870](#)), a proponent of a view at the time of blending inheritance, the concept that determinants come together in hybrids and mix irreversibly, but because hawkweed reproduces asexually, hybrids resemble the maternal parent and do not usually produce intermediate phenotypes that were the hallmark in the perpetuation of the blending concept.

Mendel could not have made sense of his observations without setting aside quantitative traits and heterosis although his article states that he did just that for many aspects of hybrid plants, apparently realizing this need. These three “menaces” to Mendel, quantitative inheritance, heterosis, and apomixis represent three little understood aspects of genetics to this day and are worthy of investigation. The number of genes and their intricate interactions affecting quantitative traits ([Mackay, 2014](#)) and the potential non-linearities that they exhibit ([Birchler and Veitia, 2012](#)) are yet to be fully elucidated. Heterosis, despite being the foundation of world food production, has managed to conceal its secrets ([Birchler, 2015](#)). Likewise, apomixis ([Ronceret and Viegas-Calzada, 2015](#)), which has been proposed to fix heterosis for clonal propagation over multiple generations, is equally mysterious.

Mechanism

In the highly speculative scenario that Mendel had submitted his manuscript to a present day high impact journal, it would no doubt be dismissed as “descriptive,” “premature,” and “lacking in mechanistic insight” with the result that what is considered to be a seminal contribution to science would be relegated to a specialty journal. However, all of science is descriptive; it just varies in the level and magnitude of detail. Every novel discovery is premature in understanding and lacking in details of mechanism.

It would not have been possible to define much in the way of mechanism at the time. Mendel’s work preceded the discovery of meiosis in 1876 by Hertwig and its explanation by Weismann in

1890. Even after the rediscovery of Mendel’s work, it took the suggestion of Sutton, Boveri, and Wilson that Mendel’s factors reside on chromosomes and the formulation of the chromosome theory of inheritance to gain an appreciation of why Mendel’s factors behaved as they do. Perhaps a lesson to be learned is that valid observations existing in a mechanistic vacuum are to be valued and used as an inspiration for experiments to understand them better.

Models

Although the details are missing and will never be known for certain, Mendel’s Introduction to his paper ([Mendel, 1866](#)) suggests that he was aware of the phenomenon of “reversion” and had a “model” to explain this phenomenon. The model was useful in finding a good organism for the experiments (i.e., peas because they have concealed self-pollination but can be crossed when desired) and selecting the plant characters to examine. Yet Mendel went on to attempt to explain, using his model, the commonly known observation that hybrids could often be intermediate (now referred to as semidominant, additive, or dosage sensitive) in phenotype between the parents. While there is a partial insight in his explanation of multifactorial basis, his attempted explanation likely was unpersuasive in the context of his time.

Darwin conducted extensive studies of intentional self-pollination of a wide variety of plant species ([Darwin, 1877](#)) that naturally outbreed and documented the changes seen. He clearly found everything that Mendel did but not in as systematic way. For flower morphs, called pins and thrums, that foster outcrossing by their alternately placed stigmas and anthers, Darwin found what we now call dominant and recessive forms, which when hybrids were made and the progeny self-pollinated, the next generation “reverted” to both grandparental types but favoring one in number (i.e., the dominant form). In *Primula vulgaris*, he studied these flower morphs, which also differed in the parents for purple and yellow flower color, which, upon selfing the hybrids, the progeny showed a “3:1” ratio of purple to yellow. Further self pollination showed that the yellow form bred true and the purple again “reverted” with a preference for the purple

form. The flower color characteristic was independent of the flower morphs. In his study of tristylous with three morphs, he also clearly states that "it is the rule that plants thus derived usually consist of both parental forms, but not of the third form," illustrating he recognized that only two types could be present in any one individual. The flower morph forms could breed true while the flower color reverted, which we now call independent assortment. Thus, one can recognize in Darwin's data, dominant and recessive characters, the fact that only two forms are present in a hybrid, their reappearance in the next generation and the independence of different characters. But Darwin did not subscribe any "law" to these observations; he entered the study concerned that these plants did not naturally inbreed and were often highly sterile when they did—facts that he sought to understand within the context of his concept of natural selection. His "model," if one will allow the analogy, made him focus on his issue of concern and therefore he did not recognize the same principles of inheritance that Mendel did.

Models are good for designing experiment to test the limits and validity of a hypothesis. However, the originators of models often overextend their explanatory power. On the other hand, they also restrict one's thinking to a particular intellectual framework leaving potentially informative experiments unimagined. The examples of Mendel and Darwin illustrate both of these points. This in no way diminishes their respective contributions to science.

Marketing

Scientific acceptance depends on when, where, and by whom new knowledge is proposed. With regard to Mendel, Cock, and Forsdyke (Cock and Forsdyke, 2008) noted: "Then, as now, in marketing, simple messages worked. Then, as now, the same applied to the marketing of scientific ideas. Accordingly, subtle scientific ideas tended to lose out to simple scientific ideas and subtle scientists tended to lose out to the unsubtle."

While there was an excitement that followed the "re-discovery" of Mendel's

laws in 1900, there were many skeptics. The British biologist, William Bateson, who had been studying discontinuous variation in *Brassica* and who coined the term "genetics," became a traveling salesman for Mendelian principles speaking in favor far and wide with great zeal (Cock and Forsdyke, 2008). Ironically, Bateson himself was skeptical of the chromosome theory of inheritance, preferring instead to think in terms of many independent factors determining organismal characters (Cock and Forsdyke, 2008). Eventually, the *Drosophila* work of the T.H. Morgan lab showing association of genetic factors with chromosomes in various ways convinced Bateson (Cock and Forsdyke, 2008).

It is often stated that seminal scientific discoveries would not go unnoticed for long because, if they are important, others will soon find them. But is that true? In the last paragraph of his paper, Mendel described white flowers with red stripes, which was likely due to a transposable element insertion into a flower pigment gene. Yet, it was not until the 1940's that Barbara McClintock recognized the subtle patterns required to decipher mobile genetic elements (McClintock, 1950) that this phenomenon began to be understood. Yet again, it took decades further before the significance of McClintock's discoveries was realized and their generalization was appreciated.

A common principle often invoked in scientific discourse is Occum's Razor. This principle dictates that the simplest or most parsimonious explanation should be favored. However, one should keep in mind that a simple explanation that does not explain the facts is to be discarded. Sydney Brenner introduced the concept of "Occum's Broom," which is used to sweep inconvenient truths under the rug to salvage the "simplest" explanation. Recognizing when to use the razor and avoid the broom is a useful reflection in evaluating scientific models as the subtle Mendel and McClintock examples attest.

And More

In his garden
Mendel planted his peas
And made many crosses

As he would please
Next generation
Let them self pollinate
And counted the types
For factors particulate
Some seeds were yellow
And some were green
Three to one ratios
In the numbers were seen
More factors were added
One—by—one
Independent assortment
When all said and done
Some doubted his findings
So were lost from sight
But upon rediscovery
Mendel was right!

REFERENCES

- Birchler, J.A. (2015). *Nat. Plants* 1, 15020.
- Birchler, J.A., and Veitia, R.A. (2012). *Proc. Natl. Acad. Sci. USA* 109, 14746–14753.
- Cock, A.G., and Forsdyke, D.R. (2008). Treasure your exceptions, The science and life of William Bateson (New York, New York: Springer).
- Darwin, C. (1868). The variation of animals and plants under domestication (London: Murray).
- Darwin, C. (1876). The effects of cross and self fertilization in the vegetable kingdom (London: Murray).
- Darwin, C. (1877). The different forms of flowers on plants of the same species (London: Murray).
- Dorshorst, B., Okimoto, R., and Ashwell, C. (2010). *J. Hered.* 101, 339–350.
- Endersby, J. (2007). A guinea pig's history of biology (Cambridge, MA: Harvard University Press).
- Galatin, W.C. (1998). *Maize Genet. Coop. News Lett.* 72, 83–84.
- Mackay, T.F. (2014). *Nat. Rev. Genet.* 15, 22–33.
- McClintock, B. (1950). *Proc. Natl. Acad. Sci. USA* 36, 344–355.
- Mendel, G. (1866). Experiments in plant hybridization. Proceedings of the Natural History Society of Brunn. (Translated by William Bateson and corrected by Roger Blumberg) <http://www.netSpace.org/MendelWeb>.
- Mendel, G. (1870). On Hieracium-Hybrids obtained by artificial fertilization. Translated and reprinted as an appendix to Bateson, W. 1909. Mendel's Principles of Heredity. Cambridge University Press.
- Ronceret, A., and Vielle-Calzada, J.-P. (2015). *Plant Reprod.* 28, 91–102.

Morgan's Legacy: Fruit Flies and the Functional Annotation of Conserved Genes

Hugo J. Bellen^{1,2,3,4,5,*} and Shinya Yamamoto^{1,2,4}

¹Program in Developmental Biology, Baylor College of Medicine, Houston, Texas 77030, USA

²Department of Molecular and Human Genetics, Baylor College of Medicine, Houston, Texas 77030, USA

³Department of Neuroscience, Baylor College of Medicine, Houston, Texas 77030, USA

⁴Jan and Dan Duncan Neurological Research Institute, Texas Children's Hospital, Houston, TX 77030, USA

⁵Howard Hughes Medical Institute (HHMI), Houston, TX, 77030, USA

*Correspondence: hbellen@bcm.edu

<http://dx.doi.org/10.1016/j.cell.2015.09.009>

In 1915, “The Mechanism of Mendelian Heredity” was published by four prominent *Drosophila* geneticists. They discovered that genes form linkage groups on chromosomes inherited in a Mendelian fashion and laid the genetic foundation that promoted *Drosophila* as a model organism. Flies continue to offer great opportunities, including studies in the field of functional genomics.

This year we celebrate the 100th anniversary of the publication of the book “The Mechanism of Mendelian Heredity” by Thomas H. Morgan, Alfred H. Sturtevant, Hermann J. Muller, and Calvin B. Bridges (Morgan et al., 1915). The work published by these four giants in the *Drosophila* field was the most influential scientific work in the field of genetics since Gregor Mendel’s work in 1866. Although the achievements of Mendel were ignored in the 19th century, the rediscovery of Mendel’s law in 1900 led to the foundation of the field of genetics. Morgan, who initiated his work on *Drosophila* in 1909, was an embryologist who became attracted to flies because of the discovery of genetic variants. Interestingly, in his early career (1900–1910), Morgan was critical of the Mendelian theory of heredity and skeptical of the fact that species arise by natural selection as postulated by Charles Darwin. Moreover, in his acceptance speech for the Nobel Prize of 1933, he downplayed the contribution of *Drosophila* research to human biology and medicine with one exception: genetic counseling. Morgan quickly changed his mind and became an advocate of Mendel’s and Darwin’s work, while researchers later showed that he was overly modest about the implications of *Drosophila* research on human biology.

***Drosophila* Research in the 20th Century**

Morgan initiated his work on *Drosophila* in 1909 at Columbia University. He quickly

attracted a set of superb scientists, and together, they elegantly documented many of the basic tenets of genetics, discovering that factors (now known as alleles of genes) form linkage groups, and that these linkage groups exhibited the same inheritance pattern as the chromosomes to which they mapped. Experimental data with mutants that map to sex chromosomes in *Drosophila* provided the central support for their hypothesis that genes are independent physical entities present in a linear array on chromosomes that follow Mendel’s law of independent segregation. They concluded their book by stating that: “Although Mendel’s law does not explain the phenomena of development, and does not pretend to explain them, it stands as a scientific explanation of heredity, because it fulfills all the requirements of any causal explanation” (Morgan et al., 1915). Despite the criticism toward Mendel’s work—that he had ignored or failed to report data that did not support his hypothesis—Morgan and colleagues gave Mendel the proper credit for discovering the principles of heredity, as is obvious from this statement as well as from the title of their book.

Muller, Sturtevant, and Bridges as well as other fly geneticists continued to perform experiments that laid the basis of much of eukaryotic genetics between 1910 and 1940. Muller developed the first balancer chromosomes which allowed him to discover that X-rays are mutagenic (Muller, 1927), for which he was awarded

the Nobel Prize in 1946. Balancer chromosomes are still the most elegant means of preventing the exchange of genetic information between two homologous chromosomes, thereby giving researchers an efficient method to maintain thousands of recessive lethal and sterile stocks without the need of molecular genotyping. Sturtevant demonstrated that the Bar eye phenotype is caused by unequal crossover, a phenomenon which plays an important role in the generation of small chromosomal duplications and deletions linked to human diseases (Lupski et al., 1996). Bridges constructed the first physical map of chromosomes for any organism by describing the banding pattern of the polytene chromosomes in the salivary gland of flies and provided a physical map of genes on the banded chromosomes (Bridges, 1935). Bridges’ work demonstrated the correlation between the physical structure of chromosomes and genetically defined linkage groups.

Drosophila research lost prominence in the 1940s as phages and bacteria dominated the field of genetics. However, a rebirth occurred in the early 1970s as two fields, neuroscience and developmental biology, converged onto *Drosophila* research. This resurgence was in part because of the reagents created by the founders, the availability of many mutations affecting numerous traits, and the ability to efficiently create new mutations (Lewis and Bacher, 1968). Indeed, no higher eukaryotic model

organism in the seventies had the tools that allowed the manipulation of genes as elegantly and probingly as in *Drosophila*.

The use of *Drosophila* as a model organism for neuroscience and developmental biology led to discoveries that provided a lasting impact. Seymour Benzer and colleagues studied genes affecting visual behavior, olfaction, sexual behavior, learning and memory, diurnal rhythms, aging, and neurodegeneration (Jan and Jan, 2008). Their work led to the discovery of numerous important genes and proteins such as the first potassium and transient receptor potential (TRP) channels, key circadian clock genes, and genes required for learning and memory. Similarly, in 1978 Christiane Nüsslein-Volhard and Eric Wieschaus decided to pursue a systematic genetic strategy to screen for mutants that affect the development of the embryo pattern and discovered many of the genes that are key players of developmental signaling pathways such as Notch, Wnt, Hedgehog, TGF- β /BMP, and Toll/TLR (Nüsslein-Volhard and Wieschaus, 1980). The impact of these discoveries have permeated almost every area of biology, including medical genetics and cancer biology (Wangler et al., 2015).

The ability to manipulate the *Drosophila* genome was bolstered tremendously by the technology to introduce any type of DNA into the fly genome using *P*-element-mediated transposition (Rubin and Spradling, 1982). Since then numerous technologies have been developed that allow extensive biological and genetic manipulation (Perrimon, 2014). The ability to manipulate the fly genome has enabled numerous scientists to contribute significantly to almost all areas of biology, including genetics, developmental biology, cell biology, neuroscience, physiology and metabolism, disease mechanisms, population genetics, and evolution.

***Drosophila* as a Model System for In Vivo Functional Genomics**

The breadth of tools that have been developed and that are shared among the members of the fly community, in the tradition of the founders, permits sophisticated experiments that can be performed in very few model organisms. For

example, these tools are being used to tease apart neuronal networks, assess and control specific behaviors, determine gene function in specific cells, and study physiological functions of proteins and metabolites. An area that has expanded significantly in the past 10 years is the study of fly genes whose human homologs cause genetic disorders. These studies attempt to better understand the basic biology of these genes and products, and attempt to probe the mechanism by which specific mutations cause pathological phenomena such as neurodegeneration (Jaiswal et al., 2012). Approximately 60% of the ~13,000 protein coding fly genes are evolutionarily conserved in human, yet, a functional annotation of most of these genes is still lacking (Yamamoto et al., 2014). Better and more detailed annotations of function and expression of thousands of *Drosophila* genes would help not only to better understand fly biology, but also to functionally annotate the human genome. Here, we will expand on some recently developed strategies that aim at providing functional data on fly genes and their expression patterns. These strategies also attempt to assess the function of human genes and provide data about the pathogenic impact of human mutations or variants.

In his 2015 State of the Union Address, President Obama announced the launch of the “Precision Medicine Initiative,” with the ultimate goal of improving medical care by providing individuals with tailor-made prevention and treatment strategies. Due to the resources generated through the human genome project and the recent advances in sequencing technology and bioinformatics, human geneticists can quickly identify the majority of the polymorphisms and variants in a personal genome. The real challenge in precision medicine, however, is the interpretation of such genomic data. Our ability to extract meaningful data from whole-exome sequencing data is damped by the existence of numerous rare variants of uncertain/unknown significance and, more importantly, by the lack of in vivo functional information of the majority of human genes. Hence, high-throughput strategies to quickly assess whether or not a variant of interest have functional effects is in high demand.

Although functional information can be obtained using cultured human cells, such as iPSCs, these experiments do not provide in vivo information. *Drosophila* is an ideal model organism to fill this niche, thanks to its short-life cycle, low maintenance costs, conserved biology, and powerful genetic toolbox.

Functional annotation of genes is typically done one by one, with individual laboratories devoting years to study the role of one or a few genes in a specific biological process or pathway. As most genes are also pleiotropic, different labs often study the same genes in different processes. This level of annotation has been the mainstay and the foundation of success of *Drosophila* research. In addition to this detailed level of gene characterization, cursory but rapid function examination of conserved genes in *Drosophila* can also provide important data to fill the gap between genetic and phenotypic information.

A cursory functional annotation of genes should start with the generation of null alleles or strong loss-of-function (LOF) mutations since this will provide a reference point and a context to study the in vivo function of a gene. Once a phenotype is identified, integration and expression of human cDNA homologous to the fly gene can be tested for its rescuing ability. An example of a simple strategy is shown in Figure 1. Integration of the yeast GAL4 transcription factor with a ribosome skipping peptide (2A) in a gene of interest will create a severe LOF allele (Diao et al., 2015). Upon identification of the phenotype in the fly, rescue experiments by the UAS-human cDNA transgene that is expressed in the proper spatial and temporal domain permit testing the conservation of gene function between fly and human. Comparing the rescue efficiency of human cDNAs with reference (wild-type) versus variant (mutant) sequences is a rapid method of assessing whether a particular variant found in a human patient might be affecting the normal function of this gene. Finally, overexpression of reference and variant human cDNA sequences in wild-type flies can also lead to detection of dominant phenotypes associated with variants found in human patients.

Another key step in the functional annotation of genes is to determine the

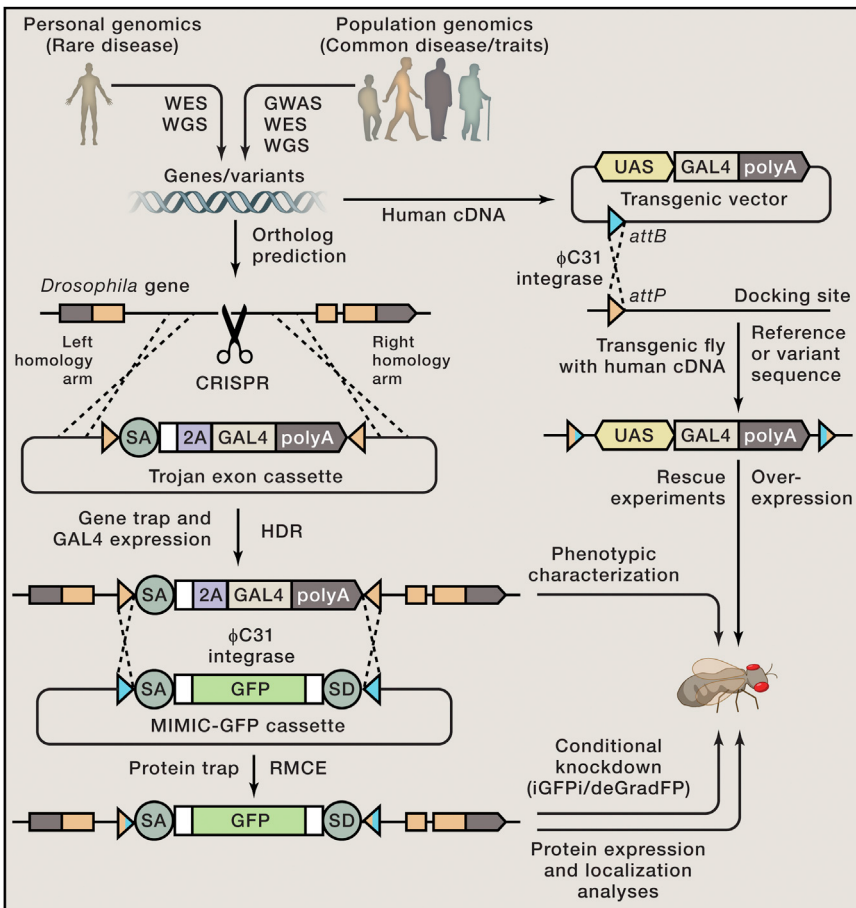


Figure 1. Functional Annotation of Conserved Genes using *Drosophila*

Rapid functional annotation of conserved genes is possible in *Drosophila* by combining a number of technologies and resources. First, the potential fly ortholog of a human gene of interest is identified. An insertion of an artificial exon that functions as a gene trap and allows expression of GAL4 (Trojan exon cassette (Diao et al., 2015)) can be introduced in an intron between two coding exons via Recombination Mediated Cassette Exchange (RMCE) of available MiMIC (Minos Mediated Integration Cassette) insertions (Venken et al., 2011). Alternatively, this can be achieved via Homology Directed Repair (HDR) using CRISPR. This Trojan exon consist of splice acceptor (SA) followed by a ribosomal skipping peptide (2A), the GAL4 gene, and a polyadenylation (polyA) sequence, allowing the expression of GAL4 in the pattern of the gene of interest in loss-of-function (LOF) mutants. By crossing these lines with flies that carry a transgene of the human cDNA under the control of UAS (DNA sequence recognized by GAL4), it can be determined if a human cDNA is able to rescue the fly mutant phenotype. If rescue is achieved with the wild-type (reference sequence) protein, one can further assess the function of variants found in human patients. UAS-human cDNA lines can also be used to assess dominant phenotypes (antimorphic, hypermorphic, or neomorphic) by overexpressing the human gene in a wild-type fly. MiMIC or Trojan gene-traps can be converted into protein-traps via RMCE, allowing intronic tagging of the gene of interest. GFP-tagged genes/proteins can be further knocked down using strategies to degrade the transcript (iGFPi) or protein (deGradFP) in a conditional and tissue specific manner (Nagarkar-Jaiswal et al., 2015), providing stage and tissue specific gene function information.

temporal, cellular, and subcellular distribution of the protein of interest. The simplest strategy is to tag genes in genomic constructs (plasmids, fosmids, or BAC clones), generate transgenic strains, and monitor the tag (e.g., GFP) in vivo. Alternatively, the above mentioned GAL4 cassette can be modified to be replaced with an artificial exon that

contains a protein tag (Venken et al., 2011). These tagged proteins are expressed under the control of endogenous regulatory elements, allowing documentation of protein expression patterns and subcellular localization without overexpression. Although the tag is internal to the protein, 75% of the proteins tagged with GFP tested so far have been shown

to be functional in vivo (Nagarkar-Jaiswal et al., 2015). In summary, by combining genomic technologies, one should be able to quickly assess the LOF phenotypes and expression pattern of a yet uncharacterized gene, identify the human ortholog, and assess the function of human variants.

Morgan may have been modest about the impact of *Drosophila* research in human physiology and medicine but the long-term impact is obvious: he selected a cost-effective model organism that has provided countless insights into biology, many of which have been directly applicable to human biology and medicine. Going forward, *Drosophila* has the potential to keep on making great contributions, and the era of functional genomics is no exception.

REFERENCES

- Bridges, C.B. (1935). J. Hered. 26, 60–64.
- Diao, F., Ironfield, H., Luan, H., Diao, F., Shropshire, W.C., Ewer, J., Marr, E., Potter, C.J., Landgraf, M., and White, B.H. (2015). Cell Rep. 10, 1410–1421.
- Jaiswal, M., Sandoval, H., Zhang, K., Bayat, V., and Bellen, H.J. (2012). Annu. Rev. Genet. 46, 371–396.
- Jan, Y.N., and Jan, L. (2008). Science 319, 45.
- Lewis, E.B., and Bacher, F. (1968). Drosoph. Inf. Serv. 43, 193.
- Lupsik, J.R., Roth, J.R., and Weinstock, G.M. (1996). Am. J. Hum. Genet. 58, 21–27.
- Morgan, T.H., Sturtevant, A.H., Muller, H.J., and Bridges, C.B. (1915). The Mechanism of Mendelian Heredity (New York, NY: Henry Holt and Company).
- Muller, H.J. (1927). Science 66, 84–87.
- Nagarkar-Jaiswal, S., Lee, P.T., Campbell, M.E., Chen, K., Anguiano-Zarate, S., Gutierrez, M.C., Busby, T., Lin, W.W., He, Y., Schulze, K.L., et al. (2015). eLife 4, e05338.
- Nüsslein-Volhard, C., and Wieschaus, E. (1980). Nature 287, 795–801.
- Perrimon, N. (2014). Methods: Drosophila developmental biology methods, Volume 68 (Amsterdam: Elsevier).
- Rubin, G.M., and Spradling, A.C. (1982). Science 218, 348–353.
- Venken, K.J., Schulze, K.L., Haelterman, N.A., Pan, H., He, Y., Evans-Holm, M., Carlson, J.W., Levis, R.W., Spradling, A.C., Hoskins, R.A., and Bellen, H.J. (2011). Nat. Methods 8, 737–743.
- Wangler, M.F., Yamamoto, S., and Bellen, H.J. (2015). Genetics 199, 639–653.
- Yamamoto, S., Jaiswal, M., Charng, W.L., Gambin, T., Karaca, E., Mirzaa, G., Wiszniewski, W., Sandoval, H., Haelterman, N.A., Xiong, B., et al. (2014). Cell 159, 200–214.

Planet of the Microbes

Life's Engines: How Microbes Made Earth Habitable

Author: Paul G. Falkowski

Princeton University Press (2015).

203 pp. \$24.95

Regardless of where you find yourself at the moment while reading these lines, visually inspect your surroundings and you will see signs of life. I ask you now to, for a moment, imagine planet Earth devoid of all plant and animal life. For all the desolation such an image will conjure in your mind, such an Earth would still be teeming with life—life unseen, microbial life. Yet, attempt to imagine an Earth without microbes and then, indeed, you will have to confront a lifeless planet. Microbial activities throughout much of our planet's history yielded the setting propitious for the evolution of plants and animals, the setting that we constantly appreciate in our daily lives. This wonderful and awe-inspiring universe of the microbes, unseen creatures that have shaped the planet such that we may live in it, is engagingly presented by Paul G. Falkowski in a remarkable text entitled *Life's Engines: How Microbes Made Earth Habitable*.

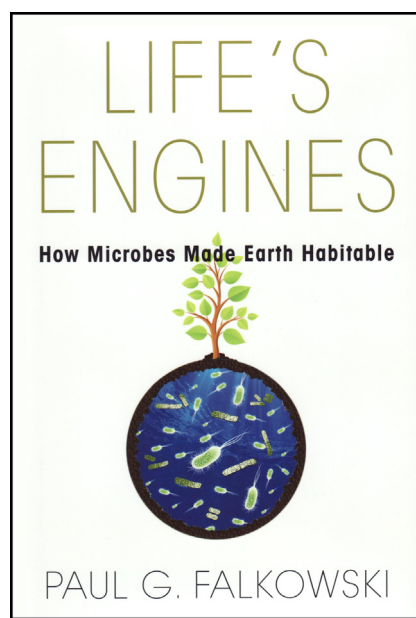
What is it that makes this text remarkable? In the opening pages, the author pointedly notes two major deficiencies of many past and present textbooks of biology. First, microbes have been largely forgotten. "...I realized that books on biology, which were assigned to me in college, mostly ignored microbes, except as carriers of disease...". Second, and perhaps much more importantly, in their effort of to be comprehensive, such textbooks end up being intensely soporific, efficient cures for insomnia. "The biology texts I was required to read were not only inaccessible, they were downright boring. I couldn't understand how one could take such an exciting subject, the study of life, and turn it into something so filled with irrelevant jargon." In bringing these two problems of textbooks to the fore early on, the author is—intentionally or not—setting himself up to the challenge of coming up with something radically different. Without a doubt, he has succeeded in doing that. I, for one, fully agree

with his assessment that the most widely used textbooks of biology are indeed quite boring. Over the years, I have steadfastly refused to use textbooks in my teaching, aside from placing a copy or two on "reserve shelves," where they tend to gather dust. But *Life's Engines* is different, and I most likely will make this book required reading for my courses in the future. Not since I read the text that would propel me into my lifelong study of microbes (Gunther Stent's *Molecular Genetics, an Introductory Narrative*) in the early 1970s have I been so completely taken by a textbook of biology.

The book's success is based on its utter simplicity. It tells the story of the history of life on our planet from a very personal perspective. Coming from the heart, as it is, the story is not constrained by order, though there is certainly a nice progression in the way the story unfolds. Thus, you will be transported from a vessel exploring microbial life in the depths of the Black Sea to Istanbul, admiring Turkish rugs. As merchants "unroll" rugs

depicting biblical stories, you will be reminded that "evolution" means "to unroll." But, understanding the origin of life on Earth will not come from stories depicted on those rugs. Rather, the perspective of scientific study of the evolution of microbes will be needed. And so your voyage will lead you through Darwin's fascination with fossils and the age of the Earth, and you will accompany Darwin on the Beagle and through his musings on the origin of life. And suddenly you will encounter Miller and Urey making amino acids from ammonia, methane, hydrogen, and a spark. All of this beautifully sets the stage for the simple fact that the unifying concept in biology, evolution, developed for over a century without including microbes that had been on Earth for billions of years before the first animal evolved. And that is just the first chapter, making the reader yearn to "meet the microbes and see how they played an outsized role in making this planet function. Without microbes, we would not be here."

Because of their size and their invisibility, microbes—the oldest residents of Earth—are relative newcomers as subjects of study. Following the same narrative style that introduced the fact that microbes were largely absent from the early development of evolutionary thought, Falkowski comprehensively relates the key roles that microbes have played in Earth's history. In this fashion, we explore early lens crafters and microscopes and launch into the history of microbiology. From simple observation to cultivation to molecular analyses, we are swept along three centuries to the revolutionary change in worldview brought about by Carl Woese's approach to re-drawing the "Tree of Life." From this universal phylogeny, it is easy to visualize the dominance of microbes in the diversity of life and to pose the question of when life originated. And so, you will take a fresh look at the composition of rocks and go back 3.5 billion years to the beginning of life, of life microbial. You will then be ready to explore the function of those *Life's Engines* cells from an evolutionary perspective. And we all know that "nothing in biology makes sense except in the light of evolution." Even if you feel that you know all there is to be known about cell biology,



I assure you that you will find amazing surprises in this gem of a book—not the least of which, I think, is the story of the history of the processes that led to the oxygenation of our atmosphere. Take a deep breath, appreciate the oxygen, and thank the microbes.

Here's a suggestion. I was so enthralled by this book from the get-go that I invite

you have a short taste of it. These days, it is easy to access some pages of almost any new book online. I know from having done this myself that the Prologue to this book is readily available. I suggest you take a look inside and savor this section. In it, you will discover a young boy who became fascinated with guppies and green algae “all because of a chance

encounter by my nosey, loquacious mother with a couple of graduate students in an elevator.” This boy grew up driven by a curiosity about the world around him and has now decided to share his life experience with all of us lucky enough to get our hands on this book. After reading the Prologue, I am pretty sure you will want to read the whole thing.

Roberto Kolter^{1,*}

¹Department of Microbiology, Harvard Medical School, 77 Avenue Louis Pasteur, Boston, MA 02115, USA

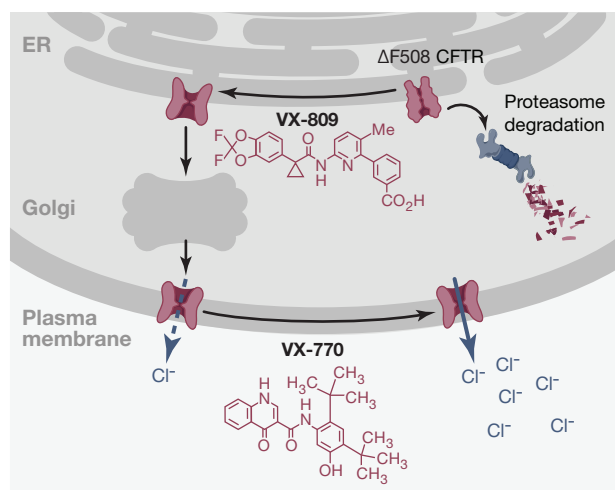
*Correspondence: roberto_kolter@hms.harvard.edu
<http://dx.doi.org/10.1016/j.cell.2015.09.006>

A Combination Therapy for Cystic Fibrosis

Jeffrey L. Brodsky^{1,*} and Raymond A. Frizzell²

¹Department of Biological Sciences, University of Pittsburgh, Pittsburgh, PA 15260, USA; ²Department of Cell Biology, University of Pittsburgh School of Medicine, Pittsburgh, PA 15261, USA; *Correspondence: jbrodsky@pitt.edu

<http://dx.doi.org/10.1016/j.cell.2015.09.003>



The most prevalent form of cystic fibrosis arises from an amino acid deletion in the cystic fibrosis transmembrane conductance regulator, CFTR. A recently approved treatment for individuals homozygous for this mutation combines a chemical corrector, which helps CFTR fold, and a potentiator that increases CFTR channel activity.

NAME

Orkambi, a combination of VX-809 (Lumacaftor) and VX-770 (Ivacaftor)

APPROVED FOR

Cystic fibrosis (CF) in patients older than 12 with two copies of the $\Delta F508$ *CFTR* gene

TYPE

Small-molecules

MOLECULAR TARGETS

CFTR, an anion channel in the ATP binding cassette transporter family

CELLULAR TARGETS

Various epithelial tissues in which CFTR regulates chloride, bicarbonate, and fluid secretion

EFFECTS ON TARGETS

Lumacaftor corrects mutant CFTR folding, and Ivacaftor potentiates CFTR channel activity. Restored CFTR trafficking and activity counters the fluid secretion defects in pancreas, intestine, sweat glands, and lung, where it improves airway surface liquid formation and productive mucus and microbe clearance.

DEVELOPED BY

Vertex Pharmaceuticals and Cystic Fibrosis Foundation Therapeutics

Lumacaftor rescues

30%
from degradation

Ivacaftor

2-fold
increase in
channel activity

Individuals with cystic fibrosis

28,000



5% have benefited
from Ivacaftor

50% may benefit
from Orkambi

1989

Cloning of the *CFTR* gene

1996

Chemical chaperones rescue $\Delta F508$ trafficking to the cell surface

1990

$\Delta F508$ CFTR is prematurely degraded and fails to traffic to the cell membrane

2011

VX-809 (Lumacaftor) facilitates $\Delta F508$ mutant protein folding

2009

VX-770 (Ivacaftor) augments CFTR channel opening

2012

Ivacaftor approved for patients with a channel gating mutation

2015

Orkambi (Ivacaftor/Lumacaftor) approved by the FDA for $\Delta F508$ homozygous patients

The Next Top Models

Extreme Farming

**Jian-Kang Zhu**

Shanghai Center for Plant Stress Biology

With the advent of global warming and climate change, more frequent episodes of extreme weather are predicted. That will dramatically affect food security. In addition, there will soon be more people, more meat diets, and less land for crops. Yet, food production needs to be doubled to feed the growing population by 2050. Big improvements in crop productivity under harsh environments will be required.

Model plants like *Arabidopsis* and rice have already paved the way to many genetic improvements in crops. Unfortunately, these model plants have not evolved to thrive in extreme environments. Some *Arabidopsis* relatives, specifically *Thellungiella* sp., can instead serve as model systems for understanding how plants cope with high salinity, extreme cold, and water shortage. Besides being capable of resisting extreme environments, these small plants (with their genomes sequenced) have short life cycles, produce large numbers of seeds, and can be genetically transformed easily in large numbers. Studies on their salt tolerance revealed that these plants appear to take advantage of pre-primed stress response genes and pathways present but less effective in glycophytes, such as *Arabidopsis* and rice. Future work on these extremophile plants promises to elucidate strategies plants use to adapt to extreme environments and to improve crops to better cope with future harsh weather.

Axolotl Legwork

**Jessica Whited**

Harvard Medical School

Axolotl salamanders (*Ambystoma mexicanum*) can regenerate limbs throughout life following amputation. Their limbs are remarkably anatomically similar to human limbs, containing the full repertoire of tissues and patterned in similar ways. A vast amount of experimentation in the field of amphibian limb regeneration was conducted by some of the leading biologists of the time in previous centuries. These older experiments at a pre-molecular level are a goldmine for modern studies. From these perspectives, axolotl is an ideal model for understanding natural regeneration.

Axolotls form a transient niche-like structure called "blastema" to localize and multiply activated progenitor cells. We are approaching the questions of blastema formation and function with no a priori assumptions about the genes that drive these processes as the axolotl genome is enormous (~32 Gb) and largely unsequenced. Taking an a priori approach has only become feasible in the last several years with the advent of next-gen sequencing and the development of powerful new technologies for functional experimentation, such as transgenesis, viral transduction, and gene editing. Thus, this is the perfect time to be using axolotls to elucidate the mechanisms underlying the fascinating process of regeneration. The hope is that, in the future, this information will help in formulating hypotheses about why humans and other mammals have much more restricted natural regenerative abilities and eventually taking effective approaches to circumvent these limitations.

The Naked Truth

**Andrei Seluanov and Vera Gorbunova**

University of Rochester

Naked mole rat (*Heterocephalus glaber*) is a mouse-size rodent, but it lives ten times longer than mouse and is resistant to multiple age-related diseases, most notably cancer. Traditionally, molecular biologists focused their work on short-lived organisms, such as mice and rats, which reproduce and die rapidly, making them convenient genetic models. Although major aspects of genetics and physiology are conserved among mammals, short-lived species lack adaptations that confer long life. Since the ultimate goal of biomedical research is to prevent disease and extend lifespan, investigating mechanisms that confer longevity and disease resistance in long-lived species has tremendous potential. The discovery of high-molecular-mass hyaluronan that provides cancer resistance to naked mole rats exemplifies how studying a nonstandard species leads to a clinically relevant molecule.

Switching to nonstandard models may seem challenging, but it is also extremely rewarding as there is so much novel biology to be unearthed. The tools from whole-genome sequencing to RNAi and CRISPR/Cas9 technologies to study these atypical organisms are rapidly improving. The naked mole rat is just one example of a mammal that evolutionarily adapted to a long and healthy life. Many other long-lived species that have evolved unique mechanisms to stall aging and prevent disease such as beaver, gray squirrel, blind mole rat, Brandt's bat, and bowhead whale await future investigation.

Ancient Immunity

Masanori Kasahara
Hokkaido University

Jawed vertebrates ranging from sharks to humans mount adaptive immune responses using antigen receptors of the immunoglobulin superfamily. In contrast, the antigen receptors known as variable lymphocyte receptors (VLRs) in jawless vertebrates such as lampreys and hagfish generate diversity comparable to that of T cell and B cell receptors by assembling multiple leucine-rich repeat modules. This highlights the striking difference between the adaptive immune systems of jawed and jawless vertebrates and catapults lampreys and hagfish into the limelight in the immunology field. Interestingly, like jawed vertebrates, lampreys have three lineages of lymphocytes: one lineage of B-like lymphocytes and two lineages of T-like lymphocytes resembling $\alpha\beta$ and $\gamma\delta$ T cells, respectively. Therefore, it appears that specialized lymphocyte lineages emerged in a common vertebrate ancestor and that jawed and jawless vertebrates evolutionarily co-opted different antigen receptors within the context of such lymphocyte lineages.

Many questions remain unanswered. Do lampreys have antigen-presenting molecules with functions equivalent to those of major histocompatibility complex molecules? What is the chemical nature of ligands recognized by VLRs expressed on $\alpha\beta$ T-like lymphocytes? Do they recognize peptides like their gnathostome counterparts? How do lamprey lymphocytes undergo selection during their development in central lymphoid organs? Investigation of the immune system of these ancient jawless fishes will yield many more surprises and keep inspiring us for years to come.

Hive's Logic of Life

Gro V. Amdam
Arizona State University and Norwegian University of Life Sciences

Honey bees (*Apis mellifera*) provide remarkable opportunities for understanding complex behavior, with systems of division of labor, communication, decision making, and social aging/immunity. They teach us how social behaviors develop from solitary behavioral modules, with only minor “tweaking” of molecular networks. They help us unravel the fundamental properties of learning, memory, and symbolic language. They reveal the dynamics of collective decision making and how social plasticity can change epigenetic brain programming or reverse brain aging. They show us the mechanistic basis of trans-generational immune priming in invertebrates, perhaps facilitating the first vaccines for insects.

These processes and more can be studied across the levels of biological complexity—from genes to societies and over multiple timescales—from action potential to evolutionary. As models in neuroscience and animal behavior, honey bees have batteries of established research tools for brain/behavioral patterns, sensory perception, and cognition. Genome sequence, molecular tools, and a number of functional genomic tools are also available. With a relatively large-sized body (~1.5 cm) and brain (~1 mm³), this fascinating animal is, additionally, easy to work with for students of all ages.

Beekeeping practices date as early as the Minoan Civilization, where the bee symbolized a Mother Goddess. Today, we increasingly value honey bees as essential pollinators of commercial crops and for their ecosystem services. Honey bees have been called keepers of the logic of life. They are truly.

Natural Neuroscience

Nachum Ulanovsky
Weizmann Institute of Science

Through a reductionist approach, we made great progress in brain research by focusing on simple sensory stimuli and simplified, highly controlled laboratory behaviors. However, this reductionism came at a cost: it neglected what real brains evolved for—guiding behavior in real-world, complex natural environments. We know surprisingly little about natural behaviors of mice and rats—a fundamental gap in our understanding of brain and behavior in these “standard mammalian models.” It is therefore crucial to study the neural basis of behavior under real-life, naturalistic conditions: a “Natural Neuroscience” approach.

One way would be to study wild rodents outdoors and then implement more naturalistic experiments indoors. Another way is to use “atypical” mammalian models, such as bats. Why bats? First, much is known about bats’ natural behaviors in the field; in fact, the same species (and even same individuals) can be studied both outdoors and in the lab. Second, their 3D flight behaviors and long-distance navigational skills make bats excellent models for studying the neural basis of navigation. Third, bat sensory inputs (biosonar) can be recorded with sub-millisecond precision, making them great models for “active sensing.” Finally, studying bats allows a “sanity check” of a key hidden assumption in modern biology—that all mammals are alike, from mouse to human. Comparative studies of bat and rodent brains—e.g., the role of hippocampal oscillations—have begun to argue against that assumption. This highlights the importance of studying circuits, networks, and neural codes across species.

Monkey Mind: A Memoir of Aging

Guoping Feng
MIT

The lack of successful translation of findings from Alzheimer's disease rodent models to clinical trials has sparked interest in finding better animal models. Although studying large non-human primates such as macaques and Caribbean vervets has revealed important insights, their long life expectancy (up to 30 years in captivity) is a major drawback for longitudinal aging studies. Circumventing this problem, the short-lived gray mouse lemur (*Microcebus murinus*) has been developed as an alternative primate model for studying cerebral aging and Alzheimer's disease. Aged mouse lemurs (>6 years) show many human aging conditions, including cataracts, loss of olfactory acuity, reduced fine motor skills, and cognitive deficits. In addition, about 5%–10% of aged mouse lemurs develop abnormal behaviors indicative of "pathologic aging" such as aggressiveness, loss of social contact, and loss of biorhythm. Intriguingly, other pathological alterations, including massive brain atrophy, loss of cholinergic neurons, β -amyloid accumulation, and Tau aggregation, are similar to those associated with patients of Alzheimer's disease.

Features of mouse lemurs, such as small size (60–120 g), short lifespan (8–12 years in captivity), high fecundity (2–4 offspring per year), and early sexual maturity (10 months), make them more advantageous and suitable for genetic manipulations using CRISPR genome-editing technology. There are several laboratory-raised colonies around the world that would facilitate the expansion of this model for aging research.

A Fish in the Fountain of Youth

Anne Brunet
Stanford University

The African turquoise killifish (*Nothobranchius furzeri*) is a fascinating organism. It lives in Zimbabwe and Mozambique in ponds that are only present during the brief rainy season and has evolved a naturally compressed lifespan adapted to this unusual habitat. The African killifish is an attractive new model to study aging and age-dependent diseases in vertebrates. Aging studies have long benefited from invertebrate models, such as worms and flies. But those organisms lack organs or systems, including bones, blood, and adaptive immune system, that are involved in age-related diseases. On the other hand, vertebrate models—mice and zebrafish—are limited by their longer life (2.5 and 4–5 years, respectively).

In developing new model organisms, it is important to consider what unique aspect they bring. The African killifish provides a natural short lifespan (4–6 months in optimal laboratory conditions) and recapitulation of age-dependent phenotypes and pathologies, including cognitive decline, sarcopenia, and cancerous lesions. It also replicates certain aspects of human biology better than current models. For example, its telomeres are comparable in size to those of humans. These characteristics, coupled with the ease of generating many offspring and low maintenance costs, make the African killifish a promising alternative vertebrate model for genetic and drug screening. The recent development of a genome-editing pipeline in this fish has the potential to transform how we explore aging and disease-related genes. The African killifish could also provide novel insight into the differences in lifespan strategies between species.

Vocal Learning

Daniel Margoliash
University of Chicago

Speech and language are central to the human experience, commanding extensive study in the realm of learning and memory. Songbirds have emerged as a powerful model for analogous animal research, informed by and informing the work in humans. Research in songbirds has identified how individual variation in vocal behavior arises from genetic and epigenetic factors. This includes not just the well-known zebra finch (*Taeniopygia guttata*) but also birds of all stripes, with extensive species-level variation in learned behavior representing a unique opportunity for study in the animal kingdom.

Combining the study of brain and learned behavior is also a powerful approach for addressing many questions of general interest to neurobiology. Songbird research is providing insight into systems-level questions such as how auditory memories are initially established, are consolidated, and influence motor output; computational questions such as how motor commands relate to movements and how a common time frame is maintained given that motor command, muscle activation, and sensory feedback progressively lag in time; and in-depth analysis of how network properties emerge from the interactions of single cells— influenced by a rich soup of transmitters and modulators; and a great many others. Recently, the zebra finch genome has been sequenced. Coupled with molecular and genomic approaches that are being adopted, this is providing for additional elegant experimental designs possible with songbirds. The sky is indeed the limit, and the future is melodious for this attractive model system.

From Scientific Discovery to Cures: Bright Stars within a Galaxy

R. Sanders Williams,^{1,2,*} Samad Lotia,¹ Alisha K. Holloway,^{1,2} and Alexander R. Pico^{1,2}

¹Gladstone Institutes, San Francisco, CA 94158, USA

²University of California, San Francisco, San Francisco, CA 94143, USA

*Correspondence: rs.williams@gladstone.ucsf.edu

<http://dx.doi.org/10.1016/j.cell.2015.09.007>

We propose that data mining and network analysis utilizing public databases can identify and quantify relationships between scientific discoveries and major advances in medicine (cures). Further development of such approaches could help to increase public understanding and governmental support for life science research and could enhance decision making in the quest for cures.

Governments and philanthropists provide financial support for life sciences primarily with the expectation that research will lead to cures—defined broadly here as measures to prevent, eradicate, or ameliorate serious diseases. However, public understanding of how scientific discoveries actually result in cures is limited, and research to elucidate principles of biological processes may appear to non-scientists as esoteric and irrelevant to public expectations. Recent examples of important cures are evident, but public support for biomedical research as reflected by federal funding for the U.S. National Institutes of Health has eroded over the past decade (FASEB 2015), indicating the absence of a strong electoral consensus that the life science enterprise is meeting public expectations. Why is public support for life science research wavering at a time when the pace of discovery is strong and scientists see expanding opportunity, and can actions to increase public understanding of how new cures are developed lead to more sustained and predictable funding of life science?

We propose that data mining and network analytics (Nicholson 2006; Nishi-kawa and Motter, 2011) applied to what we call “cure network informatics” could help to increase public appreciation of the societal value of life science discoveries. Thoughtful metrics emerging from this concept perhaps can be developed and molded into forms embraced broadly among life scientists and by those providing their funding and can be used to guide decision making in ways that would accelerate progress toward cures.

Here, we describe a step in this direction by means of an analytical model and topology-based algorithms that quantify relationships between scientific discoveries and cures.

We established and automated data collection and network analysis protocols utilizing publicly accessible databases, including www.fda.gov, www.clinicaltrials.gov, www.ncbi.nlm.nih.gov/pubmed, and www.webofknowledge.com. In a pilot study, we considered the recently successful applications for regulatory approval of two new drugs: ipilimumab in oncology and ivacaftor for cystic fibrosis. These medical advances are sufficiently novel and important to be reasonably characterized as “cures” (*vide supra*). Ipilimumab is the first successful entry into the new and burgeoning field of immunotherapy (Sharma and Allison, 2015) by which sustained clinical remissions are being induced in patients with previously intractable cancers by releasing immune effector cells from checkpoint inhibition. Ivacaftor corrects the structure of a specific loss-of-function mutation in the cystic fibrosis transmembrane conductance regulator and is the first targeted therapy of this heritable disease. Beginning with the references cited in clinical trials and information provided to the U.S. Federal Drug Administration (FDA) for regulatory approval of these drugs (FDA, 2011; FDA, 2012), we extracted two consecutive rounds of retrospective citations and constructed network models of articles, authors, and institutions contributing to the network. Assumptions underlying this approach are: (1) that the authors of FDA applications and clinical trials will

appropriately cite publications reporting new knowledge critical to the development of a new drug candidate and (2) that further retrospective rounds of citations will identify previous discoveries that were most important in establishing the base of knowledge that enabled the successful drug development program.

We learned that the nature of a cure discovery citation network is complex and fundamentally collaborative with respect to the number of different scientists and institutions making contributions to a cure. For example, the citation network leading to ipilimumab includes 7,067 different scientists who listed 5,666 different institutional and departmental affiliations and includes discoveries spanning 104 years of research (Figure 1A). Results for ivacaftor are similar: 2,857 different scientists from 2,516 different institutional and departmental affiliations, with discoveries spanning 59 years of research (Figure 1B).

We next characterized individual scientists within each citation network by two metrics. Propagated in-degree rank (PIR) is based on the number and citation count of articles that a given author published within the citation network and is a measure of influence within this selective set of publications. Ratio of basic rankings (RBR) is based on how selectively a given author published within the cure discovery citation network relative to background networks of topically related publications similar in size, scope, and structure. This ratio helps to normalize their overall publication output.

By applying the metrics of PIR and RBR to the entire cure discovery citation

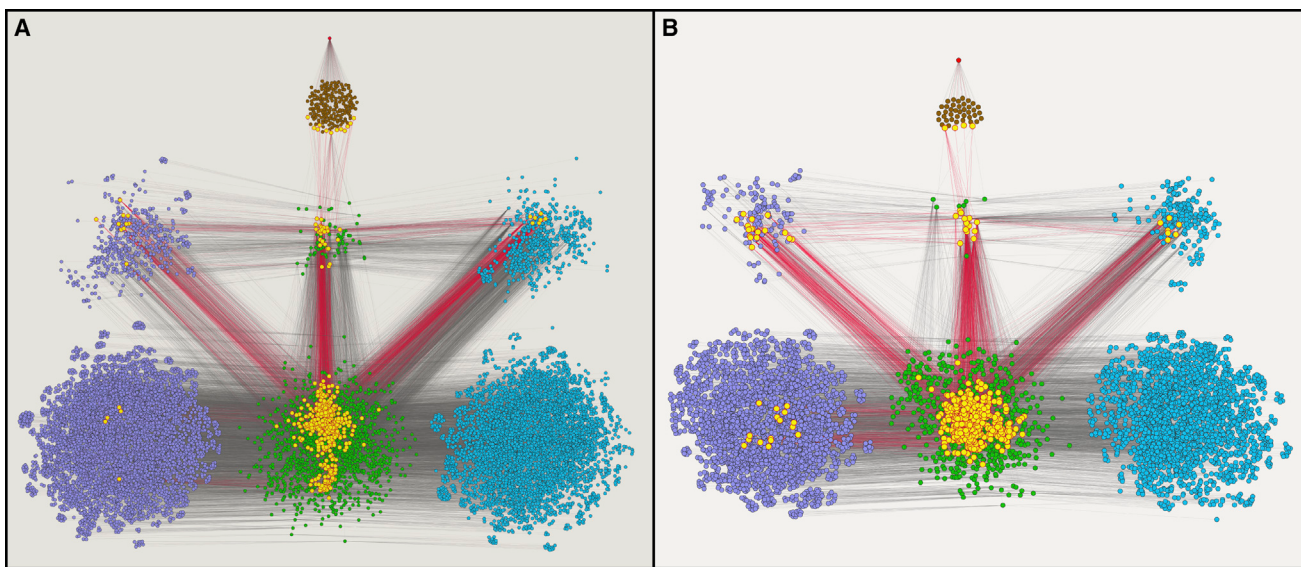


Figure 1. Cure Networks: The Constellation of Publications, Scientists, and Institutions Contributing to Drug Discovery

The red dot at the apex of the cluster is the drug ipilimumab (A) or ivacaftor (B). Relevant clinical trials and the FDA application are illustrated in brown. Publications cited in the clinical trials and FDA applications are shown in green. Likewise, papers cited by those publications are also shown in green. Authors of the papers are shown in purple, and institutional affiliations listed on the papers are shown in blue. The most influential contributors to the network as assessed by PIR and RBR (see Table S1), their articles, and their institutions are highlighted in yellow with red connecting lines.

network, the most influential and selective contributors to these massive networks emerge. Thus, in the case of ipilimumab, 15 scientists and 7 institutions associated with 433 articles spanning 46 years are characterized as elite performers (Figure 1A and Table S1). Elite performers within the ivacaftor network exhibiting similar properties as defined by the same metrics include 33 scientists and 7 institutions associated with 355 articles spanning 47 years (Figure 1B and Table S1). These elite performer subnetworks are integral to their overall citation networks, serving as hubs for 31% of the ipilimumab network and 49% of the ivacaftor network.

These data quantify how the knowledge base on which important advances in medicine ("cures") depend includes contributions from a large and diverse set of individual scientists working in many locales. This insight should be instructive for policy makers by suggesting that future cures will depend on broadly based public support of life sciences. Narrowly targeted funding initiatives may well have value but are unlikely in isolation to generate the breadth of new knowledge required to lay the foundation for future cures.

We call on the scientific community to embrace and advance the concept of

cure network informatics so as to develop advanced and sophisticated analytical tools to increase understanding of how scientific discoveries lead to cures, including predictive metrics that may guide decision making with respect to work in progress. All of the code necessary to reproduce and extend this initial effort is freely available and open source ([Lotia and Pico, 2015](#)). This network informatics approach can be applied to any "cure" with a cited publication trail. Curators of publicly available databases could play important roles in these efforts by considering cure network informatics in the design of database architecture and embedded tools. It will be important to identify trends that hold across all cures and ones that are specific to certain types of cures. It will also be useful to identify features of hubs within cure networks that are essential to the flow of knowledge required to create a cure.

A need for better metrics for assessing performance and for decision support within the life sciences is widely acknowledged by leaders and commentators in biomedicine ([Sarli and Carpenter, 2014; University of Gothenburg, 2013](#)). Metrics that are readily understandable by non-scientists, grounded in outcomes that the general public values highly (cures),

and faithful to what scientists know to be the richly intersecting and often unpredictable nature of scientific discovery should be more useful for influencing policy makers than currently available alternatives. Further development of new and useful tools for cure network informatics should contribute to increased public trust in, and support for, the life science enterprise.

SUPPLEMENTAL INFORMATION

Supplemental Information includes one table and can be found with this article online at <http://dx.doi.org/10.1016/j.cell.2015.09.007>.

ACKNOWLEDGMENTS

We are grateful for financial support of this project from the Schwab Foundation, Bruce and Martha Atwater account. We also thank Eleanor Prezant for project management and communications relating to this research.

REFERENCES

- FASEB (2015). <http://www.faseb.org/Portals/2/PDFs/opa/2015/2.10.15%20NIH%20Funding%20Cuts%202-pager.pdf>.
- FDA (2011). http://www.accessdata.fda.gov/drugsatfda_docs/nda/2011/125377Orig1s00TOC.cfm.

FDA (2012). http://www.accessdata.fda.gov/drugsatfda_docs/nda/2012/203188s000TOC.cfm.

Lotia, S., and Pico, A.P. (2015). <https://github.com/gladstone-institutes/bibliometrics/tree/1.0.1>.

Nicholson, S. (2006). Inf. Process. Manage. 42, 785–804.

Nishikawa, T., and Motter, A.E. (2011). Sci. Rep. 1, 151.

Sarli, C., and Carpenter, C.R. (2014). Mo. Med. 111, 399–403. http://digitalcommons.wustl.edu/cgi/viewcontent.cgi?article=1048&context=becker_pubs.

Sharma, P., and Allison, J.P. (2015). Cell 161, 205–214.

University of Gothenburg. (2013). ScienceDaily. <http://www.sciencedaily.com/releases/2013/10/131014094212.htm>.

Coordinating the Human Looks

Vanja Haberle¹ and Alexander Stark^{1,*}

¹Research Institute of Molecular Pathology (IMP), Vienna Biocenter (VBC), Dr Bohr-Gasse 7, 1030 Vienna, Austria

*Correspondence: stark@starklab.org

<http://dx.doi.org/10.1016/j.cell.2015.09.010>

Prescott et al. take a step forward in studying primate morphological evolution by a cellular anthropology approach. Through epigenomic profiling of in-vitro-derived cells, the authors identify and characterize candidate *cis*-regulatory elements underlying divergence in facial morphology between human and chimp, shedding new light on what makes us (look) human.

The difference between human genomic sequence and that of the chimpanzee is surprisingly small (< 2%), yet we differ greatly in appearance from our closest living relative. Although one could argue that the most discriminating feature is the human's cognitive ability, we all would probably distinguish humans from chimps in an instance by just a brief glance at their faces. It is therefore interesting and important to study the genes and DNA sequence changes involved in defining and creating our faces and how they differ between individuals and between chimps and humans.

It was suggested 40 years ago that the observed differences in physical appearance, cognition, and behavior arise from changes in genomic regulatory elements that control gene expression rather than changes in protein-coding regions themselves (King and Wilson, 1975). Today, the availability of genomic sequences and the advancements in genome-wide mapping of candidate regulatory elements provide the means to test this hypothesis and address the functional outcome of the sequence divergence (Carroll, 2008). In this issue, Prescott et al. shed light on how the distinct human and chimp facial characteristics might arise through changes in *cis*-regulatory elements by a comprehensive comparative epigenomic profiling of an in-vitro-derived embryonic cell type: the cranial neural crest cells (CNCCs) (Prescott et al., 2015).

CNCCs arise during neural tube formation in early embryogenesis and migrate to the developing head, where they differentiate into nerves, bones, cartilage, and connective tissue, establishing the facial morphology (Santagati and Rijli, 2003). Qualitative and/or quantitative differences in gene expression in these

cells might thus directly affect the shape of the face, contributing to inter- and intra-species variation in appearance and other CNCC-related human traits. Following a strategy of comparative epigenomic profiling applied previously in mammalian cell lines and organs (Villar et al., 2015) and primate corticogenesis (Reilly et al., 2015), Prescott et al. use the in-vitro-derived human and chimp CNCCs—a tightly matched pair of orthologous cell types—and map several transcription factors and histone modifications genome wide to predict distal-acting regulatory elements, also known as enhancers (Figure 1). Using established enhancer-associated chromatin characteristics, including p300 binding, chromatin accessibility, and increased H3K4me1/H3K4me3 ratio (Shlyueva et al., 2014), the authors predict CNCC enhancers genome wide. They further use H3K27ac as a predictor of enhancer activity to assess species-specific bias and identify *cis*-regulatory elements with putative functional divergence.

To exclude experimental and intra-species variability, Prescott et al. use cells derived from two chimp individuals and three humans. The high similarity between human and chimp genomic sequence further allows the authors to map reads from each species to both reference genomes, which circumvents problems that might arise during coordinate translation based on whole-genome sequence alignments but potentially restricts the analysis to the more conserved parts of the genome. With this approach, Prescott et al. predict ~14,500 CNCC enhancers, of which 13% showed species-biased H3K27ac enrichment, about half for human or chimp, respectively. The functional relevance of identified species-

biased enhancers is supported by the observation that nearby genes, which are enriched for craniofacial functions, are more likely to be differentially expressed, with the direction of expression change being in agreement with the enhancer bias. Indeed, testing nine chimp-biased and eight human-biased enhancers by luciferase assays suggests that >80% of the candidates have species-biased enhancer activity. Together, this supports the notion that quantitative modulation of enhancer activity is the main source of functional divergence between closely related species. It will be interesting and important to explore how many of the almost 2,000 species-biased candidates differ in enhancer activity (Arnold et al., 2014) and cause differential expression of their target genes.

To assess the activity of predicted enhancers *in vivo*, the authors tested several species-biased CNCC enhancers in mouse embryos and showed their differential activity in head and face regions. This further demonstrates that the respective cell types exist also in mice and that the enhancer divergence is a result of sequence changes between human and chimp and not the differences in *trans*-regulatory environments of their CNCCs. This is in line with the model that the evolution of morphological diversity is driven by *cis*-regulatory mutations that affect developmental expression patterns (Carroll, 2008). Prescott et al. further explore sequence features underlying enhancer divergence with a focus on transcription factor (TF) binding sites, which are central to enhancer function. They show that species-biased enhancers harbor very few (three to six) substitutions that nevertheless cause dramatic changes in chromatin signatures

associated with active enhancers if they affect binding sites of key TFs, emphasizing these TFs' importance for gene expression in CNCCs. The authors make an important distinction between TF motifs that are depleted in species-biased enhancers likely due to selective pressure, as they play a central role in establishing CNCC identity, and those that are enriched and thus more likely involved in regulating species-specific CNCC gene expression.

Among the later group, a novel binding motif stands out as highly enriched in divergent enhancers and shows strong correlation with enhancer activity. Interestingly, this coordinator motif, as the authors termed it, is present in species-biased enhancers of both human and chimp, and the motif strength in either species correlates with H3K27ac levels. The coordinator motif is therefore not species specific but is redirected in a species-specific fashion to distinct sets of enhancers that likely regulate different subsets of genes and drive the divergence of primate CNCCs

and their descendants. Considering that the coordinator motif is a combination of two very prominent binding sites, the E-box and homeodomain binding motif that are both bound by many different TFs, it will be interesting to identify the specific TFs that bind to the coordinator. These TFs likely play a more general role in CNCCs and in establishing facial morphology and are through mutations that modulate their binding sites at divergent enhancers deployed to regulate species-specific CNCC expression patterns.

There are several evolutionary mechanisms by which such an extensive CNCC enhancer divergence might have emerged in such a short evolutionary time. Regions of the human genome that evolve unexpectedly fast, termed human

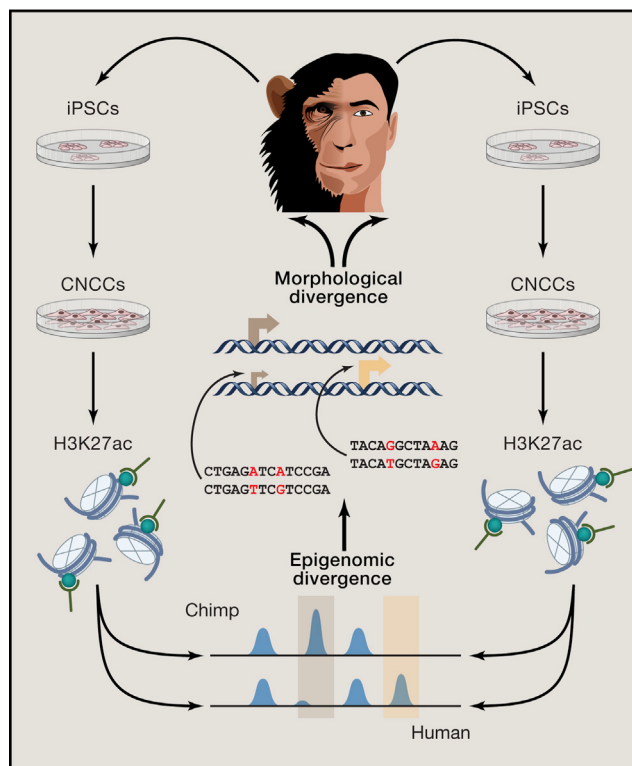


Figure 1. The Cellular Anthropology Approach

By deriving cranial neural crest cells (CNCC) for both human and chimp *in vitro*, Prescott et al. gain insight into the gene regulatory processes that lead to the establishment of species-specific facial morphology during embryogenesis (Prescott et al., 2015). Through epigenomic profiling of these cells, the authors identify distal-acting regulatory elements, known as enhancers, that show species-biased activity and likely drive species-specific CNCC gene expression. The observed epigenomic divergence allows them to link sequence changes in *cis*-regulatory elements with changes in gene expression that underlie differences between the human and chimp face.

accelerated regions (HARs), have been shown to be involved in regulating human-specific traits, including the development of the human brain (Pollard et al., 2006). Prescott et al. now show that they might also be involved in the development of human-specific facial morphology. Even though only 20 HARs overlap the species-biased CNCC enhancers, their relative enrichment is significant, and additional HARs might fall into regions with larger sequence divergence than those considered here (due to the cross-mapping requirement). Another important aspect of *cis*-regulatory evolution are transposable elements, whose involvement in gene regulation has long been postulated (Davidson and Britten, 1979), and their role in the evolution of regulatory elements has been demonstrated in

multiple studies since. In line with this, Prescott et al. reveal significant enrichment of specific classes of retrotransposons in species-biased enhancers. More than half of the divergent enhancers overlap with at least one of the major retrotransposon families, including endogenous retroviruses and L1 elements. As these were present in the primate lineage before human and chimp separated, they possibly contain progenitor sequences that evolved into CNCC enhancers. Indeed, the authors show that LTR9 retroelements, which are enriched at species-biased enhancers, often harbor a variant of the coordinator motif independently of whether they reside in CNCC enhancers or elsewhere in the genome. It is thus likely that some of these elements evolved into CNCC enhancers by acquiring mutations that converted a progenitor sequence into a strong coordinator motif capable of binding key TFs. Although this gain of function happened in both species, the loss of coordinator motif function is equally likely to have contributed to enhancer

divergence between human and chimp through disruption of the original ancestral motif in one of the species.

Interestingly, the authors show that the strongly divergent enhancers tend to cluster along the genome according to their species bias, forming larger genomic regions that often overlap genes critical for facial morphogenesis, which are differentially expressed between human and chimp. Some of these genes, for instance *PAX3*, have been previously associated with intra-human facial variation and were implied in the development of facial malformations. It will be interesting in the future to link specific regulatory regions and the genes that they regulate to the different morphological and physiological traits of the human face, which given the contribution of CNCCs to

nerves, muscles, and throat cartilages might even include aspects of verbal and non-verbal communication. Taken together, the CNCC enhancers identified by Prescott et al. represent a comprehensive resource for studies of human evolution and the genetic basis of variations in facial morphology. Their work also introduces the concept of cellular anthropology that, by studying developmentally relevant cell types in vitro, attempts to elucidate mechanisms underlying morphological evolution in primates. Together with the recent advances in molecular paleontology enabling the sequencing of genomes

of extinct close human relatives, these novel approaches make this a very exciting time to study human evolution.

REFERENCES

Arnold, C.D., Gerlach, D., Spies, D., Matts, J.A., Sytnikova, Y.A., Pagani, M., Lau, N.C., and Stark, A. (2014). *Nat. Genet.* 46, 685–692.

Carroll, S.B. (2008). *Cell* 134, 25–36.

Davidson, E.H., and Britten, R.J. (1979). *Science* 204, 1052–1059.

King, M.C., and Wilson, A.C. (1975). *Science* 188, 107–116.

Pollard, K.S., Salama, S.R., Lambert, N., Lambot, M.-A., Coppens, S., Pedersen, J.S., Katzman, S., King, B., Onodera, C., Siepel, A., et al. (2006). *Nature* 443, 167–172.

Prescott, S.L., Srinivasan, R., Marchetto, M.C., Grishina, I., Narvaiza, I., Selleri, L., Gage, F.H., Swigut, T., and Wysocka, J. (2015). *Cell* 163, this issue, 68–83.

Reilly, S.K., Yin, J., Ayoub, A.E., Emera, D., Leng, J., Cotney, J., Sarro, R., Rakic, P., and Noonan, J.P. (2015). *Science* 347, 1155–1159.

Santagati, F., and Rijli, F.M. (2003). *Nat. Rev. Neurosci.* 4, 806–818.

Shlyueva, D., Stampfel, G., and Stark, A. (2014). *Nat. Rev. Genet.* 15, 272–286.

Villar, D., Berthelot, C., Aldridge, S., Rayner, T.F., Lukk, M., Pignatelli, M., Park, T.J., Deaville, R., Erichsen, J.T., Jasinska, A.J., et al. (2015). *Cell* 160, 554–566.

A Sympathetic View on Fat by Leptin

Luis Varela¹ and Tamas L. Horvath^{1,*}

¹Program in Integrative Cell Signalling and Neurobiology of Metabolism, Section of Comparative Medicine, Yale University School of Medicine, New Haven, CT 06520, USA

*Correspondence: tamas.horvath@yale.edu
<http://dx.doi.org/10.1016/j.cell.2015.09.016>

Zeng et al. reveal that the lipolytic effect of the hormone leptin is mediated by sympathetic nerve fibers that directly “envelope” white adipocytes. Local activation of the sympathetic input to the fat opens new venues to circumvent central leptin resistance in obesity.

In the past 20 years, scientists have uncovered the mechanisms by which the hormone leptin affects different brain areas. Although it is also well known that central administration of leptin results in a myriad of effects at the periphery level (Halaas et al., 1995, 1997), the mechanism of action of these peripheral effects at the various tissue sites has remained elusive (Balthasar et al., 2004; Cowley et al., 2001). In particular, the exact mode of signaling by which leptin triggers changes in white adipose tissue (WAT) function was yet to be identified. In this issue of *Cell*, Zeng et al. (2015) resolve the mystery, showing that the sympathetic nervous system (SNS) is the fine effector of leptin’s action on WAT.

The authors begin by visualizing the sympathetic innervation of the inguinal WAT. Then, applying state-of-the-stimulating and inhibiting optogenetic ap-

proaches at peripheral sites, they reproduce or block, respectively, the effects of leptin on the WAT (Figure 1). Their study goes beyond just the delineation of how leptin triggers lipolysis in WAT. It puts forward an exciting experimental design, which adapts very advanced and powerful techniques to the study of the sympathetic innervation of peripheral tissues, in this case the WAT. First, they use optical projection tomography, or two-photon microscopy, to identify the precise sites of SNS innervation of WAT *in vivo*, a feat that could not be accomplished before. Then they apply optogenetics to stimulate axonal projections at the post-ganglionic level. To date, optogenetic approaches have been predominantly used to interrogate neuronal function in circuits of the central nervous system. This paper sets the stage for the application of optogenetics to interrogate the functional role

of various peripheral neuronal circuits in system physiology.

Many efforts have been put forth during the last decades to identify the type of innervation that is present in the WAT. Some studies erroneously postulated the existence of parasympathetic innervation associated with the vasculature (Giordano et al., 2006). Conversely, other studies investigated the role of the SNS innervation of WAT (Bartness et al., 2014; Diculescu and Stoica, 1970). It has been reported that through the manipulation of sympathetic efferents, it is possible to alter lipid mobilization in different fat depots (Bartness et al., 2014). Other studies have shown SNS innervation of WAT through the use of neuroanatomical methods, using retrograde tracers and immunohistochemical analyses (Bartness et al., 2014; Diculescu and Stoica, 1970). Nonetheless Zeng et al. are the first to

nerves, muscles, and throat cartilages might even include aspects of verbal and non-verbal communication. Taken together, the CNCC enhancers identified by Prescott et al. represent a comprehensive resource for studies of human evolution and the genetic basis of variations in facial morphology. Their work also introduces the concept of cellular anthropology that, by studying developmentally relevant cell types in vitro, attempts to elucidate mechanisms underlying morphological evolution in primates. Together with the recent advances in molecular paleontology enabling the sequencing of genomes

of extinct close human relatives, these novel approaches make this a very exciting time to study human evolution.

REFERENCES

Arnold, C.D., Gerlach, D., Spies, D., Matts, J.A., Sytnikova, Y.A., Pagani, M., Lau, N.C., and Stark, A. (2014). *Nat. Genet.* 46, 685–692.

Carroll, S.B. (2008). *Cell* 134, 25–36.

Davidson, E.H., and Britten, R.J. (1979). *Science* 204, 1052–1059.

King, M.C., and Wilson, A.C. (1975). *Science* 188, 107–116.

Pollard, K.S., Salama, S.R., Lambert, N., Lambot, M.-A., Coppens, S., Pedersen, J.S., Katzman, S., King, B., Onodera, C., Siepel, A., et al. (2006). *Nature* 443, 167–172.

Prescott, S.L., Srinivasan, R., Marchetto, M.C., Grishina, I., Narvaiza, I., Selleri, L., Gage, F.H., Swigut, T., and Wysocka, J. (2015). *Cell* 163, this issue, 68–83.

Reilly, S.K., Yin, J., Ayoub, A.E., Emera, D., Leng, J., Cotney, J., Sarro, R., Rakic, P., and Noonan, J.P. (2015). *Science* 347, 1155–1159.

Santagati, F., and Rijli, F.M. (2003). *Nat. Rev. Neurosci.* 4, 806–818.

Shlyueva, D., Stampfel, G., and Stark, A. (2014). *Nat. Rev. Genet.* 15, 272–286.

Villar, D., Berthelot, C., Aldridge, S., Rayner, T.F., Lukk, M., Pignatelli, M., Park, T.J., Deaville, R., Erichsen, J.T., Jasinska, A.J., et al. (2015). *Cell* 160, 554–566.

A Sympathetic View on Fat by Leptin

Luis Varela¹ and Tamas L. Horvath^{1,*}

¹Program in Integrative Cell Signalling and Neurobiology of Metabolism, Section of Comparative Medicine, Yale University School of Medicine, New Haven, CT 06520, USA

*Correspondence: tamas.horvath@yale.edu
<http://dx.doi.org/10.1016/j.cell.2015.09.016>

Zeng et al. reveal that the lipolytic effect of the hormone leptin is mediated by sympathetic nerve fibers that directly “envelope” white adipocytes. Local activation of the sympathetic input to the fat opens new venues to circumvent central leptin resistance in obesity.

In the past 20 years, scientists have uncovered the mechanisms by which the hormone leptin affects different brain areas. Although it is also well known that central administration of leptin results in a myriad of effects at the periphery level (Halaas et al., 1995, 1997), the mechanism of action of these peripheral effects at the various tissue sites has remained elusive (Balthasar et al., 2004; Cowley et al., 2001). In particular, the exact mode of signaling by which leptin triggers changes in white adipose tissue (WAT) function was yet to be identified. In this issue of *Cell*, Zeng et al. (2015) resolve the mystery, showing that the sympathetic nervous system (SNS) is the fine effector of leptin’s action on WAT.

The authors begin by visualizing the sympathetic innervation of the inguinal WAT. Then, applying state-of-the-stimulating and inhibiting optogenetic ap-

proaches at peripheral sites, they reproduce or block, respectively, the effects of leptin on the WAT (Figure 1). Their study goes beyond just the delineation of how leptin triggers lipolysis in WAT. It puts forward an exciting experimental design, which adapts very advanced and powerful techniques to the study of the sympathetic innervation of peripheral tissues, in this case the WAT. First, they use optical projection tomography, or two-photon microscopy, to identify the precise sites of SNS innervation of WAT *in vivo*, a feat that could not be accomplished before. Then they apply optogenetics to stimulate axonal projections at the post-ganglionic level. To date, optogenetic approaches have been predominantly used to interrogate neuronal function in circuits of the central nervous system. This paper sets the stage for the application of optogenetics to interrogate the functional role

of various peripheral neuronal circuits in system physiology.

Many efforts have been put forth during the last decades to identify the type of innervation that is present in the WAT. Some studies erroneously postulated the existence of parasympathetic innervation associated with the vasculature (Giordano et al., 2006). Conversely, other studies investigated the role of the SNS innervation of WAT (Bartness et al., 2014; Diculescu and Stoica, 1970). It has been reported that through the manipulation of sympathetic efferents, it is possible to alter lipid mobilization in different fat depots (Bartness et al., 2014). Other studies have shown SNS innervation of WAT through the use of neuroanatomical methods, using retrograde tracers and immunohistochemical analyses (Bartness et al., 2014; Diculescu and Stoica, 1970). Nonetheless Zeng et al. are the first to

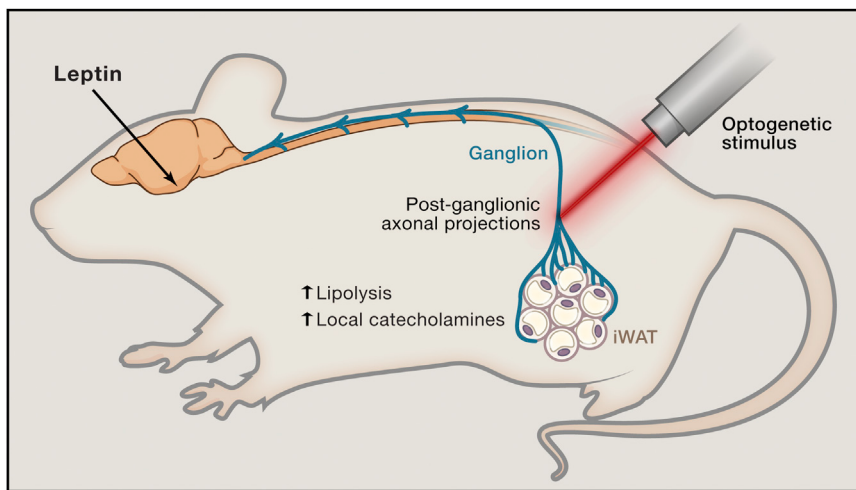


Figure 1. Post-ganglionic Axonal Projections Innervate Fat Depots

Stimuli from the different areas of the brain reach fat depots. Zeng et al. provide evidence that the WAT is innervated by axonal projections from ganglionic neurons. Optogenetic stimulation and genetic, chemical, or physical inhibition of these axons at the post-ganglionic level can mimic or block leptin effects on lipolysis in WAT, respectively.

provide direct evidence for the link between central effects of leptin and lipid mobilization in the different fat depots. The fact that central leptin promotes lipolysis in fat, together with the evidence showing an increase of sympathetic activity after leptin treatment (Pellegrino et al., 2014), led the authors to investigate whether the SNS mediates the lipolytic effects of leptin. They find that the release of sympathetic catecholamines in the fat depots plays a mandatory role in the lipolytic effects of leptin. These data challenge previous hypotheses that the lipolysis in WAT induced by leptin is due to the effects of other circulating hormones. Rather the new data show that signals from different areas of the brain reach the WAT through the SNS. Axonal projections form neural-adipose junctions, where catecholamines (in this case norepinephrine) are released to trigger

lipolysis. Because leptin impacts systemic metabolism by action in many other peripheral tissues, it will be intriguing to apply the same approach to other systems as well. In the future, improvement of this technology could allow selective altering of impaired functionality of peripheral tissues, which may vary between patients with metabolic disturbances such as obesity.

Since the discovery of leptin in 1994 (Zhang et al., 1994), thousands of studies have set out to understand the mechanisms of action of leptin at the central level as well in peripheral tissues. Despite all the advances, many questions remain to be answered to fully unravel the mechanism by which leptin controls integrative physiology (Balthasar et al., 2004; Cowley et al., 2001). Investigators continue to utilize elaborate and complicated genetic models to this end. However, fewer

studies have been done to dynamically identify the signaling modalities of leptin in control lipid mobilization and other peripheral functions. This paper is an excellent example for this latter approach, looking beyond individual steps of this process and focusing on the whole body. By default, the implications of this study are not limited to leptin and lipolysis but rather offer a new approach and vista for the investigation of the actions of other peripheral hormones in integrative physiology.

REFERENCES

- Balthasar, N., Coppari, R., McMinn, J., Liu, S.M., Lee, C.E., Tang, V., Kenny, C.D., McGovern, R.A., Chua, S.C., Jr., Elmquist, J.K., and Lowell, B.B. (2004). *Neuron* 42, 983–991.
- Bartness, T.J., Liu, Y., Shrestha, Y.B., and Ryu, V. (2014). *Front. Neuroendocrinol.* 35, 473–493.
- Cowley, M.A., Smart, J.L., Rubinstein, M., Cerdán, M.G., Diano, S., Horvath, T.L., Cone, R.D., and Low, M.J. (2001). *Nature* 411, 480–484.
- Diculescu, I., and Stoica, M. (1970). *J. Neurovisc. Relat.* 32, 25–36.
- Giordano, A., Song, C.K., Bowers, R.R., Ehlen, J.C., Frontini, A., Cinti, S., and Bartness, T.J. (2006). *Am. J. Physiol. Regul. Integr. Comp. Physiol.* 291, R1243–R1255.
- Halaas, J.L., Gajiwala, K.S., Maffei, M., Cohen, S.L., Chait, B.T., Rabinowitz, D., Lallone, R.L., Burley, S.K., and Friedman, J.M. (1995). *Science* 269, 543–546.
- Halaas, J.L., Boozer, C., Blair-West, J., Fidahusein, N., Denton, D.A., and Friedman, J.M. (1997). *Proc. Natl. Acad. Sci. USA* 94, 8878–8883.
- Pellegrino, M.J., McCully, B.H., and Habecker, B.A. (2014). *Neurosci. Lett.* 566, 1–5.
- Zeng, W., Pirzgalska, R.M., Pereira, M.M.A., Kubasova, N., Barateiro, A., Seixas, E., Lu, Y.-H., Kozlova, A., Voss, H., Martins, G.G., et al. (2015). *Cell* 163, this issue, 84–94.
- Zhang, Y., Proenca, R., Maffei, M., Barone, M., Leopold, L., and Friedman, J.M. (1994). *Nature* 372, 425–432.

No Driver behind the Wheel? Targeting Transcription in Cancer

Hector L. Franco¹ and W. Lee Kraus^{1,*}

¹Laboratory of Signaling and Gene Regulation, Cecil H. and Ida Green Center for Reproductive Biology Sciences and Division of Basic Reproductive Biology Research, Department of Obstetrics and Gynecology, University of Texas Southwestern Medical Center, Dallas, TX 75390, USA

*Correspondence: lee.kraus@utsouthwestern.edu
<http://dx.doi.org/10.1016/j.cell.2015.09.013>

Exploiting the dependence of cancer cells on transcription can be used as an effective strategy for targeting aggressive and therapeutically recalcitrant tumors. Wang et al. show that inhibiting transcription using THZ1, a small-molecule inhibitor of cyclin-dependent kinase CDK7, induces apoptotic cell death in triple-negative breast cancers.

Large-scale, deep-sequencing-based genomic analyses have revealed a surprising level of genetic heterogeneity in cancers. In some cancers, “driver” mutations in key oncogenes can be parsed out from the background of genetic heterogeneity. Some of these oncogenes (such as BRAF and EGFR) encode mutant proteins that provide opportunities for rational targeting by drugs (for instance, targeting BRAF V600E by Vemurafenib and Dabrafenib in melanoma; targeting EGFR L858R or exon 19 deletions by Afatinib and Gefitinib in non-small-cell lung cancer) (Bollag et al., 2012; Sordella et al., 2004). For other cancers, such as triple-negative breast cancer (TNBC), definitive driver mutations have not been identified and thus lack targeted therapies. In spite of a high level of genetic heterogeneity, TNBCs maintain a characteristic and readily identifiable pattern of gene expression. In this issue of *Cell*, Wang et al. (2015) hypothesize that maintenance of a uniform gene expression program in TNBCs requires continually active transcription, which might make these cancers highly sensitive to drugs that inhibit transcription (Figure 1A).

Recent studies using small-molecule inhibitors of the transcriptional machinery have shown promising selectivity for cancer cells and potent antiproliferative effects. For example, targeting bromodomain and extra-terminal proteins (BET) family members, such as BRD4, with JQ1 has exploited the dependence of certain cancers on the transcription of critical driver oncogenes (e.g., c-Myc), rendering these cancers sensitive to tran-

scriptional inhibition (Delmore et al., 2011). More recently, THZ1, a selective covalent inhibitor of cyclin-dependent kinase CDK7, has been shown to be effective in inhibiting the growth of several cancers, such as T cell acute lymphoblastic leukemia (Kwiatkowski et al., 2014), MYCN-amplified neuroblastoma (Chipumuro et al., 2014), and small-cell lung cancer (Christensen et al., 2014).

Wang et al. (2015) explore the therapeutic potential of targeting CDK7 in TNBC, a therapeutically recalcitrant subtype of breast cancer that does not express estrogen receptors (ERs, the target of the first-line therapeutic Tamoxifen), progestin receptors (PRs), or the HER2 receptor (ERBB2; a receptor tyrosine-protein kinase). Using THZ1 and CRISPR/Cas9-mediated gene editing, the authors observe that TNBC cells, but not ER-positive/PR-positive breast cancer cells, are highly dependent on the transcriptional functions of CDK7. Inhibition of CDK7 with THZ1 promotes apoptotic cell death in both TNBC cell lines and patient-derived tumor samples.

CDK7 is a cyclin-dependent kinase (CDK) and a subunit of the multi-protein basal transcription factor TFIID. As such, it plays dual roles in the regulation of cell-cycle progression and transcription. As a component of the CDK Activating Kinase (CAK), CDK7 is involved in control of the cell cycle by phosphorylating other cell-cycle CDKs, such as CDK1 and CDK2 (Malumbres, 2014). As a component of TFIID, CDK7 regulates transcription initiation by phosphorylating serines 5 and 7 of the heptapeptide repeat in the

C-terminal domain (CTD) of the largest subunit (RPB1) of RNA polymerase II (Pol II) (Malumbres, 2014) (Figure 1B). In their study, Wang et al. (2015) demonstrate that THZ1-mediated inhibition of CDK7 does not alter the cell cycle in TNBC cells, suggesting that the sensitivity of TNBCs to THZ1 is mediated through transcriptional inhibition.

Following from their initial observations, the authors postulate that TNBCs are dependent on the uninterrupted transcription of a key set of genes whose expression supports the cancer phenotype. Indeed, they identified a set of ~450 genes whose expression is highly sensitive to inhibition of CDK7 by THZ1, which they refer to as an “Achilles cluster” of TNBC-specific genes (Figure 1A). Gene ontology analyses revealed that this gene set is enriched for factors involved in signaling and transcription regulation, including genes encoding signaling molecules and transcription factors with established roles in breast cancer (e.g., *TGFB*, *STAT*, and *WNT*). Interestingly, these genes are associated with large clustered enhancer regions (so-called “super enhancers”), which are required to drive high-level expression of these genes. The authors posit that targeting CDK7-dependent transcription is an effective way to collectively suppress the expression of multiple genes that are critical for the proliferation of TNBC cells. As such, this gene set may have utility as a prognostic signature for tumors that can be treated effectively with THZ1.

Recent studies have suggested that cancer cells have a higher overall

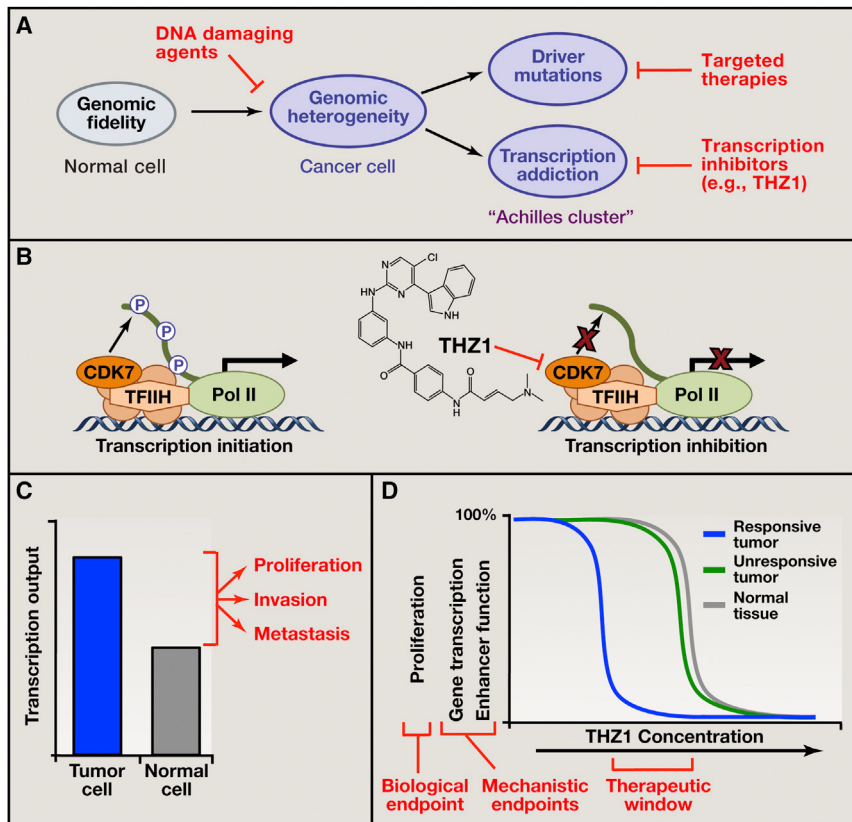


Figure 1. Inhibition of CDK7 by THZ1 and Its Therapeutic Implications

(A) Cancer cells are characterized by increased genomic heterogeneity compared to normal cells. In some cancers, driver mutations in key oncogenes can be targeted therapeutically to inhibit cancer cell growth or induce apoptosis. In cancers with no clear driver mutations, such as TNBC, inhibitors such as THZ1 can be used to target “transcription addiction” to a set of “Achilles cluster” genes that encode for factors involved in signaling and transcription regulation. Many cancer cells can be killed with DNA-damaging agents, which wreak havoc on the genome.

(B) THZ1 covalently binds to and inhibits the activity of CDK7 (a subunit of TFIID), preventing phosphorylation of the C-terminal domain (CTD) of the largest subunit (RPB1) of RNA polymerase II (Pol II) and inhibiting productive transcription initiation.

(C) Current models posit that tumor cells have a higher overall transcription output than normal cells, allowing for more opportunities to engage oncogenic pathways. General inhibition of transcription can have a therapeutic benefit by decreasing the overall transcription output to levels similar to those observed normal cells.

(D) Due to the universal role and biological importance of transcription in all cells, the therapeutic window between efficacy and toxicity for malignant and non-malignant cells will determine if THZ1 can be used to treat human patients.

transcriptional output than non-malignant cells (Lin et al., 2012). This may increase the likelihood of these cancer cells to engage in oncogenic pathways (Figure 1C). Inhibition of transcription may, therefore, reduce the transcriptional output of cancer cells to levels that are less likely to feed into oncogenic pathways (Figure 1C). However, due to the universal role and biological importance of transcription in all cells, targeting transcription as a therapeutic strategy may be challenging due to the potential lack of selectivity for cancer cells over normal

cells. Therefore, it is imperative to determine if the therapeutic window between efficacy and toxicity for malignant and non-malignant cells is large enough to produce a therapeutically efficacious effect (Figure 1D).

This situation is analogous, in some respects, to the use of DNA-damaging therapeutics. All cells need to maintain a certain level of genome integrity to survive, but highly proliferative cells, such as cancer cells, are more sensitive to the effects of DNA-damaging drugs. In fact, this is the basis of synthetic lethality with

PARP inhibitors in BRCA1/2-depleted cancers. While current chemotherapeutic agents used to induce DNA damage exploit the requirement for cancer cells to frequently replicate their genomes, a similar dependence on transcription can now be exploited with transcription inhibitors, such as THZ1.

In spite of recent advances in genomic sequencing, clear driver mutations have yet to be discovered for TNBCs. While ER-positive/PR-positive breast cancers are effectively treated with hormone therapies, the more aggressive TNBCs lack targeted therapies, and cytotoxic chemotherapy remains the standard treatment (Mayer et al., 2014). Thus, THZ1 and its derivatives are promising candidates for the treatment of TNBCs. Wang et al. (2015) have developed an analog of THZ1 (THZ2) with improved pharmacokinetics that has few side effects in mouse xenograft models, which may be more useful clinically. The growth-promoting pathways that are activated in cancer cells involve multiple redundancies. Therefore, the use of a targeted therapeutic agent that selectively inhibits one pathway may be undermined by the activation of a compensatory pathway (Mayer et al., 2014). The strategy of targeting transcription more generally may be effective in these cases. Moreover, combining targeted agents with transcriptional inhibitors may be an effective approach for the treatment of TNBC, which may minimize therapeutic resistance of these difficult-to-treat cancers. If THZ1-based therapy can be effectively translated into the clinic, the identification of biomarkers, perhaps an enhancer signature, that can predict if a given tumor will be sensitive to CDK7 inhibition will be essential.

In sum, this study highlights the enormous potential for targeting transcriptional addiction in aggressive tumors.

ACKNOWLEDGMENTS

We would like to thank Bryan A. Gibson and Ken Y. Lin for their insightful comments and critical reading of this article.

REFERENCES

Bollag, G., Tsai, J., Zhang, J., Zhang, C., Ibrahim, P., Nolop, K., and Hirth, P. (2012). *Nat. Rev. Drug Discov.* **11**, 873–886.

Chipumuro, E., Marco, E., Christensen, C.L., Kwiatkowski, N., Zhang, T., Hatheway, C.M., Abraham, B.J., Sharma, B., Yeung, C., Altabef, A., et al. (2014). *Cell* 159, 1126–1139.

Christensen, C.L., Kwiatkowski, N., Abraham, B.J., Carretero, J., Al-Shahrour, F., Zhang, T., Chipumuro, E., Herter-Sprie, G.S., Akbay, E.A., Altabef, A., et al. (2014). *Cancer Cell* 26, 909–922.

Delmore, J.E., Issa, G.C., Lemieux, M.E., Rahl, P.B., Shi, J., Jacobs, H.M., Kastritis, E., Gilpatrick, T., Paranal, R.M., Qi, J., et al. (2011). *Cell* 146, 904–917.

Kwiatkowski, N., Zhang, T., Rahl, P.B., Abraham, B.J., Reddy, J., Ficarro, S.B., Dastur, A., Amzallag, A., Ramaswamy, S., Tesar, B., et al. (2014). *Nature* 511, 616–620.

Lin, C.Y., Lovén, J., Rahl, P.B., Paranal, R.M., Burge, C.B., Bradner, J.E., Lee, T.I., and Young, R.A. (2012). *Cell* 151, 56–67.

Malumbres, M. (2014). *Genome Biol.* 15, 122.

Mayer, I.A., Abramson, V.G., Lehmann, B.D., and Pienpol, J.A. (2014). *Clin. Cancer Res.* 20, 782–790.

Sordella, R., Bell, D.W., Haber, D.A., and Settleman, J. (2004). *Science* 305, 1163–1167.

Wang, Y., Zhang, T., Kwiatkowski, N., Abraham, B.J., Lee, T.I., Xie, S., Yuzugullu, H., Von, T., Li, H., Lin, Z., et al. (2015). *Cell* 163, this issue, 174–186.

Revealing the Complexity of Retroviral Repression

Gernot Wolf¹ and Todd S. Macfarlan^{1,*}

¹The Eunice Kennedy Shriver National Institute of Child Health and Human Development, The National Institutes of Health, Bethesda, MD 20892, USA

*Correspondence: todd.macfarlan@nih.gov
<http://dx.doi.org/10.1016/j.cell.2015.09.014>

Retroviral restriction is a complex phenomenon that, despite remarkable recent progress, is far from being well understood. In this Preview, we introduce an insightful study by Yang et al. that represents the first attempt to identify the global determinants of retroviral repression in pluripotent mammalian cells.

To protect their genomic integrity, animals control retroviral infections by establishing heritable epigenetic silencing of the integrated provirus in early embryonic development. In mouse embryonic stem cells (ESCs), KAP1 (Trim28) is targeted to newly integrated Moloney murine leukemia virus (MMLV) by the Krueppel-associated box (KRAB) zinc finger protein ZFP809. KAP1, in turn, recruits histone-modifying enzymes, including the histone methyl transferase SETDB1 (ESET), that deposit repressive histone 3 lysine 9 trimethylation (H3K9me3) marks at the provirus (Figure 1) (Matsui et al., 2010; Rowe et al., 2010; Wolf and Goff, 2009). The KRAB/KAP1 system also represses endogenous retroviruses (ERVs), which are potentially hazardous remnants of retroviral germline infections (Matsui et al., 2010; Rowe et al., 2010; Wolf et al., 2015). Additionally, several cofactors of the KRAB/KAP1 system, but also KAP1-independent retroviral repression pathways, have been identified over the last few years. Indeed, the abundance and sequence diversity of exogenous and endogenous retroviruses likely drove

evolution of complex and partially redundant repression mechanisms that keep these elements under control. Moreover, some ERVs have been adapted as new regulatory elements and, in some cases, have re-wired entire transcriptional networks (Macfarlan et al., 2012). Retroviral repression mechanisms might therefore also regulate transcription of cellular genes. Despite recent progress in the field, deciphering the complexity and interconnectivity of retroviral repression pathways and networks remains an outstanding problem of mammalian genome biology. The Resource article by Yang et al. (2015) performs a genome-wide small interfering RNA (siRNA) knockdown screen in a first attempt to determine in a global manner the components of retroviral repression machinery in mammalian pluripotent cells.

The siRNA screen was performed using a MMLV reporter that is repressed by ZFP809/KAP1 and is therefore primarily aimed at identifying cofactors acting upstream and downstream of the KRAB/KAP1 system, but also at potentially overlapping

KAP1-independent repression pathways. Apart from previously known factors, including ZFP809, KAP1, and SETDB1, hundreds of new repression candidates were identified. As expected, many candidates are associated with chromatin modification, DNA methylation, and regulation of transcription. Additionally, the screen identified genes involved in protein sumoylation, DNA repair, and DNA replication and even factors located outside of the nucleus (e.g., plasma membrane, cytoskeletal, and organelle proteins). These findings highlight the complexity of retroviral restriction networks in mammalian cells, although many of these factors may not primarily, specifically, and/or directly repress retroviruses. Without a doubt, the provided candidate list is a potentially valuable resource for future studies that may address how these factors mediate retroviral restriction and ultimately help us to better understand how epigenetic silencing of retroviruses is established, maintained, and inherited during development.

Two of the newly identified repression mechanisms are subsequently analyzed

Chipumuro, E., Marco, E., Christensen, C.L., Kwiatkowski, N., Zhang, T., Hatheway, C.M., Abraham, B.J., Sharma, B., Yeung, C., Altabef, A., et al. (2014). *Cell* 159, 1126–1139.

Christensen, C.L., Kwiatkowski, N., Abraham, B.J., Carretero, J., Al-Shahrour, F., Zhang, T., Chipumuro, E., Herter-Sprie, G.S., Akbay, E.A., Altabef, A., et al. (2014). *Cancer Cell* 26, 909–922.

Delmore, J.E., Issa, G.C., Lemieux, M.E., Rahl, P.B., Shi, J., Jacobs, H.M., Kastritis, E., Gilpatrick, T., Paranal, R.M., Qi, J., et al. (2011). *Cell* 146, 904–917.

Kwiatkowski, N., Zhang, T., Rahl, P.B., Abraham, B.J., Reddy, J., Ficarro, S.B., Dastur, A., Amzallag, A., Ramaswamy, S., Tesar, B., et al. (2014). *Nature* 511, 616–620.

Lin, C.Y., Lovén, J., Rahl, P.B., Paranal, R.M., Burge, C.B., Bradner, J.E., Lee, T.I., and Young, R.A. (2012). *Cell* 151, 56–67.

Malumbres, M. (2014). *Genome Biol.* 15, 122.

Mayer, I.A., Abramson, V.G., Lehmann, B.D., and Pienpol, J.A. (2014). *Clin. Cancer Res.* 20, 782–790.

Sordella, R., Bell, D.W., Haber, D.A., and Settleman, J. (2004). *Science* 305, 1163–1167.

Wang, Y., Zhang, T., Kwiatkowski, N., Abraham, B.J., Lee, T.I., Xie, S., Yuzugullu, H., Von, T., Li, H., Lin, Z., et al. (2015). *Cell* 163, this issue, 174–186.

Revealing the Complexity of Retroviral Repression

Gernot Wolf¹ and Todd S. Macfarlan^{1,*}

¹The Eunice Kennedy Shriver National Institute of Child Health and Human Development, The National Institutes of Health, Bethesda, MD 20892, USA

*Correspondence: todd.macfarlan@nih.gov
<http://dx.doi.org/10.1016/j.cell.2015.09.014>

Retroviral restriction is a complex phenomenon that, despite remarkable recent progress, is far from being well understood. In this Preview, we introduce an insightful study by Yang et al. that represents the first attempt to identify the global determinants of retroviral repression in pluripotent mammalian cells.

To protect their genomic integrity, animals control retroviral infections by establishing heritable epigenetic silencing of the integrated provirus in early embryonic development. In mouse embryonic stem cells (ESCs), KAP1 (Trim28) is targeted to newly integrated Moloney murine leukemia virus (MMLV) by the Krueppel-associated box (KRAB) zinc finger protein ZFP809. KAP1, in turn, recruits histone-modifying enzymes, including the histone methyl transferase SETDB1 (ESET), that deposit repressive histone 3 lysine 9 trimethylation (H3K9me3) marks at the provirus (Figure 1) (Matsui et al., 2010; Rowe et al., 2010; Wolf and Goff, 2009). The KRAB/KAP1 system also represses endogenous retroviruses (ERVs), which are potentially hazardous remnants of retroviral germline infections (Matsui et al., 2010; Rowe et al., 2010; Wolf et al., 2015). Additionally, several cofactors of the KRAB/KAP1 system, but also KAP1-independent retroviral repression pathways, have been identified over the last few years. Indeed, the abundance and sequence diversity of exogenous and endogenous retroviruses likely drove

evolution of complex and partially redundant repression mechanisms that keep these elements under control. Moreover, some ERVs have been adapted as new regulatory elements and, in some cases, have re-wired entire transcriptional networks (Macfarlan et al., 2012). Retroviral repression mechanisms might therefore also regulate transcription of cellular genes. Despite recent progress in the field, deciphering the complexity and interconnectivity of retroviral repression pathways and networks remains an outstanding problem of mammalian genome biology. The Resource article by Yang et al. (2015) performs a genome-wide small interfering RNA (siRNA) knockdown screen in a first attempt to determine in a global manner the components of retroviral repression machinery in mammalian pluripotent cells.

The siRNA screen was performed using a MMLV reporter that is repressed by ZFP809/KAP1 and is therefore primarily aimed at identifying cofactors acting upstream and downstream of the KRAB/KAP1 system, but also at potentially overlapping

KAP1-independent repression pathways. Apart from previously known factors, including ZFP809, KAP1, and SETDB1, hundreds of new repression candidates were identified. As expected, many candidates are associated with chromatin modification, DNA methylation, and regulation of transcription. Additionally, the screen identified genes involved in protein sumoylation, DNA repair, and DNA replication and even factors located outside of the nucleus (e.g., plasma membrane, cytoskeletal, and organelle proteins). These findings highlight the complexity of retroviral restriction networks in mammalian cells, although many of these factors may not primarily, specifically, and/or directly repress retroviruses. Without a doubt, the provided candidate list is a potentially valuable resource for future studies that may address how these factors mediate retroviral restriction and ultimately help us to better understand how epigenetic silencing of retroviruses is established, maintained, and inherited during development.

Two of the newly identified repression mechanisms are subsequently analyzed

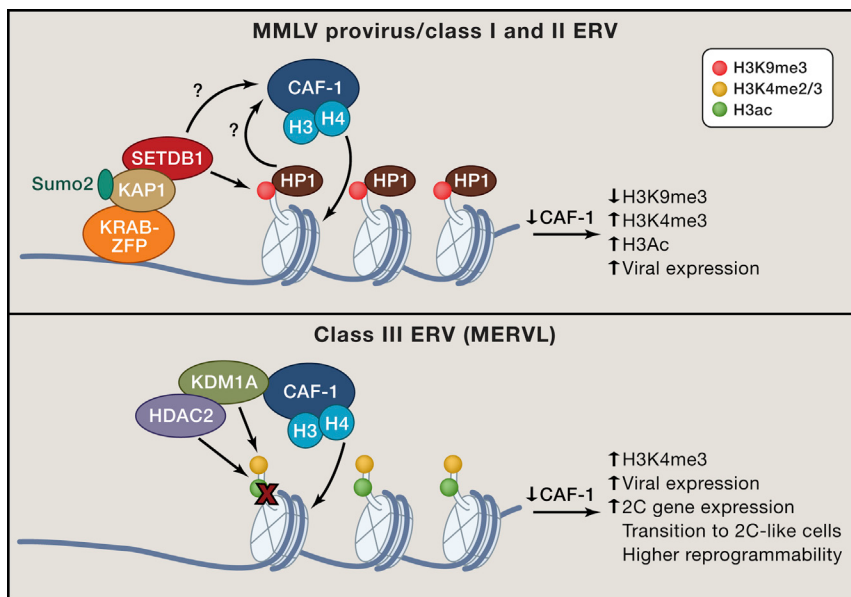


Figure 1. SUMO2/CAF-1-Assisted Retroviral Silencing

Simplified models of SUMO2/CAF-1-assisted retroviral silencing are depicted. (Top) The MMLV provirus and some endogenous retroviruses are targeted by various KRAB zinc finger proteins (KRAB-ZFPs) that recruit the KAP1 corepressor. KAP1, among other functions, recruits SETDB1, which deposits the repressive H3K9me3 mark at histone H3. HP1, a reader of the H3K9me3 mark, may recruit CAF-1. Alternatively, SETDB1, which immunoprecipitates with CAF-1, might be involved in CAF-1 recruitment to the proviral DNA. In concert with other factors, CAF-1 delivers a H3-H4 dimer onto the retroviral DNA during replication to maintain the repressive mark. (Bottom) MERVL elements are not repressed by the KRAB/KAP1/SETDB1 complex and lack the H3K9me3 mark. Instead, MERVL ERVs are repressed by the H3K4 lysine demethylase KDM1A and histone deacetylases, such as HDAC2, which both remove histone modifications associated with open chromatin and transcription. CAF-1 knockdown results in epigenetic changes and retroviral de-repression, but also to the activation of MERVL-regulated 2C genes. This ultimately facilitates the transition of ESCs to a more epigenetically pliable state, similar to 2C embryos.

in detail to validate the significance of the screen: KAP1 sumoylation and chromatin assembly at proviruses. Yang et al. show that KAP1 sumoylation by SUMO2 is required for KAP1 recruitment to the MMLV provirus and ERVs and thus for epigenetic silencing of these elements. This supports previous findings that sumoylation of KAP1 by SUMO2 is essential for forming a stable KRAB/KAP1/SETDB1 repression complex (Ivanov et al., 2007). CHAF1A, one of the top hits in the screen, is the core component of the chromatin assembly factor-1 (CAF-1). CAF-1 depletion impairs repression of newly integrated proviruses and also promotes reactivation of several ERV families, many of which are bound by both CAF-1 and KAP1 (Yang et al., 2015). Although this implies that CAF-1 is a component of the KRAB/KAP1 silencing system, SUMO2 knockdown, which results in KAP1 loss at the MMLV provirus, does not disrupt CAF-1 binding

(Yang et al., 2015). This indirectly indicates that CAF-1 recruitment to retroviruses is independent of KAP1 binding. The question remains: how is CAF-1 targeted to retroviral elements? One possibility is that CAF-1 re-assembles histones at repressed retroviral elements after DNA replication and thus aids to maintain heterochromatin marks, as previously suggested (Yu et al., 2015). In this model, free histone H3, mono-methylated by SETDB1, is incorporated into newly synthesized heterochromatic DNA by CAF-1 and is further methylated to form stable heterochromatin on the newly synthesized strand via heterochromatin protein 1 (HP1), which binds to the H3K9me3 mark (Yu et al., 2015). CAF-1 immunoprecipitates with both SETDB1 and HP1, possibly explaining its localization at retroviral elements (Figure 1) (Yang et al., 2015; Yu et al., 2015). However, it has yet to be determined whether CAF-1 localization at KAP1-controlled

ERVs is indeed replication dependent and whether the chromatin assembly function and/or the PCNA-HP1 interacting function of CAF-1 is required for ERV silencing. Furthermore, it remains open whether CAF-1 localizes exclusively at ERV-associated heterochromatin or also at non-viral genes that are repressed by KRAB/KAP1, for example, at imprinted genes. Nevertheless, the findings provided by Yang et al. strongly support a role for CAF-1 in the establishment and/or maintenance of heterochromatin at ERVs after DNA replication.

Interestingly, CAF-1 is also recruited to ERVs that are not bound by KAP1, SETDB1, or H3K9me3—especially class III ERVs, which consist primarily of MERVL elements (Figure 1). These elements are among the ERVs with the highest reactivation levels in CAF-1-depleted cells (Yang et al., 2015), an observation supported by a recent report (Ishiuchi et al., 2015). This indicates that CAF-1 may target and repress different ERV classes by entirely different mechanisms. Previously, it has been shown that MERVL repression by CAF-1 requires the chromatin-assembly activity of CAF-1, but not its functional interaction with HP1 and PCNA (Ishiuchi et al., 2015). Moreover, growth arrest of CAF-1 knockdown ESCs at G1-S prevented MERVL reactivation, indicating that CAF-1 acts to repress MERVL elements during or after DNA replication (Ishiuchi et al., 2015). Yang et al. also show that KDM1A (LSD1), which physically interacts with CAF-1, is strongly enriched at CAF-1-bound MERVL elements (Yang et al., 2015). KDM1A represses MERVL elements in ESCs (Macfarlan et al., 2011), but KDM1A binding at MERVL ERVs has not been previously demonstrated. However, it remains open how CAF-1 and KDM1A are targeted to these elements.

Depletion of KDM1A in ESCs leads to de-repression of MERVL transcripts and MERVL-associated genes, but also to an increased number of spontaneously arising cells resembling two-cell-stage embryos (2C-like cells) within the ESC population (Macfarlan et al., 2012). Interestingly, CAF-1 knockdown ESCs exhibited similar phenotypes (Ishiuchi et al., 2015). Moreover, the nuclei of 2C-like cells originating from CAF-1 knockdown ESCs are also

shown to lack chromocenters and are more efficiently reprogrammed by nuclear transfer into enucleated oocytes (Ishiuchi et al., 2015), supporting the important link between CAF-1/KDM1A-mediated retroviral repression and cellular epigenetic potential in early development.

Altogether, Yang et al. provide a valuable source for retroviral repression candidates using a genome-wide siRNA knockdown screen. Importantly, several of the newly identified factors are confirmed to function in pathways that have not been directly associated with retroviral repression before. This validation strongly supports that the screen identified bona fide candidates, whose further investigation will not only deepen our understanding of the complex retroviral restriction networks,

but also reveal new regulatory mechanisms in retrovirus-derived transcriptional networks.

REFERENCES

- Ishiuchi, T., Enriquez-Gasca, R., Mizutani, E., Boskovic, A., Ziegler-Birling, C., Rodriguez-Terres, D., Wakayama, T., Vaquerizas, J.M., and Torres-Padilla, M.E. (2015). *Nat. Struct. Mol. Biol.* 22, 662–671.
- Ivanov, A.V., Peng, H., Yurchenko, V., Yap, K.L., Negorev, D.G., Schultz, D.C., Psulkowski, E., Fredericks, W.J., White, D.E., Maul, G.G., et al. (2007). *Mol. Cell* 28, 823–837.
- Macfarlan, T.S., Gifford, W.D., Agarwal, S., Driscoll, S., Lettieri, K., Wang, J., Andrews, S.E., Franco, L., Rosenfeld, M.G., Ren, B., and Pfaff, S.L. (2011). *Genes Dev.* 25, 594–607.
- Macfarlan, T.S., Gifford, W.D., Driscoll, S., Lettieri, K., Rowe, H.M., Bonanomi, D., Firth, A., Singer, O., Trono, D., and Pfaff, S.L. (2012). *Nature* 487, 57–63.
- Matsui, T., Leung, D., Miyashita, H., Maksakova, I.A., Miyachi, H., Kimura, H., Tachibana, M., Lorincz, M.C., and Shinkai, Y. (2010). *Nature* 464, 927–931.
- Rowe, H.M., Jakobsson, J., Mesnard, D., Rougemont, J., Reynard, S., Aktas, T., Maillard, P.V., Layard-Liesching, H., Verp, S., Marquis, J., et al. (2010). *Nature* 463, 237–240.
- Wolf, D., and Goff, S.P. (2009). *Nature* 458, 1201–1204.
- Wolf, G., Yang, P., Füchtbauer, A.C., Füchtbauer, E.M., Silva, A.M., Park, C., Wu, W., Nielsen, A.L., Pedersen, F.S., and Macfarlan, T.S. (2015). *Genes Dev.* 29, 538–554.
- Yang, B.X., EL Farran, C.A., Guo, H.C., Yu, T., Fang, H.T., Wang, H.F., Schlesinger, S., Seah, Y.F.S., Goh, G.Y.L., Neo, S.P., et al. (2015). *Cell* 163, this issue, 230–245.
- Yu, Z., Liu, J., Deng, W.M., and Jiao, R. (2015). *Cell Mol. Life Sci.* 72, 327–337.

Mitochondrial DNA Variation in Human Radiation and Disease

Douglas C. Wallace^{1,*}

¹Center for Mitochondrial and Epigenomic Medicine, The Children's Hospital of Philadelphia and Department of Pathology and Laboratory Medicine, University of Pennsylvania, Philadelphia, PA 19104, USA

*Correspondence: wallaced1@email.chop.edu

<http://dx.doi.org/10.1016/j.cell.2015.08.067>

Environmental adaptation, predisposition to common diseases, and, potentially, speciation may all be linked through the adaptive potential of mitochondrial DNA (mtDNA) alterations of bioenergetics. This Perspective synthesizes evidence that human mtDNA variants may be adaptive or deleterious depending on environmental context and proposes that the accrual of mtDNA variation could contribute to animal speciation via adaptation to marginal environments.

The mitochondrial DNA (mtDNA) genes of different human populations encompass polymorphisms that alter amino acids, which appear invariant in diverse animal species. Given the functional importance of the 13 mtDNA oxidative phosphorylation (OXPHOS) genes, it would be expected that purifying selection would ensure that the functionally important amino acids would be conserved across species and thus should be invariant among individuals within the same species. Yet this is not the case. Why?

mtDNA Variation and the History of Women

The maternal inheritance of the human mtDNA and its high mutation rate has resulted in the sequential accumulation of mtDNA genetic variants along radiating maternal lineages. The resulting mtDNA mutational tree encompasses clusters of related mtDNA haplotypes, known as haplogroups, which arose in geographically localized indigenous populations. Hence, the human mtDNA phylogeny and the geographic distribution of associated indigenous populations have permitted the reconstruction of the origins and ancient migrations of women (Figure 1).

The mtDNA tree is rooted in Africa about 130,000 and 170,000 years before present (YBP). For the first ~100,000 years, mtDNAs radiated within Africa, generating a plethora of African-specific mtDNA haplogroups (L0, 1, 2, 3, etc.) that, in aggregate, are referred to as macrohaplogroup L. Between 45,000 and 65,000 YBP, two mtDNAs, M and N, emerged from within L3 in northeast Africa and successfully left Africa, founding macrohaplogroups M and N, which colonized the rest of the world. Macrohaplogroup N gave rise to multiple European, Asian, and Native American mtDNA lineages, while macrohaplogroup M gave rise to only Asian and Native American haplogroups.

The migration of women out of Africa and around the world was associated with four striking regional mtDNA discontinuities. First, only M and N mtDNAs colonized Eurasia and the Americas. Second, while N haplogroups dispersed throughout Europe and Asia, M haplogroups were confined to Asia. Third, of all of the Asian M and N mtDNA lineages, only haplogroups A, C, and D became enriched in Northeast Siberia and were poised at around 20,000 YBP to cross the Bering Land Bridge into the

Americas. Finally, only haplogroup B mtDNAs colonized the Pacific Islands. Discovery of these striking mtDNA haplogroup regional discontinuities has led to the hypothesis that specific mtDNA haplogroups may have been functionally constrained by regional environmental selection (Cann et al., 1987; Denaro et al., 1981; Kivisild et al., 2006; Merriwether et al., 1991; Mishmar et al., 2003; Wallace, 2005, 2013a, 2013b).

Mitochondrial Genetics and Bioenergetics

The mtDNA codes for the most important polypeptides of the mitochondrial energy generating system OXPHOS: the ND1, 2, 3, 4, 4L, 5, and 6 genes of complexes I; the *cytochrome b* gene of complex III; the *COI*, *COII*, and *COIII* genes of complex IV; and the *ATP6* and *ATP8* genes of complex V. In addition, the mtDNA codes for the 22 tRNAs and two rRNAs for mitochondrial protein synthesis plus an ~1,000 nucleotide “control region” that regulates mtDNA transcription and replication (Wallace et al., 2013).

Mitochondrial OXPHOS generates much of cellular energy by the oxidation of dietary calories with oxygen. As electrons pass down the electron transport chain (ETC) through complexes I, III, and IV to reduce oxygen, the energy released is used to pump protons out across the mitochondrial inner membrane to generate a proton electrochemical gradient. This electrochemical gradient can be employed by the ATP synthase (complex V) to drive ATP synthesis. However, mitochondria OXPHOS also modulates cellular REDOX and reactive oxygen species (ROS) production, pH and Ca²⁺ levels, apoptotic initiation, and, via tricarboxylic cycle intermediates, signal transduction pathways and the epigenome (Picard et al., 2014; Wallace, 2005; Wallace and Fan, 2010; Wallace et al., 2010, 2013).

The critical role played by the mtDNA genes in OXPHOS means that the mtDNA polypeptide genes should be highly evolutionarily conserved. Yet the mtDNA has a very high sequence evolution rate. Since most functional mtDNA mutations would be deleterious, the high mutation rate should create a high genetic load and imperil the survival of the species (Wallace, 2013a). This conundrum is resolved by the unique

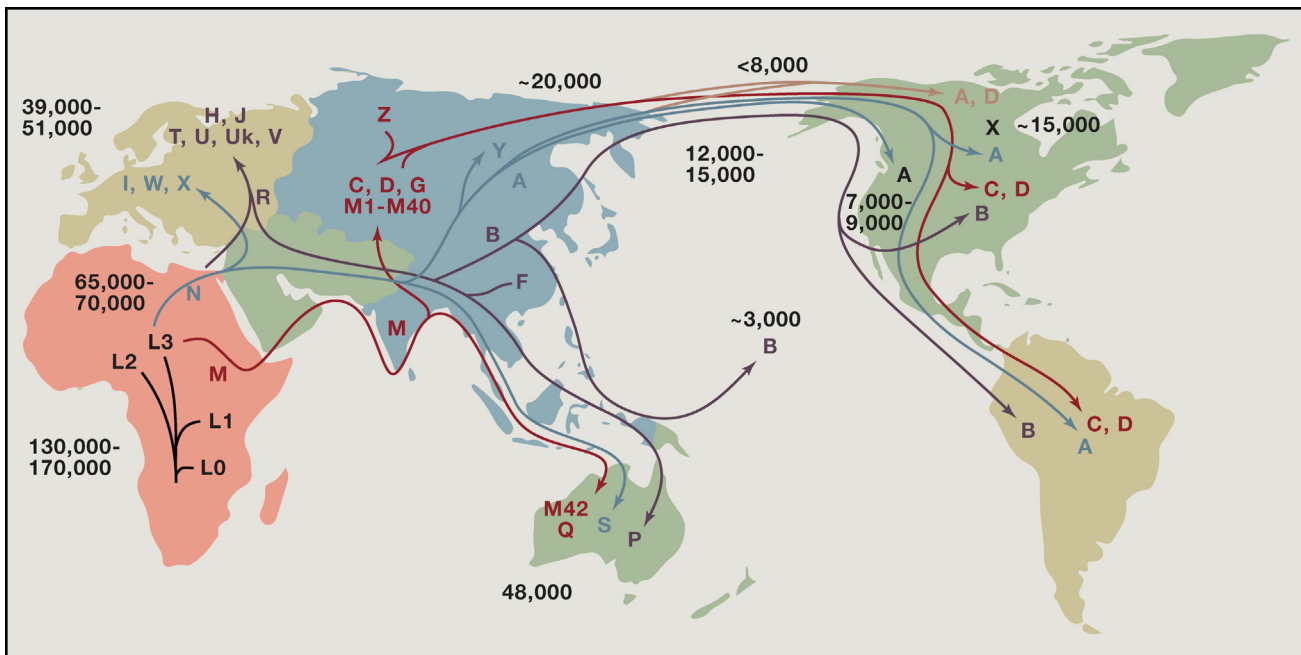


Figure 1. Regional Radiation of Human mtDNAs from their Origin in Africa and Colonization of Eurasia and the Americas Implies that Environmental Selection Constrained Regional mtDNA Variation

All African mtDNAs are subsumed under macrohaplogroup L and coalesce to a single origin about 130,000–170,000 YBP. African haplogroup L0 is the most ancient mtDNA lineage found in the Koi-San peoples, L1 and L2 in Pygmy populations. The M and N mtDNA lineages emerged from Sub-Saharan African L3 in northeastern Africa, and only derivatives of M and N mtDNAs successfully left Africa, giving rise to macrohaplogroups M and N. N haplogroups radiated into European and Asian indigenous populations, while M haplogroups were confined to Asia. Haplogroups A, C, and D became enriched in northeastern Siberia and were positioned to migrate across the Bering Land Bridge 20,000 YBP to found Native Americans. Additional Eurasian migrations brought to the Americas haplogroups B and X. Finally, haplogroup B colonized the Pacific Islands. Figure reproduced from (MITOMAP, 2015).

intracellular mtDNA population genetics of the female germline (Wallace and Chalkia, 2013).

Maternally inherited mtDNA mutations arise among the hundreds to thousands of mtDNAs within the female germline cells, each new mutation creating a mixture of normal and mutant mtDNAs, a state known as heteroplasmy. As a heteroplasmic mitotic or meiotic cell divides, the mutant and normal mtDNAs undergo replicative segregation, becoming randomly distributed among the daughter cells. The mammalian oocyte contains several hundred thousand mtDNAs, which do not actively replicate after fertilization until the blastocyst stage. Hence, the resulting primordial germ cells contain only a couple of hundred mtDNAs. Subsequent mtDNA replication in the derived oogonia leads to proto-oocytes with re-expanded mtDNA populations of several thousand mtDNAs. This repeated contraction and expansion of the intracellular mtDNA populations causes rapid genetic drift of heteroplasmic mtDNAs generating proto-oocytes enriched for either the mutant or normal mtDNAs (Wallace and Chalkia, 2013).

The proto-oocytes and/or oocytes with the most severe mtDNA mutations are then selectively eliminated prior to or soon after fertilization. This is possible because, unlike anatomical alterations that require developmental elaboration of structures before they can be acted on by selection, mitochondrial physiological alterations are expressed at the single-cell level. Hence, cells with highly deleterious mtDNA mutations and asso-

ciated bioenergetic perturbations can be detected and eliminated within the ovary. This permits the mtDNA to have a high mutation rate without the species acquiring excessive genetic load (Fan et al., 2008; Sharpley et al., 2012; Stewart et al., 2008). Through this system, bioenergetic variation is continuously introduced into the population, thus providing a powerful tool for animal adaption to changing environments.

Regional mtDNA Variation and Functional Consequences

The central role of the mtDNA genes in OXPHOS and of OXPHOS in cellular physiology means that functional variants in the mtDNA can have profound effects on human biology. For example, the efficiency with which the ETC generates the proton gradient and by which the proton gradient is converted into ATP is referred to as the coupling efficiency, and humans can differ in their coupling efficiency due to mtDNA polymorphisms. Since a dietary calorie is a unit of heat, every calorie burned by the mitochondrion generates one calorie of body heat. Tightly coupled mitochondria generate the maximum ATP and minimum heat per calorie burned and thus could be beneficial in warmer climates, while loosely coupled mitochondria must burn more calories for the same amount of ATP, generating more heat, and could be of benefit in colder climates. Variation in OXPHOS can also affect ROS production, which affects cell growth, signaling, inflammation, and predilection to infection; Ca^{2+}

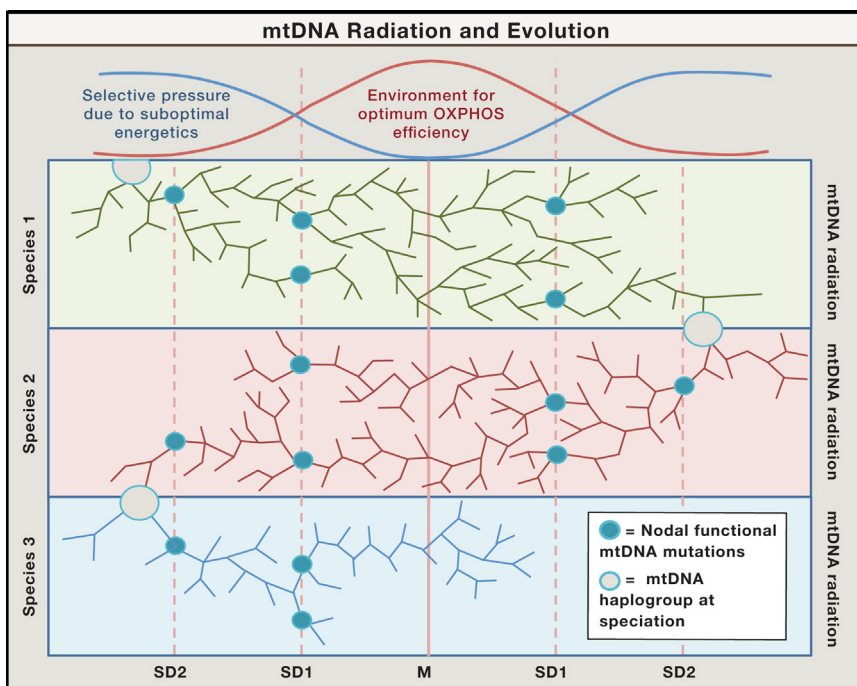


Figure 2. Hypothesized Role of mtDNA Variation in Animal Environmental Adaptation and Speciation

This figure portrays the environmental space (niche) of successively evolving species (green, orange, and blue horizontal bands). The left-to-right expanse represents the range of ecological zones for each species, with the center (M) being the optimal environment and the two left and right vertical dashed lines (SD1 and SD2) representing increasingly marginal environments. Successive mtDNA mutations occurring over time are represented by branch points on black lines, with most of them being neutral. As a new species expands from its optimal niche into more marginal environments, occasional mtDNA mutations arise, which are physiologically beneficial in the suboptimal environment (blue circles at branch points). These lineages become enriched by adaptive selection with additional neutral and adaptive mutations accumulating, creating a haplogroup. The same environmental constraint can select for the same mutation on different mtDNA lineages. Occasionally, one mtDNA lineage located at the extreme edge of the species' niche (left and right edges) permits a subpopulation to persist long enough for nDNA variants to arise that permit switching of food source (energy reservoir), leading to speciation (open circle crossing species boundaries). Previously adaptive mtDNA variants now become suboptimal in the new niche and revertants are selected, permitting energetic re-adaptation back to M.

levels, which regulate cellular and organ homeostasis; and high-energy intermediate levels that can regulate the epigenome.

Consistent with the proposed importance of mtDNA variation in human adaptation, regional haplogroups are generally founded by one or more functionally significant polypeptide, tRNA, rRNA, and/or control region variants. These variants are retained in the descendant mtDNAs creating the haplogroups. For example, at the macrohaplogroup level, the out-of-Africa macrohaplogroup N was founded by two amino acid variants: *ND3* nucleotide (nt) 10389G>A (A114T) and *ATP6* nt 8701G>A (A59T). These variants alter mitochondrial membrane potential and Ca²⁺ regulation (Kazuno et al., 2006), potentially changing the coupling efficiency and being advantageous in colder climates. The European macrohaplogroup N-derived haplogroup J was founded by the reversion of the N-defining *ND3* 10389G>A variant and the acquisition of a new *ND5* 13708G>A (A458T) variant. Haplogroup J radiation gave rise to subhaplogroup J1c founded by a *cytochrome b* variant at 14798T>C (F18L) and subhaplogroup J2 with a *cytochrome b* variant at 15257G>A (D171N). European haplogroup U was founded by the *tRNA^{Leu(CUN)}* 12308A>G variant and gave rise to subhaplogroup Uk, which encompasses the *ATP6* 9055G>A (A177T) variant and an independent recurrence of the *cytochrome b* 14798T>C (F18L) variant (Ruiz-Pesini et al., 2004; Ruiz-Pesini and Wallace, 2006). These haplogroup-founding polypeptide variants change amino acids that otherwise show high interspecific evolutionary conservation—in some cases, even to bacteria. Yet these and multiple other variants of highly conserved amino acids have been retained in the human population in the face of purifying selection for tens of thousands of years, recurred multiple times, and have become enriched in regional

populations to generate regional haplogroups (Kivisild et al., 2006; Mishmar et al., 2003; Ruiz-Pesini et al., 2004, 2007; Ruiz-Pesini and Wallace, 2006; van Oven and Kayser, 2009).

That haplogroups have physiological consequences is suggested by haplogroups T and U, which are associated with reduced sperm motility (Montiel-Sosa et al., 2006; Ruiz-Pesini et al., 2000); haplogroups J and Uk being enriched in Finnish sprinters and haplogroup I in distance runners; and haplogroup L0 being enriched in Kenyan elite distance runners (Table S1). Moreover, climatic differences correlate with mtDNA rather than nDNA variation (Balloux et al., 2009), and the basal metabolic rate of Siberian populations that are enriched for haplogroups A, C, and D is higher than that of more southern populations (Leonard et al., 2002; Snodgrass et al., 2005, 2008).

A more direct demonstration of the adaptive importance of mtDNA variants comes from studies on the mtDNA *ND1* nt 3394T>C (Y30H) variant. In high-altitude Tibetans, the rare 3394C allele is greatly enriched over low altitude Asians (OR ~24), arose three independent times on macrohaplogroup M mtDNAs, and increases in frequency with the altitude of Tibetan villages; an analogous variant (*ND1* Y30C) having been found in the high-altitude Ethiopian monkey, *Theropithecus gelada*. This suggests that the 3394C allele is adaptive at high altitudes when it arises on M haplogroups. However, the 3394C allele has not been observed in Tibetan N haplogroups, suggesting that it may be deleterious when it arises on macrohaplogroup N mtDNAs (Ji et al., 2012).

To determine the physiological consequences of the 3394C variant in association with various mtDNA haplogroups, the mtDNAs of interest have been established in cultured cell lines by transmtochondrial cybrid production (Trounce et al., 1996).

Transfer of 3394T>C (Y30H) mtDNAs into an osteosarcoma nuclear environment revealed that the *ND1* 3394C allele on macrohaplogroup N haplogroup B or F mtDNAs reduced complex I activity between 7% and 28%. However, the complex-I-specific activity between haplogroups B and F harboring the 3394T allele differed by 30%, a greater difference than seen for either haplogroups B or F when comparing the 3394T versus C allele. Moreover, when the 3394C variant occurred on the macrohaplogroup M background, as in Tibetan haplogroup M9, the complex-I-specific activity was as high as that of the most active macrohaplogroup N haplogroup B mtDNA with the 3394T allele (Ji et al., 2012). Hence, both individual mtDNA single-nucleotide polymorphisms, as well as the haplogroup background, interact to modulate mitochondrial bioenergetics.

Functional differences have been observed between other haplogroups with the osteosarcoma cybrids. Comparison of H versus J cybrids revealed that J mtDNA cells have reduced mtDNA, mtDNA transcripts, mitochondrial translation products, oxygen consumption, membrane potential, and ATP levels (Gómez-Durán et al., 2012). Haplogroup H cybrids differ from Uk cybrids by the Ux cybrids having lower mtDNA, mitochondrial RNA, and mitochondrial protein synthesis levels; reduced complex IV activity; increased oxygen consumption; and reduced inner membrane potential, suggesting reduced coupling efficiency (Gómez-Durán et al., 2010). The control region variant, 295C>T, is associated with increased TFAM transcription factor binding to the L-strand promoter, increased L-strand transcripts, and increased mtDNA copy number (Suisse et al., 2009).

Comparison of haplogroup H and J mtDNAs on a retinal pigment epithelial (RPE) nuclear background revealed that J mtDNA cells have reduced ATP, ROS, and reactive nitrogen species levels; increased lactate and growth rate; reduced expression of macular degeneration gene CFH; altered expression of genes involved in cell signaling, inflammation, and metabolism; and altered UV exposure response (Kenney et al., 2014a; Malik et al., 2014). Comparison of European H versus African L mtDNAs in RPE cells showed that the L mtDNA cells had lower ATP turnover rates; reduced spare respiratory capacity; reduced mtDNA copy number; increased mtDNA mRNA levels; and altered expression of nuclear complement, inflammation, and autoimmunity genes (Kenney et al., 2014b). Transfer of mouse mtDNAs from one inbred nucleus to another or mixing of two normal mtDNAs within the mouse germline resulted in significant phenotypic differences (Fischer Lindahl et al., 1991; Roubertoux et al., 2003; Sharpley et al., 2012), an effect also seen in *Drosophila* (Meiklejohn et al., 2013; Zhu et al., 2014). Therefore, naturally occurring mtDNA variation can have profound effects on cellular physiology, growth characteristics, and inflammatory systems.

While the population substructure of mtDNA variation can result from genetic drift (Cann et al., 1987; Kivisild et al., 2006; Wallace, 2013a), in this Perspective, I am exploring the hypothesis that a portion of mtDNA sequence variation, particularly among the haplogroup-founding functional mtDNA variants, has been acted on by adaptive selection. This is because these mtDNA variants fulfill all of the criteria currently used to argue for positive selection acting on protein-coding genes (Nielsen et al., 2007). They change evolutionarily conserved amino acids; they

have recurred multiple times throughout human radiation; they are associated with expansion of a rare haplotype into regional polymorphic haplogroups; they lead to geographically constrained population haplogroups; they increase in frequency in cases in which the environmental challenge is apparent (e.g., altitude); and they change physiological phenotypes, cellular functions, and nuclear gene expression profiles of direct relevance to regional environmental challenges (Nielsen et al., 2007).

mtDNA Variation in Disease

The importance of mtDNA variation is demonstrated by the wide range of common clinical phenotypes that have been associated with mtDNA haplogroups. The penetrance of the milder Leber hereditary optic neuropathy (LHON) complex I gene mtDNA mutations is increased if the LHON mutation arose on haplogroup J or a *ND1* 3394C-bearing mtDNA (Ji et al., 2012; Sadun et al., 2011; Wallace et al., 1988). In fact, mtDNA haplogroups have been associated with a wide range of metabolic, degenerative, infectious, and autoimmune diseases, selected examples of which are listed in Table S2.

Specific mtDNA haplogroups have also been associated with predisposition to various cancers (Table S2). Additionally, cancer cells can acquire de novo mtDNA mutations within the control region and the tRNA, rRNA, and protein-coding genes, a subset of which may be the same or similar to variants associated with regional haplogroups (Brandon et al., 2006).

One mechanism by which mtDNA variation can have such profound effects on cellular and organismal phenotypes is through retrograde signaling to the nucleus. Patients heteroplasmic for the mtDNA tRNA^{Leu(UUR)} nt 3243A>G mutation harboring 20%–30% mutant (3243G) mtDNAs can present with diabetes, 50%–90% of mutant mitochondria with neuromuscular degenerative disease, and ~100% with lethal perinatal disease. Relative to osteosarcoma cybrids with 0% mutant mtDNAs, physiological and molecular analysis of 20%–30% mutant cybrids revealed reduced OXPHOS without glycolytic compensation; 50%–90% mutant cybrids showed strong glycolytic gene induction with declining OXPHOS; and 100% mutant cybrids experienced severe reductions in both glycolysis and OXPHOS. These marked changes in patient phenotypes associated with mtDNA genotypes correlate with four dramatic phase changes in transcriptional patterns corresponding to 0%, 20%–30%, 50%–90%, and 100% 3243 mutant. Thus, the continuous changes in the mtDNA genotype must signal to the nucleus through the cellular signal transduction pathways and epigenome to regulate gene expression. However, the nucleus appears to only be able to respond in four finite ways, thus creating the abrupt phase changes in gene expression and phenotype (Picard et al., 2014).

mtDNA Variation and Speciation

The discoveries that the female germline generates a high frequency of mild functional mtDNA variants, that functionally important OXPHOS gene variants have arisen repeatedly within the mtDNA phylogeny throughout human history, and that selected variants become regionally enriched has led to the hypothesis that the mtDNA provides a powerful adaptive engine

for mammals to cope with environmental change (Figure 2). As a corollary to this hypothesis, the rapid elaboration of adaptive mtDNA variants could permit subpopulations of a species to survive and prosper in “marginal” environments, becoming progressively isolated from parent populations. These metastable peripheral populations could then, in theory, have sufficient longevity for the much slower accumulation of adaptive nDNA gene mutations in both bioenergetic (Gershoni et al., 2010, 2014; Mishmar et al., 2006) and structural genes (Nielsen et al., 2007; Sabeti et al., 2007). Ultimately, the accumulated mtDNA and nDNA adaptive variants could alter a subpopulation’s physiology and anatomy sufficiently to permit a switch to a new primary food source (energy resource), resulting in a new niche and thus speciation.

How then could the conservation of mitochondrial DNA sequence be explained? With the acquisition of a more abundant energy resource, many of the selective pressures that originally drove the enrichment of regional mtDNA variants would be relieved for the new species. The high mtDNA sequence evolution rate plus adaptive selection would then favor in the new species the reversion of previously adaptive but now maladaptive variants back to more commonly optimal bioenergetics alleles. By sequencing only mtDNAs from the central populations of different species, only the common optimal allele would be observed, thus giving the false impression of the invariance of the amino acid at that site.

Conclusion

The process of mtDNA adaptive radiation, combined nDNA-mtDNA coevolution to speciation, and reversion of intraspecific adaptive mtDNA mutations can explain several seemingly anomalous facts. These include why mutations in apparently highly conserved OXPHOS amino acids can occur multiple times within a species and repeatedly increase to polymorphic frequencies; why mtDNA phylogenies coalesce with the origins of species (Cann et al., 1987; Merriwether et al., 1991; Mishmar et al., 2003) while nDNA variants such as HLA alleles or the Tibetan Denisovan *EPAS1* allele (Huerta-Sánchez et al., 2014) are retained across related species; and why a mtDNA variant can be advantageous in one environmental context and deleterious in another. This latter phenomenon may be relevant to the rise of common disease phenotypes such as diabetes, obesity, and neurodegenerative disease, as globalization of regional diets encompasses non-regional mtDNA haplogroups or as migration transfers regional mtDNA haplotypes to new environments, thus converting an adaptive mtDNA genotype into a maladaptive one. Thus, the unique features of the mtDNA may require a reassessment of some of our core assumptions about human genetics and evolutionary theory.

SUPPLEMENTAL INFORMATION

Supplemental Information includes two tables and can be found with this article online at <http://dx.doi.org/10.1016/j.cell.2015.08.067>.

ACKNOWLEDGMENTS

This work was supported by NIH grants R01NS021328 and R33CA182384 and by a Simon Foundation grant 205844.

REFERENCES

- Balloux, F., Handley, L.J., Jombart, T., Liu, H., and Manica, A. (2009). Climate shaped the worldwide distribution of human mitochondrial DNA sequence variation. *Proc. Biol. Sci.* **276**, 3447–3455.
- Brandon, M., Baldi, P., and Wallace, D.C. (2006). Mitochondrial mutations in cancer. *Oncogene* **25**, 4647–4662.
- Cann, R.L., Stoneking, M., and Wilson, A.C. (1987). Mitochondrial DNA and human evolution. *Nature* **325**, 31–36.
- Denaro, M., Blanc, H., Johnson, M.J., Chen, K.H., Wilmsen, E., Cavalli-Sforza, L.L., and Wallace, D.C. (1981). Ethnic variation in Hpa 1 endonuclease cleavage patterns of human mitochondrial DNA. *Proc. Natl. Acad. Sci. USA* **78**, 5768–5772.
- Fan, W., Waymire, K.G., Narula, N., Li, P., Rocher, C., Coskun, P.E., Vannan, M.A., Narula, J., Macgregor, G.R., and Wallace, D.C. (2008). A mouse model of mitochondrial disease reveals germline selection against severe mtDNA mutations. *Science* **319**, 958–962.
- Fischer Lindahl, K., Hermel, E., Loveland, B.E., and Wang, C.R. (1991). Maternally transmitted antigen of mice: a model transplantation antigen. *Annu. Rev. Immunol.* **9**, 351–372.
- Gershoni, M., Fuchs, A., Shani, N., Fridman, Y., Corral-Debrinski, M., Aharoni, A., Frishman, D., and Mishmar, D. (2010). Coevolution predicts direct interactions between mtDNA-encoded and nDNA-encoded subunits of oxidative phosphorylation complex i. *J. Mol. Biol.* **404**, 158–171.
- Gershoni, M., Levin, L., Ovadia, O., Toiv, Y., Shani, N., Dadon, S., Barzilai, N., Bergman, A., Atzman, G., Wainstein, J., et al. (2014). Disrupting mitochondrial-nuclear coevolution affects OXPHOS complex I integrity and impacts human health. *Genome Biol. Evol.* **6**, 2665–2680.
- Gómez-Durán, A., Pacheu-Grau, D., López-Gallardo, E., Diez-Sánchez, C., Montoya, J., López-Pérez, M.J., and Ruiz-Pesini, E. (2010). Unmasking the causes of multifactorial disorders: OXPHOS differences between mitochondrial haplogroups. *Hum. Mol. Genet.* **19**, 3343–3353.
- Gómez-Durán, A., Pacheu-Grau, D., Martínez-Romero, I., López-Gallardo, E., López-Pérez, M.J., Montoya, J., and Ruiz-Pesini, E. (2012). Oxidative phosphorylation differences between mitochondrial DNA haplogroups modify the risk of Leber’s hereditary optic neuropathy. *Biochim. Biophys. Acta* **1822**, 1216–1222.
- Huerta-Sánchez, E., Jin, X., Asan, Bianba, Z., Peter, B.M., Vinckenbosch, N., Liang, Y., Yi, X., He, M., Somel, M., et al. (2014). Altitude adaptation in Tibetans caused by introgression of Denisovan-like DNA. *Nature* **512**, 194–197.
- Ji, F., Sharpley, M.S., Derbeneva, O., Alves, L.S., Qian, P., Wang, Y., Chalkia, D., Lvova, M., Xu, J., Yao, W., et al. (2012). Mitochondrial DNA variant associated with Leber hereditary optic neuropathy and high-altitude Tibetans. *Proc. Natl. Acad. Sci. USA* **109**, 7391–7396.
- Kazuno, A.A., Munakata, K., Nagai, T., Shimozono, S., Tanaka, M., Yoneda, M., Kato, N., Miyawaki, A., and Kato, T. (2006). Identification of mitochondrial DNA polymorphisms that alter mitochondrial matrix pH and intracellular calcium dynamics. *PLoS Genet.* **2**, e128.
- Kenney, M.C., Chwa, M., Atilano, S.R., Falatoonzadeh, P., Ramirez, C., Malik, D., Tarek, M., Cáceres-del-Carpio, J., Nesburn, A.B., Boyer, D.S., et al. (2014a). Inherited mitochondrial DNA variants can affect complement, inflammation and apoptosis pathways: insights into mitochondrial-nuclear interactions. *Hum. Mol. Genet.* **23**, 3537–3551.
- Kenney, M.C., Chwa, M., Atilano, S.R., Falatoonzadeh, P., Ramirez, C., Malik, D., Tarek, M., Del Carpio, J.C., Nesburn, A.B., Boyer, D.S., et al. (2014b). Molecular and bioenergetic differences between cells with African versus European inherited mitochondrial DNA haplogroups: implications for population susceptibility to diseases. *Biochim. Biophys. Acta* **1842**, 208–219.
- Kivisild, T., Shen, P., Wall, D.P., Do, B., Sung, R., Davis, K., Passarino, G., Underhill, P.A., Scharfe, C., Torroni, A., et al. (2006). The role of selection in the evolution of human mitochondrial genomes. *Genetics* **172**, 373–387.

Leonard, W.R., Sorensen, M.V., Galloway, V.A., Spencer, G.J., Mosher, M.J., Osipova, L., and Spitsyn, V.A. (2002). Climatic influences on basal metabolic rates among circumpolar populations. *Am. J. Hum. Biol.* 14, 609–620.

Malik, D., Hsu, T., Falatoonzadeh, P., Cáceres-del-Carpio, J., Tarek, M., Chwa, M., Atilano, S.R., Ramirez, C., Nesburn, A.B., Boyer, D.S., et al. (2014). Human retinal transmtochondrial cybrids with J or H mtDNA haplogroups respond differently to ultraviolet radiation: implications for retinal diseases. *PLoS ONE* 9, e99003.

Meiklejohn, C.D., Holmbeck, M.A., Siddiq, M.A., Abt, D.N., Rand, D.M., and Montooth, K.L. (2013). An Incompatibility between a mitochondrial tRNA and its nuclear-encoded tRNA synthetase compromises development and fitness in *Drosophila*. *PLoS Genet.* 9, e1003238.

Merriwether, D.A., Clark, A.G., Ballinger, S.W., Schurr, T.G., Soodyall, H., Jenkins, T., Sherry, S.T., and Wallace, D.C. (1991). The structure of human mitochondrial DNA variation. *J. Mol. Evol.* 33, 543–555.

Mishmar, D., Ruiz-Pesini, E., Golik, P., Macaulay, V., Clark, A.G., Hosseini, S., Brandon, M., Easley, K., Chen, E., Brown, M.D., et al. (2003). Natural selection shaped regional mtDNA variation in humans. *Proc. Natl. Acad. Sci. USA* 100, 171–176.

Mishmar, D., Ruiz-Pesini, E., Mondragon-Palomino, M., Procaccio, V., Gaut, B., and Wallace, D.C. (2006). Adaptive selection of mitochondrial complex I subunits during primate radiation. *Gene* 378, 11–18.

MITOMAP (2015). A Human Mitochondrial Genome Database. <http://www.mitomap.org>.

Montiel-Sosa, F., Ruiz-Pesini, E., Enríquez, J.A., Marcuello, A., Díez-Sánchez, C., Montoya, J., Wallace, D.C., and López-Pérez, M.J. (2006). Differences of sperm motility in mitochondrial DNA haplogroup U sublineages. *Gene* 368, 21–27.

Nielsen, R., Hellmann, I., Hubisz, M., Bustamante, C., and Clark, A.G. (2007). Recent and ongoing selection in the human genome. *Nat. Rev. Genet.* 8, 857–868.

Picard, M., Zhang, J., Hancock, S., Derbeneva, O., Golhar, R., Golik, P., O'Hearn, S., Levy, S., Potluri, P., Lvova, M., et al. (2014). Progressive increase in mtDNA 3243A>G heteroplasmy causes abrupt transcriptional reprogramming. *Proc. Natl. Acad. Sci. USA* 111, E4033–E4042.

Roubertoux, P.L., Sluyter, F., Carlier, M., Marcket, B., Maarouf-Veray, F., Chérif, C., Marican, C., Arrechi, P., Godin, F., Jamon, M., et al. (2003). Mitochondrial DNA modifies cognition in interaction with the nuclear genome and age in mice. *Nat. Genet.* 35, 65–69.

Ruiz-Pesini, E., and Wallace, D.C. (2006). Evidence for adaptive selection acting on the tRNA and rRNA genes of human mitochondrial DNA. *Hum. Mutat.* 27, 1072–1081.

Ruiz-Pesini, E., Lapeña, A.C., Díez-Sánchez, C., Pérez-Martos, A., Montoya, J., Alvarez, E., Díaz, M., Urriés, A., Montoro, L., López-Pérez, M.J., and Enríquez, J.A. (2000). Human mtDNA haplogroups associated with high or reduced spermatozoa motility. *Am. J. Hum. Genet.* 67, 682–696.

Ruiz-Pesini, E., Mishmar, D., Brandon, M., Procaccio, V., and Wallace, D.C. (2004). Effects of purifying and adaptive selection on regional variation in human mtDNA. *Science* 303, 223–226.

Ruiz-Pesini, E., Lott, M.T., Procaccio, V., Poole, J.C., Brandon, M.C., Mishmar, D., Yi, C., Kreuziger, J., Baldi, P., and Wallace, D.C. (2007). An enhanced MITOMAP with a global mtDNA mutational phylogeny. *Nucleic Acids Res.* 35, D823–D828.

Sabeti, P.C., Varilly, P., Fry, B., Lohmueller, J., Hostetter, E., Cotsapas, C., Xie, X., Byrne, E.H., McCarroll, S.A., Gaudet, R., et al.; International HapMap Consortium (2007). Genome-wide detection and characterization of positive selection in human populations. *Nature* 449, 913–918.

Sadun, A.A., La Morgia, C., and Carelli, V. (2011). Leber's Hereditary Optic Neuropathy. *Curr. Treat. Options Neurol.* 13, 109–117.

Sharpley, M.S., Marcinia, C., Eckel-Mahan, K., McManus, M., Crimi, M., Waymire, K., Lin, C.S., Masubuchi, S., Friend, N., Koike, M., et al. (2012). Heteroplasmy of mouse mtDNA is genetically unstable and results in altered behavior and cognition. *Cell* 151, 333–343.

Snodgrass, J.J., Leonard, W.R., Tarskaia, L.A., Alekseev, V.P., and Krivoshekin, V.G. (2005). Basal metabolic rate in the Yakut (Sakha) of Siberia. *Am. J. Hum. Biol.* 17, 155–172.

Snodgrass, J.J., Leonard, W.R., Sorensen, M.V., Tarskaia, L.A., and Mosher, M.J. (2008). The influence of basal metabolic rate on blood pressure among indigenous Siberians. *Am. J. Phys. Anthropol.* 137, 145–155.

Stewart, J.B., Freyer, C., Elson, J.L., Wredenberg, A., Cansu, Z., Trifunovic, A., and Larsson, N.G. (2008). Strong purifying selection in transmission of mammalian mitochondrial DNA. *PLoS Biol.* 6, e10.

Suissa, S., Wang, Z., Poole, J., Wittkopp, S., Feder, J., Shutt, T.E., Wallace, D.C., Shadel, G.S., and Mishmar, D. (2009). Ancient mtDNA genetic variants modulate mtDNA transcription and replication. *PLoS Genet.* 5, e1000474.

Trounce, I.A., Kim, Y.L., Jun, A.S., and Wallace, D.C. (1996). Assessment of mitochondrial oxidative phosphorylation in patient muscle biopsies, lymphoblasts, and transmtochondrial cell lines. *Methods Enzymol.* 264, 484–509.

van Oven, M., and Kayser, M. (2009). Updated comprehensive phylogenetic tree of global human mitochondrial DNA variation. *Hum. Mutat.* 30, E386–E394.

Wallace, D.C. (2005). A mitochondrial paradigm of metabolic and degenerative diseases, aging, and cancer: a dawn for evolutionary medicine. *Annu. Rev. Genet.* 39, 359–407.

Wallace, D.C. (2013a). Bioenergetics in human evolution and disease: implications for the origins of biological complexity and the missing genetic variation of common diseases. *Philos. Trans. R. Soc. Lond. B Biol. Sci.* 368, 20120267.

Wallace, D.C. (2013b). A mitochondrial bioenergetic etiology of disease. *J. Clin. Invest.* 123, 1405–1412.

Wallace, D.C., and Chalkia, D. (2013). Mitochondrial DNA genetics and the heteroplasmy conundrum in evolution and disease. *Cold Spring Harb. Perspect. Biol.* 5, a021220.

Wallace, D.C., and Fan, W. (2010). Energetics, epigenetics, mitochondrial genetics. *Mitochondrion* 10, 12–31.

Wallace, D.C., Singh, G., Lott, M.T., Hodge, J.A., Schurr, T.G., Lezza, A.M., Elias, L.J., 2nd, and Nikoskelainen, E.K. (1988). Mitochondrial DNA mutation associated with Leber's hereditary optic neuropathy. *Science* 242, 1427–1430.

Wallace, D.C., Fan, W., and Procaccio, V. (2010). Mitochondrial energetics and therapeutics. *Annu. Rev. Pathol.* 5, 297–348.

Wallace, D.C., Lott, M.T., and Procaccio, V. (2013). *Mitochondrial Medicine: The Mitochondrial Biology and Genetics of Metabolic and Degenerative Diseases, Cancer, and Aging*. In Emery and Rimoin's Principles and Practice of Medical Genetics, D.L. Rimoin, R.E. Pyeritz, and B.R. Korf, eds. (Philadelphia: Churchill Livingstone Elsevier).

Zhu, C.T., Ingelmo, P., and Rand, D.M. (2014). G×G×E for lifespan in *Drosophila*: mitochondrial, nuclear, and dietary interactions that modify longevity. *PLoS Genet.* 10, e1004354.

Preclinical Mouse Cancer Models: A Maze of Opportunities and Challenges

Chi-Ping Day,¹ Glenn Merlino,^{1,*} and Terry Van Dyke^{2,*}

¹Laboratory of Cancer Biology and Genetics

²Center for Advanced Preclinical Research

Center for Cancer Research, National Cancer Institute, NIH, Bethesda, MD, USA

*Correspondence: gmerlino@helix.nih.gov (G.M.), vandyket@mail.nih.gov (T.V.D.)

<http://dx.doi.org/10.1016/j.cell.2015.08.068>

Significant advances have been made in developing novel therapeutics for cancer treatment, and targeted therapies have revolutionized the treatment of some cancers. Despite the promise, only about five percent of new cancer drugs are approved, and most fail due to lack of efficacy. The indication is that current preclinical methods are limited in predicting successful outcomes. Such failure exacts enormous cost, both financial and in the quality of human life. This Primer explores the current status, promise, and challenges of preclinical evaluation in advanced mouse cancer models and briefly addresses emerging models for early-stage preclinical development.

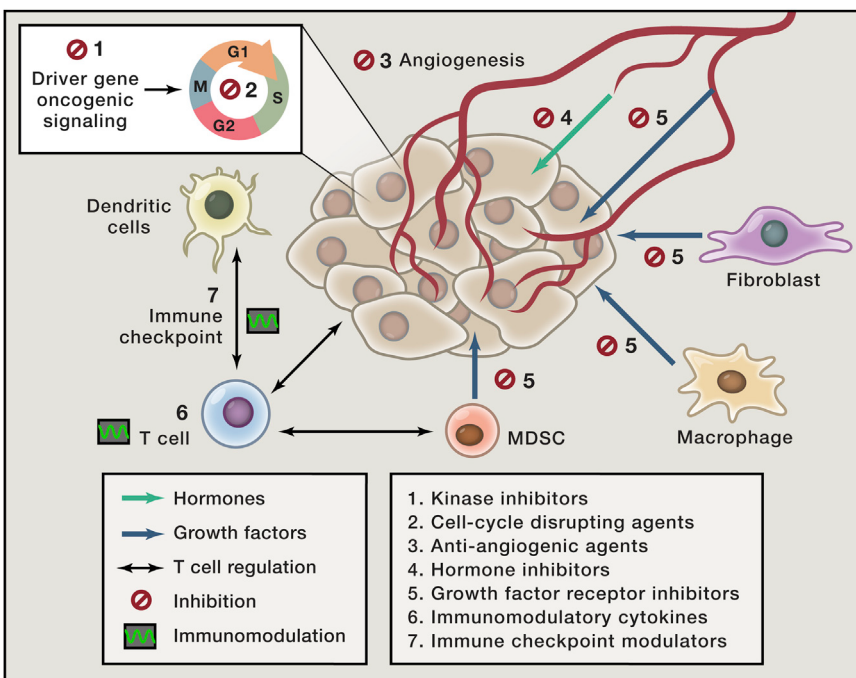
Explosion of Cancer Therapies and Challenges to Clinical Success

Ever-increasing knowledge of cancer biology has yielded countless possibilities for diagnostic and therapeutic strategies (Figure 1), while at the same time revealing enormous disease complexities that challenge clinical success. Such challenges include tumor microenvironment complexities, intra- and inter-tumor molecular and biological heterogeneity, systemic and tumoral immune and metabolic response heterogeneity, and the ability of drug-resistant stem-like cancer-initiating cells to repopulate treated cancers (Pattabiraman and Weinberg, 2014). Too often, experimental targeted therapies designed to assimilate known disease complexity have proven ineffective, only to highlight the limitations in our understanding. In contrast to most experimental targeted therapies, encouraging advancements have been made using a number of cell-based and targeted immunotherapies, which have produced sustained responses in patients (Page et al., 2014). However, only a fraction of patients respond to these therapies.

Over the last decade, cancer classification has shifted from relying solely on histopathologic properties to including key molecular attributes that can predict therapeutic outcomes. That certain molecular aberrations are targets for effective therapy first led to clinical practice in 1995 after a leukemia (APL) bearing the PML-RAR α translocation was shown to be sensitive to retinoic acid (tretinoin) (Quignon et al., 1997), which targets the RAR α component to effect leukemic cell differentiation. Soon thereafter, Herceptin (a Her2 inhibitor) was approved for treating Her2+ breast cancer (1998), and Gleevec (a BCR-ABL inhibitor) was approved for CML treatment (2001). These highly effective drugs rapidly became the standard of care. Although these successes establish the promise of targeted therapies, most attempts to attain similar results targeting known molecular drivers have failed, and the reasons are often elusive because of human research limitations. Some general principles have been recognized that emphasize the need for preclinical platforms approx-

imating human cancers. For example, in each of the noted successes, single potent cancer drivers present in a significant fraction of patient malignancies were targeted; however, when a minor fraction of patients are responsive, all-comer clinical trial data may mask the responders. This was first demonstrated in non-small-cell lung cancer (NSCLC) patient trials that initially failed to show significant responsiveness to EGFR-targeted tyrosine kinase inhibitors; however, the ~10% of patients whose tumors actually harbored activating EGFR mutations were uniquely sensitive (Lynch et al., 2004; Paez et al., 2004). Now, screening of lung cancers for such mutations prior to therapy is routine practice. Lung cancer is the most prevalent US cancer; if limited to clinical trials, accurate identification of therapies effective in a fraction of less-common cancer types may not be possible. Nonetheless, when a specific target was known, stratification of patients has identified additional effective therapies, such as inhibitors for BRAF mutant melanomas and ALK translocation-positive NSCLCs (Pagliarini et al., 2015). Unfortunately, patients treated with single targeted therapies inevitably relapse with cancers that are resistant to the original drug.

Another challenge in targeting single drivers is the feedback response upon molecular network disruption that prevents efficacy or causes increased severity. Understanding such molecular responses can aid in the discovery of more effective combination therapies. In addition, unbiased molecular queries are showing promise in identifying signatures that correspond to prognosis and/or therapeutic outcomes. For example, in some cases, unique transcriptome signatures stratify cancers into distinct therapeutic and/or prognostic categories and thus improve patient management (e.g., Garraway, 2013). Thus far, this approach has been used primarily for determining which patients require aggressive chemotherapy treatment, hence reducing the frequency of over-treatment. Oncotype DX and FDA-approved MammaPrint tests, both based on distinguishing transcriptome signatures, are now utilized in the clinic to identify the low risk breast cancer patients to be excluded from aggressive treatment.



T cells or PD-L1 in cancer cells). The immunosuppressive environment can be reversed via treatment of immunomodulatory cytokines (6, modulator sign; e.g., IL-2, IL-15) or immune checkpoint inhibitors (7, modulator sign; e.g., anti-CTLA-4, anti-PD-1, or anti-PD-L1), resuming anti-cancer activity of T cells. Right inset: targeting agents. (Artwork adapted from design by Jonathan Marie).

Yet, accuracy is not optimal, and numerous challenges currently prevent broad implementation of molecular signature diagnostics ([van't Veer and Bernards, 2008](#)). Additionally, the hope is that molecular signatures can be identified via unbiased compound or molecular screens that will dictate specific effective treatments even when the targets are unknown.

Thus, although clearly impactful, the use of cancer molecular constitution to guide clinical practice is in its infancy, and research to identify parameters that hone specificity and improve accuracy is ongoing. If confined to human research, achieving maximum effectiveness is likely impossible due to low frequencies of each molecular subtype within most cancers and limitations associated with clinical trials. More challenging is understanding the impact of complex and varied inherited genetic constitution on clinical outcomes with subsequent conversion to clinical practice ([Hood and Friend, 2011](#)). In this regard, the sophistication of complex trait evaluation in mice using the collaborative and diversity crosses may offer a path to discovery ([Churchill et al., 2004; Svenson et al., 2012](#)).

The above summary provides only a cross-section of the therapeutic and diagnostic possibilities currently under investigation, and the reader is referred to current review articles for more comprehensive information ([Chin et al., 2011; Hood and Friend, 2011; Yap et al., 2013](#)). Ultimately, the current limitation to improving cancer patient care within reasonable timeframes may not be the availability of potentially efficacious therapies; rather, a major blockade is the lack of a fully developed and integrated set of reliable preclinical technologies that can navigate complex variables in therapeutic responses and diagnostic ac-

Figure 1. Targeting the Tumor and Its Microenvironment

Genetic alterations produce oncogenes that drive signaling pathways in cancer cells facilitating survival and growth. However, tumor cells also cooperate with stromal cells, including vessels, fibroblasts, and various immune cells, to acquire growth factors, an energy supply and protection from host defenses. These key autonomous and stromal mechanisms constitute potential therapeutic targets both locally, and for immune cells also in the circulating blood and distant immune organs, as shown by indicated numbers. (1) Cancer cell growth driven by an aberrant kinase ("Driver Gene") can be targeted by small-molecule inhibitors. (2) Oncogenic signaling promoting uncontrolled cell cycling can be disrupted (e.g., anti-metabolites, anti-microtubule agents, DNA-damaging agents). (3) Tumor growth requires development of new vasculature for enhanced nutrient demands, which can be blocked by anti-angiogenic agents. (4 and 5) Growth of cancer cells stimulated by release of either host-derived hormones (4, green arrow) or growth factors (5, blue arrows from blood vessels, fibroblasts, macrophages, and myeloid-derived suppressor cells [MDSC]) can be targeted by hormone inhibitors (e.g., anti-hormones or biosynthesis inhibitors) or growth factor receptor inhibitors, respectively. (6 and 7) Tumor cells can shift the inflammatory response to an immunosuppressive mode (e.g., activation of CTLA-4 and PD-1 in

accuracy. To optimally develop efficacious therapies, preclinical research must utilize a diversity of models that collectively incorporate the biology and genetics dictating therapeutic outcomes for specific cancers, and yet achieve sufficient throughput. Here we summarize the value and constraints of mouse cancer models, highlight recent progress indicating promise, summarize non-mammalian and ex vivo preclinical models, and explore the needs for, and challenges to, developing robust multi-faceted preclinical platforms for routine use.

Mouse Cancer Models in Preclinical Research

Murine cancer models designed to capture the complexities of human cancers currently offer the most advanced preclinical opportunity for navigating diverse mechanisms that provide rationale for therapeutic development ([Van Dyke and Jacks, 2002](#)). One approach is to probe pathobiology mechanisms to design effective treatments by perturbation with molecularly targeted therapies ([Olive and Tuvesson, 2006](#)). Additionally, the models are being used/developed as preclinical efficacy determination platforms to guide clinical trial designs ([Singh et al., 2012](#)). However, the application of complex cancer models to clinical research directives is an emerging science, currently executed in individual settings and with limited resources. Significant research, ideally in a team-directed, multi-institutional effort, is required to hone existing technologies into integrated preclinical workflows to optimally accelerate positive clinical outcomes.

A variety of approaches to mouse cancer modeling are now available ([Figure 2](#)), and each has strengths and weaknesses ([Table 1](#)). Here, we address the limitations of standard Cell

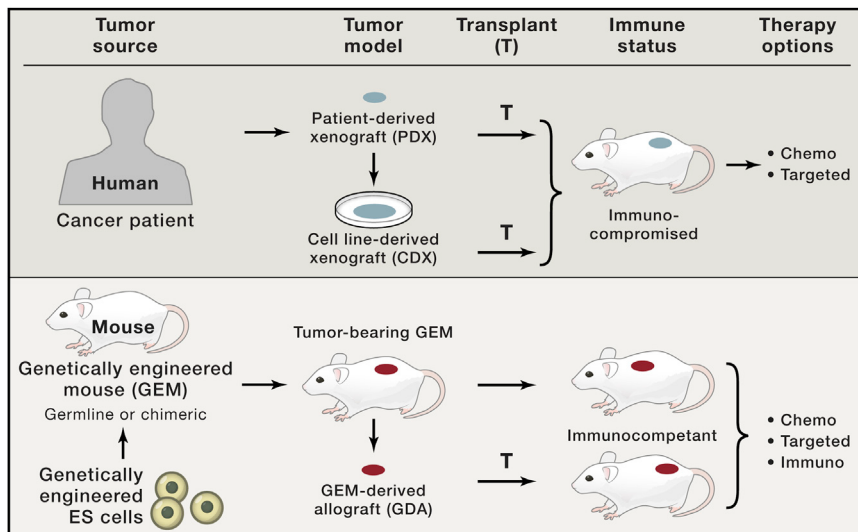


Figure 2. Current State of Preclinical Cancer Modeling

Preclinical mouse models can be defined according to the species source of tumor, how it is created, and how it is manipulated. (Upper panel) Tumors derived from human patients, and other non-murine species, can be directly transplanted into immunocompromised mice to form patient-derived xenograft (PDX) models; PDXs can also be established from circulating tumor cells (CTCs). Alternatively, these same tumors can produce established cell lines maintained in vitro as cell cultures, and transplanted into immunocompromised mice to form cell line-derived xenograft (CDX) models. Since the hosts of these tumors need to be immunocompromised, they are useful only for testing the efficacy of chemotherapeutics (Chemo) and targeted small-molecule inhibitors (Targeted). Xenograft models derived from canine patients also belong to this category, but are not shown here. (Lower panel) Mice can be engineered to generate tumors of human relevance with respect to histopathology, etiology, and molecular wiring. Offspring of such genetically engineered mice (GEM) can serve directly as pre-

clinical models themselves, in which case the tumor is treated at its precise point of origin. Notably, model building can be streamlined by using non-germline approaches, one of which is to genetically modify ES cells and study the arising chimeric mice without time-consuming breeding schemes. Alternatively, tumors harvested from GEMs can be transplanted and expanded into fully immunocompetent syngeneic hosts, forming GEM-derived allograft (GDA) models. Syngeneic models allow preclinical studies of not only chemotherapeutic and small-molecule drugs, but also of all varieties of immunotherapeutic agents (Immuno).

line-Derived Xenograft (CDX) models, describe genetically and biologically engineered mouse cancer models [Genetically Engineered Mouse (GEM), GEM-Derived Allograft (GDA), Patient-Derived Xenograft (PDX) models], review values and constraints, and highlight recent progress. Thus far, results indicate promise in understanding cancer pathobiology and in the enhancement of clinical efficacy prediction, but also underscore the need for further development to achieve consistent reliability.

Traditional Mouse Models in Therapeutic Development

Historically, preclinical mouse models have co-evolved with cancer therapy development (Figure 3). The earliest models were built through transplantation of murine tumors into immunocompetent host mice (DeVita and Chu, 2008; Talmadge et al., 2007). These early mouse-in-mouse isograft models served as workhorses for drug screening during the 1960s and 1970s, and were successful in identifying a number of effective cytotoxic drugs such as vincristine and procarbazine (DeVita and Chu, 2008). During the 1980s, researchers explored mechanisms of metastasis using selected murine and human tumor cell lines. A series of investigations by Fidler and colleagues demonstrated that metastasis is not random but site-selective (Fidler and Hart, 1982), and that metastatic patterns are injection site-dependent, supporting the establishment of “orthotopic” models (Talmadge et al., 2007). Since then, cancer therapeutic development has relied upon the more tractable CDX transplantation models, in which tumors develop after subcutaneous injection of in vitro-established human cancer cells into immunocompromised mice (Figure 2). The cell lines have been selected over many passages for rapid 2D growth on plastic in serum-containing media. The NCI60 cell line panel (DeVita and Chu, 2008; Talmadge et al., 2007) provided a valuable resource from which most CDXs were generated, and recent efforts have greatly expanded the repertoire (Reinhold et al., 2015).

These models are easily established in a wide variety of laboratory settings and have been successfully used to identify an abundance of cytotoxic drugs leading to chemotherapy treatments that still dominate clinical cancer management (Figure 3).

Unfortunately, CDXs have failed to predict human efficacy for most therapies targeted to cancer-driving proteins (Johnson et al., 2001), as evidenced by the low FDA approval rate of 5%–7% for targeted therapeutics (Sharpless and Depinho, 2006). With an average time from discovery to clinical practice of 12 years, at an average estimated cost of \$0.5–\$2.0 billion (Adams and Brantner, 2006) and an immeasurable human price, this low yield forestalls even a goal to chronically manage, rather than cure, cancers. The observation that most cancer therapeutics fail in clinical phase II and III efficacy assessment indicates that current standard preclinical practice inadequately addresses complex challenges to successful treatment, such as host immune responses, cancer heterogeneity, and drug resistance. Consequently, the system cannot be used to optimize a multitude of variables known to influence therapeutic outcomes, such as combinatorial therapies, dosing schedules, and drug delivery methods (Al-Lazikani et al., 2012). CDXs continue to be valuable in identifying non-targeted cytotoxic agents and in primary assessment of drug toxicity (Teicher, 2006), for analyzing resistance mechanisms (Garraway and Jänne, 2012) and in triaging potentially effective targeted therapies for evaluation in more representative models.

Mouse Models Designed after Patient Cancers

Mice and humans are believed to have diverged from each other ~87 million years ago (Bailey et al., 2013), so naturally there are numerous significant similarities between the two species, and also many marked disparities, including differences in immune systems and drug metabolism. Based on the premise that many cancers have been cured in mice and not in people, many argue

Table 1. Comparison of Clinical and Preclinical Model Properties

	Immune Status of the Host	Micro-environment Context	Human Relevance	Tissue Availability	Disease Complexity	Experimental Robustness	Initiation/Progression	Feasibility in Pathway Engineering	Cost
Clinical Trials	Functional	Natural	Standard	Highly Limited	High	Low	Intact	Irrelevant	Very High
Cancer Cell Line-Derived Xenografts (CDX)	Deficient	Xenogenic	Situational* (passage number dependent)	Expandable	Low	High	Bypassed	Yes	Low
Patient cancer-Derived Xenografts (PDX)	Deficient	Xenogenic	High	Expandable/ Limited	Moderate	High	Bypassed	No	High
Genetically Engineered Mice (GEM)	Functional	Natural	High/ Variable (model dependent)	Limited	High	Moderate/ Variable	Intact	Yes	High
GEM-Derived Allografts (GDA)	Functional	Allogeneic	Low/ Variable	Expandable	Moderate	High	Bypassed	Yes	Moderate

*CDX models have been shown to be limited as predictors of clinical outcome. However, they continue to be valuable for evaluating resistance mechanisms, for identifying non-targeted cytotoxic agents, for assessing drug toxicity, and as a platform to triage potentially effective targeted therapies. In general, the longer cells are in culture, the further they drift from normal tumor evolution, and the less relevant they become.

that mice are inappropriate for use in therapeutic development (Leaf, 2004). However, it is critical to understand that “cures” have been attained only in CDX models, thus dismissal of *all* mouse cancer models as irrelevant is unwarranted. Human cancers are enormously complex, and their evolutionary etiology generates vast diversity among and within them, thus challenging the attainment of successful treatments. However, as knowledge of cancer complexities has increased, so has the ability to design mouse models that better represent cancer patients. PDX and GEM models develop tumors with the greatest similarity to human diseases yet achieved, and the past 5 years have seen an increase in their employment in preclinical research. As with all models, each approach has its strengths and limitations (Table 1). Early studies suggest promise for improved guidance in the development of successful clinical treatments (Table 2), and yet also emphasize the need for further scrutiny and refinement. The following provides a balanced consideration of model advantages and limitations, their ramifications in obtaining optimally accurate preclinical data, and the logistical requirements for achieving efficiency, accuracy, and reproducibility.

Patient-Derived Xenograft Models

Relative to CDX models, immunocompromised mice bearing subcutaneous surgically derived clinical tumor samples (PDX models) are better aligned with human disease, since intact tissue that preserves tumor architecture is transferred directly to recipient mice and not compromised by *in vitro* adaptation (Figure 2). PDXs are the only models harboring bona fide tumor targets directly from the patient, and hence their use in drug discovery is expanding rapidly. Promise for such models, first developed by Fiebig (Fiebig et al., 1984), was demonstrated when chemotherapeutic agents, such as alkaloids and anti-metabolites, were shown to elicit similar responses in mice and patients (Mattern et al., 1988). In contrast, a study of responses to numerous cytotoxic agents in NCI60-based CDX models showed that the predictive value for efficacy was much less impressive (Johnson et al., 2001). Unfortunately, early studies utilizing PDXs were limited by difficulties in collecting clinical samples and in achieving sufficient take rates.

The recent resurgence of PDX model use for therapeutic evaluation has been fueled by significant improvements in clinical sample access and transplantation technology. Cancers established as PDXs can, in early passages, retain the stromal composition and histologic and molecular heterogeneity characteristic of those in patients (Hidalgo et al., 2014; Tentler et al., 2012). Since these properties critically impact therapeutic responses and biomarker specificity, PDX models provide a preclinical venue for addressing some of the most challenging barriers to successful patient therapy. Furthermore, human target specificity allows for direct evaluation of lead human-specific therapeutics, such as antibodies, in clinical development.

Methodologies for PDX establishment and characterization are detailed elsewhere (Hidalgo et al., 2014; Tentler et al., 2012; Zhang et al., 2013). For some cancers, such as certain melanomas, lung, and colorectal cancers, transplant take rates can reach ≥ 75%, and the time required for tumor growth can be as little as 2–4 months. However, these attributes vary widely depending on sample type and amount (e.g., fresh biopsy tissue, fine needle aspirate, circulating tumor cells), tumor origin, molecular properties, and recipient strain (see *Supplemental Information*).

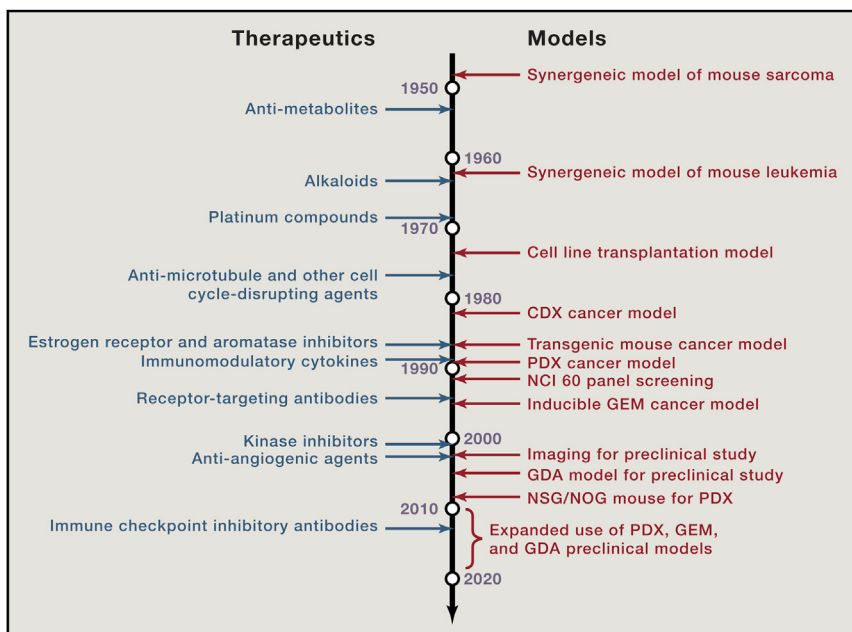


Figure 3. Timeline of Key Preclinical Cancer Model Developments since 1950

As the conceptual targets of cancer treatment progressed from actively dividing cells to oncogenic signaling and immune checkpoints, pre-clinical models (right side) and cancer therapies (left side) co-evolved accordingly. This evolution was highly dependent on technical advances, resulting in waves of activity. For example, recent development of fully immunocompromised mice and diverse syngeneic GEM models has significantly promoted PDX and GDA models, respectively, for preclinical cancer studies (the bracket).

Consequently, some cancers, such as neuroendocrine, luminal ER+ breast, and prostate cancers (Rosfjord et al., 2014) are under-represented. Notably, PDX engraftability appears to significantly correlate with clinical aggressiveness (Ilie et al., 2015).

Relative to subcutaneous transplants, cancers orthotopically transferred into organs of origin are more likely to maintain tumor microenvironment characteristics that impact therapeutic outcomes (Talmadge et al., 2007). However, orthotopic PDX production is technically challenging, and, for most cancer types, tumor growth and responses must be monitored via expensive and often laborious longitudinal imaging. Thus, preclinical therapeutic studies currently exclusively utilize subcutaneous models.

Production of PDX cohorts is by serial tumor transplantation, and, given the likelihood of change with each passage, therapeutic studies are most representative in low-passage models. Additionally, human stromal components are maintained for only 2–3 passages, with mouse stromal elements becoming dominant thereafter (Rosfjord et al., 2014). Unfortunately, if limited to early passage use, each model represents a limited resource. Hence, most preclinical studies utilize models that have been expanded, banked, and developed into significantly sized cohorts. The extent of sacrifice in accurately predicting efficacy is presently undefined and likely depends on the mechanism of therapeutic activity. As such, in propagating PDXs, parental tumor traits should be routinely monitored, and deviations must be considered in interpreting therapeutic and biomarker data.

To circumvent immune rejection, human cancers must be transplanted into immunocompromised mice. Commonly used recipients, such as nude, SCID, and NOD/SCID strains, vary in the extent of immune impairment (detailed in *Supplemental Information*). IL-2R γ -deficient NOD/SCID mice (NSG and NOG strains) are the most severely impaired, and often yield improved take rates. Critically, the requirement for immunocompromised

hosts precludes assessment of arising therapies designed to modulate immune function (e.g., immune checkpoint inhibitors α -CTLA-4, α -PD-1, α -PD-L1). Moreover, therapeutic responses in general are likely influenced by preexisting cancer-dependent immune phenotypes and immune responses elicited upon therapy-induced tumor perturbation (Zitvogel et al., 2008). The extent to which compromised immune systems limit predictive value for a given therapeutic will be determined as comparisons between PDX and clinical outcomes are expanded. Technologies to “humanize” the mouse immune system by transplanting purified human CD34 $^{+}$ hematopoietic stem cells into myeloablated NSG/NOG recipients (e.g., “BLT” mice: <http://jaxservices.jax.org/invivo/humanized-BLT-mice.html>) and other chimeric strategies have been developed (Legrand et al., 2009; Shultz et al., 2014). However, the high cost of recipient mice, limitations on human bone marrow acquisition, engraftment variability, and technical demands currently preclude use of these models in preclinical therapeutic discovery.

Despite the challenges to routine preclinical application, several PDX studies have proven effective in paralleling human outcomes (Malaney et al., 2014), in exploring drug resistance mechanisms (Das Thakur et al., 2013) and in identifying targets for second-line treatment (Girotti et al., 2015). Programs are also underway to employ PDX models in individualized precision cancer care. To date, this approach has been most successfully applied to pediatric patients with advanced sarcomas who have demonstrated the predicted response, sometimes to drugs not previously associated with this indication (Tentler et al., 2012). Patient-specific studies are currently limited by expense and relatively long and unpredictable times for establishing test animals. Since current clinical trials generally involve patients who have undergone prior failed treatments, results may not always be obtainable in a beneficial timeframe.

Genetically Engineered Mouse Cancer Models

Of all murine cancer models, GEMs provide the most complete representation of cancer development; cancers develop from initiation through progression, co-evolve with intrinsic stroma, and possess an intact immune system (Figures 1 and 2). However, GEM models are the most challenging to work with effectively, and species differences must be carefully considered in

Table 2. Representative Clinically Relevant Mouse Trials

Trial Design	Cancer Type	Model Type	Engineered Drivers	Drugs/ Treatment	Significance	Relevant Publications
Preclinical	Hematopoietic (APL)	GEM	PML-RAR α fusion PLZF-RAR α fusion	Retinoic acid	Demonstrated the efficacy of retinoic acid plus As ₂ O ₃ in specific APL subtypes, validated in clinic	(Ablain and de Thé, 2014; Pandolfi, 2001)
Preclinical	Pancreas (Neuro-endocrine)	GEM	RIP1-Tag2	Sunitinib	Demonstrated the efficacy of Sunitinib plus Imatinib, validated in clinic. FDA approved for pancreatic cancer treatment in 2011.	(Pietras and Hanahan, 2005; Raymond et al., 2011)
Preclinical	Medulla-blastoma	GEM	Ptc1 ^{+/−} P53 ^{−/−}	GDC-0449 (SMO inhibitor)	Demonstrated the efficacy of an Shh pathway small molecule inhibitor, validated in clinic	(Romer et al., 2004; Rudin et al., 2009)
Preclinical	Pancreas (Neuro-endocrine)	GEM	RIP1-Tag2	Erlotinib Rapamycin	Demonstrated efficacy of combining drugs targeting EGFR and mTOR	(Chiu et al., 2010)
Co-clinical	Pancreas (PDA)	GEM	LSL-Kras ^{G12D} LSL-Trp53 ^{R172H} Pdx-1-Cre	Gemcitabine Nab-Paclitaxel	Provided mechanistic insight into clinical cooperation between Gemcitabine and Nab-Paclitaxel	(Frese et al., 2012; Goldstein et al., 2015)
Co-clinical	Pancreas (PDA)	GEM	LSL-Kras ^{G12D} LSL-Trp53 ^{R172H} Pdx-1-Cre	CD40 monoclonal antibody Gemcitabine	Demonstrated that targeting stroma was effective in treatment of metastatic PDA	(Beatty et al., 2013)
Co-clinical	Lung (NSCLC)	GEM	KRAS ^{G12D} p53 ^{f/f} Lkb1 ^{f/f}	Selumetinib Docetaxel	Validation of improved response of adding Selumetinib to Docetaxel treatment	(Chen et al., 2012; Jänne et al., 2013)
Co-clinical	Lung (NSCLC)	GEM	EML4-ALK fusion	Crizotinib Docetaxel Pemetrexed	GEM model predicted clinical outcome of drug combinations	(Chen et al., 2014; Lunardi and Pandolfi, 2015)
Co-clinical	Various Sarcomas	PDX	N/A	Various chemotherapies	PDX testing predicted clinical outcome of drug combinations	(Stebbing et al., 2014)
Postclinical	Ovarian (SEOC)	GDA; PDX	RB/p53-deficient BRCA1/2-deficient	Olaparib Cisplatin	Validation of treatment efficacy in BRCA mutant tumors in both GDA and PDX models	(Kortmann et al., 2011; Szabova et al., 2014)
Postclinical	Pancreas (Neuro-endocrine)	GDA	RIP1-Tag2	Anti-VEGFR1 and anti-VEGFR2 antibodies	Identification of mechanisms of resistance to anti-angiogenic therapies	(Casanovas et al., 2005)
Biomarker	Lung (NSCLC)	GEM; Carcinogen-induced	Various Models	N/A	Used in-depth quantitative MS-based proteomics to profile plasma proteins	(Hanash and Taguchi, 2011)
Biomarker	Pancreas (PDA)	GEM	Kras ^{G12D} Ink4a/Arf ^{f/f} Pdx-1-Cre	N/A	Used in-depth proteomic analyses to identify candidate markers applicable to human cancer	(Faca et al., 2008)

experimental designs and interpretations. Extensive experience and infrastructure are required to ensure the use of optimally accurate models and to achieve sufficiently populated well-controlled preclinical studies. Yet, GEM cancer models provide the only opportunity to evaluate drug delivery, therapeutic response, and biomarker expression for cancers evolving within their natural microenvironment (autochthonous cancers). These complex dynamic processes contribute to overall disease properties, and in particular, constitute a source of the inter- and intra-tumoral heterogeneity that challenges successful therapeutic development. Additionally, the accuracy of some therapeutic interventions, such as those targeting the immune system, may depend on the constitution of evolutionary, rather than transplanted, disease. Indeed, overall, GEMs and GEM-derived models are currently the *only* preclinical platform for evaluation and optimization of immunomodulatory therapies. Although some immune properties differ in mouse and human, there is significant conservation (Bailey et al., 2013); moreover, many differences can be managed via data interpretation or minimized by using genetically engineered “humanized” models (Scheer et al., 2013). Finally, autochthonous GEMs are the only viable models for evaluating prevention therapies.

Several reports show that well-designed GEM studies can contribute to improved clinical trials (Table 2), not only in identifying potentially efficacious therapies but also in predicting both positive and detrimental effects in molecular subclasses. A major power of GEM approaches is in the flexibility to create models with precise molecular specificity. With increasing sophistication, several strategies (summarized below and detailed elsewhere [Abate-Shen et al., 2014]) have been employed over the past three decades to significantly enrich our understanding of cancer mechanisms. A plethora of genes frequently altered in human cancers have been validated as disease drivers in GEMs, thereby facilitating the evaluation of cancer evolutionary mechanisms and kinetics, susceptible cell and molecular targets, relative cancer cell and microenvironment roles, and mechanisms of invasion and metastasis. Indeed, entire natural disease histories can be mapped (Stiedl et al., 2015; Van Dyke and Jacks, 2002).

In the process of basic discovery, countless GEM cancer models representing a variety of histiocytic cancer types driven by multiple independent drivers have been produced, and many are currently used in preclinical evaluations. Although *no model* can perfectly capture the human condition, several GEM models tractable for preclinical studies develop cancers with remarkable molecular and pathologic similarity to their human counterparts. However, since most established GEMs were created to address basic mechanisms, many do not accurately model human disease and/or are intractable for effective preclinical evaluation. Furthermore, each engineering approach can elicit untoward anomalies. Such circumstances can be accommodated in the interpretation of mechanistic studies, but are the basis for exclusion of many models for effective pre-clinical research. Thus, choosing appropriate models as subjects for preclinical discovery requires a deep understanding of cancer biology and genetics *and also* of engineering modalities. The following provides a reasonable guide for optimizing the value of GEM-based preclinical platforms.

Germline GEMs

An extensive array of technologies is employed to engineer the mouse germline with great precision. By editing the genome of embryonic stem (ES) cells or zygotes, mice can be programmed for cell-type-specific disruption of tumor suppressor genes via direct mutation or expression of interfering non-coding RNAs (RNAi) (Walrath et al., 2010) and for oncogene expression at physiological or cancer-analogous levels. Furthermore, mice can be “humanized” by engineering the expression of drug targets in relevant cell types (Scheer et al., 2013) so that human-specific targeted therapies, such as antibody-based drugs, can be tested in GEM models. While traditional methods for constructing locus-specific genetic changes require significant lead times for engineering, the recent development of rapid sequence-targeted approaches (Mou et al., 2015) has significantly reduced this time to weeks instead of many months. In particular, clustered regularly interspaced short palindromic repeats (CRISPR)/Cas9 technology, which is efficient and versatile, is accelerating germline engineering and also facilitating rapid somatic engineering (see below).

Depending on the strategy, expression of an engineered “event” can be constitutive or inducible, although gene induction with cell-type and temporal specificity provides the best possibility for accurately modeling disease development. Inducibility is achieved by combining cell-specific expression of transcription factors (e.g., doxycycline-modulated tet-transactivators) or recombinases (Cre-lox or Flp-FRT) with cognate *cis* elements linked to a target gene, or by expressing proteins fused with a hormone-responsive domain (e.g., the tamoxifen-inducible estrogen receptor domain) (see *Supplemental Information*). When multiple distinct inducible systems are combined within the same cancer model, cancer-specific mutations can be induced sequentially in order to map and emulate cancer evolution (e.g., [Young et al., 2011]) and thus to generate increasingly relevant preclinical models. Reversible inducibility can be achieved with each of these technologies, although small molecule-mediated modulation of transcription factors and hormone-responsive domains are the most tractable for toggling expression on and off (Abate-Shen et al., 2014; Texidó, 2013). This approach facilitates the identification of events required to sustain tumor growth (“oncogene addiction”) (e.g., Soucek et al., 2008) and thus of potential therapeutic targets (e.g., Kwong et al., 2012). Tumor responses to the shutdown of oncogenes or restoration of functional tumor suppressors within tumors, or appropriate effector cells, indicate the potential efficacy of targeted therapies, while genetic ablation in the entire animal predicts the overall toxic effects of specific inhibitors. However, since off-target effects will not register in this approach, results only indicate whether a given therapy is *potentially* efficacious.

A critical, often overlooked, consideration when building GEM cancer models is the incorporation of known environmental etiologies. However, there are notable examples wherein certain environmental factors were validated as etiologic agents and thus produced representative cancer models, including HPV E6/E7-induced cervical cancer (Riley et al., 2003), UV accelerated melanomas (BRAFV600E [Cao et al., 2013], mutant HRAS [Kannan et al., 2003], and HGF/MET [Noonan et al.,

2001] models), and *Helicobacter*-fueled gastrointestinal cancers (Rogers and Fox, 2004). Exposure of GEM cancer models to environmental mutagens can be used to approximate the mutation load of many human cancers (e.g., Westcott et al., 2015), which influences therapeutic outcomes such as in drug-resistant relapse and neoantigen load-dependent immunomodulation.

The extent to which findings in GEMs extend to patients depends on engineering mice based on our understanding of human cancer etiologic drivers, cellular origins, heterogeneity, pathogenesis, and clinical properties. To recapitulate human cancer development, clinically relevant driver gene(s) or pathways must be perturbed in relevant target cells. For adult cancers, gene expression should be targeted to adult, rather than developing, organs. Furthermore, for optimal modeling, cancers should progress in a relevant sequence, since the order of events impacts properties of evolving tumors. Ideally, both initiation and progression to aggressive cancer should be evaluated using individual and relevant combinations of molecular aberrations thought to be causal in humans. High phenotypic penetrance and consistency among animals within a lineage are essential for tractability.

The accuracy of disease modeling depends on *actually achieving* the specificity envisioned in experimental designs, which is not always realized because of technical limitations and/or gaps in current knowledge. Of course, engineered sequences must be validated, but it is also critical that expected transcriptional specificities be confirmed. Unless targeted to specific genomic locations, transgenes insert randomly, and expression can be dramatically altered depending on insertion sites. Furthermore, transgenes may not carry all necessary regulatory signals. Hence, several founder lines should be established and fully characterized before selecting accurate representative lines for modeling cancers. Even targeted genetic changes have the potential to alter gene regulation. Thus, specificity, levels, and range of expression must be evaluated for each model; aberrant expression usually alters disease and can also yield ectopic phenotypes that hinder tractability and invalidate data. Yet, a surprising number of existing engineered strains, including those driving inducible expression, are not fully characterized. Hence, when choosing cancer models for preclinical studies, it is essential that expression and disease patterns are well established and accurately represented (see Supplemental Information).

Non-Germline GEM Models

While autochthonous GEM models have great utility, most are not tractable for large-scale screening of multiple anti-cancer drug candidates due to high cost, long timelines, extensive complex breeding, and/or difficulties in obtaining synchronous tumorigenesis. Preclinical analysis of metastatic lesions is particularly challenging; primary tumors arise stochastically with no reliable timetable, as in humans, and multiple tumors often develop. Thus, extensive longitudinal tomographic imaging is required to enroll mice bearing similarly sized tumors for therapeutic evaluation (e.g., Weaver et al., 2012). Such procedures require specialized expertise and can be too expensive and time-consuming for first-line drug screening. Several strategies to produce “non-germline” GEMs have been developed that bypass breeding, reduce expense, and, in some cases, improve flexibility, uniformity, and timelines (Heyer et al., 2010).

GEM-Derived Allograft Models. GEM-derived allograft (GDA) models marry the genetic and biologic human cancer similarities of GEM models with the relative ease of transplantation technology of PDXs (Heyer et al., 2010). Without in vitro manipulation, tissue fragments derived from tailor-made GEM tumors are expanded by transplantation, orthotopically or subcutaneously, into immunocompetent syngeneic hosts (Figure 2). Thus, tumors can be banked to facilitate large cohort production, and efficacy studies can be performed in industry-friendly timeframes (~3–8 weeks), allowing for increased throughput. Indeed, a battery of treatments can be evaluated in GDAs prior to (preclinical) or parallel with (“co-clinical”) clinical trials (Table 2). As with GEMs, immune systems are fully functional in GDAs, and interactions among tumor cells and their intrinsic microenvironments are maintained.

GDAs are particularly amenable to the evaluation of metastatic disease, which is responsible for most cancer-related deaths and is rarely assessed preclinically. In GDAs, metastases occur from *single* primary tumors, which can be resected to allow time for metastatic progression (Day et al., 2012). This approach also emulates clinical care standards for many cancers and facilitates comparing therapeutic responses of both primary and metastatic disease derived from the same GEM cancer (Figure 4).

As with PDXs, serial passaging increases the likelihood that tumor properties will deviate from parental samples due to further evolution and/or selection of sub-compartment growth; thus, transplanted tumors should be monitored for molecular and biological similarity to founding tumors. Additionally, since transplanted tumors do not evolve *in situ*, GDAs cannot legitimately be used for prevention studies, and some therapeutic outcomes may differ between autochthonous GEMs and GDAs. Given the potential tradeoff of accuracy for tractability, candidate therapies efficacious in GDAs should be subsequently validated in the original GEM models prior to clinical studies.

Stem Cell-Derived Chimeras and Somatic Models. Mice chimeric for genetically engineered cells are created through implantation of GEM-derived or genetically manipulated ES cells into pre-implantation embryos. Since oncogenic alleles are engineered *ex vivo* in ES cells, many mice with the desired genetic composition can be generated in the absence of complex, laborious, and long-term breeding schemes. The potential value of this approach was first highlighted in the production, analysis, and preclinical evaluation of lung adenocarcinoma (Zhou et al., 2010). Once constructed, ES cells harboring the desired alleles can be derived from blastocysts produced by a penultimate cross. In turn, this bankable resource can be used to generate mice chimeric for mutant and wild-type cells (Premrirut et al., 2011), facilitating conditional RNAi-mediated knockdown of target expression via manipulation of ES cells, which can then be used to generate chimeric mouse cohorts (Dow et al., 2012).

Notably, the advent of CRISPR/Cas9 technology, and with it the ability to perform complex gene editing with relative ease and speed, has dramatically enhanced the value of non-germline GEM approaches. Several groups have precisely modified oncogenes and tumor suppressor genes directly in somatic cells of adult mice, significantly improving the feasibility and flexibility of this genetic engineering approach (Chen et al., 2015; Dow

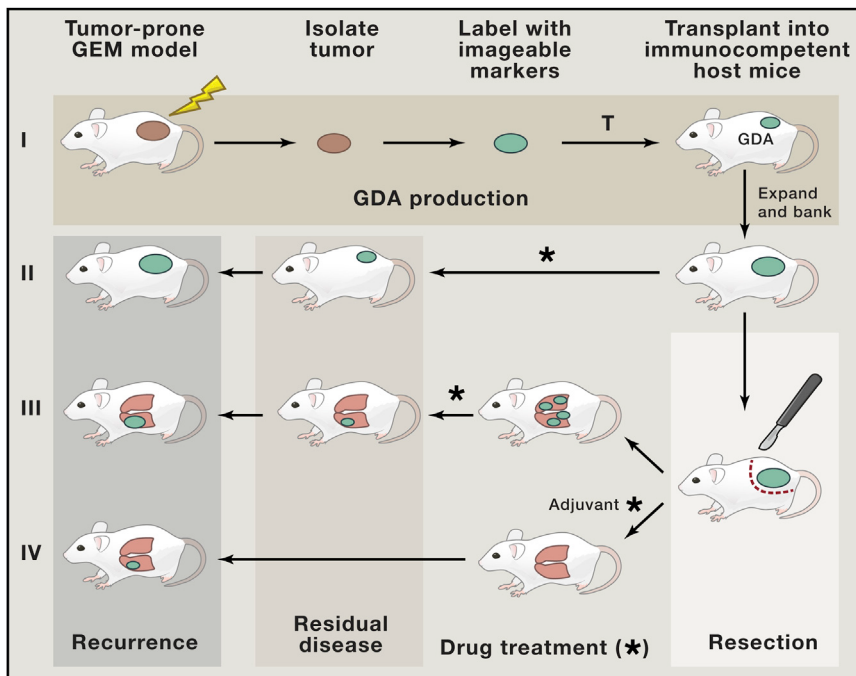


Figure 4. Generation and Application of Metastatic GDA Models

(I) GDAs are derived from tumors arising in mice genetically tailored to produce human-relevant models. Relevance can be further enhanced by including appropriate etiological agents (lightning bolt). Arising tumors are resected, labeled with imageable markers (green), and directly transplanted into fully immunocompetent syngeneic mice at either subcutaneous or orthotopic sites. The imageable markers allow monitoring of tumor growth and drug response, and/or FACS purification for analysis. Once successfully transplanted, GDAs can be expanded for banking and/or preclinical studies. Mice bearing GDAs can be treated directly with individual or combination drugs (*) to study therapeutic efficacy at the “primary” tumor site (II). (III and IV) Alternatively, GDAs can be resected using survival surgery, and treatments focused on metastatic disease, simulating first-line treatment in human patients following primary tumor resection. GDA models allow for interventional treatment of metastatic disease once detected (III), or preventive adjuvant treatment initiated immediately following surgical resection (IV). GDA models are thus well suited for studying primary or metastatic disease, with interventional or preventive approaches using pathway-targeted small molecule and/or immuno-therapeutic agents.

et al., 2015; Maddalo et al., 2014; Platt et al., 2014). These models also better mimic human cancer relative to standard germline GEMs in that tumors typically arise from fewer cells in the context of normal stroma

In a variation of the non-germline GEM approach, genetically engineered stem or progenitor cells can be transplanted into syngeneic mice, where they can home to appropriate tissue targets and become the cells of origin for developing tumors (Heyer et al., 2010). These models are especially amenable for studying hematopoietic cancers, where the stem cells are well characterized and the host can be prepared for receiving transplanted cells by using irradiation to create a favorable niche for the engineered hematopoietic stem/progenitor cells to colonize. Successes have also been reported for other cancers (Heyer et al., 2010).

Logistics for Optimizing Preclinical Studies

Extensive complexities that impede successful drug development in cancer patients dictate that faithful murine cancer models must themselves be complex. Both PDX- and GEM-based models offer this opportunity. However, their very complexity warrants that informative models are generated and characterized with substantial knowledge of cancer mechanisms and modeling limitations, rigorous animal maintenance and production, routine phenotypic and genetic monitoring, appropriate strategies for therapeutic response evaluation, and consideration of multiple variables that impact data interpretation. To achieve routine therapeutic and biomarker development that positively influence patient care, preclinical studies must be (1) well-powered with significant cohort sizes and several evaluation parameters, (2) goal-oriented and efficiently executed, and (3) highly reproducible.

Experimental Considerations

Once models that optimally represent human disease have been selected, clinical relevance relies on experimental parameters that are comparable and/or translatable to human practice. These include, but are not limited to, dosing levels and schedules, drug pharmacology, response evaluation methods, and endpoint choices. Therapeutic agents' pharmacokinetics (PK) and ability to modify targets when known (pharmacodynamics; PD) should be measured in tumor-bearing mice. The fate of administered drugs is largely determined by drug metabolizing enzymes essential for their absorption, distribution, metabolism, and excretion (ADME). Therefore, the differences that exist between the central metabolizing enzymes in mice and humans, the cytochrome P450 (CYP) family, constitute a confounding factor in extrapolating drug PKs and the responses they elicit. Since the maximum tolerated dose (MTD) of many drugs in mice is significantly higher than in humans, it is essential to evaluate efficacy by using doses achievable in patients. However, this is possible only when human PKs are known; for example, for repurposing FDA-approved drugs, for preclinical evaluation of combination therapies that comprise single phase II agents, and for co-clinical experimentation wherein mouse and human evaluations are performed in parallel, such that clinical toxicity results are available. Even when appropriate human dosing is known, there is no simple formula for approximating comparable doses to achieve the same PK in mice, and instead experimental determination is required (Sparreboom et al., 1996). Yet, when evaluating numerous agents, this approach is not possible; rather, subsequent coordination of clinical results and further preclinical dose escalation experiments are needed for optimal response assessment.

In an effort to apply a genetic solution to the PK problem, a number of humanized CYP GEMs have been developed (Gonzalez, 2004; Scheer and Wolf, 2014). Despite these advances, the humanized alleles have not yet been incorporated into GEM cancer models or PDX recipients. Such an undertaking will require significant resources, substantial time, and community effort to generate and evaluate revised models. Nonetheless, the investment will be worthwhile if the gap between laboratory mice and patients is narrowed.

The choice of preclinical experimental endpoints to determine therapeutic responses is also critical for achieving outcomes most representative of those in patients (Talmadge et al., 2007). In prevention studies, efficacy is based on disease-free or minimized status. For intervention therapy, efficacy is justified by overall survival and should not be judged solely on tumor growth inhibition. The importance of survival endpoints is highlighted by a pancreatic cancer clinical trial designed based on short-term GEM studies demonstrating reduced tumor volumes in response to sonic hedgehog pathway inhibition combined with gemcitabine (standard of care) compared to gemcitabine alone (Olive et al., 2009). Unfortunately, the trial terminated early due to increased disease dissemination and poor patient survival. However, subsequent survival studies in the GEM model replicated the clinical result, demonstrating that initial drug effects did not predict survival outcomes. Hence, the model appropriately predicted patient responses, but only with a meaningful endpoint (Couzin-Frankel, 2014).

Tumor growth and therapeutic responses in subcutaneous transplant models, such as CDXs, PDXs, and GDAs can be monitored by standard caliper measurement. Tumor growth in autochthonous and orthotopic transplant models (other than skin and breast models) and in all metastatic models must be monitored by longitudinal imaging strategies (Wang et al., 2015). High-resolution 3D images are compiled from sectional images generated by tomographic scanning of signals from X-ray (CAT), magnetic field-excited atoms (MRI), or injected radioactive tracers (SPECT; PET) (Supplemental Information). Tomographic imaging requires specific expertise for accurate execution and is relatively expensive and time-consuming. Optical imaging, which detects visualized wavelengths generated from excited fluorescent chromophores (e.g., jellyfish GFP) or firefly luminescent reactions (e.g., luciferase), can be employed for detection in real-time and is cost- and time-effective; however, these methods do not produce accurate tomographic data and are limited by tissue absorption. Notably, traceable marker proteins required for optical imaging are xenogeneic with respect to mammals and can induce immune responses in immunocompetent mice, which can result in inconsistent activity, graft rejection and/or inhibition of metastasis, confounding data interpretation. Hence, effective employment of xenogeneic reporters is restricted to short-term studies or studies in immunocompromised models, limiting their usefulness in pre-clinical science (Steinbauer et al., 2003). However, this problem can be circumvented, at least in part, by employing host mice genetically engineered to express respective markers at an early age, which elicits tolerance and thus recognition as "self" (Day et al., 2014).

Several additional points associated with preclinical trial design are worth emphasizing. Tumor mass is a critical factor in preclinical studies; vastly different outcomes can result from initiating drug dosing when tumors are different sizes. Moreover, human tumors are typically much larger than their mouse counterparts, which could affect how preclinical data translates to the clinic. It is also vital to run preclinical trials with a sufficient number of animals in each experimental arm to achieve statistically significant results; ensuring statistical power must be considered a priority for any preclinical study. Therefore, it is prudent to consult biostatisticians prior to finalizing study designs. Finally, the influence of genetic background on tumor behavior can be significant, and must be considered when designing model systems. Generation and analysis of mouse cancer models within the collaborative cross, a large panel of inbred mouse strains (Churchill et al., 2004), could also provide important insights into the impact of complex germline genetics on tumor predisposition and drug response.

Infrastructure

Critical work establishing the utility of murine cancer models in preclinical research has taken place in independent laboratories over the last 20 years. However, because of severe resource limitations, the absolute need to perpetuate basic investigator-driven mechanistic discovery, and an increasingly competitive environment wherein success is measured by individual merit, the opportunity for laboratories to execute preclinical studies beyond the pilot level is limited. Recent reports indicate that most preclinical outcomes at this level are not reproduced when studies are not conducted with robust experimental standards, such as inclusion of appropriate positive and negative controls, execution with sufficient statistical power, attention to pharmacological considerations, and implementation of blind evaluations (Begley and Ellis, 2012; Begley and Ioannidis, 2015). Adherence to *all* these standards is simply not possible in individual laboratories under current conditions. To increase accessibility to preclinical evaluation in murine cancer models, several institutions have established core facilities that perform studies using dedicated staff and common methodologies. These cores represent a necessary step to improve reproducibility in preclinical outcomes. Yet, most core facilities do not have the resources to instate the full range of skills and technologies indicated in "*Experimental Considerations*" above to ensure optimal quality and replication of clinical approaches. Additionally, conducting well-powered blinded studies requires a sizable dedicated staff, which is generally not achievable in academic cores. Finally, global improvement of murine preclinical research must include the generation of an increased range of well-characterized, technically tractable and optimally accurate models vetted for preclinical evaluation, along with the development of exportable standard operating procedures (SOPs).

To address these needs, over the past decade several organized efforts have been established that are dedicated to: (1) improving the accuracy and reproducibility of preclinical drug development platforms; (2) developing and exporting SOPs and models; (3) understanding cancer pathobiology through targeted therapeutics; and/or (4) applying the outcomes of optimized preclinical therapeutic and biomarker studies to clinical research for improved patient care. Common attributes in each

Table 3. Future Challenges and Possible Solutions for Mouse Preclinical Cancer Trials

Issue	Challenges	Possible Solutions
Model improvement	More precise spatial and temporal control of genetic alterations in mouse tissues	Improve technologies for genomic editing (e.g., CRISPR) and regulating gene activity
	Human relevance of stroma, immune system, and therapeutic targets in mouse cancer models	“Humanize” genes via genetic engineering and immune system by reconstitution with human hematopoietic stem cells
	Recapitulation of the tumor heterogeneity found in human cancers	Introduce environmental etiological factors (e.g., UV in skin cancer models); allow tumor evolution by avoiding inappropriately dominant oncogenic drivers
Study setting	Difficulties in diagnosis and treatment of large cohorts of mice as individual patients	Synchronize tumorigenesis by adopting inducible GEM or transplantable GDA systems
	Disease progression and clinically relevant endpoints in preclinical study	Improve biomarkers and imaging techniques for tumor tracking; adopt clinically relevant endpoints (e.g., progression-free survival)
	Integration of pathologic, genomic, bioinformatic, molecular, and immunological analyses	Develop/share improved and standardized protocols; organize workflows with core facilities
Extrapolation to human disease	Evaluating effects of life style on therapeutic outcomes	Consider gender, diet, and exposure to environmental factors in protocol development; consider effects of microbiota
	Physiological difference between mouse and human	“Humanize” aspects of mice; consider scaling law in PD/PK, lifespan, hemodynamics, etc.

case include: (1) a sufficient number of dedicated staff covering a broad range of expertise; (2) access to sophisticated instrumentation and technology for a full range of small animal imaging modalities, histological and molecular pathology, genomic technologies, pharmacological methods, model generation, and appropriate maintenance and quality control for a large “bank” of models; and (3) data management strategies. Examples of such organizations include the Center for Advanced Pre-clinical Research (CAPR; Center for Cancer Research, National Cancer Center and the Frederick National Laboratory for Cancer Research, <https://ccr.cancer.gov/capr-home>); Mouse Clinic for Cancer and Aging research (MCCA; Netherlands Cancer Institute and the European Research Institute for the Biology of Aging, <http://www.mccanet.nl/>); Center for Co-Clinical Trials (MD Anderson, <http://www.cancermoonshots.org/platforms/center-for-co-clinical-trials/>); and the Co-Clinical Project: Informing Clinical Trials Using Preclinical Mouse Models (Harvard Medical School). Similar efforts focused specifically on pancreatic ductal carcinoma include the Mouse Hospitals (Columbia Medical School, <http://www.olivelab.org/mouse-hospital.html>, and Cold Spring Harbor Laboratories).

Emerging and Future Prospects

This PRIMER focuses on the attributes and limitations of murine cancer models that currently best emulate our existing understanding of human cancers, an ever-expanding awareness of which is required to drive development of effective preclinical platforms. The high cost and low yield of efficacious therapies, despite clinical evaluation of countless potential therapeutics, motivate the use and development of preclinical PDX and GEM in the guidance of clinical research. Ultimately, collective employment of a variety of model systems will likely be required to successfully impact clinical outcomes.

Optimal mouse studies are sufficiently cumbersome so as to preclude the simultaneous evaluation of numerous drugs and unbiased libraries; high-throughput *in vitro* screening systems are essential precursors to *in vivo* evaluations. Despite their limitations, cancer cell lines have proven valuable in uncovering mechanisms of acquired drug resistance for *in vitro* drug screens (Torrance et al., 2001), and several technologies such as RNAi and CRISPR/Cas9 methods have enhanced their versatility (Corcoran et al., 2013; Shalem et al., 2014). However, cancer cell-line screens identify only drugs that target intrinsic cancer cell functions. Targeting tumor stroma or microenvironment/tumor cell interactions requires the use of *in vitro* systems that approximate the composition of cancers that preserve important cancer constituents, cell-cell interactions, and architectural features. To this end, several *ex vivo* platforms have been developed, including spheroids, organoids, microtumors (tumor tissue in synthetic matrix), and tissue slices (Burdett et al., 2010; Mendoza et al., 2010; Yamada and Cukierman, 2007). While optimization and validation of emerging *ex vivo* models in drug screening is ongoing, many may be incorporated into early phases of drug development, resulting in efficient triage and increased success *in vivo*.

In addition to *ex vivo* systems, non-murine whole organism drug screens have shown promise for early triage (Gao et al., 2014). Due to their relatively small size, low cost, and high fecundity, invertebrates such as flies (*Drosophila*) and nematodes (*C. elegans*) have shown promise. Furthermore, zebrafish (*Danio rerio*) are particularly well suited for high throughput screens because of rapid extra-uterine development, embryonic transparency, and recently developed pigment deficiency to facilitate imaging (Barriuso et al., 2015). Using automated high content and high throughput platforms, zebrafish can be used for chemical, genetic, and pathway-based screens (Lieschke and Currie,

2007). Notably, data generated from zebrafish models have been used in clinical trials. For example, the pyrimidine biosynthesis enzyme DHODH was identified in zebrafish screens as a novel melanoma drug target, and a clinical trial is underway in which patients are being treated with the DHODH inhibitor leflunomide (Hagedorn et al., 2014; White et al., 2011). Zebrafish have also been used as hosts for human and mouse xenografts to monitor invasiveness, angiogenesis, and drug responses in real time (Zhang et al., 2015). However, as with xenotransplantation of human cells into mice, inappropriate tumor-host interactions could limit the relevance and translational value of fish models.

Optimization of preclinical models that can impact clinical practice will require overcoming challenges in several arenas (Table 3). However, achieving this goal will undoubtedly require expansion and integration of organized efforts by many factions. The sophistication of such preclinical studies requires expertise in many disparate fields and necessitates involvement of scientists in the public sector, who often possess critical expertise and mechanisms not available in the private sector. However, communication and data-sharing among investigators and organizations, though essential for efficient optimization of effective pre-clinical standard operating procedures, are limited. A future priority will be to develop interactive web-based systems to house and mine experimental databases and SOPs for community sharing. Such organized initiatives will begin to meet the significant and immediate need to revolutionize the accuracy of preclinical assessment and to develop and utilize PDX- and GEM-based disease models in research to increase the number of effective treatments reaching clinical trials and thus, cancer patients.

In summary, we now have a wealth of model systems that show early promise in establishing robust preclinical assessment platforms for improving clinical success. Each system has specific and sometimes unique value, and all will undoubtedly play a significant role in varied aspects of future preclinical studies. At this junction, systematic comparisons in the prediction of human outcomes by distinct model systems has not been carried out and is needed in order to construct sound preclinical operating principles. The selection of models for a given study will undoubtedly depend on the required purpose. While 2D cell cultures are useful for identifying cancer cell-intrinsic vulnerabilities, 3D ex vivo methods incorporate assessment of multicellular interactions. Non-mammalian animals further offer reasonable throughput in complex biological systems, while PDX and GEM models provide the best representation of tumor microenvironments, physiological responses, and disease pathology. GEMs further allow for evaluation of immune system interventions and of responses unique to *in situ* developed disease. Ultimately, the complementary use of many of these models and continual efforts to improve their effectiveness will propel preclinical studies to a new era of cancer therapeutics development. This is a uniquely exciting era wherein preclinical models, rather than serving simply to confirm clinical outcomes, have the potential to routinely fuel optimized clinical success.

SUPPLEMENTAL INFORMATION

Supplemental Information can be found with this file at <http://dx.doi.org/10.1016/j.cell.2015.08.068>.

ACKNOWLEDGMENTS

We thank Mr. Jonathan Marie (www.thefrenzybear.com) for Figure 1 prototype, Drs. James Doroshow (Developmental Therapeutic Program [DTP], National Cancer Institute), Melinda Hollingshead (DTP), and Neal Goodwin (Champions Oncology, Inc.) for guidance on PDX studies, Yurong Song for Table 2 information, and Anton Berns (Netherlands Cancer Institute), Pier-Paolo Pandolfi (Harvard University), and David Tuveson (Cold Spring Harbor Laboratory) for insightful discussions.

REFERENCES

- Abate-Shen, C., Politi, K., Chodosh, L., and Olive, K. (2014). *Mouse Models of Cancer: A Laboratory Manual* (CSHL Press).
- Ablain, J., and de Thé, H. (2014). Retinoic acid signaling in cancer: The parable of acute promyelocytic leukemia. *Int. J. Cancer* **135**, 2262–2272.
- Adams, C.P., and Brantner, V.V. (2006). Estimating the cost of new drug development: is it really 802 million dollars? *Health Aff. (Millwood)* **25**, 420–428.
- Al-Lazikani, B., Banerji, U., and Workman, P. (2012). Combinatorial drug therapy for cancer in the post-genomic era. *Nat. Biotechnol.* **30**, 679–692.
- Bailey, M., Christoforidou, Z., and Lewis, M.C. (2013). The evolutionary basis for differences between the immune systems of man, mouse, pig and ruminants. *Vet. Immunol. Immunopathol.* **152**, 13–19.
- Barriuso, J., Nagaraju, R., and Hurlstone, A. (2015). Zebrafish: a new companion for translational research in oncology. *Clin. Cancer Res.* **21**, 969–975.
- Beatty, G.L., Torigian, D.A., Chiorean, E.G., Saboury, B., Brothers, A., Alavi, A., Troxel, A.B., Sun, W., Teitelbaum, U.R., Vonderheide, R.H., and O'Dwyer, P.J. (2013). A phase I study of an agonist CD40 monoclonal antibody (CP-870,893) in combination with gemcitabine in patients with advanced pancreatic ductal adenocarcinoma. *Clin. Cancer Res.* **19**, 6286–6295.
- Begley, C.G., and Ellis, L.M. (2012). Drug development: Raise standards for preclinical cancer research. *Nature* **483**, 531–533.
- Begley, C.G., and Ioannidis, J.P.A. (2015). Reproducibility in science: improving the standard for basic and preclinical research. *Circ. Res.* **116**, 116–126.
- Burdett, E., Kasper, F.K., Mikos, A.G., and Ludwig, J.A. (2010). Engineering tumors: a tissue engineering perspective in cancer biology. *Tissue Eng. Part B Rev.* **16**, 351–359.
- Cao, J., Wan, L., Hacker, E., Dai, X., Lenna, S., Jimenez-Cervantes, C., Wang, Y., Leslie, N.R., Xu, G.X., Widlund, H.R., et al. (2013). MC1R is a potent regulator of PTEN after UV exposure in melanocytes. *Mol. Cell* **51**, 409–422.
- Casanovas, O., Hicklin, D.J., Bergers, G., and Hanahan, D. (2005). Drug resistance by evasion of antiangiogenic targeting of VEGF signaling in late-stage pancreatic islet tumors. *Cancer Cell* **8**, 299–309.
- Chen, Z., Cheng, K., Walton, Z., Wang, Y., Ebi, H., Shimamura, T., Liu, Y., Tupper, T., Ouyang, J., Li, J., et al. (2012). A murine lung cancer co-clinical trial identifies genetic modifiers of therapeutic response. *Nature* **483**, 613–617.
- Chen, Z., Akbay, E., Mikse, O., Tupper, T., Cheng, K., Wang, Y., Tan, X., Altabef, A., Woo, S.-A., Chen, L., et al. (2014). Co-clinical trials demonstrate superiority of crizotinib to chemotherapy in ALK-rearranged non-small cell lung cancer and predict strategies to overcome resistance. *Clin. Cancer Res.* **20**, 1204–1211.
- Chen, S., Sanjana, N.E., Zheng, K., Shalem, O., Lee, K., Shi, X., Scott, D.A., Song, J., Pan, J.Q., Weissleder, R., et al. (2015). Genome-wide CRISPR screen in a mouse model of tumor growth and metastasis. *Cell* **160**, 1246–1260.
- Chin, L., Andersen, J.N., and Futreal, P.A. (2011). Cancer genomics: from discovery science to personalized medicine. *Nat. Med.* **17**, 297–303.
- Chiu, C.W., Nozawa, H., and Hanahan, D. (2010). Survival benefit with proapoptotic molecular and pathologic responses from dual targeting of mammalian target of rapamycin and epidermal growth factor receptor in a preclinical model of pancreatic neuroendocrine carcinogenesis. *J. Clin. Oncol.* **28**, 4425–4433.

Churchill, G.A., Airey, D.C., Allayee, H., Angel, J.M., Attie, A.D., Beatty, J., Beavis, W.D., Belknap, J.K., Bennett, B., Berrettini, W., et al.; Complex Trait Consortium (2004). The Collaborative Cross, a community resource for the genetic analysis of complex traits. *Nat. Genet.* 36, 1133–1137.

Corcoran, R.B., Cheng, K.A., Hata, A.N., Faber, A.C., Ebi, H., Coffee, E.M., Greninger, P., Brown, R.D., Godfrey, J.T., Cohoon, T.J., et al. (2013). Synthetic lethal interaction of combined BCL-XL and MEK inhibition promotes tumor regressions in KRAS mutant cancer models. *Cancer Cell* 23, 121–128.

Couzin-Frankel, J. (2014). The littlest patient. *Science* 346, 24–27.

Das Thakur, M., Salangsang, F., Landman, A.S., Sellers, W.R., Pryer, N.K., Levesque, M.P., Dummer, R., McMahon, M., and Stuart, D.D. (2013). Modelling vemurafenib resistance in melanoma reveals a strategy to forestall drug resistance. *Nature* 494, 251–255.

Day, C.P., Carter, J., Bonomi, C., Hollingshead, M., and Merlino, G. (2012). Preclinical therapeutic response of residual metastatic disease is distinct from its primary tumor of origin. *Int. J. Cancer* 130, 190–199.

Day, C.P., Carter, J., Weaver Ohler, Z., Bonomi, C., El Meskini, R., Martin, P., Graff-Cherry, C., Feigenbaum, L., Tütting, T., Van Dyke, T., et al. (2014). "Glowing head" mice: a genetic tool enabling reliable preclinical image-based evaluation of cancers in immunocompetent allografts. *PLoS ONE* 9, e109956.

DeVita, V.T., Jr., and Chu, E. (2008). A history of cancer chemotherapy. *Cancer Res.* 68, 8643–8653.

Dow, L.E., Premsrirut, P.K., Zuber, J., Fellmann, C., McJunkin, K., Miethling, C., Park, Y., Dickins, R.A., Hannon, G.J., and Lowe, S.W. (2012). A pipeline for the generation of shRNA transgenic mice. *Nat. Protoc.* 7, 374–393.

Dow, L.E., Fisher, J., O'Rourke, K.P., Muley, A., Kastenhuber, E.R., Livshits, G., Tschaharganeh, D.F., Socci, N.D., and Lowe, S.W. (2015). Inducible in vivo genome editing with CRISPR-Cas9. *Nat. Biotechnol.* 33, 390–394.

Faca, V.M., Song, K.S., Wang, H., Zhang, Q., Krasnoselsky, A.L., Newcomb, L.F., Plentz, R.R., Gurumurthy, S., Redston, M.S., Pitteri, S.J., et al. (2008). A mouse to human search for plasma proteome changes associated with pancreatic tumor development. *PLoS Med.* 5, e123.

Fidler, I.J., and Hart, I.R. (1982). Biological diversity in metastatic neoplasms: origins and implications. *Science* 217, 998–1003.

Fiebig, H.H., Schuchhardt, C., Henss, H., Fiedler, L., and Löhr, G.W. (1984). Comparison of tumor response in nude mice and in the patients. *Behring Inst. Mitt.* 74, 343–352.

Frese, K.K., Neesse, A., Cook, N., Bapiro, T.E., Lolkema, M.P., Jodrell, D.I., and Tuveson, D.A. (2012). nab-Paclitaxel potentiates gemcitabine activity by reducing cytidine deaminase levels in a mouse model of pancreatic cancer. *Cancer Discov.* 2, 260–269.

Gao, G., Chen, L., and Huang, C. (2014). Anti-cancer drug discovery: update and comparisons in yeast, *Drosophila*, and zebrafish. *Curr. Mol. Pharmacol.* 7, 44–51.

Garraway, L.A., and Jänne, P.A. (2012). Circumventing cancer drug resistance in the era of personalized medicine. *Cancer Discov.* 2, 214–226.

Garraway, L.A. (2013). Genomics-driven oncology: framework for an emerging paradigm. *J. Clin. Oncol.* 31, 1806–1814.

Girotti, M.R., Lopes, F., Preece, N., Niculescu-Duvaz, D., Zambon, A., Davies, L., Whittaker, S., Saturno, G., Viros, A., Pedersen, M., et al. (2015). Paradox-breaking RAF inhibitors that also target SRC are effective in drug-resistant BRAF mutant melanoma. *Cancer Cell* 27, 85–96.

Goldstein, D., El-Maraghi, R.H., Hammel, P., Heinemann, V., Kunzmann, V., Sastre, J., Scheithauer, W., Siena, S., Tabernero, J., Teixeira, L., et al. (2015). nab-Paclitaxel plus gemcitabine for metastatic pancreatic cancer: long-term survival from a phase III trial. *J. Natl. Cancer Inst.* 107.

Gonzalez, F.J. (2004). Cytochrome P450 humanised mice. *Hum. Genomics* 1, 300–306.

Hagedorn, E.J., Durand, E.M., Fast, E.M., and Zon, L.I. (2014). Getting more for your marrow: boosting hematopoietic stem cell numbers with PGE2. *Exp. Cell Res.* 329, 220–226.

Hanash, S., and Taguchi, A. (2011). Application of proteomics to cancer early detection. *Cancer J.* 17, 423–428.

Heyer, J., Kwong, L.N., Lowe, S.W., and Chin, L. (2010). Non-germline genetically engineered mouse models for translational cancer research. *Nat. Rev. Cancer* 10, 470–480.

Hidalgo, M., Amant, F., Biankin, A.V., Budinská, E., Byrne, A.T., Caldas, C., Clarke, R.B., de Jong, S., Jonkers, J., Mælandsmo, G.M., et al. (2014). Patient-derived xenograft models: an emerging platform for translational cancer research. *Cancer Discov.* 4, 998–1013.

Hood, L., and Friend, S.H. (2011). Predictive, personalized, preventive, participatory (P4) cancer medicine. *Nat. Rev. Clin. Oncol.* 8, 184–187.

Ilie, M., Nunes, M., Blot, L., Hofman, V., Long-Mira, E., Butori, C., Selva, E., Merino-Trigo, A., Vénissac, N., Mouroux, J., et al. (2015). Setting up a wide panel of patient-derived tumor xenografts of non-small cell lung cancer by improving the preanalytical steps. *Cancer Med.* 4, 201–211.

Jänne, P.A., Shaw, A.T., Pereira, J.R., Jeannin, G., Vansteenkiste, J., Barrios, C., Franke, F.A., Grinsted, L., Zazulina, V., Smith, P., et al. (2013). Selumetinib plus docetaxel for KRAS-mutant advanced non-small-cell lung cancer: a randomised, multicentre, placebo-controlled, phase 2 study. *Lancet Oncol.* 14, 38–47.

Johnson, J.I., Decker, S., Zaharevitz, D., Rubinstein, L.V., Venditti, J.M., Scheパート, S., Kalyanrug, S., Christian, M., Arbuck, S., Hollingshead, M., and Sausville, E.A. (2001). Relationships between drug activity in NCI preclinical in vitro and in vivo models and early clinical trials. *Br. J. Cancer* 84, 1424–1431.

Kannan, K., Sharpless, N.E., Xu, J., O'Hagan, R.C., Bosenberg, M., and Chin, L. (2003). Components of the Rb pathway are critical targets of UV mutagenesis in a murine melanoma model. *Proc. Natl. Acad. Sci. USA* 100, 1221–1225.

Kortmann, U., McAlpine, J.N., Xue, H., Guan, J., Ha, G., Tully, S., Shafait, S., Lau, A., Cranston, A.N., O'Connor, M.J., et al. (2011). Tumor growth inhibition by olaparib in BRCA2 germline-mutated patient-derived ovarian cancer tissue xenografts. *Clin. Cancer Res.* 17, 783–791.

Kwong, L.N., Costello, J.C., Liu, H., Jiang, S., Helms, T.L., Langsdorf, A.E., Jakubosky, D., Genovese, G., Muller, F.L., Jeong, J.H., et al. (2012). Oncogenic NRAS signaling differentially regulates survival and proliferation in melanoma. *Nat. Med.* 18, 1503–1510.

Leaf, C. (2004). Why we're losing the war on cancer (and how to win it). *Fortune* 149, 76–82, 84–86, 88 passim.

Legrand, N., Ploss, A., Balling, R., Becker, P.D., Borsotti, C., Brezillon, N., Debarry, J., de Jong, Y., Deng, H., Di Santo, J.P., et al. (2009). Humanized mice for modeling human infectious disease: challenges, progress, and outlook. *Cell Host Microbe* 6, 5–9.

Lieschke, G.J., and Currie, P.D. (2007). Animal models of human disease: zebrafish swim into view. *Nat. Rev. Genet.* 8, 353–367.

Lunardi, A., and Pandolfi, P.P. (2015). A co-clinical platform to accelerate cancer treatment optimization. *Trends Mol. Med.* 21, 1–5.

Lynch, T.J., Bell, D.W., Sordella, R., Gurubhagavatula, S., Okimoto, R.A., Brannigan, B.W., Harris, P.L., Haserlat, S.M., Supko, J.G., Haluska, F.G., et al. (2004). Activating mutations in the epidermal growth factor receptor underlying responsiveness of non-small-cell lung cancer to gefitinib. *N. Engl. J. Med.* 350, 2129–2139.

Maddalo, D., Manchado, E., Concepcion, C.P., Bonetti, C., Vidigal, J.A., Han, Y.-C., Ogródowski, P., Crippa, A., Rekhrtman, N., de Stanchina, E., et al. (2014). In vivo engineering of oncogenic chromosomal rearrangements with the CRISPR/Cas9 system. *Nature* 516, 423–427.

Malaney, P., Nicosia, S.V., and Davé, V. (2014). One mouse, one patient paradigm: New avatars of personalized cancer therapy. *Cancer Lett.* 344, 1–12.

Mattern, J., Bak, M., Hahn, E.W., and Volm, M. (1988). Human tumor xenografts as model for drug testing. *Cancer Metastasis Rev.* 7, 263–284.

Mendoza, A., Hong, S.-H., Osborne, T., Khan, M.A., Campbell, K., Briggs, J., Eleswarapu, A., Buquo, L., Ren, L., Hevitt, S.M., et al. (2010). Modeling metastasis biology and therapy in real time in the mouse lung. *J. Clin. Invest.* 120, 2979–2988.

Mou, H., Kennedy, Z., Anderson, D.G., Yin, H., and Xue, W. (2015). Precision cancer mouse models through genome editing with CRISPR-Cas9. *Genome Med.* 7, 53.

Noonan, F.P., Recio, J.A., Takayama, H., Duray, P., Anver, M.R., Rush, W.L., De Fabo, E.C., and Merlino, G. (2001). Neonatal sunburn and melanoma in mice. *Nature* 413, 271–272.

Olive, K.P., and Tuveson, D.A. (2006). The use of targeted mouse models for preclinical testing of novel cancer therapeutics. *Clin. Cancer Res.* 12, 5277–5287.

Olive, K.P., Jacobetz, M.A., Davidson, C.J., Gopinathan, A., McIntyre, D., Honess, D., Madhu, B., Goldgraben, M.A., Caldwell, M.E., Allard, D., et al. (2009). Inhibition of Hedgehog signaling enhances delivery of chemotherapy in a mouse model of pancreatic cancer. *Science* 324, 1457–1461.

Paez, J.G., Jänne, P.A., Lee, J.C., Tracy, S., Greulich, H., Gabriel, S., Herman, P., Kaye, F.J., Lindeman, N., Boggon, T.J., et al. (2004). EGFR mutations in lung cancer: correlation with clinical response to gefitinib therapy. *Science* 304, 1497–1500.

Page, D.B., Postow, M.A., Callahan, M.K., Allison, J.P., and Wolchok, J.D. (2014). Immune modulation in cancer with antibodies. *Annu. Rev. Med.* 65, 185–202.

Pagliarini, R., Shao, W., and Sellers, W.R. (2015). Oncogene addiction: pathways of therapeutic response, resistance, and road maps toward a cure. *EMBO Rep.* 16, 280–296.

Pandolfi, P.P. (2001). Oncogenes and tumor suppressors in the molecular pathogenesis of acute promyelocytic leukemia. *Hum. Mol. Genet.* 10, 769–775.

Pattabiraman, D.R., and Weinberg, R.A. (2014). Tackling the cancer stem cells - what challenges do they pose? *Nat. Rev. Drug Discov.* 13, 497–512.

Pietras, K., and Hanahan, D. (2005). A multitargeted, metronomic, and maximum-tolerated dose “chemo-switch” regimen is antiangiogenic, producing objective responses and survival benefit in a mouse model of cancer. *J. Clin. Oncol.* 23, 939–952.

Platt, R.J., Chen, S., Zhou, Y., Yim, M.J., Swiech, L., Kempton, H.R., Dahlman, J.E., Parnas, O., Eisenhaure, T.M., Jovanovic, M., et al. (2014). CRISPR-Cas9 knockin mice for genome editing and cancer modeling. *Cell* 159, 440–455.

Premsrirut, P.K., Dow, L.E., Kim, S.Y., Camiolo, M., Malone, C.D., Miethling, C., Scuoppo, C., Zuber, J., Dickins, R.A., Kogan, S.C., et al. (2011). A rapid and scalable system for studying gene function in mice using conditional RNA interference. *Cell* 145, 145–158.

Quignon, F., Chen, Z., and de Thé, H. (1997). Retinoic acid and arsenic: towards oncogene-targeted treatments of acute promyelocytic leukaemia. *Biochim. Biophys. Acta* 1333, M53–M61.

Raymond, E., Dahan, L., Raoul, J.-L., Bang, Y.-J., Borbath, I., Lombard-Bonias, C., Valle, J., Metrakos, P., Smith, D., Vinik, A., et al. (2011). Sunitinib maleate for the treatment of pancreatic neuroendocrine tumors. *N. Engl. J. Med.* 364, 501–513.

Reinhold, W.C., Varma, S., Rajapakse, V.N., Luna, A., Sousa, F.G., Kohn, K.W., and Pommier, Y.G. (2015). Using drug response data to identify molecular effectors, and molecular “omic” data to identify candidate drugs in cancer. *Hum. Genet.* 134, 3–11.

Riley, R.R., Duensing, S., Brake, T., Münger, K., Lambert, P.F., and Arbeit, J.M. (2003). Dissection of human papillomavirus E6 and E7 function in transgenic mouse models of cervical carcinogenesis. *Cancer Res.* 63, 4862–4871.

Rogers, A.B., and Fox, J.G. (2004). Inflammation and Cancer. I. Rodent models of infectious gastrointestinal and liver cancer. *Am. J. Physiol. Gastrointest. Liver Physiol.* 286, G361–G366.

Romer, J.T., Kimura, H., Magdaleno, S., Sasai, K., Fuller, C., Baines, H., Connally, M., Stewart, C.F., Gould, S., Rubin, L.L., and Curran, T. (2004). Suppression of the Shh pathway using a small molecule inhibitor eliminates medulloblastoma in Ptc1(+/-)p53(-/-) mice. *Cancer Cell* 6, 229–240.

Rosfjord, E., Lucas, J., Li, G., and Gerber, H.-P. (2014). Advances in patient-derived tumor xenografts: from target identification to predicting clinical response rates in oncology. *Biochem. Pharmacol.* 91, 135–143.

Rudin, C.M., Hann, C.L., Laterra, J., Yauch, R.L., Callahan, C.A., Fu, L., Holcomb, T., Stinson, J., Gould, S.E., Coleman, B., et al. (2009). Treatment of medulloblastoma with hedgehog pathway inhibitor GDC-0449. *N. Engl. J. Med.* 361, 1173–1178.

Scheer, N., and Wolf, C.R. (2014). Genetically humanized mouse models of drug metabolizing enzymes and transporters and their applications. *Xenobiotica* 44, 96–108.

Scheer, N., Snaith, M., Wolf, C.R., and Seibler, J. (2013). Generation and utility of genetically humanized mouse models. *Drug Discov. Today* 18, 1200–1211.

Shalem, O., Sanjana, N.E., Hartenian, E., Shi, X., Scott, D.A., Mikkelsen, T.S., Heckl, D., Ebert, B.L., Root, D.E., Doench, J.G., and Zhang, F. (2014). Genome-scale CRISPR-Cas9 knockout screening in human cells. *Science* 343, 84–87.

Sharpless, N.E., and Depinho, R.A. (2006). The mighty mouse: genetically engineered mouse models in cancer drug development. *Nat. Rev. Drug Discov.* 5, 741–754.

Shultz, L.D., Goodwin, N., Ishikawa, F., Hosur, V., Lyons, B.L., and Greiner, D.L. (2014). Human cancer growth and therapy in immunodeficient mouse models. *Cold Spring Harb. Protoc.* 2014, 694–708.

Singh, M., Murriel, C.L., and Johnson, L. (2012). Genetically engineered mouse models: closing the gap between preclinical data and trial outcomes. *Cancer Res.* 72, 2695–2700.

Soucek, L., Whitfield, J., Martins, C.P., Finch, A.J., Murphy, D.J., Sodir, N.M., Karnezis, A.N., Swigart, L.B., Nasi, S., and Evan, G.I. (2008). Modelling Myc inhibition as a cancer therapy. *Nature* 455, 679–683.

Sparreboom, A., van Tellingen, O., Nooitjien, W.J., and Beijnen, J.H. (1996). Nonlinear pharmacokinetics of paclitaxel in mice results from the pharmaceutical vehicle Cremophor EL. *Cancer Res.* 56, 2112–2115.

Stebbing, J., Paz, K., Schwartz, G.K., Wexler, L.H., Maki, R., Pollock, R.E., Morris, R., Cohen, R., Shankar, A., Blackman, G., et al. (2014). Patient-derived xenografts for individualized care in advanced sarcoma. *Cancer* 120, 2006–2015.

Steinbauer, M., Guba, M., Cernaianu, G., Köhl, G., Cetto, M., Kunz-Schughart, L.A., Geissler, E.K., Falk, W., and Jauch, K.W. (2003). GFP-transfected tumor cells are useful in examining early metastasis in vivo, but immune reaction precludes long-term tumor development studies in immunocompetent mice. *Clin. Exp. Metastasis* 20, 135–141.

Stiedl, P., Grabner, B., Zboray, K., Bogner, E., and Casanova, E. (2015). Modeling cancer using genetically engineered mice. *Methods Mol. Biol.* 1267, 3–18.

Svenson, K.L., Gatti, D.M., Valdar, W., Welsh, C.E., Cheng, R., Chesler, E.J., Palmer, A.A., McMillan, L., and Churchill, G.A. (2012). High-resolution genetic mapping using the Mouse Diversity Outbred population. *Genetics* 190, 437–447.

Szabova, L., Bupp, S., Kamal, M., Householder, D.B., Hernandez, L., Schlorer, J.J., Baran, M.L., Yi, M., Stephens, R.M., Annunziata, C.M., et al. (2014). Pathway-specific engineered mouse allograft models functionally recapitulate human serous epithelial ovarian cancer. *PLoS ONE* 9, e95649.

Talmadge, J.E., Singh, R.K., Fidler, I.J., and Raz, A. (2007). Murine models to evaluate novel and conventional therapeutic strategies for cancer. *Am. J. Pathol.* 170, 793–804.

Teicher, B.A. (2006). Tumor models for efficacy determination. *Mol. Cancer Ther.* 5, 2435–2443.

Tentler, J.J., Tan, A.C., Weekes, C.D., Jimeno, A., Leong, S., Pitts, T.M., Arcaroli, J.J., Messersmith, W.A., and Eckhardt, S.G. (2012). Patient-derived tumour xenografts as models for oncology drug development. *Nat. Rev. Clin. Oncol.* 9, 338–350.

Texidó, G. (2013). Genetically engineered animal models for in vivo target identification and validation in oncology. *Methods Mol. Biol.* 986, 281–305.

Torrance, C.J., Agrawal, V., Vogelstein, B., and Kinzler, K.W. (2001). Use of isogenic human cancer cells for high-throughput screening and drug discovery. *Nat. Biotechnol.* 19, 940–945.

Van Dyke, T., and Jacks, T. (2002). Cancer modeling in the modern era: progress and challenges. *Cell* 108, 135–144.

van't Veer, L.J., and Bernards, R. (2008). Enabling personalized cancer medicine through analysis of gene-expression patterns. *Nature* 452, 564–570.

Walrath, J.C., Hawes, J.J., Van Dyke, T., and Reilly, K.M. (2010). Genetically engineered mouse models in cancer research. *Adv. Cancer Res.* 106, 113–164.

Wang, Y., Tseng, J.-C., Sun, Y., Beck, A.H., and Kung, A.L. (2015). Noninvasive imaging of tumor burden and molecular pathways in mouse models of cancer. *Cold Spring Harb. Protoc.* 2015, 135–144.

Weaver, Z., Difilippantonio, S., Carretero, J., Martin, P.L., El Meskini, R., Iacovelli, A.J., Gumprecht, M., Kulaga, A., Guerin, T., Schlomer, J., et al. (2012). Temporal molecular and biological assessment of an erlotinib-resistant lung adenocarcinoma model reveals markers of tumor progression and treatment response. *Cancer Res.* 72, 5921–5933.

Westcott, P.M.K., Halliwill, K.D., To, M.D., Rashid, M., Rust, A.G., Keane, T.M., Delrosario, R., Jen, K.-Y., Gurley, K.E., Kemp, C.J., et al. (2015). The mutational landscapes of genetic and chemical models of Kras-driven lung cancer. *Nature* 517, 489–492.

White, R.M., Cech, J., Ratanasirintrawoot, S., Lin, C.Y., Rahl, P.B., Burke, C.J., Langdon, E., Tomlinson, M.L., Mosher, J., Kaufman, C., et al. (2011). DHODH modulates transcriptional elongation in the neural crest and melanoma. *Nature* 471, 518–522.

Yamada, K.M., and Cukierman, E. (2007). Modeling tissue morphogenesis and cancer in 3D. *Cell* 130, 601–610.

Yap, T.A., Omlin, A., and de Bono, J.S. (2013). Development of therapeutic combinations targeting major cancer signaling pathways. *J. Clin. Oncol.* 31, 1592–1605.

Young, N.P., Crowley, D., and Jacks, T. (2011). Uncoupling cancer mutations reveals critical timing of p53 loss in sarcomagenesis. *Cancer Res.* 71, 4040–4047.

Zhang, X., Claerhout, S., Prat, A., Dobrolecki, L.E., Petrovic, I., Lai, Q., Landis, M.D., Wiechmann, L., Schiff, R., Giuliano, M., et al. (2013). A renewable tissue resource of phenotypically stable, biologically and ethnically diverse, patient-derived human breast cancer xenograft models. *Cancer Res.* 73, 4885–4897.

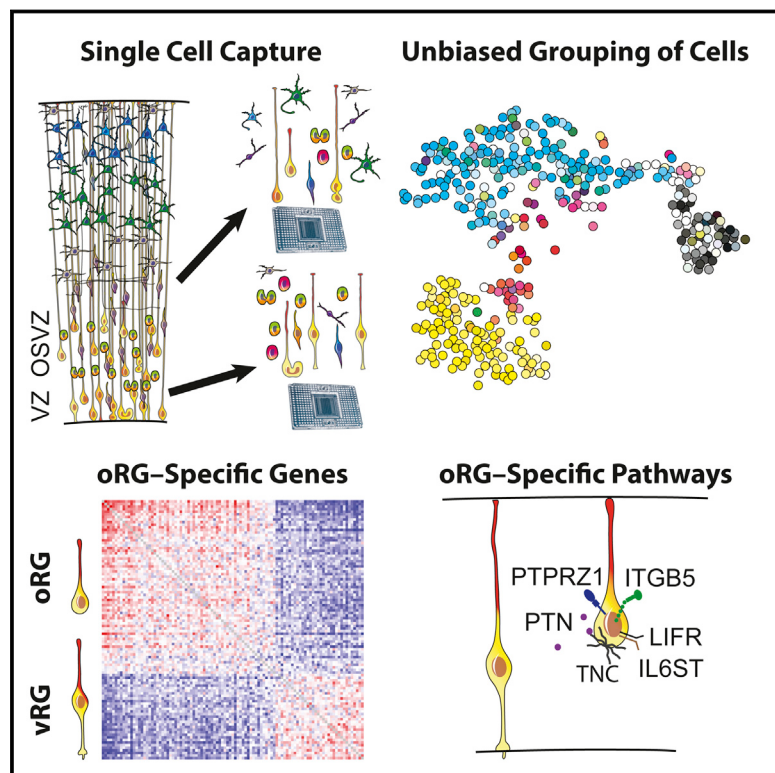
Zhang, B., Xuan, C., Ji, Y., Zhang, W., and Wang, D. (2015). Zebrafish xenotransplantation as a tool for in vivo cancer study. *Fam. Cancer* 14, 487–493.

Zhou, Y., Rideout, W.M., 3rd, Zi, T., Bressel, A., Reddypalli, S., Rancourt, R., Woo, J.-K., Horner, J.W., Chin, L., Chiu, M.I., et al. (2010). Chimeric mouse tumor models reveal differences in pathway activation between ERBB family- and KRAS-dependent lung adenocarcinomas. *Nat. Biotechnol.* 28, 71–78.

Zitvogel, L., Apetoh, L., Ghiringhelli, F., and Kroemer, G. (2008). Immunological aspects of cancer chemotherapy. *Nat. Rev. Immunol.* 8, 59–73.

Molecular Identity of Human Outer Radial Glia during Cortical Development

Graphical Abstract



Highlights

- oRG and vRG cells represent molecularly distinct subpopulations of human radial glia
- oRG transcriptional state first emerges in VZ during early cortical development
- Single oRG cells generate hundreds of daughter cells of diverse types
- Molecular profile suggests that oRG cells sustain proliferative niche in primate OSVZ

Authors

Alex A. Pollen, Tomasz J. Nowakowski, Jiadong Chen, ..., Anne A. Leyrat, Jay A. West, Arnold R. Kriegstein

Correspondence

alex.pollen@gmail.com (A.A.P.), kriegsteina@stemcell.ucsf.edu (A.R.K.)

In Brief

Single-cell transcriptomics reveals molecular distinctions between human radial glia residing in the ventricular and outer subventricular zones, suggesting that outer radial glia may generate a self-sustaining proliferative niche that supports primate brain expansion during development of the cerebral cortex.

Accession Numbers

[phs000989.v1.p1](https://www.ncbi.nlm.nih.gov/pmc/articles/PMC4563000/)

Molecular Identity of Human Outer Radial Glia during Cortical Development

Alex A. Pollen,^{1,2,5,*} Tomasz J. Nowakowski,^{1,2,5} Jiadong Chen,^{1,2} Hanna Retallack,^{1,2} Carmen Sandoval-Espinosa,^{1,2} Cory R. Nicholas,^{1,6} Joe Shuga,³ Siyuan John Liu,^{1,2} Michael C. Oldham,¹ Aaron Diaz,^{1,4} Daniel A. Lim,^{1,4} Anne A. Leyrat,³ Jay A. West,³ and Arnold R. Kriegstein^{1,2,*}

¹Eli and Edythe Broad Center of Regeneration Medicine and Stem Cell Research, University of California, San Francisco, San Francisco, CA 94143, USA

²Department of Neurology, University of California, San Francisco, San Francisco, CA 94158, USA

³Fluidigm Corporation, South San Francisco, CA 94080, USA

⁴Department of Neurological Surgery, University of California, San Francisco, San Francisco, CA 94143, USA

⁵Co-first author

⁶Present address: Neurona Therapeutics, South San Francisco, CA 94080, USA

*Correspondence: alex.pollen@gmail.com (A.A.P.), kriegsteina@stemcell.ucsf.edu (A.R.K.)

<http://dx.doi.org/10.1016/j.cell.2015.09.004>

SUMMARY

Radial glia, the neural stem cells of the neocortex, are located in two niches: the ventricular zone and outer subventricular zone. Although outer subventricular zone radial glia may generate the majority of human cortical neurons, their molecular features remain elusive. By analyzing gene expression across single cells, we find that outer radial glia preferentially express genes related to extracellular matrix formation, migration, and stemness, including *TNC*, *PTPRZ1*, *FAM107A*, *HOPX*, and *LIFR*. Using dynamic imaging, immunostaining, and clonal analysis, we relate these molecular features to distinctive behaviors of outer radial glia, demonstrate the necessity of STAT3 signaling for their cell cycle progression, and establish their extensive proliferative potential. These results suggest that outer radial glia directly support the subventricular niche through local production of growth factors, potentiation of growth factor signals by extracellular matrix proteins, and activation of self-renewal pathways, thereby enabling the developmental and evolutionary expansion of the human neocortex.

INTRODUCTION

The human neocortex contains 16 billion neurons of diverse types that develop from an initially uniform neuroepithelium. In the ventricular zone (VZ), radial glia undergo interkinetic nuclear migration and possess apical processes that contact the ventricle and form adherens junctions. Apical complex proteins transduce signals from the cerebrospinal fluid that are critical for the survival, proliferation, and neurogenic capacity of ventricular radial glia (vRG) (Lehtinen et al., 2011). However, the majority of human radial glia are located in the outer subventricular zone (OSVZ) (Lewitus et al., 2013). These outer radial glia (oRG) retain basal processes but lack apical junctions and undergo a distinct

migratory behavior, mitotic somal translocation, directly preceding cell division (Hansen et al., 2010). Thus, vRG and oRG cells reside in distinct niches defined by differences in anatomical location, provision of growth factors, cell morphology, and behavior (Fietz et al., 2010). Although oRG cells may generate the majority of cortical neurons (Lewitus et al., 2013; Smart et al., 2002), the molecular features sustaining neural stem cell properties of oRG cells in the OSVZ niche are largely unknown and the long-term proliferative capacity of these cells has not been examined.

Understanding the molecular programs specifically employed by oRG cells would provide insights into mechanisms of cortical development and support strategies to generate this cell type *in vitro*. Previous studies have attempted to identify genes uniquely expressed in oRG cells using a variety of transcriptional profiling strategies, including comparisons between microdissected samples (Fietz et al., 2012; Miller et al., 2014) and between cell populations expressing particular surface proteins (Florio et al., 2015; Johnson et al., 2015), but the difficulty of isolating bona fide oRG cells has made clear definition of their gene expression profiles challenging.

To specifically compare molecular features of radial glia in the VZ and OSVZ, we performed RNA sequencing of single cells captured from these two zones without additional enrichment steps. We then classified cells by analyzing thousands of genes that vary across cells and isolated radial glia from other cell types *in silico* (Pollen et al., 2014). We find that the proneural gene networks recently attributed to oRG cells are largely restricted to intermediate progenitor cells. Within classically defined radial glia, we discover molecular distinctions between vRG and oRG cells. The transcriptional state enriched in oRG cells includes genes involved in extracellular matrix production, epithelial-to-mesenchymal transition, and stem cell maintenance. Surprisingly, we find that components of the LIFR/STAT3 self-renewal pathway are selectively expressed by oRG but not vRG cells, and we confirm that STAT3 signaling is necessary for oRG cell-cycle progression. We further find that single oRG cells have the capacity to produce hundreds of deep and upper cortical layer neurons. Based on these results, we propose that oRG cells directly support the development of an enlarged OSVZ

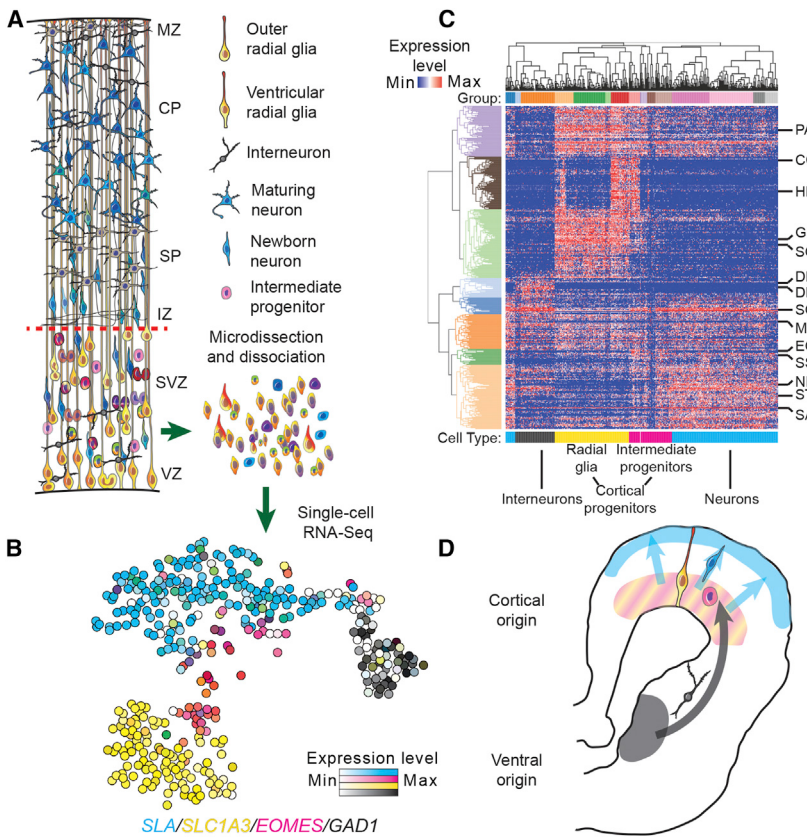


Figure 1. Molecular Diversity of Single Cells from Human Cortical Germinal Zone

(A) Schematic representation of major cell populations of developing cortex. VZ, ventricular zone; SVZ, subventricular zone; IZ, intermediate zone; SP, subplate; CP, cortical plate; MZ, marginal zone.

(B) Representation of transcriptional heterogeneity of germinal zone cells profiled by single-cell mRNA-seq. Cells are arranged according to their position determined using t-distributed stochastic neighbor embedding.

(C) Heatmap showing gene expression levels for 1% of genes most strongly contributing to PC1–4. Select marker genes are highlighted. Groups represent clusters with highest approximately unbiased p values following multiscale bootstrapping of hierarchical clustering based on expectation-maximization cluster assignments (see also Figure S1).

(D) Interpretation of distinct cortical and ventral telencephalic lineages detected among germinal zone cells.

neural stem cell niche through the local production of growth factors, the expression of extracellular matrix proteins that potentiate growth factor signaling, and the activation of the LIFR/STAT3 signaling pathway.

RESULTS

Molecular Diversity of Cells in the Cortical Germinal Zones

To analyze molecular features of cells in the germinal zones during human cortical neurogenesis, we captured single cells from microdissected VZ and SVZ specimens of human cortex at gestational weeks 16–18 (GW16–18) and generated sequencing libraries (schematic Figure 1A). We subsequently analyzed 393 single cells from three individuals in which we detected at least 1,000 genes (Table S1). To classify cells, we performed principal component analysis (PCA) and used expectation-maximization clustering to group cells based on their position in PC space (Figure S1 and Experimental Procedures). Based on the expression of known marker genes, we interpreted groups to represent cells along the cortical excitatory lineage and inhibitory interneurons generated in the ventral telencephalon (Figures 1B–1D and S1 and Table S2).

We further examined groups of cells expressing known markers of the cortical excitatory neuron lineage (schematic, Figure 2A). Four groups robustly expressed markers of human radial glia *SLC1A3*, *PAX6*, *SOX2*, *PDGFD*, and *GLI3* (yellow

bar, Figure 2A). Another four groups retained a reduced level of *PAX6*, *SOX2*, and *SLC1A3* expression, but also expressed early neuronal markers such as *STMN2* and *NEUROD6*. These groups were also characterized by the absence of canonical radial glia marker expression, including *VIM* and *HES1*, and by the specific expression of canonical and novel intermediate progenitor markers *EOMES* (*TBR2*), *ELAVL4*, *NEUROG1*, *NEUROD1*, *NEUROD4*, *PPP1R17*, and *PENK* (magenta bar, Figures 2A, 2B, and S1) (Hevner et al., 2006; Kawaguchi et al., 2008). We found that the vast majority of cells expressing *EOMES* and *PPP1R17* mRNA also expressed *EOMES* protein with variable *SOX2* expression (Figure S2). Immunostaining for *PPP1R17* revealed diverse morphologies of these cells, including multipolar cells with short processes, as well as unipolar and bipolar cells with one or two radially or tangentially oriented processes. Regardless of morphology, these progenitor cells did not express the classical molecular signature of radial glia (Figure S2). Thus, our analysis provides a clear distinction between radial glia and intermediate progenitors. Future studies may relate the molecular heterogeneity of intermediate progenitors and the relative expression of radial glial and proneuronal genes to the diverse and dynamic morphological features reported in OSVZ progenitors (Betizeau et al., 2013).

Major Sources of Transcriptional Variation among Radial Glia Relate to Cell Cycle and Stem Cell Niche

We next analyzed variation in gene expression across 107 cells from the four groups that robustly expressed canonical markers of radial glia. We anticipated that cell cycle would be the major source of transcriptional variation across proliferative populations (Pollen et al., 2014). Indeed, genes involved in cell-cycle regulation, mitosis, and DNA replication explained most variation

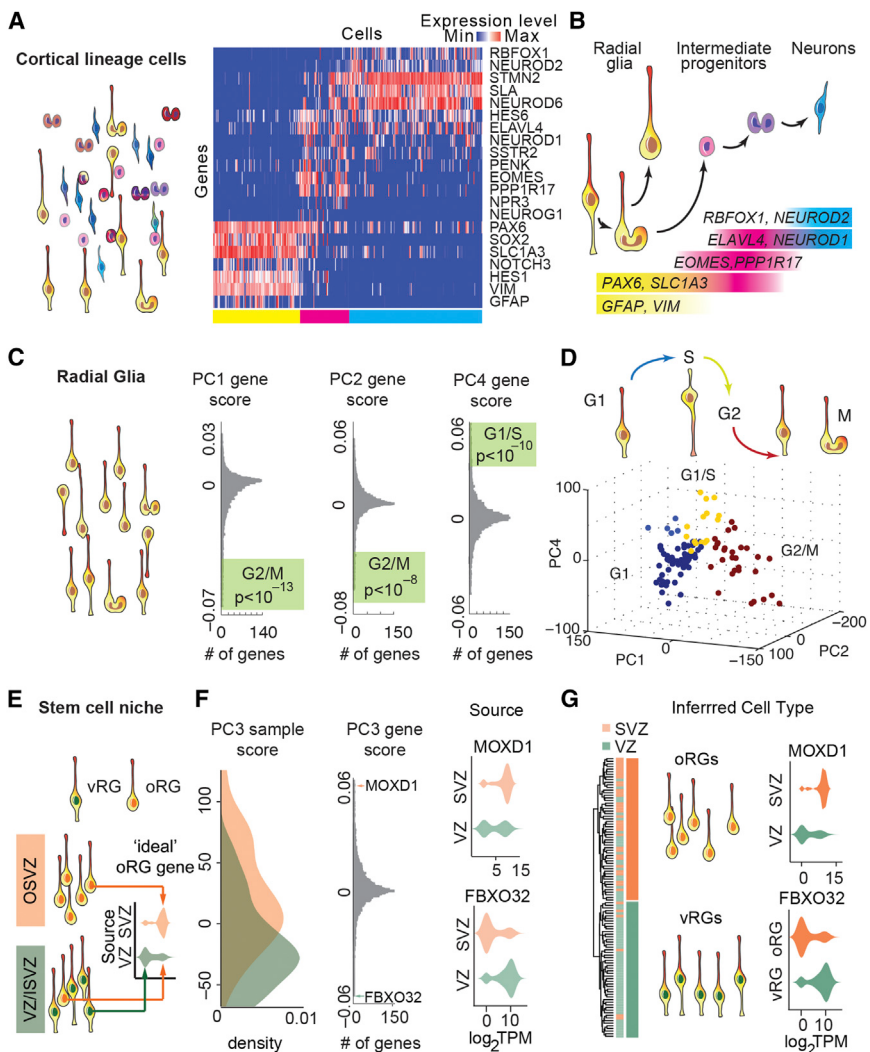


Figure 2. Major Sources of Transcriptional Heterogeneity among Radial Glia

(A) Analysis of cell-type identity of in-silico-sorted cortical lineage cells (schematic); heatmap illustrates expression of identity genes across cells. Colored bars below heatmap highlight membership of cells into major groups (Figure S1).

(B) Interpretation of sequential gene expression changes during cortical excitatory neuron differentiation (see also Figure S2).

(C) Schematic illustrating in silico sorting of classically defined radial glia from the set of cortical lineage cells. Radial glia themselves display heterogeneity with respect to cell-cycle progression, morphology, anatomical position, and behavior, and PCA reveals major sources of transcriptional variation among radial glia. Histogram of PCA gene loading scores with gene ontology enrichments highlighted (adjusted p value, Fisher's exact test).

(D) Interpretation of cell-cycle phases for radial glia based on clustering according to sample scores along PC1, 2, and 4 (see also Figure S3).

(E) Schematic of the anatomical sources of radial glia and violin plots illustrate prediction that VZ and adjacent inner SVZ contain a mixed population of vRG and oRG cells.

(F) Histogram of VZ and OSVZ radial glia sample scores and gene loading scores along PC3. Radial glia from OSVZ ($n = 39$) have significantly higher PC3 scores than radial glia from VZ ($n = 68$) across 3 samples ($p < 10^{-4}$, Welch t test, see also Figure S3). Violin plots show distribution of expression values for strongly loading genes across cells from VZ and OSVZ sources.

(G) Interpretation of oRG and vRG identity based on clustering cells according to top 1% of genes loading PC3. Schematic highlights the grouping of radial glia by inferred cell type rather than by anatomical source. Violin plots show distribution of expression values within inferred cell types.

along PC1, PC2, and PC4 (Figure 2C and Table S3). Clustering radial glia based on variation along these axes revealed cell groups representing G1, G1/S checkpoint, and G2/M checkpoint (Figures 2D and S3). During interkinetic nuclear migration, the cell bodies of radial glia migrate away from the ventricle during G1, toward the ventricle during S/G2 phase, and divide at the ventricular surface. We examined the expression of a novel predicted G1 marker, *CRYAB*, and found that cells expressing *CRYAB* transcript were displaced from the ventricle, rarely expressed the G2/M marker phospho-histone H3, and rarely incorporated BrdU, a label for DNA replication, consistent with the G1 specificity of this transcript (Figure S3). Thus, differentiation and cell cycle are major sources of transcriptional heterogeneity among cells in the germinal zone, and single-cell analysis reveals novel molecular features of these states.

We hypothesized that differences in stem cell niche occupancy would also contribute to variation among radial glia. Descriptions of cell behavior and morphology suggest that the VZ and adjacent inner SVZ contain mixed populations of vRG cells and oRG cells destined to migrate to the OSVZ (Reillo et al.,

2011) (Figure 2E). In contrast, the OSVZ contains a more pure population of oRG cells that lack apical processes (Fietz et al., 2010; Hansen et al., 2010), although the morphology of these cells may also be dynamic and diverse (Betizeau et al., 2013; Gertz et al., 2014). We found that the anatomical source of radial glia was significantly associated with the position of cells along PC3 (Figures 2F and S3). Indeed, many of the genes with strong positive and negative loading scores along PC3 showed differential expression patterns between radial glia collected from VZ and SVZ (Figure 2F). By clustering radial glia based on the 1% of genes most strongly loading PC3, we identified two transcriptionally distinct groups, one almost purely composed of cells from VZ that we interpreted as vRG cells and another composed of cells from both VZ and SVZ that we interpreted as oRG cells (Figure 2G).

Predicted Markers Relate to Position, Morphology, and Behavior of oRG Cells

To relate these distinct transcriptional states to the stem cell niches of the developing neocortex, we first searched for genes

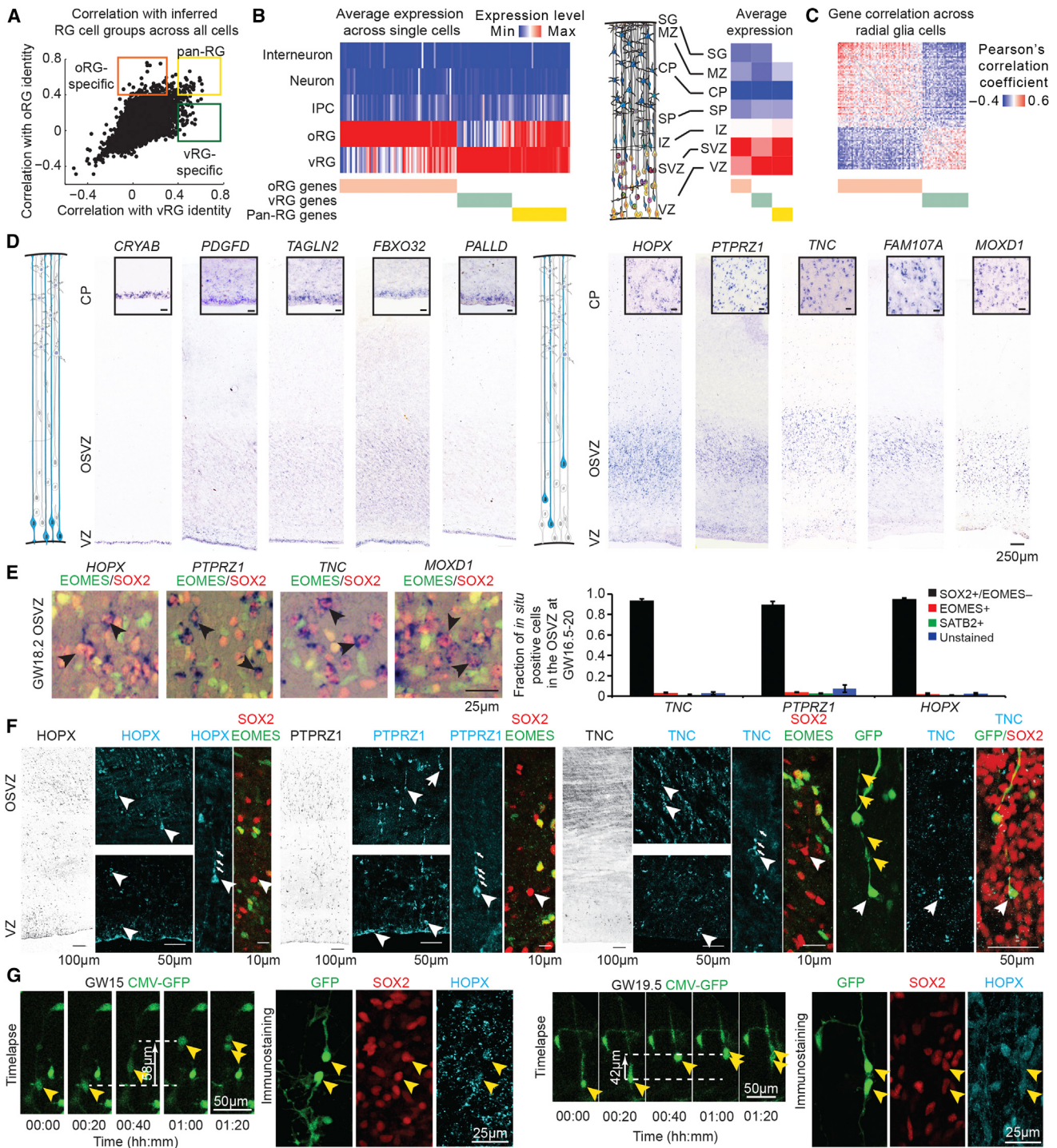


Figure 3. Candidate oRG Markers Relate to Position, Morphology, and Behavior of Cell Type

(A) Scatterplot highlighting specificity of genes to inferred radial glia subpopulations. Specificity is calculated by Pearson correlation with an idealized marker gene expressed only in candidate oRG cells (y axis) or candidate vRG cells (x axis). Orange, green, and yellow boxes highlight genes with predicted specificity for oRG, vRG, and all radial glia cells (pan-RG), respectively (see also Figure S3).

(B) Left heatmap showing expression of oRG, vRG, and pan-RG genes across inferred cell types and their average expression in microdissected cortical tissue samples (right heatmap) (Miller et al., 2014).

(C) Similarity matrix of oRG- and vRG-specific gene expression levels across radial glia cells.

(D) Representative examples of in situ hybridization staining for candidate vRG and oRG markers in human cortical tissue sections at GW18.2. Inset shows higher magnification of positively stained region (scale bar, 25 μm).

(legend continued on next page)

likely to distinguish predicted radial glia subtypes. We measured the specificity of genes by their correlation with an ideal marker gene uniformly expressed in only one putative radial glia subpopulation across all 393 cells (Figures 3A and S3). We identified 67 candidate marker genes strongly correlated with the oRG population, 33 candidate genes strongly correlated with the vRG population, and 31 genes strongly correlated with both radial glia populations (Figure 3A, green, orange, and yellow boxes, respectively; Table S3). In support of these predictions, we observed that candidate vRG markers showed higher expression in the VZ, whereas candidate oRG markers showed higher expression in the SVZ across tissue samples collected from developing human cortex, and their expression levels were inversely correlated across radial glia cells (Figures 3B and 3C) (Miller et al., 2014).

To further investigate candidate marker genes, we performed *in situ* hybridization at GW17–19, stages of peak neurogenesis. We found that expression of vRG candidates, *CRYAB*, *PDGFD*, *TAGLN2*, *FBXO32*, and *PALLD*, was strongest in the VZ, whereas expression of oRG candidates, *HOPX*, *PTPRZ1*, *TNC*, *FAM107A*, and *MOXD1*, was strongest in the OSVZ (Figure 3D). Quantification revealed that the vast majority of cells expressing *TNC*, *PTPRZ1*, or *HOPX* also expressed the radial glia marker *SOX2*, but not the intermediate progenitor marker *EOMES* or neuronal marker *SATB2* (Figures 3E and S4). Immunostaining revealed expression of *HOPX*, *PTPRZ1*, and *TNC* proteins in cells with basal fibers that lacked *EOMES* expression, linking this molecular identity to the typical morphology of oRG cells (Figure 3F). To next relate this molecular identity to distinctive oRG behaviors, we performed time-lapse imaging of organotypic cortical slices from GW15, GW17, GW18, GW18.7, and GW19.5 specimens infected with GFP-expressing adenovirus and then examined the expression of the most specific oRG marker, *HOPX*. We observed that cells undergoing mitotic somal translocation behavior can generate *SOX2/HOPX* double-positive daughter cells with long basal processes characteristic of oRG cells throughout neurogenesis (Figures 3G and S4). Together, these results connect the molecular identity determined from single-cell RNA sequencing to the anatomical location, morphology, and behavior of oRG cells.

Specific Expression of Stemness Pathways Suggests Mechanism for Maintaining the OSVZ Stem Cell Niche

Because oRG cells lack direct access to trophic factors distributed by the cerebrospinal fluid (Lehtinen et al., 2011), we explored whether genes enriched in oRG cells relate to known functional categories related to growth factor signaling (Figure 4A). We found that protein products of many genes enriched in oRG cells mediate interactions with the extracellular matrix (Figures 4B–4D and Table S3). These proteins included *TNC*, *PTPRZ1*, *SDC3*, *HS6ST1*, and *ITGB5*, which cooperate to pro-

mote neural stem cell maturation by controlling local concentrations of fibroblast and epidermal growth factors (Barros et al., 2011; Garwood et al., 2004; Milev et al., 1998; Szklarczyk et al., 2015). Furthermore, the PTPRZ1 ligand PTN was expressed in both radial glia populations but was the most significantly upregulated gene in oRG cells (Table S4). We confirmed by immunostaining that *TNC* and *PTPRZ1* are expressed in a subset of *ITGB5*-positive oRG cells (Figure 4E). Many of the cell-surface proteins enriched in oRG cells are also highly overexpressed in glioblastomas compared with normal human astrocytes, including *TNC*, *PTPRZ1*, and *LGALS3BP* (Autelitano et al., 2014; Nie et al., 2015), and PTN stimulation of PTPRZ1 is sufficient to stimulate the coordinated processes of epithelial-to-mesenchymal transition in a glioblastoma cell line (Perez-Pinera et al., 2006). Therefore, we investigated whether human glioblastoma samples contain cell populations that co-express oRG markers. In a recent study of five primary glioblastoma samples, *PTN*, *PTPRZ1*, and *FABP7* were the genes most correlated with a stemness signature across single tumor cells (Patel et al., 2014). We extended this analysis to all predicted oRG and vRG markers (Figure 4F) and found that oRG markers were more highly correlated with both the stemness and general radial glia signatures than vRG markers (Figure 4G), suggesting that oRG-enriched genes are associated with stemness pathways and growth factor signaling in both the developing OSVZ stem cell niche and in primary glioblastoma.

We next explored whether additional signaling pathways were upregulated in oRG cells. We found that *LIFR* and its co-receptor *IL6ST* (GP130) were specifically expressed in oRG cells (Figures 4H and 4I). LIF signaling through LIFR and IL6ST phosphorylates STAT3 at tyrosine 705 (p-Y705) to promote stem cell maintenance (Huang et al., 2014). Immunostaining revealed that p-Y705-STAT3 was specifically localized at the nuclei of oRG cells and not detected in other cell types (Figures 4I and S5). To investigate the function of STAT3 in oRG cells, we pharmacologically blocked STAT3 phosphorylation in human slice cultures. After 2 days, we observed a reduction in the proportion of oRG cells that incorporated bromodeoxyuridine (BrdU) (Figure 4J), which is consistent with the proposed role of phosphorylated STAT3 in neural stem cell maintenance (Hong and Song, 2015; Huang et al., 2014). In addition, we found that expression of constitutively active Stat3 in developing mouse cortex increased the proportion of electroporated cells expressing *Sox2*, but not *Eomes*, compared with expression of only the fluorescent reporter (Figure S5). Together, these results support a role for STAT3 (p-Y705) in maintaining stemness of human oRG cells.

Extensive Neurogenic Capacity of oRG Cells

We next examined the differentiation potential and proliferative capacity of human oRG cells (Figure 5A). Many oRG-enriched

(E) *In situ* hybridization combined with immunostaining for identity markers. Black arrows highlight cells expressing marker transcript and *SOX2*, but not *EOMES* (see also Figure S4 containing further examples). Bar chart shows quantification of molecular identity of OSVZ cells positive for oRG marker mRNA. Values represent mean \pm SEM; n = 3 biological replicates, GW16.7, GW18.2, and GW20.

(F) Immunostaining of GW18 cortex for candidate oRG proteins and identity markers. White arrows highlight examples of immunopositive radial glia with staining in basal fiber. Yellow arrows indicate varicosities of the basal fiber of an oRG cell infected with adenovirus-GFP, with *TNC* immunostaining in the cell body.

(G) Time-lapse imaging of oRG cells undergoing MST and post-staining for *HOPX*, *SOX2*, and GFP. Yellow arrows highlight GFP-expressing cells. See also Figure S4.

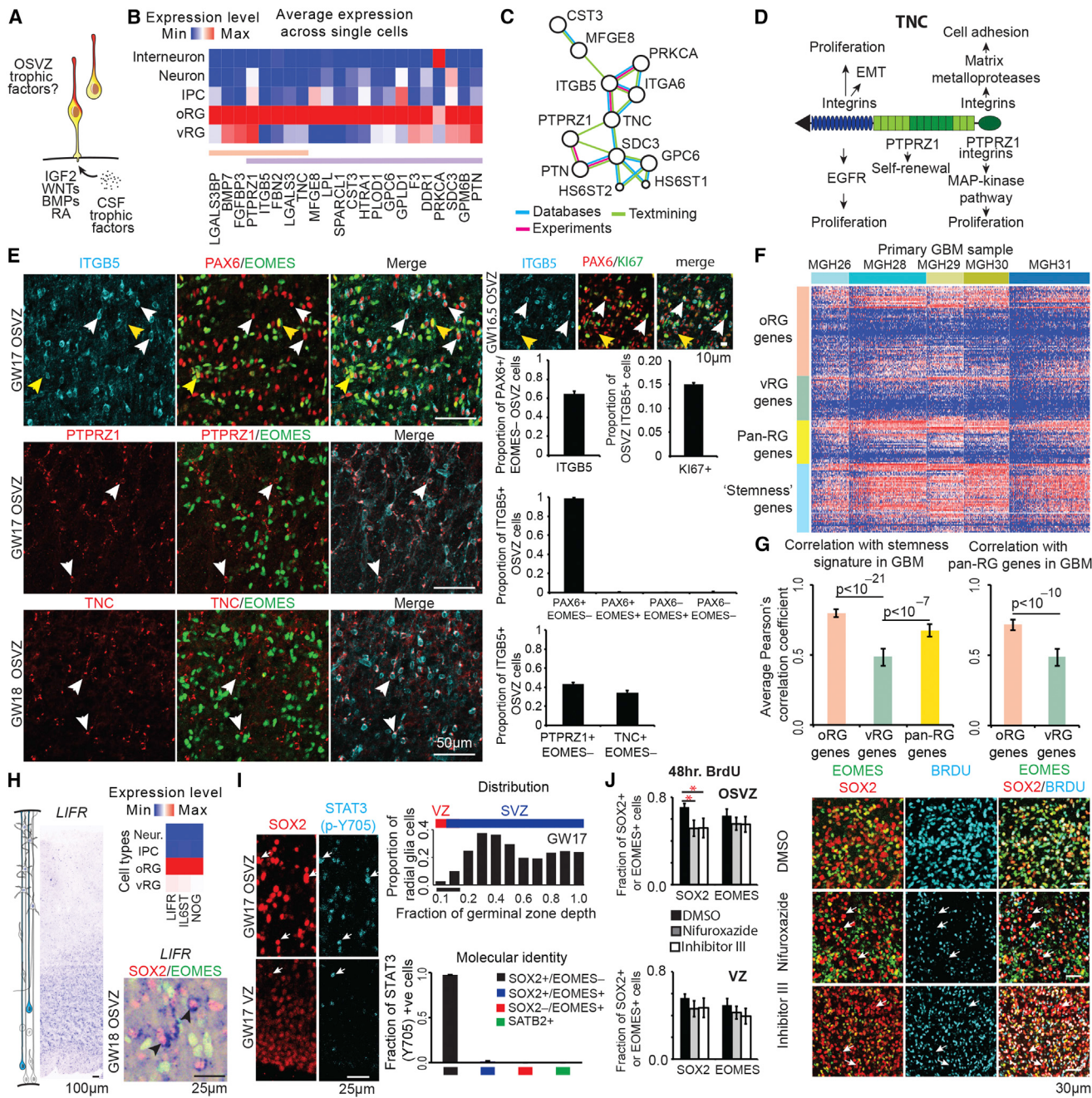


Figure 4. Pathways Enriched in oRG Cells Relate to Growth Factor Signaling and Maintenance of Proliferation

(A) Schema: oRG cells lack apical processes that transduce signals mediated by trophic factors in ventricular cerebrospinal fluid (CSF).

(B) Heatmap of extracellular matrix gene expression across inferred cell types. Orange bar highlights genes with high oRG specificity across all cells, and purple bar highlights genes differentially expressed by DESeq.

(C) Functional protein association network generated using String-db (Szklarczyk et al., 2015).

(D) Model of TNC protein, interaction partners, and downstream pathways.

(E) Immunolabeling of human OSVZ tissue sections reveals expression of ITGB5 by radial glia, including proliferating KI67+ and KI67- (top row, examples indicated with arrows), but not EOMES+ intermediate progenitors (yellow arrowheads denote PAX6+, EOMES+ intermediate progenitor cells, which do not express ITGB5, see also Figure S2). Top right panels show immunolabeling for ITGB5 and proliferation marker Ki67 (white arrows indicate proliferating radial glia expressing ITGB5, and yellow arrow indicates non-actively proliferating radial glia expressing ITGB5). Bottom left rows show expression of TNC and PTPRZ1 in a subset of ITGB5+ radial glia (examples indicated with arrowheads). Bar charts represent quantification (mean ± SEM) across three biological replicates between GW16.5 and GW18.

(F) Heatmap of oRG, vRG, pan-RG, and glioblastoma multiforme (GBM) stemness gene expression signatures across 598 cells from five primary GBM tumors (Patel et al., 2014).

(legend continued on next page)

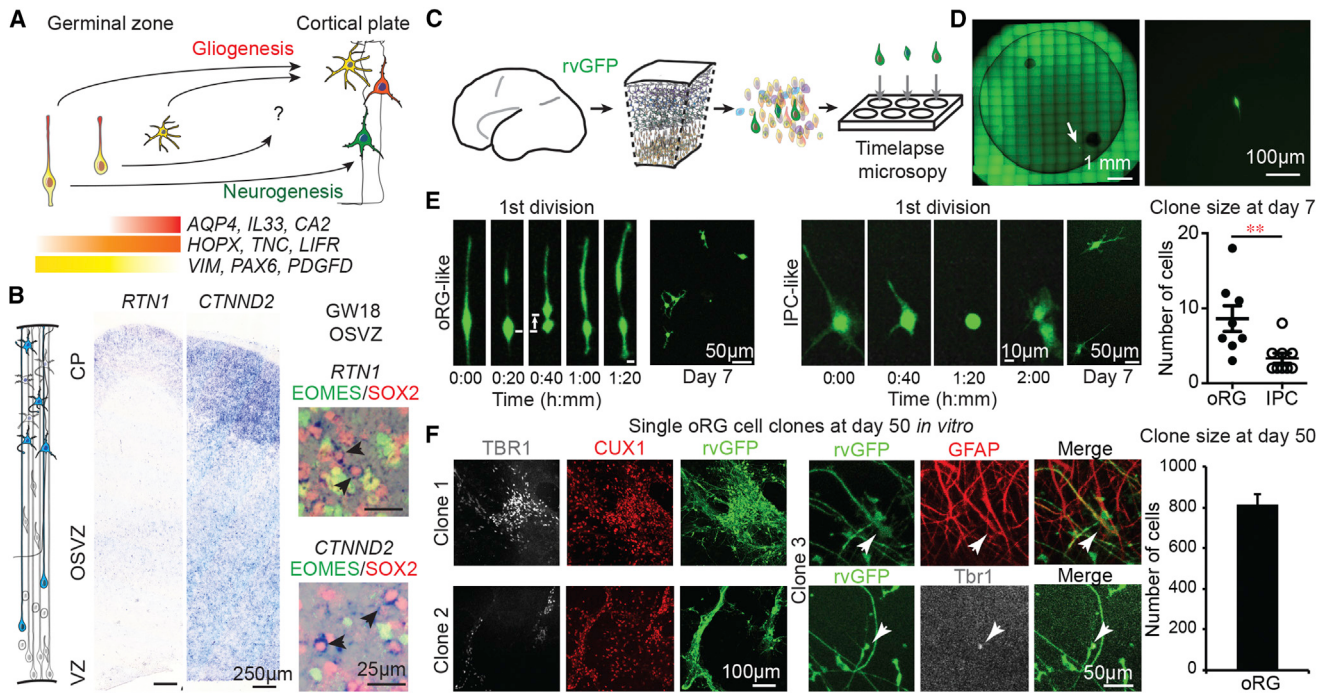


Figure 5. Extensive Proliferative and Neurogenic Capacity of oRG Cells

(A) Schema representing progenitor cell competence of radial glia, oRG cells, and glial progenitors (see also Figure S5).

(B) In situ hybridization for genes expressed by oRG and other cell types but depleted in vRG cells and immunolabeling of GW18 human cortical sections (see also Figure S6). Black arrows indicate examples of mRNA expressing oRG cells.

(C) Experimental design for single-cell clonal lineage analysis of oRG cells labeled with retrovirus GFP (rvGFP).

(D) Image and magnification of a well containing a single purified GFP-positive cell. Time-lapse imaging of single cell with arrow highlighting MST preceding first division.

(E) Images show movie frames capturing the initial division and a resulting clone after 7 days in culture of a cell exhibiting oRG specific mitotic somal translocation (left) and a cell undergoing an initial stationary division with fiber retraction characteristic of intermediate progenitors and a resulting clone after 7 days in culture (right). Chart shows clone sizes at 7 days for cells classified as oRGs and IPCs based on first division and morphology.

(F) Immunostaining for neuronal or glial markers of 3 oRG cell clones after 50 days in vitro. Bar chart represents quantification of the average clone size of oRG cells.

See also Figure S6.

genes are also associated with astrocytes later in development, including *TNC*, *ITGB5*, *DIO2*, and *ACSBG1* (Cahoy et al., 2008), and LIFR signaling through STAT3 can promote gliogenesis in combination with BMP signaling (Bonaguidi et al., 2005). However, oRG cells did not express other astrocyte markers such as *AQP4*, *CA2*, *IL33*, and *ALDOC*, which we observed in putative astrocytes later in development (Figure S5). In addition, oRG cells strongly expressed *NOG* (Figure 4H), which inhibits BMP signaling and promotes neurogenesis in GFAP-expressing pro-

genitors (Bonaguidi et al., 2005; Bonaguidi et al., 2008; Lim et al., 2000). We further noted that many genes upregulated in oRG cells relative to vRG cells were also strongly expressed by cortical neurons such as *NPY*, *RTN1*, *CTNNND2*, *SEZ6L*, and *NRCAM* (Figures 5B and S6), suggesting a relationship between neurons and oRG cells.

To further examine the neurogenic potential of oRG cells, we isolated single cells from the germinal zone by fluorescence-activated cell sorting (FACS) and cultured them on a feeder cell layer

(G) Bar graphs show that the oRG signature has the strongest correlation with the GBM stemness signature and with the pan-RG signature across GBM tumor samples. p values report significance of difference between standardized correlation coefficients; error bars represent 95% confidence interval.

(H) Heatmap showing average expression of selected genes across inferred cell types and validation of *LIFR* expression in oRG cells by in situ hybridization (examples indicated by arrows).

(I) Immunostaining of human tissue section for phosphorylated STAT3 (p-Y705) and SOX2 (see also Figure S5). Top bar graph represents quantification of nuclear immunostaining for phosphorylated STAT3 across germinal zone depth starting from ventricular edge (0.0) to the basal edge of the OSVZ (1.0). Bottom graph represents the molecular identity of STAT3+ Y705+ cells quantified in the OSVZ of three biological replicates between GW16.5 and GW18. Data represent mean \pm SEM.

(J) Inhibition of STAT3 phosphorylation in organotypic OSVZ slice cultures reduces BrdU incorporation by radial glia. Images show representative examples of immunostained experimental sections. Bar graphs display quantification of BrdU incorporation by radial glia and intermediate progenitors in presence of STAT3 phosphorylation inhibitors or control DMSO ($n = 4$, * $p < 0.05$, paired Student's t test, error bars represent SEM). Arrows indicate examples of cells expressing SOX2 but not EOMES or SATB2 that did not incorporate BrdU over 48 hr period in inhibitor-treated slices.

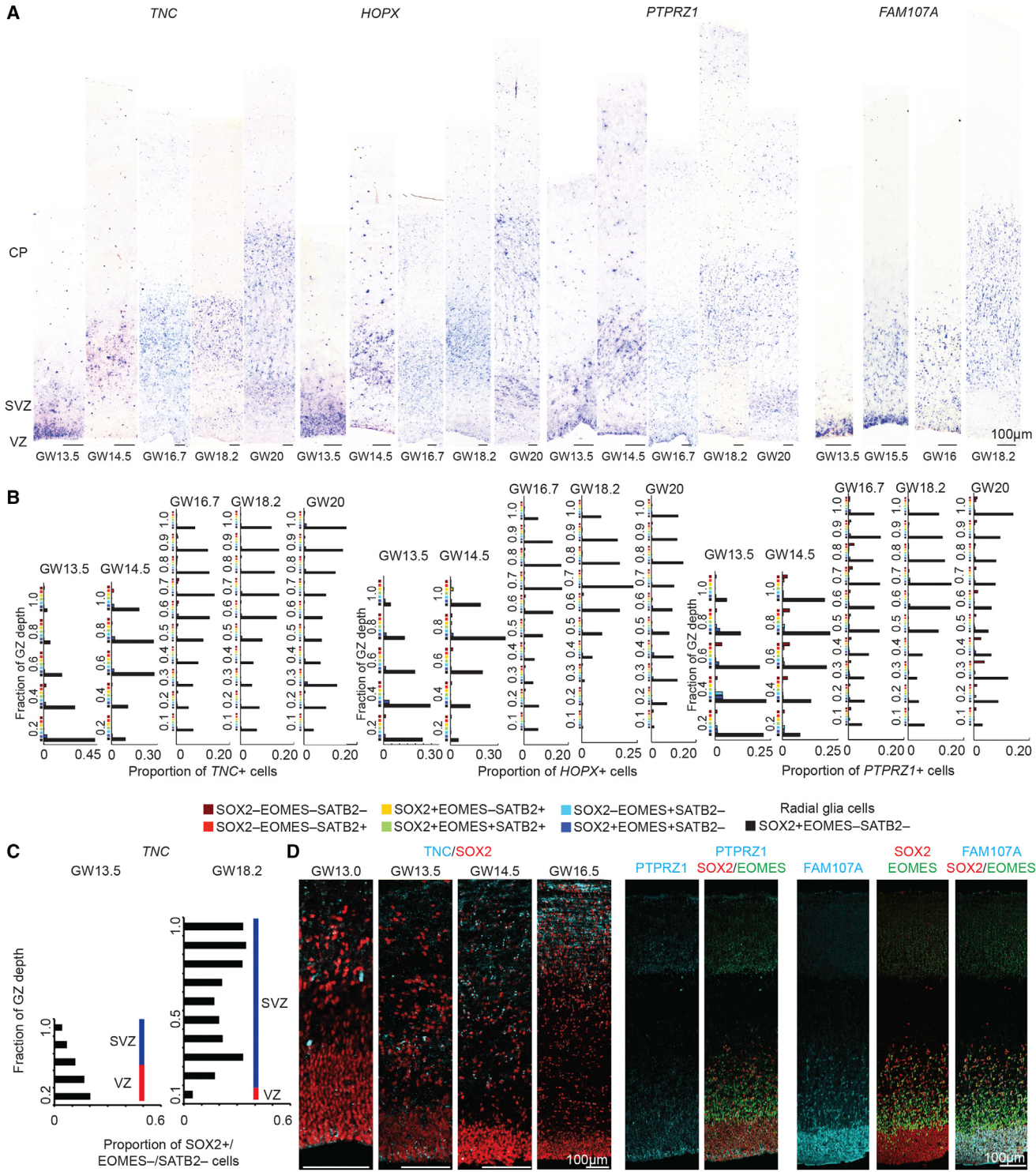


Figure 6. Molecular Signature of oRG Cells Emerges in VZ

(A) *In situ* hybridization for genes enriched in oRG cells across multiple developmental time points corresponding to human cortical neurogenesis. Sections were stained with antibodies against SOX2, EOMES, and SATB2 to identify major cell populations (see also Figures S4 and S7).

(B) The proportion of oRG marker cells that express all combinations of protein markers was quantified across ten bins that span the germinal zone throughout neurogenesis. In all cases, oRG marker transcripts are almost exclusively expressed by SOX2+/EOMES-/SATB2- cells (black bars). Bar graphs highlight that, at GW13.5, oRG markers predominantly label radial glia in the VZ, but by GW14.5, oRG markers predominantly label radial glia cells in the SVZ.

(legend continued on next page)

(Figures 5C and 5D). Using time-lapse imaging, we followed individual cells for 1 week in vitro. Cells that displayed the distinctive somal translocation directly preceding the first division were classified as oRGs, whereas cells that retracted processes and underwent stationary first division were classified as intermediate progenitors. Consistent with their stem-like character, single oRG cells gave rise to larger clones than intermediate progenitor cells (Figure 5E). We followed three oRG clones in vitro for an additional 6 weeks, and they generated hundreds of daughter cells, including deep and upper layer neurons, as well as glial cells (Figures 5F and S6). Thus, human oRG cells express self-renewal pathways not detected in vRG cells during peak upper cortical layer neurogenesis, generate diverse neural daughter cells, and have the capacity for extensive proliferation.

oRG Signature Emerges in VZ and Is Conserved in Primates

To further investigate the developmental and evolutionary origin of the transcriptional signature of oRG cells, we examined the expression of oRG marker genes across different stages of human corticogenesis and in different species. Surprisingly, we observed strong expression of transcripts encoding oRG marker genes in the VZ at early stages of human cortical development. This expression became progressively restricted to the OSVZ at later stages, with *FAM107A* persisting the longest in the VZ (Figures 6A, 6B, and S7). *TNC*, *FAM107A*, and *PTPRZ1* protein expression followed a similar developmental progression, but *TNC* and *PTPRZ1* antibodies only labeled subsets of radial glia cells in the VZ (Figure 6C). The coordinated expression of these genes in the VZ around GW13.5 coincides with the elaboration of the OSVZ (Bayatti et al., 2008; Martínez-Cerdeño et al., 2012; Shitamukai et al., 2011; Zecevic et al., 2005) and may represent a molecular program involved in oRG specification.

During mouse development, oRG cells are rare and there is not a distinct OSVZ. To investigate whether human oRG markers are expressed in mouse radial glia, we used recently published gene coexpression networks (Lui et al., 2014) and found that, on average, human oRG markers are less likely to show specific expression in mouse radial glia than general radial glia markers (Figure 7A). Nonetheless, *TNC* expression has previously been detected in radial glia of the mouse ventral pallium (Garcion et al., 2004; Götz et al., 1998; Wiese et al., 2012). Immunostaining for *TNC* and *PTPRZ1* revealed that both proteins are most strongly detected in the VZ and SVZ of the lateral and ventral pallium (Figure 7B), where mouse oRG cells are most common (Wang et al., 2011b). Closer examination of SOX2-positive cells in the SVZ revealed examples of putative mouse oRG cells expressing *TNC* and *PTPRZ1* (Figure 7B, insets). More widespread transcription of *TNC*, *PTPRZ1*, and *HOPX* throughout the mouse cortical VZ coincides with the conclusion of cortical neurogenesis (Figure S7). Thus, conserved elements of the oRG signature may reflect regional and temporal heterogeneity of mouse radial glia, but many genes enriched in human oRG cells are

not expressed in mouse radial glia, including *MOXD1* (Wang et al., 2011a), *FAM107A*, *FBN2*, *BMP7*, *HS6ST2*, *LGALS3*, and *TKTL1* (Figure S7). In contrast to mouse, the developing macaque cortex contains a large OSVZ region and prominent oRG population (Betizeau et al., 2013; Smart et al., 2002). Using microarray data from developing macaque cortex, we found that the expression of oRG marker genes in macaque development mirrors that of human development (Figure 7C). We confirmed this pattern for select oRG marker genes by analyzing primary tissue samples. We detected expression of *TNC*, *PTPRZ1*, and *HOPX* in macaque VZ early in development but found that OSVZ expression of these markers, along with *FAM107A*, predominates at later stages of corticogenesis (Figure 7D). Together, our data indicate that major elements of the transcriptional signature of human oRG cells are conserved in primates.

DISCUSSION

Our study identifies neuronal differentiation, cell-cycle progression, and anatomical position as major sources of transcriptional variation across single cells sampled from germinal niches of the developing human cortex. The transcriptional state associated with neuronal differentiation involves reduced expression of classical radial glia markers such as *VIM* and *HES1* and upregulation of proneuronal transcription factors such as *NEUROG1*, *NEUROD4*, and *EOMES* and neuropeptide signaling genes *PENK*, *SSTR2*, and *OXTR*. This transcriptional state was recently attributed to heterogeneity among oRG cells (Johnson et al., 2015). However, based on expression of mRNA, EOMES protein, and the novel marker PPP1R17, which reveals diverse multipolar morphologies, we interpret this transcriptional state to represent intermediate progenitor cells.

In contrast, we identify a novel transcriptional state, independent of neuronal differentiation, that distinguishes oRG from vRG cells by analyzing the major sources of variation among classically defined radial glia. We relate this transcriptional state to the position, morphology, and dynamic behavior of oRG cells. Together, this multimodal characterization establishes an integrative identity for oRG cells. These neural stem cells are characterized by the expression of novel markers, including *HOPX*, *TNC*, *ITGB5*, as well as pan-radial glia markers such as *VIM*, *HES1*, and *ATP1A2*; the presence of a basal, but not apical fiber; mitotic-somal translocation behavior; and extensive proliferative and neurogenic capacity. This cell type is most abundant in the OSVZ stem cell niche for which it was named but also resides in the inner SVZ and VZ, and the transcriptional state first emerges in the VZ during early cortical neurogenesis. The oRG marker genes may enable the construction of molecular tools for selectively visualizing, manipulating, or purifying oRG cells in tissue and for evaluating the identity of human cortical progenitor cells generated from pluripotent stem cells. In addition, these genes may provide insights into the cell types affected in neurodevelopmental disorders.

(C) The proportion of SOX2+/EOMES-/SATB2- that expressed *TNC* was quantified across the span of the germinal zone at GW13.5 and GW18.

(D) Immunolabeling of early developmental time points for oRG markers and SOX2. At GW13.5, *TNC* and *PTPRZ1* protein show limited expression in radial glia close to the ventricular edge, whereas *FAM107A* protein is widely expressed in GW13.5 VZ.

See also Figure S7.

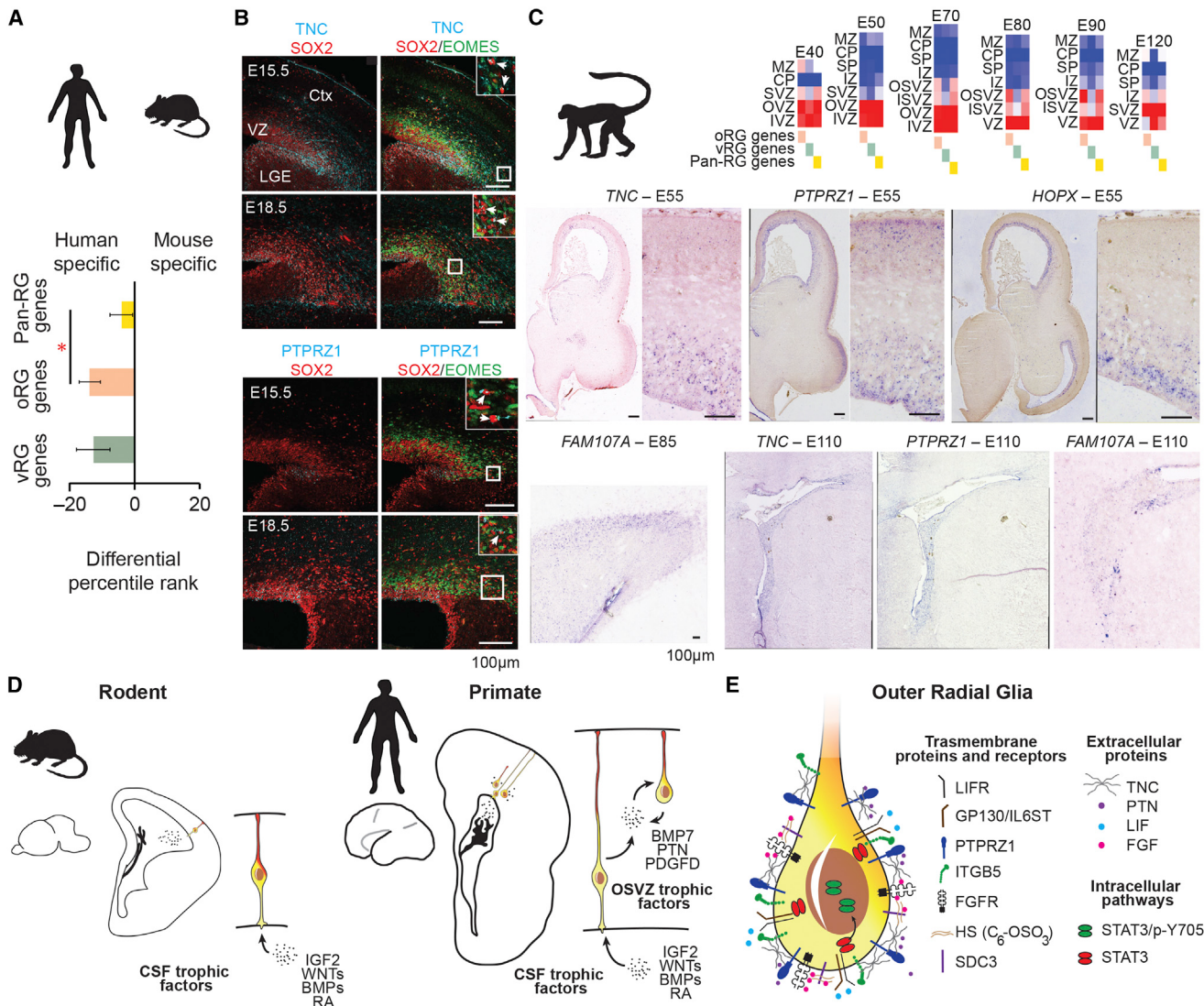


Figure 7. Conservation of oRG Marker Gene Expression in Primates

(A) Bar graph indicates average differential percentile rank of pan-RG, oRG, and vRG genes for radial glia gene coexpression network specificity in human and mouse. Compared with pan-RG genes ($n = 29$), human oRG genes ($n = 66$) show reduced conservation with mouse radial glia signature ($p < 0.05$, Wilcoxon rank sum test).

(B) Mouse E15.5 and E18.5 cortical sections immunoreacted for Tnc and Ptprz1 along with Sox2 and Eomes. Inset images show a magnified view of SVZ region, and arrows highlight examples of Sox2-positive, Eomes-negative cells that co-label for Tnc or Ptprz1. LGE, lateral ganglionic eminence; Ctx, cortex.

(C) Heatmaps show average expression level of oRG, vRG, and pan-RG genes in distinct regions of developing macaque cortex. IVZ, inner VZ; OVZ, outer VZ; the NIH Blueprint Non-Human Primate (NHP) Atlas. In situ hybridization of macaque cortex showing expression of oRG marker genes mirrors human trajectory.

(D) Radial glia in small rodent brains are concentrated along the ventricle and access cerebrospinal fluid trophic factors directly via apical processes. In contrast, large primate brains contain numerous radial glia in the OSVZ. Local production of growth factors by radial glia may provide additional trophic support to oRG cells in the OSVZ niche.

(E) Increased expression of extracellular matrix proteins that potentiate growth factor signaling and activation of LIFR/STAT3 pathway may further maintain stemness in oRG cells.

See also Figure S7.

Beyond simply marking oRG cells, the genes we identify belong to common pathways that suggest mechanisms by which human oRG cells actively maintain the OSVZ as a neural stem cell niche. Many of these genes promote growth factor signaling, including *TNC*, *PTPRZ1*, *ITGB5*, *SDC3*, *HS6ST1*,

IL6ST, and *LIFR* (Sim et al., 2006; Wiese et al., 2012). For example, *TNC* potentiates FGF signaling to support the maturation of neural stem cells (Garcion et al., 2004), whereas integrin signaling along the basal fiber promotes radial glia identity (Fietz et al., 2010). Interestingly, *TNC* contains EGF-like repeats and

multiple binding domains for PTPRZ1, syndecans, integrins, and other cell-surface receptors (Besser et al., 2012; von Holst, 2008). Thus, TNC expression in oRG cells may couple key protein networks regulating growth factor signaling, migration, and self-renewal. In addition, LIFR/STAT3 signaling is known to maintain radial glia neural stem cell identity (Bonaguidi et al., 2005), and we show that p-Y705-STAT3 signaling is necessary for normal cell-cycle progression in oRG cells but is surprisingly absent in vRG cells. Although STAT3 signaling can also contribute to gliogenesis, we speculate that expression of NOG may inhibit gliogenesis as observed in the rodent adult neurogenic germinal zones (Bonaguidi et al., 2008; Lim et al., 2000). We directly examined the neural stem cell properties of oRG cells using single-cell clonal analysis. We find that single oRG cells at mid-neurogenesis can generate clones of nearly 1,000 neuronal and glial daughter cells. This highlights the remarkable proliferative capacity of human oRG cells compared to mouse radial glia that typically generate 10–100 daughter cells throughout the neurogenic period (Gao et al., 2014; Qian et al., 2000; Vasistha et al., 2014).

The cell behaviors that distinguish oRG from vRG cells—loss of adhesion, delamination, and rapid migratory bursts preceding cell division—have been compared to epithelial-to-mesenchymal transition (Itoh et al., 2013). Recent work suggests that oRG and glioma cells both undergo myosin-II-dependent migratory movements (Beadle et al., 2008; Ostrem et al., 2014). Interestingly, many of the genes and proteins we detected in oRG cells have been implicated in invasive migratory behavior, including genes expressed in the VZ when oRG cells first emerge. For example, TNC, ITGB5, and PTN/PTPRZ1 signaling promotes multiple aspects of epithelial-to-mesenchymal transition (Bianchi et al., 2010; Katoh et al., 2013; Perez-Pinera et al., 2006), PRKCA is necessary for the upregulation of SNAI1 and downregulation of CLDN1 during these transitions (Kyuno et al., 2013), and FAM107A establishes focal adhesions and increases glioma invasiveness (Le et al., 2010). The expression of these genes suggests possible mechanisms by which oRG cells emerge from the VZ and undergo mitotic somal translocation. More generally, we found the oRG transcriptional signature to be enriched in cells from primary glioblastoma and conserved in macaque, suggesting that the development of invasive glioblastoma and the evolutionary expansion of the OSVZ may recruit common sets of genes controlling migration and self-renewal.

Sequencing of single-cell mRNA while retaining cell position information provides a general method for identifying distinct subpopulations whose molecular identity may relate to microenvironment. Here, we explored variation in radial glia gene expression while considering stem cell niche as a covariate. Our results revealed novel molecular features of neural stem cell populations previously distinguished only by cell behavior, morphology, and position. Together with recent findings (Fietz et al., 2012; Lui et al., 2014), these results highlight three mechanisms that may maintain stemness of the expanded oRG population in the OSVZ stem cell niche: local production of trophic factors such as PTN and BMP7 by radial glia, expression of extracellular matrix proteins that potentiate growth factor signaling, and activation of the LIFR/p-STAT3 signaling pathway (Figures 7D and

7E). Because the oRG population is thought to be responsible for the majority of human cortical neurogenesis and OSVZ size correlates with the evolutionary expansion of the brain, future studies can investigate the role of these genes in neurodevelopmental disorders and cortical evolution.

EXPERIMENTAL PROCEDURES

Single-Cell Analysis

Micro-dissected VZ and SVZ tissue samples were dissociated using Papain (Worthington). Single-cell sequencing libraries were generated using the C₁ Single-Cell Auto Prep Integrated Fluidic Circuit (Fluidigm), the SMARTer Ultra Low RNA Kit (Clontech), and the Nextera XT DNA Sample Preparation Kit (Illumina). Reads were aligned using Tophat2, and the expression of RefSeq genes was quantified by the featureCounts routine. Gene expression values were normalized based on library size as counts per million reads (CPM). Libraries with fewer than 1,000 genes detected above 1 CPM were eliminated as outliers. Cells were assigned to groups using PCA and Expectation-Maximization clustering, and groups were interpreted based on the expression of known marker genes and tissue validation. The specificity of genes to each group was determined using the Pearson's correlation and confirmed with DESeq2. The expression of cell-type markers was evaluated *in silico* using the Allen Institute Prenatal LMD Microarray Atlas (Miller et al., 2014) and NIH Blueprint NHP Atlas, as well as human and mouse gene coexpression networks (Lui et al., 2014) and single-cell glioblastoma data (Patel et al., 2014), and *in tissue* using immunohistochemistry and *in situ* hybridization as described in the *Supplemental Experimental Procedures*.

STAT3 Signaling

To examine the function of decreased STAT3 signaling in oRG cells, we cultured fetal cortical slices for 48 hr in the presence of inhibitors and then performed immunostaining. *In utero* electroporation was performed at E13.5 of a mutated form of STAT3, which mimics the Y705 phosphorylation state driven by the EF1a promoter (Addgene, 24983). Timed-pregnant Swiss-Webster mice were obtained from Simonsen Laboratories and maintained according to protocols approved by the UCSF Institutional Animal Care and Use Committee.

Single-Cell Clonal Analysis

Cells dissociated from cortical germinal zone were infected cells with a pNIT-GFP retrovirus for 2–4 hr, cultured on matrigel (BD Biosciences) for 3 days in media containing DMEM (Invitrogen, 11965), 1% B-27 supplement (Invitrogen, 12587-010), 1% N-2 supplement (17502-048), and recombinant human FGF-basic (10 ng/ml, Peprotech, AF-100-18B). We then used FACS (ARIA, BD Biosciences) to sort GFP-expressing cells at 1 cell/well into 96-well plates pre-seeded with feeder cells. We used time-lapse microscopy to identify the mitotic behavior of the initial cell divisions for each clone. After 1 week, the cells were cultured for 6 weeks in media without FGF.

ACCESSION NUMBERS

The accession number for the RNA sequencing data reported in this paper is dbGaP: phs000989.v1.p1.

SUPPLEMENTAL INFORMATION

Supplemental Information includes Supplemental Experimental Procedures, seven figures, and four tables and can be found with this article online at <http://dx.doi.org/10.1016/j.cell.2015.09.004>.

AUTHOR CONTRIBUTIONS

A.A.P., T.J.N., and A.R.K. conceived and supervised the project. A.A.P., T.J.N., J.S., A.A.L., and J.A.W. performed single-cell RNA-seq experiments. J.C. and C.R.N. designed and performed single-cell clonal lineage experiments.

T.J.N., A.A.P., and H.R. designed and performed tissue validation and functional experiments with input from A.R.K. and D.A.L. Bioinformatic analysis was performed by A.A.P., T.J.N., H.R., C.S.-E., M.C.O., S.J.L., and A.D. Manuscript was prepared by A.A.P. and T.J.N. with input from all authors.

ACKNOWLEDGMENTS

We thank Stephen Noctor, Marc Unger, Bob Jones, Beatriz Alvarado, Tricia Sun, Mercedes Paredes, Becky Anderson, Raphael Kohler, Jerry Wang, Shaohui Wang, Yingying Wang, and Simone Mayer for providing resources, suggestions, and technical assistance and the staff at the San Francisco General Hospital for providing access to donated tissue samples. A.A.P. is supported by a Damon Runyon Cancer Research Foundation postdoctoral fellowship (DRG-2166-13). A.D. is partially supported by UCSF-CTSI UL1 TR000004. This research was supported by NIH awards U01 MH105989 and R01NS075998 to A.R.K. A.A.L., J.A.W., and J.S. have a financial interest in Fluidigm Corporation as employees and/or stockholders.

Received: July 13, 2015

Revised: August 4, 2015

Accepted: August 31, 2015

Published: September 24, 2015

REFERENCES

Autelitano, F., Loyaux, D., Roudières, S., Déon, C., Guette, F., Fabre, P., Ping, Q., Wang, S., Auvergne, R., Badarinayrayana, V., et al. (2014). Identification of novel tumor-associated cell surface sialoglycoproteins in human glioblastoma tumors using quantitative proteomics. *PLoS ONE* 9, e110316.

Barros, C.S., Franco, S.J., and Müller, U. (2011). Extracellular matrix: functions in the nervous system. *Cold Spring Harb. Perspect. Biol.* 3, a005108.

Bayatti, N., Moss, J.A., Sun, L., Ambrose, P., Ward, J.F., Lindsay, S., and Clowry, G.J. (2008). A molecular neuroanatomical study of the developing human neocortex from 8 to 17 postconceptional weeks revealing the early differentiation of the subplate and subventricular zone. *Cereb. Cortex* 18, 1536–1548.

Beadle, C., Assanah, M.C., Monzo, P., Vallee, R., Rosenfeld, S.S., and Canoll, P. (2008). The role of myosin II in glioma invasion of the brain. *Mol. Biol. Cell* 19, 3357–3368.

Besser, M., Jagatheaswaran, M., Reinhard, J., Schaffelke, P., and Faissner, A. (2012). Tenascin C regulates proliferation and differentiation processes during embryonic retinogenesis and modulates the de-differentiation capacity of Müller glia by influencing growth factor responsiveness and the extracellular matrix compartment. *Dev. Biol.* 369, 163–176.

Betizeau, M., Cortay, V., Patti, D., Pfister, S., Gautier, E., Bellemain-Ménard, A., Afanassieff, M., Huisoud, C., Douglas, R.J., Kennedy, H., and Dehay, C. (2013). Precursor diversity and complexity of lineage relationships in the outer subventricular zone of the primate. *Neuron* 80, 442–457.

Bianchi, A., Gervasi, M.E., and Bakin, A. (2010). Role of β 5-integrin in epithelial-mesenchymal transition in response to TGF- β . *Cell Cycle* 9, 1647–1659.

Bonaguidi, M.A., McGuire, T., Hu, M., Kan, L., Samanta, J., and Kessler, J.A. (2005). LIF and BMP signaling generate separate and discrete types of GFAP-expressing cells. *Development* 132, 5503–5514.

Bonaguidi, M.A., Peng, C.Y., McGuire, T., Falciglia, G., Gobeske, K.T., Czeisler, C., and Kessler, J.A. (2008). Noggin expands neural stem cells in the adult hippocampus. *J. Neurosci.* 28, 9194–9204.

Cahoy, J.D., Emery, B., Kaushal, A., Foo, L.C., Zamanian, J.L., Christopher, K.S., Xing, Y., Lubischer, J.L., Krieg, P.A., Krupenko, S.A., et al. (2008). A transcriptome database for astrocytes, neurons, and oligodendrocytes: a new resource for understanding brain development and function. *J. Neurosci.* 28, 264–278.

Fietz, S.A., Kelava, I., Vogt, J., Wilsch-Bräuninger, M., Stenzel, D., Fish, J.L., Corbeil, D., Riehn, A., Distler, W., Nitsch, R., and Huttner, W.B. (2010). OSVZ progenitors of human and ferret neocortex are epithelial-like and expand by integrin signaling. *Nat. Neurosci.* 13, 690–699.

Fietz, S.A., Lachmann, R., Brandl, H., Kircher, M., Samusik, N., Schröder, R., Lakshmanaperumal, N., Henry, I., Vogt, J., Riehn, A., et al. (2012). Transcriptomes of germinal zones of human and mouse fetal neocortex suggest a role of extracellular matrix in progenitor self-renewal. *Proc. Natl. Acad. Sci. USA* 109, 11836–11841.

Florio, M., Albert, M., Taverna, E., Namba, T., Brandl, H., Lewitus, E., Haffner, C., Sykes, A., Wong, F.K., Peters, J., et al. (2015). Human-specific gene ARHGAP11B promotes basal progenitor amplification and neocortex expansion. *Science* 347, 1465–1470.

Gao, P., Postiglione, M.P., Krieger, T.G., Hernandez, L., Wang, C., Han, Z., Streicher, C., Papusheva, E., Insolera, R., Chugh, K., et al. (2014). Deterministic progenitor behavior and unitary production of neurons in the neocortex. *Cell* 159, 775–788.

Garcion, E., Halilagic, A., Faissner, A., and ffrench-Constant, C. (2004). Generation of an environmental niche for neural stem cell development by the extracellular matrix molecule tenascin C. *Development* 131, 3423–3432.

Garwood, J., Garcion, E., Dobbertin, A., Heck, N., Calco, V., ffrench-Constant, C., and Faissner, A. (2004). The extracellular matrix glycoprotein Tenascin-C is expressed by oligodendrocyte precursor cells and required for the regulation of maturation rate, survival and responsiveness to platelet-derived growth factor. *Eur. J. Neurosci.* 20, 2524–2540.

Gertz, C.C., Lui, J.H., LaMonica, B.E., Wang, X., and Kriegstein, A.R. (2014). Diverse behaviors of outer radial glia in developing ferret and human cortex. *J. Neurosci.* 34, 2559–2570.

Götz, M., Stoykova, A., and Gruss, P. (1998). Pax6 controls radial glia differentiation in the cerebral cortex. *Neuron* 21, 1031–1044.

Hansen, D.V., Lui, J.H., Parker, P.R., and Kriegstein, A.R. (2010). Neurogenic radial glia in the outer subventricular zone of human neocortex. *Nature* 464, 554–561.

Hevner, R.F., Hodge, R.D., Daza, R.A., and Englund, C. (2006). Transcription factors in glutamatergic neurogenesis: conserved programs in neocortex, cerebellum, and adult hippocampus. *Neurosci. Res.* 55, 223–233.

Hong, S., and Song, M.R. (2015). Signal transducer and activator of transcription-3 maintains the stemness of radial glia at mid-neurogenesis. *J. Neurosci.* 35, 1011–1023.

Huang, G., Yan, H., Ye, S., Tong, C., and Ying, Q.L. (2014). STAT3 phosphorylation at tyrosine 705 and serine 727 differentially regulates mouse ESC fates. *Stem Cells* 32, 1149–1160.

Itoh, Y., Moriyama, Y., Hasegawa, T., Endo, T.A., Toyoda, T., and Gotoh, Y. (2013). Scratch regulates neuronal migration onset via an epithelial-mesenchymal transition-like mechanism. *Nat. Neurosci.* 16, 416–425.

Johnson, M.B., Wang, P.P., Atabay, K.D., Murphy, E.A., Doan, R.N., Hecht, J.L., and Walsh, C.A. (2015). Single-cell analysis reveals transcriptional heterogeneity of neural progenitors in human cortex. *Nat. Neurosci.* 18, 637–646.

Katoh, D., Nagaharu, K., Shimojo, N., Hanamura, N., Yamashita, M., Kozuka, Y., Imanaka-Yoshida, K., and Yoshida, T. (2013). Binding of $\alpha v\beta 1$ and $\alpha v\beta 6$ integrins to tenascin-C induces epithelial-mesenchymal transition-like change of breast cancer cells. *Oncogenesis* 2, e65.

Kawaguchi, A., Ikawa, T., Kasukawa, T., Ueda, H.R., Kurimoto, K., Saitou, M., and Matsuzaki, F. (2008). Single-cell gene profiling defines differential progenitor subclasses in mammalian neurogenesis. *Development* 135, 3113–3124.

Kyuno, D., Kojima, T., Yamaguchi, H., Ito, T., Kimura, Y., Imamura, M., Takanawa, A., Murata, M., Tanaka, S., Hirata, K., and Sawada, N. (2013). Protein kinase C α inhibitor protects against downregulation of claudin-1 during epithelial-mesenchymal transition of pancreatic cancer. *Carcinogenesis* 34, 1232–1243.

Le, P.U., Angers-Loustau, A., de Oliveira, R.M., Ajlan, A., Brassard, C.L., Dudley, A., Brent, H., Siu, V., Trinh, G., Mölenkamp, G., et al. (2010). DRR drives brain cancer invasion by regulating cytoskeletal-focal adhesion dynamics. *Oncogene* 29, 4636–4647.

Lehtinen, M.K., Zappaterra, M.W., Chen, X., Yang, Y.J., Hill, A.D., Lun, M., Maynard, T., Gonzalez, D., Kim, S., Ye, P., et al. (2011). The cerebrospinal fluid provides a proliferative niche for neural progenitor cells. *Neuron* 69, 893–905.

Lewitus, E., Kelava, I., and Huttner, W.B. (2013). Conical expansion of the outer subventricular zone and the role of neocortical folding in evolution and development. *Front. Hum. Neurosci.* 7, 424.

Lim, D.A., Tramontin, A.D., Trevejo, J.M., Herrera, D.G., García-Verdugo, J.M., and Alvarez-Buylla, A. (2000). Noggin antagonizes BMP signaling to create a niche for adult neurogenesis. *Neuron* 28, 713–726.

Lui, J.H., Nowakowski, T.J., Pollen, A.A., Javaherian, A., Kriegstein, A.R., and Oldham, M.C. (2014). Radial glia require PDGFD-PDGFR β signalling in human but not mouse neocortex. *Nature* 515, 264–268.

Martinez-Cerdeño, V., Cunningham, C.L., Camacho, J., Antczak, J.L., Prakash, A.N., Czep, M.E., Walker, A.I., and Noctor, S.C. (2012). Comparative analysis of the subventricular zone in rat, ferret and macaque: evidence for an outer subventricular zone in rodents. *PLoS ONE* 7, e30178.

Milev, P., Monnerie, H., Popp, S., Margolis, R.K., and Margolis, R.U. (1998). The core protein of the chondroitin sulfate proteoglycan phosphacan is a high-affinity ligand of fibroblast growth factor-2 and potentiates its mitogenic activity. *J. Biol. Chem.* 273, 21439–21442.

Miller, J.A., Ding, S.L., Sunkin, S.M., Smith, K.A., Ng, L., Szafer, A., Ebbert, A., Riley, Z.L., Royall, J.J., Alona, K., et al. (2014). Transcriptional landscape of the prenatal human brain. *Nature* 508, 199–206.

Nie, S., Gurrea, M., Zhu, J., Thakolwiboon, S., Heth, J.A., Muraszko, K.M., Fan, X., and Lubman, D.M. (2015). Tenascin-C: a novel candidate marker for cancer stem cells in glioblastoma identified by tissue microarrays. *J. Proteome Res.* 14, 814–822.

Ostrem, B.E., Lui, J.H., Gertz, C.C., and Kriegstein, A.R. (2014). Control of outer radial glial stem cell mitosis in the human brain. *Cell Rep.* 8, 656–664.

Patel, A.P., Tirosh, I., Trombetta, J.J., Shalek, A.K., Gillespie, S.M., Wakimoto, H., Cahill, D.P., Nahed, B.V., Curry, W.T., Martuza, R.L., et al. (2014). Single-cell RNA-seq highlights intratumoral heterogeneity in primary glioblastoma. *Science* 344, 1396–1401.

Perez-Pinera, P., Alcantara, S., Dimitrov, T., Vega, J.A., and Deuel, T.F. (2006). Pleiotrophin disrupts calcium-dependent homophilic cell-cell adhesion and initiates an epithelial-mesenchymal transition. *Proc. Natl. Acad. Sci. USA* 103, 17795–17800.

Pollen, A.A., Nowakowski, T.J., Shuga, J., Wang, X., Leyrat, A.A., Lui, J.H., Li, N., Szpankowski, L., Fowler, B., Chen, P., et al. (2014). Low-coverage single-cell mRNA sequencing reveals cellular heterogeneity and activated signaling pathways in developing cerebral cortex. *Nat. Biotechnol.* 32, 1053–1058.

Qian, X., Shen, Q., Goderie, S.K., He, W., Capela, A., Davis, A.A., and Temple, S. (2000). Timing of CNS cell generation: a programmed sequence of neuron and glial cell production from isolated murine cortical stem cells. *Neuron* 28, 69–80.

Reillo, I., de Juan Romero, C., García-Cabezas, M.A., and Borrell, V. (2011). A role for intermediate radial glia in the tangential expansion of the mammalian cerebral cortex. *Cereb. Cortex* 21, 1674–1694.

Shitamukai, A., Konno, D., and Matsuzaki, F. (2011). Oblique radial glial divisions in the developing mouse neocortex induce self-renewing progenitors outside the germinal zone that resemble primate outer subventricular zone progenitors. *J. Neurosci.* 31, 3683–3695.

Sim, F.J., Lang, J.K., Walda, B., Roy, N.S., Schwartz, T.E., Pilcher, W.H., Chandross, K.J., Natesan, S., Merrill, J.E., and Goldman, S.A. (2006). Complementary patterns of gene expression by human oligodendrocyte progenitors and their environment predict determinants of progenitor maintenance and differentiation. *Ann. Neurol.* 59, 763–779.

Smart, I.H., Dehay, C., Giroud, P., Berland, M., and Kennedy, H. (2002). Unique morphological features of the proliferative zones and postmitotic compartments of the neural epithelium giving rise to striate and extrastriate cortex in the monkey. *Cereb. Cortex* 12, 37–53.

Szklarczyk, D., Franceschini, A., Wyder, S., Forslund, K., Heller, D., Huerta-Cepas, J., Simonovic, M., Roth, A., Santos, A., Tsafou, K.P., et al. (2015). STRING v10: protein-protein interaction networks, integrated over the tree of life. *Nucleic Acids Res.* 43, D447–D452.

Vasistha, N.A., Garcia-Moreno, F., Arora, S., Cheung, A.F., Arnold, S.J., Robertson, E.J., and Molnar, Z. (2014). Cortical and clonal contribution of Tbr2 expressing progenitors in the developing mouse brain. *Cereb. Cortex*. Published online June 13, 2014. <http://dx.doi.org/10.1093/cercor/bhu125>.

von Holst, A. (2008). Tenascin C in stem cell niches: redundant, permissive or instructive? *Cells Tissues Organs (Print)* 188, 170–177.

Wang, W.Z., Oeschger, F.M., Montiel, J.F., García-Moreno, F., Hoerder-Suabedissen, A., Krubitzer, L., Ek, C.J., Saunders, N.R., Reim, K., Villalón, A., and Molnár, Z. (2011a). Comparative aspects of subplate zone studied with gene expression in sauropsids and mammals. *Cereb. Cortex* 21, 2187–2203.

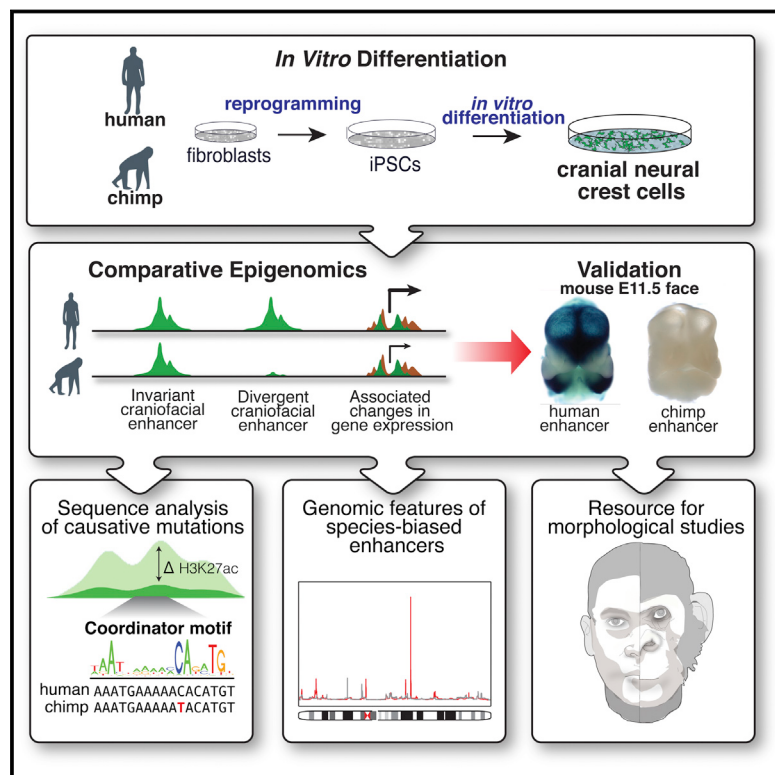
Wang, X., Tsai, J.W., LaMonica, B., and Kriegstein, A.R. (2011b). A new subtype of progenitor cell in the mouse embryonic neocortex. *Nat. Neurosci.* 14, 555–561.

Wiese, S., Karus, M., and Faissner, A. (2012). Astrocytes as a source for extracellular matrix molecules and cytokines. *Front. Pharmacol.* 3, 120.

Zecevic, N., Chen, Y., and Filipovic, R. (2005). Contributions of cortical subventricular zone to the development of the human cerebral cortex. *J. Comp. Neurol.* 497, 109–122.

Enhancer Divergence and *cis*-Regulatory Evolution in the Human and Chimp Neural Crest

Graphical Abstract



Highlights

- Aspects of higher primate embryogenesis can be recapitulated *in vitro* using iPSCs
- Epigenomic profiling from human and chimp CNCCs reveals divergent facial enhancers
- Recently diverging CNCC enhancers have distinct sequence features
- Species-biased enhancers cluster near loci affecting intra-human facial variation

Authors

Sara L. Prescott, Rajini Srinivasan,
Maria Carolina Marchetto, ...,
Fred H. Gage, Tomek Swigut,
Joanna Wysocka

Correspondence

swigut@stanford.edu (T.S.),
wysocka@stanford.edu (J.W.)

In Brief

Epigenomic and transcriptome profiling from *in-vitro*-derived human and chimpanzee cranial neural crest cells (CNCCs) allows for the identification and mechanistic exploration of recent *cis*-regulatory landscape divergence underlying human craniofacial evolution.

Accession Numbers

GSE70751

Enhancer Divergence and *cis*-Regulatory Evolution in the Human and Chimp Neural Crest

Sara L. Prescott,¹ Rajini Srinivasan,¹ Maria Carolina Marchetto,² Irina Grishina,³ Iñigo Narvaiza,² Licia Selleri,³ Fred H. Gage,^{2,4} Tomek Swigut,^{1,*} and Joanna Wysocka^{1,5,6,*}

¹Department of Chemical and Systems Biology and Department of Developmental Biology, Stanford University School of Medicine, Stanford, CA 94305, USA

²Laboratory of Genetics, The Salk Institute for Biological Studies, 10010 North Torrey Pines Road, La Jolla, CA 92037, USA

³Department of Cell and Developmental Biology, Weill Cornell Medical College, Cornell University, New York, NY 10065, USA

⁴Center for Academic Research and Training in Anthropogeny (CARTA), University of California, San Diego, 9500 Gilman Drive, La Jolla, CA 92093, USA

⁵Howard Hughes Medical Institute, Stanford University School of Medicine, Stanford, CA 94305, USA

⁶Institute of Stem Cell Biology and Regenerative Medicine, Stanford University School of Medicine, Stanford, CA 94305, USA

*Correspondence: swigut@stanford.edu (T.S.), wysocka@stanford.edu (J.W.)

<http://dx.doi.org/10.1016/j.cell.2015.08.036>

SUMMARY

cis-regulatory changes play a central role in morphological divergence, yet the regulatory principles underlying emergence of human traits remain poorly understood. Here, we use epigenomic profiling from human and chimpanzee cranial neural crest cells to systematically and quantitatively annotate divergence of craniofacial *cis*-regulatory landscapes. Epigenomic divergence is often attributable to genetic variation within TF motifs at orthologous enhancers, with a novel motif being most predictive of activity biases. We explore properties of this *cis*-regulatory change, revealing the role of particular retroelements, uncovering broad clusters of species-biased enhancers near genes associated with human facial variation, and demonstrating that *cis*-regulatory divergence is linked to quantitative expression differences of crucial neural crest regulators. Our work provides a wealth of candidates for future evolutionary studies and demonstrates the value of “cellular anthropology,” a strategy of using in-vitro-derived embryonic cell types to elucidate both fundamental and evolving mechanisms underlying morphological variation in higher primates.

INTRODUCTION

Since the discovery that the protein-coding regions of the genome remain largely conserved between humans and chimpanzees, it has long been postulated that morphological divergence between closely related species is driven principally through quantitative and spatiotemporal changes in gene expression, mediated by alterations in *cis*-regulatory elements (Carroll, 2008; King and Wilson, 1975; Wray, 2007). A number of excellent case studies have validated these early predictions and demonstrated that mutations or deletions affecting distal

regulatory elements called enhancers can alter ecologically relevant traits (Gompel et al., 2005; Shapiro et al., 2004; Attanasio et al., 2013). Recent successes in full-genome sequencing and epigenomic strategies have enabled the first genome-wide comparisons of transcription factor (TF) binding and regulatory landscapes in closely related species, demonstrating the value of comparative epigenomics in the context of high-genome orthology for understanding principles of *cis*-regulatory evolution (Bradley et al., 2010; He et al., 2011; Stefflova et al., 2013). Nonetheless, despite the availability of human and chimpanzee genomes, our knowledge of *cis*-regulatory divergence between humans and our closest evolutionary relatives remains fairly speculative. Previous efforts have relied heavily on computational approaches to pinpoint conserved non-coding elements that were either deleted or had undergone accelerated change specifically in the human lineage (McLean et al., 2011; Pollard et al., 2006; Prabhakar et al., 2006). Functional epigenomic comparisons between humans and other primates have been largely limited to lymphoblastoid cell lines (Cain et al., 2011; Shibata et al., 2012; Zhou et al., 2014) or to profiling whole organs from more distantly related species (Cotney et al., 2013; Villar et al., 2015).

Recently, iPSCs were made available from our nearest living evolutionary relative, the chimpanzee (Marchetto et al., 2013), offering an opportunity to derive developmentally relevant and previously inaccessible tissue types in vitro. This allows aspects of species-specific development to be recapitulated in a dish, facilitating “cellular anthropology” through the discovery of cell-type-specific regulatory changes that occurred during recent human evolution. Here, we focus on the neural crest (NC), one of the embryonic cell populations most relevant to emergence of uniquely human traits. In vivo, NC cells (NCCs) arise during weeks ~3–5 of human gestation from the dorsal part of the neural tube ectoderm and migrate into the branchial arches and what will later become the embryonic face, consequently establishing the central plan of facial morphology (Bronner and LeDouarin, 2012; Cordero et al., 2011; Jheon and Schneider, 2009). Within our recent evolutionary history, the modern human craniofacial complex has undergone dramatic changes in shape and sensory organ function, which helped to build a recognizably

human face and were required to accommodate the transition to bipedal posture, enlargement of the brain, extension of the larynx for speech, and compensatory rotations of the orbits, olfactory bulb, and nasomaxillary complex (Bilsborough and Wood, 1988; Lieberman, 1998; Spoor et al., 1994).

To overcome the inability to obtain cranial NCCs (CNCCs) directly from higher primate embryos, we here employ a pluripotent stem-cell-based *in vitro* differentiation model in which specification, migration, and maturation of human and chimpanzee CNCCs are recapitulated in the dish (Bajpai et al., 2010; Rada-Iglesias et al., 2012; this study). We compared TF and coactivator binding, histone modifications, and chromatin accessibility genome-wide to annotate the divergent regulatory element repertoire of human and chimpanzee CNCCs. This information allowed us to explore, with unprecedented comprehensiveness and resolution, the mechanisms of tissue-specific enhancer landscape evolution within a developmentally relevant tissue type in humans and our nearest evolutionary relative.

RESULTS

Derivation of Human and Chimpanzee CNCCs

Given the similarities in hominid gestational environment, we hypothesized that non-human primate CNCCs could be derived from pluripotent cells using the same cell culture conditions that we have previously applied to human embryonic stem cells (ESCs)/iPSCs (Bajpai et al., 2010; Rada-Iglesias et al., 2012). Chimp iPSCs have recently become available and can be maintained *in vitro* under identical conditions as human ESCs/iPSCs (Marchetto et al., 2013). Upon differentiation of our chimp iPSCs, we observed formation of highly mobile stellate cells that were morphologically indistinguishable from human CNCCs, expressed a broad range of migratory NC markers at levels equivalent to those seen in human cells, and had a very low level of *HOX* gene expression, a profile consistent with CNCC identity (Figures 1A–1C and S1A). To characterize staging and homogeneity of our human and chimp CNCC populations, we identified a panel of five cluster of differentiation (CD) markers, whose expression is sensitive to the developmental progression of CNCC (see Experimental Procedures and Figure S1B). These markers provided a platform for us to monitor and optimize our cell culture protocol for derivation and maintenance of primate CNCCs achieving metrics of homogeneity greater than 90% regardless of the genetic background, initial cell source (e.g., iPSC versus ESC), or species (human versus chimp); see Figure S1C and Experimental Procedures. Cultured primate CNCCs show a high correlation of expression signatures and epigenomic profiles with CNCCs isolated from chick embryos, reinforcing the NC identity of these *in-vitro*-derived cells (Figures S2A and S2B). Importantly, derived human and chimp CNCCs are both capable of prolonged maintenance (for up to 18 passages) and sustained differentiation capacity into both mesenchymal and non-mesenchymal lineages (Figure S2C). Furthermore, xenotransplantation of cultured human and chimp CNCCs into the dorsal neural tube of early chick embryos demonstrates their ability to engraft and then follow endogenous migration cues into the distal branchial arches (Figures S2D and S2E).

Epigenomic Profiling of Human and Chimpanzee CNCCs

For epigenomic profiling, we derived CNCCs from H9 hESCs and from iPSCs from two humans and two chimpanzees (Marchetto et al., 2013). We subsequently performed chromatin immunoprecipitation and sequencing (ChIP-seq) using antibodies against CNCC TFs (TFAP2A and NR2F1), a general coactivator (p300), and histone modifications associated with active regulatory elements (H3K4me1, H3K4me3, and H3K27ac) (Figures 1A and 1E). In parallel, we mapped genome-wide chromatin accessibility using an assay for transposase-accessible chromatin (ATAC-seq) (Buenrostro et al., 2013).

One crucial advantage of performing comparative epigenomics between human and chimpanzee, as opposed to a more distant primate relative, is the large similarity between genomes, which permits reciprocal mapping of sequencing reads to the reference genomes of both species. This allows for quantification of read enrichments from each species in the context of both reference genomes, removing otherwise difficult-to-control-for biases due to mappability, ambiguous liftOver, and other technical caveats. Importantly, we could unambiguously assign one-to-one orthology between genomes for >95% of all enhancer candidates from either species, with the remaining 4%–5% representing enhancers that fall within putative species-specific structural variants. We found that enrichments for all ChIP-ed factors and for chromatin accessibility were largely independent of the chosen reference genome and excluded all candidate elements for whom enrichment divergence was dependent upon the reference (< 0.1%) or that did not map uniquely in both genomes (see Experimental Procedures). Globally, the observed epigenomic patterns at candidate regions were highly correlated for human and chimp CNCCs (Figures 1E and Figure S4A).

Genome-wide Annotation of Human and Chimpanzee CNCC Regulatory Elements Uncovers Enhancers with Craniofacial Activity

To annotate enhancers genome wide, we promiscuously identified candidate *cis*-regulatory regions by the presence of TF or p300 enrichment and/or increased chromatin accessibility. We then restricted our analysis primarily to enhancers by assessing the ratio of H3K4me1/H3K4me3 enrichment at these candidate sites, which distinguishes distal enhancers from promoters (Heintzman et al., 2007), and further using H3K27ac enrichment to differentiate active from inactive elements (Creyghton et al., 2010; Rada-Iglesias et al., 2011). The resulting enhancer candidates had enriched conservation signatures compared to surrounding genomic regions and were near genes annotated with craniofacial ontologies—consistent with bona fide NC enhancer status (Figures S3A–S3C). Furthermore, cross-referencing our enhancer list with the VISTA Enhancer Browser database (Visel et al., 2007) identified 247 regions overlapping CNCC enhancers that were functionally tested for activity in mouse embryos. Of those 247 regions: (1) 208 were active at E11.5 (odds ratio 6.33 and $p < 5 \times 10^{-32}$), and (2) these 208 active enhancers were significantly enriched for activity in NC-derived head tissues (branchial arches and facial mesenchyme; Figure 1D, examples are shown in Figures 1E [right], and Figure S3D). Thus, our analysis captures regulatory regions relevant for distinct

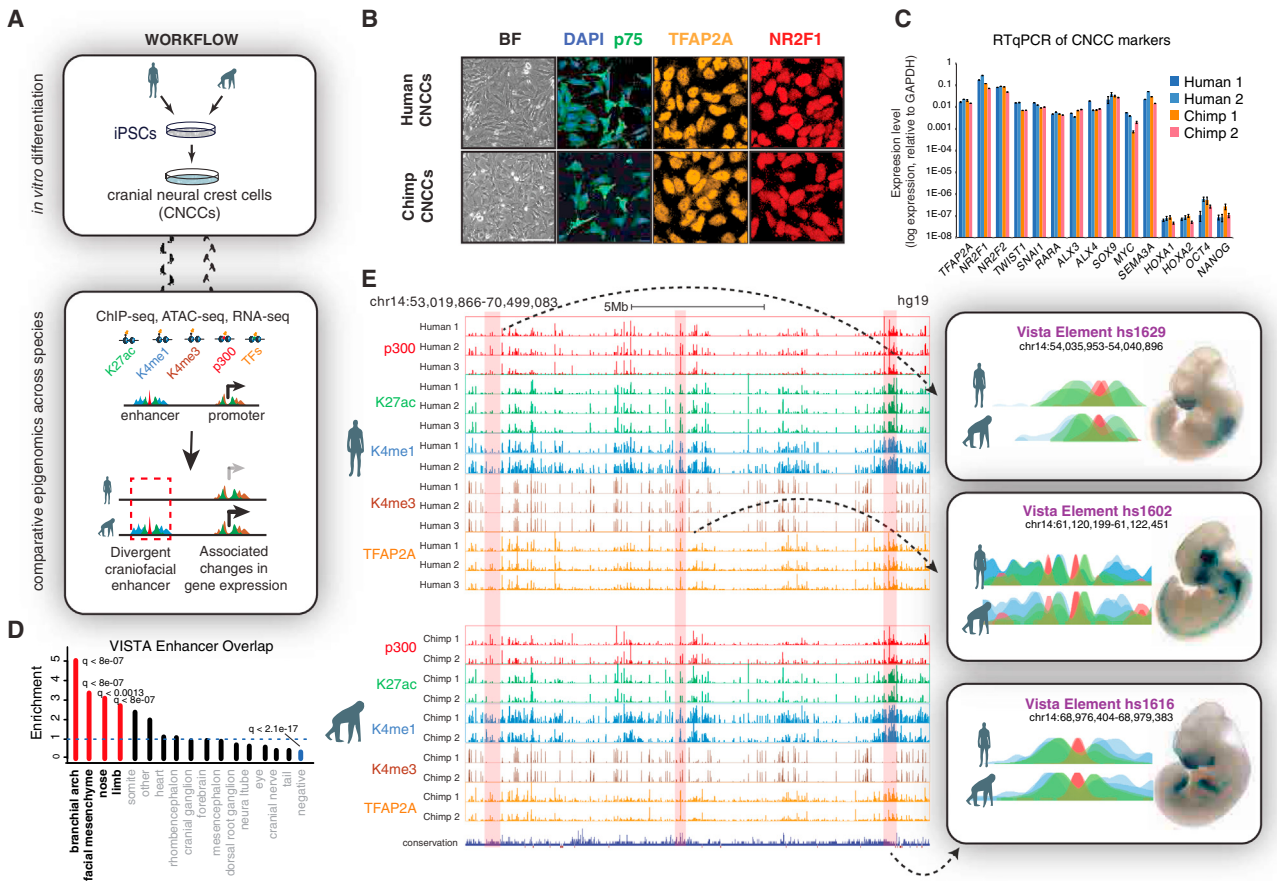


Figure 1. Derivation of Human and Chimpanzee CNCCs and Epigenomic Annotation of Craniofacial Enhancers

- (A) Workflow of comparative epigenomic strategy.
- (B) Confocal immunofluorescence detection of NC markers p75, TFAP2A, and NR2F1 in human and chimp CNCCs at passage 4.
- (C) RT-qPCR of NC markers, HOXs, and pluripotency markers OCT4 and NANOG in derived human and chimp CNCCs from two genetic backgrounds of each species. Error bars represent one SD.
- (D) Enrichment of annotated expression domain categories from overlap of top 15,000 enhancer calls with regions in the VISTA enhancer database. p values were calculated with Fisher's exact test and corrected for pFDR. Categories with q value < 0.05 are indicated in red (enrichment) or blue (depletion).
- (E) Representative UCSC Genome Browser tracks showing ChIP-seq profiles for p300 (red), H3K27ac (green), H3K4me1 (blue), H3K4me3 (brown), and TFAP2A (orange) from both species aligned to hg19 reference genome. Representative elements tested through the VISTA enhancer database (Visel et al., 2007) displayed on the right next to the reported lacZ expression domains.

spatial identities in the developing face *in vivo* (Figure 1D). Taken together, our epigenomic approach thus comprehensively annotates putative human and chimp NC enhancers, at least a subset of which is active in facial structures during embryogenesis.

Quantitative Analysis of H3K27ac Enrichments Predicts Species-Biased Enhancers

We hypothesized that, in closely related species, quantitative modulation of activity at orthologous regions is a major form of enhancer divergence. To identify such divergence, we used H3K27ac enrichment data in biological quadruplicate (i.e., independent CNCC derivations from each individual) to quantitatively approximate activity at all annotated CNCC enhancers detected for either species. Global comparisons of H3K27ac enrichments between individuals of the same species revealed high concordance of signals, with some minor variation due to either differ-

ences in genetic background or experimental variability (Figures 2A, highlighted in red, and S4A). Human and chimpanzee CNCC H3K27ac enrichment was also highly correlated when mapped to the same reference genome, and human and chimpanzee CNCC H3K27ac profiles clustered together distinctly from 49 other human cell types (Figures S4A and S4B). Despite this high conservation of profiles, a substantial subset of elements demonstrated a significant species bias (Figure 2A, FDR < 0.01 highlighted in blue), which we thereafter considered to be our species-biased enhancer candidates. H3K27ac ChIP-qPCR at select candidate enhancers from independent CNCC derivations recapitulated this species bias (Figure S4C).

Importantly, consistent with the premise that H3K27ac is a suitable readout of enhancer activity, the bias in H3K27ac status alone was highly predictive of biases in TF and p300 binding, as well as chromatin accessibility (Figure 2C; examples are shown

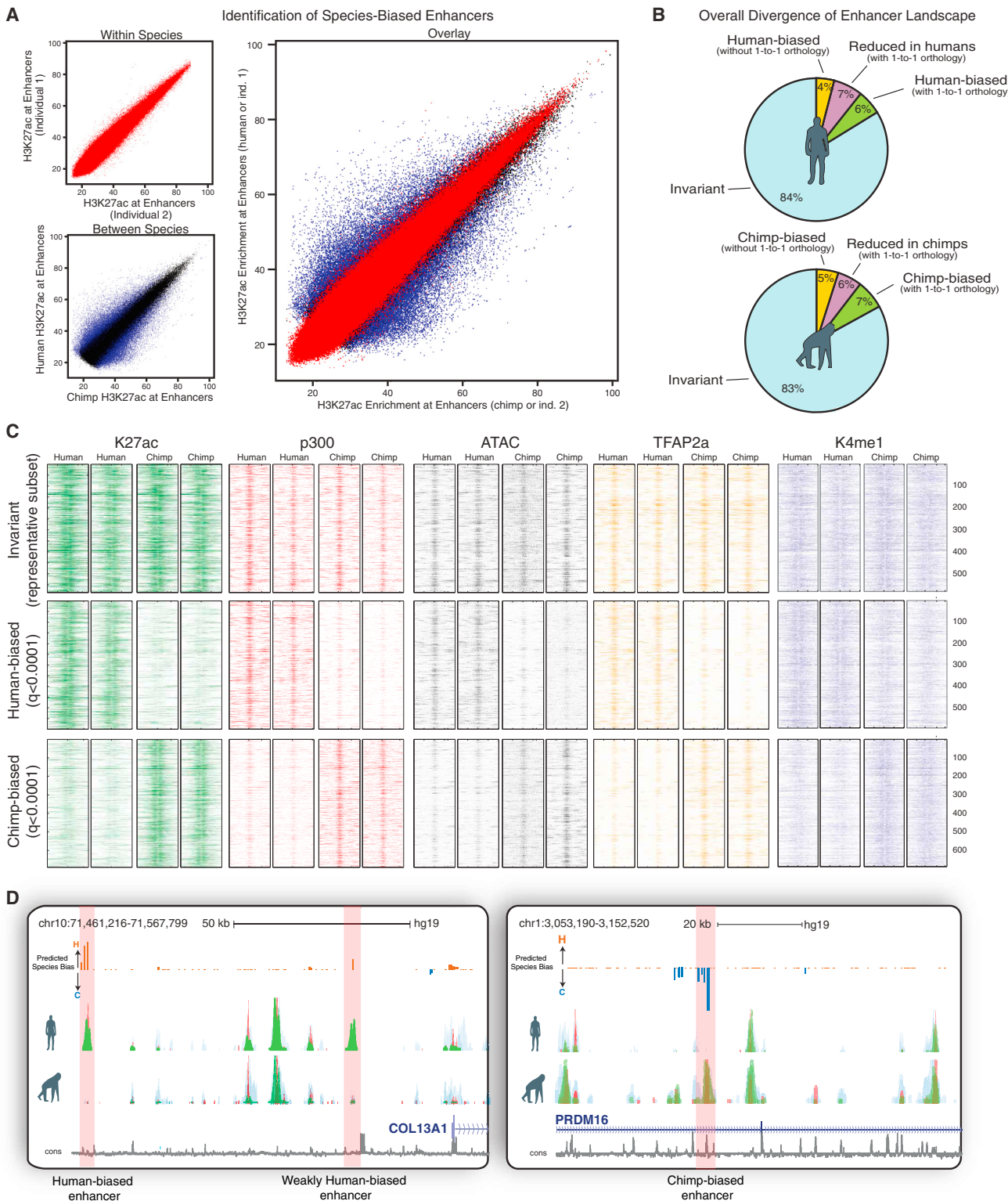


Figure 2. Identification of Species-Biased Enhancers Using H3K27ac Enrichments at Orthologous Loci

(A) Enrichment of H3K27ac at candidate enhancer elements compared within individuals of the same species (red) or across species (blue/black), with overlay shown on the right. Enhancers with significant inter-species divergence indicated in blue ($p_{adj} < 0.01$).

(legend continued on next page)

in [Figures 2D](#) and [S4D](#)). Furthermore, this approach enabled genome-wide assignment of signed significance scores on a per-enhancer basis, visualizable as a genome browser track ([Figure 2D](#), “Predicted Species Bias” track).

Altogether, of all annotated active human CNCC enhancers ($n = 14,606$), 84% were invariant, 4% fell at non-orthologous sites, and 6% and 7% demonstrated quantitative increase or decrease, respectively ([Figure 2B](#)). One limitation is the low number of currently available chimpanzee iPSC lines, especially given the high reported degree of polymorphism among chimps ([Kaessmann et al., 1999](#)). To estimate false positive rate for identifying true fixed inter-species differences, we applied our strategy to previously published ChIP-seqs from chimp lymphoblastoid cell lines and estimated a conservative FDR of 0.15 when using only two chimp genetic backgrounds. This suggests that the vast majority of identified differences represent functionally fixed differences across species (the rest represent enhancers that are still divergent but remain polymorphic within one of the species). Our observations agree with the emerging notion that quantitative modulation of enhancer activity is the prevalent source of regulatory landscape divergence among closely related species.

cis-Sequence Changes Drive Species-Biased Enhancer Activity In Vitro and In Vivo

To functionally validate our predictions, we used a luciferase reporter assay to examine activity of a selected set of orthologous pairs of species-biased human and chimpanzee enhancers. We found that >80% of tested enhancers had correlated species bias in luciferase expression, which was consistent regardless of whether the reporter assays were performed in human or chimpanzee CNCCs ([Figures 3A](#) and [3B](#)). These results further validate that H3K27ac identifies both enhancer activity and bona fide species bias; thus, for simplicity, we refer to H3K27ac enrichment interchangeably with “activity.” Importantly, these results also demonstrate that enhancer divergence can be largely explained by *cis*-sequence changes rather than differences in the *trans* regulatory environments of the human and chimp CNCCs.

The conservation of *trans*-environments across species facilitates testing of human and chimp regulatory elements *in vivo* using a mouse LacZ transgenic reporter assay. We selected two predicted human-biased enhancers near *CNTNAP2* (enhancer 1) and *PAPPA* (enhancer 2), respectively ([Figures 3C](#) and [3D](#)). For both predicted human-biased enhancers we observed gains of additional expression domains in head regions, as well as quantitative gains in enhancer strength, as evidenced by the

overall higher LacZ staining intensity for the human sequence compared to the chimp ortholog ([Figures 3C–3H](#) and [S5](#)). Notably, to ensure that the negative/weak staining results obtained with the chimp sequences were not a result of undersampling, we performed surplus embryo injections with both chimp enhancer reporters ([Figure S5A](#)). Thus, species-biased enhancers identified in our *in vitro* analysis drive distinct expression patterns within CNCC-derived tissues *in vivo*.

Human Accelerated Regions Overlap with Distal CNCC Enhancers

Our results suggest that DNA sequence is the predominant driver of enhancer divergence; therefore, we began examining sequence properties of species-biased enhancers. Although species-biased enhancers were similar in H3K27ac enrichment levels when compared to invariant enhancers, they showed a distinct reduction of sequence conservation signatures ([Figure 4A](#)). Furthermore, we identified 163 “human accelerated regions” (HARs; [Hubisz and Pollard, 2014](#)) overlapping active chromatin features in CNCCs, of which 20 showed species-biased activity (at a cutoff of $q < 0.001$; $n = 48$ with a cutoff of $q < 0.1$) ([Figures 4B](#) and [S6A–S6D](#)), representing a significant enrichment relative to the whole enhancer set ($p < 0.025$, odds ratio 1.81). It is possible that the HAR-overlapping regions without species bias in CNCC could manifest divergence in another tissue type, as exemplified by HAR2 (a.k.a., HACNS1), which overlaps an invariant CNCC enhancer ([Figure S6D](#), p value of species bias = 0.339) that has a pharyngeal arch activity domain that is conserved in primates but has human-specific activity in the embryonic limb ([Prabhakar et al., 2008](#)).

Species-Biased Enhancers Are Enriched for Specific Classes of Retroelements

Given that nearly half of the human genome is composed of transposable elements, the majority of which invaded the primate lineage prior to the separation of humans and chimpanzees ([Cordaux and Batzer, 2009](#)), we hypothesized that a subset of species-biased orthologous enhancers may be transposon derived. Interestingly, we found that, while CNCC enhancers overlapped with many different classes of repeats, specific subclasses of endogenous retroviruses (ERV1, ERVL-MaLR, and ERVK) as well as L1 elements were preferentially enriched at species-biased enhancers ([Figure 4C](#)), suggesting that these specific subclasses may harbor progenitor sequences that are prone to acquire CNCC enhancer activity over relatively short evolutionary distances.

(B) Pie charts showing the percentage of total active CNCC enhancers classified as either species-biased enhancers with gained activity (green), species-biased enhancers with decreased activity (purple), enhancers without clear orthology across genomes (yellow), or invariant enhancers (blue) using a human reference genome (above) or chimp reference genome (below).

(C) Heatmap of raw ChIP-seq and ATAC-seq counts across species-biased and invariant CNCC enhancers for two human and two chimp genetic backgrounds. Each row represents a 2 kb window (1 kb each direction) centered around the middle of human-biased ($n = 598$, $q < 0.0001$), chimp-biased ($n = 691$, $q < 0.0001$), or invariant ($n = 584$ representative subset, $q > 0.95$) enhancers for H3K27ac (green), p300 (red), TFAP2A (yellow), K4me1 (blue), and ATAC-seq (gray). All reads were aligned to hg19.

(D) Representative browser tracks showing overlaid H3K4me1 (blue), p300 (red), and H3K27ac (green) from human and chimp CNCCs mapped to hg19. Examples of strongly human-biased, weakly human-biased, or strongly chimp-biased enhancers highlighted in pink. Predicted species-bias track shown above for candidate enhancers; the magnitude of the bias track represents $-\log_{10}$ (adjusted p value of divergence) with negative sign (indigo) representing chimp bias and positive (bronze) human bias.

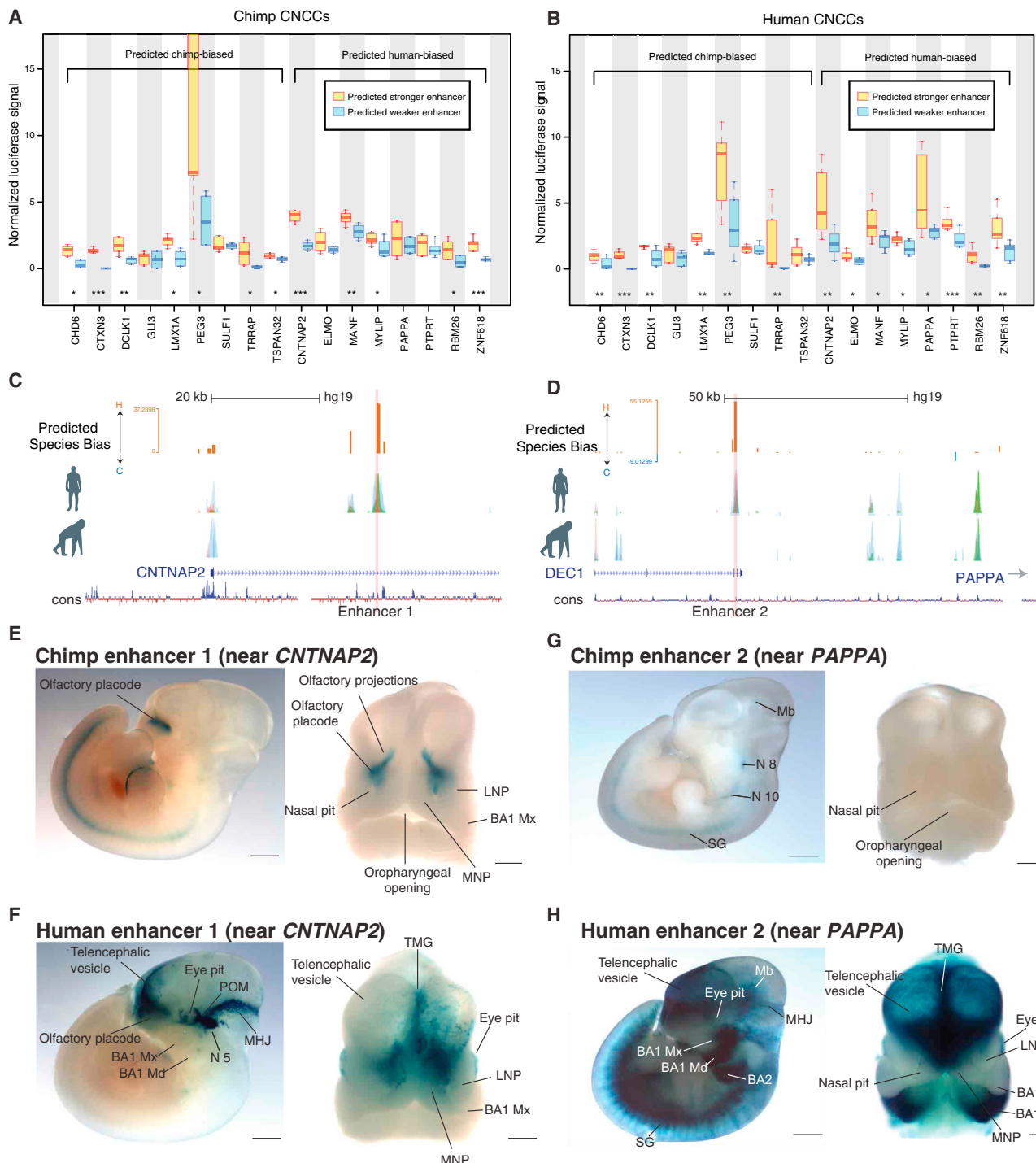


Figure 3. In Vitro and In Vivo Validations of Species-Biased Enhancers

(A and B) Luciferase reporter assays performed in chimp CNCCs (A) or human CNCCs (B) for 9 chimp-biased regions (and orthologous human regions) and 8 human-biased regions (and orthologous chimp regions). Luciferase signal was normalized to renilla transfection control. Significance tested from three biological replicates from each species with ANOVA followed by residuals testing with Student's t test. * $p < 0.05$, ** $p < 0.01$, *** $p < 0.001$. Central bar represents the median, box outline represents first and third quartile, and whiskers extend to furthest datapoint within $1.5 \times$ box length way from the box. Tested enhancers are named by nearest gene.

(C and D) Genome browser tracks showing human-biased enhancer 1 (near *CNTNAP2* gene; C) and enhancer 2 (near *PAPPA* gene; D) selected for a *lacZ* reporter mouse transgenesis assay.

(E and F) Analysis of enhancer activity for chimpanzee and human enhancer 1 in a *lacZ* reporter transgenic mouse assay. (E) Representative E11.5 transgenic embryo obtained for the chimpanzee enhancer 1 reporter, shown in lateral view (left) or frontal view (right) of the embryonic head. (F) Representative E11.5

(legend continued on next page)

Sequence Substitutions within TF Binding Motifs at Species-Biased Enhancers Contribute to Epigenomic Divergence

Consistent with the expectation that species-specific biases are largely sequence driven, we observed that the variance in H3K27ac between species at each enhancer scales proportionally with the degree of sequence dissimilarity (i.e., Levenshtein distance) at those orthologous sites, while the intra-species variance at the same regions remains unchanged (Figure 4D). Nonetheless, even at enhancers with detectable species bias, sequence substitutions were still infrequent—only ~3–6 substitutions per 500 bp enhancer—suggesting that a small number of mutations can confer substantial effects on overall enhancer activity, likely by affecting binding of key sequence-dependent TFs. We therefore interrogated how frequently sequence substitutions fall within particular classes of TF motifs and to what degree these mutations correlate, either positively or negatively, with changes in enhancer activity or other chromatin modifications (Figure 4E). This, in essence, leverages preexisting genetic variation like a large-scale mutagenesis screen.

Through this approach, we identified a large set of both known and novel motifs for which deviation from the consensus was correlated with species bias of H3K27ac and other epigenomic marks, implying functional consequences for these mutations. As expected, the correlations vary in frequency and in effect, with some motifs being frequent and having small effects (e.g., Forkhead factors) and others being infrequent but conferring large effects (e.g., TFAP2A), with one outlier motif being both very frequent and conferring large effects when mutated (see description of the “Coordinator” motif below) (Figure 4F). Among our top hits, we identified many motifs for TFs with known effects in NC regulation, including a set of TFAP2 motif variants that serve as a positive control for our approach, as we see a high correlation between TFAP2 motif mutations and inter-species divergence in TFAP2A ChIP signals at these sites (Figure 4G, group 3). We previously showed that TFAP2A participates in establishment of active chromatin states at NC enhancers (Rada-Iglesias et al., 2012), and consistently we observed that divergence from the TFAP2A consensus also correlates with the loss of H3K27ac, co-activator binding, and chromatin accessibility. Notably, TFAP2 motifs are depleted from species-biased sites, likely due to strong selective pressure to conserve TFAP2A function in the NC and possibly in other pleiotropic contexts (Figure 4F). Another interesting set of motifs, which are both frequent at species-biased sites and positively correlated with permissive chromatin states, are those recognized by ALX homeobox factors that are highly expressed in the face and mutated in severe frontonasal dysplasias in humans (Twigg et al., 2009) (Figures 4F and 4G, group 2).

Intriguingly, we also identified a group of motifs whose mutations away from the consensus were correlated with a gain in chromatin accessibility and H3K27ac, suggesting that these motifs may recruit repressive factors with negative effects on overall enhancer activity. Examples of such motifs included the SNAI2 motif, which is bound by a known transcriptional repressor, the TBX family motif bound by T-box factors, and other candidate negative regulators representing distinct TF classes, e.g., HIC1/2, MESP1, TCF3/4, and GLIS1 (Figure 4G, group 1). These results suggest an unappreciated prevalence of repressive inputs in quantitative modulation of enhancer activity.

“Coordinator”: A novel Motif that Is Highly Predictive of Active Chromatin States and Species Bias

Surprisingly, one motif stood out as an outlier in this analysis, as it was exceptionally enriched at divergent sites and was the most correlated with changes in all examined active chromatin features (Figures 4F, upper-right, and 4G, far-right). This sequence, which we termed the “Coordinator” motif, is a 17-bp-long motif, which we identified through de novo motif discovery from our CNCC-specific enhancers and was not previously annotated to a known regulatory complex. We note that portions of the Coordinator resemble an E box and HOX-like motifs; however, these represent large protein families, and the particular factors that bind at this element remain to be identified.

Sequence analysis using INSIGHT, a tool to infer signatures of recent natural selection using human polymorphism data (Gronau et al., 2013), found evidence of positive selection at the Coordinator motif occurrences within species-biased enhancers, but not within invariant enhancers, suggesting that the motif and its cognate binder(s) have played a privileged role in recent enhancer divergence in primate CNCCs (Figure 5A). When we further dissected the motif by individual bases, we found that the correlations of each nucleotide with ChIP enrichments (both for histone modifications and TF ChIPs) recapitulated the information content of the motif itself, as would be expected if Coordinator motif mutations were causal for the observed chromatin changes (Figure 5B). Fittingly, we found human mutations that strengthen the Coordinator motif within both human-biased enhancers tested in mouse transgenesis (Figure S6E). Globally, the Coordinator motif was preferentially enriched at distal regulatory elements rather than at promoters (Figure S6F) and was further enriched at enhancers that were CNCC specific as opposed to those that shared measurable H3K27ac in other tissue types (Figure 5C). Interestingly, we observe that LTR9 elements, a retroelement class enriched at species-biased enhancers, are 5× more likely to harbor a Coordinator motif variant than MER52A elements, a similar repeat

transgenic embryo obtained for the human enhancer 1 reporter, shown in lateral view (left) or frontal view (right). Midbrain/hindbrain junction (MHJ); periocular mesenchyme (POM); lateral and medial nasal processes (LNP and MNP); maxillary (Mx) and mandibular (Md) processes of branchial arch 1 (BA1) and BA2. Scale bars: 100 μm (left images) and 50 μm (right images).

(G and H) Analysis of enhancer activity for chimpanzee and human enhancer 2 in a *lacZ* reporter transgenic mouse assay. (G) Representative E11.5 transgenic embryo obtained for the chimpanzee enhancer 2 reporter, shown in lateral view (left) or frontal view (right) of the embryonic head. (H) Representative E11.5 transgenic embryo obtained for the human enhancer 2 reporter, shown in lateral view (left) or frontal view (right). Midbrain (Mb); cranial nerves 8 and 10 (N8 and N10 respectively); sympathetic ganglia (SG); telencephalic midline groove (TMG); midbrain/hindbrain junction (MHJ); maxillary (Mx) and mandibular (Md) processes of branchial arch 1 (BA1) and BA2. Scale bars: 100 μm (left images) and 50 μm (right images).

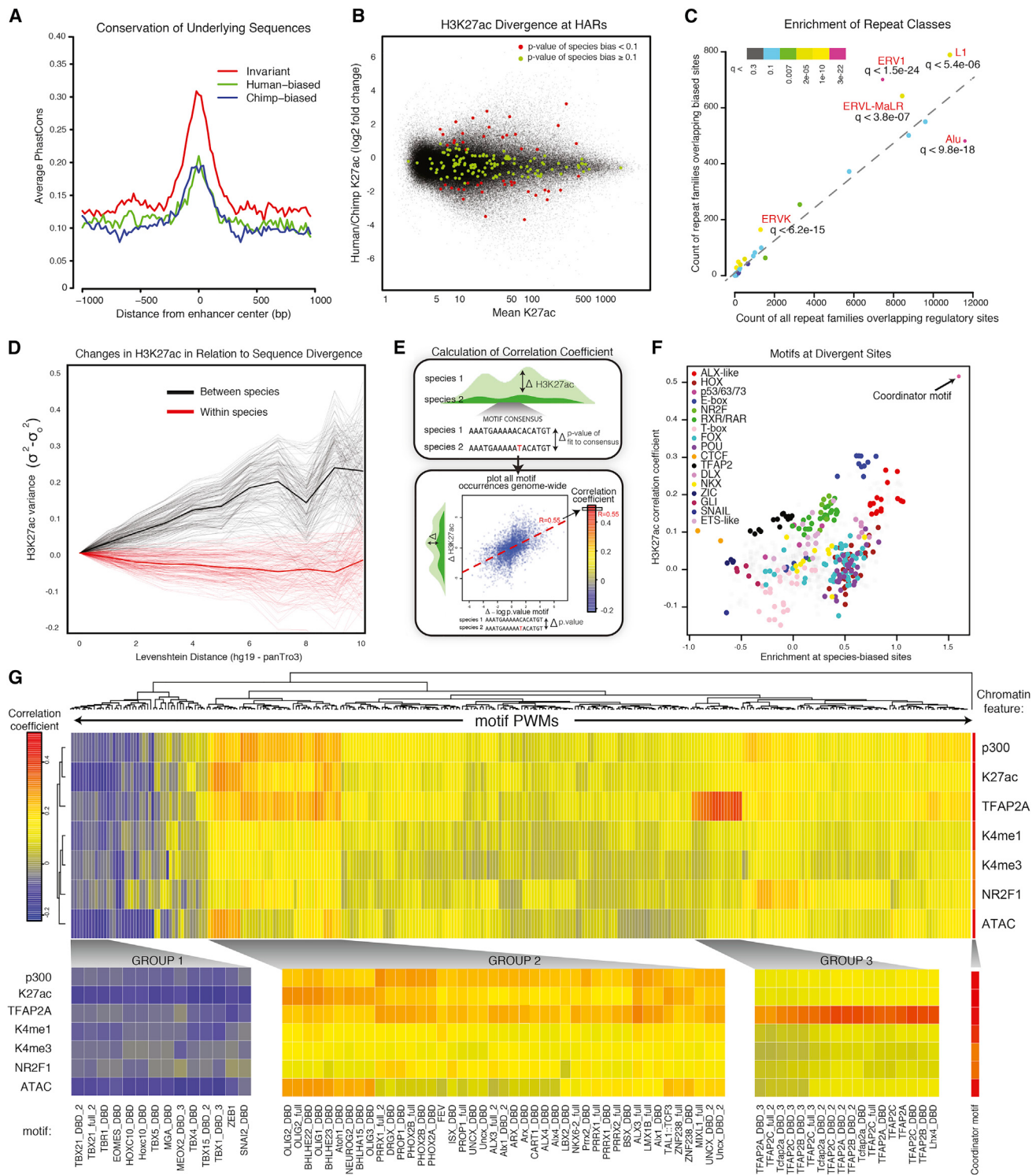


Figure 4. Global Features of Species-Biased Enhancers and Correlation of Mutations within TF Binding Motifs with Epigenomic Divergence

(A) Average PhastCons scores are shown for strong invariant enhancers ($q > 0.98$), strongly human-biased enhancers ($q < 0.0001$), or strongly chimp-biased enhancers ($q < 0.0001$) for 1 kb surrounding each enhancer center.

(B) Degree of species bias (\log_2 fold change H3K27ac human/chimp, y axis) relative to enhancer strength (human-chimp-averaged H3K27ac enrichment, x axis) for bulk CNCC elements (black) and elements overlapping HARs (color representing q value of species bias: $q < 0.1$ in red, $q \geq 0.1$ in green).

(C) Counts of repeat families overlapping species-biased enhancers (y axis) relative to counts of repeat families overlapping all CNCC regulatory sites (x axis) are plotted. q values of enrichment for different repeat classes is indicated by color.

(legend continued on next page)

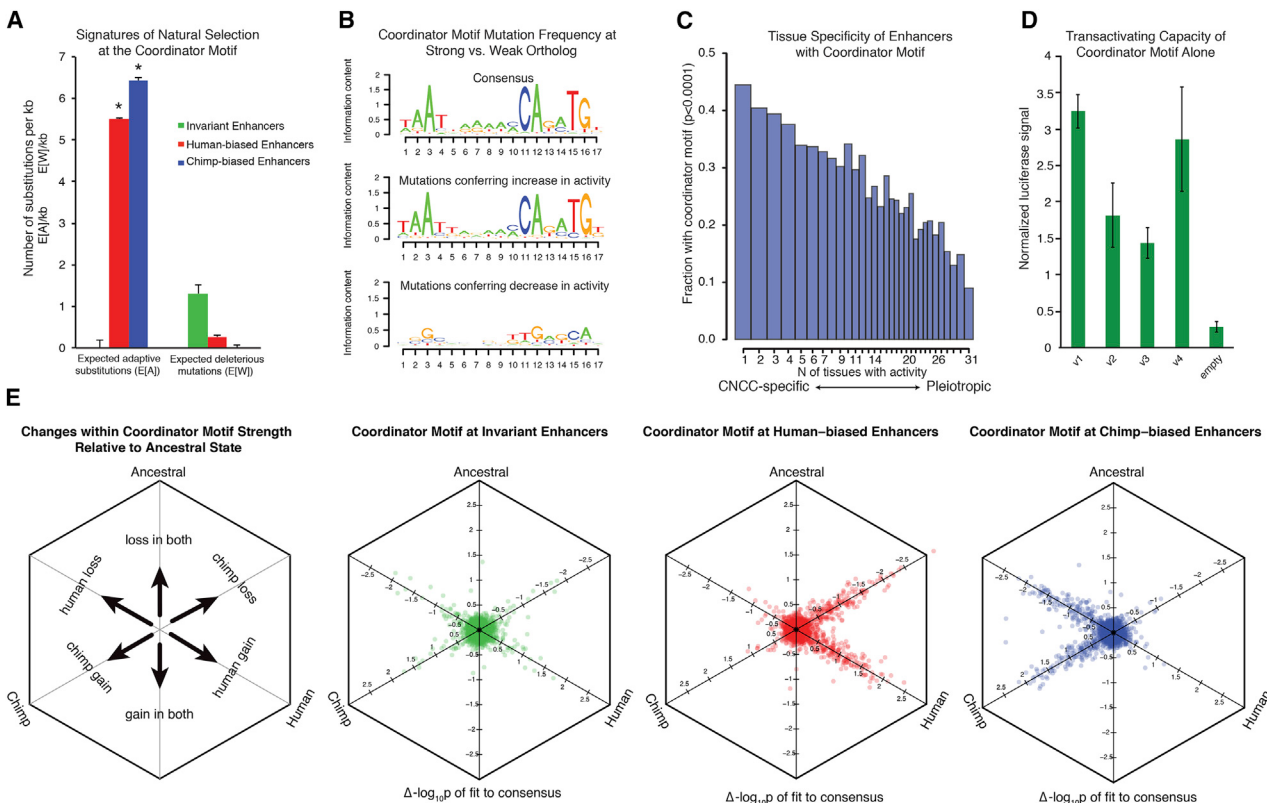


Figure 5. Properties of the Novel “Coordinator” Motif

(A) Expected number of adaptive substitutions ($E[A]$) per kilobase and expected number of deleterious mutations $E[W]$ per kilobase were calculated for all sites of the Coordinator motif at invariant enhancers (green), at human-biased enhancers (red), and at chimp-biased enhancers (blue) using default INSIGHT parameters (Gronau et al., 2013). Significance indicated by * ($p < 0.01$). Overall fractions of nucleotides under selection (ρ) not shown ($\rho_{\text{Invariant}} = 0.66$, $p < 0.01$; $\rho_{\text{Human-biased}} = 0.015$, $p < 0.01$; $\rho_{\text{Chimp-biased}} = 0.019$, $p < 0.01$). Error bars represent approximate SE.

(B) Position weight matrix of the Coordinator consensus sequence from top 3,000 CNCC specific enhancers is shown (top) relative to logo of mutations preferred at more acetylated (H3K27ac) alleles (middle) versus mutations at less acetylated alleles (bottom).

(C) Enhancers were scored for H3K27ac ChIP-seq enrichments from 30 public data set cell types and binned by number of tissues with activity (1 to 31). The fraction of enhancers per bin with recognizable Coordinator motif ($p < 0.0001$) is indicated on y axis.

(D) Four different versions (V1–V4) of the Coordinator motif were cloned in tandem into luciferase reporter vectors and were tested for transactivation activity in human CNCCs. Luciferase was normalized relative to renilla transfection control. Error bars represent one SD.

(E) Comparison of sequence changes within the Coordinator motif with a reconstructed human-chimp ancestral outgroup. Changes in fit to the Coordinator consensus compared to the ancestral ortholog ($-\log_{10} p$ value) were plotted as orthographic projections along space diagonals for all occurrences of the motif for both human and chimpanzee lineages at different classes of sites. Overlapping data points were jittered for better visualization. Schematic is shown on the far left.

class depleted from species-biased sites. Even at sites without activity in CNCCs, LTR9 sequences are 3.7× more likely to harbor a Coordinator-like motif than MER52A, consistent with the idea that a preexisting Coordinator-like progenitor sequence

contributed to the recent adaptation of some retroelements for CNCC enhancer function. Lastly, we found that the Coordinator motif alone was able to drive activity in luciferase reporter assays in CNCCs (Figure 5D).

(D) Pairwise H3K27ac variance $\sigma_2 - \sigma_{2,\text{id}} = 0$ at enhancers across samples, ranked by increasing sequence dissimilarity counted by Levenshtein distance (Id) between human (hg19) and chimp (panTro3) orthologous 200 bp enhancers, relative to $\text{Id} = 0$. Comparison between samples of different species shown in black; same species shown in red (means represented by thick lines).

(E) Schematic showing method for deriving the correlation coefficient. For a given motif, each occurrence genome wide containing a genetic change across species is plotted as $\Delta\log_{10} p$ value (human/chimp) of the fit to consensus (x axis) versus $\Delta H3K27ac$ for the overlying enhancer region (human/chimp) (y axis), then a line is fit. The slope of the line represents the correlation coefficient for that given motif and epigenomic modification genome wide.

(F) Enrichments of classes of motifs at species-biased enhancers over all enhancers (log odds ratio, x axis) plotted relative to genome-wide correlation coefficient calculated for each motif (using H3K27ac), as described in E (y axis).

(G) Genome-wide correlation coefficients were calculated for whole databases of annotated motifs and multiple chromatin features, revealing motifs with large influence on epigenomic profiles. Correlation coefficients are bi-clustered per motif, and resulting changes in enrichment of chromatin features (p300, K27ac, TFAP2A, H3K4me1, H3K4me3, NR2F1, ATAC) at all enhancers containing mutated PWMs are represented by color. Individual subclusters are magnified below with corresponding motifs indicated.

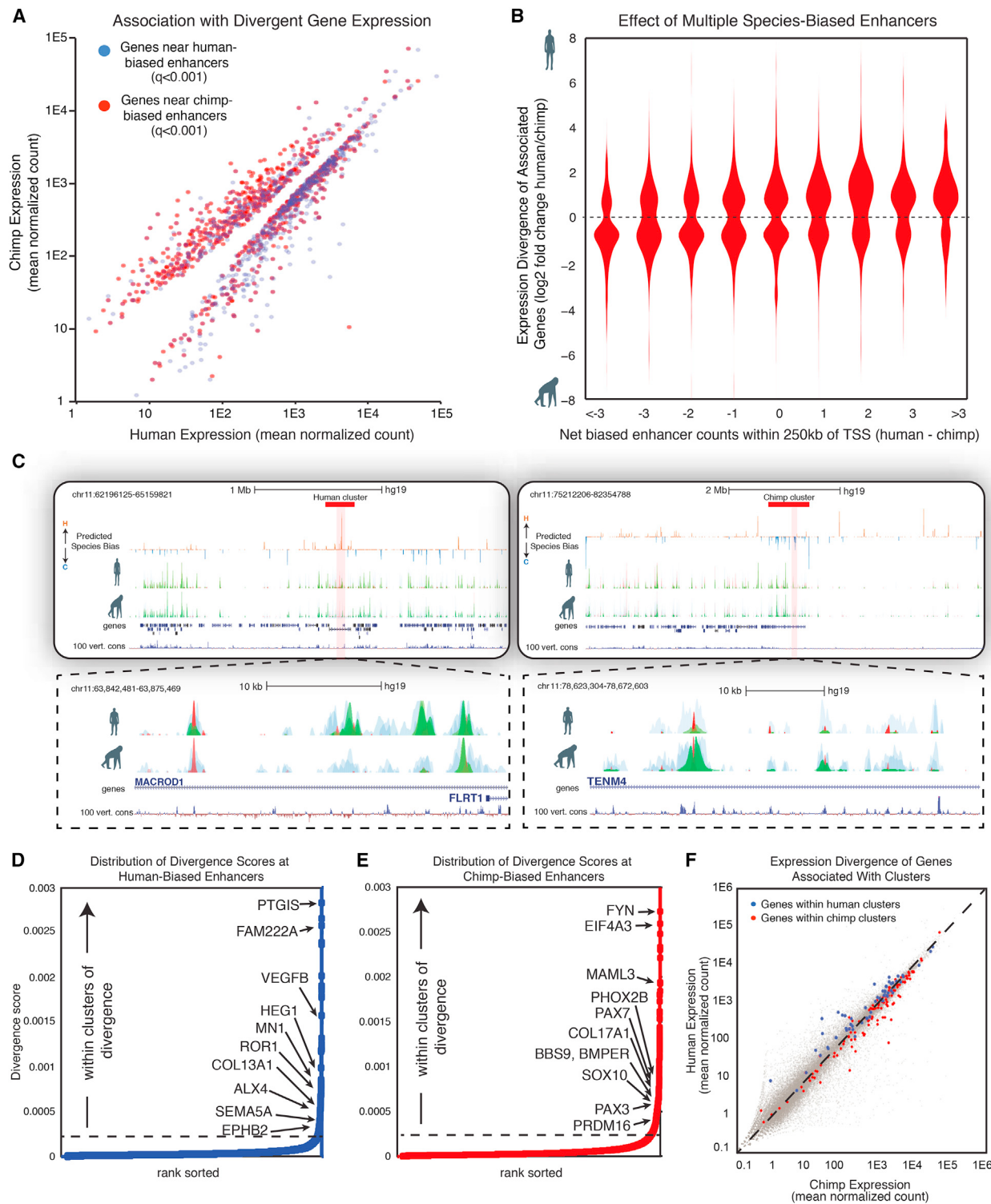


Figure 6. Clusters of Regulatory Divergence Overlap Loci with Crucial Roles in Trait Variation and Are Predictive of Expression Bias

(A) Mean normalized human expression (x axis) versus mean normalized chimp expression (y axis) for genes associated with human-biased enhancers ($q < 0.001$, blue) or with chimp-biased enhancers ($q < 0.001$, red). Only genes with significant inter-species expression change (p_{adj} value < 0.1) are shown.

(B) Violin plots showing \log_2 fold change human/chimp H3K27ac enrichment at orthologous enhancers binned by total count of biased enhancers (total number of human-biased enhancers minus total number of chimp-biased enhancers) within 250 kb of promoter regions for genes with significant differences in expression across species (p_{adj} value < 0.1).

(legend continued on next page)

Sequence Analysis Reveals the Recent Evolutionary History of Coordinator Motif Changes

Our results suggest that nucleotide changes within Coordinator motif sites represent an important class of “causative” mutations predictably associated with gain or loss of CNCC enhancer activity. Thus, by comparing the fit to the consensus for Coordinator-like motifs with a reconstructed ancestral outgroup, we can infer the polarity of enhancer activity change in each lineage relative to the common human-chimp ancestor. Using this strategy, we observed that human-biased enhancers contain Coordinator-like sequences that were equally prone to: (1) a gain in the fit in the human lineage ($n = 300$) or (2) a loss in the fit in the chimp lineage ($n = 255$) relative to the ancestral state (Figure 5E). However, human-biased enhancers contain almost no examples in which there was a gain of Coordinator fit in the chimp lineage or loss in the human lineage, an important validation of our analysis. Conversely, we see that chimp-biased enhancers are similarly prone to gains of the Coordinator motif in the chimp lineage ($n = 218$) versus losses in the human lineage ($n = 255$) and again, with almost no gains in human or losses in chimp. Thus, there appears to be no preferred direction of enhancer divergence in either lineage since the split from our common ancestor for this class of sites. We also applied our analysis to hominin outgroups such as Denisovans and Neanderthals and found that, as expected given the much more recent split from the common ancestor, these lineages primarily share the human-like variants of the Coordinator motif at species-biased sites (Figure S6G). Therefore, even for individuals substantially more diverged than any modern human, most changes are present in the hominin lineage relative to the human-chimp ancestor. However, there is a small set of changes that are unique to modern humans compared to other hominins, and those clearly merit further exploration.

Species-Biased Enhancers Flank Genes that Show Species-Biased Expression

Recent studies suggest that gene expression levels are more evolutionarily conserved than utilization of *cis*-regulatory elements and can be buffered by redundant or compensatory elements regulating the same loci (Hong et al., 2008; Odom et al., 2007; Schmidt et al., 2010; Vierstra et al., 2014; Wong et al., 2014). Nonetheless, at least some of the species-biased enhancers should be associated with transcriptional changes at nearby genes if they are responsible for morphological variation. To test this, we performed RNA-seq analyses of our human and chimp CNCC populations and identified genes whose expression significantly diverged between, but not within, species. We found that genes with significantly divergent expression between humans and chimpanzees are strongly enriched for

nearby species-biased enhancers, with human-biased genes flanked by human-biased enhancers and chimp-biased genes flanked by chimp-biased enhancers (Figure 6A). In addition, we observed that the fraction of species-biased genes (but not the degree of the expression bias) scales with the number of flanking enhancers biased toward the same species (Figure 6B).

Clusters of Regulatory Divergence Flank Loci Involved in Intra-Human Facial Variation

Interestingly, we found that strongly divergent enhancers were not distributed at random throughout the genome but instead were likely to fall in close genomic proximity to other species-biased enhancers matching in polarity (Figure S7A), suggesting that divergent enhancers fall into regulatory clusters. To systematically locate these clusters, we calculated a genome-wide divergence score using a moving window over the nearest ~10 enhancers for each species, integrating both the degree and genomic span of divergent enhancers in series (Figure S7B). This strategy revealed a low baseline encompassing the bulk of interspersed species-biased enhancers (examples of Chr11 in Figures S7C and S7D, top) but exposed a subset of regions throughout the genome (~1–4 per chromosome), with a marked increase in their divergence score resulting from presence of dense clusters of strongly biased enhancers (Figure 6C). Importantly, we find that these clusters of divergence do not emerge simply by chance due to increased frequency of enhancers near highly active CNCC genes (Figures S7C and S7D).

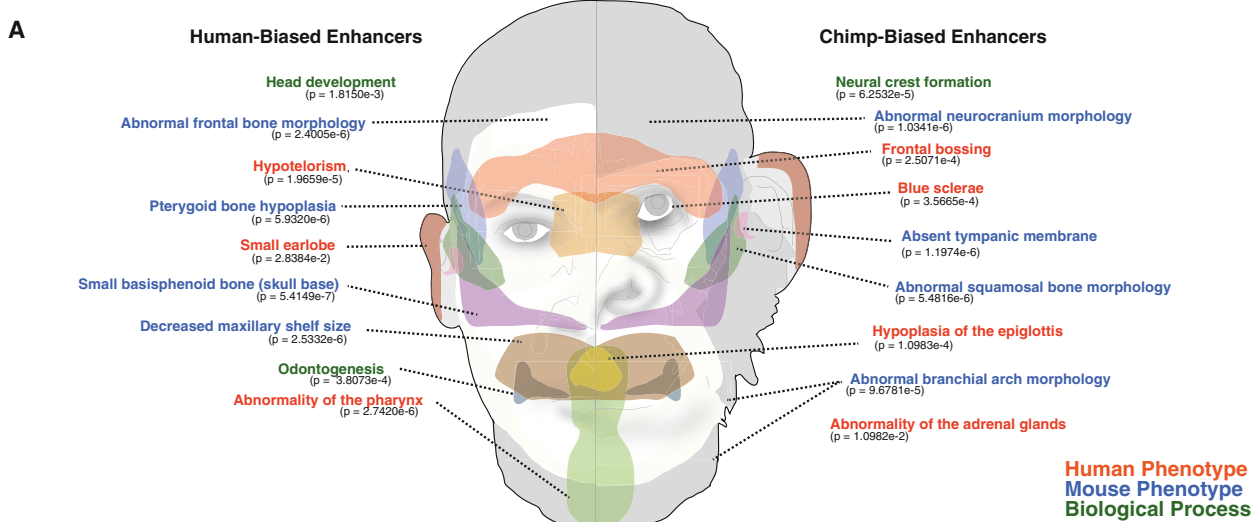
When ranking all human- and chimp-biased enhancers according to their divergence score, we observed an inflection in the distribution (Figures 6D for human, 6E for chimp). Using this inflection point as a cutoff, we identified 32 human and 65 chimp clusters of divergence, spanning genomic windows of, on average, ~500 kb and encompassing ~11.9% of all species-biased enhancers. Of note, while some clusters overlapped super-enhancers in CNCCs, most super-enhancers were not identified as a species-biased cluster and many species-biased clusters did not encompass super-enhancers, indicating that these two entities are distinct (Whyte et al., 2013).

We speculate that these species-biased enhancer clusters represent broad *cis*-regulatory regions under strong evolutionary pressure to diverge and hypothesize that they may contain genes with central roles in the regulation of NC-associated phenotypes. Indeed, these regions fall immediately over or next to genes that are critical in facial morphogenesis, including *PRDM16*, *MN1*, *COL17A1*, *EDNRA*, *PAX3*, *PAX7*, *SOX10*, and *ALX4*. Intriguingly, of five chromosomal regions linked to normal-range human facial variation in GWAS, three (*PRDM16*, *COL17A1*, and *PAX3*) fall directly within these regions of high divergence. Importantly, the clusters were highly predictive of changes in nearby gene

(C) Representative browser tracks showing clusters of species-biased enhancers. Top panel shows broad view with predicted species-bias track (human-biased in orange, chimp-biased in blue) and the corresponding H3K4me1 (blue), p300 (red), and H3K27ac (green) from two individuals of each species shown in overlay. Boundaries of the cluster are indicated by a red block. Close-up of an individual cluster of biased enhancers is shown below. All chromatin features are mapped to hg19.

(D and E) Distribution of divergence scores at human-biased enhancers (D) and chimp-biased enhancers (E). Selected genes falling within identified clusters are highlighted next to the enhancer in the cluster with highest divergence score.

(F) Mean normalized human expression (x axis) versus mean normalized chimp expression (y axis) for genes within or flanking human-biased enhancer clusters (blue) or chimp-biased enhancer clusters (red).

**B**

Gene	Expression bias:	DESEQ q value	Coordinates of nearby species-biased enhancers (hg19)	Relevant genetic phenotypes, disease associations and comments	References
PAX3	C	4.1584E-06	chr2:223983203-223983402 ; chr2:223157099-223157298 ; chr2:223148418-223148617 ; chr2:223084744-223084943 ; chr2:223060007-22306206 ; chr2:223005367-22300566 ; (see Figure S4B);	Heterozygous loss-of-function mutations cause Waardenburg syndrome, characterized by craniofacial, auditory and pigmentation defects; in model organisms Pax3 is involved in induction, specification and differentiation of neural crest cells and craniofacial development; in GWAS studies the locus was associated with normal-range variation of facial morphology in Europeans.	Asher et al., 1996; Convey et al., 1997; Liu et al., 2012; Milet et al., 2013; Paternoster et al., 2012; Tassabehji et al., 1992; Tremblay et al., 1995;
PAX7	C	0.11724596	chr1:19267843-19268042 ; chr1:19268294-19268493 ; chr1:19268849-19269047 ; chr1:19271215-19271414 ; chr1:19275542-19275741 ; chr1:19276342-19276541	Involved in early specification of the neural crest in the embryo; loss of function in the mouse leads to reduction of the maxilla and a pointed snout.	Basch et al., 2006; Mansouri et al., 1996;
EDNRA	C	1.1308E-04	chr4:148262113-148262312 ; chr4:148276381-148276580 ; chr4:148454528-148454727 ; chr4:14855160-14855259 ; chr4:148507330-148507529 ; chr4:148508238-148508437 ; chr4:148510911-148511110 (see Figure S4B);	Mouse deficient for Ednra exhibit cranial and cardiac neural crest defects. Most lower jaw structures in Ednra ^{-/-} embryos undergo a homeotic transformation into maxillary-like structures; other defects include absence of tympanic rings, malleus, and incus, and the rostral relocation of the hyoid bone.	Clothier et al., 1998, 2010; Ruest et al., 2004
EDN3	H	5.2338E-03	chr20:57723838-57724037 ; chr20:57724804-57725003 ; chr20:57726203-57726402 ; chr20:57894099-57894298 ; chr20:57988186-57988385 ; chr20:58028164-58028363 ; chr20:58028993-58029192 ; chr20:58154612-58154811 (see Figure S4B);	Heterozygous or homozygous mutations associated with several human neurocristopathies, including Waardenburg syndrome type 4B, Hirschsprung's disease, and Congenital Central Hypoventilation Syndrome (CCHS). In animal models EDN3 is involved in the regulation of coat pigmentation and enteric neuron function.	Baynash et al., 1994; Bidaud et al., 1997; Dupin et al., 2000; Edery et al., 1996; Lahav et al., 1996; Pingault et al., 2001;
NRP2	H	4.7551E-02	chr2:206515229-206515428 ; chr2:206436082-206436281 ; chr2:206266143-206266342 ; chr2:206250975-206251174	Involved in guidance of NCC migration and restricting migratory paths of cranial and trunk NCCs, positioning sensory neurons and organizing their projections.	Gammill et al., 2007; Schwarz et al., 2008; Yu and Moens, 2005;
EPHB2	H	5.1251E-02	chr1:23164766-23164965 ; chr1:23164254-23164453 ; chr1:23162983-23163182 ; chr1:23162487-23162686	Ephrin B signaling is involved in targeting and restricting neural crest migration within branchial arches; compound EphB2/B3 knockout in mice leads to cleft palate.	Orioli et al., 1996; Risley et al., 2009; Smith et al., 1997;
BMP4	H	5.4181E-02	chr14:54911474-54911673 ; chr14:55093544-55093743 ; chr14:55094758-55094957 ; chr14:55095533-55095732	Proposed to be a crucial mediator of beak shape changes in Darwin's finches and of craniofacial shape and morphological adaptive radiation in Cichlid fish. CNCC-specific overexpression of BMP4 during mouse development results in the dramatic change of facial shape, with shortening in both the mandible and maxilla, rounding of the skull shape, and more anterior orientation of the eyes. In humans, mutations/variants in BMP4 are associated with orofacial clefts, microphthalmia, and age of the primary tooth eruption.	Abzhanov et al., 2004; Albertson et al., 2005; Boell et al., 2013; Fatemifar et al., 2013; Tucker et al., 1998; Wu et al., 2004;
BMPER	C	2.2758E-05	chr7:33525807-33526006 ; chr7:33526320-33526519 ; chr7:33527256-33527455 ; chr7:33540319-33540518 ; chr7:33540928-33541127 ; (see Figure S4B)	Negative regulator of BMP4 function in osteoblast and chondrocyte differentiation (see also <i>BMP4</i>). In humans, homozygous or heterozygous mutations in <i>BMPER</i> are associated with a skeletal disorder, diaphanspondylyostosis, whose consistent craniofacial features include ocular hypertelorism, epicanthal folds, depressed nasal bridge with short nose, and low-set ears.	Binnerts et al., 2004; Funari et al., 2010; Moser et al., 2003;
PITX2	C	1.2564E-11	chr4:111230391-111230590 ; chr4:111230942-111231141 ; chr4:111280988-111281187	PITX2 haploinsufficiency is associated with Axenfeld-Rieger syndrome involving ocular anterior segment dysgenesis, tooth anomalies, and craniofacial anomalies such as maxillary hypoplasia with mid-face flattening and prominent forehead; in mice, ocular manifestations are largely recapitulated by the neural crest-specific knockout of Pitx2; genetically interacts with <i>FOXC1</i> , see also <i>FOXC1</i> .	Evans and Gage, 2005; Lu et al., 1999; Matt et al., 2005; Semina et al., 1996
FOXC1	C	3.4267E-02	chr6:1744897-1745096	Heterozygous mutations in <i>FOXC1</i> are associated with Axenfeld-Rieger syndrome (A-RS) involving ocular anterior segment dysgenesis, tooth anomalies, and maxillary and mandibular hypoplasia; dosage-dependent interactions with another A-RS gene <i>PITX2</i> have been observed; in mice, loss of FoxC1 results in bony synostosis, defects in maxillary and mandibular structures, and agenesis of the temporomandibular joint; see also <i>PITX2</i> .	Berry et al., 2006; Inman et al., 2013; Kelberman et al., 2011; Mears et al., 1998; Turner and Bach-Holm, 2009;
POU3F3	H	2.1354E-02	chr2:105024721-105024920 ; chr2:104990082-104990281 ; chr2:104989534-104989733 ; chr2:104937657-104937856	In mouse knockout leads to loss of squama temporalis and stapes fusion to styloid process.	Dheude et al., 2014; Jeong et al., 2008;

(legend on next page)

expression for the bulk of the associated genes in the region (Figure 6E), suggesting that either (1) multiple genes in the vicinity must be under coordinated selection for these super-divergent regions to emerge or, more likely, that (2) strong selection on one or a few target genes could drive changes in the local enhancer landscape that have secondary effects on other genes in the vicinity. Altogether, we provide evidence that highly divergent clusters of tissue-specific enhancers may promote inter-species and intra-species phenotypic variation.

Resource for Studies of Human Morphological Evolution

In addition to informing the basic mechanisms underlying the *cis*-regulatory divergence of human and chimpanzee NC, our study also provides a rich resource for future investigations of morphological evolution of human craniofacial traits. Ontology annotations of all significantly species-biased enhancers reveal strong associations with processes important for various craniofacial structures that are diverging in human and chimps (Figure 7A). As examples, we highlight some of the most interesting divergent candidate genes in Figure 7B. These featured loci show species-biased expression in our RNA-seq and also map to regions with species-biased enhancer divergence and are emphasized due to their known associations with CNCC development and/or facial morphology. Nonetheless, it is important to bear in mind that the biases in gene expression and enhancer states highlighted in Figure 7 refer to the relative change between human and chimpanzee CNCCs, without ascribing the polarity of the change with respect to the ancestral status.

Our divergently expressed genes are known to be involved in multiple, distinct developmental processes that cooperate to influence differential allocation of CNCCs in facial primordia and, in turn, contribute to species-specific morphology (Fish et al., 2014). These processes (and associated species-biased genes) include: (1) CNCC specification (e.g., *PAX3*, *PAX7*), (2) migration and guidance of CNCC migratory paths (e.g., *EPHB2*, *NRP2*, *EDNRA*, *EDN3*), (3) modulation of CNCC proliferation at facial primordia (e.g., *BMP4*), and (4) regulation of CNCC differentiation (e.g., *PITX2*). Moreover, heterozygous mutations in many of these genes (e.g., *PAX3*, *PITX2*, *FOXC1*, *EDN3*, *BMPER*) are associated with human syndromes that include craniofacial manifestations, suggesting that altered gene dosage can drive both morphological variation between species and, below a certain threshold, disease-associated malformations (Figure 7B). Furthermore, many phenotypes of the highlighted genes affect aspects of head morphology that have diverged between humans and chimps (e.g., size of the mandible and maxilla, skull shape, and pigmentation) (Figure 7B and Discussion). Altogether, our study provides a wealth of candidate loci for further deep exploration in studies of human evolution and variation.

DISCUSSION

Our study utilizes primate cellular models to provide a comprehensive map of human and chimp regulatory divergence in a tissue with central relevance to the development of the head and face. We show that a common mechanism of regulatory divergence in higher primates is quantitative modulation of orthologous elements, driven largely through small numbers of sequence changes that perturb tissue-specific TF binding motifs. This is consistent with previous studies from closely related *Drosophila* or mouse species demonstrating that large effects can be conferred by a small number of mutations affecting direct and cooperative binding of key TFs (Bradley et al., 2010; He et al., 2011; Stefflova et al., 2013). Interestingly, we find that not all TF binding sites contribute equally to regulatory divergence—in fact, we identify a broad spectrum of regulatory motifs that vary in frequency and effect, suggesting a mechanism through which evolution can fine-tune *cis*-regulation across an enhancer landscape. One outlier in our analysis is the Coordinator motif, a de novo consensus sequence that is strongly predictive of the surrounding chromatin features and is highly enriched at species-biased enhancers. We speculate that the factor(s) that recognize the Coordinator motif play a privileged role in the establishment of enhancer competence in this cell context, reminiscent of the *Drosophila* TAGteam motif bound by a pioneer factor Zelda (Liang et al., 2008; Satija and Bradley, 2012). Furthermore, we find evidence of repressive inputs into quantitative modulation of enhancer activity, with a sizable number of motifs whose gain in strength negatively correlates with acquisition of permissive chromatin states.

Our work provides a rich framework for future gene-centric studies on the developmental mechanisms of human morphological evolution. Indeed, our approach identified loci that are known to profoundly affect NC development and craniofacial morphology, often in a dosage-sensitive manner. For example, we observed that two genes involved in CNCC specification, *PAX3* and *PAX7*, are expressed at higher levels in chimps and are associated with clusters of chimp-biased enhancers. In mice, mutations of these TFs lead to reduction of pigmentation and snout length (*Pax3*) (Tremblay et al., 1995) and reduction of maxilla and pointed snout (*Pax7*) (Mansouri et al., 1996), features that are consistent with smaller jaw size and hypopigmentation of humans as compared to chimps. Furthermore, humans are sensitive to alterations of *PAX3* dosage, as haploinsufficiency of this gene is associated with craniofacial, auditory, and pigmentation defects (Waardenburg syndrome, OMIM #193510), and genetic variants at this locus have been identified in GWAS studies as regulators of normal-range facial shape (Liu et al., 2012; Paternoster et al., 2012). Thus, variation in

Figure 7. Species-Biased Enhancers Are Associated with Genes Affecting Craniofacial Structures

(A) GREAT term enrichments and associated facial regions indicated for human-biased enhancers ($q < 0.01$, baseMean > 300) and chimp-biased enhancers ($q < 0.01$, baseMean > 300); binomial raw p values are shown below. Ontology categories are color coded (human phenotypes, red; mouse phenotypes, blue; biological processes, green).

(B) Table of highlighted divergently expressed genes showing direction of bias (human-biased versus chimp-biased indicated by H or C, respectively), DESeq adjusted p value of expression divergence, coordinates of nearby species-biased enhancers with corresponding bias (hg19), description of genetic phenotypes, disease associations, comments, and relevant references. Full reference information can be found in Table S1.

PAX3 and PAX7 levels represents an attractive possible mechanism for mediating facial shape divergence between humans and chimpanzees.

We also find evidence that genes already known to affect facial morphology in other species, such as *BMP4*, are diverging in higher primates as well. *BMP4* is the most well-understood example of a factor that influenced craniofacial morphological change during evolution, as it has been implicated in mediating changes in beak morphology in Darwin's finches (Abzhanov et al., 2004) and in jaw shape in Cichlid fish (Albertson et al., 2005). We were therefore intrigued to note that *BMP4* is associated with strongly human-biased enhancers and is expressed at higher levels in humans than in chimps. Conversely, expression of the *BMP4* inhibitor *BMPER* was significantly chimp biased and showed dramatic strengthening of the local chimp enhancer landscape. What would be the potential effects of elevated *BMP4* expression on primate facial development? Interestingly, in the mouse, CNCC-specific overexpression of *BMP4* results in a dramatic change of facial shape, with shortening of both the mandible and maxilla, rounding of the skull, and more anterior orientation of the eyes (Bonilla-Claudio et al., 2012)—morphological changes that resemble those observed between human and chimps. Thus, the same molecular mechanism that has been postulated to influence beak morphology in Darwin's finches may also contribute to our uniquely human facial features.

Even more intriguing, of five chromosomal regions that have been associated with normal-range human facial variation in GWAS, three (*PRDM16*, *COL17A1*, and *PAX3*) coincide with clusters of species-biased enhancers uncovered in our study (Liu et al., 2012; Paternoster et al., 2012), suggesting a significant overlap between loci regulating intra- and inter-species variation of facial shape in higher primates. We therefore hypothesize that other divergent clusters identified in our study represent novel candidates for loci involved in the regulation of facial shape in humans. More broadly, we suggest that comparisons of human regulatory landscapes with those of a closely related primate in any tissue of interest may provide an effective strategy to identify candidate loci involved in normal-range and disease-associated variation.

EXPERIMENTAL PROCEDURES

CNCC Derivation

Pluripotent lines were differentiated into CNCC as previously described (Rada-Iglesias et al., 2012). Details are provided in the *Supplemental Experimental Procedures*.

Chromatin Immunoprecipitation and Preparation of ChIP-Seq Libraries

Chromatin immunoprecipitation (ChIP) was performed using ~0.5–1 × 10⁷ CNCCs per experiment, as previously described (Bajpai et al., 2010; Rada-Iglesias et al., 2011, 2012). Antibodies used for ChIPs are listed in the *Supplemental Experimental Procedures*. Sequencing libraries were prepared starting from 30 ng of ChIP DNA using the NEBNext Multiplex Oligos for Illumina kit (Cat# E7335S). Libraries were multiplexed four to six samples per lane for 1 × 50 bp next-gen sequencing on Illumina HiSeq platform.

Quantitative Analysis of H3K27ac ChIP-Seq and Identification of Divergence

All sequencing reads were aligned to both reference genomes (hg19 and pan-Tro3) using default settings with bowtie2.2.4, regardless of species of origin.

Modal peak positions for candidate regulatory elements were determined using a mean shift procedure, described in the *Supplemental Experimental Procedures*. To obtain count statistics for each H3K27ac ChIP alignment, we counted read coverage in a 1.6 kb window surrounding modal peak positions. ENCODE-blacklisted regions and outlier regions with high counts in control input sequences relative to ChIP were removed as artifacts. Scores for visualization and classification of remaining ChIPs were obtained using a kernel density estimate, as previously described (Buecker et al., 2014).

Calculations of species bias were inferred with DESeq2, based on the read counts from all replicates of H3K27ac at candidate enhancers from three human lines (one hESC, two iPSC) and two chimp lines (two iPSC). DESeq2 analysis was performed separately for panTro3 and hg19 counts; then conservatively, the higher p-adj value and lower abs(log2FoldChange) of the analysis from either hg19 or panTro3 were assigned to each region, while rare regions with discordant calls were excluded from list of biased sites (less than 0.1%).

ACCESSION NUMBERS

All sequencing data sets were deposited in the NCBI GEO repository under accession ID GEO: GSE70751.

SUPPLEMENTAL INFORMATION

Supplemental Information includes Supplemental Experimental Procedures, seven figures, and three tables and can be found with this article online at <http://dx.doi.org/10.1016/j.cell.2015.08.036>.

ACKNOWLEDGMENTS

We thank D. Kingsley, R. Greenberg, J. Buenrostro, and Wysocka lab members for comments on the manuscript. We also thank R. Aho and J.D. Benazet for help with imaging of mouse transgenic embryos and interpretation of staining patterns, as well as P. Nano and E. Grow for help generating reporter reagents. This work was supported by W.M. Keck Foundation, Stanford School of Medicine Innovation Fund, and NIH R01 GM095555 (J.W.) and U01 DE024430 (J.W. and L.S.), as well as CIRM training grant (TG2-01159) (S.L.P.). This work was also partially supported by funds from NIH TR01 MH095741, the Helmsley Charitable Fund, the Mathers Foundation, and the JPB Foundation (F.H.G.).

Received: February 3, 2015

Revised: May 6, 2015

Accepted: July 21, 2015

Published: September 10, 2015

REFERENCES

- Abzhanov, A., Protas, M., Grant, B.R., Grant, P.R., and Tabin, C.J. (2004). *Bmp4* and morphological variation of beaks in Darwin's finches. *Science* 305, 1462–1465.
- Albertson, R.C., Streelman, J.T., Kocher, T.D., and Yelick, P.C. (2005). Integration and evolution of the cichlid mandible: the molecular basis of alternate feeding strategies. *Proc. Natl. Acad. Sci. USA* 102, 16287–16292.
- Attanasio, C., Nord, A.S., Zhu, Y., Blow, M.J., Li, Z., Liberton, D.K., Morrison, H., Plajzer-Frick, I., Holt, A., Hosseini, R., et al. (2013). Fine tuning of craniofacial morphology by distant-acting enhancers. *Science* 342, 1241006.
- Bajpai, R., Chen, D.A., Rada-Iglesias, A., Zhang, J., Xiong, Y., Helms, J., Chang, C.-P., Zhao, Y., Swigut, T., and Wysocka, J. (2010). CHD7 cooperates with PBAF to control multipotent neural crest formation. *Nature* 463, 958–962.
- Bilsborough, A., and Wood, B.A. (1988). Cranial morphometry of early hominids: facial region. *Am. J. Phys. Anthropol.* 76, 61–86.
- Bonilla-Claudio, M., Wang, J., Bai, Y., Klysik, E., Selever, J., and Martin, J.F. (2012). Bmp signaling regulates a dose-dependent transcriptional program to control facial skeletal development. *Development* 139, 709–719.

Bradley, R.K., Li, X.-Y., Trapnell, C., Davidson, S., Pachter, L., Chu, H.C., Tonkin, L.A., Biggin, M.D., and Eisen, M.B. (2010). Binding site turnover produces pervasive quantitative changes in transcription factor binding between closely related *Drosophila* species. *PLoS Biol.* 8, e1000343.

Bronner, M.E., and LeDouarin, N.M. (2012). Development and evolution of the neural crest: an overview. *Dev. Biol.* 366, 2–9.

Buecker, C., Srinivasan, R., Wu, Z., Calo, E., Acampora, D., Faial, T., Simeone, A., Tan, M., Swigut, T., and Wysocka, J. (2014). Reorganization of enhancer patterns in transition from naïve to primed pluripotency. *Cell Stem Cell* 14, 838–853.

Buenrostro, J.D., Giresi, P.G., Zaba, L.C., Chang, H.Y., and Greenleaf, W.J. (2013). Transposition of native chromatin for fast and sensitive epigenomic profiling of open chromatin, DNA-binding proteins and nucleosome position. *Nat. Methods* 10, 1213–1218.

Cain, C.E., Blekhman, R., Marioni, J.C., and Gilad, Y. (2011). Gene expression differences among primates are associated with changes in a histone epigenetic modification. *Genetics* 187, 1225–1234.

Carroll, S.B. (2008). Evo-devo and an expanding evolutionary synthesis: a genetic theory of morphological evolution. *Cell* 134, 25–36.

Cordaux, R., and Batzer, M.A. (2009). The impact of retrotransposons on human genome evolution. *Nat. Rev. Genet.* 10, 691–703.

Cordero, D.R., Brugmann, S., Chu, Y., Bajpai, R., Jame, M., and Helms, J.A. (2011). Cranial neural crest cells on the move: their roles in craniofacial development. *Am. J. Med. Genet. A* 155A, 270–279.

Cotney, J., Leng, J., Yin, J., Reilly, S.K., DeMare, L.E., Emera, D., Ayoub, A.E., Rakic, P., and Noonan, J.P. (2013). The evolution of lineage-specific regulatory activities in the human embryonic limb. *Cell* 154, 185–196.

Creyghton, M.P., Cheng, A.W., Welstead, G.G., Kooistra, T., Carey, B.W., Steine, E.J., Hanna, J., Lodato, M.A., Frampton, G.M., Sharp, P.A., et al. (2010). Histone H3K27ac separates active from poised enhancers and predicts developmental state. *Proc. Natl. Acad. Sci. USA* 107, 21931–21936.

Fish, J.L., Sklar, R.S., Woronowicz, K.C., and Schneider, R.A. (2014). Multiple developmental mechanisms regulate species-specific jaw size. *Development* 141, 674–684.

Gompel, N., Prud'homme, B., Wittkopp, P.J., Kassner, V.A., and Carroll, S.B. (2005). Chance caught on the wing: cis-regulatory evolution and the origin of pigment patterns in *Drosophila*. *Nature* 433, 481–487.

Gronau, I., Arbiza, L., Mohammed, J., and Siepel, A. (2013). Inference of natural selection from interspersed genomic elements based on polymorphism and divergence. *Mol. Biol. Evol.* 30, 1159–1171.

He, Q., Bardet, A.F., Patton, B., Purvis, J., Johnston, J., Paulson, A., Gogol, M., Stark, A., and Zeitlinger, J. (2011). High conservation of transcription factor binding and evidence for combinatorial regulation across six *Drosophila* species. *Nat. Genet.* 43, 414–420.

Heintzman, N.D., Stuart, R.K., Hon, G., Fu, Y., Ching, C.W., Hawkins, R.D., Barrera, L.O., Van Calcar, S., Qu, C., Ching, K.A., et al. (2007). Distinct and predictive chromatin signatures of transcriptional promoters and enhancers in the human genome. *Nat. Genet.* 39, 311–318.

Hong, J.-W., Hendrix, D.A., and Levine, M.S. (2008). Shadow enhancers as a source of evolutionary novelty. *Science* 321, 1314.

Hubisz, M.J., and Pollard, K.S. (2014). Exploring the genesis and functions of Human Accelerated Regions sheds light on their role in human evolution. *Curr. Opin. Genet. Dev.* 29, 15–21.

Jheon, A.H., and Schneider, R.A. (2009). The cells that fill the bill: neural crest and the evolution of craniofacial development. *J. Dent. Res.* 88, 12–21.

Kaessmann, H., Wiebe, V., and Pääbo, S. (1999). Extensive nuclear DNA sequence diversity among chimpanzees. *Science* 286, 1159–1162.

King, M.C., and Wilson, A.C. (1975). Evolution at two levels in humans and chimpanzees. *Science* 188, 107–116.

Liang, H.-L., Nien, C.-Y., Liu, H.-Y., Metzstein, M.M., Kirov, N., and Rushlow, C. (2008). The zinc-finger protein Zelda is a key activator of the early zygotic genome in *Drosophila*. *Nature* 456, 400–403.

Lieberman, D.E. (1998). Sphenoid shortening and the evolution of modern human cranial shape. *Nature* 393, 158–162.

Liu, F., van der Lijn, F., Schurmann, C., Zhu, G., Chakravarty, M.M., Hysi, P.G., Wollstein, A., Lao, O., de Brujinne, M., Ikram, M.A., et al. (2012). A genome-wide association study identifies five loci influencing facial morphology in Europeans. *PLoS Genet.* 8, e1002932.

Mansouri, A., Stoykova, A., Torres, M., and Gruss, P. (1996). Dysgenesis of cephalic neural crest derivatives in *Pax7*-/- mutant mice. *Development* 122, 831–838.

Marchetto, M.C.N., Narvaiza, I., Denli, A.M., Benner, C., Lazzarini, T.A., Nathanson, J.L., Paquola, A.C.M., Desai, K.N., Herai, R.H., Weitzman, M.D., et al. (2013). Differential L1 regulation in pluripotent stem cells of humans and apes. *Nature* 503, 525–529.

McLean, C.Y., Reno, P.L., Pollen, A.A., Bassan, A.I., Capellini, T.D., Guenther, C., Indjeian, V.B., Lim, X., Menke, D.B., Schaer, B.T., et al. (2011). Human-specific loss of regulatory DNA and the evolution of human-specific traits. *Nature* 471, 216–219.

Odom, D.T., Dowell, R.D., Jacobsen, E.S., Gordon, W., Danford, T.W., MacIsaac, K.D., Rolfe, P.A., Conboy, C.M., Gifford, D.K., and Fraenkel, E. (2007). Tissue-specific transcriptional regulation has diverged significantly between human and mouse. *Nat. Genet.* 39, 730–732.

Paternoster, L., Zhurov, A.I., Toma, A.M., Kemp, J.P., St Pourcain, B., Timpton, N.J., McMahon, G., McArdle, W., Ring, S.M., Smith, G.D., et al. (2012). Genome-wide association study of three-dimensional facial morphology identifies a variant in *PAX3* associated with nasion position. *Am. J. Hum. Genet.* 90, 478–485.

Pollard, K.S., Salama, S.R., Lambert, N., Lambot, M.-A., Cappens, S., Pedersen, J.S., Katzman, S., King, B., Onodera, C., Siepel, A., et al. (2006). An RNA gene expressed during cortical development evolved rapidly in humans. *Nature* 443, 167–172.

Prabhakar, S., Poulin, F., Shoukry, M., Afzal, V., Rubin, E.M., Couronne, O., and Pennacchio, L.A. (2006). Close sequence comparisons are sufficient to identify human cis-regulatory elements. *Genome Res.* 16, 855–863.

Prabhakar, S., Visel, A., Akiyama, J.A., Shoukry, M., Lewis, K.D., Holt, A., Plajzer-Frick, I., Morrison, H., Fitzpatrick, D.R., Afzal, V., et al. (2008). Human-specific gain of function in a developmental enhancer. *Science* 321, 1346–1350.

Rada-Iglesias, A., Bajpai, R., Swigut, T., Brugmann, S.A., Flynn, R.A., and Wysocka, J. (2011). A unique chromatin signature uncovers early developmental enhancers in humans. *Nature* 470, 279–283.

Rada-Iglesias, A., Bajpai, R., Prescott, S., Brugmann, S.A., Swigut, T., and Wysocka, J. (2012). Epigenomic annotation of enhancers predicts transcriptional regulators of human neural crest. *Cell Stem Cell* 11, 633–648.

Satija, R., and Bradley, R.K. (2012). The TAGteam motif facilitates binding of 21 sequence-specific transcription factors in the *Drosophila* embryo. *Genome Res.* 22, 656–665.

Schmidt, D., Wilson, M.D., Ballester, B., Schwalie, P.C., Brown, G.D., Marshall, A., Kutter, C., Watt, S., Martinez-Jimenez, C.P., Mackay, S., et al. (2010). Five-vertebrate ChIP-seq reveals the evolutionary dynamics of transcription factor binding. *Science* 328, 1036–1040.

Shapiro, M.D., Marks, M.E., Peichel, C.L., Blackman, B.K., Nereng, K.S., Jónsson, B., Schluter, D., and Kingsley, D.M. (2004). Genetic and developmental basis of evolutionary pelvic reduction in threespine sticklebacks. *Nature* 428, 717–723.

Shibata, Y., Sheffield, N.C., Fedrigo, O., Babbitt, C.C., Wortham, M., Tewari, A.K., London, D., Song, L., Lee, B.-K., Iyer, V.R., et al. (2012). Extensive evolutionary changes in regulatory element activity during human origins are associated with altered gene expression and positive selection. *PLoS Genet.* 8, e1002789.

Spoor, F., Wood, B., and Zonneveld, F. (1994). Implications of early hominid labyrinthine morphology for evolution of human bipedal locomotion. *Nature* 369, 645–648.

Stefflova, K., Thybert, D., Wilson, M.D., Streeter, I., Aleksic, J., Karagianni, P., Brazma, A., Adams, D.J., Talianidis, I., Marioni, J.C., et al. (2013). Cooperativity

and rapid evolution of cobound transcription factors in closely related mammals. *Cell* 154, 530–540.

Tremblay, P., Kessel, M., and Gruss, P. (1995). A transgenic neuroanatomical marker identifies cranial neural crest deficiencies associated with the Pax3 mutant Splotch. *Dev. Biol.* 171, 317–329.

Twigg, S.R.F., Versnel, S.L., Nürnberg, G., Lees, M.M., Bhat, M., Hammond, P., Hennekam, R.C.M., Hoogeboom, A.J.M., Hurst, J.A., Johnson, D., et al. (2009). Frontorhiny, a distinctive presentation of frontonasal dysplasia caused by recessive mutations in the ALX3 homeobox gene. *Am. J. Hum. Genet.* 84, 698–705.

Vierstra, J., Rynes, E., Sandstrom, R., Zhang, M., Canfield, T., Hansen, R.S., Stehling-Sun, S., Sabo, P.J., Byron, R., Humbert, R., et al. (2014). Mouse regulatory DNA landscapes reveal global principles of cis-regulatory evolution. *Science* 346, 1007–1012.

Villar, D., Berthelot, C., Aldridge, S., Rayner, T.F., Lukk, M., Pignatelli, M., Park, T.J., Deaville, R., Erichsen, J.T., Jasinska, A.J., et al. (2015). Enhancer evolution across 20 mammalian species. *Cell* 160, 554–566.

Visel, A., Minovitsky, S., Dubchak, I., and Pennacchio, L.A. (2007). VISTA Enhancer Browser—a database of tissue-specific human enhancers. *Nucleic Acids Res.* 35, D88–D92.

Whyte, W.A., Orlando, D.A., Hnisz, D., Abraham, B.J., Lin, C.Y., Kagey, M.H., Rahl, P.B., Lee, T.I., and Young, R.A. (2013). Master transcription factors and mediator establish super-enhancers at key cell identity genes. *Cell* 153, 307–319.

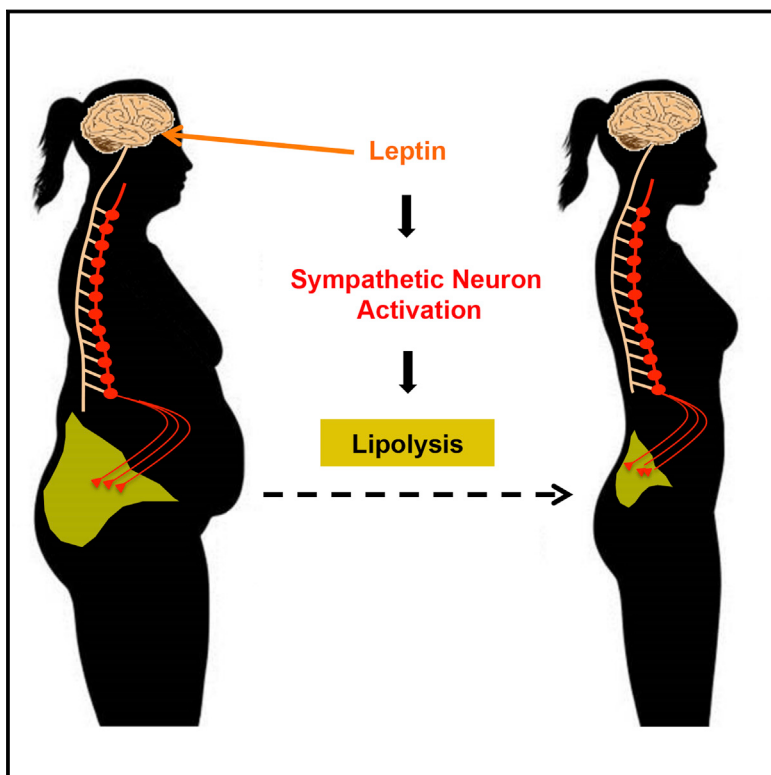
Wong, E.S., Thybert, D., Schmitt, B.M., Stefflova, K., Odom, D.T., and Flórek, P. (2014). Decoupling of evolutionary changes in transcription factor binding and gene expression in mammals. *Genome Res.*

Wray, G.A. (2007). The evolutionary significance of cis-regulatory mutations. *Nat. Rev. Genet.* 8, 206–216.

Zhou, X., Cain, C.E., Myrthil, M., Lewellen, N., Michelini, K., Davenport, E.R., Stephens, M., Pritchard, J.K., and Gilad, Y. (2014). Epigenetic modifications are associated with inter-species gene expression variation in primates. *Genome Biol.* 15, 547.

Sympathetic Neuro-adipose Connections Mediate Leptin-Driven Lipolysis

Graphical Abstract



Authors

Wenwen Zeng, Roksana M. Pirzgalska,
Mafalda M.A. Pereira, ...,
Gabriel G. Martins, Jeffrey M. Friedman,
Ana I. Domingos

Correspondence

dominan@igc.gulbenkian.pt

In Brief

The lipolytic effect of leptin is mediated by sympathetic neurons that innervate adipocytes, forming neuro-adipose junctions that directly mediate fat breakdown. Anti-obesity strategies targeting the sympathetic neurons in fat have the potential to circumvent central leptin resistance.

Highlights

- The neuro-adipose junction in white adipose tissue is visualized *in vivo*
- Adipocyte-projecting neurons can completely envelop an adipocyte
- Leptin stimulates lipolysis via sympathetic neurons in fat
- Optogenetic activation of sympathetic fibers in fat drives lipolysis and fat mass reduction



Sympathetic Neuro-adipose Connections Mediate Leptin-Driven Lipolysis

Wenwen Zeng,^{2,3,7} Roksana M. Pirzgalska,^{1,7} Mafalda M.A. Pereira,¹ Nadiya Kubasova,¹ Andreia Barateiro,^{1,6} Elsa Seixas,¹ Yi-Hsueh Lu,² Albina Kozlova,² Henning Voss,⁵ Gabriel G. Martins,⁴ Jeffrey M. Friedman,^{2,3,8} and Ana I. Domingos^{1,8,*}

¹Obesity Laboratory, Instituto Gulbenkian de Ciéncia, Oeiras 2780-156, Portugal

²Laboratory of Molecular Genetics, The Rockefeller University, New York, NY 10021, USA

³Howard Hughes Medical Institute, The Rockefeller University, New York, NY 10021, USA

⁴Advanced Microscopy Unit, Instituto Gulbenkian de Ciéncia, Oeiras 2780-156, Portugal

⁵Department of Radiology, Weill Cornell Medical College, New York, NY 10021, USA

⁶Research Institute for Medicines (iMed.ULisboa), Faculty of Pharmacy, Universidade de Lisboa, Avenue Professor Gama Pinto, Lisbon 1649-003, Portugal

⁷Co-first author

⁸Co-senior author

*Correspondence: dominan@igc.gulbenkian.pt

<http://dx.doi.org/10.1016/j.cell.2015.08.055>

SUMMARY

Leptin is a hormone produced by the adipose tissue that acts in the brain, stimulating white fat breakdown. We find that the lipolytic effect of leptin is mediated through the action of sympathetic nerve fibers that innervate the adipose tissue. Using intravital two-photon microscopy, we observe that sympathetic nerve fibers establish neuro-adipose junctions, directly “enveloping” adipocytes. Local optogenetic stimulation of sympathetic inputs induces a local lipolytic response and depletion of white adipose mass. Conversely, genetic ablation of sympathetic inputs onto fat pads blocks leptin-stimulated phosphorylation of hormone-sensitive lipase and consequent lipolysis, as do knockouts of dopamine β -hydroxylase, an enzyme required for catecholamine synthesis. Thus, neuro-adipose junctions are necessary and sufficient for the induction of lipolysis in white adipose tissue and are an efferent effector of leptin action. Direct activation of sympathetic inputs to adipose tissues may represent an alternative approach to induce fat loss, circumventing central leptin resistance.

INTRODUCTION

White adipose tissues (WATs) serve as a storage depot for energy-rich triglycerides. In times of privation, this lipid storage can be released as part of an adaptive response to the energy shortage. Lipolysis, the process of hydrolyzing stored triglycerides in adipocytes, is regulated by several G-protein-coupled receptors, including adrenergic receptors, all of which activate protein kinase A (PKA) and elevate the intracellular levels of cyclic adenosine monophosphate (cAMP) (Brasaemle, 2007). PKA also phosphorylates several key target proteins, including

lipid-droplet-associated protein perilipin, hormone-sensitive lipase (HSL), and a set of esterases that collectively promote the hydrolysis of triglycerides into free fatty acids (FFAs) and glycerol, which are then released into plasma to meet the energy demands of other tissues (Brasaemle, 2007). HSL is a canonical target of PKA in adipocytes, and this enzyme catalyzes the conversion of diacylglycerol to monoacyl glycerol (Brasaemle, 2007).

Adipose tissue mass is homeostatically controlled by an endocrine loop in which leptin acts on neural circuits in the hypothalamus and elsewhere in brain to regulate food intake and peripheral metabolism (Friedman and Halaas, 1998). In wild-type (WT) and leptin-deficient *ob* animals, leptin treatment reduces food intake and leads to a rapid depletion of fat mass (Halaas et al., 1995, 1997; Montez et al., 2005). Of note, the depletion of fat mass after leptin treatment is distinct from that observed after food restriction in a number of respects: leptin treatment spares lean body mass and also potently stimulates glucose metabolism, while starvation results in a loss of lean body mass and causes insulin resistance (Newman and Brodows, 1983; Koffler and Kisch, 1996; Awad et al., 2009; Elia et al., 1999). In addition, leptin-deficient *ob/ob* mice pair-fed to leptin-treated *ob* mice lose only half the weight of those treated with leptin, further implicating a mechanism beyond a reduced food intake (Rafael and Herling, 2000). Because leptin has been shown to increase the sympathetic efferent signal to brown adipose tissues (BAT) (Scarpace and Matheny, 1998; Rezai-Zadeh and Münzberg, 2013), it has been suggested that leptin also activates sympathetic efferents to WAT to increase lipolysis in WAT. However, this has not been directly shown, and the nature of the effector mechanism underlying leptin-stimulated lipolysis in WAT has not been defined. In particular, it has not been established whether the increased lipolysis in WAT in response to leptin is due to a circulating hormone (or hormones) such as norepinephrine (NE) and/or another mediator that is released either centrally or peripherally (adrenal gland or macrophages), or specific efferent neural inputs to WAT, which mediates central leptin action. However, the effect of leptin on energy balance does not

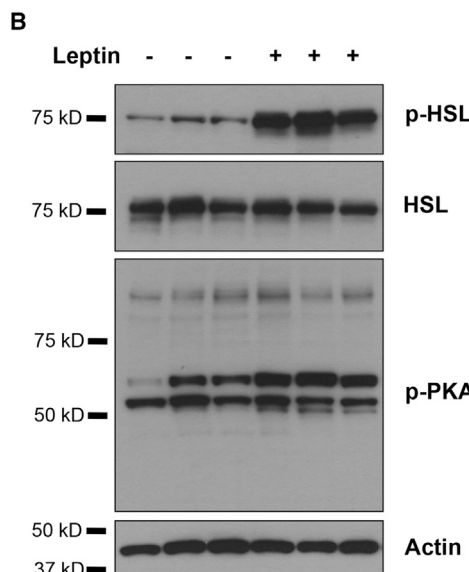
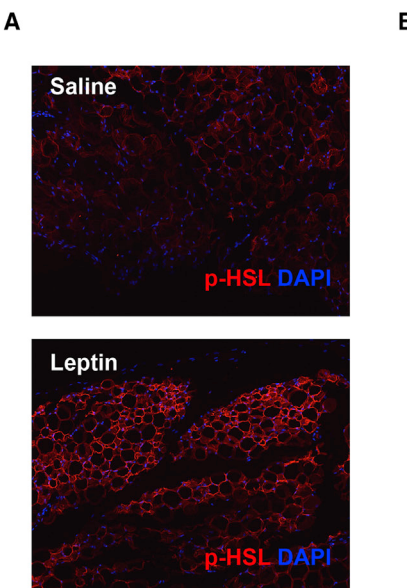


Figure 1. Leptin Stimulates HSL Phosphorylation in WAT

(A) Immunostaining of p-HSL (red) in paraffin sections of epididymal fat of C57BL/6J mice that were peripherally administrated with 500 ng/hr recombinant leptin for 2 days.

(B) p-HSL and phosphorylated PKA substrates in total protein extracts of epididymal fats were examined by immunoblot analysis.

require the presence of intact adrenals, suggesting that this organ is unlikely to be the source of the lipolytic signal (Arvaniti et al., 1998).

While numerous previous studies have shown dense neural innervation of BAT, both functionally and anatomically, the innervation of WAT has been difficult to visualize. Thus, it has been suggested that neural inputs to WAT are either very sparse or difficult to be distinguished from en passant axons with terminals on other cell types, such as those in vasculature (Bartness et al., 2005; Bartness and Song, 2007; Youngstrom and Bartness, 1995; Giordano et al., 1996). Indeed, some reports have suggested that the only innervation of WAT is perivascular and that white adipocytes themselves are not directly innervated (Giordano et al., 2005). This controversy has heightened the uncertainty as to the relative roles of sympathetic neural activity to regulate WAT metabolism. Alternatively, macrophages in adipose tissue account for about 10% of the stromal vascular fraction (SVF); hence, local catecholamines produced by these cells could also contribute to lipolysis in WAT in vivo (Weisberg et al., 2003; Nguyen et al., 2011). Thus, the dramatic decrease of adipose tissue mass observed after leptin treatment could, in principle, be mediated by catecholamines or other mediators that are either locally produced or produced by neurons.

In this study, we use anatomic, optogenetic, biochemical, and genetic approaches to show that the catecholamines released at heretofore-unidentified neuro-adipose junctions mediates the lipolytic effect of leptin, thus establishing the effector mechanism underlying the depletion of fat mass by leptin and, potentially, other stimuli. Our data demonstrate that the local sympathetic activity in WAT is necessary and sufficient for the lipolytic effect of leptin. In addition, genetic evidence shows that the β -adrenergic, but not α -adrenergic, receptors partially constitute a signaling pathway that accounts for the lipolytic effect of leptin. Moreover, the effect of pre-synaptic manipulations, such as neural gain of function or loss of function, is more profound than that of post-synaptic manipulations, thus suggesting direct activa-

tion of sympathetic inputs to adipose tissues as a strategy for the induction of fat loss.

RESULTS

Phosphorylation of HSL in WAT as a Lipolysis Marker for Leptin Action

To directly assess the cellular effect of leptin on lipolysis in white adipocytes and provide a marker for leptin action, we searched for biochemical responses in white adipocytes that were specifically activated by leptin treatment. We used a battery of phospho-specific antibodies and found that the phosphorylation of HSL was robustly increased in adipose tissue in response to leptin treatment. Note that our ability to define a biochemical effect of leptin is dependent on the quality of the antibodies, and we found that the anti-pHSL antibody was extremely robust. As shown, peripheral administration of leptin led to a significant increase of phosphorylated HSL (p-HSL) in WAT that could be visualized by immunohistochemistry (Figure 1A) and quantified by immunoblot analysis (Figure 1B). We set out to investigate whether the effect of leptin to increase HSL phosphorylation was mediated by neural efferent outputs onto WAT.

Axonal Bundles Project to WAT and Form Sympathetic Neuro-adipose Junctions

We first used tomography methods to determine whether fat pads were innervated. By coupling optical projection tomography (OPT) to a fat-clearing method that renders whole organs transparent, we were able to macroscopically visualize and document the nerve bundles that innervate the inguinal fat pad (Figure 2A; Experimental Procedures; Supplemental Experimental Procedures for details) (Gualda et al., 2013; Quintana and Sharpe, 2011). A full series of projections of the whole organ are acquired from multiple angles, typically 800–1,600 angles, and from this series of projections, a stack of axial slices can be visualized through back-projection reconstruction (Figure 2B).

From an OPT series of coronal optical sections of inguinal fat organ, we performed a 3D reconstruction, which enabled the visualization of thick axon bundles targeting the fat pad (Figures 2C and 2D). Axon bundles can be identified based on the gray threshold level and morphological features that distinguish them from the vasculature (Figure 2E). These structures within the fat were then segmented using semi-automated software (see Experimental Procedures).

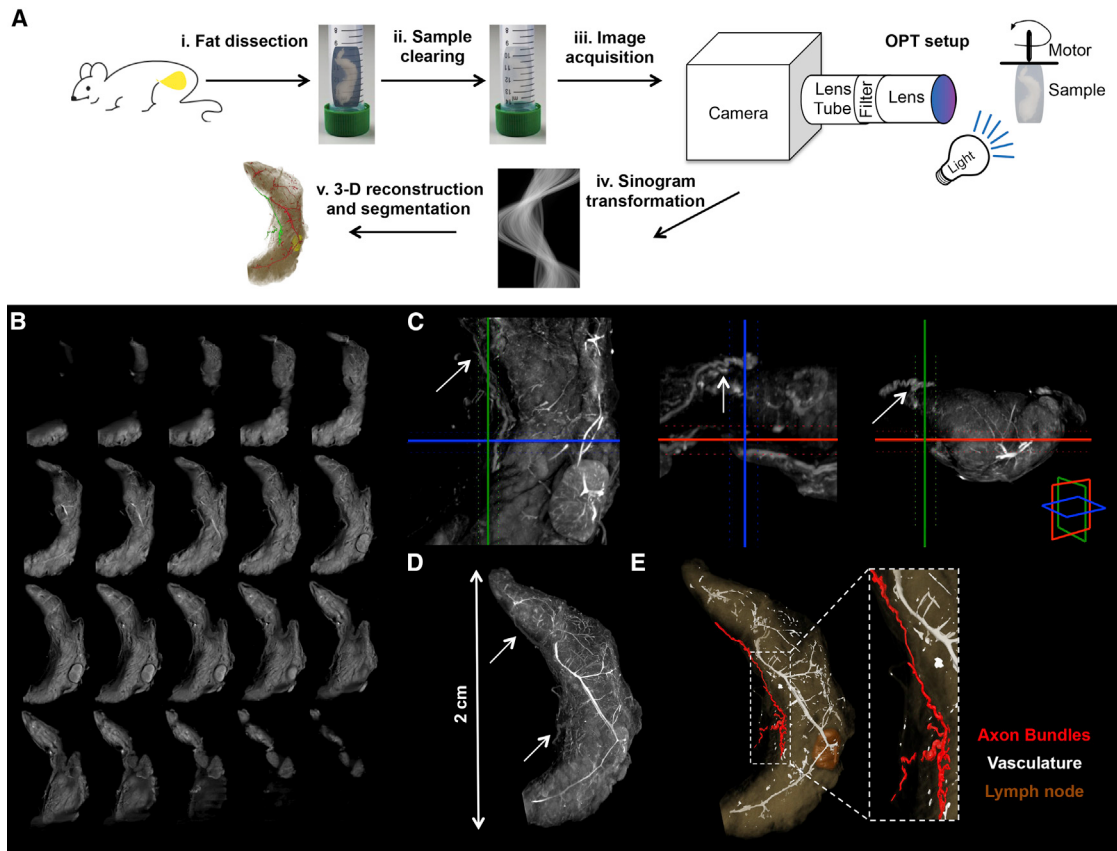


Figure 2. Neural Projections in Fat Detected with OPT

(A) Schematic representation of the OPT method applied to the subcutaneous inguinal fat. (i) Tissue dissection. (ii) Sample clearing. (iii) Image acquisition. (iv) Sinogram transformation. (v) 3D reconstruction and segmentation.

(B) OPT series of coronal sections of inguinal fat organ after 3D reconstruction.

(C) Orthogonal 400- μ m OPT slabs of inguinal fat in coronal, axial, and sagittal views. Axon bundles were identified based on the gray threshold level (arrows).

(D) 3D reconstruction in maximal intensity projection of the OPT coronal sections.

(E) Surface view of segmented structures within inguinal fat.

The neural bundles were micro-dissected from the subcutaneous fat pads and subjected to immunostaining for tyrosine hydroxylase (TH), a marker of sympathetic neurons, and β 3-tubulin (Tub-3), a general marker for the peripheral nervous system (PNS) (Figure 3A). We found that, overall, ~50% of the Tub-3-positive neurons also expressed TH, thus establishing the presence of both catecholaminergic and non-catecholaminergic axons innervating subcutaneous fat pads (Figure 3A). Then, we used multi-photon microscopy on the intact inguinal WAT of a living mouse to visualize sympathetic neuro-adipose connections (Figures 3B and 3C; Experimental Procedures). We labeled adipocytes with LipidTOX, a lipophilic dye, and sympathetic axons by crossing TH Cre-recombinase mice (*TH-Cre*) with a Tdtomato-reporter line (*Rosa26-LSL-Tdtomato*) (Figure 3C). We observed that Tdtomato-positive axons in fat pads made dense contacts with adipocytes through bouton-like structures that had the anatomic appearance of neuro-adipocyte junctions, resembling synapses (Figure 3C). We quantified these from eight independent two-photon micrographs and determined that $8\% \pm 4.6\%$ of adipocytes are in direct contact with sympathetic nerves.

Optogenetic Stimulation of Sympathetic Inputs to WAT Leads to Catecholamine Release, HSL Phosphorylation, and Fat Mass Depletion

We assessed the function of the catecholaminergic fibers by crossing the *TH-Cre* mice to a channelrhodopsin (ChR2) reporter line, *Rosa26-LSL-ChR2-YFP*. ChR2-YFP (yellow fluorescent protein) showed a complete co-localization with the endogenous TH, as determined by immunostaining of YFP and TH (Figure 4A). ChR2-YFP-expressing axons that projected onto subcutaneous WAT were then optogenetically activated using a subcutaneously implanted optical fiber targeting the right inguinal fat depot (see Experimental Procedures for surgical details).

While optogenetic tools have been widely used in the CNS, it has not been used as frequently to probe the function of peripheral cells, including sympathetic neurons. We began by validating the use of optogenetic stimulation of sympathetic neurons in primary cultures of superior cervical ganglia (SCG) of *TH-Cre X Rosa26-LSL-ChR2-YFP* mice; SCG can be dissected with less difficulty compared to other sympathetic ganglia (see Supplemental Experimental Procedures for culture details). We found

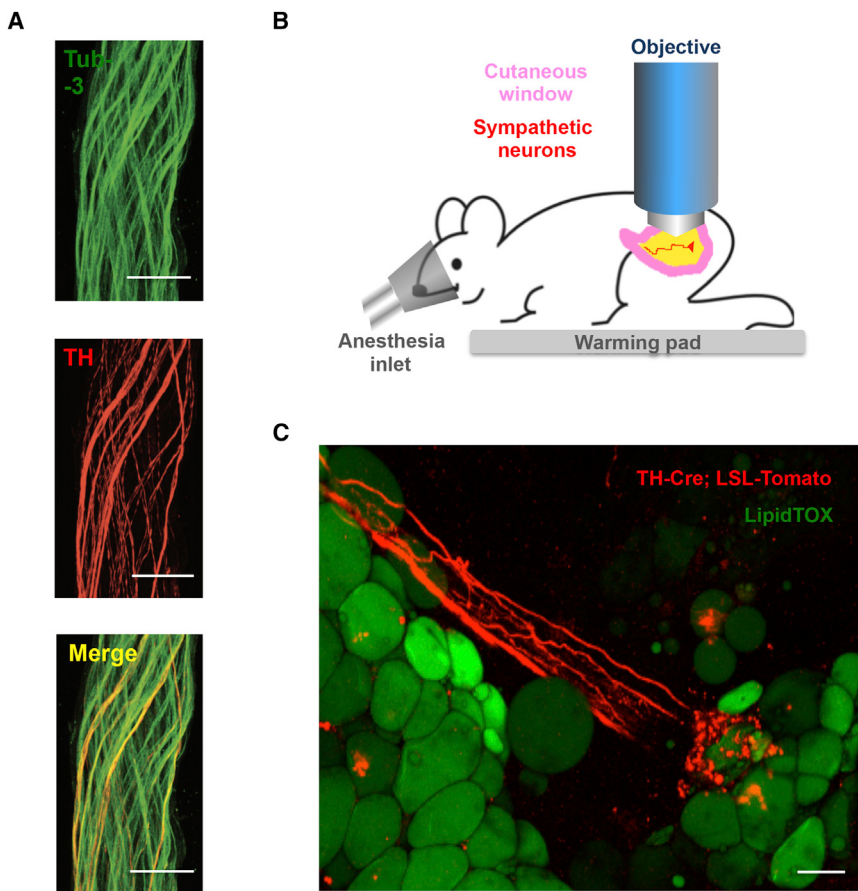


Figure 3. Catecholaminergic Neurons Innervating Adipocytes Integrate Nerve Bundles of Mixed Molecular Identity

(A) Partial co-localization of TH (red), an SNS marker, and Tub-3 (green), a general PNS marker, shown by immunohistochemistry of nerve bundles dissected from the inguinal fat pads of WT mice. Scale bars, 50 μ m.

(B) Schematic representation of the two-photon intra-vital imaging of neurons in the inguinal fat pad.

(C) Intra-vital two-photon microscopy visualization of a neuro-adipose connection in the inguinal fat pad of a live *TH-Cre; LSLS-Tomato* mouse; LipidTOX (green) labels adipocytes. Scale bar, 100 μ m.

that optogenetic stimulation of cultured sympathetic neurons increased expression of c-Fos, a marker for neuronal activity, in TH-positive cells and significantly stimulated NE release ex vivo, as assayed with ELISA (Figures 4B and 4C). NE release of ChR2-positive neurons was significantly higher relative to that of ChR2-negative cells (749.6 ± 170.1 pg/ml versus 4.8 ± 1.7 pg/ml, $p < 0.05$) (Figures 4B and 4C; see Experimental Procedures for culture and stimulation details).

Next, we stimulated ChR2-YFP-expressing axons in vivo unilaterally by placing optical fibers subcutaneously, aiming at inguinal fat pads located in the supra-pelvic flank of *TH-Cre X Rosa26-LSL-ChR2-YFP* mice (see Experimental Procedures for stimulation details). Activation of the ChR2-positive axons in subcutaneous WAT led to a significant increase of NE in the stimulated fat pad, relative to the contralateral un-stimulated control side (2.7 ± 0.5 versus 1.1 ± 0.2 , $p < 0.05$; Figure 4D). We also observed a significant increase of HSL phosphorylation of fat on the side ipsilateral to the optical fiber, compared to the contralateral un-stimulated side (Figure 4E). These data show that local activation of catecholaminergic inputs to fat could locally mimic the biochemical effect of leptin (Figures 4D and 4E). Then, we tested whether a more prolonged (4-week) optogenetic stimulation of ChR2-positive neurons in WAT could deplete fat mass (Figure 4F). The optical stimulation protocol was set to deliver light for every other second at 20 Hz, and

the volume of subcutaneous WAT was determined using MRI with 3D reconstruction (Figures 4F and 4G; see Experimental Procedures for details). After chronic activation, the size of the optogenetically stimulated ipsilateral fat pads of *TH-Cre; Rosa26-LSL-ChR2-YFP* mice was $23\% \pm 3.4\%$ that of the contralateral control side, representing a statistically and biologically significant decrease in fat mass (Figures 4F and 4G, $p < 0.0001$). This effect depended on ChR2 expression, as the fat pad volume of stimulated fat pads in ChR2-negative mice was unchanged ($86\% \pm 4.3\%$ of the size of the contralateral control fat pad), ruling

out a potential nonspecific effect of laser stimulation (Figure 4G; see Experimental Procedures for details). Together, the results provide anatomical and functional evidence that there are synapse-like sympathetic inputs onto white adipocytes and that their activation is sufficient to promote local NE release, HSL phosphorylation, and a reduction in the mass of an adipose tissue depot.

Local Sympathetic Inputs Are Required for Leptin-Stimulated HSL Lipolysis in WAT

Similarly to optogenetic stimulation of sympathetic innervation in white fat, leptin treatment led to an increase in NE levels in the subcutaneous adipose organ. NE levels in WATs dissected from leptin-treated animals were significantly higher than those in controls (78.7 ± 16.8 pg NE/ μ g of protein versus 30.7 ± 4.1 pg NE/ μ g of protein, $p < 0.05$; Figure 5A). Interestingly, leptin treatment did not affect serum NE levels (Figure 5B), indicating that leptin locally increases NE release in white fat, but not systemically.

Next, we evaluated whether sympathetic activation is necessary for leptin-stimulated lipolysis by disrupting the neural inputs in WAT, using a pharmacologic blockade or local genetic ablation. First, we observed that administration of hexamethonium, a non-depolarizing anti-cholinergic ganglion blocker, significantly decreased the leptin-stimulated phosphorylation of HSL

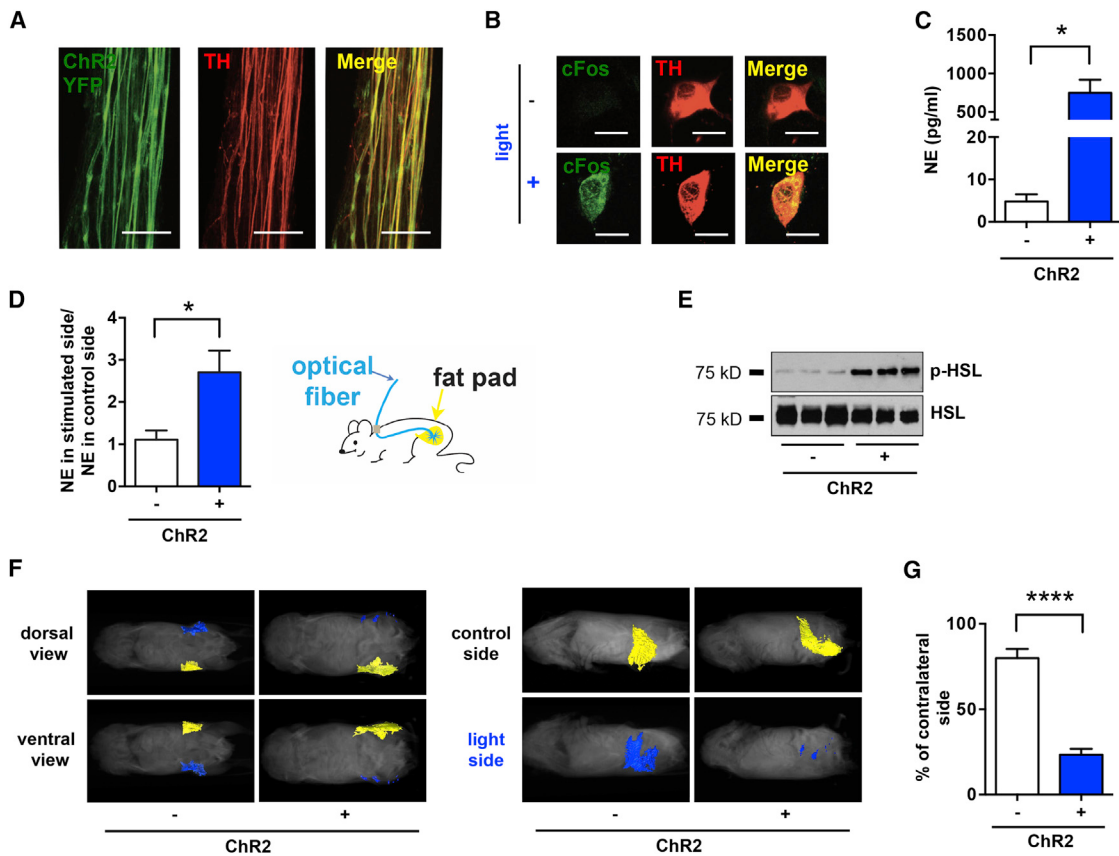


Figure 4. Optogenetic Stimulation of SNS Neurons in Fat Is Sufficient to Drive Lipolysis

(A) Complete co-localization of YFP (green) and TH (red) shown by immunohistochemistry of nerve bundles dissected from the inguinal fat pads of *TH-Cre; LSL-ChR2-YFP*. Scale bars, 50 μ m.

(B) c-Fos (green) induction in cultured SNS neurons after optogenetic activation. Scale bars, 10 μ m.

(C) Ex vivo NE release upon optogenetic stimulation of sympathetic SCG explants isolated from *TH-Cre; LSL-ChR2-YFP* mice and *LSL-ChR2-YFP* control mice (* $p < 0.05$; $n = 3\text{--}6$). Results are shown as mean \pm SEM.

(D) In vivo NE release in subcutaneous fat upon optogenetic stimulation of sympathetic neurons in WATs of *TH-Cre; LSL-ChR2-YFP* and *LSL-ChR2-YFP* control mice that were subcutaneously implanted with optical fibers targeting the inguinal fat pad (* $p < 0.05$; $n = 8$). Results are shown as mean \pm SEM.

(E) Immunoblot analysis of p-HSL in total protein extracts of subcutaneous fats of *TH-Cre; LSL-ChR2-YFP* and *LSL-ChR2-YFP* control mice that were subcutaneously implanted with optical fibers targeting the inguinal fat pad and optogenetically stimulated for 2 weeks (details are given in *Experimental Procedures*).

(F) MRI-guided visualization of fat in *TH-Cre; LSL-ChR2-YFP* and *LSL-ChR2-YFP* control mice that were optogenetically stimulated for 4 weeks (yellow indicates control inguinal fat pad, blue indicates light-stimulated fat pad; details are given in *Experimental Procedures*).

(G) Quantification of fat reduction in stimulated side versus the contralateral control side (** $p < 0.0001$; $n = 6$). Results are shown as mean \pm SEM. See also *Movies S1* and *S2*.

in adipose tissue (Figure 5C). However, as the action of hexamethonium is systemic and is not cell type specific, affecting all ganglionic transmission, we took a complementary approach by introducing a local neural crush injury to the fibers innervating epididymal fat pads. Because of the anatomy of the fat pad, nerve fibers in the distal portion of the tissues can be efficiently eliminated by a surgical crush of the perivascular axons running parallel to the main vessels (see *Experimental Procedures*). We carried out physical denervation with a forceps crushing the fibers 2 mm from the distal tip for 30 s. Leptin was delivered 3 days post-surgery through osmotic pump for 2 days. Consistent with the effect of hexamethonium, after a crush injury to the local nerve, leptin treatment failed to increase HSL phosphorylation on the denervated side compared to the intact contralateral control

(Figure 5D). This showed that local neural activation to WAT is required for the biochemical changes associated with leptin treatment.

To confirm that leptin-mediated lipolysis is the result of activation of sympathetic neural outputs to fat, we ablated these neurons by crossing the *TH-Cre* line with the diphtheria toxin receptor (DTR) mice, *Rosa26-LSL-DTR*, and injected diphtheria toxin (DT) locally in subcutaneous inguinal WAT (Buch et al., 2005). Local treatment with DT eliminated only those sympathetic axons in the regions of the injection site, without effects on other local neuronal populations as shown by the sparing TH-negative Tub-3-positive axons at the site of injection (Figure 5E, $p < 0.001$; see *Supplemental Experimental Procedures* for details). These injections were administered peripherally at

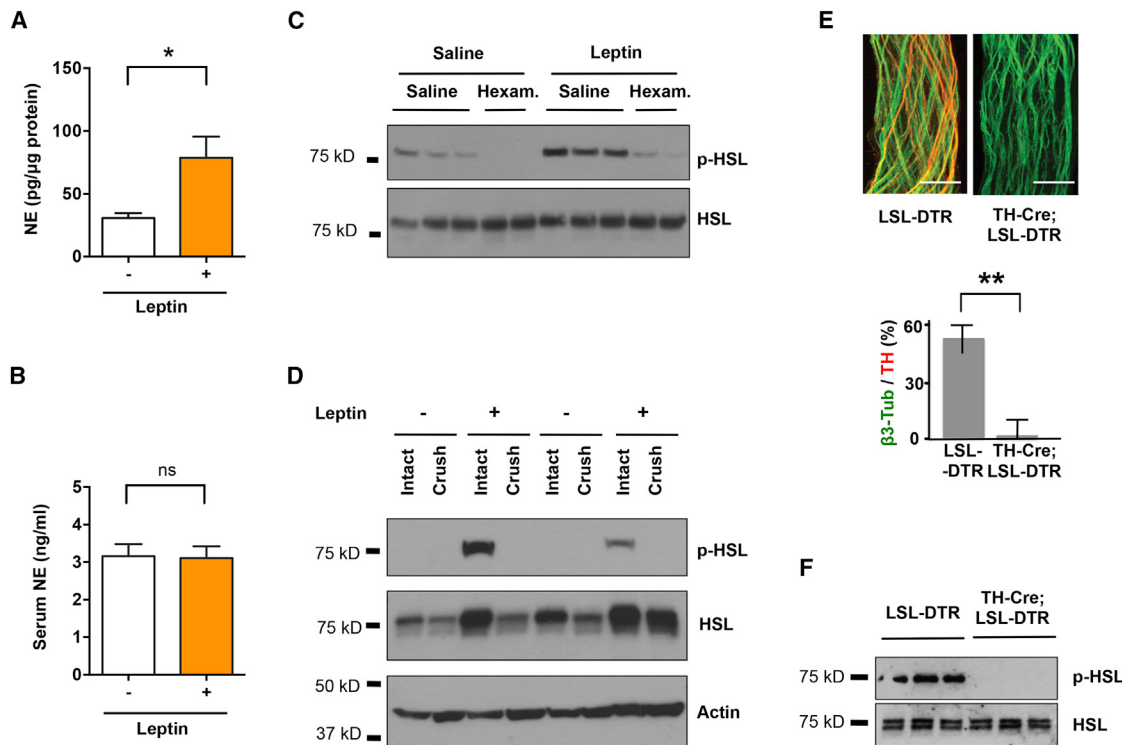


Figure 5. Sympathetic Neurons Are Locally Required for Leptin-Induced Lipolysis

(A and B) C57BL6/J mice were peripherally administrated with 500 ng/hr recombinant leptin or saline for 2 days. (A) NE content in subcutaneous fat pads (*p < 0.05; n = 5) and (B) NE serum levels were measured by NE ELISA (n = 4). Results are shown as mean ± SEM. ns, not significant.

(C and D) C57BL6/J mice were peripherally administrated with 500 ng/hr recombinant leptin (C) in combination with 500 μg/hr ganglionic blocker hexamethonium (Hexam.) or (D) at 3 days after local crush injury of nerves in fat pads. p-HSL in total protein extracts of epididymal fats were examined by immunoblot analysis.

(E) Fat pads in TH-Cre; LSL-DTR mice were locally treated with DT. Tissue-specific ablation of SNS axons confirmed by immunostaining for Tub-3 and TH (**p < 0.001; n = 6). Results are shown as mean ± SEM.

(F) Immunoblot analysis of p-HSL in total protein extracts of subcutaneous fats of TH-Cre; LSL-DTR and control mice injected with DT following leptin treatment (500 ng/hr).

See also Figure S1.

low doses (10 ng/g) to ensure that the effect was local and to also spare TH-positive neurons in CNS (Figure S1; Domingos et al., 2013). Genetic ablation of sympathetic input to adipose tissue completely blocked the effect of leptin on HSL phosphorylation on the ipsilateral compared to the contralateral untreated side (Figure 5F). Together, these results demonstrate that activation of sympathetic neurons in fat is necessary for leptin to stimulate HSL phosphorylation in adipose tissue.

β-Adrenergic Signaling Influences Leptin-Stimulated Lipolysis in WAT

Consistent with a sympathetic mechanism for the leptin-mediated stimulation of lipolysis, systemic administration of the β-adrenergic agonist isoproterenol resulted in the rapid induction of p-HSL. As previously reported, isoproterenol also increased FFA release from WAT in vitro and in vivo (Figure S2).

Therefore, we set out to test whether β-adrenergic signaling was required for leptin-stimulated lipolysis.

We first examined the lipolytic response to leptin in mice with a knockout (KO) of dopamine β-hydroxylase (*DBH*), a key enzyme in the synthesis of NE and epinephrine from dopamine (Figure 6).

After peripheral administration of leptin, there was a dramatic increase of HSL phosphorylation in WAT in the WT or *DBH*^{+/+} animals but a markedly diminished response in the *DBH*^{-/-} littermates (Figure 6A). Consistent with this, the total fat composition dramatically decreased in the WT mice treated with leptin, while there was only a slight change of fat mass in mice with the *DBH* deletion (p < 0.05; Figure 6B). Also consistent with a diminished lipolytic effect of leptin, there was also a lower amount of weight loss in the *DBH*^{-/-} mice (Figure 6C). After 2 days of leptin treatment, the body weight of WT mice decreased more than 6%, while the weight loss of *DBH*^{-/-} was less than 2% (p < 0.05). The data suggest that catecholamines contribute to more than 50% of leptin's effect on body weight. Altogether, the results confirm that catecholamines are required for the leptin-stimulated lipolysis and HSL phosphorylation in WAT.

To test whether the action of leptin to drive lipolysis is mediated through β-adrenergic signaling, we crossed the β1/β2 double-KO to β3 KO to generate animals with a deletion of all three β-adrenergic receptors (Figure 7). Animals with a deletion of all three isoforms of the β-adrenergic receptors showed

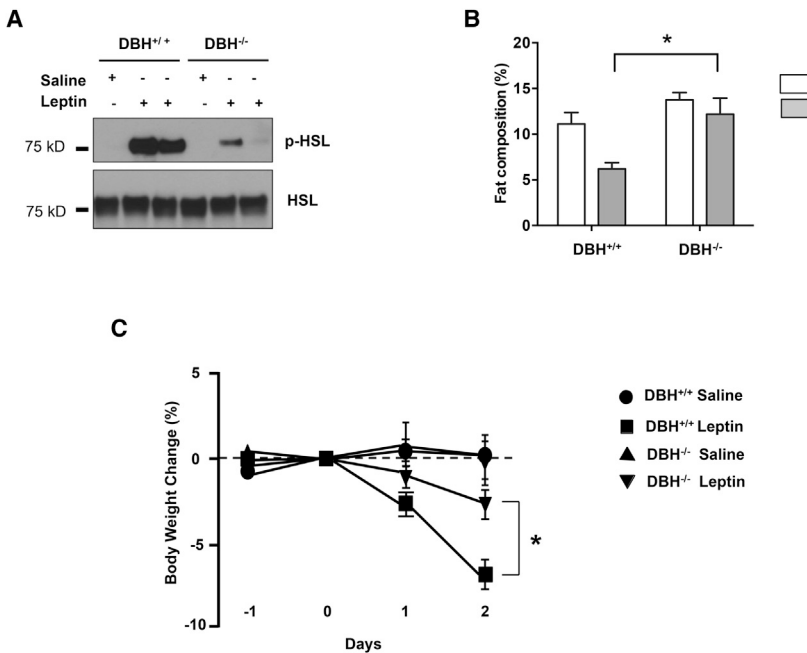


Figure 6. Norepinephrine Deficiency Impairs Leptin-Induced Lipolysis

(A) Immunoblot analysis of p-HSL in total protein extracts of fat pads of dopamine β -monoxygenase mutant and control littermates ($DBH^{-/-}$ and $DBH^{+/+}$, respectively) mice that were treated with 500 ng/hr recombinant leptin.

(B) Whole-body fat composition (*p < 0.05). Results are shown as mean \pm SEM (n = 4–5).

(C) Body weight change after leptin treatment (*p < 0.05). Results are shown as mean \pm SEM (n = 5).

significantly decreased HSL phosphorylation after leptin treatment in comparison to the double-KO controls (Figure 7A). However, this decrease was not as marked as that seen in individual depots after local ablation of sympathetic fibers using DT (Figure 5F). While leptin treatment significantly decreased total fat mass in $\beta 1^{-/-}\beta 2^{-/-}$ mice, this effect was significantly reduced in $\beta 1^{-/-}\beta 2^{-/-}\beta 3^{-/-}$ triple-KO mice (Figure 7B; paired ANOVA post hoc test, p < 0.01, comparing $\beta 1^{-/-}\beta 2^{-/-}\beta 3^{-/-}$ with $\beta 1^{-/-}\beta 2^{-/-}\beta 3^{+/+}$ mice after leptin treatment). In contrast, α -adrenergic receptors appeared to play only a minor role in the leptin-stimulated loss of fat mass, because the α -adrenergic blockers phentolamine (5 mg/kg, intraperitoneally [i.p.]) and phenoxylbenzamine (10 mg/kg i.p.) failed to diminish the catabolic responses to leptin treatment in $\beta 1^{-/-}\beta 2^{-/-}\beta 3^{+/+}$ control mice or $\beta 1^{-/-}\beta 2^{-/-}\beta 3^{-/-}$ mice (Figure 7C). There was also a small suppression of body weight loss in response to leptin in the $\beta 1^{-/-}\beta 2^{-/-}\beta 3^{-/-}$ mice (Figure 7D). These results showed that the β -adrenergic receptors are only partially necessary for leptin-mediated lipolysis of WAT but that the magnitude of the effect of a loss of β -adrenergic signaling is not as great as that observed by interfering with local neural outputs, thus suggesting that there could also be other neural mediators or interacting receptors on adipocytes (Figure 5).

DISCUSSION

Leptin is known to stimulate lipolysis and reduce fat mass, though the physiologic mechanisms responsible for this have not been fully delineated. In this study, we present data using functional, anatomic, biochemical, and genetic approaches to show that leptin increases lipolysis via the actions of sympathetic neuronal efferents to adipose tissue. These data also provide molecular, cellular, and anatomic evidence confirming the exis-

tence of neuronal projections onto adipocytes, which have been the subject of conjecture but which have not been directly visualized.

The existence of neuro-adipose junctions in WAT had been inferred based on the fact that a pseudorabies retrograde-tracing virus can visualize a set of neural projections in the brain (Bartness and Song, 2007). In addition, immunohistochemistry, and immunofluorescence have been used to visualize contacts between sympathetic neurons and adipocytes in sliced tissue (Giordano et al., 1996, 2005; Thompson, 1986). However, these methods, which require tissue slicing and fixation, do not distinguish en passant neurons from those that directly project onto adipocytes. The visualization of adipocyte-projecting neurons that can completely envelop an adipocyte has not been accomplished so far. We were able to directly visualize neural termini onto adipocytes using intra-vital multiphoton microscopy, which allows deep penetration onto the live intact tissue, allowing us to visualize deeper structures without the perturbations associated with classical histological methods, which, in past studies, may have compromised the integrity of the neuro-adipose termini (Helmchen and Denk, 2005).

Confocal or multiphoton microscopy methods are suitable for histological analysis at a microscopic spatial scale, but do not give a 3D perspective of the organization of the organ as a whole. At a macroscopic spatial scale, methods such as MRI or computed tomography (CT) allow for measurement of whole-body fat distribution. However, all of these methods lack the spatial resolution that is required for visualizing structures such as nerve bundles. OPT is a technique with physical principles similar to those of X-ray CT/gamma radiation, which uses visible light instead of radiation (Gualda et al., 2013). Scattering of light passing through tissues is minimized by clearing lipids from the whole organ (Quintana and Sharpe, 2011). Unlike most currently available methods, OPT coupled to tissue clearing allows imaging of whole-mount samples with a spatial scale in the order of centimeters.

It has been previously shown that electrical stimulation of WAT nerve bundles can drive lipolysis (Correll, 1963). However, as shown here, nerve bundles in WAT have mixed molecular identity, making it difficult to ascertain the identity of the neurons responsible for this effect. To address this limitation, we used

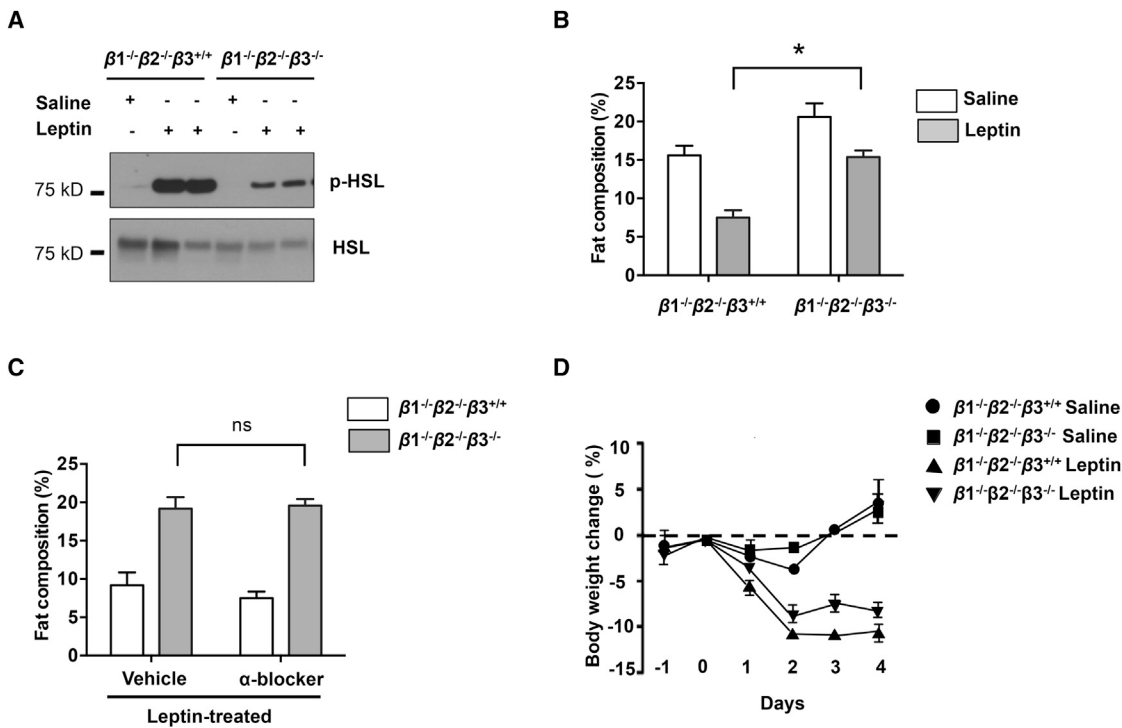


Figure 7. Deficiency of All β -Adrenergic Receptors Influences Leptin-Induced Lipolysis

(A) Immunoblot analysis of p-HSL in total protein extracts of fat pads of $\beta 1^{-/-}\beta 2^{-/-}\beta 3^{+/+}$ and $\beta 1^{-/-}\beta 2^{-/-}\beta 3^{-/-}$ mice that were treated with 500 ng/hr recombinant leptin.

(B) Whole-body fat composition (* $p < 0.05$, $n = 4-5$). Results are shown as mean \pm SEM.

(C) α -Adrenergic receptors had a minor function in leptin-induced lipolysis (* $p > 0.05$, $n = 4-5$). Results are shown as mean \pm SEM. ns, not significant.

(D) Whole-body fat composition of mice peripherally treated with recombinant leptin and α -blockers (phentolamine, 5 mg/kg, i.p.; and phenoxybenzamine, 10 mg/kg, i.p.) was measured ($n = 4-5$). Results are shown as mean \pm SEM.

See also Figure S2.

optogenetics, which allows for cell-specific stimulation of neurons (Domingos et al., 2011, 2013). In the present study, we used optogenetics to specifically activate sympathetic neurons in TH-Cre mice. Another advantage of this approach is that it enables the specific activation of axonal projections and does not require stimulation of neuronal cell bodies (Petreanu et al., 2007; Vrontou et al., 2013). This feature is particularly convenient for autonomic neurons, given the deep localization of their cell bodies along the anterior face of the spinal cord and the intrinsic difficulty of implanting optical fibers in this location. Previous studies using neural tracing have revealed that sympathetic neurons innervating the subcutaneous inguinal fat pads localize to the 13th thoracic ganglia, which localizes at the dorsal edge of the diaphragm muscle, in the transition between the thorax and the abdomen (Youngstrom and Bartness, 1995). This anatomical location is particularly inaccessible and unsuitable for chronic implants of optical fibers or equivalent devices. However, as we show here, subcutaneous implant of optical fibers for stimulation of nerve terminals is feasible and effective. We used this approach to show that optogenetic gain of function of the catecholaminergic signaling to the neuro-adipose junction can lead to the phosphorylation of HSL and lipolysis of WAT. Similarly, previous loss-of-function experiments that assessed the effect of

sympathetic input on lipolysis also did not allow analysis of the effect of specific cells in the way that optogenetics can. Thus, the use of mechanical denervation does not distinguish between neurons that directly innervate adipocytes versus those that are passing through. We have not yet profiled the non-TH nerve fibers, but it is reasonable to expect that some might be parasympathetic, nociceptive, sensory fibers and/or en passant axons. The function of these fibers could be assessed similarly to those that we report, using optogenetics, to activate other populations, including cholinergic neurons, by studying choline acetyltransferase (ChAT)-Cre mice and/or neurons expressing other molecular markers. Chemical ablation with capsaicin also has limitations, as this treatment is not specific to sympathetic neurons and affects all transient-receptor-potential-vanilloid (TRPV)-expressing fibers (Holzer, 1991). Chemical ablation with 6-hydroxydopamine is likely to affect dopaminergic as well as enteric neurons, creating secondary systemic effects (Ding et al., 2004).

To avoid these limitations and gain local control over sympathetic neural activity, we used additional molecular genetic tools that combine tissue specificity with a localized effect. We show that ablation of the sympathetic neurons by DTR expression in TH-positive neurons followed by local DT injection in WAT abolishes the effect of leptin on HSL phosphorylation. We also noted

that the loss of function due to post-synaptic manipulations (i.e., the triple β -adrenergic receptor KO in Figure 7) has a lesser effect on the size of adipose tissue depots than that seen after pre-synaptic manipulations such as a loss of *DBH* or pharmacologic or mechanical ablation of neural input to fat (Figure 6). This suggests that leptin-induced production of NE from sympathetic neurons could act through additional receptors that are not one of the three β -adrenergic receptors that we tested, which have been suggested by others (Tavernier et al., 2005). Alternatively, sympathetic neurons may co-release other neurotransmitters or neuropeptides that signal through non-adrenergic receptors. This could account for the residual leptin-induced weight loss seen in *DBH*^{-/-}, although this effect is not significant when compared to controls. Thus, an in-depth knowledge of the underlying sympathetic neural circuits could provide strategies to pharmacologically activate specific sympathetic neuronal population, thus circumventing leptin resistance, as potential treatment of obesity.

A canonical effect of leptin is to increase sympathetic signaling to BAT, thus promoting thermogenesis (Bachman et al., 2002; Landsberg et al., 1984). However the role of autonomic stimulation of white fat has been less well studied. We now show that the sympathetic activity is also responsible for the leptin-stimulated lipolysis in WAT. While leptin has been assumed to increase lipolysis via activation of sympathetic efferent fibers, this has not been directly shown. Adrenergic agonists have been shown to induce the formation of beige (brite) fat, and these data suggest that sympathetic innervation may also stimulate this phenotypic change in adipose tissue (Bachman et al., 2002; Giralt and Villarroya, 2013; Dempersmier et al., 2015). Consistent with this, leptin has also been suggested to increase the formation of beige fat (Dodd et al., 2015).

Because brown adipocytes have relatively smaller fat storages compared to white adipocytes, while having higher metabolic demand, the continuous thermogenic response of BAT might require the supply of FFA from WAT mobilized in other parts of the body. Therefore, it is reasonable to speculate that the coordinated sympathetic actions in BAT and WAT in response to leptin could help maximize the hormone's effect on energy expenditure and fat metabolism. Future studies delineating the neural circuits connecting the central action of leptin with the peripheral activation of sympathetic system will be necessary to test this hypothesis. Particularly, it would be of great importance to develop technologies that would allow whole-body visualization and mapping of peripheral neuronal circuits using some of the approaches presented here.

In summary, we provide direct evidence that the sympathetic neuro-adipose junction is both necessary and sufficient for leptin to drive lipolysis in WAT.

EXPERIMENTAL PROCEDURES

Antibodies and Drugs

The antibodies were obtained from the following vendors: HSL (Cell Signaling Technology), phospho-HSL (Cell Signaling Technology), phospho-PKA substrate (Cell Signaling Technology), TH (Pel-Freez Biologicals), and actin (Sigma). Hexamethonium chloride, phentolamine, and phenoxybenzamine were from Sigma-Aldrich. DT was purchased from Merck Millipore. Recombinant mouse leptin was obtained from Amylin Pharmaceuticals.

Mice

DBH KO mice were kindly provided by Steve Thomas at the University of Pennsylvania. *Adr β 1*^{-/-}*2*^{-/-} and *Adr β 3*^{-/-} were kindly provided by Bruce Spiegelman at Harvard Medical School. *TH-Cre*, Rosa26-LSL-ChR2-YFP (Stock No. 012-569; Daou et al., 2013), Rosa26-LSL-DTR, and C57BL/B6J mice at 6–10 weeks old were purchased from The Jackson Laboratory. Animal procedures were approved by the ethics committee of Instituto Gulbenkian de Ciéncia and the Institutional Animal Care and Use Committee of Rockefeller University.

OPT

Six-week-old C57BL/6 mice were sacrificed with carbon dioxide. The inguinal fat pads were dissected from the mice with Dumont #5 Forceps, fixed in 4% paraformaldehyde (PFA; Sigma-Aldrich) for 3 hr at room temperature (RT) and subjected to the OPT clearing protocol as described in the *Supplemental Experimental Procedures*. Images of the whole fat tissue were acquired using a 1× lens mounted on an Infinitube tube lens and projected into a Hamamatsu FlashLT sCMOS camera. A total of 1,600 images were acquired for a full rotation (0.25° steps). The series of projections were then pre-processed for back-projection using FIJI in order to remove hot pixels and re-align the axis of rotation in relation to the camera chip, and finally the back-projection reconstruction was conducted using the Skyscan's NRecon software (Schindelin et al., 2012). The stack of slices was further processed with FIJI to increase contrast and saved to posterior analysis with the software Amira V5.3. Using this software, 3D reconstructions and image segmentation were performed to identify and reconstruct individual parts of the fat organs. Detailed instructions for setting up an OPT system can be found at <https://sites.google.com/site/openSpinMicroscopy/home/opt>.

In Vivo Two-Photon Microscopy

Two-month-old mice were kept anesthetized with 2% isoflurane. During surgery, body temperature was maintained at 37°C with a warming pad. After application of local anesthetics (lidocaine), a sagittal incision of the skin was made above the supra-pelvic flank to expose the subcutaneous inguinal fat pad. An imaging chamber was custom built to minimize fat movement. Warm imaging solution (in millimolar: 130 NaCl, 3 KCl, 2.5 CaCl₂, 0.6 MgCl₂ • 6H₂O, 10 HEPES without Na, 1.2 NaHCO₃, 10 glucose (pH 7.45), with NaOH) (37°C) mixed with a fat dye (LipidTOX) was applied to label adipocytes, maintain tissue integrity, and allow the use of immersion objective. Imaging experiments were performed under a two-photon laser-scanning microscope (Ultima, Prairie Instruments). Live images were acquired at 8–12 frames per second, at depths below the surface ranging from 100 to 250 mm, using an Olympus 20× 0.8 N.A. water immersion objective, with a laser tuned to 860–940 nm wavelength, and emission filters 525/50 nm and 595/50 nm for green and red fluorescence, respectively. Laser power was adjusted to be 20–25 mW at the focal plane (maximally, 35 mW), depending on the imaging depth and level of expression of *tdTomato* and LipidTOX spread. *tdTomato* fluorescence was used to identify TH-positive fibers until photobleaching occurred.

Leptin Treatment and Lipolysis Analysis

To examine the effect of leptin treatment on lipolysis, leptin (delivery rate of 500 ng/hr) or saline was delivered through osmotic pumps (Alzet) subcutaneously for 2 days. Body weight was recorded daily. Body fat composition was measured using the EchoMRI body analyzer at end point before subcutaneous or epididymal adipose tissues were collected. HSL phosphorylation was detected by immunohistochemistry of paraffin sections at 6-μm thickness and/or western blot of subcutaneous or epididymal adipose tissues. NE levels in serum and subcutaneous fat pads were determined with an NE ELISA kit (Labor Diagnostika Nord GmbH). Tissues were homogenized and sonicated in homogenization buffer (1 N HCl, 1 mM EDTA), and cellular debris was pelleted by centrifugation at 13,000 rpm for 15 min at 4°C. All tissue samples were normalized to total tissue protein concentration.

Mechanical Denervation

The nerve bundle 2 mm distal from the tip of the epididymal fat was physically crushed for 30 s and then released using a forcep. Leptin was administrated through osmotic pump 3 days after nerve crush. HSL phosphorylation was detected 2 days upon leptin treatment.

Hexamethonium Chloride, Isoproterenol, and α -Blocker Treatment

Hexamethonium chloride (500 μ g/hr) was administrated during leptin treatment through a separate osmotic pump, and the α -blockers phentolamine (5 mg/kg, intraperitoneally [i.p.]) and phenoxybenzamine (10 mg/kg; i.p.) were administrated twice a day during the course of leptin treatment (500 ng/hr). Isoproterenol (250 μ g per mouse) was delivered in saline through jugular vein injection. Blood was drawn through tail bleeding, and plasma FFA was measured using a NETO kit (Wako Pure Chemicals Industries). For FFA release upon isoproterenol treatment in vitro, adipose tissue explants were dissected and cultured in Hank's medium and stimulated with isoproterenol at 10 μ g/ml for 3 hr. FFA was measured in the medium.

NE Measurements after Optogenetic Stimulation Ex Vivo

SCG were removed from 28- to 30-day-old *TH-Cre X Rosa26-LSL-ChR2-YFP* mice under a stereomicroscope and placed in DMEM (Invitrogen). Ganglia were cleaned from the surrounding tissue capsule and transferred into eight-well tissue culture chambers (Sarstedt) that were previously coated with poly-D-lysine (Sigma-Aldrich) in accordance to the manufacturer's instructions. Ganglia were then covered with 5 μ l Matrigel (BD Biosciences) and incubated for 7 min at 37°C. DMEM without phenol red (Invitrogen) supplemented with 10% fetal bovine serum (Invitrogen), 2 mM L-glutamine (Biowest), and nerve growth factor (Sigma-Aldrich) was subsequently added. SCG ganglia were cultured for a minimum of 24 hr prior to further manipulation. Depolarization of sympathetic neurons in explant cultures was performed on a Yokogawa CSU-X1 Spinning Disk confocal system using the 488-nm laser line and pointing at the region of interest (ROI) for 200 μ s. Stimulation was repeated five times using 40% of laser intensity. NE in the SCG explant culture medium was determined with an NE ELISA kit (Labor Diagnostika Nord GmbH). The same procedure was performed for *LSL-ChR2-YFP* control mice.

Surgeries and Optogenetic Stimulation

General anesthesia was induced and maintained with isoflurane. After application of local anesthetics (lidocaine), a sagittal incision of the skin was made above the neck and supra-pelvic flank. A hemostat was inserted into the incision and, by opening and closing the jaws of the hemostat, spread the subcutaneous tissue to create a longitudinal pocket for the optical fiber. The pocket was made long enough to allow about 4–6 cm of fiber (Thorlabs FT200). The tip of the fiber targeted the anatomical location of the inguinal fat pad. The other end of the fiber, the ferrule-connector end, was secured along the skin via sutures and dermal staples. Appropriate local analgesic was used post-surgically. Optogenetical stimulations were performed 48 hr after surgical procedures.

The stimulation session in Figure 4D lasted 4–6 hr and was performed via a 1-s 20-Hz pulse of blue laser every other second, originating from a 473-nm solid laser source (OEM-BL-473-00100-CWM-SD-05). The laser source had an output power of 100 mW. Ferrule-coupled optical fibers of 200- μ m diameter (Thorlabs; FT200EMT-CANNULA-TS1031629) were connected to ferrule patch cords (Thorlabs; FT200EMT-FC/PC-ferrule) with mating sleeves (Thorlabs; ADAF1), and the later to the laser source via FC/PC adaptor.

NE in subcutaneous fat pads was determined with an NE ELISA kit (Labor Diagnostika Nord GmbH) as described earlier.

Stimulation protocol in Figure 4E took place every day for 2 weeks and solely during the rodent rest period. Longer sessions, as in Figure 4F, had a duration of 4 weeks. Stimulation sessions lasted 4–6 hr and were performed as described earlier.

MRI Fat Measurements and Fat Pad Segmentation

Mice were subjected to optogenetic stimulation as stated earlier, perfused with 4% PFA/PBS, post-fixed over 2–3 days, and embedded in Fomblin Oil (Sigma-Aldrich) for scanning. Imaging was performed on a 7.0 T 70/30 Bruker Biospec small-animal MRI system with a 12-cm diameter 450 mT/m amplitude and 4,500 T/m/s slew rate actively shielded gradient subsystems with integrated shim capability. A linear coil with 7-cm diameter and a length sufficient to cover the whole body of the animal was used for excitation and reception of the magnetic resonance signal. Two image sets were acquired, one with fat suppression and one without. Axial images, covering the whole animal in 75 0.4-mm-thick slices without gap, were acquired in an interleaved

way by using a RARE (rapid acquisition with relaxation enhancement) pulse sequence with RARE factor 2. Four averages with a flip angle of 90°—echo time (TE) = 10 ms, repetition time (TR) = 2,468 ms, field of view = 10 \times 3 cm, and matrix size = 256 \times 128 (acquisition matrix size = 256 \times 96), resulting in a spatial resolution of 0.391 \times 0.234 \times 0.4 mm—were acquired. The fat suppression, added to the second scan, consists of a 90° Gaussian pulse with 2.6067-ms duration and 1051.1-Hz bandwidth. Data were converted into .tif files by FIJI software. The subcutaneous inguinal fat distribution was determined with semi-automated Amira V5.3 software segmentation of scanned images. Amira V5.3 software segmentation relies on the automated grouping of pixels with the same index of intensity in the grayscale. An automatic segmentation based on the gray threshold levels, which decomposes the image domain into subsets, allowed us to define the right and the left inguinal fat depots, which were further saved as unique fields. Volumes of the right and the left subcutaneous fat pads were defined as the number of voxels multiplied by the size of a single voxel. The size of stimulated fat pads was determined, and the effect of optogenetic stimulation of neurons on fat mass was calculated in the same animal relative to non-stimulated contralateral side.

Statistical Methods

Statistics were performed in GraphPad Prism and involved the computation of means and SEM, which accompany each figure legend. Student's t tests and ANOVAs were used where appropriate, and p values are indicated in text.

SUPPLEMENTAL INFORMATION

Supplemental Information includes Supplemental Experimental Procedures, two figures, and two movies and can be found with this article online at <http://dx.doi.org/10.1016/j.cell.2015.08.055>.

AUTHOR CONTRIBUTIONS

Two-photon microscopy and optogenetics were performed by A.I.D. and R.M.P., and related rodent husbandry was performed by N.K. and E.S. OPT was performed by R.M.P., M.M.A.P., and G.G.M.; MRI scans were conducted by H.V.; Amira segmentation of MRI data was performed by R.M.P. and M.M.A.P.; cell cultures and neuronal explants were developed by A.B. and R.M.P. Biochemical analyses and measurement of whole body fat composition and body weights were performed by W.Z., N.K., E.S., Y.H.L., and A.K.; A.I.D. and J.M.F. wrote the manuscript.

ACKNOWLEDGMENTS

This work was supported by the Fundação para a Ciência e Tecnologia (FCT), the European Molecular Biology Organization (EMBO), and the JPB Foundation. The FCT supported A.I.D., R.M.P., M.M.A.P., N.K., G.G.M., A.B., and E.S. The JPB Foundation supported the work of W.Z., Y.H.L., and A.K. J.M.F. is a Howard Hughes Medical Institute (HHMI) investigator.

Received: May 6, 2015

Revised: July 17, 2015

Accepted: August 6, 2015

Published: September 24, 2015

REFERENCES

- Arvaniti, K., Deshaies, Y., and Richard, D. (1998). Effect of leptin on energy balance does not require the presence of intact adrenals. *Am. J. Physiol.* 275, R105–R111.
- Awad, S., Constantin-Teodosiu, D., Macdonald, I.A., and Lobo, D.N. (2009). Short-term starvation and mitochondrial dysfunction – a possible mechanism leading to postoperative insulin resistance. *Clin. Nutr.* 28, 497–509.
- Bachman, E.S., Dhillon, H., Zhang, C.Y., Cinti, S., Bianco, A.C., Kobilka, B.K., and Lowell, B.B. (2002). betaAR signaling required for diet-induced thermogenesis and obesity resistance. *Science* 297, 843–845.

Bartness, T.J., and Song, C.K. (2007). Thematic review series: adipocyte biology. Sympathetic and sensory innervation of white adipose tissue. *J. Lipid Res.* 48, 1655–1672.

Bartness, T.J., Kay Song, C., Shi, H., Bowers, R.R., and Foster, M.T. (2005). Brain-adipose tissue cross talk. *Proc. Nutr. Soc.* 64, 53–64.

Brasaemle, D.L. (2007). Thematic review series: adipocyte biology. The perilipin family of structural lipid droplet proteins: stabilization of lipid droplets and control of lipolysis. *J. Lipid Res.* 48, 2547–2559.

Buch, T., Heppner, F.L., Tertiit, C., Heinen, T.J., Kremer, M., Wunderlich, F.T., Jung, S., and Waisman, A. (2005). A Cre-inducible diphtheria toxin receptor mediates cell lineage ablation after toxin administration. *Nat. Methods* 2, 419–426.

Correll, J.W. (1963). Adipose tissue: ability to respond to nerve stimulation in vitro. *Science* 140, 387–388.

Daou, I., Tuttle, A.H., Longo, G., Wieskopf, J.S., Bonin, R.P., Ase, A.R., Wood, J.N., De Koninck, Y., Ribeiro-da-Silva, A., Mogil, J.S., and Séguéla, P. (2013). Remote optogenetic activation and sensitization of pain pathways in freely moving mice. *J. Neurosci.* 33, 18631–18640.

Dempersmier, J., Sambeat, A., Gulyaeva, O., Paul, S.M., Hudak, C.S., Raposo, H.F., Kwan, H.Y., Kang, C., Wong, R.H., and Sul, H.S. (2015). Cold-inducible Zfp516 activates UCP1 transcription to promote browning of white fat and development of brown fat. *Mol. Cell* 57, 235–246.

Ding, Y.M., Jaumotte, J.D., Signore, A.P., and Zigmond, M.J. (2004). Effects of 6-hydroxydopamine on primary cultures of substantia nigra: specific damage to dopaminergic neurons and the impact of glial cell line-derived neurotrophic factor. *J. Neurochem.* 89, 776–787.

Dodd, G.T., Decherf, S., Loh, K., Simonds, S.E., Wiede, F., Balland, E., Merry, T.L., Münzberg, H., Zhang, Z.Y., Kahn, B.B., et al. (2015). Leptin and insulin act on POMC neurons to promote the browning of white fat. *Cell* 160, 88–104.

Domingos, A.I., Vaynshteyn, J., Voss, H.U., Ren, X., Gradinariu, V., Zang, F., Deisseroth, K., de Araujo, I.E., and Friedman, J. (2011). Leptin regulates the reward value of nutrient. *Nat. Neurosci.* 14, 1562–1568.

Domingos, A.I., Sordillo, A., Dietrich, M.O., Liu, Z.W., Tellez, L.A., Vaynshteyn, J., Ferreira, J.G., Ekstrand, M.I., Horvath, T.L., de Araujo, I.E., and Friedman, J.M. (2013). Hypothalamic melanin concentrating hormone neurons communicate the nutrient value of sugar. *eLife* 2, e01462.

Elia, M., Stubbs, R.J., and Henry, C.J. (1999). Differences in fat, carbohydrate, and protein metabolism between lean and obese subjects undergoing total starvation. *Obes. Res.* 7, 597–604.

Friedman, J.M., and Halaas, J.L. (1998). Leptin and the regulation of body weight in mammals. *Nature* 395, 763–770.

Giordano, A., Morroni, M., Santone, G., Marchesi, G.F., and Cinti, S. (1996). Tyrosine hydroxylase, neuropeptide Y, substance P, calcitonin gene-related peptide and vasoactive intestinal peptide in nerves of rat periovarian adipose tissue: an immunohistochemical and ultrastructural investigation. *J. Neurocytol.* 25, 125–136.

Giordano, A., Frontini, A., Murano, I., Tonello, C., Marino, M.A., Carruba, M.O., Nisoli, E., and Cinti, S. (2005). Regional-dependent increase of sympathetic innervation in rat white adipose tissue during prolonged fasting. *J. Histochem. Cytochem.* 53, 679–687.

Giralt, M., and Villarrota, F. (2013). White, brown, beige/brite: different adipose cells for different functions? *Endocrinology* 154, 2992–3000.

Gualda, E.J., Vale, T., Almada, P., Feijó, J.A., Martins, G.G., and Moreno, N. (2013). OpenSpinMicroscopy: an open-source integrated microscopy platform. *Nat. Methods* 10, 599–600.

Halaas, J.L., Gajiwala, K.S., Maffei, M., Cohen, S.L., Chait, B.T., Rabinowitz, D., Lallone, R.L., Burley, S.K., and Friedman, J.M. (1995). Weight-reducing effects of the plasma protein encoded by the obese gene. *Science* 269, 543–546.

Halaas, J.L., Boozer, C., Blair-West, J., Fidahusein, N., Denton, D.A., and Friedman, J.M. (1997). Physiological response to long-term peripheral and central leptin infusion in lean and obese mice. *Proc. Natl. Acad. Sci. USA* 94, 8878–8883.

Helmchen, F., and Denk, W. (2005). Deep tissue two-photon microscopy. *Nat. Methods* 2, 932–940.

Holzer, P. (1991). Capsaicin: cellular targets, mechanisms of action, and selectivity for thin sensory neurons. *Pharmacol. Rev.* 43, 143–201.

Koffler, M., and Kisch, E.S. (1996). Starvation diet and very-low-calorie diets may induce insulin resistance and overt diabetes mellitus. *J. Diabetes Complications* 10, 109–112.

Landsberg, L., Saville, M.E., and Young, J.B. (1984). Sympathoadrenal system and regulation of thermogenesis. *Am. J. Physiol.* 247, E181–E189.

Montez, J.M., Soukas, A., Asilmaz, E., Fayzikodjaeva, G., Fantuzzi, G., and Friedman, J.M. (2005). Acute leptin deficiency, leptin resistance, and the physiologic response to leptin withdrawal. *Proc. Natl. Acad. Sci. USA* 102, 2537–2542.

Newman, W.P., and Brodows, R.G. (1983). Insulin action during acute starvation: evidence for selective insulin resistance in normal man. *Metabolism* 32, 590–596.

Nguyen, K.D., Qiu, Y., Cui, X., Goh, Y.P., Mwangi, J., David, T., Mukundan, L., Brombacher, F., Locksley, R.M., and Chawla, A. (2011). Alternatively activated macrophages produce catecholamines to sustain adaptive thermogenesis. *Nature* 480, 104–108.

Petreanu, L., Huber, D., Sobczyk, A., and Svoboda, K. (2007). Channelrhodopsin-2-assisted circuit mapping of long-range callosal projections. *Nat. Neurosci.* 10, 663–668.

Quintana, L., and Sharpe, J. (2011). Optical projection tomography of vertebrate embryo development. *Cold Spring Harb. Protoc.* 2011, 586–594.

Rafael, J., and Herling, A.W. (2000). Leptin effect in ob/ob mice under thermo-neutral conditions depends not necessarily on central satiation. *Am. J. Physiol. Regul. Integr. Comp. Physiol.* 278, R790–R795.

Rezai-Zadeh, K., and Münzberg, H. (2013). Integration of sensory information via central thermoregulatory leptin targets. *Physiol. Behav.* 121, 49–55.

Scarpace, P.J., and Matheny, M. (1998). Leptin induction of UCP1 gene expression is dependent on sympathetic innervation. *Am. J. Physiol.* 275, E259–E264.

Schindelin, J., Arganda-Carreras, I., Frise, E., Kaynig, V., Longair, M., Pietzsch, T., Preibisch, S., Rueden, C., Saalfeld, S., Schmid, B., et al. (2012). Fiji: an open-source platform for biological-image analysis. *Nat. Methods* 9, 676–682.

Tavernier, G., Jimenez, M., Giacobino, J.P., Hulo, N., Lafontan, M., Muzzin, P., and Langin, D. (2005). Norepinephrine induces lipolysis in beta1/beta2/beta3-adrenoceptor knockout mice. *Mol. Pharmacol.* 68, 793–799.

Thompson, G.E. (1986). Vascular and lipolytic responses of the inguinal fat pad of the sheep to adrenergic stimulation, and the effects of denervation and autotransplantation. *Q. J. Exp. Physiol.* 71, 559–567.

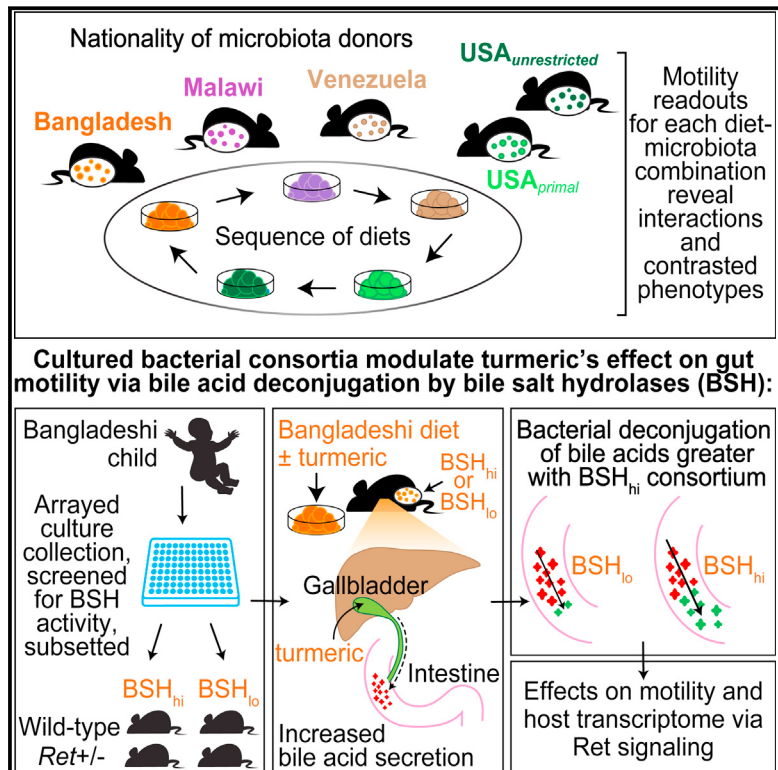
Vrontou, S., Wong, A.M., Rau, K.K., Koerber, H.R., and Anderson, D.J. (2013). Genetic identification of C fibres that detect massage-like stroking of hairy skin in vivo. *Nature* 493, 669–673.

Weisberg, S.P., McCann, D., Desai, M., Rosenbaum, M., Leibel, R.L., and Ferrante, A.W., Jr. (2003). Obesity is associated with macrophage accumulation in adipose tissue. *J. Clin. Invest.* 112, 1796–1808.

Youngstrom, T.G., and Bartness, T.J. (1995). Catecholaminergic innervation of white adipose tissue in Siberian hamsters. *Am. J. Physiol.* 268, R744–R751.

Regulators of Gut Motility Revealed by a Gnotobiotic Model of Diet-Microbiome Interactions Related to Travel

Graphical Abstract



Authors

Neelendu Dey, Vitas E. Wagner,
Laura V. Blanton, ..., Rashidul Haque,
Tahmeed Ahmed, Jeffrey I. Gordon

Correspondence

jgordon@wustl.edu

In Brief

A mouse model of short-term dietary changes, which happen when humans are traveling to places with different culinary traditions, reveals how a single food ingredient interacts with a functional microbiota trait to regulate host physiology.

Highlights

- Gut motility is affected by different human gut microbiota-diet combinations
- Turmeric slows motility in gnotobiotic mice with a Bangladeshi microbiota/diet
- Turmeric's effect involves bile acid secretion/deconjugation and Ret signaling
- Gnotobiotic mice can define key interactions between traditional foods and microbiota

Regulators of Gut Motility Revealed by a Gnotobiotic Model of Diet-Microbiome Interactions Related to Travel

Neelendu Dey,^{1,2,3} Vitas E. Wagner,^{1,2} Laura V. Blanton,^{1,2} Jiye Cheng,^{1,2} Luigi Fontana,³ Rashidul Haque,⁴ Tahmeed Ahmed,⁴ and Jeffrey I. Gordon^{1,2,*}

¹Center for Genome Sciences and Systems Biology

²Center for Gut Microbiome and Nutrition Research

³Department of Medicine

Washington University School of Medicine, St. Louis, MO 63108, USA

⁴Centre for Nutrition and Food Security, International Centre for Diarrhoeal Disease Research, Dhaka 1212, Bangladesh

*Correspondence: jgordon@wustl.edu

<http://dx.doi.org/10.1016/j.cell.2015.08.059>

SUMMARY

To understand how different diets, the consumers' gut microbiota, and the enteric nervous system (ENS) interact to regulate gut motility, we developed a gnotobiotic mouse model that mimics short-term dietary changes that happen when humans are traveling to places with different culinary traditions. Studying animals transplanted with the microbiota from humans representing diverse culinary traditions and fed a sequence of diets representing those of all donors, we found that correlations between bacterial species abundances and transit times are diet dependent. However, the levels of unconjugated bile acids—generated by bacterial bile salt hydro-lases (BSH)—correlated with faster transit, including during consumption of a Bangladeshi diet. Mice harboring a consortium of sequenced cultured bacterial strains from the Bangladeshi donor's microbiota and fed a Bangladeshi diet revealed that the commonly used cholekinetic spice, turmeric, affects gut motility through a mechanism that reflects bacterial BSH activity and Ret signaling in the ENS. These results demonstrate how a single food ingredient interacts with a functional microbiota trait to regulate host physiology.

INTRODUCTION

Gut motility, a key physiologic parameter governing digestion and absorption of nutrients, is affected by diet (Cummings et al., 1976, 1978), gut microbes (Husebye et al., 1994, 2001; Wichmann et al., 2013), the enteric nervous system (ENS) (Edery et al., 1994; Romeo et al., 1994), and host genetics (Levy et al., 2000; Whorwell et al., 1986). At present, we lack detailed understanding of the complex and dynamic interrelationships between these factors, particularly in the global context of diverse cultural

traditions concerning foods, their methods of preparation, and the varied human gut microbiota that have evolved under these dietary conditions. Intestinal transit times measured in >1,000 healthy individuals representing diverse populations worldwide varied within and between groups, likely reflecting a combination of these factors (Burkitt et al., 1972). The advent of culture-independent methods for characterizing the structure and expressed functions of a gut microbiota creates an opportunity to identify new approaches for understanding gut motility and optimizing the nutritional benefits derived from different dietary practices.

In the present study, we began by modeling short-term diet changes associated with global human travel in gnotobiotic mice colonized with gut microbiota from healthy human donors from around the world. We hypothesized that with an international focus, we could conduct a screen of food types and microbiota for potential mediators of motility common to diverse diets and gut communities. Without making any assumptions regarding the healthiness of faster or slower motility, our strategy was to identify diets and microbiota whose interactions result in highly contrasting transit times in order to subsequently home in on specific dietary ingredients and microbiota-encoded metabolic capacities that affect motility. We reasoned that by generating clonally arrayed collections of bacterial strains cultured from donor microbiota that transmitted disparate motility phenotypes in different dietary settings, we could deliberately manipulate which members of the collection were used for colonization of mice based on specific metabolic attributes that could be identified from their genomes and confirmed by direct biochemical assays *in vitro*. Colonization with different subsets of the community could then be performed in the context of concurrently manipulated diets, either in wild-type animals or in those with deliberately manipulated genetic features known to affect ENS function. Our immediate goal for this type of preclinical modeling was to decipher the mechanisms by which diet-by-microbiota interactions can regulate gut motility. Our long-term goal was to implement an approach that could, in principle, be generalized to dissect the effects of interactions between (1) ingredients represented in established as well as emerging dietary traditions/trends, (2) members of consumers' gut microbiota, and (3) gut motility and potentially other aspects of human physiology.



Figure 1. Compositions of Diets Used in the Six-Phase Travel Experiment

In the foreground, word clouds convey the specific ingredients used; font sizes depict the weight-based proportional representations of ingredients within each diet. Pie charts in the background represent the macromolecular compositions. See also [Table S1](#).

RESULTS

Modeling Diet and Motility Changes Associated with Global Human Travel in Gnotobiotic Mice

In an initial “travel” experiment, intact uncultured fecal microbiota samples obtained from six healthy adults representing different geographic locations and cultural/culinary traditions were transplanted into adult germ-free C57BL/6 male mice ($n = 6$ recipient mice/donor microbiota). Microbiota donors included (1) three residents of the USA (a twin pair stably discordant for obesity with both co-twins consuming an American diet without self-imposed dietary restrictions ($\text{USA}_{\text{unrestricted}}$) ([Ridaura et al., 2013](#)) plus another lean individual who had consumed a protein- and fat-rich primal diet for a number of years ($\text{USA}_{\text{primal}}$), (2) an Amerindian living in a remote rural village in the Amazonas State of Venezuela ([Yatsunenko et al., 2012](#)), (3) a Bangladeshi resident of an urban slum ([Subramanian et al., 2014](#)), and (4) a Malawian from a rural village in the southern part of the country ([Yatsunenko et al., 2012](#)) (see [Table S1A](#) for a description of donor characteristics and [Table S1B](#) for analysis of microbiota transplantation efficiency). The six groups of transplant recipients were fed a sequence of six sterilized diets formulated to represent those consumed by the microbiota donors ([Figure 1](#); [Tables S1C](#) and [S1D](#)), in essence simulating the varying dietary experiences of humans and their microbiota during travel. In each case, the initial and final diets in the sequence represented the native or home diet of the donor, in order to characterize the longer-term effects of dietary exposures during travel and the degree to which transit times recover. In between, travel diets were given in the same sequence, in an order chosen randomly but executed uniformly for all mice, as permitted by the type of home diet ([Figure 2A](#)). The starting and ending home diets were given for 14 and 8 days, respectively, while each travel diet was administered for 8 days. Intestinal transit times were measured at the end of each diet phase by gavaging mice with non-absorbable red carmine dye and recording the time from gavage to first appearance of the dye in their feces ([Kashyap et al., 2013](#); [Li et al., 2011](#); [Yano et al., 2015](#)) ([Figure 2B](#); [Table S2A](#)). Carmine dye does not perturb the structure of the gut bacterial community; 16S rRNA analysis of fecal samples, collected before and after carmine administration from 9-week-old gnotobiotic mice colonized with a fecal microbiota from a conventionally raised C57BL/6 donor,

showed no significant effect of the dye as judged by weighted UniFrac distances ($p > 0.05$, two-tailed Student’s t test). Moreover, fecal samples collected on the days of transit time measurements were taken prior to carmine administration.

Aggregating data from all animals at all time points of this six-phase travel experiment revealed a normal distribution of transit times ([Figure 2C](#)). The average within-mouse variance throughout the experiment was 27.7 min, while the average between-mouse variance at a given time point was 29.3 min. Repeated-measures ANOVA in which transit time was the dependent variable demonstrated that diet ($p = 5.6 \times 10^{-5}$), the donor microbiota ($p = 2.3 \times 10^{-3}$), and the interaction of diet and microbiota ($p = 2.6 \times 10^{-3}$) were all significant factors ([Table S3A](#)). The most contrasted diet-by-microbiota effects on transit times were documented in mice colonized with the Bangladeshi compared to the $\text{USA}_{\text{unrestricted}}$ microbiota when they consumed Bangladeshi and primal diets ([Figure 2D](#)). Specifically, mice colonized with the $\text{USA}_{\text{unrestricted}}$ microbiota had significantly faster motility (i.e., shorter transit times) when consuming the Bangladeshi diet compared to primal diet ($p < 0.002$, two-tailed Student’s t test); the opposite was observed in mice colonized with a Bangladeshi microbiota ($p < 0.006$, two-tailed Student’s t test). We tested the robustness of these most contrasted motility phenotypes by colonizing animals with fecal microbiota obtained from three healthy Bangladeshi adults (including the donor tested in the first experiment) and three healthy $\text{USA}_{\text{unrestricted}}$ adults (a repeat of the obese co-twin in the discordant pair, plus a new obese and a new lean donor; see [Table S1A](#) for donor characteristics). Recipients ($n = 5$ mice/donor microbiota) were subjected to three diet phases beginning and ending with a “local” diet (i.e., the primal diet for mice colonized with a $\text{USA}_{\text{unrestricted}}$ microbiota or the Bangladeshi diet for mice colonized with a Bangladeshi microbiota) and including an interval “non-native” diet ([Figure S1A](#)). The results of this three-phase travel experiment confirmed that significantly contrasted transit times were imparted by the interactions of these diets and microbiota ($p < 2.6 \times 10^{-5}$, $F = 19.8$, analysis of covariance [ANCOVA]), although the effect size and statistical significance of differences in transit time varied by the individual microbiota donor ([Figure S1B](#); [Table S2B](#)).

Correlations between the Relative Abundances of Gut Bacterial Strains and Transit Times Are Diet Dependent

To identify relationships between specific bacterial taxa, diet, and transit time phenotypes, we sequenced PCR amplicons generated from the V4 region of bacterial 16S rRNA genes

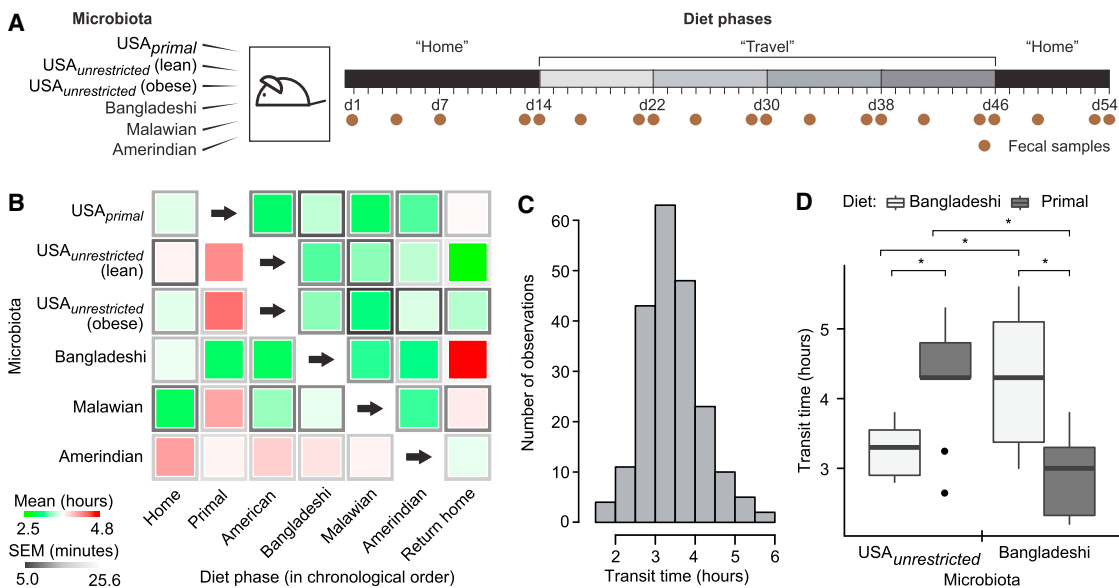


Figure 2. Diet and Microbiota Significantly Impact Intestinal Transit Times

(A) Schematic of the six-phase travel experiment. Groups of adult germ-free C57BL/6 mice were colonized with fecal microbiota from six healthy donors and fed diets representative of those consumed by all donors in the sequence shown in (B).

(B) The central squares of this heatmap represent means of transit times for each diet-microbiota combination as measured by a carmine red dye assay; the frames of the squares represent SEM ($n = 6$ mice/donor microbiota). Microbiota are represented along rows and diet phases along columns. Each group of mice consumed human diets in the order shown from left to right; home diets were always consumed during the initial and final diet phases but skipped in the intervening travel diet progression (primal diet → unrestricted American diet → Bangladeshi diet → Malawian diet → Amerindian diet).

(C) Histogram showing distribution of all transit times recorded throughout the six-phase travel experiment.

(D) The most contrasted diet-by-microbiota effects on transit times were observed in mice colonized with a Bangladeshi or USA_{unrestricted} microbiota and fed Bangladeshi versus primal diets. Results for USA_{unrestricted} (lean) and USA_{unrestricted} (obese) were aggregated and are represented together as USA_{unrestricted}. Results from the "home" and "return home" phases for mice colonized with a Bangladeshi microbiota and fed a Bangladeshi diet were also aggregated. Statistical significance was determined using a two-tailed Student's t test; * $p < 0.05$. Within each box, the horizontal line denotes the mean value of the transit times. The lower and upper boundaries of each box represent the 25th and 75th percentiles, respectively, while whiskers represent 1.5 times the interquartile range.

See also Figures 1, 3, S1, and S2 and Tables S1, S2, S3, S4, and S5.

present in fecal microbiota collected throughout the course of the six-phase as well as three-phase travel experiments (984 fecal samples; $22,470 \pm 630$ reads per sample [mean \pm SEM]; Table S4). 16S rRNA reads were grouped into operational taxonomic units based on whether they shared $\geq 97\%$ nucleotide sequence identity (97%ID OTUs). Principal coordinates analysis (PCoA) based on unweighted UniFrac, a phylogenetic metric that computes similarity between any two microbiota based on the degree to which their component OTUs share branch length on a bacterial tree (Lopupone and Knight, 2005), indicated that community assembly was rapid and highly reproducible within a given group of mice that received the same donor microbiota in both the six-phase and three-phase travel experiments (Figures S2A and S2C).

The microbiota donor was the predominant factor explaining variance in unweighted UniFrac distances between samples from the different experimental groups ($p < 0.001$ within-group as compared to between-group similarity, permutational multivariate analysis of variance using distance matrices [PERMANOVA]; Figures S2B and S2D). Nonetheless, diet had consistent effects across different treatment groups and phenotypes: 87 diet-discriminatory 97%ID OTUs that were robust to donor microbiota

and motility phenotypes were identified by applying a machine learning algorithm (Random Forests) to the 16S rRNA dataset generated from all fecal microbiota samples collected from all mouse recipients of all human donor microbiota throughout the six-phase travel experiment (Figure 3; Table S5). We elected to apply a decision-tree-based algorithm for feature selection (i.e., in this case, the most diet-discriminatory OTUs) so that we would not have to make any distributional assumptions regarding our dataset of proportional OTU abundances. The Random Forests-derived model predicted which diet was being consumed in the subsequent three-phase travel experiment with a mean accuracy of $83\% \pm 0.02\%$ (range 79%–86%; 10,000 replications), significantly better than the null distribution ($p < 2.2 \times 10^{-16}$). These 87 diet-discriminatory OTUs were not significantly correlated with transit times across all diet-microbiota combinations in either experiment. In an analysis of all 416 97%ID OTUs with relative abundances above the limit of detection (0.01%) in mouse fecal samples collected throughout both travel experiments, just a single OTU, *Parabacteroides gordonii* (OTU ID 240), was significantly correlated, after Bonferroni correction for multiple comparisons, with transit times across the highly contrasted diet-microbiota combinations ($\rho = 0.3$, $p = 0.02$). This

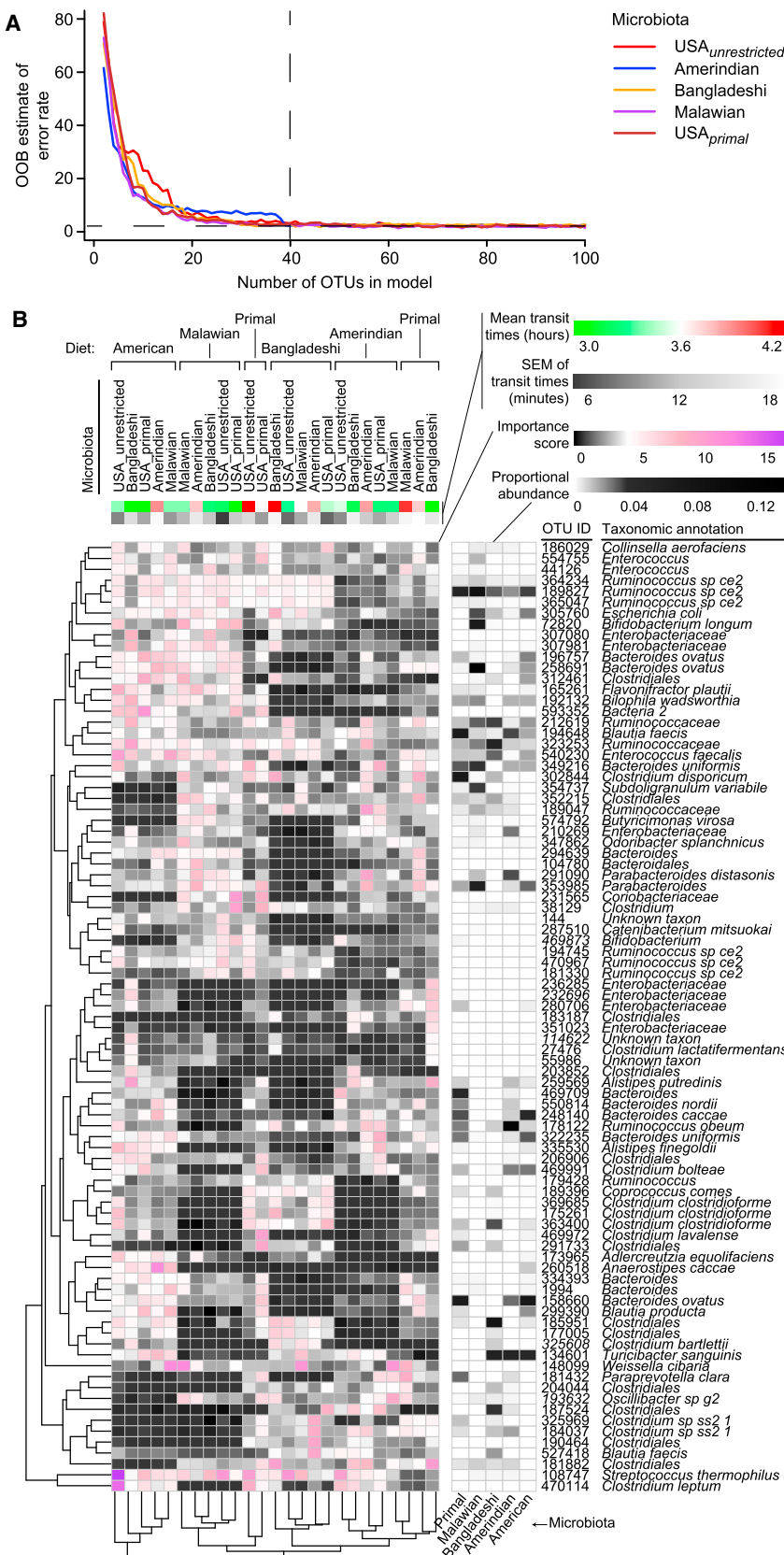


Figure 3. Diet-Discriminatory OTUs Are Robust to Different Donor Microbiota and Motility Phenotypes

(A) Out-of-bag (OOB) estimated error rates in a Random Forests model for predicting diet, stratified by donor microbiota, as a function of numbers of diet-discriminatory OTUs. For each microbiota, 40 OTUs were sufficient to discriminate diet, yielding a total of 87 unique OTUs across six microbiota donors from five cultural/dietary traditions in the six-phase travel experiment.

(B) Evidence for the robustness of diet-discriminatory OTUs to donor microbiota and motility phenotype. Feature importance scores of 87 diet-discriminatory OTUs in each diet-microbiota context are represented in this heatmap, which was generated following unsupervised hierarchical clustering. A sparse Random Forests model built using these diet-discriminatory OTUs accurately predicted diet in the three-phase travel experiment.

See also Table S5.

organism has not been reported to be associated with altered intestinal motility in humans.

We identified 27 OTUs present in both the USA_{unrestricted} and Bangladeshi microbiota that had significant *diet-dependent* correlations with transit times documented in the context of either the Bangladeshi or primal diets, but not both (Table S3B). The relationships of bacteria to transit times were strain specific: two strains of *Eubacterium desmolans* (OTU IDs 170124 and 158946) had opposing relationships with transit times within the setting of primal diet consumption. A single OTU, *E. desmolans* (OTU ID 158946), was significantly correlated with transit times in both diets, but remarkably, the correlations were opposite in the Bangladeshi versus primal diet contexts ($p < 9.3 \times 10^{-6}$, $F = 9.6$, ANCOVA testing interaction of *E. desmolans* abundance with diet). In the unrestricted USA diet context, yet another OTU in the USA_{unrestricted} and Bangladeshi microbiota (*Clostridiales*, OTU ID 261590) was correlated with transit times ($\rho = -0.57$, $p = 0.04$). Hence, a next-generation probiotic strain designed to impact motility may require simultaneous consumption of a specific diet or diet ingredient to exert its effect.

Transit times at the ends of the initial and final home diets often varied. This finding could not be ascribed to increasing age ($p = 0.7$, $F = 0.1$, one-way ANOVA of transit time as a function of age). Mathematically, if we consider two functions $h(m)$ and $t(m)$, then $h(m)$ need not necessarily equal $h(t(h(m)))$. We postulated that if these two functions represent the effects of home (h) and travel (t) diets, respectively, on a microbiota m , then the result of a home diet may depend on whether intervening travel diets were consumed. Indeed, an analysis comparing fecal microbiota at the ends of the initial and final home phases in the six-phase travel experiment disclosed that community structure, while largely similar, always exhibited statistically significant changes ($p < 0.05$, paired two-tailed Student's t test after Bonferroni correction) in the proportional abundances of one or more OTUs. For example, mice colonized with fecal microbiota from both USA_{unrestricted} individuals exhibited a significant increase in the relative abundance of *Bacteroides ovatus* between the first and last home diet periods, while mice colonized with microbiota from the adult Bangladeshi donor exhibited significantly increased abundances of an OTU classified as *Clostridiales*, and a decrease in *Ruminococcus obeum*.

The imperfect recovery of transit time following diverse dietary exposures during travel could reflect not only these structural differences but also functional differences in the microbiota. Therefore, we characterized metabolic features of the microbiota in the context of the most highly contrasted motility phenotypes.

Microbially Deconjugated Bile Acid Metabolites Are Correlated with Faster Gut Transit

To identify metabolic features that correlate with motility phenotypes, we applied ultra-high-performance liquid chromatography mass spectrometry (UPLC-MS) to fecal samples collected from mice in the three-phase travel experiment on the same days when their transit times were measured (three USA_{unrestricted} and three Bangladeshi donor microbiota; five mice/donor microbiota; three fecal samples analyzed/mouse). We observed

>2,500 unique m/z peaks that were present in more than one mouse. Spearman's rank correlations (without Bonferroni correction) yielded 599 m/z peaks that were significantly correlated with transit times, of which 67 (11%) were putatively identified as bile acid metabolites (Tables S6A and S6B). In mice, the predominant primary bile acids are beta-muricholic acid and cholic acid, while in humans they are chenodeoxycholic acid and cholic acid (Haslewood, 1967). Prior to secretion from hepatocytes into biliary canaliculi, bile acids are conjugated with either taurine (predominant in mice; Falany et al., 1997) or glycine (predominant in humans; Falany et al., 1994) to decrease passive absorption by intestinal enterocytes. Bile acids have microbicidal activity; members of the gut microbiota neutralize these effects by metabolizing host bile acids, beginning with deconjugation catalyzed by microbial bile salt hydrolases (BSHs) (Drasar et al., 1966). Since bile acids are modified by the microbiota, we considered whether differences in bile acid metabolite profiles could explain discordant microbiota-associated motility phenotypes.

To gain insights into the relationships between OTUs and bile acid metabolites as they pertain to transit times, we calculated Spearman's rank correlation coefficients between the proportional abundances of 97%ID OTUs in fecal microbiota, the peak intensities of fecal bile acids, and transit times in the three-phase travel experiment (Figure 4; Table S6B). After Bonferroni correction, we identified 118 OTUs with significant correlations between their abundances and levels of one or more fecal bile acids; only one of these OTUs, *Blautia* (OTU ID 296977), also had a significant correlation between its abundance and transit times (slower transit) (Table S6B). A sparse linear model, built after regressing transit times against all bile acid metabolite levels then simplified by applying stepwise backward feature selection, demonstrated that levels of just five bile acids (7-ketodeoxycholic acid, muricholic acid, taurocholic acid, tauro-beta-muricholic acid, and tauro-muricholic acid sulfate) accurately predicted transit times in the three-phase travel experiment ($\rho = 0.54$, $p = 1.8 \times 10^{-7}$, Spearman's rank correlation), outperforming a linear model built with an equivalent number of randomly selected non-bile-acid metabolites ($\rho = 0.17$, $p = 0.47$, Spearman's rank correlation; mean values over 1,000 replications) (Figure S1C; Table S6C). Of these five bile acids, none was significantly associated with either diet. Only one bile acid species, tauro-muricholic acid sulfate, was significantly associated with the geographic origin of the microbiota donor; it was found at significantly higher concentrations in fecal specimens collected from mice colonized with subjects residing in Bangladesh (Figure 4). Bile acids that were correlated with faster transit times were unconjugated (7-ketodeoxycholic acid and muricholic acid), whereas those that correlated with slower transit times were conjugated (tauro-beta-muricholic acid, taurocholic acid, and tauro-muricholic acid sulfate) (Figure 4; Table S6B). Levels of multiple bile acids, including these five bile acids, were significantly correlated with multiple OTUs (Figure 4), underscoring the complexity of microbial bile acid metabolism.

Turmeric Alters Gut Motility

Intestinal bile acid concentrations are largely dictated by dietary components (e.g., peptides and fats) that trigger intestinal

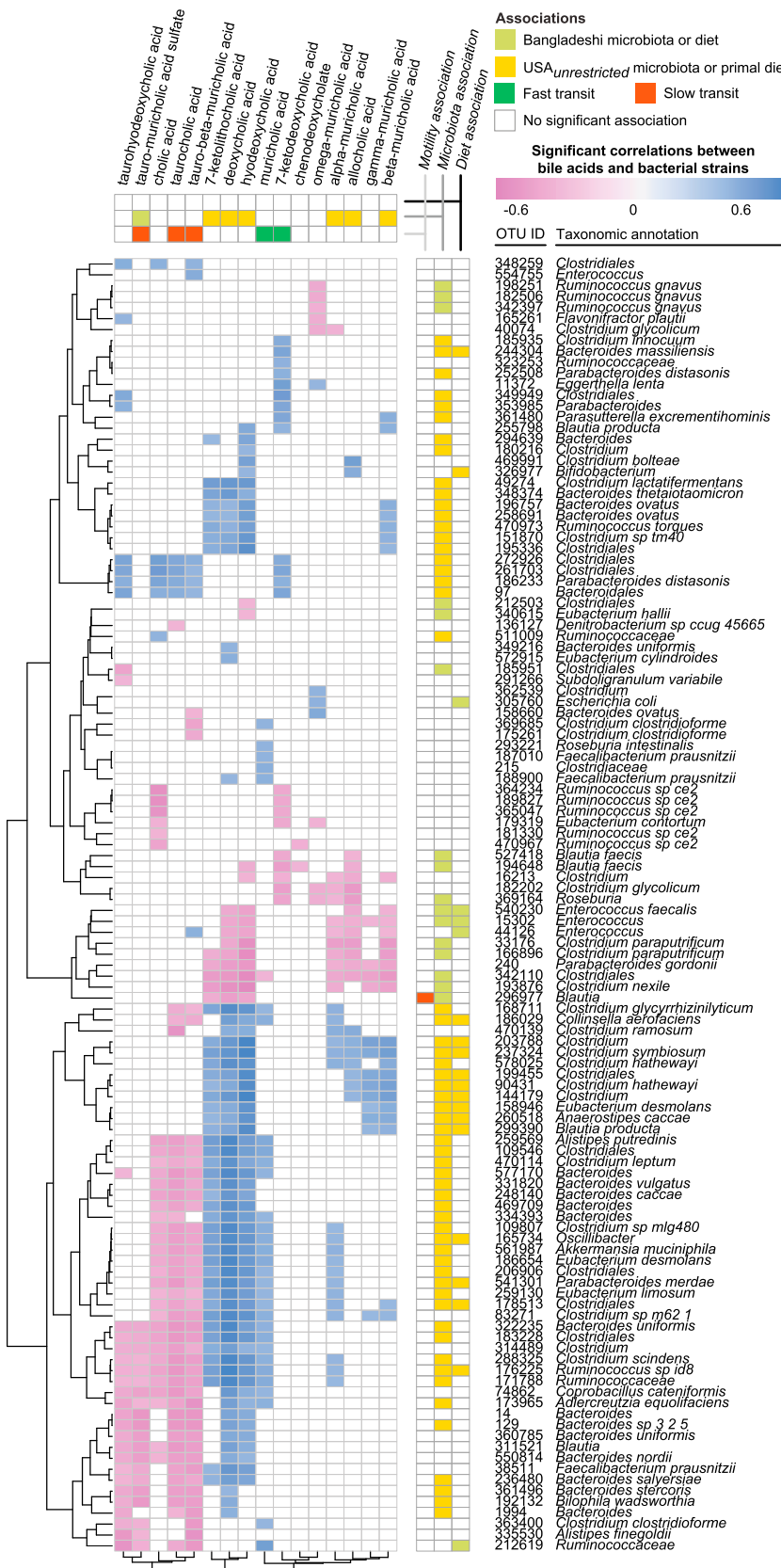


Figure 4. Significant Correlations between Fecal Bile Acid Metabolite Concentrations and the Relative Abundances of Bacterial 97%ID OTUs

Bile acid metabolite profiling and 16S rRNA analysis was performed on fecal samples collected from mice in the three-phase travel experiment (Figure S1). Spearman rank correlations were calculated between bile acid concentrations and relative abundances of 97%ID OTUs. Unsupervised hierarchical clustering was applied. Significant associations ($p < 0.05$ calculated by two-tailed Student's t test, with Bonferroni correction) between microbiota/diet and bile acids/OTUs are represented in the vertical and horizontal side panels. Associations between bile acid levels and transit times were calculated by linear modeling with stepwise backward feature selection, as detailed in the text and [Supplemental Experimental Procedures](#).

See also Figures S1 and Tables S4 and S6.

signals (e.g., cholecystokinin), which, in turn, influence gallbladder contraction and release of bile into the lumen of the proximal small intestine. To further characterize interactions between specific OTUs, bile acid metabolism, and diet, we examined the effects of turmeric on transit time. We selected turmeric, a spice with cultural significance commonly used in Bangladeshi cuisine, because it has a dose-dependent cholekinetic effect; i.e., its active ingredient, curcumin, stimulates gallbladder contraction and thus increases luminal bile acid levels. The effect sizes of turmeric's cholekinesis vary between reported studies, possibly due to population-based differences (e.g., European versus Asian subjects) or differences in how the spice was administered (Marciani et al., 2013; Rasyid and Lelo, 1999; Rasyid et al., 2002). In a study using serial hydrogen breath tests to assess carbohydrate fermentation and small bowel transit time, investigators observed that turmeric-containing Japanese-style curry fed to Japanese individuals increased fermentation and shortened small bowel transit time compared to curry prepared without turmeric (Shimouchi et al., 2009). The microbial underpinnings of these observations in human subjects are unknown, as metagenomic or metabolomic analyses of their gut microbiota were not performed.

We initially defined the effect of turmeric in adult male C57BL/6 gnotobiotic mice colonized with a collection of anaerobic bacterial strains cultured from the fecal microbiota of a healthy 2-year-old Bangladeshi child (Table S7A). We generated this culture collection from a child rather than an adult to avoid the potential confounding effects of chronic antecedent turmeric exposure on microbiota features. This child, like the three Bangladeshi adults whose microbiota were tested in the earlier experiments, lived in Mirpur, an urban sub-district of Dhaka. The sequenced, clonally arrayed bacterial culture collection gave us the capacity to perform follow-up experiments in which specific strains were selected for colonization based on their capacity to metabolize bile acids.

Following gavage of the entire culture collection, composed of 53 bacterial strains (Table S7A), mice were initially fed a Bangladeshi diet lacking turmeric for 10 days (diet phase 1), then the same diet containing turmeric for 10 days (diet phase 2), and finally the unsupplemented Bangladeshi diet again for 10 days (diet phase 3). A control group was maintained under germ-free conditions and subjected to the same sequence of diets ($n = 6$ animals/group). To limit carryover of turmeric from the prior diet, old bedding was replaced with fresh new bedding at the start of each diet phase.

Colonization was highly reproducible between animals, with community assembly completed within 3–5 days after gavage. At the end of the first diet phase, 44 ± 1.2 (mean \pm SEM) of the 53 input strains were detectable in fecal samples collected from recipient animals, based on community profiling by shotgun sequencing (COPRO-seq) of fecal DNA (see [Experimental Procedures](#)). Colonized mice had significantly faster transit times at each diet phase compared to their germ-free counterparts ($p = 5.0 \times 10^{-6}$, $p < 4.7 \times 10^{-7}$, and $p < 1.7 \times 10^{-5}$ for diet phases 1, 2, and 3, respectively, two-tailed Student's t test; Table S2C). Consumption of turmeric was associated with a significant slowing of motility (i.e., longer transit time) (Table S2C). UPLC-MS of fecal samples collected from germ-free mice at

the end of each diet phase disclosed that ingestion of this cholekinetic spice was associated with significantly increased levels of taurohyodeoxycholic acid ($p = 0.003$, one-tailed Student's t test) and tauro-muricholic acid sulfate ($p = 0.03$, one-tailed Student's t test) compared to the period of unsupplemented diet consumption (Table S6A). As expected, no unconjugated bile acids were detected in the germ-free group during any of the diet phases. We included a curcumin standard in order to quantify fecal curcumin levels; however, curcumin was undetectable in all samples.

To directly test the hypothesis that microbiota with different capacities to deconjugate bile acids transmit distinct transit time phenotypes, we first used a UPLC-MS-based in vitro assay to screen all members of the clonally arrayed culture collection for their BSH (EC 3.5.1.24) activities. The screen demonstrated that OTUs representing a number of phylotypes had the ability to deconjugate at least one of the two primary bile acids found in mice (Table S7A). BLAST predictions, based on the presence in a strain's genome of homologs of known BSH genes (E-value threshold cutoff $\leq 10^{-5}$) were correct in predicting in vitro BSH enzymatic activity for 85% of the bacterial strains. Only ten strains did not deconjugate either bile acid in vitro (six members of the genus *Enterococcus*, three members of *Eggerthella*, and one belonging to *Enterobacteriaceae*). The strains with BSH activity were largely members of the genera *Bifidobacterium* and *Enterococcus*. We then assembled two bacterial consortia, each composed of seven strains representing the taxonomic diversity of the BSH-positive and BSH-negative subsets within the culture collection: the "BSH_{hi}" consortium contained four members of *Enterococcus* and three members of *Bifidobacterium*, and the "BSH_{lo}" consortium had five members of *Enterococcus*, one *Eggerthella* species, and one *Enterobacteriaceae* (see Table S7B for a summary of KEGG-based annotations of the sequenced genomes of these 14 strains). Members of the two consortia had in vitro growth rates under anaerobic conditions in rich medium that were not significantly different from one another ($p = 0.92$, two-tailed Student's t test).

Age-matched adult male C57BL/6 gnotobiotic mice were colonized with either the BSH_{hi} or BSH_{lo} consortium (assembled prior to gavage by combining equal numbers of colony-forming units of each component strain). A positive control group was colonized with the entire culture collection. As before, mice in each of these three groups ($n = 5$ /group) were given the unsupplemented Bangladeshi diet for 3 days prior to gavage of the cultured organisms. Following gavage, mice were maintained on the unsupplemented Bangladeshi diet for 8 days, followed by the turmeric-supplemented diet for 8 days, and then returned to the starting Bangladeshi diet for another 8 days. The complete culture collection produced a transit time that was significantly faster than that measured with the BSH_{lo} consortium in all three diet phases ($p < 0.002$, one-tailed Student's t test; Table S2D). While mice harboring the BSH_{lo} consortium had the same transit time as the BSH_{hi} consortium in the absence of turmeric, addition of this spice to the Bangladeshi diet produced significantly slower transit times in BSH_{lo} animals ($p = 0.02$, one-tailed Student's t test comparing phase 1 versus phase 2 transit times; Figure 5A) but no significant effects in BSH_{hi} mice ($p = 0.7$, one-tailed Student's t test). These findings indicate that a gut microbiota capable of

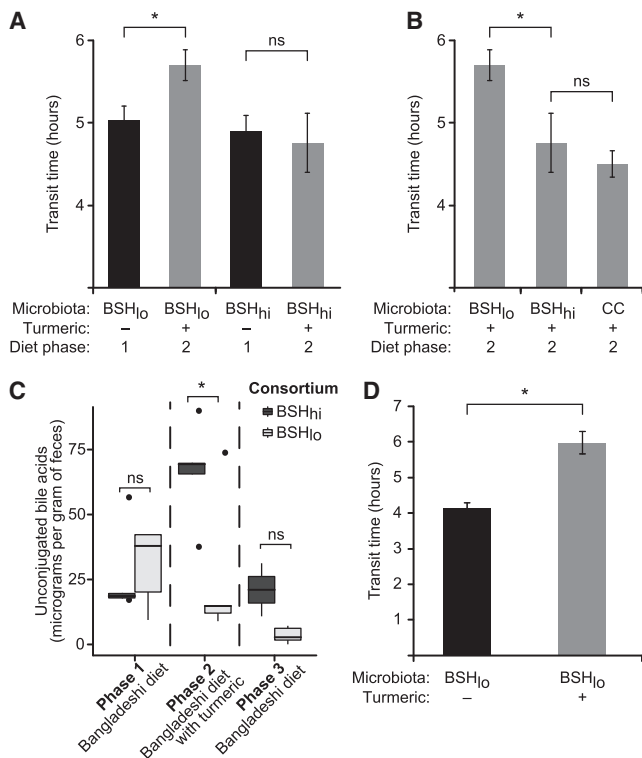


Figure 5. An Interaction Between Diet, Bile Acid Metabolism, and Gut Motility Revealed by Colonizing Germ-free Mice with a BSH_{hi} or BSH_{lo} Consortium and Feeding Them a Representative Bangladeshi Diet with or without Turmeric

- (A) Turmeric consumption resulted in significantly slower motility in mice colonized with the BSH_{lo}, but not the BSH_{hi} consortium.
- (B) While consuming the turmeric-supplemented Bangladeshi diet, BSH_{hi} mice had transit times comparable to mice colonized with the complete 53-strain culture collection ("CC") and faster motility (i.e., shorter transit times) than BSH_{lo} mice ($n = 5$ animals/microbiota). In this comparison, data for BSH_{lo} and BSH_{hi} are the same as in (A).
- (C) Turmeric consumption is associated with a significant increase in total fecal unconjugated bile acid concentrations in gnotobiotic wild-type mice colonized with the BSH_{hi} consortium, but not the BSH_{lo} consortium.
- (D) Transit times measured for two groups of gnotobiotic mice colonized with BSH_{lo} consortium and fed the unsupplemented or turmeric-containing Bangladeshi diet. Measurements occurred at the end of the 10-day monotonous diet experiment.

Statistical significance was determined using a one-tailed Student's t test. * $p < 0.05$. In (A), (B), and (D), transit times are represented by mean values \pm SEM. In (C), the horizontal line within each box denotes the mean value of the measured transit times. The lower and upper boundaries of each box represent the 25th and 75th percentiles, respectively, while whiskers represent 1.5 times the interquartile range. See also Tables S4, S6, S7, and S8.

deconjugating bile acids could modify the response to turmeric, which through its cholekinetic effects delivers increased amounts of conjugated bile acids to the proximal intestine.

Mice colonized with the BSH_{lo} consortium had significantly slower motility than BSH_{hi} animals only in the setting of turmeric ($p < 0.03$, one-tailed Student's t test; Figure 5B). UPLC-MS confirmed that BSH_{hi} mice had significantly higher total concentrations of fecal unconjugated bile acids ($p = 0.01$, one-tailed Student's t test) and significantly lower total concentrations of

conjugated bile acids ($p = 0.02$, one-tailed Student's t test) compared to mice colonized with the BSH_{lo} consortium (Figure 5C; Table S6A). Total concentrations of the two unconjugated primary bile acids (cholic acid and beta-muricholic acid) were significantly negatively correlated with transit times ($\rho = -0.76$, $p = 3.6 \times 10^{-9}$, Spearman's rank correlation). COPRO-Seq revealed that turmeric had no statistically significant effects on the representation of any strain in either consortium when compared to the unsupplemented diet phases ($p > 0.15$, two-tailed Student's t test).

Applying microbial RNA sequencing (RNA-seq) to fecal samples collected at the same time points as those used for the COPRO-seq analysis, we confirmed significantly greater overall levels of community BSH expression in the BSH_{hi} compared to the BSH_{lo} consortium's meta-transcriptome (145-fold; $p = 0.006$, two-tailed Student's t test). However, turmeric did not result in significant changes in the levels of BSH transcripts in the fecal meta-transcriptomes of BSH_{lo} and BSH_{hi} animals ($p > 0.05$, two-tailed Student's t test). *Enterococcus faecalis* (isolate ID hG2) was the only member of the BSH_{lo} consortium that expressed BSH, albeit at low levels (thus explaining the presence of fecal unconjugated bile acids in these animals; Figure 5C). In the BSH_{hi} consortium, the principal contributors of BSH transcripts to the community meta-transcriptome were three *Bifidobacteria* (isolate IDs hB1, hB8, and hF8), which together accounted for $76\% \pm 1\%$ (mean \pm SEM) of these transcripts. In mice colonized with the BSH_{lo} consortium, turmeric resulted in significant reductions in expression of two transcripts in the meta-transcriptome assigned to the KEGG "dioxin degradation pathway" (5.7-fold; $p = 0.004$, two-tailed Student's t test): salicylate 1-monooxygenase (EC 1.14.13.1, a oxidoreductase that produces catechol) and 4-oxalocrotonate tautomerase (EC 5.3.2.6; part of a metabolic pathway that generates tricarboxylic acid cycle intermediates). In mice colonized with the BSH_{hi} consortium, no KEGG pathways were significantly differentially expressed as a function of turmeric consumption. Together, these results suggest that turmeric enhances the discordance in motility phenotypes between BSH_{lo} and BSH_{hi} mice not by changing expression of bacterial BSH genes but rather through its cholekinetic effect, thereby providing conjugated bile acids to the two consortia with markedly different BSH gene content and deconjugation capacities.

Effects of Turmeric on Host Gene Expression

To assess the effects of turmeric on host gene expression, we focused on the BSH_{lo} consortium because, in the previous experiment, it transmitted a turmeric-responsive transit time phenotype. BSH_{lo} mice were monotonously fed either the unsupplemented or turmeric-supplemented Bangladeshi diet for 10 days. The capacity of turmeric to significantly slow motility was replicated in this new, single-diet-phase experiment ($p = 0.003$, one-tailed Student's t test comparing transit times between the two diet-treatment groups; Figure 5D). RNA-seq datasets were generated from the liver and terminal ileum, essential components of the enterohepatic circulation. Differentially expressed genes were identified using the exact negative binomial test. Genes that satisfied our criteria for significant differences in expression (after correcting for multiple comparisons) are listed

in Table S8. Transcriptional data generated from the livers of mice from the 10-day-long monotonous-diet experiment indicated that turmeric consumption was followed by a homeostatic response designed to maintain bile acid pool size at constant levels: i.e., consistent with the increased fecal bile acid levels elicited by turmeric consumption, *Cyp7a1* (cholesterol 7 α -hydroxylase) expression was 3.3-fold lower ($p = 0.00002$). *Cyp7A1* converts cholesterol into 7 α -hydroxycholesterol in the rate-limiting first step of hepatic bile acid synthesis, a step subject to feedback inhibition by increased bile acid concentrations.

In the terminal ileum, a total of 96 genes exhibited significant differential expression in the face of turmeric consumption (Table S8A), including greater expression of multiple genes involved in gut mucosal immune/barrier function: *Retnlb* (resistin-like molecule β , with 410-fold higher expression), *Siglec5* (sialic acid binding Ig-like lectin 5, an eosinophil marker), *Fut2* (α -1,2-fucosyltransferase; a null allele of this gene in humans confers non-secretor status and is associated with Crohn's disease [Tong et al., 2014]), while *Fut2* deficiency in mice enhances susceptibility to infection with eukaryotic and bacterial pathogens [Goto et al., 2014; Hurd and Domino, 2004]), *Nfil3* (nuclear factor, interleukin 3, a transcription factor that directs development of innate lymphoid cells [ILCs]; Geiger et al., 2014; Klose et al., 2014), *Tnfrsf21* (tumor necrosis factor receptor superfamily member 21, involved in T helper cell function), and *Irf2* (interferon regulatory factor 2). *Retnlb* is expressed by intestinal goblet cells and enterocytes (Hogan et al., 2006) and appears to have various effects on immunity, including maintenance of mucosal barrier function (Hogan et al., 2006), macrophage activation to produce tumor necrosis factor α (TNF- α) (McVay et al., 2006; Steinbrecher et al., 2011), and protection from gut helminthic infections (e.g., by inhibiting migration of worms; Artis et al., 2004; Herbert et al., 2009). Eosinophils, which, as noted above, express *Siglec5*, contribute to protective immunity against parasites (Knott et al., 2007). *Nfil3* expression is linked to ILC accumulation; group 2 ILCs have been implicated in development of protective immunity to parasites (Olyphant et al., 2014), while group 3 ILCs promote *Fut2* expression and mediate resistance to bacterial pathogens such as *Salmonella* (Goto et al., 2014). Turmeric's ability to modulate the distal ileal transcriptome is interesting in light of the South Asian Ayurvedic tradition of using crushed turmeric as an anti-helminthic (Handral et al., 2013; Nadkarni and Nadkarni, 1976). The burden of parasitic infection in this population is great (Roy et al., 2011); our findings offer one potential biological insight about why turmeric came to be ubiquitously represented in Bangladeshi cuisine. Though it is unclear whether these findings relate to our observed motility phenotypes, they may be of anthropologic significance.

Interplay of the Microbiota, Bile Acids, and the ENS

To assess the degree to which the effect of turmeric on motility was dependent upon ENS-based signaling (Alemi et al., 2013), we turned to mice heterozygous for a null allele of the Ret receptor (Tsuzuki et al., 1995). *Ret*, which encodes a transmembrane protein that binds glial cell-derived neurotrophic factor family ligands, is the gene most commonly implicated in Hirschsprung's disease (Edery et al., 1994; Romeo et al., 1994), a developmental disorder associated with absent peristalsis in the distal colon.

Heuckeroth and colleagues have reported that *Ret*^{+/−} mice exhibit >90% reductions in longitudinal and circular gut muscle contractility and 70%–95% reductions in the release of two neurotransmitters (substance P and VIP) compared to *Ret*^{+/+} animals despite having equivalent numbers of enteric neurons (Gianino et al., 2003). We found that conventionally raised wild-type (*Ret*^{+/+}) mice have significantly slower transit times than their conventionally raised heterozygous (*Ret*^{+/−}) littermates ($p = 0.05$, one-tailed Student's t test; Table S2F).

We re-derived C57BL/6 *Ret*^{+/−} mice as germ-free and colonized the heterozygotes and their wild-type littermates with either the seven-member BSH_{lo} or seven-member BSH_{hi} consortium. Animals were subjected to a three-phase diet oscillation as in the experiments described above (unsupplemented → turmeric-supplemented → unsupplemented Bangladeshi diet; 10 days/phase). We hypothesized that if enteric neurons were key mediators of the observed phenotypes, then the difference in transit times seen between wild-type mice colonized with the two different seven-member consortia (Figure 5B) might be mitigated in *Ret*^{+/−} animals. Indeed, in contrast to wild-type mice, transit times were not significantly different between *Ret*^{+/−} mice harboring the two different consortia (Table S2D) despite the same pattern of differences in fecal bile acids concentrations documented by UPLC-MS in wild-type mice: *Ret*^{+/−} mice colonized with the BSH_{lo} consortium had significantly lower fecal concentrations of unconjugated bile acids compared to *Ret*^{+/−} mice colonized with the BSH_{hi} consortium in the setting of turmeric consumption ($p = 0.009$, one-tailed Student's t test). As in wild-type mice, COPRO-seq analysis showed that turmeric consumption had no significant effects on the abundances of any of the bacterial strains in the *Ret*^{+/−} mice. Notably, a significant difference in transit times between *Ret*^{+/−} and wild-type mice was only seen when animals were colonized with the BSH_{hi} bacterial consortium (diet phase 1: $p = 0.009$, phase 2: $p = 0.02$, phase 3: $p = 0.09$, one-tailed Student's t test; $p > 0.05$ in all analogous comparisons of *Ret*^{+/−} versus wild-type mice colonized with the BSH_{lo} consortium). Thus, while turmeric consumption has a cholekinetic effect in both wild-type and *Ret*^{+/−} mice, the transit time phenotype it produces in wild-type mice is mediated by gut microbial bile acid metabolism and a functionally intact ENS.

DISCUSSION

Intestinal motility is a key physiologic parameter impacting nutritional status and gut health. The travel-associated diet changes that we model here are increasingly relevant to our daily lives during this period of rapid globalization, in which a day spent entirely in one's hometown may nonetheless consist of consumption of foods representing several of the world's cultures. A gnotobiotic mouse model of global travel could also incorporate additional factors that impact the gut microbiota, such as disruption of circadian rhythm (Thaiss et al., 2014) or the order in which different diets are experienced. Using gnotobiotic mice colonized with microbiota obtained from healthy individuals representing different geographic and cultural traditions and diets representative of those consumed by these donors, we were able to dissect factors that interact to define a motility

phenotype. These diet-microbiota-metabolic interactions were resolved in the context of Bangladeshi microbiota through a multi-pronged strategy that involved (1) manipulating the dietary representation of a single culturally relevant spice, turmeric; (2) selecting members of a clonally arrayed culture collection generated from a Bangladeshi donor's microbiota, based on whether or not they were able to support BSH-mediated bile acid deconjugation; and (3) colonizing germ-free mice with or without a mutation in *Ret*, a key regulator of ENS function, with a BSH_{hi} or BSH_{lo} consortium.

The simulation of global-travel-associated short-term diet shifts revealed that (1) diet-discriminatory bacterial strains were represented across microbiota from individuals raised in environments that are geographically and culturally distinct and (2) correlations between individual bacterial species abundances and transit times are largely diet dependent, e.g., a given bacterial strain can have contrasting correlations with transit times depending upon the diet context. These findings suggest that future use of bacterial strains derived from the human gut as probiotic agents for motility disorders will require thoughtful consideration of an individual's dietary practices and/or adjunct dietary recommendations. Reciprocally, our preclinical data suggest that dietary treatments for motility disorders need to be calibrated based on structural and functional features of an individual's microbiota. In this respect, we find that unconjugated bile acids resulting from bacterial metabolism are consistently correlated with faster transit times across different diets and microbiota. In patients with irritable bowel syndrome, a limited number of clinical trials have suggested that a subset of patients respond to oral administration of the unconjugated bile acid chenodeoxycholate with accelerated transit times (Odunsi-Shiyanbade et al., 2010; Rao et al., 2010), consistent with our observations. Our results point to fecal BSH activity as a functional microbiota parameter that could be useful for categorizing individuals with motility disorders, allowing correlation analyses to be performed between the levels of its conjugated substrates and/or its various unconjugated bile acid products and transit time. If significantly correlated within a population, this metabolic activity could be used as a target or biomarker in clinical studies testing the effects, both short- and long-term, of various therapeutic interventions.

The imperfect recovery of transit times following consumption of travel diets, initially noted in the context of the six-phase and three-phase travel experiments, was also seen in our experiments involving sequential presentation of an unsupplemented, turmeric-supplemented, and unsupplemented Bangladeshi diet. Across ecosystems, history (i.e., order and temporal features of perturbations) is well known to impact community structure and function (Chase, 2003; Fukami and Morin, 2003; Pagaling et al., 2014). In this context, turmeric may influence alternative stable states (Staver et al., 2011) of the gut microbiota and ENS. Despite our practice of changing bedding between diet phases to limit carryover of ingredients, turmeric may have long-lived effects on host physiology. A sustained increase in total bile acid pool size evoked by turmeric's cholekinetic effects seems an unlikely explanation for these observations, as bile acid concentrations in the final diet phase returned to pre-turmeric levels (Figure 5C). Follow-up experiments examining the duration of

turmeric's effects on the transcriptome of purified enteric neurons (including the TGR5 bile acid receptor; Alemi et al., 2013) in combination with analyses of the microbiota and its metabolic features, localization of motility effects (i.e., gastric, small intestinal, and/or colonic), and production of neuroactive compounds such as serotonin by enteroendocrine cells (Yano et al., 2015) could reveal and help characterize this postulated turmeric-induced alternative stable state.

Other dietary ingredients (e.g., polysaccharides; Kashyap et al., 2013) and products of bacterial metabolism (e.g., butyrate; Soret et al., 2010) have been previously described to impact motility in mouse models. Populations experiencing shifting cultural/culinary traditions through travel, immigration, or emigration are susceptible to marked changes in their gut microbiota, both structural and functional, which may have downstream health consequences. In principle, our approach could be used to identify and characterize the biological activities and microbiota interactions of dietary components characteristic of dietary/cultural traditions established over centuries but now vulnerable to diminished use due to Westernization. Their exclusion from modern diets may represent a loss of key food ingredients that could be used to promote health in contemporary societies. These ingredients may also serve as valuable tools for identifying and characterizing mechanisms by which food and the microbiota interact to affect various features of our physiology.

EXPERIMENTAL PROCEDURES

Measurement of Gastrointestinal Transit Times Using Non-absorbable Red Carmine Dye

Carmine red (Sigma-Aldrich) was prepared as a 6% (w/v) solution in 0.5% methylcellulose (Sigma-Aldrich) and autoclaved prior to import into gnotobiotic isolators. Mice were maintained on a strict 12-hr light cycle (lights on between 06:00 and 18:00) and gavaged with 150 µl of the carmine solution between 08:00 and 08:30 local time. Animals were not fasted beforehand. Feces were collected every 30 min (up to 8 hr from time of gavage) and streaked across a sterile white napkin to assay for the presence of the red carmine dye. The time from gavage to initial appearance of carmine in the feces was recorded as the total intestinal transit time for that animal.

Generating a Clonally Arrayed Culture Collection of Anaerobic Bacterial Strains from the Fecal Microbiota of a Healthy 24-Month-Old Bangladeshi Child

A clonally arrayed culture collection was generated using methods described in an earlier publication (Goodman et al., 2011). A given well of the 96-well plate used to archive the collection contained a monoculture of a single isolate. Each isolate's genome was sequenced using an Illumina MiSeq or HiSeq instrument (250-nt and 101-nt paired end reads, respectively; 53 ± 4.8-fold (mean ± SEM) genome coverage). Genomes were assembled using MIRA (Chevreux et al., 1999) (N50 contig length: 23,253 ± 2,669 bp; range, 735–112,622 bp). Assemblies were annotated using Prokka (version 1.10) (Seemann, 2014). Predicted genes were mapped to KEGG pathways by querying the KEGG reference database (release 72.1) and assigning their protein products to KEGG Ortholog (KO) groups (BLAST 2.2.29+, blastp E-value threshold ≤ 10⁻¹⁰, single best hit defined by E-value and bit score) (Kanehisa and Goto, 2000; Kanehisa et al., 2014). Species-level taxonomic identities of bacterial isolates were defined by Sanger capillary sequencing of full-length 16S rRNA gene amplicons generated using the universal 8F and 1391R PCR primers, with classifications performed using the Ribosomal Database Project (RDP) version 2.4 classifier (Ridaura et al., 2013). Strain-level taxonomic classifications were subsequently determined based on a minimum 96% overall genome sequence identity (calculated by the software package NUCmer; Kurtz et al., 2004) between isolates bearing the same 16S rRNA-based taxonomy. A total of 53 unique strains

were identified using this 96% identity cutoff threshold and grown in modified gut microbiota medium (mGMM) containing ingredients described in a previous publication (Goodman et al., 2011) but without short-chain fatty acid supplementation. Strains were stored at -80°C in 15% glycerol (v/v) in reduced PBS until used for gavage of germ-free mice.

In Vitro Assays for Bile Acid Deconjugation

We screened each of the 91 isolates, comprising 53 strains, in the clonally arrayed culture collection for their capacity to deconjugate bile acids. The two predominant primary bile acids in mice, taurocholic acid (TCA; Sigma-Aldrich) and tauro-beta-muricholic acid (TbMCA; Santa Cruz Biotechnology), were dissolved in water at concentrations of 100 mg/ml and 10 mg/ml, respectively. Each isolate was first incubated in 1 ml mGMM containing 100 μM TCA for 48 hr in an anaerobic Coy chamber (75% N_2 , 20% CO_2 , and 5% H_2) with growth monitored based on optical densities at 600 nm (OD_{600}). Cells were then pelleted by centrifugation ($17,900 \times g$ for 7 min at 4°C), and the resulting supernatant was subjected to UPLC-MS (see *Supplemental Experimental Procedures*) to assess levels (peak intensities) of unconjugated and conjugated bile acids (cholic acid and TCA, respectively). For the vast majority of isolates, bile acid profiles at 48 hr were either all conjugated or unconjugated. Growth of bacterial isolates was simultaneously assessed by measuring OD_{600} to ensure that a lack of deconjugation was not simply a reflection of a lack of bacterial viability. If no deconjugation was observed, we performed a secondary screen where isolates were incubated in 1 ml mGMM containing 100 μM TbMCA for 48 hr in an anaerobic chamber, followed by UPLC-MS quantitation of the levels of unconjugated (beta-muricholic acid) and conjugated (TbMCA) bile acids. Bacterial isolates that did not deconjugate either bile acid in vitro were considered as eligible for the BSH_{io} consortium. See *Supplemental Experimental Procedures* for additional protocols.

ACCESSION NUMBERS

The study accession number for the bacterial V4-16S rRNA amplicon datasets, whole-genome shotgun sequencing datasets from cultured bacterial strains, and microbial and host RNA-seq datasets reported in this paper is ENA: PRJEB9169.

SUPPLEMENTAL INFORMATION

Supplemental Information includes Supplemental Experimental Procedures, two figures, and eight tables and can be found with this article online at <http://dx.doi.org/10.1016/j.cell.2015.08.059>.

AUTHOR CONTRIBUTIONS

N.D., L.V.B., J.C., and J.I.G. designed the experiments; N.D., V.E.W., L.V.B., and J.C. generated the data; V.E.W. generated the clonally arrayed bacterial culture collection; L.F. provided microbiota samples and dietary data from primal dieters; T.A. and R.H. provided microbiota samples and dietary data from Bangladeshi individuals; and N.D. and J.I.G. analyzed the data and wrote the paper.

ACKNOWLEDGMENTS

We are grateful to Robert Heuckeroth (University of Pennsylvania) for generously providing *Ret*^{+/−} mice; Maria Gloria Dominguez-Bello (New York University) for her leadership in obtaining fecal samples from Amerindians in an earlier collaborative study; Andreea Soare for her assistance in obtaining fecal samples and diet records from individuals consuming a primal diet; David O'Donnell and Maria Karlsson for their assistance with gnotobiotic husbandry; Sabrina Wagoner, Janaki Lelwala-Guruge, Martin Meier, and Jessica Hoisington-Lopez for their invaluable technical assistance; and Vanessa Ridaura, Sathish Subramanian, Ansel Hsiao, Matthew Hibberd, Nicholas Griffin, Nathan McNulty, Philip Ahern, and other members of the Gordon lab for their helpful suggestions. This work was supported by grants from the NIH (DK30292, DK70977, DK078669, and P30 DK052574), the Bill and Melinda Gates Foun-

dation, and the Crohn's and Colitis Foundation of America. N.D. is the recipient of a Young Investigator Grant for Probiotics Research from the Global Probiotics Council. J.I.G. is cofounder of Matatu Inc., a company characterizing the role of diet-by-microbiota interactions in animal health.

Received: April 21, 2015

Revised: July 20, 2015

Accepted: August 17, 2015

Published: September 24, 2015

REFERENCES

- Alemi, F., Poole, D.P., Chiu, J., Schoonjans, K., Cattaruzza, F., Grider, J.R., Bunnett, N.W., and Corvera, C.U. (2013). The receptor TGR5 mediates the prokinetic actions of intestinal bile acids and is required for normal defecation in mice. *Gastroenterology* **144**, 145–154.
- Artis, D., Wang, M.L., Keilbaugh, S.A., He, W., Brenes, M., Swain, G.P., Knight, P.A., Donaldson, D.D., Lazar, M.A., Miller, H.R.P., et al. (2004). RELM β /FIZZ2 is a goblet cell-specific immune-effector molecule in the gastrointestinal tract. *Proc. Natl. Acad. Sci. USA* **101**, 13596–13600.
- Burkitt, D.P., Walker, A.R.P., and Painter, N.S. (1972). Effect of dietary fibre on stools and the transit-times, and its role in the causation of disease. *Lancet* **2**, 1408–1412.
- Chase, J.M. (2003). Community assembly: when should history matter? *Oecologia* **136**, 489–498.
- Chevreux, B., Wetter, T., and Suhai, S. (1999). Genome sequence assembly using trace signals and additional sequence information. *Comput. Sci. Biol. Proc. Ger. Conf. Bioinforma. GCB* **99**, 45–56.
- Cummings, J.H., Jenkins, D.J., and Wiggins, H.S. (1976). Measurement of the mean transit time of dietary residue through the human gut. *Gut* **17**, 210–218.
- Cummings, J.H., Wiggins, H.S., Jenkins, D.J., Houston, H., Jivraj, T., Drasar, B.S., and Hill, M.J. (1978). Influence of diets high and low in animal fat on bowel habit, gastrointestinal transit time, fecal microflora, bile acid, and fat excretion. *J. Clin. Invest.* **61**, 953–963.
- Drasar, B.S., Hill, M.J., and Shiner, M. (1966). The deconjugation of bile salts by human intestinal bacteria. *Lancet* **1**, 1237–1238.
- Edery, P., Lyonnet, S., Mulligan, L.M., Pelet, A., Dow, E., Abel, L., Holder, S., Nihoul-Fékété, C., Ponder, B.A., and Munnich, A. (1994). Mutations of the RET proto-oncogene in Hirschsprung's disease. *Nature* **367**, 378–380.
- Falany, C.N., Johnson, M.R., Barnes, S., and Diasio, R.B. (1994). Glycine and taurine conjugation of bile acids by a single enzyme. Molecular cloning and expression of human liver bile acid CoA:amino acid N-acyltransferase. *J. Biol. Chem.* **269**, 19375–19379.
- Falany, C.N., Fortinberry, H., Leiter, E.H., and Barnes, S. (1997). Cloning, expression, and chromosomal localization of mouse liver bile acid CoA:amino acid N-acyltransferase. *J. Lipid Res.* **38**, 1139–1148.
- Fukami, T., and Morin, P.J. (2003). Productivity-biodiversity relationships depend on the history of community assembly. *Nature* **424**, 423–426.
- Geiger, T.L., Abt, M.C., Gasteiger, G., Firth, M.A., O'Connor, M.H., Geary, C.D., O'Sullivan, T.E., van den Brink, M.R., Pamer, E.G., Hanash, A.M., and Sun, J.C. (2014). Nfil3 is crucial for development of innate lymphoid cells and host protection against intestinal pathogens. *J. Exp. Med.* **211**, 1723–1731.
- Gianino, S., Grider, J.R., Cresswell, J., Enomoto, H., and Heuckeroth, R.O. (2003). GDNF availability determines enteric neuron number by controlling precursor proliferation. *Development* **130**, 2187–2198.
- Goodman, A.L., Kallstrom, G., Faith, J.J., Reyes, A., Moore, A., Dantas, G., and Gordon, J.I. (2011). Extensive personal human gut microbiota culture collections characterized and manipulated in gnotobiotic mice. *Proc. Natl. Acad. Sci. USA* **108**, 6252–6257.
- Goto, Y., Obata, T., Kunisawa, J., Sato, S., Ivanov, I.I., Lamichhane, A., Takeyama, N., Kamioka, M., Sakamoto, M., Matsuki, T., et al. (2014). Innate lymphoid cells regulate intestinal epithelial cell glycosylation. *Science* **345**, 1254009.

Handral, H.K., Duggi, S., Handral, R., Tulsianand, G., and Shruthi, S.D. (2013). Turmeric: nature's precious medicine. *Asian J. Pharm. Clin. Res.* 6, 10–16.

Haslewood, G.A. (1967). Bile salt evolution. *J. Lipid Res.* 8, 535–550.

Herbert, D.R., Yang, J.-Q., Hogan, S.P., Groschwitz, K., Khodoun, M., Munitz, A., Orekov, T., Perkins, C., Wang, Q., Brombacher, F., et al. (2009). Intestinal epithelial cell secretion of RELM-beta protects against gastrointestinal worm infection. *J. Exp. Med.* 206, 2947–2957.

Hogan, S.P., Seidu, L., Blanchard, C., Groschwitz, K., Mishra, A., Karow, M.L., Ahrens, R., Artis, D., Murphy, A.J., Valenzuela, D.M., et al. (2006). Resistin-like molecule β regulates innate colonic function: barrier integrity and inflammation susceptibility. *J. Allergy Clin. Immunol.* 118, 257–268.

Hurd, E.A., and Domino, S.E. (2004). Increased susceptibility of secretor factor gene *Fut2*-null mice to experimental vaginal candidiasis. *Infect. Immun.* 72, 4279–4281.

Husebye, E., Hellström, P.M., and Midtvedt, T. (1994). Intestinal microflora stimulates myoelectric activity of rat small intestine by promoting cyclic initiation and aboral propagation of migrating myoelectric complex. *Dig. Dis. Sci.* 39, 946–956.

Husebye, E., Hellström, P.M., Sundler, F., Chen, J., and Midtvedt, T. (2001). Influence of microbial species on small intestinal myoelectric activity and transit in germ-free rats. *Am. J. Physiol. Gastrointest. Liver Physiol.* 280, G368–G380.

Kanehisa, M., and Goto, S. (2000). KEGG: kyoto encyclopedia of genes and genomes. *Nucleic Acids Res.* 28, 27–30.

Kanehisa, M., Goto, S., Sato, Y., Kawashima, M., Furumichi, M., and Tanabe, M. (2014). Data, information, knowledge and principle: back to metabolism in KEGG. *Nucleic Acids Res.* 42, D199–D205.

Kashyap, P.C., Marcabal, A., Ursell, L.K., Larauche, M., Duboc, H., Earle, K.A., Sonnenburg, E.D., Ferreyra, J.A., Higginbottom, S.K., Million, M., et al. (2013). Complex interactions among diet, gastrointestinal transit, and gut microbiota in humanized mice. *Gastroenterology* 144, 967–977.

Klose, C.S.N., Flach, M., Möhle, L., Rogell, L., Hoyler, T., Ebert, K., Fabiunke, C., Pfeifer, D., Sexl, V., Fonseca-Pereira, D., et al. (2014). Differentiation of type 1 ILCs from a common progenitor to all helper-like innate lymphoid cell lineages. *Cell* 157, 340–356.

Knott, M.L., Matthaei, K.I., Giacomin, P.R., Wang, H., Foster, P.S., and Dent, L.A. (2007). Impaired resistance in early secondary *Nippostrongylus brasiliensis* infections in mice with defective eosinophilopoeisis. *Int. J. Parasitol.* 37, 1367–1378.

Kurtz, S., Phillippe, A., Delcher, A.L., Smoot, M., Shumway, M., Antonescu, C., and Salzberg, S.L. (2004). Versatile and open software for comparing large genomes. *Genome Biol.* 5, R12.

Levy, R.L., Whitehead, W.E., Von Korff, M.R., and Feld, A.D. (2000). Intergenerational transmission of gastrointestinal illness behavior. *Am. J. Gastroenterol.* 95, 451–456.

Li, Z., Chalazonitis, A., Huang, Y.Y., Mann, J.J., Margolis, K.G., Yang, Q.M., Kim, D.O., Côté, F., Mallet, J., and Gershon, M.D. (2011). Essential roles of enteric neuronal serotonin in gastrointestinal motility and the development/survival of enteric dopaminergic neurons. *J. Neurosci.* 31, 8998–9009.

Lozupone, C., and Knight, R. (2005). UniFrac: a new phylogenetic method for comparing microbial communities. *Appl. Environ. Microbiol.* 71, 8228–8235.

Marciani, L., Cox, E.F., Hoad, C.L., Totman, J.J., Costigan, C., Singh, G., Shepherd, V., Chalkley, L., Robinson, M., Ison, R., et al. (2013). Effects of various food ingredients on gall bladder emptying. *Eur. J. Clin. Nutr.* 67, 1182–1187.

McVay, L.D., Keilbaugh, S.A., Wong, T.M.H., Kierstein, S., Shin, M.E., Lehrke, M., Leferova, M.I., Shifflett, D.E., Barnes, S.L., Cominelli, F., et al. (2006). Absence of bacterially induced RELM β reduces injury in the dextran sodium sulfate model of colitis. *J. Clin. Invest.* 116, 2914–2923.

Nadkarni, K.M., and Nadkarni, A.K. (1976). Indian Materia Medica (Popular Prakashan).

Odunsi-Shiyanbade, S.T., Camilleri, M., McKinzie, S., Burton, D., Carlson, P., Busciglio, I.A., Lamsam, J., Singh, R., and Zinsmeister, A.R. (2010). Effects of chenodeoxycholate and a bile acid sequestrant, colestevam, on intestinal transit and bowel function. *Clin. Gastroenterol. Hepatol.* 8, 159–165.

Oliphant, C.J., Hwang, Y.Y., Walker, J.A., Salimi, M., Wong, S.H., Brewer, J.M., Englezakis, A., Barlow, J.L., Hams, E., Scanlon, S.T., et al. (2014). MHCII-mediated dialog between group 2 innate lymphoid cells and CD4(+) T cells potentiates type 2 immunity and promotes parasitic helminth expulsion. *Immunity* 41, 283–295.

Pagaling, E., Strathdee, F., Spears, B.M., Cates, M.E., Allen, R.J., and Free, A. (2014). Community history affects the predictability of microbial ecosystem development. *ISME J.* 8, 19–30.

Rao, A.S., Wong, B.S., Camilleri, M., Odunsi-Shiyanbade, S.T., McKinzie, S., Ryks, M., Burton, D., Carlson, P., Lamsam, J., Singh, R., et al. (2010). Cheno-deoxycholate in females with irritable bowel syndrome-constipation: a pharmacodynamic and pharmacogenetic analysis. *Gastroenterology* 139, 1549–1558.e1.

Rasyid, A., and Lelo, A. (1999). The effect of curcumin and placebo on human gall-bladder function: an ultrasound study. *Aliment. Pharmacol. Ther.* 13, 245–249.

Rasyid, A., Rahman, A.R.A., Jaalam, K., and Lelo, A. (2002). Effect of different curcumin dosages on human gall bladder. *Asia Pac. J. Clin. Nutr.* 11, 314–318.

Ridaura, V.K., Faith, J.J., Rey, F.E., Cheng, J., Duncan, A.E., Kau, A.L., Griffin, N.W., Lombard, V., Henrissat, B., Bain, J.R., et al. (2013). Gut microbiota from twins discordant for obesity modulate metabolism in mice. *Science* 341, 1241214.

Romeo, G., Ronchetto, P., Luo, Y., Barone, V., Seri, M., Ceccherini, I., Pasini, B., Bocciardi, R., Lerone, M., Kääriäinen, H., et al. (1994). Point mutations affecting the tyrosine kinase domain of the RET proto-oncogene in Hirschsprung's disease. *Nature* 367, 377–378.

Roy, E., Hasan, K.Z., Haque, R., Haque, A.F., Siddique, A.K., and Sack, R.B. (2011). Patterns and risk factors for helminthiasis in rural children aged under 2 in Bangladesh. *South Afr. J. Child Health* 5, 78–84.

Seemann, T. (2014). Prokka: rapid prokaryotic genome annotation. *Bioinformatics* 30, 2068–2069.

Shimouchi, A., Nose, K., Takaoka, M., Hayashi, H., and Kondo, T. (2009). Effect of dietary turmeric on breath hydrogen. *Dig. Dis. Sci.* 54, 1725–1729.

Soret, R., Chevalier, J., De Copet, P., Poupeau, G., Derkinderen, P., Segain, J.P., and Neunlist, M. (2010). Short-chain fatty acids regulate the enteric neurons and control gastrointestinal motility in rats. *Gastroenterology* 138, 1772–1782.

Staver, A.C., Archibald, S., and Levin, S. (2011). Tree cover in sub-Saharan Africa: rainfall and fire constrain forest and savanna as alternative stable states. *Ecology* 92, 1063–1072.

Steinbrecher, K.A., Harmel-Laws, E., Garin-Laflam, M.P., Mann, E.A., Bezerra, L.D., Hogan, S.P., and Cohen, M.B. (2011). Murine guanylate cyclase C regulates colonic injury and inflammation. *J. Immunol.* 186, 7205–7214.

Subramanian, S., Huq, S., Yatsunenko, T., Haque, R., Mahfuz, M., Alam, M.A., Benzeira, A., DeStefano, J., Meier, M.F., Muegge, B.D., et al. (2014). Persistent gut microbiota immaturity in malnourished Bangladeshi children. *Nature* 510, 417–421.

Thaissa, C.A., Zeevi, D., Levy, M., Zilberman-Schapira, G., Suez, J., Tengeler, A.C., Abramson, L., Katz, M.N., Korem, T., Zmora, N., et al. (2014). Transkingdom control of microbiota diurnal oscillations promotes metabolic homeostasis. *Cell* 159, 514–529.

Tong, M., McHardy, I., Ruegger, P., Goudarzi, M., Kashyap, P.C., Haritunians, T., Li, X., Graeber, T.G., Schwager, E., Huttenhower, C., et al. (2014). Reprogramming of gut microbiome energy metabolism by the FUT2 Crohn's disease risk polymorphism. *ISME J.* 8, 2193–2206.

Tsuzuki, T., Takahashi, M., Asai, N., Iwashita, T., Matsuyama, M., and Asai, J. (1995). Spatial and temporal expression of the ret proto-oncogene product in embryonic, infant and adult rat tissues. *Oncogene* 10, 191–198.

Whorwell, P.J., McCallum, M., Creed, F.H., and Roberts, C.T. (1986). Non-colonic features of irritable bowel syndrome. *Gut* 27, 37–40.

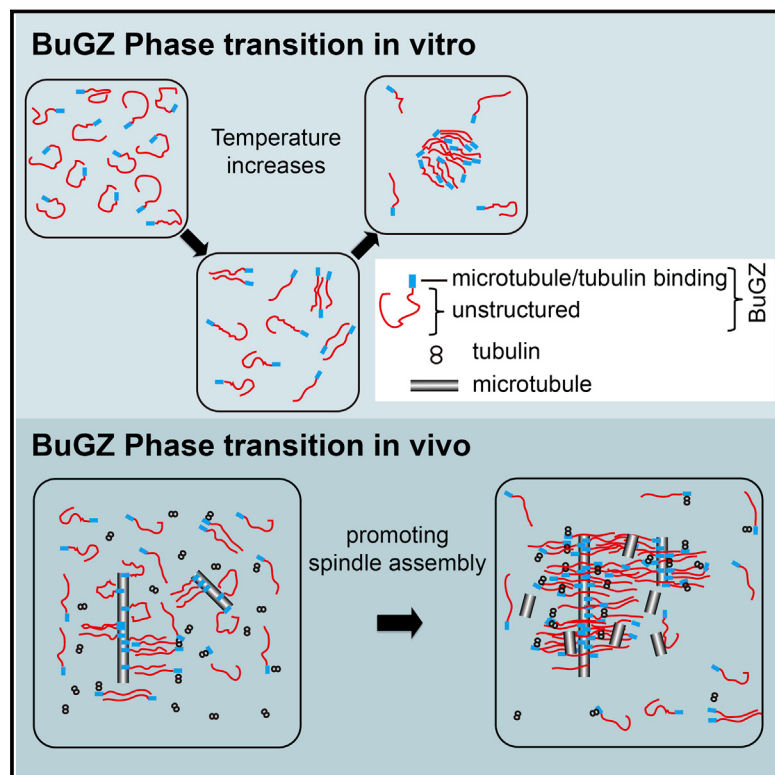
Wichmann, A., Allahyar, A., Greiner, T.U., Plovier, H., Lundén, G.Ö., Larsson, T., Drucker, D.J., Delzenne, N.M., Cani, P.D., and Bäckhed, F. (2013). Microbial modulation of energy availability in the colon regulates intestinal transit. *Cell Host Microbe* 14, 582–590.

Yano, J.M., Yu, K., Donaldson, G.P., Shastri, G.G., Ann, P., Ma, L., Nagler, C.R., Ismagilov, R.F., Mazmanian, S.K., and Hsiao, E.Y. (2015). Indigenous bacteria from the gut microbiota regulate host serotonin biosynthesis. *Cell* 161, 264–276.

Yatsunenko, T., Rey, F.E., Manary, M.J., Trehan, I., Dominguez-Bello, M.G., Contreras, M., Magris, M., Hidalgo, G., Baldassano, R.N., Anokhin, A.P., et al. (2012). Human gut microbiome viewed across age and geography. *Nature* 486, 222–227.

Phase Transition of Spindle-Associated Protein Regulate Spindle Apparatus Assembly

Graphical Abstract



Authors

Hao Jiang, Shusheng Wang,
Yuejia Huang, ..., Honggang Cui,
Xueliang Zhu, Yixian Zheng

Correspondence

xlzhu@sibcb.ac.cn (X.Z.),
zheng@ciwemb.edu (Y.Z.)

In Brief

A protein associated with the mitotic spindle must undergo a phase transition to promote microtubule polymerization and spindle assembly, suggesting that the biophysical properties associated with liquid demixing may shape the characteristics of a hypothesized but elusive spindle matrix.

Highlights

- The spindle regulator BuGZ undergoes temperature-dependent phase transition
- Phase transition of BuGZ relies on the aromatic and hydrophobic Phe and Tyr
- BuGZ droplets promote microtubule polymerization
- Phase transition of BuGZ promotes assembly of spindle and its matrix

Phase Transition of Spindle-Associated Protein Regulate Spindle Apparatus Assembly

Hao Jiang,^{1,2,4} Shusheng Wang,^{2,4} Yuejia Huang,² Xiaonan He,¹ Honggang Cui,³ Xueliang Zhu,^{1,*} and Yixian Zheng^{2,*}

¹State Key Laboratory of Cell Biology, CAS Center for Excellence in Molecular Cell Science, Institute of Biochemistry and Cell Biology, Shanghai Institutes for Biological Sciences, Chinese Academy of Sciences, 320 Yueyang Road, Shanghai 200031, China

²Department of Embryology, Carnegie Institution for Science, 3520 San Martin Drive, Baltimore, MD 21218, USA

³Department of Chemical and Biomolecular Engineering and Institute for NanoBioTechnology, Johns Hopkins University, 3400 North Charles Street, Baltimore, MD 21218, USA

⁴Co-first author

*Correspondence: xlzhu@sibcb.ac.cn (X.Z.), zheng@ciwemb.edu (Y.Z.)

<http://dx.doi.org/10.1016/j.cell.2015.08.010>

SUMMARY

Spindle assembly required during mitosis depends on microtubule polymerization. We demonstrate that the evolutionarily conserved low-complexity protein, BuGZ, undergoes phase transition or coacervation to promote assembly of both spindles and their associated components. BuGZ forms temperature-dependent liquid droplets alone or on microtubules in physiological buffers. Coacervation *in vitro* or in spindle and spindle matrix depends on hydrophobic residues in BuGZ. BuGZ coacervation and its binding to microtubules and tubulin are required to promote assembly of spindle and spindle matrix in *Xenopus* egg extract and in mammalian cells. Since several previously identified spindle-associated components also contain low-complexity regions, we propose that coacervating proteins may be a hallmark of proteins that comprise a spindle matrix that functions to promote assembly of spindles by concentrating its building blocks.

INTRODUCTION

Since the discovery of spindle apparatus in the 1800s (Lukács, 1981), much attention has focused on how microtubules (MT) interact with chromosomes to ensure equal partitioning of chromosomes into daughter cells. Investigation of the mechanisms by which MTs and MT-associated proteins regulate mitosis (Walczak et al., 2010) is fueled by the ease of visualizing the spindle-shaped MT fibers, the disruption of chromosome segregation and cell division upon MT perturbation, and the discovery of tubulin (Oakley, 2000). In addition to spindle MTs, a set of material that surrounds and permeates spindle MTs have periodically drawn attention (Goldman and Rebhun, 1969; Schibler and Pickett-Heaps, 1980; Scholey et al., 2001; Johansen and Johansen, 2007; Johansen et al., 2011; Leslie et al., 1987; Pickett-Heaps et al., 1984; Pickett-Heaps and Forer, 2009; Schweizer et al., 2014; Wein et al., 1998; Zheng, 2010; Zheng and Tsai, 2006).

Historically, this ill-defined spindle-associated material has been referred to as spindle matrix. One vague but generally

accepted feature of spindle matrix is that it retains some integrity upon MT disassembly. Based on this criterion, several spindle matrix proteins have been identified and studied in the context of spindle assembly and chromosome segregation. For example, among the *Drosophila* spindle matrix proteins (Fabian et al., 2007; Johansen et al., 2011; Qi et al., 2004, 2005; Rath et al., 2004; Walker et al., 2000; Yao et al., 2012, 2014), Megator regulates spindle assembly checkpoints (SAC) (Lince-Faria et al., 2009). A conserved protein, BuGZ, which was identified as part of the lamin-B (LB) spindle matrix in *Xenopus* (Tsai et al., 2006; Ma et al., 2009), has recently been shown to facilitate chromosome alignment by controlling both stability and kinetochore loading of the SAC component Bub3 (Jiang et al., 2014; Toledo et al., 2014). Additionally, LB (Tsai et al., 2006) and poly ADP-ribose (Chang et al., 2004), along with other spindle assembly factors (SAFs), such as dynein, Nudel, NuMA, and kinesin Eg5 (Civelekoglu-Scholey et al., 2010; Goodman et al., 2010; Ma et al., 2009; Tsai et al., 2006), may regulate spindle morphogenesis. Despite these studies, the structural nature of the spindle matrix remains undefined and whether it constitutes a cohesive functional unit is unclear. In fact, some modeling and biophysical probing of spindle apparatus have not provided evidence for the existence of spindle matrix (Brugués and Needleman, 2014; Gatlin et al., 2010; Shimamoto et al., 2011). Thus, whether spindle matrix is a real structural element of spindle apparatus or a mere artifact induced upon depolymerization of spindle MTs remains an open question.

Unlike membranous organelles, the spindle apparatus is not surrounded by membrane barrier during vertebrate mitosis. However, spindles may need to concentrate many components in order to support spatially and temporally diverse reactions. Consistently, tubulin and some SAFs are shown to be concentrated in the region where nascent spindle begins to assemble in *Caenorhabditis elegans* embryos (Hayashi et al., 2012). This concentration process is independent of MTs but it requires nuclear envelope permeabilization and RanGTPase, which stimulates spindle assembly (Kalab et al., 1999; Ohba et al., 1999; Wilde and Zheng, 1999).

Proteins, such as elastin and elastin-like peptides, can undergo liquid-liquid phase transition or coacervation to form liquid droplets (Yeo et al., 2011). The phase separation has been proposed to promote concentration of molecules into the liquid droplets, which can then facilitate biochemical reactions

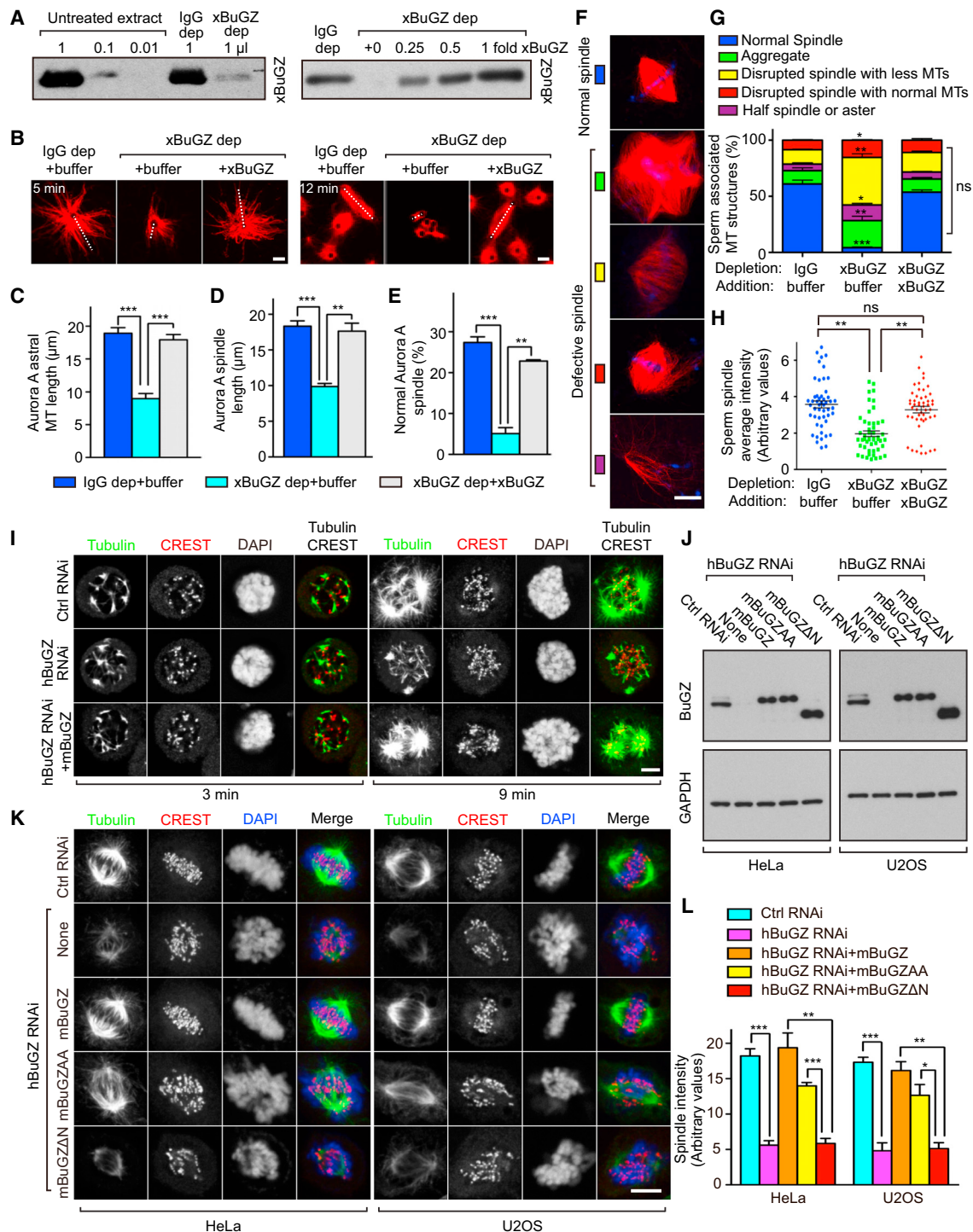


Figure 1. BuGZ Promotes Spindle Assembly Independent of Kinetochores

(A) Western blotting of xBuGZ depletion (left) and add-back (right) in extracts. xBuGZ depletion (dep) efficiency and xBuGZ addition are shown in titrations. (B–E) Representative images (B) show that xBuGZ depletion reduced astral MT length, bipolar spindle formation and length, which were all rescued by His-xBuGZ. Approximately 50 (C and D) or 500 (E) structures were measured in each experiment and condition. White dashed lines in (B) indicate Aurora A spindle length and longest astral MTs measured. (F–H) xBuGZ depletion caused multiple sperm spindle defects (F), which was rescued by His-xBuGZ (G and H). Approximately 500 (G) and 50 (H) structures were analyzed in each experiment and condition.

(legend continued on next page)

([Hyman et al., 2014](#)). Indeed, the liquid droplet feature of P granules and nucleoli is consistent with the idea that assembly and function of these non-membranous organelles could be driven by the phase transition of some of their structural components ([Brangwynne et al., 2009, 2011](#)). No proteins of these organelles, however, have yet been shown to undergo functionally relevant phase transition. Interestingly, when engineered as multiple tandem repeats, SRC homology 3 (SH3) domains of NCK and proline-rich motif (PRM) of N-WASP form multivalent interactions, which allow the protein mixture to undergo phase transition to form liquid droplets. These droplets concentrate actin to promote F-actin assembly *in vitro* ([Li et al., 2012](#)). Despite the observed *in vitro* phase transition into liquid droplets, proteins have been shown to function *in vivo* via phase transition.

Here, we examine the spindle regulatory protein BuGZ, which we noted contains evolutionarily conserved low complexity sequence, and demonstrate that it forms a MT-independent structure through temperature- and hydrophobic residue-dependent coacervation. This phase transition property allows the concentration of tubulin along MTs and supports assembly of spindle MTs and of the biochemically defined spindle matrix structure. Based on these results, we propose a model and line of investigation for further developing our understanding of observed properties and possible functions of spindle matrix.

RESULTS

BuGZ Promotes Assembly of Spindle Apparatus

Our previous studies show that BuGZ binds MTs to promote kinetochore loading of Bub3 and chromosome alignment ([Jiang et al., 2014](#)). We noticed that human BuGZ (hBuGZ) depletion in HeLa cells resulted in a more severe disruption of spindle morphology and reduction of MT intensity than those depleted of Bub3, especially when RNAi treatment was extended to 72 hr ([Figures S1A and S1B](#)). The more severe spindle defects in hBuGZ-depleted cells were consistent with a stronger chromosome misalignment than those depleted of hBub3 ([Figure S1C](#)). This suggests that BuGZ could directly regulate spindle assembly independent of Bub3's kinetochore function.

Previously, we developed a bead-based spindle assembly assay ([Tsai and Zheng, 2005](#)) by tethering the mitotic kinase Aurora A to 2.8-μm magnetic beads via antibodies. These beads function as MT organizing centers to induce efficient spindle assembly in the cytostatic factor (CSF) arrested *Xenopus* egg extract (referred to as extract below) in the presence of RanGTP. Since spindles induced by Aurora A beads and RanGTP do not have chromosomes and kinetochores, we can test the kinetochore-independent function of BuGZ in spindle assembly. Immunodepletion of *Xenopus* BuGZ (xBuGZ) by ~90% ([Figure 1A](#)) resulted in a significant reduction of astral MT length and bipolar

spindle numbers ([Figures 1B, 1C, and 1E](#)). Most bipolar spindles formed in the absence of xBuGZ were also significantly shorter than those of controls ([Figure 1D](#)). These defects were fully rescued by purified xBuGZ ([Figures 1A–E](#)). xBuGZ depletion also disrupted spindle assembly induced by sperm chromatin. Major phenotypes included spindles with MT aggregates surrounding sperm chromatin or spindles with reduced MTs, followed by asters, half spindles, or abnormal spindle shapes with normal MT density ([Figures 1F–1H](#)), and all of the defects were also rescued by purified xBuGZ ([Figures 1F–1H](#)). Thus BuGZ promotes spindle assembly independent of its kinetochore function.

BuGZ-MT Interaction Promotes Spindle Assembly

To understand how BuGZ promotes spindle assembly, we treated HeLa cells with control or hBuGZ siRNA and then depolymerized MTs in the cold. MT regrowth was examined after returning cells to 37°C. hBuGZ depletion greatly reduced astral MT regrowth, which was rescued by expressing the RNAi-insensitive wild-type mouse BuGZ (mBuGZ, [Figures 1I and 1J](#)). The N-terminal 92 amino acids of BuGZ bind directly to MTs, while the Gle2-binding sequence (GLEBS) within the C terminus of BuGZ directly binds and stabilizes Bub3 ([Jiang et al., 2014](#)). Replacing the two highly conserved glutamic acids (E) in GLEBS with alanine (A) results in a mutant (mBuGZAA) that fails to bind and stabilize Bub3, while mBuGZΔN lacking the N-terminal 92 amino acids does not bind to spindles *in vivo* and MTs *in vitro* ([Jiang et al., 2014](#)). The wild-type mBuGZ and mBuGZAA bound to spindle MTs and MTs assembled from pure tubulin ([Figures S1D–S1F](#)). To analyze which of these two known domains in BuGZ promotes assembly of spindle, we depleted endogenous hBuGZ from HeLa or U2OS cells by RNAi. BuGZ RNAi-induced spindle defects, judged by spindle MT intensity, were rescued fully by wild-type mBuGZ and partially by mBuGZAA, but not by mBuGZΔN ([Figures 1J–1L](#)). hBuGZ depletion did not alter interphase MT densities ([Figure S1G](#)). Thus MT binding of BuGZ promotes spindle MT assembly.

Spindle Matrix Assembly and Stability Require BuGZ and a Physiological Temperature

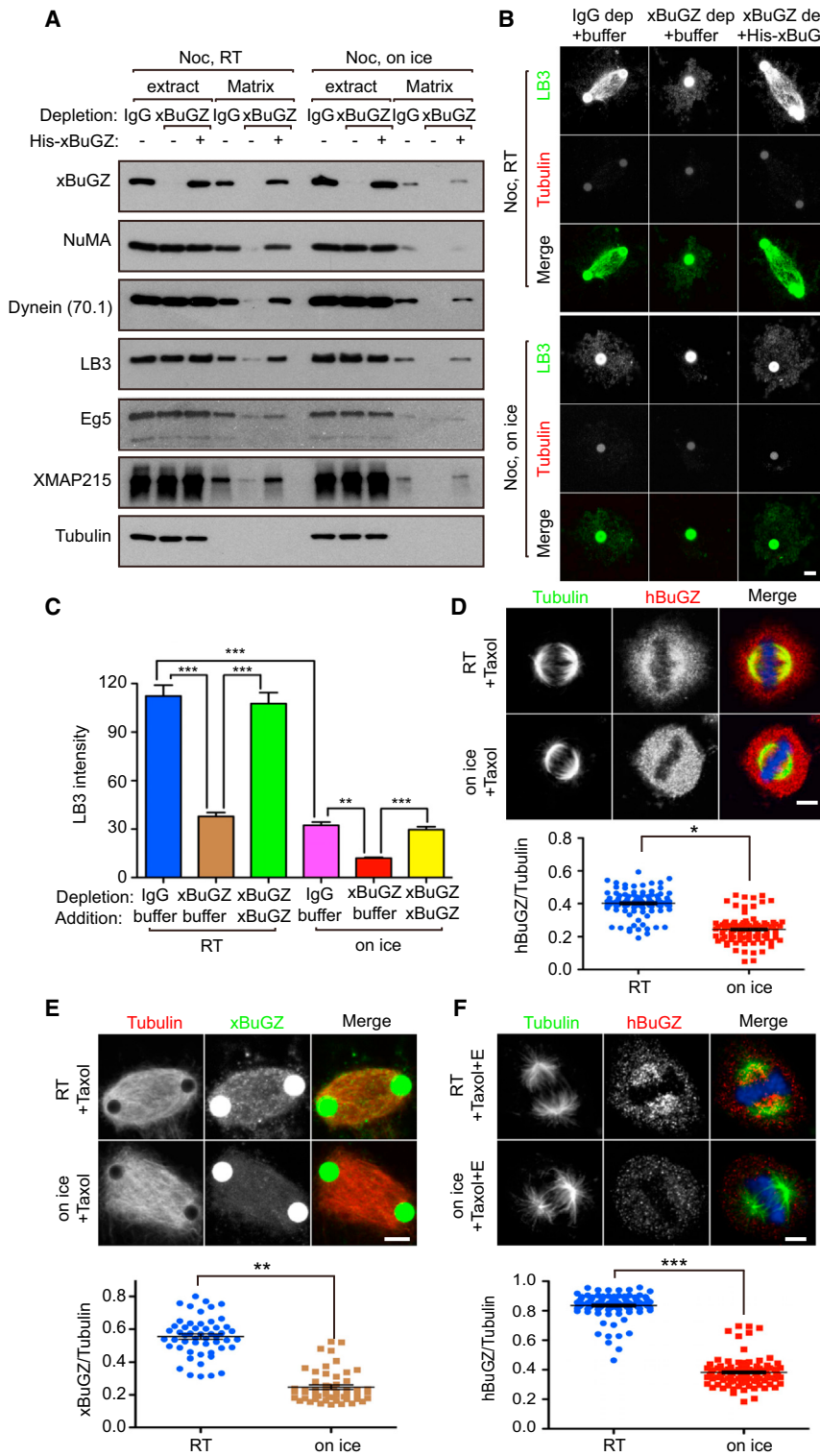
Since BuGZ was identified as a spindle matrix component, we assayed for spindle matrix by assembling Aurora A-bead spindles in extract and then depolymerizing MTs using nocodazole at room temperature (RT) ([Ma et al., 2009; Tsai et al., 2006](#)). The nocodazole-insensitive material that remains on the Aurora A beads, i.e., the spindle matrix, was isolated using a magnet and analyzed by western blotting or immunostaining probing known spindle matrix markers, lamin-B3 (LB3, the major lamin in extracts), dynein, Eg5, NuMA, and XMAP215 ([Ma et al., 2009; Tsai et al., 2006](#)). Depleting xBuGZ greatly diminished recovery of the spindle matrix, but this was rescued by purified xBuGZ (see the Noc, RT panels in [Figures 2A–2C](#)). Although

(I) hBuGZ depletion reduced astral MT re-growth in mitotic HeLa cells and was rescued by mBuGZ. Cold-treated cells were examined at 3 or 9 min after returning to 37°C. MTs, centromeres, and chromosomes were stained by tubulin antibody, CREST serum, and DAPI, respectively.

(J) Western blotting analyses of HeLa and U2OS cells treated by hBuGZ siRNA and transfected with indicated plasmids.

(K and L) HeLa or U2OS images (K) show that hBuGZ depletion by 72 hr of RNAi diminished MT intensity in spindles and was rescued fully by mBuGZ, partially by mBuGZAA, but not by mBuGZΔN. Cells were blocked with 10 μM MG132 for 1 hr before immunostaining. Approximately 30 cells were measured for each experiment and condition (L).

Error bars, SEM. Student's t test: *p < 0.05, **p < 0.01, ***p < 0.001, three independent experiments. Scale bars, 5 μm. See also [Figure S1](#).



xBuGZ depletion diminished the recovery of LB3, depleting LB3 did not affect association of xBuGZ with the spindle matrix (Figure S2A). Thus, BuGZ may function upstream of LB3 to promote spindle matrix assembly.

Figure 2. Effects of BuGZ and Temperature on Spindle Matrix

(A–C) Both BuGZ and temperature influenced spindle matrix assembly. Spindle matrices were prepared with or without xBuGZ after nocodazole (Noc) treatment at RT or on ice and assayed by western blotting (A) or immunostaining (B) using indicated markers. Tubulin, negative control. LB3 intensity of ~30 spindle matrices associated with one or two beads was quantified (C). Less spindle matrix was present in the cold than at RT. Green Aurora A beads appear larger than 2.8 μ m due to secondary anti-rabbit antibody staining.

(D) Taxol-treated HeLa cells were incubated at RT or on ice. Metaphase cells were visualized by immunostaining with tubulin (green), hBuGZ (red) and DAPI (blue). Approximately 100 cells were quantified for each condition.

(E) Treatment of Taxol-stabilized Aurora A spindles on ice for 5 min diminished xBuGZ signal on spindles visualized by fluorescein-labeled MTs (red) and xBuGZ immunostaining (green). Approximately 50 spindles were quantified for each condition.

(F) Extraction of Taxol-stabilized and cold-treated metaphase spindles in HeLa cells diminished hBuGZ signal on spindles compared to RT extraction. Metaphase cells shown were immunostained using tubulin and hBuGZ antibodies and DAPI. Approximately 100 cells were quantified for each condition. Error bars, SEM. Student's t test: p^* < 0.05, $**p$ < 0.01, $***p$ < 0.001, three independent experiments. Scale bar, 5 μ m. See also Figure S2.

When spindle MTs were depolymerized by nocodazole on ice, less matrices were associated with Aurora A beads than those incubated at RT (compare IgG matrix panels in Figures 2A and 2B). Quantification of LB3 staining revealed a significant reduction of matrices around beads upon cold treatment or upon xBuGZ depletion (Figure 2C). xBuGZ depletion plus cold treatment caused an additional matrix reduction that could be rescued by purified xBuGZ (Figure 2C). Thus spindle matrix assembly and stability require BuGZ and a physiological temperature.

BuGZ Exhibits Temperature-Sensitive Binding to Spindle MTs

Unlike many MT-associated SAFs that decorate MT fibers densely and brightly, BuGZ appears as a loose “haze” enriched on spindles (Figure S1E) (Jiang et al., 2014). When HeLa cells were incubated at RT or on ice for 5 min followed by immunostaining, we found that cold treatment diminished BuGZ signal on spindles, whether or not the spindle MTs were stabilized with Taxol (Figures 2D and S2B).

xBuGZ signal was also reduced on cold-treated Aurora A-bead spindles stabilized by Taxol (Figure 2E).

We then treated HeLa cells by Taxol and collected mitotic cells by shake-off. Detergent extraction of these cells on ice or at RT in the presence of Taxol followed by immunoblotting showed that more hBuGZ was extracted in the cold as compared to tubulin or CENP-A controls (Figure S2C). Immunostaining further indicated that spindle-associated hBuGZ was more sensitive to the extraction on ice than at RT (Figure 2F).

BuGZ Exhibits Temperature-Dependent Phase Transition via Conserved Phenylalanine and Tyrosine

We analyzed vertebrate BuGZ protein sequences using PONDR and SEG, programs designed to predict the disordered (Xue et al., 2010) and low complexity regions (Wootton, 1994) in proteins, respectively. The N terminus of BuGZ, containing the MT binding domain and zinc fingers, was predicted to have normal amino acid complexity, while the rest of BuGZ was largely unstructured with low amino acid complexity (Figure 3A). Since some disordered and low complexity (DLC) proteins can undergo phase transition, we examined Sf9 cells expressing YFP-tagged xBuGZ (YFP-xBuGZ) via baculovirus. YFP-xBuGZ formed bright droplet-like spheres in the cytosol, whereas YFP was evenly distributed (Figure 3B).

We purified His-, GST-, GFP-, or YFP-tagged xBuGZ or mBuGZ expressed in either Sf9 cells or bacteria (Figures 3C and S3A). Upon warming, each protein formed droplets of varying sizes in physiologically relevant buffers and the droplet size increased over time (Figures 3D, S3B, and S3C). When the solutions were cooled on ice, the droplets disintegrated over time, as judged by the disappearance of fluorescence in the droplets (Figure S3D). Under the same conditions and the same or much higher concentrations, purified GST, GFP, YFP, or other SAFs such as GFP-EB1 did not form droplets (Figure S3E). Live imaging showed that at 100 μM of YFP-xBuGZ small droplets became visible at ~10°C and larger droplets formed upon further increase in temperature (Figure 3E).

Turbidity assay showed that purified YFP-xBuGZ underwent an abrupt increase in solution turbidity above a critical temperature, and the process was reversible upon cooling to the same temperature (Figure 3F). After dissolution of droplets on ice, BuGZ underwent the same degree of phase transition upon warming, indicating that the phase separation was repeatable (Figure 3G). Formation of coacervates at high concentrations of YFP-xBuGZ eventually led to large-scale phase separation that become visible to the naked eye due to protein settlement at the bottom of cuvettes (Figure 3H). By varying protein concentrations and temperature, we found that a lower concentration of YFP-xBuGZ required a higher temperature for coacervation (Figure 3I). YFP-xBuGZΔN exhibited similar coacervation properties as YFP-xBuGZ, especially at higher protein concentrations (Figures 3I, 3J, and 3N), indicating that the MT-binding sequence is dispensable for phase transition in vitro. By contrast, YFP did not undergo any noticeable phase transition at equivalent concentrations and temperatures (Figure 3K).

The above findings suggest that BuGZ could undergo intermolecular interactions mediated by hydrophobic residues. We found that BuGZ orthologs are all abundant in proline (P). For

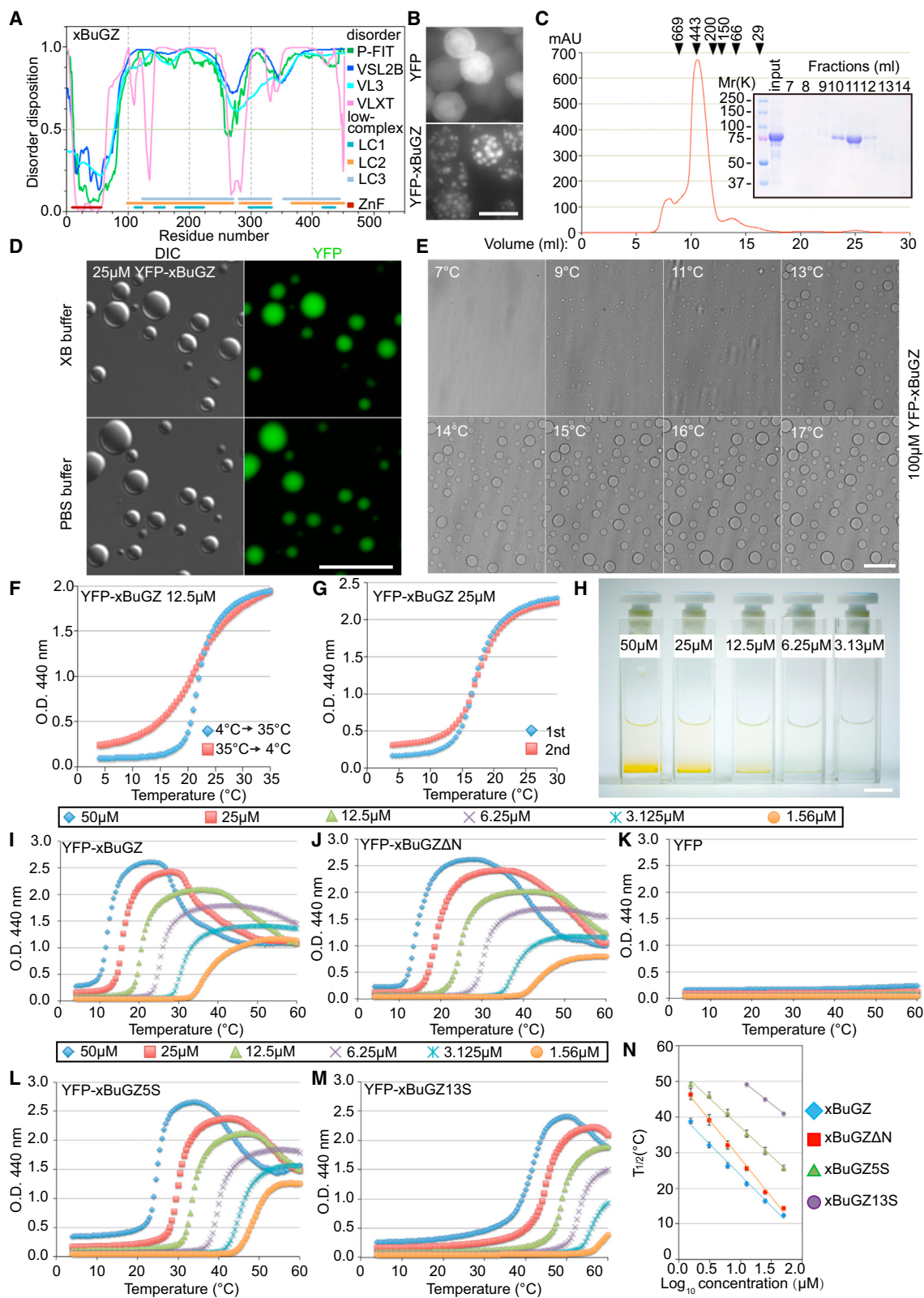
example, mBuGZ and xBuGZ contain 15%–19% P, which often occur next to hydrophobic residues (Figure S3F). The hydrophobic and aromatic residues phenylalanine (F) and tyrosine (Y) are implicated in hydrogel formation of some nucleoporins (Frey and Görlich, 2007), transcription factors, and RNA binding proteins (Kato et al., 2012; Kwon et al., 2013). Since both F and Y are highly conserved among vertebrate BuGZ (Figure S3F), we mutated the last 5 or all 13 conserved Fs and Ys in the predicted DLC region of xBuGZ to serine (S) to create YFP-xBuGZ5S or YFP-xBuGZ13S (Figure S3F). Coacervation of YFP-xBuGZ5S and YFP-xBuGZ13S required increasingly higher concentration and temperature (Figures 3L–3N). Thus conserved Fs and Ys are required for BuGZ phase transition.

We found that a fragment of xBuGZ corresponding to amino acids 258–334 (xBuGZ-B) (Figure S3F, black underline), which did not form droplets on its own (Figure S3E), inhibited the phase transition of YFP-xBuGZ when used at high concentrations (Figure S3G). Replacing the 2F and 1Y by S in xBuGZ-B (xBuGZ-B3S, also did not form droplets on its own, Figure S3E) largely disrupted the inhibitory property (Figures S3G–S3I). At concentrations that did not fully block His-xBuGZ droplet formation, GFP-xBuGZ-B strongly incorporated into the droplets as compared to GFP-xBuGZ-B3S (Figure S3J). Thus, intermolecular BuGZ interactions in droplets may be mediated, in part, by Fs and Ys. Moreover, xBuGZ-B may disrupt droplet formation by blocking proper alignment of full-length xBuGZ molecules critical for coacervation.

BuGZ Bundles MTs via MT Binding and Phase Transition

We incubated 0–4 μM YFP-xBuGZ, YFP-xBuGZΔN, YFP-xBuGZ13S, or YFP with rhodamine-labeled and Taxol-stabilized short MTs at 37°C. BuGZ (4 μM), but not xBuGZΔN, xBuGZ13S, or YFP, caused prominent MT bundling, although careful inspection showed that some MT bundles were formed even at 1 μM xBuGZ (Figure 4A). The bundled MTs were longer and brighter than the input MT fragments. To quantify the bundling activity, we measured the length and average brightness of individual MTs or MT bundles formed with 2 μM of different xBuGZ proteins and YFP because MT bundles at higher xBuGZ concentrations became a network. xBuGZ increased MT bundle length and average intensity, but xBuGZΔN, xBuGZ13S, or YFP did not (Figures 4B and 4C). xBuGZ-B inhibited MT bundling induced by xBuGZ, while xBuGZ-B3S was much less effective (Figures 4B and 4C). Thus, MT binding and phase transition of BuGZ promote MT bundling.

Although 2 or 4 μM YFP-xBuGZ, YFP-xBuGZΔN, YFP-xBuGZ13S, and YFP did not form visible droplets at 37°C (Figure S4A), when incubated with MT seeds, YFP-xBuGZ was enriched on MT bundles and small YFP-xBuGZ droplets were visible along some bundles (arrowheads, Figures 4D and S4B). Line scan showed that the droplets tended to appear at sites of thicker MT bundles flanked by thinner regions (Figure 4D). YFP-xBuGZΔN and YFP-xBuGZ13S failed to form MT-associated droplets, even though YFP-xBuGZ13S showed MT association (Figure S4B). MT pelleting also showed that, despite intact MT binding domain and similar MT binding at 4°C, significantly less YFP-xBuGZ13S bound to MTs at 37°C than did YFP-xBuGZ (Figures 4E and 4F). When high concentrations (60–100 μM) of



(legend on next page)

YFP-xBuGZ were used to induce MT bundling, large deformed BuGZ droplets extended beyond the associated MT bundles (Figure S4C), suggesting that the MT bundles could flatten the droplets when local BuGZ was not in excess. Thus BuGZ preferably undergoes phase transition along MTs, while the multivalent MT binding sites in BuGZ coacervates in turn promote MT bundling.

BuGZ Phase Transition Concentrates Tubulin and Promotes MT Polymerization

When different xBuGZ were incubated with rhodamine-tubulin in the presence of nocodazole to prevent MT assembly, tubulin was concentrated in YFP-xBuGZ, but not in YFP-xBuGZ Δ N, droplets (Figure 5A). When incubated with beads coated with different forms of BuGZ at 4°C in the presence of nocodazole, purified tubulin was pulled down by YFP-xBuGZ or YFP-xBuGZ13S, but not by YFP-xBuGZ Δ N (Figure 5B).

Next, purified BuGZ and tubulin were combined on ice in the presence of nocodazole and incubated at 37°C followed by pelleting the droplets (Figure 5C). Both YFP-xBuGZ and YFP-xBuGZ Δ N were enriched in droplets by many fold than the initial solution concentrations (Figures 5D and 5E). Tubulin was greatly enriched in the YFP-xBuGZ, but not the YFP-xBuGZ Δ N, droplets (Figures 5D and 5E). Neither YFP-xBuGZ13S nor tubulin was enriched in the pellet fractions (Figure 5F).

Since MT assembly is greatly aided by high tubulin concentrations (Caudron et al., 2000), the concentration of tubulin by BuGZ droplets could lead to enhanced MT assembly. Indeed, *in vitro* MT assembly assays (Oegema et al., 1999; Zheng et al., 1995) showed that mBuGZ and xBuGZ, but not YFP, YFP-xBuGZ Δ N, or YFP-xBuGZ13S, stimulated MT assembly even at low concentrations (Figures 5G, 5H, and S5A–S5C). xBuGZ-B, when present in excess, inhibited the xBuGZ-stimulated MT polymerization, whereas xBuGZ-B3S was much less effective (Figure S5D). Thus, the BuGZ-stimulated tubulin concentration and MT polymerization require both MT/tubulin binding and phase transition of BuGZ.

We estimated endogenous xBuGZ in extracts to be ~0.1 μM and polyethylene glycol, a crowding agent, induced purified xBuGZ at this concentration to undergo phase transition *in vitro* (Figures S5E and S5F). Importantly, spindle concentration

of xBuGZ was estimated as 0.5–0.86 μM (Figure S5G). Thus, endogenous BuGZ could undergo phase transition to promote MT polymerization during spindle assembly.

BuGZ Exhibits Phase Transition Property in Spindle Matrix

If BuGZ in droplets could undergo continuous exchange with solution BuGZ, wild-type and mutant forms of YFP-xBuGZ should have different abilities to exchange into preformed His-xBuGZ droplets. Indeed, YFP-xBuGZ and YFP-xBuGZ Δ N exchanged into the His-xBuGZ droplets efficiently, while YFP-xBuGZ5S and YFP-xBuGZ13S exhibited weak and background incorporations, respectively (Figure 6A). We also created two additional GFP-tagged fragments, xBuGZ-A and xBuGZ-C, corresponding to 111–187 aa and 376–452 aa in the DLC region (Figure S3F, pink and orange underlines), and their F/Y mutants: xBuGZ-A3S and xBuGZ-C5S, respectively. Similar to xBuGZ-B these fragments did not form droplets on their own (Figure S6A). GFP-xBuGZ-A, GFP-xBuGZ-B, and GFP-xBuGZ-C, but not their mutants, exchanged into and disrupted the His-xBuGZ droplets (Figure S6B; also see Figure S3G).

Next, we incubated isolated spindle matrices with 0.1 μM wild-type or mutant YFP-xBuGZ. YFP-xBuGZ and YFP-xBuGZ Δ N exchanged into spindle matrices (marked by LB3) strongly, while YFP-xBuGZ5S exhibited weak exchange (Figure 6B). YFP-xBuGZ13S exhibited only background incorporation into the matrix, similar to the YFP control (Figure 6B). When isolated spindle matrices were incubated with 0.5 μM GFP-xBuGZ-A, GFP-xBuGZ-B, or GFP-xBuGZ-C to disrupt the coacervation of endogenous xBuGZ, each fragment, but not their mutants, incorporated into and reduced the size of the matrix (Figure S6C). Therefore, phase transition is required for both BuGZ incorporation into and the maintenance of preformed spindle matrix, indicating that BuGZ exhibits a phase transition property in the spindle matrix.

Phase Transition and Tubulin Binding of BuGZ Promote MT Assembly from Spindle Matrix

The exchange of YFP-xBuGZ or YFP-xBuGZ Δ N into the spindle matrix replaced most endogenous xBuGZ, while YFP-xBuGZ5S and YFP-xBuGZ13S exhibited increasingly less replacement of

Figure 3. Temperature- and Concentration-Dependent Phase Transition of BuGZ

- (A) Sequence features of xBuGZ. The line at 0.5 (y axis) is the cutoff for disorder (>0.5) and order (<0.5) predictions. P-FIT, VSL2B, VL3, and VLXT, predictors for disordered dispositions. LC1, LC2, and LC3 indicate low complexity regions determined at three stringencies. ZnF, zinc fingers, predicted structured region.
- (B) YFP-xBuGZ formed spheres in S9 cells. YFP served as control. Scale bar, 20 μm.
- (C) Gel filtration chromatography of YFP-xBuGZ. Arrowheads, positions of size markers (in kDa): thyroglobulin, apoferritin, amylase, alcohol dehydrogenase, albumin, and carbonic anhydrase. Fractions 7–14 were analyzed by gel electrophoresis and Coomassie staining.
- (D) YFP-xBuGZ formed droplets *in vitro* as visualized by DIC and fluorescence microscopy. Scale bar, 20 μm.
- (E) Temperature-dependent droplet formation by YFP-xBuGZ in XB buffer as visualized by Hoffman modulation contrast microscopy. Temperature ramp, 4°C–20°C at 1°C/min. Scale bar, 20 μm.
- (F and G) Turbidity assay of reversibility (F) and repeatability (G) of phase transition by YFP-xBuGZ. Increase (4°C–35°C) and decrease (35°C–4°C) in temperature in (F) had the same temperature ramp. The temperature ramp in (G) was 4°C–30°C. Ramp rate, 0.5°C/min.
- (H) Concentration-dependent accumulation of YFP-xBuGZ coacervates at the bottom of cuvettes after turbidity measurements. Scale bar, 1 cm.
- (I–K) Concentration- (color-coded) and temperature-dependent phase transition of YFP-xBuGZ (I) and YFP-xBuGZ Δ N (J), but not YFP (K), based on the turbidity assay.
- (L and M) xBuGZ5S (L) and xBuGZ13S (M) coacervation at increasingly higher protein concentrations and temperatures.
- (N) The temperature at which the turbidity was half ($T_{1/2}$) of the difference between maximum and 4°C absorbance was plotted against \log_{10} protein concentration. YPF-xBuGZ13S did not reach maximum turbidity at 3.125 and 1.56 μM even at 60°C. Error bars, SD from three independent experiments.

See also Figure S3.

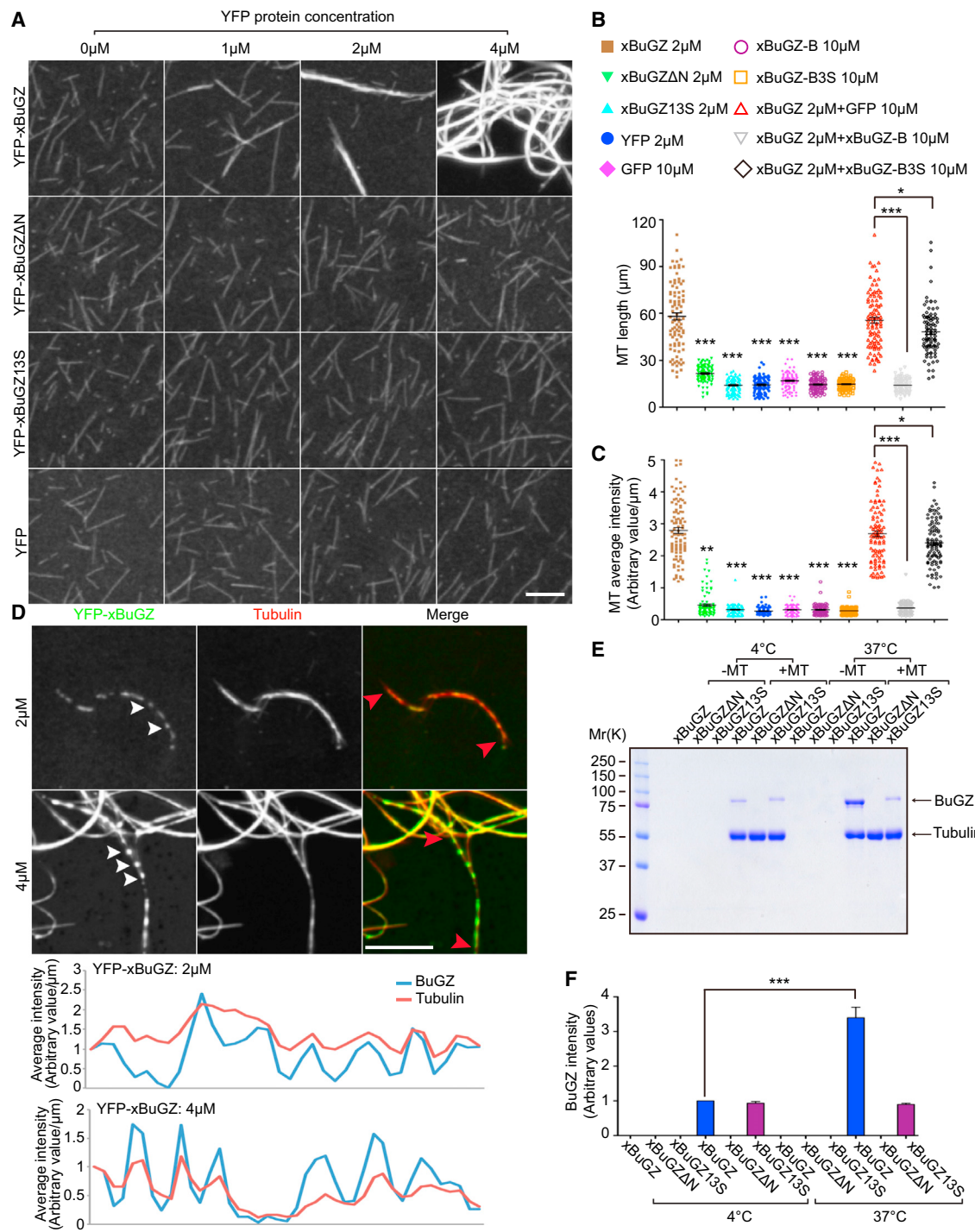


Figure 4. Bundling of MTs by BuGZ Depends on Its MT Binding and Phase Transition

(A) YFP-xBuGZ, but not YFP-BuGZ Δ N, YFP-BuGZ13S, or YFP, induced MT bundling from Taxol-stabilized and rhodamine-labeled MT seeds.

(B and C) Quantifications of length (B) and average intensity (C) of MTs or MT bundles formed in the presence of indicated proteins and concentrations. MT images were randomly captured under a 63 \times objective. Approximately 100 individual MTs or MT bundles were measured.

(D) YFP-xBuGZ droplets (green, white arrowheads) along some MT bundles (red). Line scans of tubulin and YFP-BuGZ intensity of the indicated segments of MTs (red arrowheads) are shown.

(E and F) Purified YFP-xBuGZ, but not YFP-xBuGZ13S, had increased binding to preformed MTs at 37°C compared to 4°C, but YFP-BuGZ Δ N fail to bind. Quantification is shown in (F).

Error bars, SEM. Student's t test: *p < 0.05, **p < 0.01, ***p < 0.001, three independent experiments. Scale bars, 10 μ m. See also Figure S4.

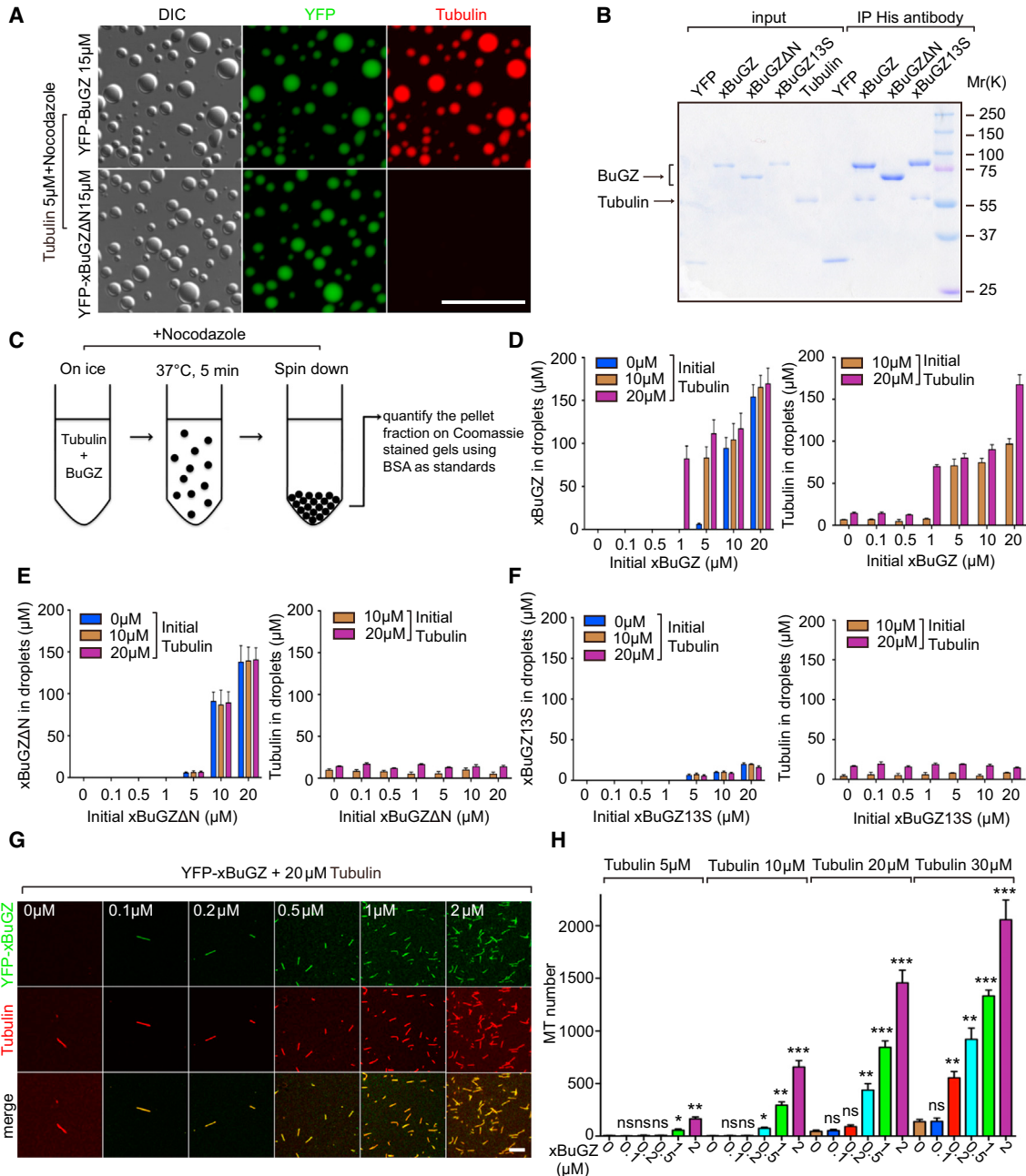


Figure 5. BuGZ Coacervation Promotes MT Polymerization by Concentrating Tubulin

(A) Tubulin was concentrated in droplets formed by YFP-xBuGZ, but not by YFP-xBuGZ Δ N. Scale bar, 20 μ m.

(B) Anti-His-tag antibody pulled down indicated xBuGZ and tubulin at 4°C.

(C) Illustration of the spin down assay.

(D) Higher concentrations of YFP-xBuGZ and tubulin are found in droplets (y axis) than in initial solution concentrations (x axis).

(E and F) Compared to initial solution concentrations (x axis), YFP-xBuGZ Δ N (E) coacervation only concentrated itself, but not tubulin, in droplets (y axis), whereas YFP-xBuGZ Δ S (F) did not coacervate or concentrate itself or tubulin (y axis).

(G and H) Representative fields of MTs polymerized. MTs were counted in 20 random microscopic fields using a 63 \times objective. Scale bar, 10 μ m.

Error bars, SEM. Student's t test: ns, not significant, *p < 0.05, **p < 0.01, ***p < 0.001, three independent experiments. See also Figure S5.

endogenous xBuGZ (Figures 6B and S6D). The total BuGZ levels in the matrices, however, remained similar to controls (Figure S6D). After incubating isolated spindle matrices with

0.1 μ M of different YFP-xBuGZs followed by addition of 25 μ M tubulin with or without nocodazole, the YFP-xBuGZ Δ N-incorporated spindle matrices had greatly diminished abilities to

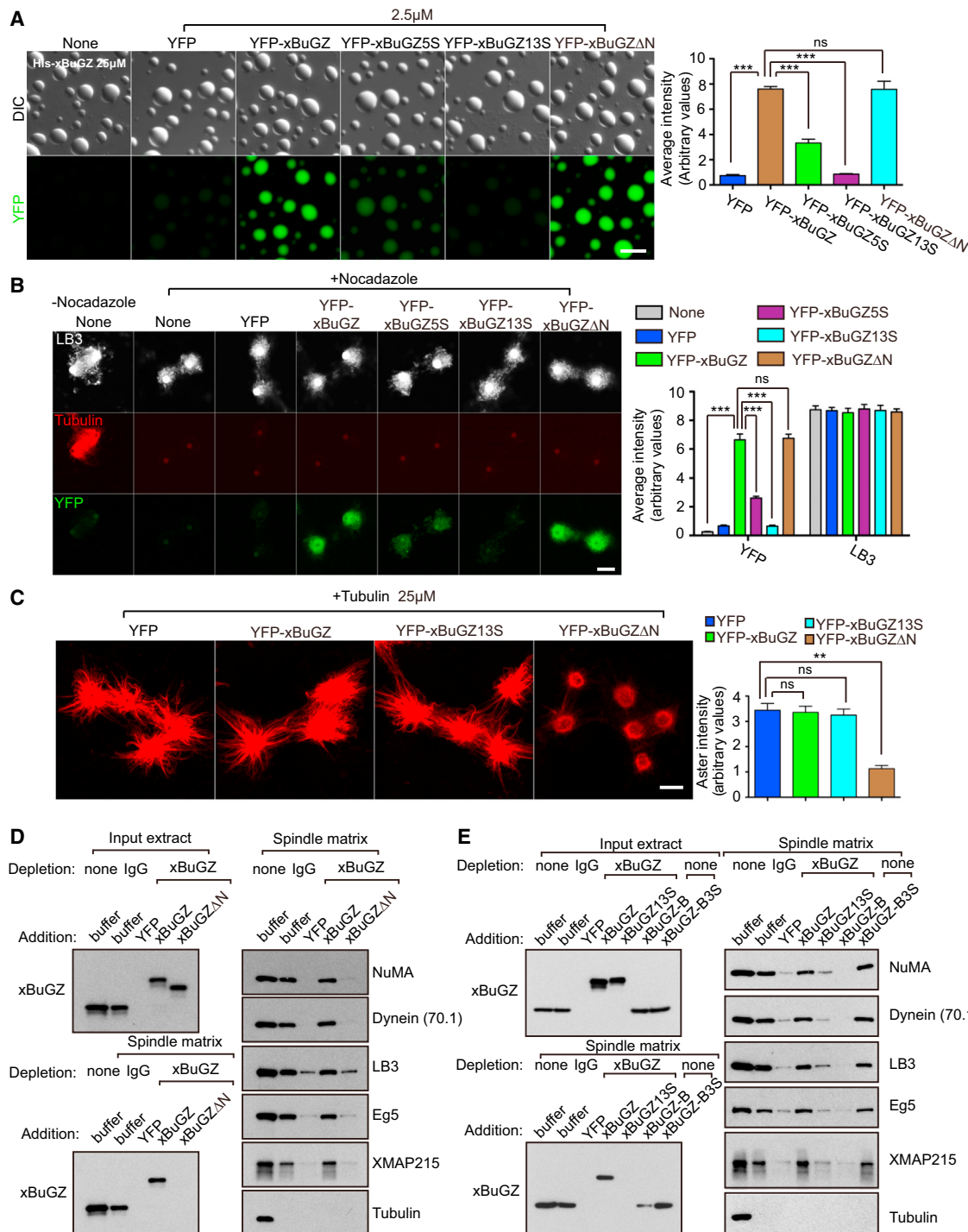


Figure 6. Tubulin/MT Binding and Phase Transition of BuGZ Promote Spindle Matrix Assembly and Function

(A) Incorporation of YFP-xBuGZ into preformed His-xBuGZ droplets in vitro required Fs and Ys but not the N terminus of xBuGZ. YFP intensity was quantified in ~50 droplets.

(B) Incorporation of 0.1 μM YFP-xBuGZ into isolated spindle matrix required Fs and Ys but not the N terminus of xBuGZ. Approximately 30 structures were analyzed.

(C) Incubation of YFP-xBuGZΔN, but not YFP, YFP-xBuGZ, or YFP-xBuGZ13S, with isolated spindle matrix disrupted matrix-mediated MT assembly. Approximately 30 asters were analyzed.

(D) Spindle matrix assembly required MT-binding of BuGZ. YFP-xBuGZ, but not YFP-xBuGZΔN, rescued spindle matrix assembly upon endogenous xBuGZ depletion, as assayed by western blotting analyses using spindle matrix markers.

(legend continued on next page)

concentrate tubulin and to promote MT polymerization (Figures 6C and S6E). YFP-xBuGZ13S did not affect such abilities of the matrices (Figures 6C and S6E), consistent with its failure to incorporate (Figure 6B and S6D). Thus phase transition and tubulin-binding of BuGZ are required for the spindle matrix to concentrate tubulin and promote MT assembly.

Phase Transition and MT Binding of BuGZ Promote Spindle Matrix Assembly

To test whether phase transition of xBuGZ is critical for spindle matrix assembly, extract depleted of endogenous xBuGZ was supplemented with purified YFP-xBuGZ, YFP-xBuGZΔN, or YFP-xBuGZ13S. Alternatively, 2 μM of purified BuGZ-B or BuGZ-B3S were added to unperturbed extract. We found that YFP-xBuGZ, but not xBuGZΔN or xBuGZ13S, rescued spindle matrix assembly (Figures 6D and 6E). xBuGZ-B, but not xBuGZ-B3S, disrupted spindle matrix assembly (Figure 6E). Therefore, both MT binding and phase transition of BuGZ are required for spindle matrix assembly.

Phase Transition and MT Binding of BuGZ Promote Spindle Assembly

To understand whether phase transition of BuGZ is important for spindle assembly, we used GFP-xBuGZ-A, GFP-xBuGZ-B, and GFP-xBuGZ-C to disrupt phase transition of endogenous xBuGZ in extract. One micromolar each of the fragments disrupted spindle assembly induced by Aurora A beads or sperm, whereas their mutants were much less effective (Figures S7A–S7D). When isolated spindles were incubated with 0.2 μM GFP-xBuGZ-A, GFP-xBuGZ-B, or GFP-xBuGZ-C, a concentration that did not disrupt spindle assembly, we found efficient spindle incorporation of these fragments, whereas their mutants incorporated poorly (Figure S7E). Thus, these fragments may bind to endogenous BuGZ to disrupt phase transition and spindle assembly.

Next, we incubated isolated Aurora A-bead spindles with 0.1 μM YFP-xBuGZ or mutants. YFP-xBuGZ, YFP-xBuGZ5S, and YFP-xBuGZ13S sequentially showed decreasing exchanges into spindles (Figure 7A), confirming the importance of BuGZ phase transition in spindle association. YFP-xBuGZΔN exhibited the weakest exchange of all (Figure 7A), consistent with the idea that MT binding of BuGZ facilitates its phase transition. We then depleted endogenous xBuGZ in extract and induced spindle formation by Aurora A beads or sperm. Spindle defects due to xBuGZ depletion were fully rescued by purified xBuGZ, but not by xBuGZΔN or YFP-xBuGZ13S (Figures 7B–7F).

In the predicted DLC region, mBuGZ has extra 15 amino acids (including 1Y and 1F) not found in xBuGZ (see Figure S3F). We replaced these two and the other 13 Fs and Ys with S to create mBuGZ15S. HeLa cells were transfected with control or hBuGZ siRNAs followed by expression of RNAi-insensitive Flag-mBuGZ or -mBuGZ15S. Reduction of MT intensity due to hBuGZ RNAi was rescued by wild-type mBuGZ but not by mBuGZ15S (Fig-

ures 7G–7I). Since xBuGZΔN also failed to rescue MT intensity (Figures 1J–1L), both MT binding and phase transition of BuGZ are required to promote spindle assembly in cells.

DISCUSSION

The vague structure-function definitions and uncertain composition of the spindle matrix have made its study both challenging and controversial. Among the studied spindle matrix proteins, LB was initially suggested to be a structural component of the matrix because its depletion resulted in reduced spindle matrix as judged by markers, such as NuMA and Eg5 (Tsai et al., 2006). However, due to the difficulties in studying lamins biochemically, the structural role that LB assumes in the spindle matrix remains challenging to decipher. Similarly, despite the identification of several spindle matrix proteins in *Drosophila*, the assembly mechanism of these proteins remains unknown (Johansen and Johansen, 2007). Through analyses of the spindle matrix component BuGZ, which can be expressed and purified as a soluble protein, we have uncovered its phase transition property in spindle and spindle matrix assembly.

Based on our *in vitro* studies, we propose that at low temperature the DLC region of BuGZ assumes a variety of quasi-folded states in solution due to weak intra-molecular hydrophobic interactions and a water shell surrounding the molecule, which limits intermolecular interactions (Figure 7J). Temperature increase disrupts (or denatures) the quasi-folded BuGZ and the water shell to allow intermolecular interactions, leading to phase transition (Figure 7K). By studying phase transition of BuGZ in spindle and matrix, we propose that during spindle assembly, the binding of N-terminal BuGZ to MTs limits quasi-folding of BuGZ. By bringing BuGZ molecules close to one another on MTs, intermolecular interactions and phase transition of BuGZ are enhanced (Figure 7L), which in turn bundles MTs and concentrates tubulin (Figure 7M). The elevated tubulin concentration near existing MTs then promotes MT polymerization during spindle assembly.

Our mutational analyses show that BuGZ coacervation depends on highly conserved Fs and Ys in the DLC region of BuGZ. Hydrophobicity-dependent phase transition has been studied in various proteins and polymers. In the well-characterized phase transition of elastin, hydrophobic patches are required for its coacervation, which is critical for subsequent filament assembly (Yeo et al., 2011). Our analyses of the predicted DLC region of BuGZ revealed that highly conserved hydrophobic residues and prolines (P) are enriched in two segments that flank a region with relatively low P and hydrophobicity. This suggests that intermolecular hydrophobic interactions mediated by the hydrophobic patches contribute to BuGZ coacervation. Consistent with this, BuGZ coacervation is dependent on temperature, protein concentration, and Fs and Ys. The aromatic feature of these residues may also mediate phase transition independent of their hydrophobicity. Inhibition of BuGZ coacervation by the

(E) Spindle matrix assembly required BuGZ coacervation. YFP-xBuGZ, but not YFP-xBuGZ13S, rescued spindle matrix assembly upon endogenous xBuGZ depletion. The addition of GFP-BuGZ-B, but not -BuGZ-B3S, into unperturbed extract disrupted spindle matrix assembly.

Error bars, SEM. Student's t test: ns, not significant, **p < 0.01, ***p < 0.001, three independent experiments. The numbers of structures quantified are for each experiment and condition. Scale bars, 10 μm. See also Figure S6.

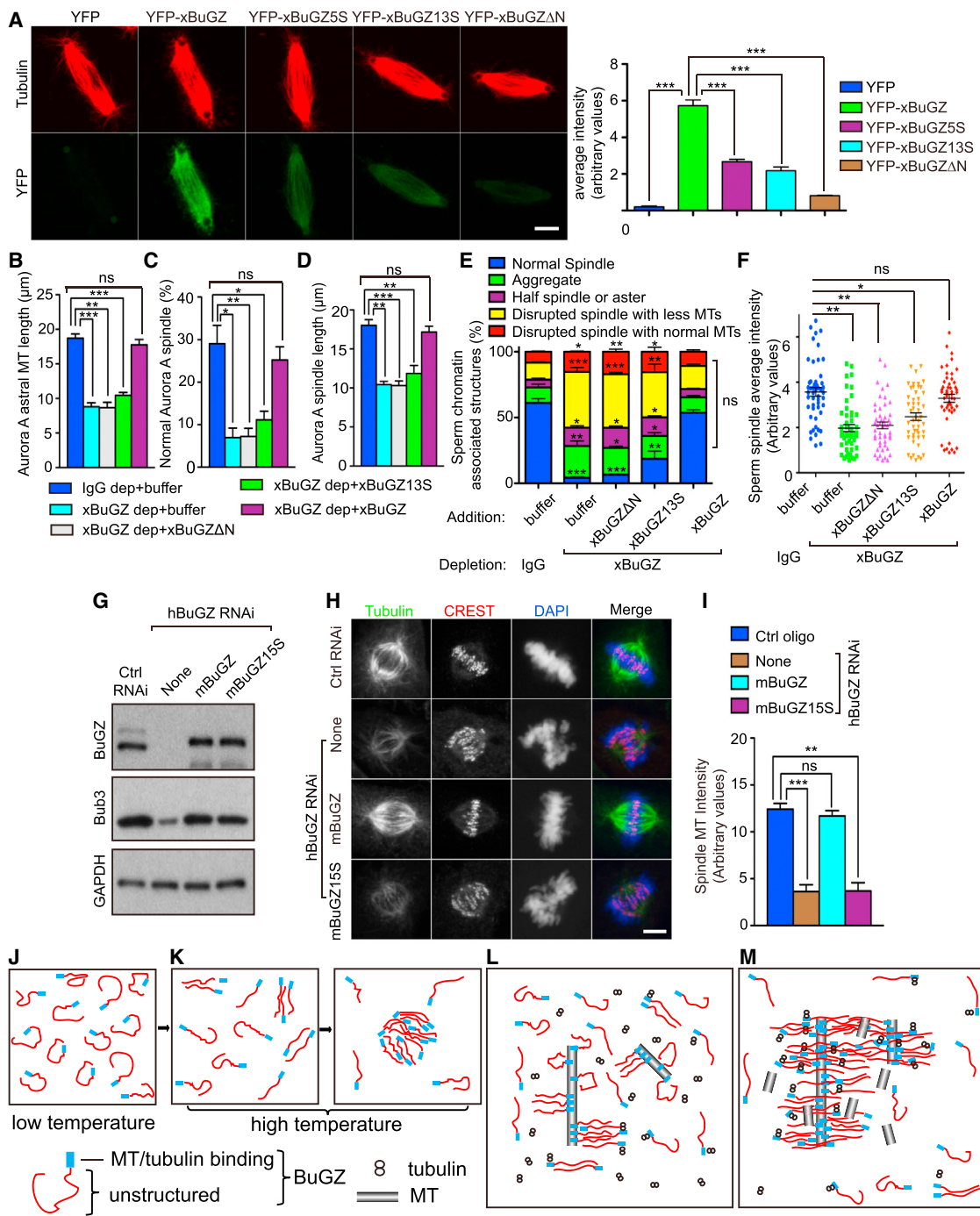


Figure 7. Tubulin/MT Binding and Coacervation of BuGZ Promotes Spindle Assembly

(A) Incorporation of 0.1 μM YFP-xBuGZ into isolated spindles required Fs and Ys and MT binding. Approximately 30 spindles were analyzed. Scale bar, 10 μm.

(B–D) xBuGZ, but not xBuGZΔN or xBuGZ13S, rescued astral MT length (B), percentages of normal spindles (C), and length of spindles (D) induced by Aurora A beads. Approximately 50 (B and D) or 500 (C) structures were analyzed.

(E and F) Only wild-type xBuGZ, but not xBuGZΔN or xBuGZ13S, rescued defective morphology (E) or MT intensity (F) of spindles in xBuGZ-depleted extracts. Approximately 500 sperm-associated MT structures (E) or 50 spindles (F) were analyzed.

(G–I) Expression of mBuGZ, but not mBuGZ15S, in hBuGZ depleted HeLa cells (G) rescued normal spindle MT intensity (H and I). Approximately 30 spindles were analyzed. Spindles, centromeres, and chromosomes were stained. Scale bars, 5 μm.

(J–M) Models for BuGZ phase transition in vitro (J and K) or during spindle assembly (L and M). See explanations in the Discussion.

Error bars, SEM. Student's t test: ns, not significant; *p < 0.05, **p < 0.01, ***p < 0.001 from three independent experiments. The numbers of structures analyzed are for each experiment and condition. See also Figure S7.

xBuGZ fragments containing F and Y could be caused by disruption of proper alignment of hydrophobic and aromatic residues important for intermolecular BuGZ interactions. BuGZ droplets formed *in vitro* do not appear to further form filaments based on our preliminary analyses by electron microscopy (unpublished data). Although additional studies are required to fully understand the biophysical properties that underline BuGZ phase transition, our findings suggest that unfolding of BuGZ at elevated temperature could drive coacervation through intermolecular hydrophobic interactions.

The temperature-dependent BuGZ phase transition and spindle matrix stability suggest that BuGZ is a structural component of spindle matrix. Indeed, based on known markers of *Xenopus* spindle matrix, we show that BuGZ in spindle matrix exhibits a phase transition property, which is required for assembly and stability of spindle matrix. The MT-independent and temperature-dependent phase transition of BuGZ that we uncover here also help to explain why upon MT depolymerization the spindle matrix can retain its structural integrity better at RT than on ice. Our findings beg the question whether phase transition represent a key structural property of spindle matrix.

Using PONDR and SEG, we found additional DLC-containing proteins in the proteome of *Xenopus* spindle matrix (unpublished data). Similar analyses revealed the presence of long stretches of DLC regions in several *Drosophila* spindle matrix proteins, such as Megator, Chromator, EAST, and Skeletor (unpublished data). Since multiple proteins can undergo phase transition together through complicated intermolecular interactions, we speculate that the spindle matrix could be a complex coacervate, whose formation relies on various combinations of proteins depending on organisms and cell types. These coacervates could contain different phases to segregate different biochemical reactions that could communicate with one another. This idea may explain the apparent un-relatedness of some spindle matrix components. Formation of complex coacervates may involve both DLC and structured proteins, which could explain why the largely structured proteins, such as lamin and actin, are found in the spindle and spindle matrix (Zheng and Tsai, 2006; Pickett-Heaps and Forer, 2009). Additionally, proteins participating in phase transition in the spindle and spindle matrix could undergo rapid flux in and out of the structures. The phase transition features may explain the lack of a discrete localization of BuGZ on spindle MTs and a lack of a clearly defined morphology of the spindle matrix upon MT depolymerization.

We show that phase transition of BuGZ does not require MTs, but the MT binding domain of BuGZ helps to not only facilitate BuGZ phase transition along MTs but to concentrate tubulin. Both phase transition and MT binding of BuGZ are required for promoting MT polymerization and bundling *in vitro*. Importantly, we show that all of these properties are also required for BuGZ to promote spindle assembly. Therefore, one functional consequence of BuGZ-mediated spindle matrix assembly along existing MTs appears to allow efficient polymerization and bundling of MTs in the spindle. By increasing local tubulin concentration, BuGZ could also promote MT nucleation from microtubule nucleators such as γ TuRC (Zheng et al., 1995).

Recent studies have shown that MT-dependent branched MT nucleation facilitates spindle assembly (Petry et al., 2013). Since

BuGZ could concentrate tubulin along existing MTs, it would be interesting to further study whether BuGZ-mediated phase transition could help to concentrate other SAFs known to promote branched MT nucleation. Additionally, we have shown that BuGZ interacts with Bub3 to promote the binding of Bub3 to kinetochores in a MT-dependent manner (Jiang et al., 2014). Purified BuGZ-Bub3 complex undergoes more efficient phase transition than BuGZ alone *in vitro* (unpublished data). It would be interesting to further study whether increasing Bub3 concentration along spindle MTs via phase transition could promote assembly of the Bub3-Bub1-BubR1 complex for its kinetochore loading.

We have shown that nuclear transport receptors such as importin α and β disrupt spindle matrix assembly, which is attenuated by RanGTP (Tsai et al., 2006). Since BuGZ and some other known spindle matrix components are nuclear proteins in interphase, it will be important to further explore whether the RanGTP-importin system regulates phase transition of BuGZ and other spindle matrix proteins in mitosis. As a conserved protein found in both vertebrates and invertebrates, our study of BuGZ here should open a door to further characterize the structural properties and functions of the spindle matrix in different organisms.

EXPERIMENTAL PROCEDURES

Expression Vectors

For all expression constructs see Table S1.

Cell Culture and *Xenopus* Egg Extract

All cells were grown under standard culturing conditions. CSF egg extracts were prepared as described before and only those that were tested to support spindle assembly were used for further experiments. All assays in egg extracts are detailed in the Supplemental Experimental Procedures.

Immunofluorescence and Quantifications

Cells were fixed by 4% paraformaldehyde in PBS for 7 min, followed by extraction in 0.5% Triton in PBS for 10 min. *Xenopus* MT structures were fixed by ice cold methanol for 5 min. Samples were then blocked in 4% BSA in PBS for >1 hr followed by primary antibody (Table S2) incubation overnight at 4°C. Nikon ECLIPSE E800 or Leica SP5 microscopes were used for imaging. To quantify spindle MT intensity or the ratio of BuGZ and MT immunostaining intensities, metaphase spindles in cells, Aurora A, or sperm MT structures were captured at the same exposure using a 63 \times objective on Nikon ECLIPSE E800. Two 15 \times 15 pixel regions, corresponding to the brightest areas of each half spindle was chosen based on tubulin or BuGZ intensity and the average intensities in these areas were determined. The background fluorescence was subtracted using the intensity measured in areas away from the spindle.

Protein Expression, Purification, and Interaction

Proteins were purified using Glutathione agarose (Sigma) or Ni-NTA agarose (QIAGEN) according to manufacturer's protocols. Some proteins were further purified by gel filtration. To study tubulin and xBuGZ interaction, cycled tubulin was added to beads coated with purified His-tagged YFP-xBuGZ, YFP-BuGZ Δ N, or YFP via antibody to 6His and incubated. See details in the Supplemental Experimental Procedures.

BuGZ Phase Transition

Purified mBuGZ, xBuGZ, or control proteins were thawed on ice and diluted into ice-cold buffers on ice followed by incubation at 37°C for 5 min and differential interference contrast (DIC) or fluorescence microscopy. For turbidity assay, purified proteins were diluted in XB buffer on ice (300 μ l final) and then loaded into 750- μ l cuvettes (28F-Q-10, Starna Cells) in a cold room.

Turbidity was measured at 440 nm using a Cary 300 UV-VIS spectrophotometer with a Peltier-Thermostatted Multi-cell Holder (Agilent Technologies). Temperature ramp rate was 0.5°C/min from 4°C to 60°C. To estimate protein concentrations in BuGZ droplets, 100 µl of protein samples were incubated at 37°C for 5 min followed by centrifugation at 2,000 rpm in a microfuge (Eppendorf E5430) for 5 min at room temperature (RT). Proteins in pellet fractions were quantified by Coomassie blue staining using BSA as standard. See details in the [Supplemental Experimental Procedures](#).

MT Polymerization, Bundling, and Binding

Purified xBuGZ and cycled tubulin were mixed on ice. MT polymerization was performed at 37°C for 5 min. After fixation, MTs were counted in 20 random microscopic fields using a 63× objective. The same amount of rhodamine-MT seeds were mixed with different purified xBuGZ proteins and incubated at 37°C for 5 min and imaged immediately. MT length and intensity were measured based on micrographs. To visualize the binding of wild-type and mutant xBuGZ to MTs, rhodamine-labeled and Taxol-stabilized MTs were mixed with different versions of YFP-xBuGZ. See details in the [Supplemental Experimental Procedures](#).

Sequence Analysis for Protein Disorder and Low Complexity

The PONDR (<http://www.disprot.org/index.php>) (Xue et al., 2010) and SEG programs (<http://mendel.imp.ac.at/METHODS/seg.server.html>) (Wootton, 1994) were used to analyze the DLC regions of BuGZ and other spindle matrix proteins at default settings. See details in the [Supplemental Experimental Procedures](#).

SUPPLEMENTAL INFORMATION

Supplemental Information includes Supplemental Experimental Procedures, seven figures, and two tables and can be found with this article online at <http://dx.doi.org/10.1016/j.cell.2015.08.010>.

AUTHOR CONTRIBUTIONS

Conceptualization, Y.Z.; Methodology, H.J., S.W., Y.Z., H.C., and X.Z.; Investigation, H.J., S.W., X.H., and Y.H.; Writing-Original draft, Y.Z., H.J., and S.W.; Writing-Review and Editing, Y.Z., X.Z., H.C., S.W., and H.J.; Funding Acquisition, Y.Z. and X.Z.; Resources, Y.Z., X.Z., and H.C.; Supervision, Y.Z. and X.Z.

ACKNOWLEDGMENTS

We thank Dr. Andreas Merdes for the NuMA antibody, Ona Martin for proof reading, Ona Martin and Lynne Hugendubler for technical support, Dr. Pengcheng Zhang for help with the turbidity assay, and the Y.Z. lab for critical reading. Supported by the Chinese Academy of Sciences (XDA01010107 to X.Z.), Ministry of Science and Technology of China (2014CB964803 to X.Z.), National Science Foundation of China (31420103916 to X.Z. and Y.Z.), and GM056312 and GM106023 (to Y.Z.).

Received: February 4, 2015

Revised: June 9, 2015

Accepted: July 31, 2015

Published: September 17, 2015

REFERENCES

Brangwynne, C.P., Eckmann, C.R., Courson, D.S., Rybarska, A., Hoege, C., Gharakhani, J., Jülicher, F., and Hyman, A.A. (2009). Germline P granules are liquid droplets that localize by controlled dissolution/condensation. *Science* **324**, 1729–1732.

Brangwynne, C.P., Mitchison, T.J., and Hyman, A.A. (2011). Active liquid-like behavior of nucleoli determines their size and shape in *Xenopus laevis* oocytes. *Proc. Natl. Acad. Sci. USA* **108**, 4334–4339.

Brugués, J., and Needleman, D. (2014). Physical basis of spindle self-organization. *Proc. Natl. Acad. Sci. USA* **111**, 18496–18500.

Caudron, N., Valiron, O., Usson, Y., Valiron, P., and Job, D. (2000). A reassessment of the factors affecting microtubule assembly and disassembly in vitro. *J. Mol. Biol.* **297**, 211–220.

Chang, P., Jacobson, M.K., and Mitchison, T.J. (2004). Poly(ADP-ribose) is required for spindle assembly and structure. *Nature* **432**, 645–649.

Civelekoglu-Scholey, G., Tao, L., Brust-Mascher, I., Wollman, R., and Scholey, J.M. (2010). Prometaphase spindle maintenance by an antagonistic motor-dependent force balance made robust by a disassembling lamin-B envelope. *J. Cell Biol.* **188**, 49–68.

Fabian, L., Xia, X., Venkitaramani, D.V., Johansen, K.M., Johansen, J., Andrew, D.J., and Forer, A. (2007). Titin in insect spermatocyte spindle fibers associates with microtubules, actin, myosin and the matrix proteins skeleto, megator and chromator. *J. Cell Sci.* **120**, 2190–2204.

Frey, S., and Görlich, D. (2007). A saturated FG-repeat hydrogel can reproduce the permeability properties of nuclear pore complexes. *Cell* **130**, 512–523.

Gatlin, J.C., Matov, A., Danuser, G., Mitchison, T.J., and Salmon, E.D. (2010). Directly probing the mechanical properties of the spindle and its matrix. *J. Cell Biol.* **188**, 481–489.

Goldman, R.D., and Rebhun, L.I. (1969). The structure and some properties of the isolated mitotic apparatus. *J. Cell Sci.* **4**, 179–209.

Goodman, B., Channels, W., Qiu, M., Iglesias, P., Yang, G., and Zheng, Y. (2010). Lamin B counteracts the kinesin Eg5 to restrain spindle pole separation during spindle assembly. *J. Biol. Chem.* **285**, 35238–35244.

Hayashi, H., Kimura, K., and Kimura, A. (2012). Localized accumulation of tubulin during semi-open mitosis in the *Caenorhabditis elegans* embryo. *Mol. Biol. Cell* **23**, 1688–1699.

Hyman, A.A., Weber, C.A., and Jülicher, F. (2014). Liquid-liquid phase separation in biology. *Annu. Rev. Cell Dev. Biol.* **30**, 39–58.

Jiang, H., He, X., Wang, S., Jia, J., Wan, Y., Wang, Y., Zeng, R., Yates, J., 3rd, Zhu, X., and Zheng, Y. (2014). A microtubule-associated zinc finger protein, BuGZ, regulates mitotic chromosome alignment by ensuring Bub3 stability and kinetochore targeting. *Dev. Cell* **28**, 268–281.

Johansen, K.M., and Johansen, J. (2007). Cell and molecular biology of the spindle matrix. *Int. Rev. Cytol.* **263**, 155–206.

Johansen, K.M., Forer, A., Yao, C., Girton, J., and Johansen, J. (2011). Do nuclear envelope and intranuclear proteins reorganize during mitosis to form an elastic, hydrogel-like spindle matrix? *Chromosome research* **19**, 345–365.

Kalab, P., Pu, R.T., and Dasso, M. (1999). The ran GTPase regulates mitotic spindle assembly. *Curr. Biol.* **9**, 481–484.

Kato, M., Han, T.W., Xie, S., Shi, K., Du, X., Wu, L.C., Mirzaei, H., Goldsmith, E.J., Longgood, J., Pei, J., et al. (2012). Cell-free formation of RNA granules: low complexity sequence domains form dynamic fibers within hydrogels. *Cell* **149**, 753–767.

Kwon, I., Kato, M., Xiang, S., Wu, L., Theodoropoulos, P., Mirzaei, H., Han, T., Xie, S., Corden, J.L., and McKnight, S.L. (2013). Phosphorylation-regulated binding of RNA polymerase II to fibrous polymers of low-complexity domains. *Cell* **155**, 1049–1060.

Leslie, R.J., Hird, R.B., Wilson, L., McIntosh, J.R., and Scholey, J.M. (1987). Kinesin is associated with a nonmicrotubule component of sea urchin mitotic spindles. *Proc. Natl. Acad. Sci. USA* **84**, 2771–2775.

Li, P., Banjade, S., Cheng, H.C., Kim, S., Chen, B., Guo, L., Llaguno, M., Hollingsworth, J.V., King, D.S., Banani, S.F., et al. (2012). Phase transitions in the assembly of multivalent signalling proteins. *Nature* **483**, 336–340.

Lince-Faria, M., Maffini, S., Orr, B., Ding, Y., Cláudia Florindo, Sunkel, C.E., Tavares, A., Johansen, J., Johansen, K.M., and Maiato, H. (2009). Spatiotemporal control of mitosis by the conserved spindle matrix protein Megator. *J. Cell Biol.* **184**, 647–657.

Lukács, D. (1981). [Walter Flemming, discoverer of chromatin and mitotic cell division]. *Orv. Hetil.* **122**, 349–350.

Ma, L., Tsai, M.Y., Wang, S., Lu, B., Chen, R., Iii, J.R., Zhu, X., and Zheng, Y. (2009). Requirement for Nudel and dynein for assembly of the lamin B spindle matrix. *Nat. Cell Biol.* **11**, 247–256.

Oakley, B.R. (2000). An abundance of tubulins. *Trends Cell Biol.* 10, 537–542.

Oegema, K., Wiese, C., Martin, O.C., Milligan, R.A., Iwamatsu, A., Mitchison, T.J., and Zheng, Y. (1999). Characterization of two related Drosophila gamma-tubulin complexes that differ in their ability to nucleate microtubules. *J. Cell Biol.* 144, 721–733.

Ohba, T., Nakamura, M., Nishitani, H., and Nishimoto, T. (1999). Self-organization of microtubule asters induced in Xenopus egg extracts by GTP-bound Ran. *Science* 284, 1356–1358.

Petry, S., Groen, A.C., Ishihara, K., Mitchison, T.J., and Vale, R.D. (2013). Branching microtubule nucleation in Xenopus egg extracts mediated by augmin and TPX2. *Cell* 152, 768–777.

Pickett-Heaps, J., and Forer, A. (2009). Mitosis: spindle evolution and the matrix model. *Protoplasma* 235, 91–99.

Pickett-Heaps, J., Spurck, T., and Tippit, D. (1984). Chromosome motion and the spindle matrix. *J. Cell Biol.* 99, 137s–143s.

Qi, H., Rath, U., Wang, D., Xu, Y.Z., Ding, Y., Zhang, W., Blacketer, M.J., Paddy, M.R., Girton, J., Johansen, J., and Johansen, K.M. (2004). Megator, an essential coiled-coil protein that localizes to the putative spindle matrix during mitosis in Drosophila. *Mol. Biol. Cell* 15, 4854–4865.

Qi, H., Rath, U., Ding, Y., Ji, Y., Blacketer, M.J., Girton, J., Johansen, J., and Johansen, K.M. (2005). EAST interacts with Megator and localizes to the putative spindle matrix during mitosis in Drosophila. *J. Cell. Biochem.* 95, 1284–1291.

Rath, U., Wang, D., Ding, Y., Xu, Y.Z., Qi, H., Blacketer, M.J., Girton, J., Johansen, J., and Johansen, K.M. (2004). Chromator, a novel and essential chromodomain protein interacts directly with the putative spindle matrix protein skeleto. *J. Cell. Biochem.* 93, 1033–1047.

Schibler, M.J., and Pickett-Heaps, J.D. (1980). Mitosis in Oedogonium: spindle microfilaments and the origin of the kinetochore fiber. *Eur. J. Cell Biol.* 22, 687–698.

Scholey, J.M., Rogers, G.C., and Sharp, D.J. (2001). Mitosis, microtubules, and the matrix. *J. Cell Biol.* 154, 261–266.

Schweizer, N., Weiss, M., and Maiato, H. (2014). The dynamic spindle matrix. *Curr. Opin. Cell Biol.* 28, 1–7.

Shimamoto, Y., Maeda, Y.T., Ishiwata, S., Libchaber, A.J., and Kapoor, T.M. (2011). Insights into the micromechanical properties of the metaphase spindle. *Cell* 145, 1062–1074.

Toledo, C.M., Herman, J.A., Olsen, J.B., Ding, Y., Corrin, P., Girard, E.J., Olson, J.M., Emili, A., DeLuca, J.G., and Paddison, P.J. (2014). BuGZ is required for Bub3 stability, Bub1 kinetochore function, and chromosome alignment. *Dev. Cell* 28, 282–294.

Tsai, M.Y., and Zheng, Y. (2005). Aurora A kinase-coated beads function as microtubule-organizing centers and enhance RanGTP-induced spindle assembly. *Curr. Biol.* 15, 2156–2163.

Tsai, M.Y., Wang, S., Heidinger, J.M., Shumaker, D.K., Adam, S.A., Goldman, R.D., and Zheng, Y. (2006). A mitotic lamin B matrix induced by RanGTP required for spindle assembly. *Science* 311, 1887–1893.

Walczak, C.E., Cai, S., and Khodjakov, A. (2010). Mechanisms of chromosome behaviour during mitosis. *Nat. Rev. Mol. Cell Biol.* 11, 91–102.

Walker, D.L., Wang, D., Jin, Y., Rath, U., Wang, Y., Johansen, J., and Johansen, K.M. (2000). Skeleto, a novel chromosomal protein that redistributes during mitosis provides evidence for the formation of a spindle matrix. *J. Cell Biol.* 151, 1401–1412.

Wein, H., Bass, H.W., and Cande, W.Z. (1998). DSK1, a kinesin-related protein involved in anaphase spindle elongation, is a component of a mitotic spindle matrix. *Cell Motil. Cytoskeleton* 41, 214–224.

Wilde, A., and Zheng, Y. (1999). Stimulation of microtubule aster formation and spindle assembly by the small GTPase Ran. *Science* 284, 1359–1362.

Wootton, J.C. (1994). Non-globular domains in protein sequences: automated segmentation using complexity measures. *Comput. Chem.* 18, 269–285.

Xue, B., Dunbrack, R.L., Williams, R.W., Dunker, A.K., and Uversky, V.N. (2010). PONDR-FIT: a meta-predictor of intrinsically disordered amino acids. *Biochim. Biophys. Acta* 1804, 996–1010.

Yao, C., Rath, U., Maiato, H., Sharp, D., Girton, J., Johansen, K.M., and Johansen, J. (2012). A nuclear-derived proteinaceous matrix embeds the microtubule spindle apparatus during mitosis. *Mol. Biol. Cell* 23, 3532–3541.

Yao, C., Wang, C., Li, Y., Ding, Y., Rath, U., Sengupta, S., Girton, J., Johansen, K.M., and Johansen, J. (2014). The spindle matrix protein, Chromator, is a novel tubulin binding protein that can interact with both microtubules and free tubulin. *PLoS ONE* 9, e103855.

Yeo, G.C., Keeley, F.W., and Weiss, A.S. (2011). Coacervation of tropoelastin. *Adv. Colloid Interface Sci.* 167, 94–103.

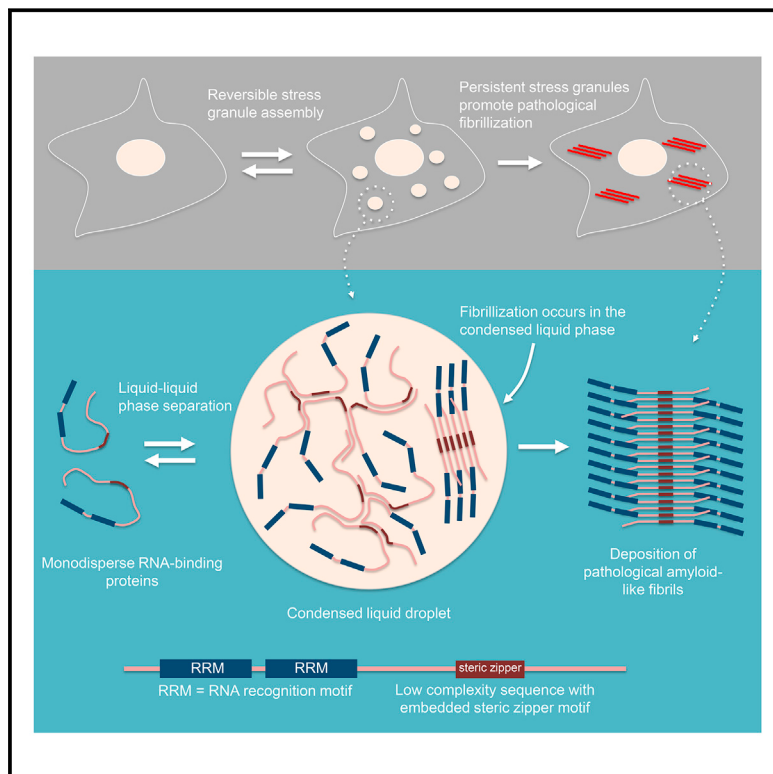
Zheng, Y. (2010). A membranous spindle matrix orchestrates cell division. *Nat. Rev. Mol. Cell Biol.* 11, 529–535.

Zheng, Y., and Tsai, M.Y. (2006). The mitotic spindle matrix: a fibro-membranous lamin connection. *Cell Cycle* 5, 2345–2347.

Zheng, Y., Wong, M.L., Alberts, B., and Mitchison, T. (1995). Nucleation of microtubule assembly by a gamma-tubulin-containing ring complex. *Nature* 378, 578–583.

Phase Separation by Low Complexity Domains Promotes Stress Granule Assembly and Drives Pathological Fibrillization

Graphical Abstract



Authors

Amandine Molliex, Jamshid Temirov, Jihun Lee, ..., Hong Joo Kim, Tanja Mittag, J. Paul Taylor

Correspondence

tanja.mittag@stjude.org (T.M.),
jpaul.taylor@stjude.org (J.P.T.)

In Brief

Liquid-liquid phase separation by RNA-binding proteins harboring low complexity sequence domains is the molecular basis for stress granule assembly, and persistent stress granules promote pathological protein fibrillization.

Highlights

- hnRNPA1 undergoes spontaneous concentration-dependent liquid-liquid phase separation
- Liquid-liquid phase separation is mediated by a low complexity sequence domain
- Stress granules assemble in a RNA-binding protein concentration-dependent manner
- Pathological fibrillization of hnRNPA1 is driven by liquid-liquid phase separation

Phase Separation by Low Complexity Domains Promotes Stress Granule Assembly and Drives Pathological Fibrillization

Amandine Molliex,¹ Jamshid Temirov,² Jihun Lee,³ Maura Coughlin,¹ Anderson P. Kanagaraj,¹ Hong Joo Kim,¹ Tanja Mittag,^{3,*} and J. Paul Taylor^{4,*}

¹Department of Cell and Molecular Biology, St. Jude Children's Research Hospital, Memphis, TN 38105, USA

²Cell and Tissue Imaging Center, St. Jude Children's Research Hospital, Memphis, TN 38105, USA

³Department of Structural Biology, St. Jude Children's Research Hospital, Memphis, TN 38105, USA

⁴Howard Hughes Medical Institute, Department of Cell and Molecular Biology, St. Jude Children's Research Hospital, Memphis, TN 38105, USA

*Correspondence: tanja.mittag@stjude.org (T.M.), jpaul.taylor@stjude.org (J.P.T.)

<http://dx.doi.org/10.1016/j.cell.2015.09.015>

SUMMARY

Stress granules are membrane-less organelles composed of RNA-binding proteins (RBPs) and RNA. Functional impairment of stress granules has been implicated in amyotrophic lateral sclerosis, frontotemporal dementia, and multisystem proteinopathy—diseases that are characterized by fibrillar inclusions of RBPs. Genetic evidence suggests a link between persistent stress granules and the accumulation of pathological inclusions. Here, we demonstrate that the disease-related RBP hnRNPA1 undergoes liquid-liquid phase separation (LLPS) into protein-rich droplets mediated by a low complexity sequence domain (LCD). While the LCD of hnRNPA1 is sufficient to mediate LLPS, the RNA recognition motifs contribute to LLPS in the presence of RNA, giving rise to several mechanisms for regulating assembly. Importantly, while not required for LLPS, fibrillization is enhanced in protein-rich droplets. We suggest that LCD-mediated LLPS contributes to the assembly of stress granules and their liquid properties and provides a mechanistic link between persistent stress granules and fibrillar protein pathology in disease.

INTRODUCTION

It has recently emerged that cells organize many biochemical processes in membrane-less compartments that have liquid-like properties, exemplified by germ granules in *C. elegans* and nucleoli in *X. laevis* (Brangwynne et al., 2009, 2011). It has been proposed that membrane-less organelles arise through a process of liquid-liquid phase separation (LLPS), which permits the requisite components of membrane-less organelles to become rapidly and reversibly concentrated in discrete loci in cells (Hyman et al., 2014). Although the molecular details under-

lying LLPS in cells are largely obscure, several recent reports indicate that constituent proteins harboring intrinsically disordered, low complexity sequence domains (LCDs) can mediate this process. For example, RNA helicase DDX4, a LCD-containing constituent of germ granules, forms phase-separated organelles that exhibit liquid properties in vitro and in live cells (Nott et al., 2015). Related, LAF-1 undergoes LLPS in vitro and is required for P granule assembly in *C. elegans* (Elbaum-Garfinkle et al., 2015). Additional RNA/protein assemblies similarly are membrane-less organelles that exhibit liquid properties and may assemble by LLPS, including stress granules, P bodies, and Cajal bodies (Hyman et al., 2014; Wippich et al., 2013).

Stress granules are membrane-less cytosolic bodies composed of mRNAs and proteins that assemble when translation initiation is limiting and are thought to represent a pool of mRNPs stalled in the process of translation initiation (Anderson and Kedersha, 2009; Buchan and Parker, 2009). A wealth of genetic evidence has emerged over the past 5 years implicating stress granules as a subcellular compartment that is central to the pathogenesis of a closely related set of degenerative diseases, including amyotrophic lateral sclerosis (ALS), frontotemporal dementia (FTD), and inclusion body myopathy (IBM) (Li et al., 2013; Ramaswami et al., 2013). These degenerative diseases are characterized pathologically by cytoplasmic inclusions composed of fibrillar deposits of heterogeneous nuclear ribonucleoproteins (hnRNPs) in affected cells (Kim et al., 2013; Ramaswami et al., 2013). Conspicuously, inherited forms of ALS, FTD, and myopathy are often caused by missense mutations impacting hnRNPs, such as TDP-43, FUS, hnRNPA1, hnRNPA2B1, hnRNPDL, and TIA-1 (Kim et al., 2013; Klar et al., 2013; Kwiatkowski et al., 2009; Sreedharan et al., 2008; Vieira et al., 2014). These hnRNPs are all components of stress granules, and disease-causing mutations in these proteins are associated with accumulation of persistent stress granules (Bosco et al., 2010; Hackman et al., 2013; Kim et al., 2013). ALS, FTD, and myopathy are also caused by mutations in VCP/p97, which are associated with impaired autophagic clearance of stress granules (Buchan et al., 2013). ALS-causing mutations in the actin-binding protein Profilin 1 similarly impair stress granule dynamics (Figley et al., 2014). Thus, a variety of genetic and cell

biological insights have focused attention on alteration in stress granule dynamics as a key defect in the pathogenesis of ALS, FTD, and myopathy, yet the mechanism that leads to accumulation of fibrillar hnRNP pathology remains obscure.

hnRNPA1 is a prototypical hnRNP consisting of two folded RNA recognition motifs (RRMs) that occupy the N-terminal half of the protein and a LCD that occupies the C-terminal half. Missense mutations in the LCD of hnRNPA1 cause ALS and multisystem proteinopathy (MSP), a pleiotropic degenerative disorder affecting muscle and brain (Kim et al., 2013). hnRNPA1 and closely related hnRNPs exhibit intrinsic propensity to assemble into amyloid-like fibrils containing cross- β structure, and this property has been proposed to mediate stress granule assembly (Kato et al., 2012). However, stress granules are dynamic assemblies; its components have residence times varying between seconds and minutes, and indeed, the assembly and disassembly of entire granules are accomplished on this same timescale (Buchan and Parker, 2009). These rapid dynamics argue in favor of a mechanism that permits rapid assembly and disassembly, such as LLPS, and suggest that, rather than accounting for their assembly, fibrillization by hnRNPA1 and related hnRNPs may represent specialized components that accrue within stress granules. Here, we demonstrate that the RBP hnRNPA1 undergoes LLPS mediated by the LCD to form protein-rich droplets. While the LCD of hnRNPA1 is sufficient to mediate phase separation, the folded RNA recognition motifs contribute to phase separation in the presence of RNA, giving rise to several mechanisms for regulating assembly. Importantly, while not required for phase separation, fibrillization is enhanced in protein-rich droplets. These results suggest that LCD-mediated LLPS contributes to the assembly of stress granules and their liquid properties and reveal the mechanistic link between persistent stress granules and fibrillar protein pathology in disease.

RESULTS

hnRNPA1 Undergoes Liquid-Liquid Phase Separation

To gain insight into the role of individual RBPs with LCDs in the assembly of stress granules, we expressed and purified hnRNPA1 and TDP-43 as fusions with solubility-enhancing His-SUMO tags (His-SUMO-hnRNPA1 and His-SUMO-TDP-43). Importantly, this purification always included careful RNA digestion followed by ion exchange and gel filtration chromatography to remove all nucleotides (Figure S1). The hnRNPA1 solution exhibited temperature-dependent reversible turbidity (Figure 1A), which was revealed by differential interference contrast microscopy to reflect the presence of numerous droplets (Figure 1B). The His-SUMO-TDP-43 solution was also turbid due to the presence of a multitude of small droplets (Figure 1C). The formation of hnRNPA1 droplets was inducible by a decrease in temperature, was rapidly reversible, and required a minimum protein concentration that was dependent on temperature (Movie S1). Droplets of hnRNPA1 exhibited wetting when they encountered the surface of the coverslip, suggesting liquid properties (Figure 1D and Movie S2). To further probe the nature of the droplets, we fluorescently labeled hnRNPA1 by conjugation to Oregon Green and observed that these protein droplets tended to fuse rapidly

into larger droplets within seconds, further reflecting liquid properties (Figure 1E and Movie S3). Removal of the His-SUMO tag from hnRNPA1 led to the same observations, demonstrating that properties intrinsic to hnRNPA1 mediate the ability for assembly into droplets (Figure S2). We assessed the mobility of hnRNPA1 molecules between the droplet and bulk phases by fluorescence recovery after photobleaching (FRAP) measurements (Figure 1F). After photobleaching a single droplet, the majority of its fluorescence signal (~80%) recovered with a characteristic recovery time of 3.7 s (Table S1). These data demonstrate that hnRNPA1 is highly dynamic, with rapid exchange of molecules between the droplets and the surrounding solution. The appearance of this second liquid phase in a temperature- and protein-concentration-dependent manner is consistent with LLPS by hnRNPA1 as described by Flory-Huggins theory (Flory, 1942; Huggins, 1942). hnRNPA1 is also able to assemble into hydrogels composed of uniformly polymerized amyloid-like fibers (Kato et al., 2012).

We produced hydrogels from purified His-SUMO-hnRNPA1 according to the protocol of (Kato et al., 2012); thus, purified hnRNPA1 was dialyzed at 4°C overnight, sonicated, concentrated, and incubated for 48 hr at room temperature, resulting in hydrogel formation. While hnRNPA1 hydrogels exhibit dynamic properties (Kato et al., 2012), they did not show any detectable fluorescence recovery after photobleaching in experiments lasting >15 min (Figures 1G and 1H), demonstrating that hnRNPA1 is more rigidly incorporated into hydrogels than into liquid droplets. These data are in agreement with the report that hnRNPA1 hydrogels are composed of cross- β fibrils, which may represent a thermodynamically stabilized or kinetically trapped state of the protein. While hnRNPA1 droplets showed a wide size distribution and grew over time by fusion events, TDP-43 droplets were similar in size with an upper limit of ~1 μ m and often appeared in strings as if fusion events into larger droplets were initiated but did not proceed (Movie S4). Their spherical nature suggested that they were also formed by LLPS, but since the material properties of TDP-43 droplets appeared more complex than classic liquid, we focused on the biophysical properties of hnRNPA1 going forward.

LLPS has been proposed as the molecular mechanism underlying formation of membrane-less cellular bodies that exhibit liquid properties, such as P granules and nucleoli (Brangwynne et al., 2009; Elbaum-Garfinkle et al., 2015; Fromm et al., 2014; Li et al., 2012; Nott et al., 2015). We observed that stress granules in cells exhibit liquid properties, regularly fusing into larger structures (Figure 1I and Movie S5). Moreover, hnRNPA1 in stress granules is in dynamic equilibrium with the surrounding cytosol, as illustrated by FRAP measurements showing similar recovery times (4.2 s) to purified hnRNPA1 in liquid droplets (Figure 1J). These classic liquid properties suggest that stress granules represent a separate liquid phase that is formed via LLPS.

The LCD of hnRNPA1 Mediates Liquid-Liquid Phase Separation and Is Sufficient for Incorporation into Stress Granules

In order to map the domains responsible for LLPS of hnRNPA1, we engineered His-SUMO fusion constructs containing either the folded N-terminal RNA recognition motifs (A1-RRM) or the

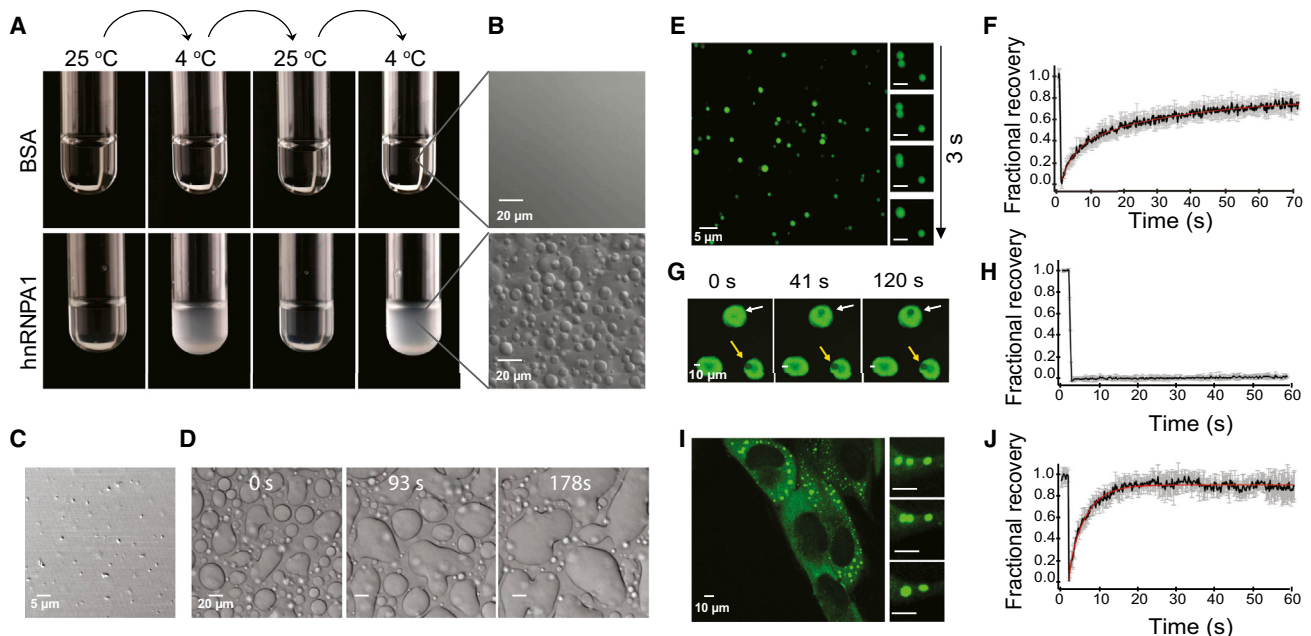


Figure 1. hnRNPA1 Spontaneously and Reversibly Assembles into Liquid Droplets

(A) Test tubes containing 500 μ M BSA or 500 μ M His-SUMO-hnRNPA1, respectively, were alternated between 4°C and 25°C.

(B) Transparent BSA or turbid hnRNPA1 solution observed by differential interference contrast (DIC) microscopy at 10°C.

(C) TDP-43 droplets observed by DIC at 25°C.

(D) 300 μ M hnRNPA1 in 100 mM NaCl exhibited wetting at the surface of the coverslip. Images were extracted from Movie S2.

(E) Fluorescence micrographs of hnRNPA1 (spiked with Oregon-green-labeled hnRNPA1 at a molar ratio of 300:1) in 150 mM NaCl buffer at 10°C reveal that the protein is enriched in the droplets; the droplets fuse over time. The main image and the panel on the right were extracted from Movie S3.

(F) FRAP of fluorescently labeled/unlabeled hnRNPA1 at a molar ratio of 1:300. The black curve is an average of FRAP events from nine distinct droplets; the error bars represent the SE. The red curve corresponds to a double exponential fit of the data. The two characteristic recovery times are 3.72 s and 31.6 s. See also Table S1.

(G) An area of hydrogel (white arrow) was photobleached over the course of 60 s. A decrease of the fluorescence intensity was observed but no recovery. The yellow arrow indicates an area of hydrogel photobleached 15 min before.

(H) FRAP of hydrogels. The black curve is an average of FRAP events from three different hydrogel pieces; the error bars represent the SE.

(I) Live imaging of U2OS cells expressing G3BP-GFP. The cells were stressed for 1 hr with 0.5 mM arsenite, and stress granule formation was observed. Stress granules fused over time. The main image and the panel on the right were extracted from Movie S5.

(J) FRAP of hnRNPA1 in stress granules. The black curve is an average of FRAP events from 12 distinct stress granules from 12 distinct cells; the error bars represent the SE. The red curve corresponds to a single exponential fit of the data. The characteristic recovery time is 4.21 s. See also Table S1.

C-terminal LCD (A1-LCD) (Table S2), which is predicted to be intrinsically disordered (Figures 2A and S3). The A1-LCD alone had the ability to form liquid droplets, whereas A1-RRM failed to undergo LLPS under comparable conditions to full-length hnRNPA1 (A1-FL) and all other conditions tested (Figure 2B).

hnRNPA1 amino acid residues 259–264 correspond to a steric zipper motif centered in the LCD and are essential to hnRNPA1's intrinsic tendency to fibrillize (Kim et al., 2013). Importantly, the corresponding deletion mutant (A1- Δ hexa), which does not fibrillize (Kim et al., 2013), readily underwent LLPS, demonstrating that LLPS and fibrillization are two mechanistically distinct processes (Figures 2A and 2B). To test the role of LCD-mediated LLPS in the formation of stress granules, we transiently expressed wild-type, GFP-tagged LCD from hnRNPA1 (GFP-LCD) or a version with deletion of aa259–264 constituting the steric zipper (GFP-LCD Δ hexa) in HeLa cells (Figure 2C). Both proteins were efficiently incorporated into stress granules, suggesting that stress granule assembly does not require fibrilli-

zation and hence is distinct from hydrogel formation (Figures 2D and 2E).

Liquid-Liquid Phase Separation by hnRNPA1 Is Based on Weak Interactions

To gain further insight into the intermolecular interactions underlying LLPS by hnRNPA1, we measured the temperature at which droplets first formed as a function of protein concentration and molecular crowding, allowing the construction of a phase diagram (Figure 3A). Whereas LLPS by hnRNPA1 occurs spontaneously in a temperature- and protein-concentration-dependent manner in the absence of a crowding agent (Figure S4A), we mapped the phase diagram in the presence of Ficoll, a typical crowding agent, to mimic the crowded cellular environment, which is thought to contain ~200 mg/ml of macromolecules (Elis, 2001). Ficoll was used for most experiments, but polyethylene glycol (PEG) was also able to promote hnRNPA1 LLPS (Figure S4B). These data demonstrated that the propensity for

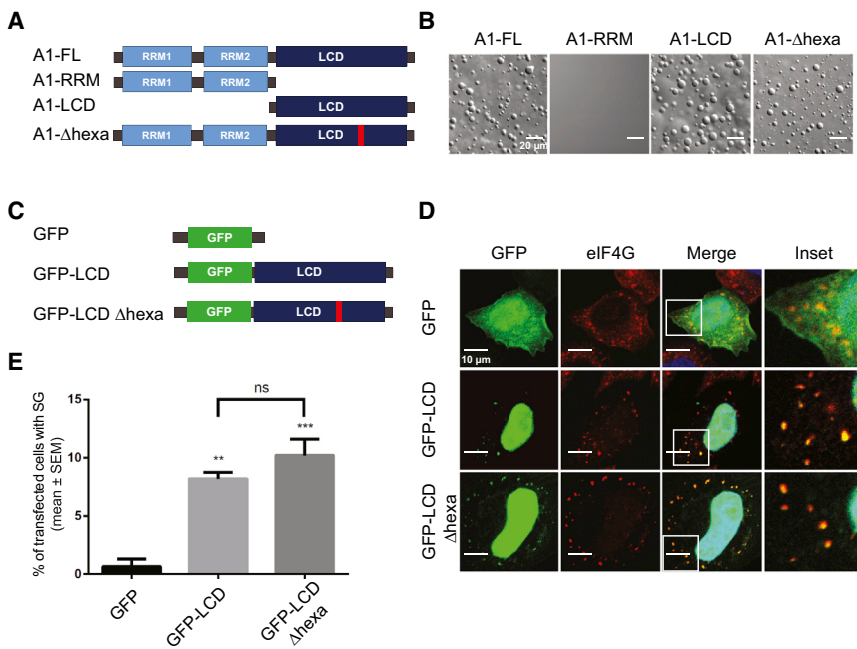


Figure 2. Liquid-Liquid Phase Separation by hnRNPA1 Is Mediated by the C-Terminal Low Complexity Sequence Domain and Is Distinct from Fibrillization

(A) Schematic of the structure of hnRNPA1 full length (A1-FL), the N terminus comprising the two folded RNA recognition motifs (A1-RRM), the low complexity sequence domain (A1-LCD), and the mutant with a deletion of residues 259–264 (Kim et al., 2013) (A1-Δhexa).

(B) DIC images of A1-FL, A1-RRM, A1-LCD, and A1-Δhexa at 140 μM protein, 150 mg/ml Ficoll in 50 mM HEPES, 300 mM NaCl, and 5 mM DTT.

(C) Schematic of the constructs transiently expressed in HeLa cells.

(D) Representative confocal microscopy images of HeLa cells transfected with constructs presented in (C), treated with 0.5 mM sodium arsenite for 15 min, and immunostained with anti-eIF4G (red) and DAPI (blue).

(E) Quantification for data in (D). The percentage of transfected cells displaying GFP signal in SGs ([number of cells with GFP-positive SGs/number of GFP-expressing cells] × 100) was plotted as mean ± SEM; n = 100 cells; **p < 0.005, ***p < 0.001 by one-way ANOVA, Tukey's post hoc test.

phase separation increased with increased molecular crowding, and the hnRNPA1 concentration necessary for phase separation drops substantially approaching conditions of intracellular molecular crowding. From the shape of the phase diagram, we conclude that hnRNPA1 has an upper critical solution temperature (UCST), i.e., a critical temperature exists, above which the two-phase regime cannot be accessed. A UCST phase diagram indicates that LLPS is driven mostly by enthalpy, with favorable interactions between protein molecules mediating assembly (Flory, 1942; Huggins, 1942). We also observed that lowering the NaCl concentration led to LLPS at lower A1-FL concentrations, suggesting that electrostatic interactions contributed to LLPS. Again, the hnRNPA1 concentration necessary for phase separation dropped substantially approaching conditions of intracellular salt concentration (Figure 3B). Interestingly, LLPS by A1-FL was disrupted by hexanediol, a compound that disables the selectivity filter of the nuclear pore complex by disrupting the interactions of phenylalanines in the FG repeats (Patel et al., 2007; Ribbeck and Görlich, 2002), suggesting that aromatic residues in the LCD contribute to LLPS of hnRNPA1 (Figure 3C). These results indicate that multiple types of favorable molecular interactions contribute to hnRNPA1 LLPS.

Increasing the Cytoplasmic Concentration of Endogenous LCD-Containing hnRNPs Is Sufficient to Drive Stress Granule Assembly

To manipulate the cytoplasmic concentration of endogenous hnRNPA1 and related hnRNPs in cells, we transiently expressed M9M peptide in HeLa cells. M9M peptide was designed to have a significantly greater affinity for Karyopherin-β2 than natural PY-NLSs present in hnRNPA1 and several closely related RNA-binding proteins (Bernis et al., 2014; Cansizoglu et al., 2007). As a result, M9M prevents Karyopherin-β2 from binding a select subset of PY-NLS-containing endogenous clients and results in their

accumulation in the cytoplasm (Cansizoglu et al., 2007; Dормann et al., 2012). We observed that transient expression of YFP-M9M in HeLa cells resulted in increased cytoplasmic concentration of hnRNPA1 and related LCD-containing RNA-binding proteins (hnRNPA2 and FUS), resulting in an increased assembly of stress granules compared to the cells transfected with YFP only (Figures 3D, 3E, S5A, and S5B). Together with the in vitro data, these observations suggest that concentration-dependent LLPS drives assembly of stress granules and requires a threshold protein concentration.

RNA Facilitates Liquid-Liquid Phase Separation by hnRNPA1 by Binding to RRM and LCD

Stress granules are enriched in RNA-binding proteins and translationally stalled mRNAs (Kedersha and Anderson, 2002). hnRNPA1 contains two RNA recognition motifs (Figure 2A) that have been shown to bind RNA (Burd and Dreyfuss, 1994); thus, we tested whether the association with RNA plays a role in hnRNPA1 phase separation properties. Based on CLIP-seq, hnRNPA1 has been shown to bind >1,000 RNA species through a relatively short, degenerate sequence motif (Huelga et al., 2012). Thus, rather than engineer a specific sequence, we used a random oligonucleotide RNA sequence. Fluorescently labeled RNA (fl-RNA⁴⁴) was recruited into the protein-dense droplets formed by hnRNPA1 (Figure 4A). Notably, the addition of RNA substantially decreased the hnRNPA1 concentration required for phase separation to as low as 500 nM, well within the estimated intracellular concentration of hnRNPA1 (Figure 4B and Supplemental Information). The increased propensity for LLPS in the presence of RNA suggested the formation of larger hetero-oligomers. Indeed, despite our previous results that A1-RRM alone was not able to undergo LLPS under any conditions when tested in isolation, it readily phase separated in the presence of RNA (Figure 4C). The two RRM domains and multiple

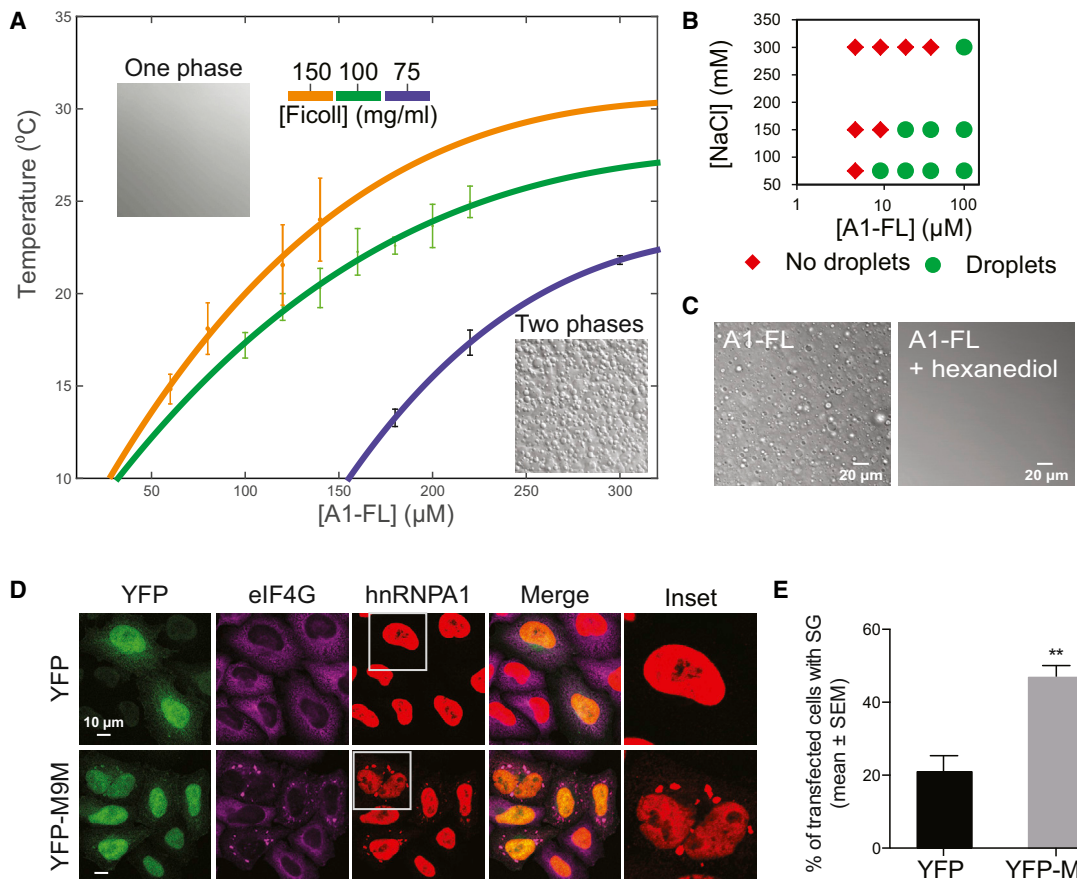


Figure 3. Molecular Crowding, Electrostatic and Hydrophobic Interactions, and Increased Cytoplasmic Concentration of hnRNPs Contribute to Liquid-Liquid Phase Separation of hnRNPA1

(A) Phase diagrams of hnRNPA1 in 50 mM HEPES, 300 mM NaCl, 5 mM DTT. The apparent cloud point, i.e., the temperature at which droplets were first observed, was determined as a function of protein concentration and molecular crowding. Each point represents the mean of a triplicate \pm SD. The solid curve represents a fit to a relation for binary demixing that describes the shape of the coexistence curve (Muscol and Rosenberger, 1997; Sengers, 1980; Stanley, 1971).

(B) Protein/NaCl concentration pairs scoring positive (green circles) or negative (red diamonds) for the appearance of droplets. The experiment was performed in 100 mg/ml Ficoll at 10°C.

(C) DIC images of 100 μM hnRNPA1 and 150 mg/ml Ficoll at 10°C; the solution returns to the one-phase regime upon the addition of 5% 1,6-hexanediol.

(D) Confocal microscopy images of HeLa cells transfected with YFP or YFP-M9M and immunostained with anti-hnRNPA1 (red) and anti-eIF4G (purple). The insets show hnRNPA1. See also Figure S5.

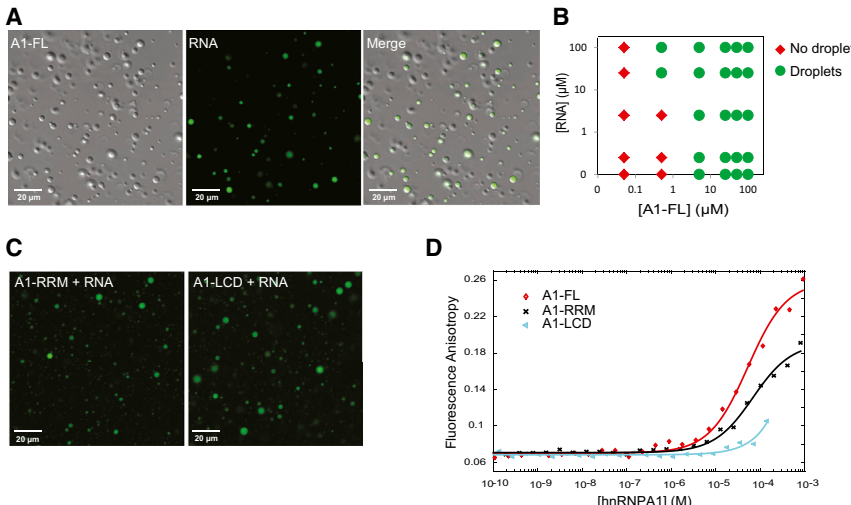
(E) Quantification for data in (D). The percentage of transfected cells displaying SGs was plotted as mean \pm SEM; n = 100 cells; **p < 0.005 by one-way ANOVA, Tukey's post hoc test.

binding motifs for RRM on the RNA likely mediate weak multivalent interactions that lead to LLPS. Droplets formed by A1-LCD also recruited RNA (Figure 4C), indicating that the LCD of hnRNPA1 binds RNA, as shown previously (Mayeda et al., 1994). Indeed, using fluorescence anisotropy, we confirmed that A1-FL, A1-RRM, and A1-LCD interacted with fl-RNA⁴⁴ with micromolar affinity (Figure 4D). In this experiment, we added increasing concentrations of the indicated proteins to fl-RNA⁴⁴. Protein binding to RNA slows the tumbling of the labeled species, and this is detected by an increase in fluorescence anisotropy; the inflection point on the curve corresponds approximately to the dissociation constant of the interaction. Thus, RNA can bind the RRM domains, as well as the LCD in hnRNPA1, and this multi-

valency likely results in the formation of large higher-order complexes that promote LLPS of hnRNPA1 more efficiently than via the LCD alone. Our findings suggest a mechanism by which multivalent interactions between RNA and some RNA-binding proteins may contribute to the formation of stress granules.

Disease-Causing Mutation to hnRNPA1 Does Not Significantly Alter Liquid-Liquid Phase Separation Properties

The disease-causing hnRNPA1 mutant, D262V, was associated with increased stress granule assembly, as well as formation of hnRNPA1 fibrils, but the relationship of these observations was unclear (Kim et al., 2013). To examine the impact of disease



solid lines are non-linear least-squares fits to a direct binding model (Roehrl et al., 2004). Importantly, LLPS did not occur under these conditions; the increase in fluorescence anisotropy is therefore caused by direct binding, not partitioning of RNA into droplets.

mutation on LLPS of hnRNPA1, we expressed and purified His-SUMO-hnRNPA1-D262V (A1-D262V) and determined that this mutant protein undergoes spontaneous temperature- and concentration-dependent LLPS to create liquid droplets that were morphologically indistinguishable from liquid droplets formed by wild-type protein (Movie S6). Assessment of A1-D262V in liquid droplets by FRAP showed a recovery time of similar duration (2.9 s) to that of wild-type hnRNPA1, illustrating that the mutation did not significantly impact dynamic exchange with the surrounding solution—at least in the time frames examined (Figure 5A). We mapped the phase diagram of mutant hnRNPA1 in the presence of molecular crowder (Ficoll at 100 mg/ml) and 300 mM NaCl and found no significant differences from that of wild-type hnRNPA1 (Figure 5B). Finally, we observed that wild-type and mutant hnRNPA1 were miscible in droplets (Figure 5C). Together, these results suggest that the disease-causing mutation does not significantly impact the interactions that drive phase separation.

Liquid-Liquid Phase Separation Promotes Fibrillization of the Disease-Causing Mutant

While examining the LLPS properties of A1-D262V, we noted that reversible droplet assembly was accompanied by the accumulation of insoluble precipitate on the coverslip surface (Figure 6A). After the temperature was raised and the droplets dispersed, the surface of the coverslip was found to be blanketed with Thioflavin-T (ThT)-positive fibrils (Figure S6). This phenomenon occurred within minutes of droplet assembly by A1-D262V and was not observed with wild-type hnRNPA1 or A1-Δhexa. We tested the fibrillization propensity of the His-SUMO-tagged proteins under agitation at 25°C by ThT fluorescence and observed substantially greater fibrillization of the mutant compared to wild-type, whereas hnRNPA1-Δhexa did not fibrillize over a period of 24 hr (Figure 6B). Fibrillization by A1-D262V under these conditions occurred on a timescale of hours, consistent with previous results (Kim et al., 2013). To

Figure 4. RNA Facilitates Liquid-Liquid Phase Separation of hnRNPA1 by Binding to RRMs and LCD

(A) DIC/Fluorescence images of 120 μM hnRNPA1 mixed with 1.2 μM fluorescein-labeled RNA at 10°C. The samples of purified hnRNPA1 were RNA free (Figure S1).

(B) Phase diagram of hnRNPA1 as a function of protein concentration and RNA concentration. Red and green symbols indicate that the sample was in the one-phase or the two-phase regime, respectively. The experiment was performed in 50 mM HEPES, 150 mM NaCl, 5 mM DTT, and 150 mg/ml Ficoll at 10°C.

(C) Fluorescence images of 100 μM fluorescein-labeled RNA mixed with 100 μM A1-RRM or A1-LCD at 10°C.

(D) A1-FL, A1-RRM, and A1-LCD binding to RNA was monitored by changes in fluorescence anisotropy of 5'-fluorescein-labeled RNA (fl-RNA⁴⁴). Symbols represent experimental data points, and

observe the effect of LLPS on fibrillation, we mixed purified wild-type hnRNPA1 and mutant hnRNPA1 under conditions that allowed LLPS and noted that fibrils of mutant hnRNPA1 formed almost immediately in the floating condensed liquid droplets (Figure 6C) and gradually deposited on the coverslip surface (Figure 6D). Interestingly, we observed that mutant hnRNPA1 fibrils eventually seeded the assembly of wild-type hnRNPA1, resulting in mixed fibrils on the coverslip surface (Figure 6D), which is consistent with the previous observation that preformed fibrils of hnRNPA1 can seed assembly (Kim et al., 2013). To further illustrate the role of phase separation in driving fibrillization, we investigated the temporal correlation of the onset of fibrillization with LLPS. The protein was held in the one-phase regime (33°C) or held in the two-phase regime (16°C) by decreasing the temperature at different time points (0 min and 20 min). Mutant hnRNPA1 always formed fibrils immediately upon LLPS at either early or late time points but never formed fibrils when the protein was maintained in the one-phase regime over the same period of time (Figure 6E). Taken together, our findings demonstrate that LLPS increases the propensity of hnRNP1-D262V to form amyloid-like fibrils, likely by increasing the local protein concentration in droplets and enhancing nucleation. The presence of wild-type protein in droplets, or presumably other RBPs at risk for aggregation in stress granules, such as TDP-43, leads to its co-recruitment into fibrils.

DISCUSSION

We showed that the RBPs hnRNPA1 and TDP-43, disease-related proteins that are typical components of stress granules, are able to assemble into protein-rich droplets via LLPS (Figure 1). The LCD of hnRNPA1 mediates LLPS in vitro and is sufficient for recruitment into stress granules in cells (Figure 2). LLPS of hnRNPA1 is tunable by environmental conditions; specifically, lower salt concentration, molecular crowding, and interaction with RNA all reduce the protein concentration required for

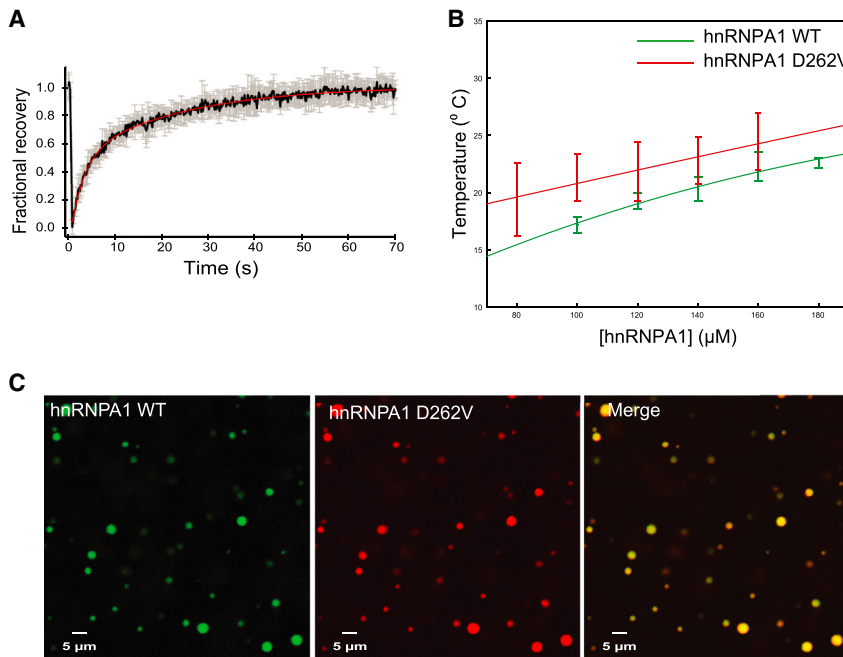


Figure 5. Disease-Causing Mutant Has Liquid-Liquid Phase Separation Properties Similar to the Wild-Type

(A) FRAP of fluorescently labeled/unlabeled A1 D262V at a molar ratio of 1:300. The black curve is an average of FRAP events from nine distinct droplets; the error bars represent the SE. The red curve corresponds to a double exponential fit of the data. The two characteristic recovery times are 2.86 s and 23.2 s. See also Table S1.

(B) Phase diagrams of wild-type hnRNP A1 and hnRNP A1-D262V. The apparent cloud point, i.e., the temperature at which droplets were first observed, was determined as a function of protein concentration. Each point represents the mean of a triplicate \pm SD. The solid curve represents a fit to a relation for binary demixing from renormalization-group theory. WT data are replotted from Figure 3A.

(C) Fluorescence images of Oregon-green-labeled/unlabeled wild-type hnRNP A1 mixed with Rhodamine-Texas red labeled/unlabeled A1-D262V (both at molar ratios of 1:300) at 10°C.

LLPS to a physiologically relevant range (Figures 3 and 4). Forced increase in the cytoplasmic concentration of hnRNP A1 and closely related RBPs is sufficient to drive stress granule assembly, which is consistent with an LLPS-mediated process (Figure 3). Fibrillation of hnRNP A1 promoted by a potent steric zipper in the LCD is dispensable for LLPS and for the recruitment of the LCD to stress granules (Figure 2). Furthermore, protein molecules can exchange between the protein-poor and protein-rich phases on a timescale of seconds, which is consistent with the dynamics observed in stress granules in cells (Figure 1). By contrast, LCD-containing RBPs are more rigidly incorporated into hydrogels composed of uniformly polymerized amyloid-like fibers (Kato et al., 2012; Figure 1). Nevertheless, it is evident that a propensity toward fibrillation is a conserved feature of LCD-containing RBPs, possibly due to the sequence features giving rise to LLPS and specific interactions with other binding partners. The fibrillation propensity may also be physiologically relevant to stress granule function as has been previously suggested (Kato et al., 2012), perhaps representing a process of maturation after assembly is initiated by LLPS. On the other hand, the propensity toward fibrillation within the condensed liquid environment of stress granules also poses a risk, particularly when the LCD contains a fibril-promoting mutation (such as the disease-causing D262V mutation in hnRNP A1), which can lead to excess, pathological fibrillation as observed in ALS, FTD, myopathy, and MSP and as predicted by Weber and Brangwynne (2012) (Figures 6 and 7).

LCD Sequence Properties Promoting LLPS

Proteins harboring LCDs are abundant in RNA granules and other membrane-less organelles (Anderson and Kedersha, 2006; Buchan and Parker, 2009; Voronina et al., 2011). Our finding that the LCD of hnRNP A1 mediates LLPS is consistent

with recent reports that LCD-mediated LLPS of the DEAD-box helicases Ddx4 and Laf-1 play roles in the assembly of P granules (Elbaum-Garfinkle et al., 2015; Nott et al., 2015). As with generic IDPs (Das and Pappu, 2013; Das et al., 2015; Müller-Späth et al., 2010), amino acid composition and sequence patterning likely determine interactions within and conformational properties of LCDs and encode their ability to undergo phase separation. What might these features be? We find that LLPS of hnRNP A1 is enthalpy driven and that aromatic and electrostatic interactions are driving forces (Figure 3). Indeed, hnRNP A1 is enriched in the aromatic residues phenylalanine and tyrosine and the positively charged residue arginine relative to the overall eukaryotic proteome (Hormoz, 2013). Moreover, the LCD sequence of hnRNP A1 is patterned; phenylalanine and tyrosine residues are relatively evenly distributed with a mean spacing of 6.2 ± 2.3 residues (Figure S7). Positively charged residues, mainly arginines, are also well distributed (Figure S7). They may thus represent reiterated interaction motifs in the background of a polar polymer and enable multivalent interactions that drive LLPS.

Multivalent RNA/RRM Domains Mediate Assembly of Large Complexes

Stress granules are, of course, composed not only of RBPs but also untranslated mRNAs (Buchan and Parker, 2009; Teixeira et al., 2005), posing the question of what role RNA plays in mediating LLPS of RBPs. Upon LLPS of a mixture of hnRNP A1 and RNA, we find that RNA not only localizes to the dense protein phase but reduces the hnRNP A1 concentrations required for LLPS. RNA likely engages hnRNP A1 in a multivalent fashion via both the RRM domains and the LCD, resulting in large, cross-linked complexes that undergo LLPS at reduced concentrations. This interpretation is supported by several

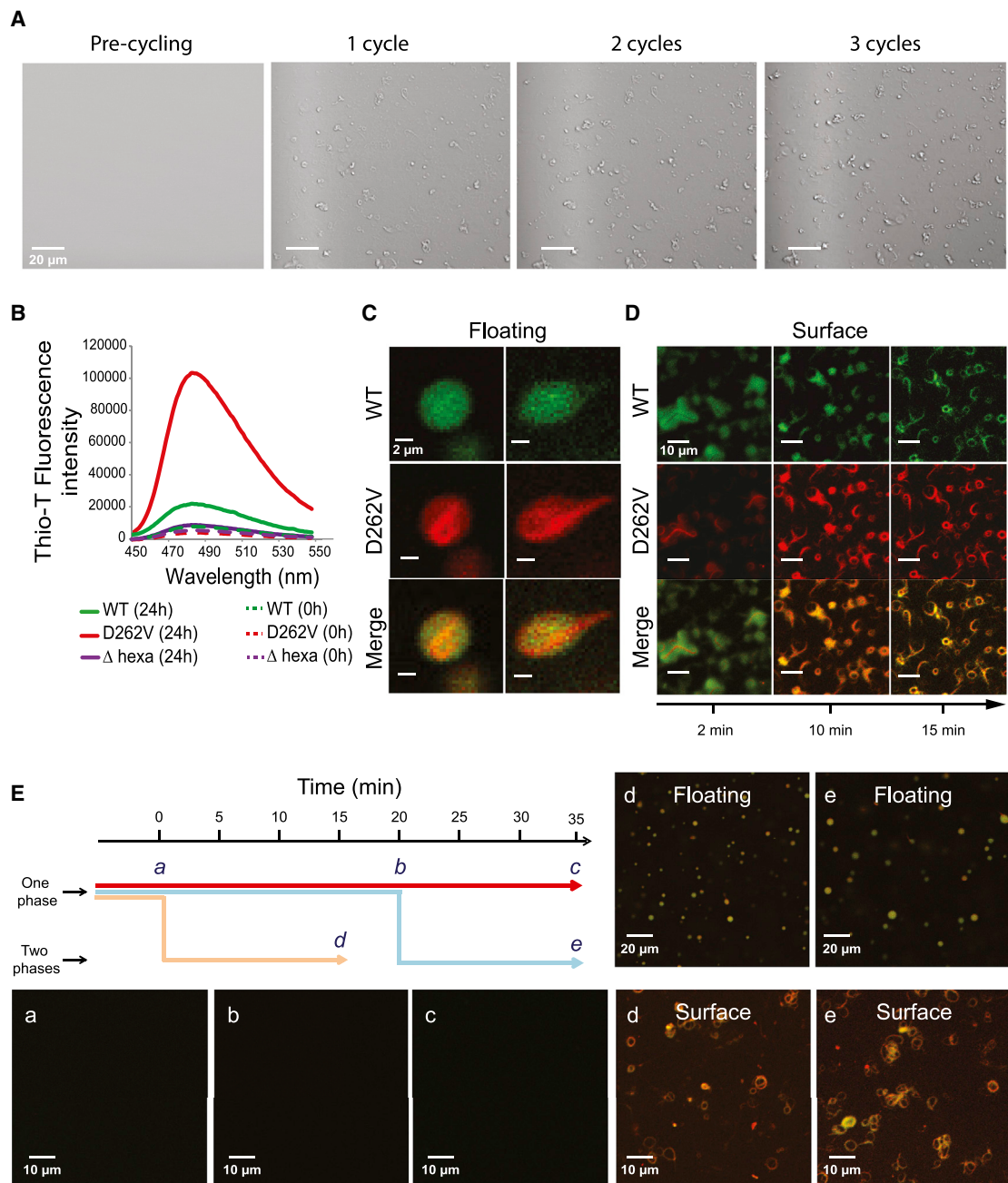


Figure 6. Phase Separation Promotes Fibrillation of hnRNPA1 D262V

All experiments were performed in 50 mM HEPES, 300 mM NaCl, 5 mM DTT, and 100 mg/ml Ficoll.

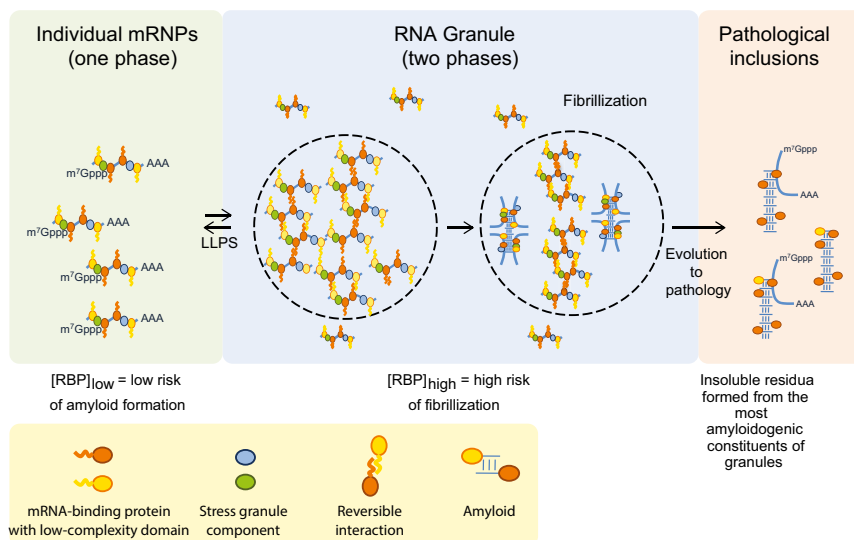
(A) A1-D262V fibril accumulation on the surface of the coverslip was monitored by cycling the temperature between 10°C and 25°C. Each cycle corresponded to a starting temperature of 25°C, subsequently decreased to 10°C to allow droplet formation and increased back to 25°C. The images were taken at 25°C in order to visualize the surface. See also [Figure S6](#).

(B) A1-FL, A1-D262V, or A1-Δhexa were agitated at 25°C for 24 hr. Fibrillization was monitored by ThT fluorescence.

(C) Fluorescence images of floating droplets of a mixture of Oregon-green-labeled/unlabeled wild-type hnRNPA1 (total concentration 160 μM, molar ratio of 1:300) mixed with Rhodamin-Texas red labeled/unlabeled A1 D262V (total concentration 160 μM, molar ratio of 1:300) at 16°C.

(D) Fluorescence images of a mixture of Oregon-green-labeled/unlabeled wild-type hnRNPA1 (total concentration 160 μM, molar ratio of 1:300) mixed with Rhodamin-Texas-red-labeled/unlabeled A1-D262V (total concentration 160 μM, molar ratio of 1:300) at 33°C. The images were taken at indicated times at the surface of the coverslips.

(E) Schematic summarizing the experiment to correlate phase separation and fibrillization. The sample was either kept in the one-phase regime (33°C) for 35 min (red arrow), kept in the one-phase regime for 20 min and then put in the two-phase regime by decreasing the temperature to 16°C for 15 min (blue arrow), or kept in the two-phase regime for 15 min (yellow arrow). The images were taken at the indicated time points (a–e).

**Figure 7. Model**

Model depicting the relationship between phase separation, fibrillization, and pathological inclusions.

stress granule formation or prolong their assembly (Figure 7) and the fibrillar pathology that dominates end-stage disease. Thus, we propose that the condensed liquid state of stress granules resulting from LLPS of hnRNP A1 and related RBPs presents a low probability risk of assembling amyloid-like fibrils that, under normal conditions, can be managed by granule disassembly and cellular proteostasis machinery. However, when stress granules are composed of RBPs that contain LCD mutations that promote fibrillization (Kim et al., 2013;

Klar et al., 2013; Kwiatkowski et al., 2009; Sreedharan et al., 2008; Vieira et al., 2014), or when stress granules persist due to disturbances in disassembly machinery (Buchan et al., 2013; Figley et al., 2014), pathogenic fibrils can assemble and escape quality control surveillance.

EXPERIMENTAL PROCEDURES

Protein Expression and Purification

A1-FL, A1-RRM, A1-LCD, A1-D262V, and A1-Δhexa were expressed as His-SUMO-tagged fusion proteins in BL21-Gold (DE3) cells (Agilent) in LB medium. Cells were lysed in 50 mM HEPES (pH 7.5), 250 mM NaCl, 30 mM imidazole, 2 mM βME, 100 µg/ml RNase, and complete protease inhibitor cocktail (Roche) with a microfluidizer. The cleared lysate was loaded onto a gravity NiNTA column, washed with lysis buffer, and eluted in 50 mM HEPES (pH 7.5), 300 mM NaCl, 300 mM imidazole, and 2 mM βME. The proteins were treated with 0.2 mg/ml RNase A (Roche) for 5 min at 37°C. The proteins were purified by ion exchange chromatography with a HiTrap SP or Q column (GE Healthcare). The fractions were analyzed by SDS-PAGE gel, pooled, and concentrated. They were then subjected to size exclusion chromatography on a Superdex 200 16/60 column (GE Healthcare) equilibrated in sample buffer, 50 mM HEPES (pH 7.5), 300 mM NaCl, and 5 mM DTT. The fractions were analyzed by SDS-PAGE gel, pooled, concentrated, and stored at -80°C. Dynamic light scattering was used to ensure that the proteins were monomeric. The RNA levels were analyzed by polyacrylamide gel (Figure S1). hnRNP A1 WT was fluorescently labeled with Oregon green 488, hnRNP A1 D262V with Rhodamine Red-X (for details, see *Supplemental Experimental Procedures*).

Formation of hnRNP A1 Hydrogels

Purified A1-FL was dialyzed against a gelation buffer containing 50 mM Tris-HCl (pH 7.5), 150 mM NaCl, 1 mM TCEP, 0.1 mM EDTA, and 1 mM benzamidine overnight at 4°C. The protein solution was sonicated 10 s at a 13% power level on a Misonix ultrasonic liquid processor Model S4000. The protein solutions were concentrated to roughly 35 mg/ml. After centrifugation, a 0.5 µl droplet of the supernatant was deposited onto a glass-bottomed microscope dish (MatTek). The dish was sealed with parafilm and incubated for 2 days at RT. The method was adapted from a previous report (Kato et al., 2012).

Cell Culture and Transfection

HeLa and U2OS G3BP-GFP cells were cultured in DMEM (Hyclone) supplemented with 10% FBS (Hyclone) and GlutaMax-1X (GIBCO). The U2OS G3BP-GFP stable line was a gift from Paul Anderson. Cells were transfected

findings: (1) the folded RRM domains alone do not phase separate in the absence of RNA under any conditions tested; (2) RNA promotes LLPS of the RRM domains, presumably by engaging the two RRM domains in a multivalent fashion via several nucleotide motifs, as was previously shown for PTB/RNA interactions (Li et al., 2012), resulting in large, cross-linked complexes; and (3) the LCD also binds RNA. Thus, our results suggest that both protein-protein and protein-RNA interactions work synergistically in the assembly of RNA granules.

Fibrillization of RBPs in Stress Granules—Pathology or Physiological Function?

hnRNP A1 is intrinsically prone to fibrillization—a propensity that is strongly enhanced by mutations that cause ALS and PSP (Kim et al., 2013). Although fibrillization is not required for LLPS, and disease mutation does not significantly impact LLPS behavior on short timescales (Figure 5), fibrillization of mutant hnRNP A1 is enhanced in the two-phase regime (Figure 6). We propose that the high local protein concentration in the condensed liquid droplets increases the probability of rare nucleation events and of the rate constant for adding monomers to a growing fibril, which is in agreement with typical nucleation-driven fibrillization processes (Eisenberg and Jucker, 2012). Changes in the conformational ensemble and dynamics of the LCD compared to the dispersed state may also play roles in enhanced nucleation (Pappu et al., 2008). Nevertheless, the fact that wild-type hnRNP A1 is prone to fibrillization on longer timescales, a behavior shared by a large number of related RBPs (Ramaswami et al., 2013), suggests that this property could occur in the context of RNA granules in cells and potentially contribute to physiological functions. For example, short length-scale dynamic fibrils might assemble in the condensed liquid phase during maturation of long-lived RNA granules and play functional roles or provide mechanical stability.

Irrespective of a potential physiological role in normal stress granules, our findings provide a model to explain the relationship between disease-associated genetic mutations that promote

using FuGENE6 transfection reagent (Roche), according to the manufacturer's instructions.

FRAP Methods and Analysis

FRAP experiments were performed using a Marianas spinning disk confocal (SDC) imaging system on a Zeiss Axio Observer inverted microscope platform. Time-lapse images of the sample were collected with 100 ms exposure time for 1 to 2 min at 5.6 frames per second using a Zeiss Plan-Apochromat 63 \times 1.4 NA oil objective and Evolve 512 EMCCD camera (Photometrics). Images were analyzed with SlideBook 6 software (3i). For FRAP analysis, mean fluorescence intensities from three regions of interests (ROIs) of time-lapse images were computed. ROI-1 was the photobleached region/droplet, and ROI-2 was drawn in the area/droplet not connected to the photobleached droplet and was used to correct for overall photobleaching due to imaging laser illumination. ROI-3 was defined as background, and its signal was subtracted from both ROI-1 and ROI-2 signals. Such background and photobleaching corrected fluorescence intensity versus time graphs were expressed in fractional form normalized by the pre-photobleach intensity (Axelrod et al., 1976) and fitted to equations for single- or double-exponential recovery. See also Table S1.

Immunofluorescence Studies

Cells were fixed in 4% paraformaldehyde in phosphate-buffered saline (PBS), permeabilized with 0.5% Triton X-100 in PBS for 10 min, blocked with 5% goat serum in PBS for 45 min, and incubated with primary antibody for 1.5 hr at RT. Primary antibodies were visualized with secondary antibodies conjugated with Alexa Fluor 488, Alexa Fluor 555, and Alexa Fluor 647 (Molecular Probes, Invitrogen), and nuclei were detected using DAPI. Stained cells were examined using a Zeiss LSM 780 NLO confocal microscope with Zeiss ZEN software.

In Vitro Determination of Phase Diagram

Samples were prepared by mixing the determined amount of protein, buffer, and Ficoll PM 400 (Sigma). Apparent cloud points were measured using a Linkam PE100 thermal stage mounted on a Zeiss LSM 780 NLO microscope. Sealed sample chambers containing protein solutions comprised coverslips sandwiching two layers of 3M 300 LSE high-temperature double-sided tape (0.34 mm) and were taped on the PE100 silver heating/cooling block. The variance in the solution conditions was monitored with temperature. For each given hnRNP A1 concentration, the sample was equilibrated at 33°C (one-phase regime). The temperature was then decreased at a rate of 2°C/min until the initial appearance of droplets at the apparent cloud point. Each set of cloud points (three independent replicates) was fitted to the scaling relation for binary demixing from renormalization-group theory (Muscollo and Rosenberger, 1997; Sengers, 1980; Stanley, 1971):

$$T = T_c \left\{ 1 - A \left| \frac{Cc - Cp}{Cc} \right|^{1/\beta} \right\}, \text{ with a critical exponent } \beta = 0.325.$$

Fluorescence Anisotropy

The N-terminally fluorescently labeled RNA fl-RNA⁴⁴ with sequence GGGC CCCCGGGUACCGAGCGUCUAAUCAAAACAAAAGCU was purchased from Sigma. For direct FA binding assays, increasing concentrations of A1-FL, A1-RRM and A1-LCD were titrated into 40 nM fl-RNA⁴⁴ in a buffer containing 50 mM HEPES (pH 7.5), 300 mM NaCl, 0.01% Triton, and 5 mM DTT, and the FA was monitored with a CLARIOstar plate reader (BMG Labtech) at 25°C. We performed a standard fluorescence anisotropy binding experiment, in which we added increasing concentrations of the indicated proteins to fluorescein-labeled RNA. Protein binding to RNA slows the tumbling of this labeled species, and this is detected by an increase in fluorescence anisotropy. Analysis was performed as described previously (Roehrl et al., 2004).

In Vitro Fibril Formation Assay with Thioflavin-T Measurements

The experiment was performed as described previously (Kim et al., 2013). In brief, 100 μM A1-WT, A1-D262V, and A1-Δhexa, respectively, were incubated at 25 °C under agitation for 24 hr. Aliquots were removed at 0 and 24 hr and added to a solution of 50 μM ThT, and the fluorescence intensity at excitation/emission wavelengths of 450/550 nm, respectively, was determined.

SUPPLEMENTAL INFORMATION

Supplemental Information includes Supplemental Experimental Procedures, seven figures, two tables, and six movies and can be found with this article online at <http://dx.doi.org/10.1016/j.cell.2015.09.015>.

AUTHOR CONTRIBUTIONS

A.M., H.J.K., T.M., and J.P.T. designed experiments. A.M., J.T., J.L., M.C., A.P.K., H.J.K., and T.M. performed the experiments. A.M., J.T., H.J.K., T.M., and J.P.T. contributed to data analysis. A.M., H.J.K., T.M., and J.P.T. wrote the manuscript.

ACKNOWLEDGMENTS

We thank J. Peng for his help in estimating the intracellular hnRNP A1 concentrations. We thank V. Frohlich and the St. Jude Cell and Tissue Imaging Shared Resource for extended access to their microscopes. We thank M. Rosen and R. Parker for comments on our manuscript and for sharing data prior to publication. We thank M. Marzahn for scientific input and E. Enemark for sharing reagents. We thank J. Parobek and A-M. Hedges in St. Jude Biomedical Communications for photography of the test tubes. This work was supported by funding from the Muscular Dystrophy Association, the Packard Center for ALS Research, Target ALS, and ALSAC.

Received: June 25, 2015

Revised: August 5, 2015

Accepted: August 25, 2015

Published: September 24, 2015

REFERENCES

- Anderson, P., and Kedersha, N. (2006). RNA granules. *J. Cell Biol.* **172**, 803–808.
- Anderson, P., and Kedersha, N. (2009). Stress granules. *Curr. Biol.* **19**, R397–R398.
- Axelrod, D., Koppel, D.E., Schlessinger, J., Elson, E., and Webb, W.W. (1976). Mobility measurement by analysis of fluorescence photobleaching recovery kinetics. *Biophys. J.* **16**, 1055–1069.
- Bernis, C., Swift-Taylor, B., Nord, M., Carmona, S., Chook, Y.M., and Forbes, D.J. (2014). Transportin acts to regulate mitotic assembly events by target binding rather than Ran sequestration. *Mol. Biol. Cell* **25**, 992–1009.
- Bosco, D.A., Lemay, N., Ko, H.K., Zhou, H., Burke, C., Kwiatkowski, T.J., Jr., Sapp, P., McKenna-Yasek, D., Brown, R.H., Jr., and Hayward, L.J. (2010). Mutant FUS proteins that cause amyotrophic lateral sclerosis incorporate into stress granules. *Hum. Mol. Genet.* **19**, 4160–4175.
- Brangwynne, C.P., Eckmann, C.R., Courson, D.S., Rybarska, A., Hoege, C., Gharakhani, J., Jülicher, F., and Hyman, A.A. (2009). Germline P granules are liquid droplets that localize by controlled dissolution/condensation. *Science* **324**, 1729–1732.
- Brangwynne, C.P., Mitchison, T.J., and Hyman, A.A. (2011). Active liquid-like behavior of nucleoli determines their size and shape in *Xenopus laevis* oocytes. *Proc. Natl. Acad. Sci. USA* **108**, 4334–4339.
- Buchan, J.R., and Parker, R. (2009). Eukaryotic stress granules: the ins and outs of translation. *Mol. Cell* **36**, 932–941.
- Buchan, J.R., Kolaitis, R.M., Taylor, J.P., and Parker, R. (2013). Eukaryotic stress granules are cleared by autophagy and Cdc48/VCP function. *Cell* **153**, 1461–1474.
- Burd, C.G., and Dreyfuss, G. (1994). RNA binding specificity of hnRNP A1: significance of hnRNP A1 high-affinity binding sites in pre-mRNA splicing. *EMBO J.* **13**, 1197–1204.
- Cansizoglu, A.E., Lee, B.J., Zhang, Z.C., Fontoura, B.M., and Chook, Y.M. (2007). Structure-based design of a pathway-specific nuclear import inhibitor. *Nat. Struct. Mol. Biol.* **14**, 452–454.

Das, R.K., and Pappu, R.V. (2013). Conformations of intrinsically disordered proteins are influenced by linear sequence distributions of oppositely charged residues. *Proc. Natl. Acad. Sci. USA* **110**, 13392–13397.

Das, R.K., Ruff, K.M., and Pappu, R.V. (2015). Relating sequence encoded information to form and function of intrinsically disordered proteins. *Curr. Opin. Struct. Biol.* **32**, 102–112.

Dormann, D., Madl, T., Valori, C.F., Bentmann, E., Tahirovic, S., Abou-Ajram, C., Kremmer, E., Ansorge, O., Mackenzie, I.R., Neumann, M., and Haass, C. (2012). Arginine methylation next to the PY-NLS modulates Transportin binding and nuclear import of FUS. *EMBO J.* **31**, 4258–4275.

Eisenberg, D., and Jucker, M. (2012). The amyloid state of proteins in human diseases. *Cell* **148**, 1188–1203.

Elbaum-Garfinkle, S., Kim, Y., Szczepaniak, K., Chen, C.C., Eckmann, C.R., Myong, S., and Brangwynne, C.P. (2015). The disordered P granule protein LAF-1 drives phase separation into droplets with tunable viscosity and dynamics. *Proc. Natl. Acad. Sci. USA* **112**, 7189–7194.

Ellis, R.J. (2001). Macromolecular crowding: an important but neglected aspect of the intracellular environment. *Curr. Opin. Struct. Biol.* **11**, 114–119.

Figley, M.D., Bieri, G., Kolaitis, R.M., Taylor, J.P., and Gitler, A.D. (2014). Profilin 1 associates with stress granules and ALS-linked mutations alter stress granule dynamics. *J. Neurosci.* **34**, 8083–8097.

Flory, P.J. (1942). Thermodynamics of high polymer solutions. *J. Chem. Phys.* **10**, 51.

Fromm, S.A., Kamenz, J., Nöldeke, E.R., Neu, A., Zocher, G., and Sprangers, R. (2014). In vitro reconstitution of a cellular phase-transition process that involves the mRNA decapping machinery. *Angew. Chem. Int. Ed. Engl.* **53**, 7354–7359.

Hackman, P., Sarparanta, J., Lehtinen, S., Virola, A., Evilä, A., Jonson, P.H., Luque, H., Kere, J., Screen, M., Chinnery, P.F., et al. (2013). Welander distal myopathy is caused by a mutation in the RNA-binding protein TIA1. *Ann. Neurol.* **73**, 500–509.

Hormoz, S. (2013). Amino acid composition of proteins reduces deleterious impact of mutations. *Sci. Rep.* **3**, 2919.

Huelga, S.C., Vu, A.Q., Arnold, J.D., Liang, T.Y., Liu, P.P., Yan, B.Y., Donohue, J.P., Shiue, L., Hoon, S., Brenner, S., et al. (2012). Integrative genome-wide analysis reveals cooperative regulation of alternative splicing by hnRNP proteins. *Cell Rep.* **23**, 167–178.

Huggins, M.L. (1942). Some properties of solutions of long-chain compounds. *J. Phys. Chem.* **46**, 151–158.

Hyman, A.A., Weber, C.A., and Jülicher, F. (2014). Liquid-liquid phase separation in biology. *Annu. Rev. Cell Dev. Biol.* **30**, 39–58.

Kato, M., Han, T.W., Xie, S., Shi, K., Du, X., Wu, L.C., Mirzaei, H., Goldsmith, E.J., Longgood, J., Pei, J., et al. (2012). Cell-free formation of RNA granules: low complexity sequence domains form dynamic fibers within hydrogels. *Cell* **149**, 753–767.

Kedersha, N., and Anderson, P. (2002). Stress granules: sites of mRNA triage that regulate mRNA stability and translatability. *Biochem. Soc. Trans.* **30**, 963–969.

Kim, H.J., Kim, N.C., Wang, Y.D., Scarborough, E.A., Moore, J., Diaz, Z., MacLea, K.S., Freibaum, B., Li, S., Molliex, A., et al. (2013). Mutations in prion-like domains in hnRNPA2B1 and hnRNPA1 cause multisystem proteinopathy and ALS. *Nature* **495**, 467–473.

Klar, J., Sobol, M., Melberg, A., Mäbert, K., Ameur, A., Johansson, A.C., Feuk, L., Entesarian, M., Orlén, H., Casar-Borota, O., and Dahl, N. (2013). Welander distal myopathy caused by an ancient founder mutation in TIA1 associated with perturbed splicing. *Hum. Mutat.* **34**, 572–577.

Kwiatkowski, T.J., Jr., Bosco, D.A., Leclerc, A.L., Tamrazian, E., Vanderburg, C.R., Russ, C., Davis, A., Gilchrist, J., Kasarskis, E.J., Munsat, T., et al. (2009).

Mutations in the FUS/TLS gene on chromosome 16 cause familial amyotrophic lateral sclerosis. *Science* **323**, 1205–1208.

Li, P., Banjade, S., Cheng, H.C., Kim, S., Chen, B., Guo, L., Llaguno, M., Hollingsworth, J.V., King, D.S., Banani, S.F., et al. (2012). Phase transitions in the assembly of multivalent signalling proteins. *Nature* **483**, 336–340.

Li, Y.R., King, O.D., Shorter, J., and Gitler, A.D. (2013). Stress granules as crucibles of ALS pathogenesis. *J. Cell Biol.* **201**, 361–372.

Mayeda, A., Munroe, S.H., Cáceres, J.F., and Krainer, A.R. (1994). Function of conserved domains of hnRNP A1 and other hnRNP A/B proteins. *EMBO J.* **13**, 5483–5495.

Müller-Späth, S., Soranno, A., Hirschfeld, V., Hofmann, H., Rüegger, S., Reymond, L., Nettels, D., and Schuler, B. (2010). From the Cover: Charge interactions can dominate the dimensions of intrinsically disordered proteins. *Proc. Natl. Acad. Sci. USA* **107**, 14609–14614.

Muschol, M., and Rosenberger, F. (1997). Liquid-liquid phase separation in supersaturated lysozyme solutions and associated precipitate formation/crystallization. *J. Chem. Phys.* **107**, 1953–1962.

Nott, T.J., Petsalaki, E., Farber, P., Jervis, D., Fussner, E., Plochowietz, A., Craggs, T.D., Bazett-Jones, D.P., Pawson, T., Forman-Kay, J.D., and Baldwin, A.J. (2015). Phase transition of a disordered nuage protein generates environmentally responsive membraneless organelles. *Mol. Cell* **57**, 936–947.

Pappu, R.V., Wang, X., Vitalis, A., and Crick, S.L. (2008). A polymer physics perspective on driving forces and mechanisms for protein aggregation. *Arch. Biochem. Biophys.* **469**, 132–141.

Patel, S.S., Belmont, B.J., Sante, J.M., and Rexach, M.F. (2007). Natively unfolded nucleoporins gate protein diffusion across the nuclear pore complex. *Cell* **129**, 83–96.

Ramaswami, M., Taylor, J.P., and Parker, R. (2013). Altered ribostasis: RNA-protein granules in degenerative disorders. *Cell* **154**, 727–736.

Ribbeck, K., and Görlich, D. (2002). The permeability barrier of nuclear pore complexes appears to operate via hydrophobic exclusion. *EMBO J.* **21**, 2664–2671.

Roehrl, M.H., Wang, J.Y., and Wagner, G. (2004). A general framework for development and data analysis of competitive high-throughput screens for small-molecule inhibitors of protein-protein interactions by fluorescence polarization. *Biochemistry* **43**, 16056–16066.

Sengers, J.V. (1980). Universality of critical phenomena in classical fluids. In *Phase Transitions Cargèse 1980*, M. Lévy, J.-C. Le Guillou, and J. Zinn-Justin, eds. (New York: Plenum Press), pp. 95–135.

Sreedharan, J., Blair, I.P., Tripathi, V.B., Hu, X., Vance, C., Rogej, B., Ackerley, S., Durnall, J.C., Williams, K.L., Buratti, E., et al. (2008). TDP-43 mutations in familial and sporadic amyotrophic lateral sclerosis. *Science* **319**, 1668–1672.

Stanley, H.E. (1971). *Introduction to Phase Transitions and Critical Phenomena* (New York: Oxford University Press).

Teixeira, D., Sheth, U., Valencia-Sánchez, M.A., Brengues, M., and Parker, R. (2005). Processing bodies require RNA for assembly and contain nontranslating mRNAs. *RNA* **11**, 371–382.

Vieira, N.M., Naslavsky, M.S., Licitio, L., Kok, F., Schlesinger, D., Vainzof, M., Sanchez, N., Kitajima, J.P., Gal, L., Cavaçana, N., et al. (2014). A defect in the RNA-processing protein HNRPD1 causes limb-girdle muscular dystrophy 1G (LGMD1G). *Hum. Mol. Genet.* **23**, 4103–4110.

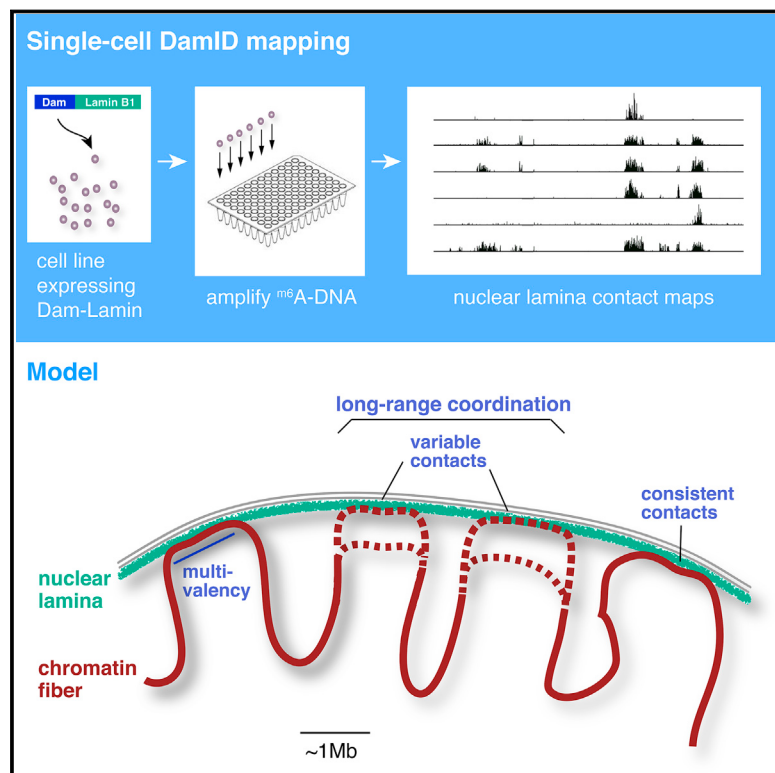
Voronina, E., Seydoux, G., Sassone-Corsi, P., and Nagamori, I. (2011). RNA granules in germ cells. *Cold Spring Harb. Perspect. Biol.* **3**, 3.

Weber, S.C., and Brangwynne, C.P. (2012). Getting RNA and protein in phase. *Cell* **149**, 1188–1191.

Wippich, F., Bodenmüller, B., Trajkovska, M.G., Wanka, S., Aebersold, R., and Pelkmans, L. (2013). Dual specificity kinase DYRK3 couples stress granule condensation/dissolution to mTORC1 signaling. *Cell* **152**, 791–805.

Genome-wide Maps of Nuclear Lamina Interactions in Single Human Cells

Graphical Abstract



Highlights

- Modified DamID method maps genome-nuclear lamina interactions in single human cells
- Nuclear lamina contact frequency is locus specific
- Stable contact sites are extremely gene poor, suggesting a structural role
- Single-cell maps point to multivalent interactions and long-range coordination

Authors

Jop Kind, Ludo Pagie,
Sandra S. de Vries, ..., Job Dekker,
Alexander van Oudenaarden,
Bas van Steensel

Correspondence

j.kind@hubrecht.eu (J.K.),
b.v.steensel@nki.nl (B.v.S.)

In Brief

A modified DamID method enables the mapping of genome-wide nuclear lamina interactions in single human cells, providing insight into the cell-to-cell variation in the interphase chromosome architecture and suggesting extensive intra-chromosomal coordination of nuclear lamina contacts.

Accession Numbers

GSE69423
GSE69841
GSE68596

Genome-wide Maps of Nuclear Lamina Interactions in Single Human Cells

Jop Kind,^{1,2,*} Ludo Pajie,¹ Sandra S. de Vries,¹ Leila Nahidiazar,³ Siddharth S. Dey,² Magda Bienko,⁷ Ye Zhan,⁴ Bryan Lajoie,⁴ Carolyn A. de Graaf,^{1,10} Mario Amendola,¹ Geoffrey Fudenberg,⁵ Maxim Imakaev,⁶ Leonid A. Mirny,^{6,8} Kees Jalink,³ Job Dekker,⁹ Alexander van Oudenaarden,² and Bas van Steensel^{1,*}

¹Division of Gene Regulation, Netherlands Cancer Institute, Plesmanlaan 121, 1066CX Amsterdam, the Netherlands

²Hubrecht Institute-KNAW (Royal Netherlands Academy of Arts and Sciences) and University Medical Center Utrecht, Cancer Genomics Netherlands, Uppsalaalaan 8, 3584CT Utrecht, the Netherlands

³Division of Cell Biology I, Netherlands Cancer Institute, Plesmanlaan 121, 1066CX Amsterdam, the Netherlands

⁴Program in Systems Biology, Department of Biochemistry and Molecular Pharmacology, University of Massachusetts Medical School, Worcester, MA 01605-0103, USA

⁵Graduate Program in Biophysics, Harvard University, Cambridge, MA 02138, USA

⁶Department of Physics, Massachusetts Institute of Technology, Cambridge, MA 02139, USA

⁷Science for Life Laboratory, Division of Translational Medicine and Chemical Biology, Department of Medical Biochemistry and Biophysics, Karolinska Institute, 171 21 Stockholm, Sweden

⁸Institute for Medical Engineering and Science, Massachusetts Institute of Technology (MIT), Cambridge, MA 02139, USA

⁹Howard Hughes Medical Institute, Program in Systems Biology, Department of Biochemistry and Molecular Pharmacology, University of Massachusetts Medical School, Worcester, MA 01605-0103, USA

¹⁰Present address: Molecular Medicine Division, The Walter and Eliza Hall Institute of Medical Research, Parkville, VIC 3052, Australia

*Correspondence: j.kind@hubrecht.eu (J.K.), b.v.steensel@nki.nl (B.V.S.)

<http://dx.doi.org/10.1016/j.cell.2015.08.040>

SUMMARY

Mammalian interphase chromosomes interact with the nuclear lamina (NL) through hundreds of large lamina-associated domains (LADs). We report a method to map NL contacts genome-wide in single human cells. Analysis of nearly 400 maps reveals a core architecture consisting of gene-poor LADs that contact the NL with high cell-to-cell consistency, interspersed by LADs with more variable NL interactions. The variable contacts tend to be cell-type specific and are more sensitive to changes in genome ploidy than the consistent contacts. Single-cell maps indicate that NL contacts involve multivalent interactions over hundreds of kilobases. Moreover, we observe extensive intra-chromosomal coordination of NL contacts, even over tens of megabases. Such coordinated loci exhibit preferential interactions as detected by Hi-C. Finally, the consistency of NL contacts is inversely linked to gene activity in single cells and correlates positively with the heterochromatic histone modification H3K9me3. These results highlight fundamental principles of single-cell chromatin organization.

INTRODUCTION

An important unresolved question in eukaryotic genome biology is how chromosomes are spatially organized inside interphase nuclei. Current evidence suggests that this organization is driven by probabilistic principles (Bickmore, 2013; Cavalli and Misteli,

2013; Gibcus and Dekker, 2013). Systematic fluorescence *in situ* hybridization (FISH) experiments have revealed that in a homogeneous cell population the nuclear positions of chromosomes are variable with respect to each other and relative to the periphery (Bolzer et al., 2005). However, this positioning is not entirely random; for example, in human lymphoid cells, chromosome 18 (chr18) tends to be located near the periphery, while chr19 shows a preference for the nuclear interior (Croft et al., 1999; Cremer et al., 2001).

At a smaller scale, certain individual genomic loci visualized by FISH also exhibit preferences for specific nuclear landmarks, such as the nuclear envelope (Marshall et al., 1996; Kosak et al., 2002) and nucleoli (Manuelidis and Borden, 1988; Ochs and Press, 1992), but usually with some degree of random variation. This variability is directly illustrated by *in vivo* tagging experiments in which loci contacting the nuclear lamina (NL) were tracked over mitosis in a clonal human cell line (Kind et al., 2013). This demonstrated that a sizeable subset of loci that were associated with the NL in mother cells relocated to the nuclear interior in daughter cells, indicating that, at least to some degree, genome contacts with the NL are intrinsically variable.

Complementary to these single-cell microscopy approaches are genome-wide mapping techniques that query the chromosome organization in large pools of cells (van Steensel and Dekker, 2010). For example, the 4C, 5C, and Hi-C technologies generate maps of the pair-wise spatial proximity of genomic loci (de Wit and de Laat, 2012; Dekker et al., 2013). Such maps have revealed global patterns that indicate that mammalian interphase chromosomes are partitioned into domains that are roughly 200 kb–2 Mb in size (Lieberman-Aiden et al., 2009; Dixon et al., 2012; Nora et al., 2012; Rao et al., 2014). Computational models of chromosome polymer folding fitted to 5C and Hi-C data generally suggest that interphase chromosomes adopt multiple configurations that vary from cell to cell

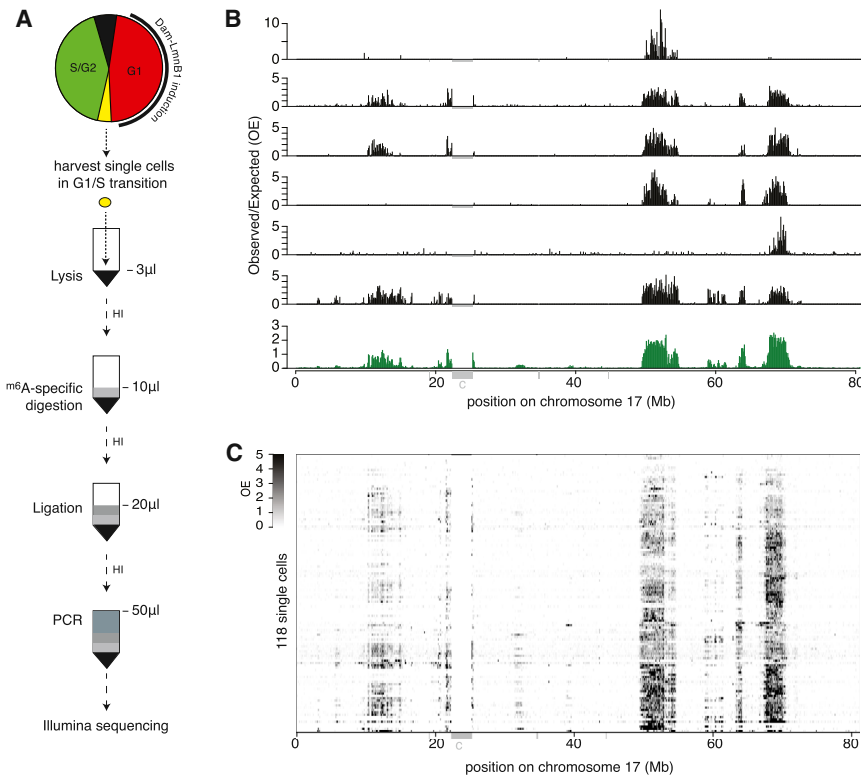


Figure 1. Single-Cell DamID Mapping of Genome-NL Interactions

(A) Schematic representation of the single-cell DamID procedure. HI, heat inactivation step. (B) NL contact maps for chr17 in six individual cells (black) and the average profile of 118 single cells (bottom track, green). OE, observed over expected read count ratio in contiguous 100-kb segments. (C) Grayscale representation of OE values for 118 single cells on chromosome 17. The gray bars underneath the axes in (B) and (C) mark unmappable regions; c, centromeric region. See also Figure S1.

ing, provide insights into the nature of LAD-NL interactions and uncover principles of cell-to-cell variation in chromosome architecture.

RESULTS

Single-Cell DamID Methodology

As a model system to develop single-cell DamID, we chose the human myeloid leukemia cell line KBM7, which is haploid for all chromosomes, except for chr8 and a small part of chr15 (Kotecki et al., 1999; Bürcstümmer et al., 2013). Even though this haploid state is unusual for human

somatic cells, it facilitates the interpretation of single-cell genome-wide maps because there is no need to discriminate the homologous chromosomes that are present in diploid cells.

We developed a DamID protocol for single cells as summarized in Figure 1A. We created a KBM7 clone (#14) that expresses an inducible fusion protein consisting of DNA adenine methyltransferase (Dam) and Lamin B1 (LmnB1) (Kind et al., 2013), as well as the Fucci two-color fluorescent reporter system to monitor the cell-cycle stage (Sakaue-Sawano et al., 2008). We then induced Dam-LmnB1 protein expression (Figures S1A and S1B), and 15 hr later we collected single cells at the onset of the S phase by fluorescence-activated cell sorting (FACS) (Figure S1C). This design ensured that the harvested cells had expressed Dam-LmnB1 for most of their recent G1 phase (which lasts on average ~14.9 hr, an estimate based on doubling time and FACS data), providing sufficient time for the accumulation of adenine methylation on the genomic loci that contact the NL. Importantly, LmnB1 was strictly confined to the nuclear periphery before and after Dam-LmnB1 induction (Figure S1D).

The single FACS-sorted cells were captured directly in a small volume of lysis buffer in a 96-well plate. Subsequent sample processing consisted of only a few steps (Figure 1A): digestion with DpnI, which is highly specific for Dam-methylated GATC sequences, followed by adaptor ligation (Figure S1E) and a total of 26 cycles of PCR amplification. A key difference with the conventional DamID protocol is that these steps are all done in the same well by sequential addition of reagents, without intermediate purification or concentration steps that could lead to loss of DNA. Gel electrophoresis showed that approximately half of the

(Lieberman-Aiden et al., 2009; Baù et al., 2011; Kalhor et al., 2012; Giorgetti et al., 2014; Nagano et al., 2013).

Another genome-wide approach to studying chromosome architecture is the mapping of interactions with the NL, mostly by means of the DamID technology (Guelen et al., 2008; Peric-Hupkes et al., 2010; Meuleman et al., 2013). The NL provides a very large surface area for potential contacts with the genome. Indeed, DamID studies have estimated that as much as ~35% of the mammalian genome can interact with the NL in any tested cell type, although it has remained unclear how much of the genome contacts the NL in a single cell. Genome-NL interactions occur through about 1,100–1,400 discrete lamina-associated domains (LADs), which have a median size of ~0.5 Mb and are scattered across all chromosomes. Most genes in LADs are expressed at very low levels, and results of various tethering experiments (Finlan et al., 2008; Reddy et al., 2008; Kind et al., 2013; Therizols et al., 2014) point to a reciprocal relationship between gene positioning at the NL and a repressive chromatin state.

The large size of LADs and their prevalence throughout the genome strongly suggest that LAD-NL interactions play an important role in interphase chromosome architecture. Insights into the single-cell behavior of these interactions will thus enhance our fundamental understanding of chromosome organization. Here, we report a modified version of the DamID technology that is sensitive enough to generate genome-wide maps of NL contacts in single human cells at a resolution of ~100 kb, which is well below the median size of LADs. We generated a total of 395 of these single-cell maps. These maps, complemented by Hi-C analysis and super-resolution microscopy imag-

wells yielded a clear smear of amplified DNA (Figure S1F). These PCR products were prepared for multiplexed Illumina sequencing by ligation of indexed adaptors, subsequently pooled, and sequenced.

Single-Cell NL Interaction Maps

In total, we generated 118 single-cell DamID maps from KBM7 clone #14. After applying quality filters (Figure S1G), we obtained a median of 5×10^5 reads per cell that could be mapped to a unique genomic location (Figure S1H). On average, 92% of the mapped locations started with a GATC motif, which is the recognition sequence of both Dam and DpnI, indicating that the detection is highly specific. For each cell, we binned these reads in 100-kb contiguous genomic segments, and then we calculated for each segment an observed over expected (OE) score based on the number of recovered unique reads, the theoretical maximum number of mappable unique reads in the segment, and the total genome-wide read count obtained from each cell. OE scores >1 indicate more Dam-LmnB1 methylation than may be expected by random chance.

Essentially, all cells showed a striking domain pattern of OE scores along most chromosomes, as illustrated for chr17 in Figures 1B and 1C. This pattern is reminiscent of the LAD profiles previously published for populations of cells. However, clear differences can be observed between individual cells (Figure 1B), often with entire megabase-sized domains missing, which is suggestive of cell-to-cell variation in NL contacts.

We note that the chosen segment size of 100 kb is a compromise between resolution and noise. Because the median human LAD size is approximately 0.5 Mb (Guelen et al., 2008), segments of 100 kb are expected to capture most of the LAD organization. Indeed, the OE scores in adjacent segments within each of the 118 single cell samples have a Pearson correlation coefficient of 0.70 ± 0.06 (mean \pm SD), indicating that neighboring segments report NL interactions in a partially redundant fashion with acceptable noise levels. For reference, at 100 kb resolution our previously published Dam-LmnB1 profiles from pools of human TIG3, hESCs, and HT1080 cells (Guelen et al., 2008; Kind et al., 2013; Meuleman et al., 2013) show a correlation of 0.88–0.90 between neighboring segments. The single-cell correlation of OE scores between adjacent segments is not related to the number of reads per cell (Pearson's correlation coefficient of 0.06, $p = 0.51$), indicating that the latter does not impose a limit to the quality of our data at 100 kb resolution.

Validation of Single-Cell Maps

To further gauge the overall quality of these data, we first reconstructed a population profile by averaging the maps of the 118 single cells and then compared it to a conventional microarray-based DamID profile generated from a large pool of KBM7 cells (Figure 2A). The highly similar domain patterns and an overall Spearman rank correlation coefficient of 0.90 demonstrate that the new protocol captures the same regions of interaction as the previous well-validated protocol.

However, in conventional DamID, a Dam-only control is typically included to normalize for chromatin accessibility and other potential biases (Vogel et al., 2007; Guelen et al., 2008). This normalization is not possible in single-cell DamID because the

Dam-LmnB1 and Dam-only profiles cannot be obtained from the same cell. Nevertheless, we established a Dam-only and Fucci-expressing KBM7 clone and mapped the adenine methylation patterns in 26 single cells. The resulting patterns are very different from the Dam-LmnB1 profiles (Figures 2B and 2C). In general, regions that have no detectable Dam-LmnB1 signal show clear Dam-only signals; hence, these regions are not intrinsically undetectable. Conversely, regions with very high Dam-only signals generally do not show a Dam-LmnB1 signal, indicating that there is no strong bias for accessibility in our Dam-LmnB1 maps. We conclude that leaving out the Dam-only normalization is acceptable for single-cell Dam-LmnB1 profiling.

Next, we performed multi-color fluorescent in situ hybridization (FISH) with probes for six genomic loci covering a broad range of average OE scores (Figures 2D–2F). Analysis of hundreds of nuclei revealed a good correspondence between the average distance to the periphery according to FISH and the average OE scores (Spearman's $\rho = 0.94$), confirming that our single-cell Dam-LmnB1 profiles provide a view of the spatial organization of the genome relative to the NL. Together these data indicate that single-cell DamID using Dam-LmnB1 generates NL interaction profiles with low noise levels, suitable resolution, acceptable bias, and with good correspondence to localization by FISH.

Cell-to-Cell Variability and Consistency of Genome-NL Associations

Visual inspection of the collection of single-cell maps suggested that some regions interact more frequently with the NL than others (Figures 1B and 1C). In order to analyze this systematically, we first converted the OE scores for each cell to a binary NL contact map. For this, we used an OE score cutoff of 1, motivated by the bimodal distribution of OE scores (Figure S2A) that suggests that loci are either in a "contact" or "no-contact" state. We then calculated for each 100-kb segment the NL contact frequency (CF), defined as the proportion of cells in which this segment contacted the NL. This data processing does not lead to a substantial loss of information content, because the Spearman rank correlation coefficient of the average radial position of the six FISH probes with CF is 0.90 (as compared to 0.94 for OE values, see above), and CF values correlate strongly with the average OE scores (Figure S2B). CF values are also highly robust with respect to sequencing read depth, because subsampling of the single-cell data to the one-but-lowest read count (1.04×10^5 reads; an average 3.1-fold downsampling) does not affect CF values (Figure S2C).

Strikingly, CFs vary widely across the genome (Figures 3A and 3B). About 23% of the 100-kb segments show no detectable contact with the NL in any of the 118 cells and thus are very stably located in the nuclear interior. Conversely, ~15% of the segments have CFs $>80\%$, representing loci that are consistently located at the NL. About 34% of the segments have contact frequencies in the range of 20%–80% and thus show high cell-to-cell variability in their NL associations. The remaining loci (29%) only occasionally contact the NL ($0 < CF < 20\%$).

These different classes of loci are scattered throughout the genome (Figure 3A), although the smaller chromosomes tend

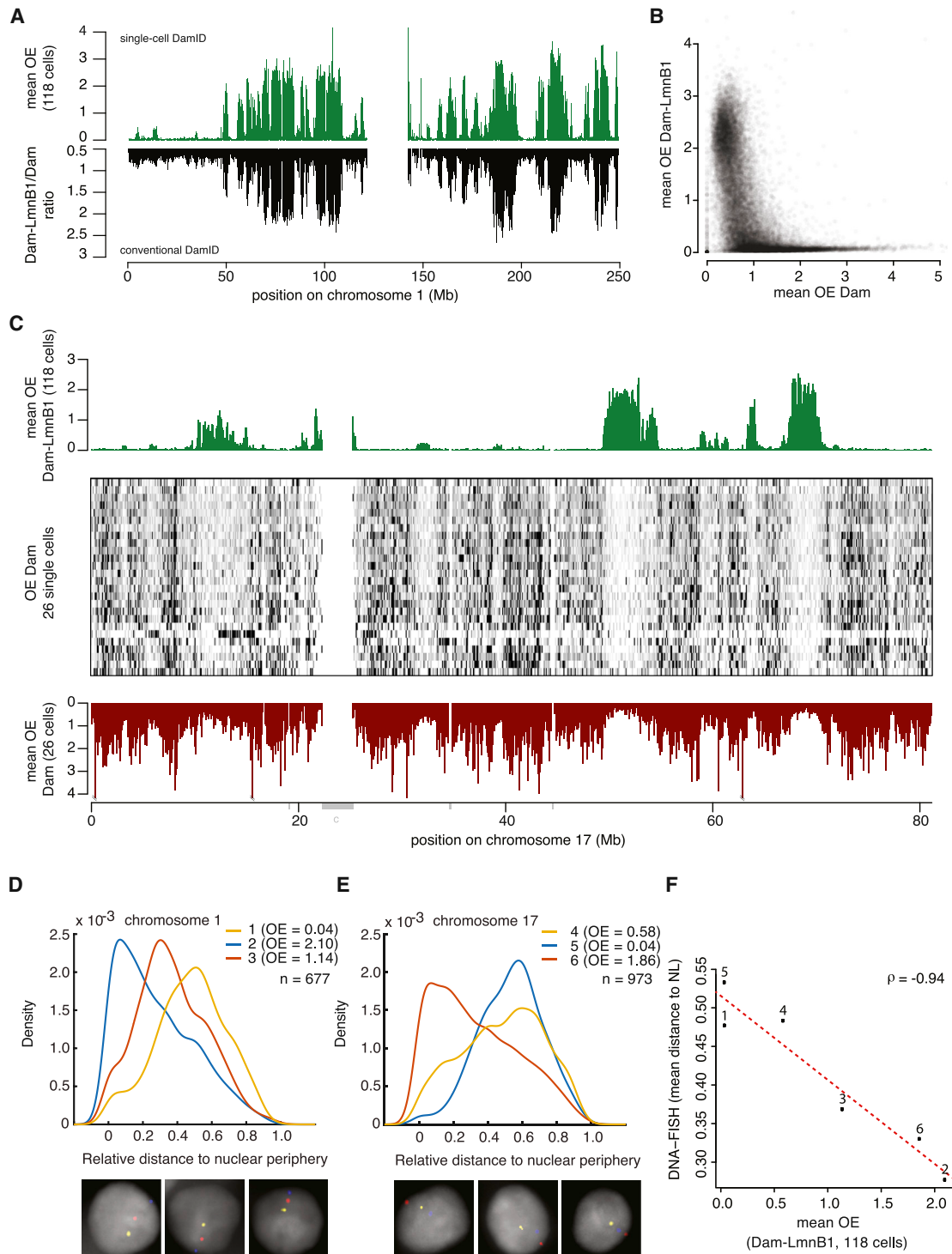


Figure 2. Validation of Single-Cell DamID Maps

(A) Comparison NL contact map for chr1 representing the average of 118 single-cell profiles (top profile) and a conventional DamID map generated with a population of $\approx 1-2 \times 10^5$ cells (bottom profile). The genome-wide correlation between the two methods is 0.90 (Spearman's ρ .)

(B) Average OE score of 118 single-cell Dam-LmnB1 samples (y axis) versus the average OE score of 26 single-cell Dam-only samples (x axis).

(C) Comparison of average OE scores obtained with Dam-LmnB1 (top track, average of 118 cells, same as in Figure 1B) and Dam-only (bottom track, average of 26 cells). OE scores for the individual Dam-only cells are shown as grayscale-encoded rows in the center frame. Gray bars underneath the bottom axis mark unmappable regions; c, centromeric region.

(legend continued on next page)

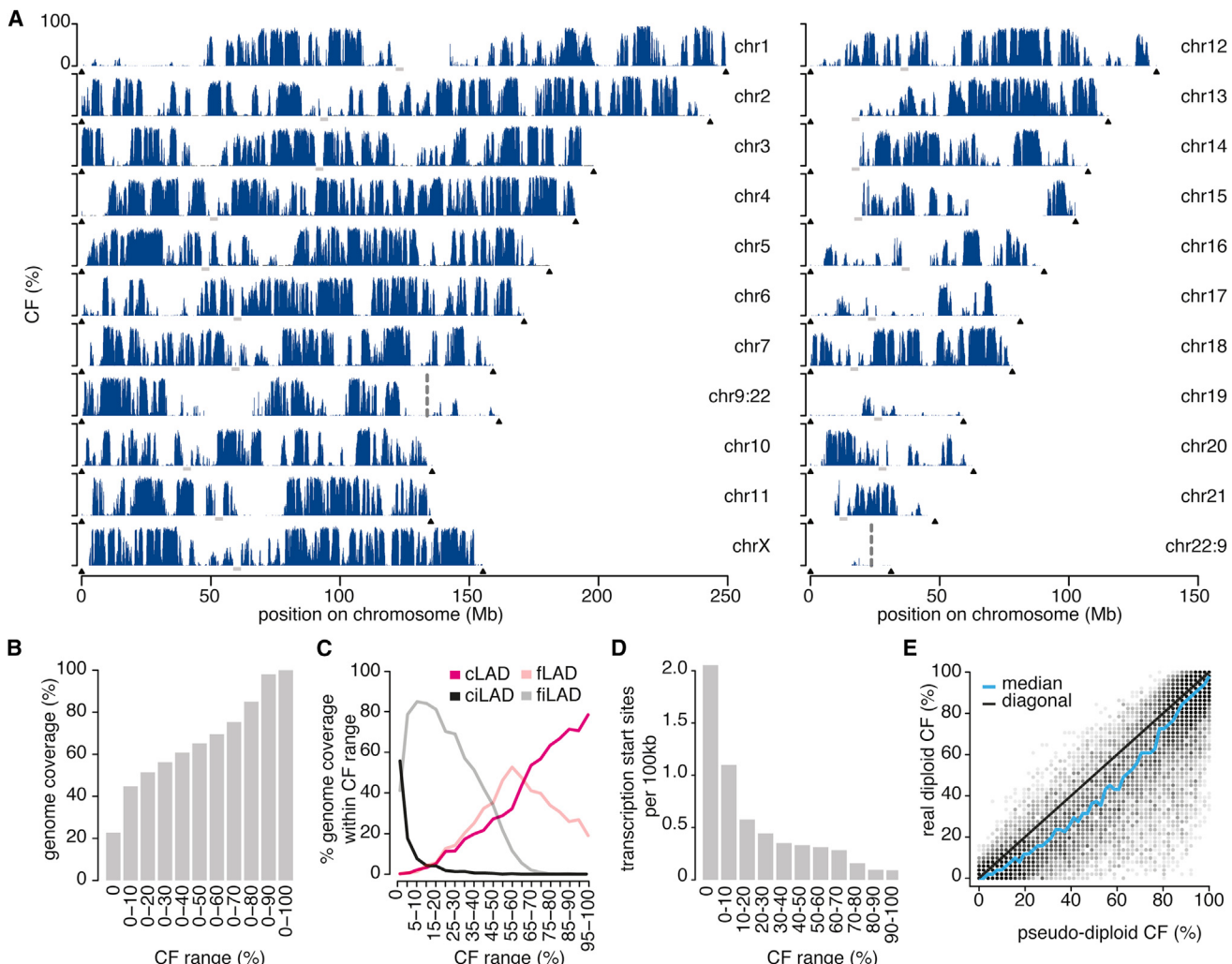


Figure 3. NL Contact Frequencies Are Linked to Developmental Dynamics, Gene Density, and Ploidy

(A) Estimated contact frequency maps for all chromosomes in clone #14 cells. KBM7 cells carry a balanced translocation between chr9 and chr22 (Bürckstümmer et al., 2013); vertical dotted lines mark the junctions. Centromeric regions are indicated by gray bars; telomeres are marked by black triangles. chr8 is not shown because it is diploid.

(B) Cumulative histogram of genome-wide CF values.

(C) Distribution of genomic segments with indicated CFs over constitutive (c) and facultative (f) LADs and inter-LADs (iLADs).

(D) Average number of transcription start sites per 100-kb segment, plotted as a function of CF.

(E) Comparison of CFs in diploid cells and pseudo-diploid cells. The latter are simulated by combining equal numbers of sequence reads from pairs of haploid cells. See also Figure S2 and Table S1.

to have a lower density of stable NL contacts than larger chromosomes. An exception to this rule is chr18, which harbors many regions with high CFs. This contrasts in particular with chr19, which only exhibits a few contact sites and very low CFs. This matches previous chromosome painting studies that found chr18 to be preferentially located at the nuclear periphery and chr19 in the nuclear interior (Croft et al., 1999; Cremer et al.,

2001). An intriguing pattern is visible on chrX (Figure 3A, bottom left). The distal arms of this chromosome have many stable NL contacts, while the centromere-proximal ~40 Mb show only variable contacts.

In order to confirm these CF patterns, we used an independently derived KBM7 clone that also expresses Dam-LmnB1 and the Fucci system (clone #5.5) to generate a total of 168

(D-F) Multi-color 3D DNA FISH microscopy with probes for six genomic loci covering a broad range of average OE scores distributed on chr1 ($n = 677$) (D) and chr17 ($n = 973$) (E). Graphs depict the distributions of radial probe positions, with zero corresponding to the nuclear edge and one to the centroid. Three representative nuclei with three-color FISH signals are displayed below the graphs; DNA staining with DAPI is shown in gray. (F) Mean radial positions of the six probes versus the mean DamID OE scores. Numbers 1–6 correspond to probe numbers in (D) and (E). The dotted line shows linear regression fit.

single-cell maps. The genome-wide CF profile of clone #5.5 is highly similar to that of clone #14 (Pearson correlation, $r = 0.97$; Figures S2D and S2E). However, the absolute CF values in clone #5.5 are systematically 1.3-fold lower than in clone #14, which we attribute to a somewhat lower activity of the Dam-LmnB1 protein in clone #5.5 (Figure S2F). Nevertheless, the relative CF differences between loci are highly consistent between the two clones. We cannot rule out that the CF values of clone #14 are underestimated, but the fact that the highest CF values of clone #14 are in the range of ~95%, combined with the tight linearity with clone #5.5, suggests that any underestimate in clone #14 is minor.

Stable and Variable NL Contacts Are Linked to Degrees of Developmental Plasticity

Previously, we reported that some LADs interact with the NL in a cell-type-specific (facultative) fashion, while other LADs do so in a cell-type invariant (constitutive) manner (Peric-Hupkes et al., 2010; Meuleman et al., 2013). We investigated whether this distinct behavior is linked to differences in CF. We used a collection of conventional microarray-based DamID maps of NL interactions in nine human cell lines of diverse origin (C.A.d.G. and B.v.S., unpublished data; see the [Supplemental Experimental Procedures](#)) to classify each 100-kb segment as constitutive LAD (cLAD), constitutive inter-LAD (ciLAD), facultative LAD (fLAD), or facultative inter-LAD (fiLAD). The latter are inter-LAD regions that are not associated with the NL in KBM7 cells, but do interact with the NL in at least one other cell type.

As expected, ciLADs have low CF values (Figure 3C), consistent with their definition as not associated with the NL. Likewise, cLADs tend to have high CF values. Thus, these constitutive regions are not only invariable between different cell types but tend to be consistently positioned relative to the NL within one cell type. In contrast, facultative LADs and iLADs have mostly intermediate CF values: fLADs generally have lower CF values than cLADs ($p < 2.2 \times 10^{-16}$, Wilcoxon test) and fiLADs have higher values than ciLADs ($p < 2.2 \times 10^{-16}$). The partial overlap in CF distributions of fLADs and fiLADs indicates that the definitions of these LAD classes are not perfect, which may be due to differences in the data types (single-cell versus population-based DamID maps; sequencing versus microarray) and resolution. These results uncover a link between CF and the consistency of NL interactions between different cell types.

We previously reported that cLADs have a ~2-fold lower gene density than ciLADs (Meuleman et al., 2013). CF values are more dramatically linked to gene density: regions with CF >80% have a ~20-fold lower gene density than regions with no NL contacts (Figure 3D). The few genes that are located in such high-CF regions are enriched for gene ontology categories very divergent from myeloid cell functions, among them most prominently the olfactory receptor genes (Table S1), which are rarely expressed.

A picture thus emerges in which most cLADs are relatively consistently associated with the NL, providing a structural backbone to chromosomes that is largely invariant between individual cells and also between cell types. In contrast, regions with cell-type-specific NL interactions generally interact less consistently with the NL, contributing to cell-to-cell variability in the spatial organization of chromosomes.

Ploidy of KBM7 Cells Primarily Affects Variable NL Contacts

We considered the possibility that competition between LADs could explain why some LADs contact the NL in only a fraction of all cells: such LADs may have lower NL binding affinities and fail to compete with stronger LADs in some of the cells. We wondered whether this balance could be altered by changing the total amount of genomic DNA in the nucleus. To test this, we took advantage of the fact that KBM7 cells spontaneously form diploid cells at low frequency (Kotecki et al., 1999). Such diploid cells should be genetically identical to the haploid cells, except for their ploidy. We derived a clonal diploid line from clone #14, with normal cell-cycle behavior (Figure S2G), and generated a total of 51 single-cell Dam-LmnB1 contact maps.

Comparison of the single-cell maps from haploid and diploid cells is not straightforward, because our current DamID method cannot determine whether the sequence reads from diploid cells are derived from one homolog or both. We therefore constructed “pseudo-diploid” reference maps by combining equal numbers of sequence reads from pairs of single haploid cells and then merged the reads and processed the data as above, as if they were derived from a single cell. Hence, these pseudo-diploid maps are simulated maps in which two homologs of each chromosome are present, but there cannot be any biological effect of increased ploidy (because the homologs were in different cells), while technical skews due to the inability to discriminate the two homologs should be identical to those in diploid cells.

Although the overall pattern of NL contacts was similar between pseudo-diploid and diploid cells, many loci showed decreased CFs in diploid cells compared to haploid cells (Figure 3E), while increased CFs were rare. Strikingly, these changes occurred preferentially in genomic segments that have intermediate CFs in pseudo-diploid (and thus haploid) cells. This result indicates that diploidization leads to preferential loss of NL interactions of LADs that contact the NL less robustly in haploid cells. We obtained similar results with 32 single cells from a diploid clonal line derived from clone #5.5 (Figure S2H). The loss of NL contacts in diploid cells suggests increased competition for NL contacts. This may be caused by a reduced surface-to-volume ratio and an increase in the average distance of loci to the NL, both of which are expected to accompany the increase in nuclear volume due to the doubled DNA content. However, other mechanisms cannot be ruled out.

Single-Cell Maps Point to a Multivalent Mechanism of LAD-NL Interactions

We wondered which biophysical principle could explain the differences in apparent NL affinity between genomic loci. The domain pattern of NL contacts suggests that these interactions are not mediated by focal attachments, but rather by multivalent interactions within each LAD. Because interactions with higher valency typically have a higher avidity, we predicted that long LADs interact more stably with the NL than short LADs. To analyze this, we defined LADs as continuous stretches of 100-kb segments with CF >1% across the 118 cells. This yielded a total of 1,358 LADs. Strikingly, the mean CF within each LAD shows a clear positive correlation with LAD length (Spearman’s $\rho = 0.81$; $p < 2.2 \times 10^{-16}$), reaching a plateau for sizes larger

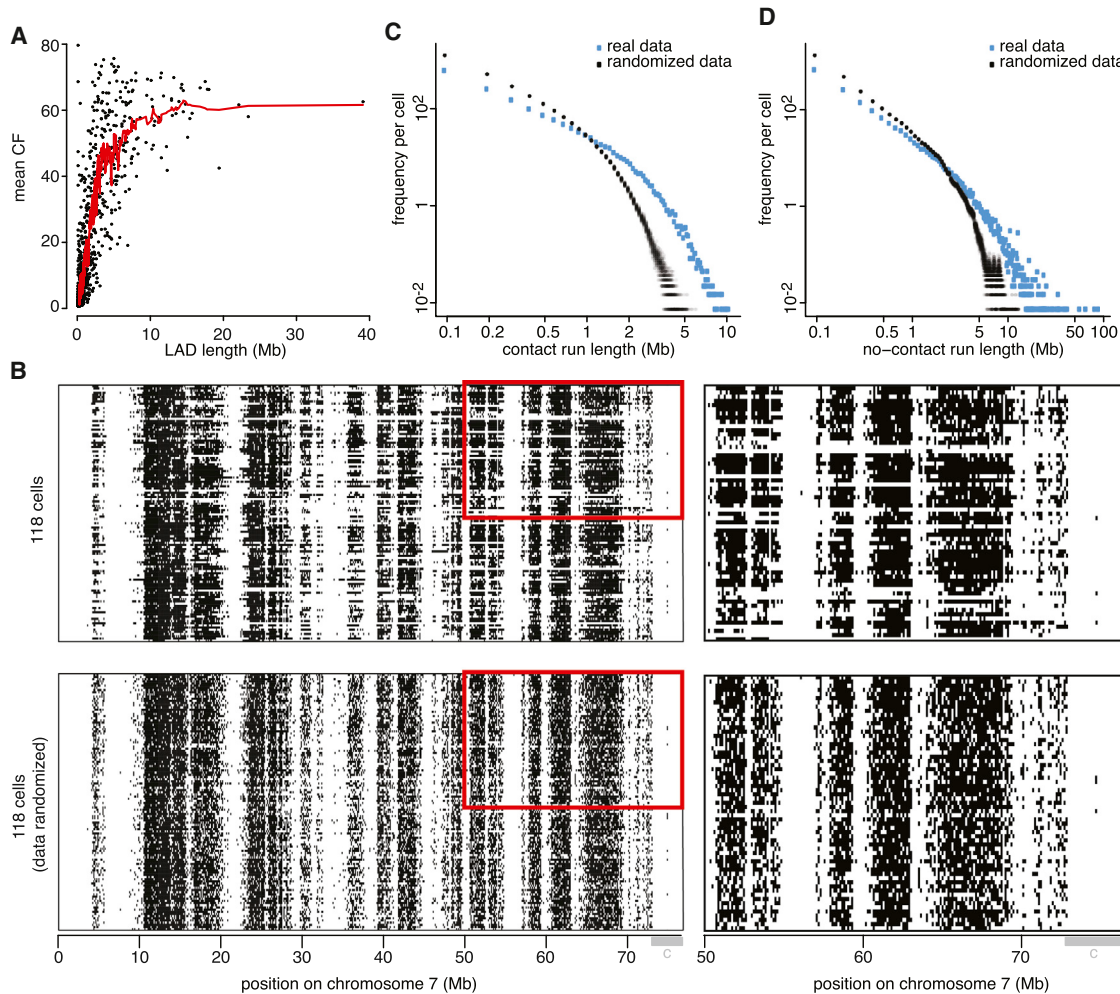


Figure 4. Evidence for Multivalent NL Interactions

(A) Correlation between the mean CF and the length of LADs. Here, LADs are defined as continuous regions in which all 100-kb segments have CF >1% across all 118 clone #14 cells. The curve shows running mean with bin size 15.

(B) Binarized NL contact map of the p arm of chr7 in 118 cells (top), and the same data after a random shuffling procedure that keeps CFs and the number of contacts per cell the same, to simulate the complete absence of coordination between neighboring segments (bottom). The gray bar marked “c” indicates the centromeric region. Right-hand panels are magnified views of the regions outlined by red boxes in the left-hand panels.

(C) Distribution of genome-wide NL contact run lengths in 118 single-cell datasets (blue) compared to 100 sets of randomized data (gray).

(D) Genome-wide length distribution of no-contact runs in real (blue) and 100 sets of randomized (gray) data. No-contact runs present in all 118 cells (i.e., regions that never contact the NL) were excluded in this analysis.

See also Figure S3.

than ~6–8 Mb (Figure 4A). This supports a model of multivalent local genome-NL interactions.

This multivalency model predicts that there are continuous stretches of contact in individual LADs in single cells. Indeed, such runs of contact could be frequently observed (black horizontal streaks in Figure 4B, top). For comparison, we randomly shuffled the contact data to simulate a “random button” model, in which each segment maintains exactly the same CF as in the real data, but contacts the NL independently of its neighboring segments (Figure 4B, bottom). This pattern has a much more fine-grained appearance than the original contact maps, with fewer long runs of contact. Quantitative analysis showed that long contact runs, particularly above ~1.5 Mb, occur more

frequently in the real data than in the simulated random button model (Figure 4C). This supports the multivalent interaction model.

Long-Range Coordination of NL Contacts within Chromosomes

Interestingly, we also observed long runs of no-contact on many single chromosomes (white horizontal streaks in Figure 4B, top). Particularly in the range of >5 Mb, such runs occur more frequently than may be expected by random chance (Figure 4D). We interpret these long runs of no-contact as large chromosomal regions (often including multiple LADs) that completely dissociate from the NL in an incidental manner. These long no-contact runs are not generally due to loss of large chromosomal

regions during sample processing, because our Dam-only single cell maps have more homogeneous methylation patterns (Figure 2C) and lack long runs that are completely devoid of mappable sequence reads (Figure S3A).

This coordinated detachment of neighboring LADs from the NL prompted us to systematically search for evidence of coordination of NL contacts, by calculating pair-wise NL contact correlations for all 100-kb segments within each chromosome, based on the binary NL contact maps of the 118 single cells. The resulting correlation matrices, which indicate how pairs of loci may coordinately attach and detach from the NL in single cells, showed remarkable plaid-like patterns on all chromosomes (Figure 5A). Along the diagonal, squares of consistently positive correlations represent units of coordinated NL contacts, which tend to be one to several megabases in size. Most of these units exhibit additional off-diagonal correlations with other units, sometimes with striking specificity (Figure 5A, examples marked with arrows and boxes). Such coordinated units can be tens of megabases apart, although the frequency decays gradually with distance (Figure 5B). Randomized contact maps yield much lower average correlation coefficients over all distances, demonstrating that the prevalence of positive correlations is not due to random chance (Figure 5B). Intra-chromosomal coordination is on average higher than inter-chromosomal coordination, and the latter is not higher than may be expected by random chance (Figure S4A). These results point to extensive coordination of NL contacts within chromosomes, often over long genomic distances.

Coordination of NL Contacts Is Partially Linked to Physical Proximity as Detected by Hi-C

The plaid-like correlation patterns reminded us of patterns commonly observed with Hi-C (Lieberman-Aiden et al., 2009; Dixon et al., 2012), a technology that maps proximity of genomic sequences in nuclear space (Dekker et al., 2013). An intriguing possibility was therefore that regions with coordinated NL contacts could be in spatial proximity to one another. To investigate this, we generated Hi-C maps from KBM7 clone #14 cells. The resulting Hi-C interaction matrices appeared partially similar to the NL contact correlation matrices (Figure 5C).

To quantify the similarity, we calculated the correlation between the degree of NL contact coordination and the Hi-C interaction frequency as a function of genomic distance (Figure 5D). The results show that Hi-C interactions correlate moderately but significantly with the degree of NL contact coordination. This correlation is most prominent at $\sim 1\text{--}2$ Mb distance and declines gradually over longer distances, but is still statistically significant ($p < 0.001$) at ~ 100 Mb. Somewhat surprisingly, this positive correlation appears absent among directly neighboring 100-kb segments. One possibility is that pairs of adjacent 100-kb segments have very high Hi-C interaction frequencies due to their physical linkage, regardless of any coordination of NL contacts; indeed, our analyses show that finer-scale features of Hi-C do not always correspond to coordination of NL contacts (see below). Together, these data indicate that over a broad range of linear distances, coordinated NL contacts have a tendency to be linked to close proximity in nuclear space.

Previous Hi-C studies have revealed multi-scale compartmentalization of chromatin. At the highest level, megabase-sized do-

mains are segregated into two main compartments that can be identified by eigenvector decomposition of the Hi-C matrix (Lieberman-Aiden et al., 2009). The CF pattern shows a remarkably tight correlation with this compartment score (Figure S4B; genome-wide Spearman's $\rho = -0.88$, weighted average of by-chromosome correlations), indicating that the two main Hi-C compartments largely correspond to NL-interacting and internally located chromatin.

At a finer scale, the genome is partitioned into topologically associated domains (TADs), which are discrete domains that have many intra-domain Hi-C interactions but relatively few interactions with neighboring TADs (Dixon et al., 2012; Nora et al., 2012). We computed TAD boundary positions and compared them to the NL contact coordination patterns. We found examples in which TAD boundaries coincide with borders of units of coordinated NL contacts, but also cases in which they do not coincide (Figure S4B). We discovered that only TAD boundaries that coincide with strong transitions in CF values also mark the edges of units of NL contact coordination, while TAD boundaries located in regions with relatively uniform CF values typically do not (Figure S4C). This is not due to a general difference in TAD boundary strength, because the average TAD boundary scores were highly similar (Figure S4C, bottom). We conclude that TADs overlap only partially with units of coordinated NL contacts.

Chromosomal CF Patterns Suggest Long-Range Cooperativity

The prevalence of intra-chromosomally coordinated NL contacts raised the possibility that multiple LADs across a chromosome associate with the NL in a cooperative manner. In support of this, we noticed a strong correlation between the average CF of all LADs along each chromosome and the overall density of LADs on the same chromosome (Figure 5E; Spearman's rho = 0.85, $p = 9 \times 10^{-7}$). This is, for example, illustrated by the stark contrast between chr18 and chr19: the former has a very high density of LADs, of which many have consistent NL contacts, while the latter has only a few LADs that infrequently contact the NL (Figure 3A). The tight correlation between chromosomal density of LADs and their average CF is suggestive of chromosome-wide cooperative LAD-NL interactions.

NL Contacts Often Involve Embedding of DNA in the NL

To gain more insight into the nature of NL contacts at the scale of single LADs, we visualized these contacts by ground state depletion (GSD) super-resolution fluorescence microscopy (Fölling et al., 2008) in combination with the ^{m6}A -Tracer method (Kind et al., 2013). We used a previously established clonal cell line (derived from HT1080 fibrosarcoma cells) that expresses inducible Dam-LmnB1, together with a GFP-tagged ^{m6}A -binding protein; this system allows for direct visualization of DNA that is, or has been, in contact with the NL (Kind et al., 2013). We labeled the NL in the same cells with an antibody against LmnB1 and used GSD microscopy to obtain super-resolution two-color images.

20 hr after Dam-LmnB1 induction, the ^{m6}A -Tracer signal exhibits a striking speckled pattern that is mostly confined to a zone of $\sim 1\text{ }\mu\text{m}$ underneath the NL (Figures 6A and 6B). The signal consists of clusters with diameters in the range of approximately

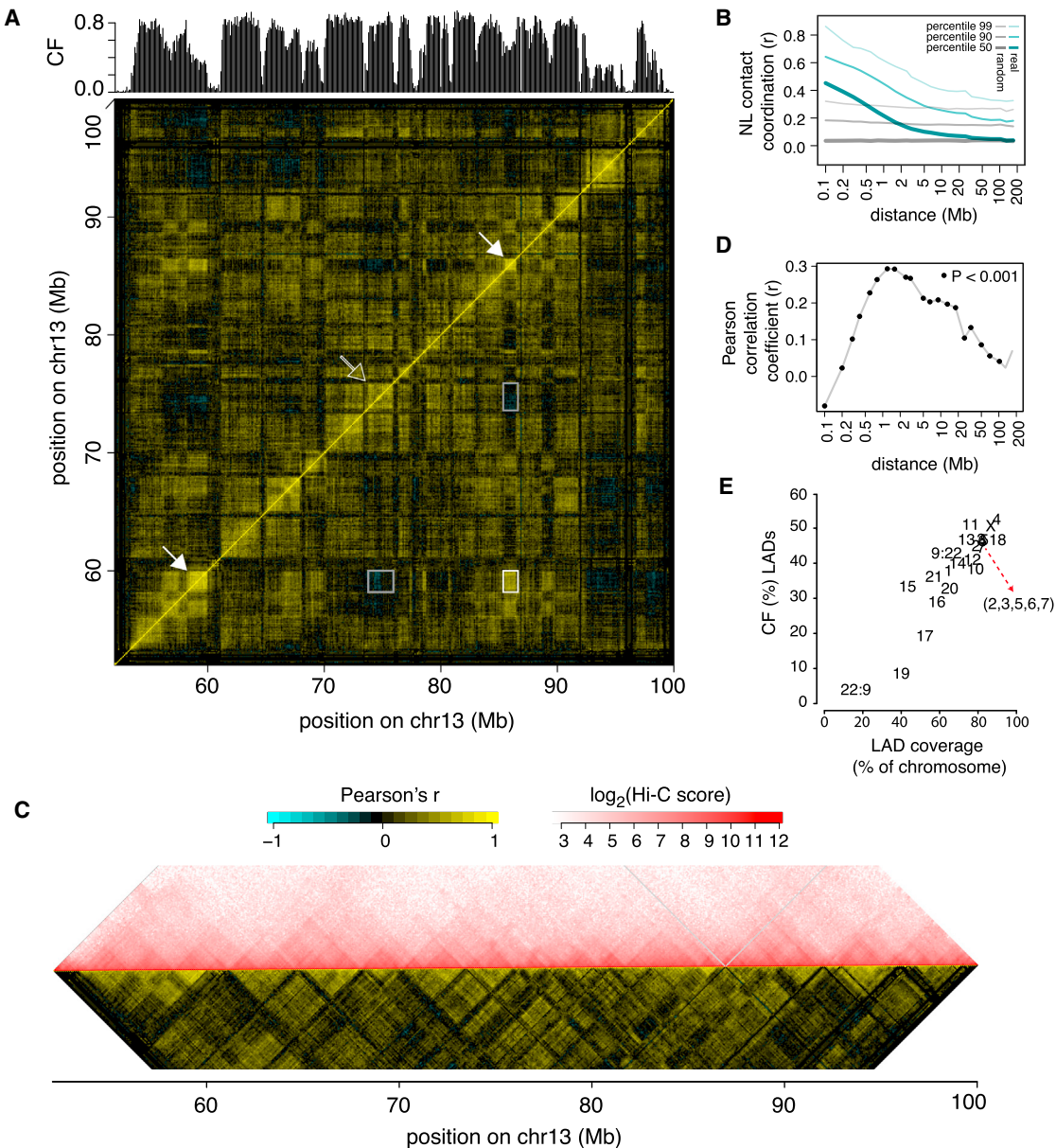


Figure 5. Intra-Chromosomal Coordination of NL Contacts over a Wide Range of Distance

(A) NL contact correlation matrix for part of chr13 in clone #14, showing the Pearson correlation of binary NL contacts across the 118 cells for all possible pairs of genomic segments. The color key is shown in panel (C). White arrows mark two example regions located ~26 Mb apart that exhibit coordinated contacts (white box); the open arrow indicates a region that is not positively correlated with these regions (gray boxes).

(B) Genome-wide coordinated NL contacts as a function of linear distance. Median, 90th percentile, and 99th percentile Pearson's r values are shown for real (cyan) and randomized (gray) binary NL contact data from 118 single cells.

(C) Comparison of NL contact coordination matrix to Hi-C interaction matrix. The matrix in (A) was turned clockwise by 45° and only a section below the diagonal is shown; the corresponding part of the Hi-C interaction matrix (white-red color scale) is juxtaposed to facilitate comparison. Gray lines mark a repetitive region.

(D) Genome-wide correlation between NL contact coordination and Hi-C interactions, plotted as function of linear distance along chromosomes. Dots mark distances at which the correlation is significantly different from zero ($p < 0.001$).

(E) Positive correlation (Spearman's $\rho = 0.85$, $p = 8.96 \times 10^{-7}$) between the fraction of each chromosome covered by LADs and the average CF in these LADs. See also Figure S4.

50–300 nm. A similar pattern is seen 10 hr after Dam-LmnB1 induction (Figure S5A), although the signals are sparser than after 20 hr. Many of the ^{m6}A-Tracer signals do not touch the NL directly, indicating that they represent loci that contacted the

NL in the recent past and subsequently moved over a short distance toward the nuclear interior, as noted previously (Kind et al., 2013). Nevertheless, close association of ^{m6}A-Tracer signals with LmnB1 staining is frequently observed (Figure 6A).

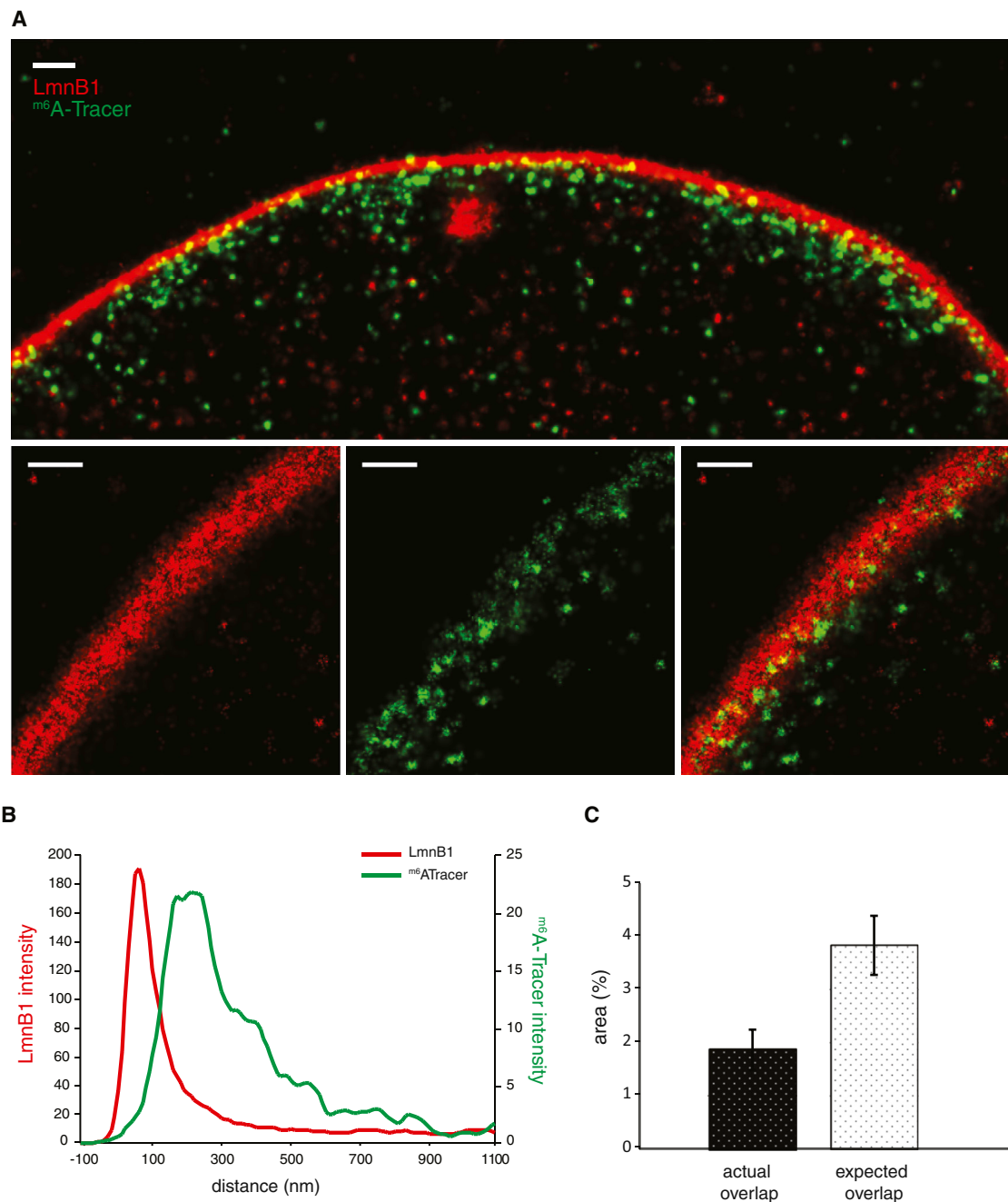


Figure 6. LAD-NL Interactions Involve Partial Embedding of Chromatin in the NL

(A) GSD microscopy image sections perpendicular (top) and oblique (bottom) to the NL. Red: LmnB1; green: m^6 A-Tracer signal 20 hr after induction of Dam-LmnB1. The large red structure in the center of the top panel may be an invagination of the NL. Scale bars represent 500 nm.

(B) Average pixel intensity of m^6 A-Tracer and LmnB1 signals as a function of the distance to the center of the NL. Curves show the average of four images.

(C) Quantification of the overlap of m^6 A-Tracer and LaminB1 signals within the confines of the NL, compared to random overlap. Data are the average of four nuclei. Error bars indicate SD.

See also Figure S5.

It is noteworthy that the edge of the LmnB1 signal at the NL is less sharply defined at the nucleoplasmic side than at the inner nuclear membrane side (Figures 6A and 6B). This could indicate that lamin filaments extend to varying degrees

into the nuclear interior, creating a somewhat fuzzy surface. Interestingly, the m^6 A-Tracer signals that abut the NL often appear partially embedded in this LmnB1 meshwork (Figure 6A, top). Oblique sections show that m^6 A-Tracer signals tend to

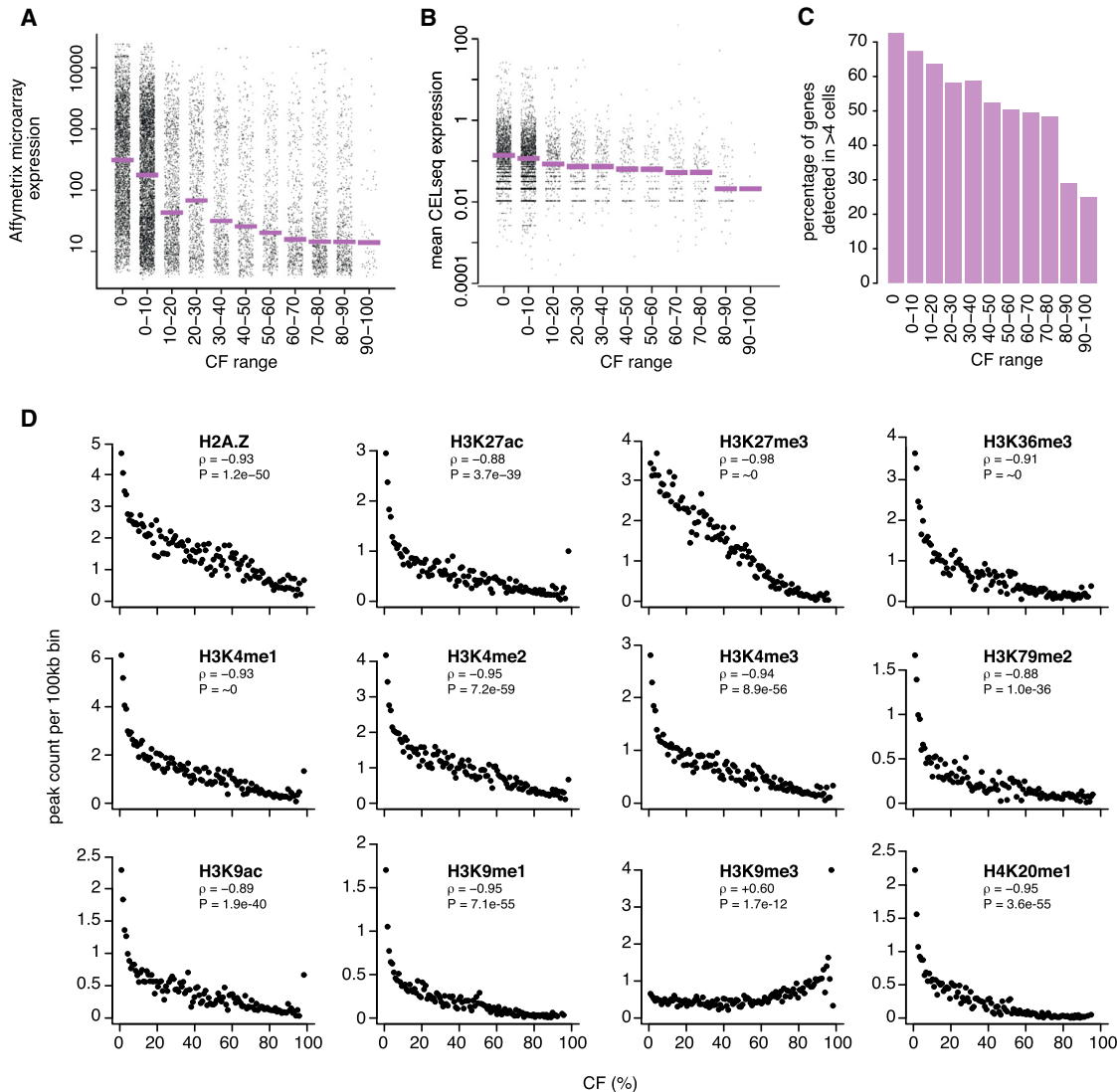


Figure 7. Links of CF to Gene Expression and Chromatin Composition in Single Cells

(A) Gene expression in pools of KBM7 cells (GEO: GSE56465; $n = 7$ independent clones) as a function of CF. Dots represent genes; purple bars show median values.

(B) Gene expression level in single clone #14 cells (mean of 96 single cells) as a function of CF. Dots represent genes; two genes with expression levels >100 are not shown. Purple bars show median values. Only genes with detectable expression in at least one cell are included.

(C) Fraction of genes with detectable expression in at least 5 out of 96 cells, as function of CF. Genes not detected in any of the 96 cells are not counted.

(D) Links of CF to epigenome mapping data from K562 cells (Consortium, 2012).

See also Figure S6.

occupy small pockets in the Lamin B1 signals (Figure 6A, bottom). Indeed, quantitative analysis of oblique sections showed that, within the confines of the NL, the overlap between m^6 A-Tracer clusters and LmnB1 is less than expected by chance (Figure 6C). This embedding is not caused by thickening of the NL due to expression of Dam-LmnB1, because the thickness of the NL is similar to that of cells in which Dam-LmnB1 is not induced (Figure S5B). Together, these results show that contact of LADs with the NL often involves embedding of chromatin in the relatively fuzzy nucleoplasmic surface of the NL.

Links between NL Contacts, Single-Cell Gene Expression, and Chromatin State

Because most NL interactions have been linked to gene repression (Finlan et al., 2008; Guelen et al., 2008; Reddy et al., 2008; Peric-Hupkes et al., 2010), we asked how transcriptional activity of genes is linked to their CF. Analysis of publicly available gene expression profiles from pools of KBM7 cells revealed that with increasing CFs the distribution of gene expression levels shifts gradually toward lower values (Figure 7A). To investigate this further, we employed a modified CEL-seq method (Grün et al., 2014) to generate genome-wide mRNA expression profiles

from 96 single KBM7 cells. These data show that the average mRNA expression level, as well as the fraction of genes with detectable mRNA, declines with increasing CF values (Figures 7B and 7C), which is in agreement with the cell pool expression analysis. Thus, in general, the more stably a gene is associated with the NL, the less active it tends to be. We considered that genes with mid-range CFs (i.e., genes that associate with the NL in only a subset of cells) might exhibit more cell-to-cell variation in gene expression. Analysis of the CEL-seq data did not uncover such a relationship (Figures S6A and S6B), although we note that technical noise in CEL-seq data may obscure such biological noise, particularly because NL-associated genes are generally expressed at very low levels.

Finally, we investigated whether CFs are linked to the presence of specific histone modifications. While no genome-wide maps of these modifications are available for KBM7 cells, extensive datasets are available from K562 cells (ENCODE Project Consortium, 2012), which is another myeloid leukemia cell line. These data reveal clear negative correlations between CFs and 10 out of 11 tested histone marks, as well as the histone variant H2A.Z (Figure 7D), most of which have previously been linked to active transcription. Only H3K9me3, which is generally linked to gene repression (ENCODE Project Consortium, 2012), is positively correlated with CF values (Spearman's rho = 0.60, p = 1.7 × 10⁻¹²). This is consistent with the previously reported role of H3K9 methylation in NL tethering (Towbin et al., 2012; Bian et al., 2013). In contrast, H3K27me3, which is also linked to gene repression, shows a strong negative correlation with CFs, suggesting that it does not play a role in NL tethering in KBM7 cells.

DISCUSSION

Single-Cell Protein-DNA Interaction Mapping by DamID

Here, we demonstrate that a modified DamID protocol can be used to map protein-DNA contacts genome-wide in single cells. At present, the resolution of the resulting maps is approximately 100 kb, which is suited to study proteins that form large domains along the genome (Bickmore and van Steensel, 2013). We expect that the resolution may be further improved by optimization of the DamID protocol and by deeper sequencing of samples so that more unique reads are recovered. It will be of interest to integrate single-cell DamID mapping with the recently reported single-cell Hi-C approach (Nagano et al., 2013).

Most Chromosomes Have a “Backbone” of Consistent NL Interactions

One interesting outcome of this study is that about 15% of the genome contacts the NL in most of the cells (CF > 80%). We propose that these consistently interacting loci together form a “backbone” that may help to shape the overall chromosome architecture. Their strong overlap with constitutive LADs suggests a common backbone function in many cell types. The extremely low gene density within these loci suggests that they may have evolved to play a structural role. Not all cLADs have high CFs, but because virtually all chromosomes have multiple cLADs, the backbone may be robust due to redundancy. The precise distribution of loci with stable NL contacts may be critical; this is suggested by the previously reported strong evolutionary

conservation of the boundaries of cLADs (Meuleman et al., 2013). It will be of interest to investigate the consequences of deleting such stable contact sites from chromosomes.

Intra-chromosomal Coordination of Variable NL Contacts and Spatial Proximity

Scattered between these stable contact sites are many loci that associate with the NL in only a subset of cells. Such loci may be subject to a balance between mechanisms that tether them to the NL and mechanisms that sequester them in the nuclear interior. These variable loci, which together cover about one-third of the genome, exhibit a complex pattern of coordinated NL contacts within chromosomes. This domain-like pattern presumably reflects the overall chromosomal architecture. Indeed, our Hi-C analysis shows that loci with intra-chromosomally coordinated NL contacts tend to be in close proximity in nuclear space, particularly in the 0.5–5 Mb distance range. Physical interactions between these loci may facilitate the coordination of their NL contacts. However, it is also possible that loci with coordinated NL contacts are more often in spatial proximity of one another simply because they are located in the same nuclear compartment.

Multivalent Interactions and Embedding of Chromatin in the NL

The non-random long runs of NL contacts observed in our single-cell maps strongly suggest a multivalent mode of interaction. Considering that both the NL and chromosomes consist of polymer structures, such a mechanism is quite plausible. The Mb range over which we find this mechanism to be active appears at odds with a report claiming that a short 400-bp repetitive sequence was sufficient to target a locus to the NL (Zullo et al., 2012). One possibility is that this sequence was integrated as a long tandem repeat, which often happens in stable transfections. Another study identified three independent “peripheral targeting regions” in a human LAD, one of which could be narrowed down to 6.3 kb (Bian et al., 2013). However, this element was unable to target a free plasmid to the NL, while in genomic context its ability to interact with the NL was strongly dependent on the integration site, indicating that this element requires support from other elements.

H3K9me3 is strongly correlated with CF values and several studies have found that di- and tri-methylation of H3K9 can promote NL interactions (Towbin et al., 2012; Bian et al., 2013; Kind et al., 2013). These histone modifications tend to cover large genomic regions (Bickmore and van Steensel, 2013) and are thus probable candidates to be involved in multivalent chromatin-NL contacts.

The largest ^{m6}A-Tracer clusters (~300 nm in size) that we observed by super-resolution microscopy may contain ~100–250 kb of DNA, a rough estimate that we infer from previous polymer modeling of FISH distance measurements in mammalian nuclei (Mateos-Langerak et al., 2009; Giorgetti et al., 2014). However, most ^{m6}A-Tracer clusters are substantially smaller. We therefore suggest that a typical long (>1 Mb) contact run as observed in the single-cell maps may consist of a string of such clusters, each typically shorter than 100 kb, that contact the NL in a multivalent manner. Future improvement

of the resolution of single-cell DamID mapping may enable the identification of individual m^6 A-Tracer clusters at the sequence level.

EXPERIMENTAL PROCEDURES

Detailed methods are described in the [Supplemental Experimental Procedures](#).

Single-Cell DamID

The protocol for the detection of Dam methylation in single-cell DamID is similar to that of conventional DamID ([Vogel et al., 2007](#)) and uses largely the same reagents. Key differences are (1) use of clonal cell lines with controlled expression of Dam-LmnB1, (2) use of the Fucci system and flow sorting to collect single cells at the G1/S transition, (3) the solution used to lyse the cells, (4) performance of all enzymatic steps to detect Dam methylation in a single well of a 96-well plate, by sequential addition of reagents without any purification of the DNA, (v) 4–6 additional PCR cycles, and (5) use of Illumina sequencing instead of microarrays as readout. Multiplexing of samples was done with indexing primers as listed in [Table S2](#). A detailed description is provided in the [Supplemental Experimental Procedures](#), which also document the processing of sequencing reads.

Hi-C, Gene Expression Analysis, and CEL-Seq

Hi-C data from clone #14 cells were generated in duplicate and processed as described ([Belton et al., 2012; Lajoie et al., 2015](#)). Gene expression profiles from pools of KBM7 cells were obtained from GEO: GSE56465. CEL-seq was done essentially as previously described ([Grün et al., 2014](#)).

GSD Microscopy

Super-resolution microscopy was performed with a Leica SR GSD microscope (Leica Microsystems) with a Sumo Stage (#11888963) for drift-free imaging. Images were collected with an EMCCD Andor iXon camera (Andor Technology) and an oil-immersion objective (PL Apo 160 \times , na 1.46). Lasers used included 405 nm/30 mW (back-pumping only), 488 nm/300 mW, and 647 nm/500 mW. Between 10,000 to 50,000 frames were collected at 100 Hz for each SR image. Data were analyzed with the ImageJ ThunderStorm analysis module ([Ovesný et al., 2014](#)).

ACCESSION NUMBERS

The accession numbers for the single-cell and conventional DamID, Hi-C, and CEL-seq reported in this paper are deposited in GEO: GSE69423, GSE69841, and GSE68596.

SUPPLEMENTAL INFORMATION

Supplemental Information includes Supplemental Experimental Procedures, six figures, two tables, and five data files and can be found with this article at <http://dx.doi.org/10.1016/j.cell.2015.08.040>.

AUTHOR CONTRIBUTIONS

J.K.: conceived of and designed the study; single-cell DamID development and experiments; data exploration; paper writing. L.P. and S.S.D.V. made equal contributions. L.P.: data processing pipeline; data analysis. S.S.D.V.: clonal cell line establishment; single-cell DamID; control experiments and experimental design. L.N.: super-resolution microscopy. S.S.D.: CEL-seq experiments and data analysis. M.B.: FISH experiments and data analysis. Y.Z.: Hi-C experiments. B.L.: Hi-C data processing. C.A.d.G.: unpublished LAD atlas; data processing support. M.A.: constructs; experimental support. G.F.: data analysis. M.I.: data analysis. L.A.M.: advisor of G.F. and M.I.; data analysis; intellectual input. K.J.: advisor of L.N.; superresolution microscopy and experimental design and image analysis. J.D.: advisor of Y.Z. and B.L.; intellectual input. A.v.O.: advisor of S.S.D. and M.B.; intellectual input. B.v.S.:

conceived of and designed study; data analysis; project coordination; paper writing.

ACKNOWLEDGMENTS

We thank the NKI Genomics Core Facility for technical assistance, Thijn Brummelkamp for help with KBM7 cells, Erik Wernersson for FISH image analysis, and members of the B.v.S. lab for helpful comments. This study was supported by a Nederlandse Organisatie voor Wetenschappelijk Onderzoek (NWO) ALW-VENI fellowship (to J.K.), an NHMRC Early Career Fellowship (to C.A.d.G.), an NWO ZonMW-TOP and European Research Council (ERC) Advanced Grant AdG 293662-CHROMATINPRINCIPLES (to B.v.S.), a STW grant (12150) (to K.J.), an ERC Advanced Grant AdG 294325-GeneNoiseControl and NWO VICI Award (to S.S.D., M.B., and A.v.O.), a NIH grant (R01 GM114190) (to L.A.M., M.I., and G.F.), and a National Human Genome Research Institute grant (R01 HG003143) (to J.D., L.A.M., M.I., and G.F.).

Received: April 22, 2015

Revised: June 27, 2015

Accepted: August 12, 2015

Published: September 10, 2015

REFERENCES

- Baù, D., Sanyal, A., Lajoie, B.R., Capriotti, E., Byron, M., Lawrence, J.B., Dekker, J., and Marti-Renom, M.A. (2011). The three-dimensional folding of the α -globin gene domain reveals formation of chromatin globules. *Nat. Struct. Mol. Biol.* 18, 107–114.
- Belton, J.M., McCord, R.P., Gibcus, J.H., Naumova, N., Zhan, Y., and Dekker, J. (2012). Hi-C: a comprehensive technique to capture the conformation of genomes. *Methods* 58, 268–276.
- Bian, Q., Khanna, N., Alvikas, J., and Belmont, A.S. (2013). β -globin cis-elements determine differential nuclear targeting through epigenetic modifications. *J. Cell Biol.* 203, 767–783.
- Bickmore, W.A. (2013). The spatial organization of the human genome. *Annu. Rev. Genomics Hum. Genet.* 14, 67–84.
- Bickmore, W.A., and van Steensel, B. (2013). Genome architecture: domain organization of interphase chromosomes. *Cell* 152, 1270–1284.
- Bolzer, A., Kreth, G., Solovei, I., Koehler, D., Saracoglu, K., Fauth, C., Müller, S., Eils, R., Cremer, C., Speicher, M.R., and Cremer, T. (2005). Three-dimensional maps of all chromosomes in human male fibroblast nuclei and prometaphase rosettes. *PLoS Biol.* 3, e157.
- Bürckstümmer, T., Banning, C., Hainzl, P., Schobesberger, R., Kerzendorfer, C., Paufer, F.M., Chen, D., Them, N., Schischlik, F., Rebsamen, M., et al. (2013). A reversible gene trap collection empowers haploid genetics in human cells. *Nat. Methods* 10, 965–971.
- Cavalli, G., and Misteli, T. (2013). Functional implications of genome topology. *Nat. Struct. Mol. Biol.* 20, 290–299.
- Cremer, M., von Hase, J., Volm, T., Brero, A., Kreth, G., Walter, J., Fischer, C., Solovei, I., Cremer, C., and Cremer, T. (2001). Non-random radial higher-order chromatin arrangements in nuclei of diploid human cells. *Chromosome Res.* 9, 541–567.
- Croft, J.A., Bridger, J.M., Boyle, S., Perry, P., Teague, P., and Bickmore, W.A. (1999). Differences in the localization and morphology of chromosomes in the human nucleus. *J. Cell Biol.* 145, 1119–1131.
- de Wit, E., and de Laat, W. (2012). A decade of 3C technologies: insights into nuclear organization. *Genes Dev.* 26, 11–24.
- Dekker, J., Marti-Renom, M.A., and Mirny, L.A. (2013). Exploring the three-dimensional organization of genomes: interpreting chromatin interaction data. *Nat. Rev. Genet.* 14, 390–403.
- Dixon, J.R., Selvaraj, S., Yue, F., Kim, A., Li, Y., Shen, Y., Hu, M., Liu, J.S., and Ren, B. (2012). Topological domains in mammalian genomes identified by analysis of chromatin interactions. *Nature* 485, 376–380.

ENCODE Project Consortium (2012). An integrated encyclopedia of DNA elements in the human genome. *Nature* 489, 57–74.

Finlan, L.E., Sproul, D., Thomson, I., Boyle, S., Kerr, E., Perry, P., Ylstra, B., Chubb, J.R., and Bickmore, W.A. (2008). Recruitment to the nuclear periphery can alter expression of genes in human cells. *PLoS Genet.* 4, e1000039.

Fölling, J., Bossi, M., Bock, H., Medda, R., Wurm, C.A., Hein, B., Jakobs, S., Eggeling, C., and Hell, S.W. (2008). Fluorescence nanoscopy by ground-state depletion and single-molecule return. *Nat. Methods* 5, 943–945.

Gibcus, J.H., and Dekker, J. (2013). The hierarchy of the 3D genome. *Mol. Cell* 49, 773–782.

Giorgetti, L., Galupa, R., Nora, E.P., Piolot, T., Lam, F., Dekker, J., Tiana, G., and Heard, E. (2014). Predictive polymer modeling reveals coupled fluctuations in chromosome conformation and transcription. *Cell* 157, 950–963.

Grün, D., Kester, L., and van Oudenaarden, A. (2014). Validation of noise models for single-cell transcriptomics. *Nat. Methods* 11, 637–640.

Guclu, L., Pagie, L., Brasset, E., Meuleman, W., Faza, M.B., Talhout, W., Eussen, B.H., de Klein, A., Wessels, L., de Laat, W., and van Steensel, B. (2008). Domain organization of human chromosomes revealed by mapping of nuclear lamina interactions. *Nature* 453, 948–951.

Kalhor, R., Tjong, H., Jayathilaka, N., Alber, F., and Chen, L. (2012). Genome architectures revealed by tethered chromosome conformation capture and population-based modeling. *Nat. Biotechnol.* 30, 90–98.

Kind, J., Pagie, L., Ortabozkoyun, H., Boyle, S., de Vries, S.S., Janssen, H., Amendola, M., Nolen, L.D., Bickmore, W.A., and van Steensel, B. (2013). Single-cell dynamics of genome-nuclear lamina interactions. *Cell* 153, 178–192.

Kosak, S.T., Skok, J.A., Medina, K.L., Riblet, R., Le Beau, M.M., Fisher, A.G., and Singh, H. (2002). Subnuclear compartmentalization of immunoglobulin loci during lymphocyte development. *Science* 296, 158–162.

Kotecki, M., Reddy, P.S., and Cochran, B.H. (1999). Isolation and characterization of a near-haploid human cell line. *Exp. Cell Res.* 252, 273–280.

Lajoie, B.R., Dekker, J., and Kaplan, N. (2015). The hitchhiker's guide to Hi-C analysis: practical guidelines. *Methods* 72, 65–75.

Lieberman-Aiden, E., van Berkum, N.L., Williams, L., Imakaev, M., Ragoczy, T., Telling, A., Amit, I., Lajoie, B.R., Sabo, P.J., Dorschner, M.O., et al. (2009). Comprehensive mapping of long-range interactions reveals folding principles of the human genome. *Science* 326, 289–293.

Manuelidis, L., and Borden, J. (1988). Reproducible compartmentalization of individual chromosome domains in human CNS cells revealed by *in situ* hybridization and three-dimensional reconstruction. *Chromosoma* 96, 397–410.

Marshall, W.F., Dernburg, A.F., Harmon, B., Agard, D.A., and Sedat, J.W. (1996). Specific interactions of chromatin with the nuclear envelope: positional determination within the nucleus in *Drosophila melanogaster*. *Mol. Biol. Cell* 7, 825–842.

Mateos-Langerak, J., Bohn, M., de Leeuw, W., Giromus, O., Manders, E.M., Verschure, P.J., Indemans, M.H., Gierman, H.J., Heermann, D.W., van Driel, R., and Goetze, S. (2009). Spatially confined folding of chromatin in the interphase nucleus. *Proc. Natl. Acad. Sci. USA* 106, 3812–3817.

Meuleman, W., Peric-Hupkes, D., Kind, J., Beaudry, J.B., Pagie, L., Kellis, M., Reinders, M., Wessels, L., and van Steensel, B. (2013). Constitutive nuclear lamina-genome interactions are highly conserved and associated with A/T-rich sequence. *Genome Res.* 23, 270–280.

Nagano, T., Lubling, Y., Stevens, T.J., Schoenfelder, S., Yaffe, E., Dean, W., Lue, E.D., Tanay, A., and Fraser, P. (2013). Single-cell Hi-C reveals cell-to-cell variability in chromosome structure. *Nature* 502, 59–64.

Nora, E.P., Lajoie, B.R., Schulz, E.G., Giorgetti, L., Okamoto, I., Servant, N., Piolot, T., van Berkum, N.L., Meisig, J., Sedat, J., et al. (2012). Spatial partitioning of the regulatory landscape of the X-inactivation centre. *Nature* 485, 381–385.

Ochs, R.L., and Press, R.I. (1992). Centromere autoantigens are associated with the nucleolus. *Exp. Cell Res.* 200, 339–350.

Ovesný, M., Krížek, P., Borkovec, J., Svindrych, Z., and Hagen, G.M. (2014). ThunderSTORM: a comprehensive ImageJ plug-in for PALM and STORM data analysis and super-resolution imaging. *Bioinformatics* 30, 2389–2390.

Peric-Hupkes, D., Meuleman, W., Pagie, L., Bruggeman, S.W., Solovei, I., Brugman, W., Gräf, S., Flück, P., Kerkhoven, R.M., van Lohuizen, M., et al. (2010). Molecular maps of the reorganization of genome-nuclear lamina interactions during differentiation. *Mol. Cell* 38, 603–613.

Rao, S.S., Huntley, M.H., Durand, N.C., Stamenova, E.K., Bochkov, I.D., Robinson, J.T., Sanborn, A.L., Machol, I., Omer, A.D., Lander, E.S., and Aiden, E.L. (2014). A 3D map of the human genome at kilobase resolution reveals principles of chromatin looping. *Cell* 159, 1665–1680.

Reddy, K.L., Zullo, J.M., Bertolino, E., and Singh, H. (2008). Transcriptional repression mediated by repositioning of genes to the nuclear lamina. *Nature* 452, 243–247.

Sakaue-Sawano, A., Kurokawa, H., Morimura, T., Hanyu, A., Hama, H., Osawa, H., Kashiwagi, S., Fukami, K., Miyata, T., Miyoshi, H., et al. (2008). Visualizing spatiotemporal dynamics of multicellular cell-cycle progression. *Cell* 132, 487–498.

Therizols, P., Illingworth, R.S., Courilleau, C., Boyle, S., Wood, A.J., and Bickmore, W.A. (2014). Chromatin decondensation is sufficient to alter nuclear organization in embryonic stem cells. *Science* 346, 1238–1242.

Towbin, B.D., González-Aguilera, C., Sack, R., Gaidatzis, D., Kalck, V., Meister, P., Askjaer, P., and Gasser, S.M. (2012). Step-wise methylation of histone H3K9 positions heterochromatin at the nuclear periphery. *Cell* 150, 934–947.

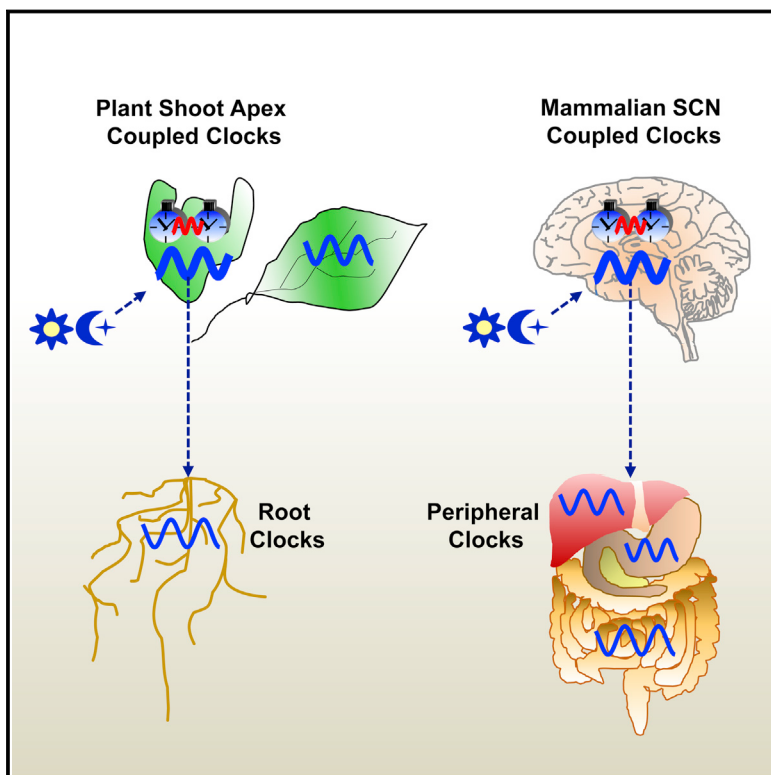
van Steensel, B., and Dekker, J. (2010). Genomics tools for unraveling chromosome architecture. *Nat. Biotechnol.* 28, 1089–1095.

Vogel, M.J., Peric-Hupkes, D., and van Steensel, B. (2007). Detection of *in vivo* protein-DNA interactions using DamID in mammalian cells. *Nat. Protoc.* 2, 1467–1478.

Zullo, J.M., Demarco, I.A., Piqué-Regi, R., Gaffney, D.J., Epstein, C.B., Spawner, C.J., Luperchio, T.R., Bernstein, B.E., Pritchard, J.K., Reddy, K.L., and Singh, H. (2012). DNA sequence-dependent compartmentalization and silencing of chromatin at the nuclear lamina. *Cell* 149, 1474–1487.

A Hierarchical Multi-oscillator Network Orchestrates the *Arabidopsis* Circadian System

Graphical Abstract



Authors

Nozomu Takahashi, Yoshito Hirata,
Kazuyuki Aihara, Paloma Mas

Correspondence

paloma.mas@cragenomica.es

In Brief

The plant shoot apex clocks resemble the suprachiasmatic nucleus in mammals in their coupling properties and their capacity to synchronize circadian rhythms in distal organs.

Highlights

- Shoot apex clocks function as the suprachiasmatic nucleus neurons in mammals
- Circadian coupling defines the high degree of synchrony among shoot apex clocks
- The shoot apex clocks influence the circadian activity in roots
- Different plant organs exhibit variations in clock precision and circadian synchrony

A Hierarchical Multi-oscillator Network Orchestrates the *Arabidopsis* Circadian System

Nozomu Takahashi,¹ Yoshito Hirata,² Kazuyuki Aihara,² and Paloma Mas^{1,3,*}

¹Centre for Research in Agricultural Genomics (CRAG), CSIC-IRTA-UAB-UB, Campus UAB, Bellaterra, 08193 Barcelona, Spain

²Institute of Industrial Science, The University of Tokyo, 4-6-1 Komaba, Meguro-ku, Tokyo 153-8505, Japan

³Consejo Superior de Investigaciones Científicas (CSIC), 08028 Barcelona, Spain

*Correspondence: paloma.mas@cragenomica.es

<http://dx.doi.org/10.1016/j.cell.2015.08.062>

SUMMARY

Short- and long-distance circadian communication is essential for integration of temporal information. However, a major challenge in plant biology is to decipher how individual clocks are interconnected to sustain rhythms in the whole plant. Here we show that the shoot apex is composed of an ensemble of coupled clocks that influence rhythms in roots. Live-imaging of single cells, desynchronization of dispersed protoplasts, and mathematical analysis using barycentric coordinates for high-dimensional space show a gradation in the strength of circadian communication in different tissues, with shoot apex clocks displaying the highest coupling. The increased synchrony confers robustness of morning and evening oscillations and particular capabilities for phase readjustments. Rhythms in roots are altered by shoot apex ablation and micrografting, suggesting that signals from the shoot apex are able to synchronize distal organs. Similarly to the mammalian suprachiasmatic nucleus, shoot apices play a dominant role within the plant hierarchical circadian structure.

INTRODUCTION

The circadian clock is a cellular mechanism able to generate rhythms in biological processes. A key function of circadian clocks is the synchronization of metabolism, physiology, and development in anticipation of the diurnal and seasonal environmental changes (Young and Kay, 2001). Over the last years, biochemical and genetic studies have provided a complex view of the circadian organization and function in several clock systems, including mammals, insects, plants, fungi, and cyanobacteria (Wijnen and Young, 2006). Rhythms in most organisms are generated by reciprocal regulations among core clock components that produce 24 hr oscillations in gene expression, mRNA processing, protein abundance, and activity (Harmer et al., 2001). Changes in chromatin architecture have also emerged as a central mechanism coupled to the rhythmic oscillation of clock gene expression (Nakahata et al., 2007; Ripperger and Merrow, 2011; Stratmann and Más, 2008).

Plants as sessile organisms perceive and adapt to the environmental changes for optimal growth and survival. Consistently, nearly all stages of plant development and many essential aspects of growth and metabolism are regulated by the clock (de Montaigu et al., 2010; Yakir et al., 2007). Among others, processes such as photo-protection, responses to biotic attacks, or the photoperiodic regulation of flowering are controlled by the clock (Kinmonth-Schultz et al., 2013). Mechanistically, a number of regulatory transcriptional modules have been defined at the basis of the *Arabidopsis thaliana* circadian oscillator. Two single MYB-domain transcription factors expressed early in the morning, known as CIRCADIAN CLOCK ASSOCIATED 1 (CCA1) (Wang and Tobin, 1998) and LATE ELONGATED HYPOCOTYL (LHY) (Schaffer et al., 1998), negatively regulate the expression (Alabadí et al., 2001) of the evening-phased PSEUDO-RESPONSE REGULATOR 1 (PRR1) or TIMING OF CAB EXPRESSION 1 (TOC1) (Makino et al., 2002; Strayer et al., 2000). TOC1 (Gendron et al., 2012; Huang et al., 2012) and the other members of the PRR family (PRR5, PRR7, and PRR9) (Nakamichi et al., 2010) also bind to the promoters of CCA1 and LHY to repress their expression. Additional components such as EARLY FLOWERING3 (ELF3), ELF4, and LUX ARRHYTHMO (LUX) interact to form the Evening Complex (EC) that represses the expression of the early day-phased clock gene PRR9 (Helfer et al., 2011; Nusinow et al., 2011).

At a cellular level, it has been assumed that virtually every plant cell might contain an endogenous clock. However, their possible circadian communication or coupling has been a matter of debate. Circadian analysis using cell cultures (Kim and Somers, 2010; Nakamichi et al., 2003), records of different rhythmic markers (Sai and Johnson, 1999), studies of clock synchronization (Wenden et al., 2012), and circadian characterization of guard cells (Yakir et al., 2011) have suggested that plant cellular clocks might be only weakly coupled. However, luminescence assays in *Arabidopsis* and analysis of chlorophyll fluorescence in *Kalanchoe daigremontiana* have shown a certain degree of cellular coupling in different parts of leaves (Fukuda et al., 2007; Rascher et al., 2001). A recent interesting report has also described particular properties of clocks in leaf veins that are able to communicate with the adjacent leaf mesophyll cells (Endo et al., 2014). Intercellular coupling opens the question about long-distance signaling and synchronization. Indeed, circadian oscillations in roots seem to be entrained by signals from shoots (James et al., 2008). This situation resembles that of the mammalian circadian system in which a master clock

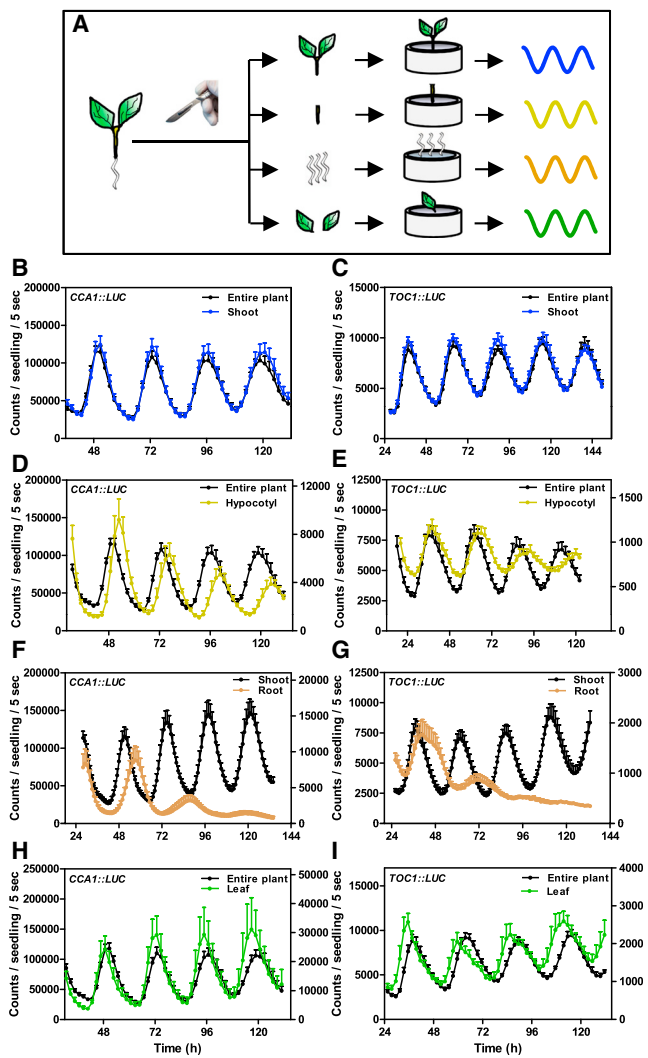


Figure 1. Disparity in the Precision and Robustness of Circadian Rhythms in Various Organs Excised from the Plant

(A) Schematic drawing depicting the dissection of the different parts of the plant and the subsequent analysis by luminescence assays. Seedlings were dissected to separate shoots, hypocotyls, roots, and leaves.

(B–I) In vivo circadian analysis of luminescent rhythms under LL from CCA1::LUC (B, D, F, and H) and TOC1::LUC (C, E, G, and I) in shoots (B and C), hypocotyls (D and E), roots (F and G), and leaves (H and I). Data are the means + SEM of the luminescence of 6–12 individual samples. Values of luminescence signals from hypocotyls, roots, and leaves are represented on the right y axes. See also Figure S1.

located at the suprachiasmatic nucleus (SCN) synchronizes peripheral clocks dispersed throughout the body (Aton and Herzog, 2005; Welsh et al., 2010).

The functional structure of a circadian system consists of a complex assembly of components and mechanisms that are precisely coordinated in cells, tissues, and organs. Intercellular coupling of circadian clocks might provide an efficient way for local synchronization in a particular tissue while long-distance signaling can aid in synchronizing distal parts. In this study, we have focused on these two particular aspects of circadian

communication in *Arabidopsis* and found that the shoot apex might act as a master clock that influences rhythms in roots.

RESULTS

Differences in Robustness and Precision of Circadian Rhythms in Dissected Organs

To determine organ-specific circadian function, we analyzed rhythms in different organs excised from the plant (Figure 1A and Supplemental Experimental Procedures). Promoter activity was monitored by in vivo luminescence assays of plants expressing the morning- (CCA1) and evening-phased (TOC1) gene promoters fused to the LUCIFERASE (LUC). Under constant light conditions (LL), CCA1::LUC and TOC1::LUC expression in excised shoots robustly oscillated without evident damping. Circadian waveforms closely matched those of whole plants (Figures 1B and 1C), suggesting that root excision did not manifestly affect oscillations in shoots. Excised hypocotyls sustained rhythms albeit with a long circadian period (27.02 ± 0.64 versus 24.61 ± 0.25 in entire plants) and a progressive decrease in amplitude over the days (Figures 1D and 1E). Rhythms in excised roots were only sustained for about 2 days, dampening low afterward (Figures 1F and 1G). The fact that oscillations in roots do not persist in the absence of sucrose could be due to energy limitation, as excised roots are a sucrose sink. Indeed, the use of the same procedure for root excision but using medium with sucrose revealed that rhythms were sustained for more than 4 days (Figure S1) with a significantly longer period (26.21 ± 0.33) than in shoots (24.63 ± 0.22). The sustained oscillations suggest that the excision per se was not responsible for the damped rhythms observed without sucrose. Adding sucrose to non-sucrose grown and arrhythmic excised roots did not restore the oscillatory pattern (Figure S1), suggesting that sugar cannot compensate for the arrhythmia. When excised leaves were analyzed in the absence (Figures 1H and 1I) or in the presence (Figure S1) of sucrose, we observed an averaged advanced phase compared to entire plants or shoots.

Specific Properties for Synchronization and Phase Readjustments of Shoot Apex Clocks

We next performed similar analysis with excised shoot apices (Figure 2A) and found that the phase, period, and amplitude remained synchronized (Figures 2B and 2C), with rhythms very similar to those of the entire plants (Figure S2) and with highly synchronous individual waveforms (Figure 2D). These results are in clear contrast with the high degree of variability observed in individual leaf waveforms, manifested by a range of phases and amplitudes from the very first day under LL (Figure 2E). As the size of the tissue might influence the circadian waveforms, we analyzed small sections of leaves (with sizes similar to those of the shoot apices). Our results showed a similar variability to that displayed by full leaves (Figure S2), which suggests that the shoot apex homogeneity in waveforms is not due to the reduced sizes of the samples. The circadian phases clustered together in shoot apices and to much less extent in leaves (Figures 2F and 2G). Similar conclusions were drawn when the average phase and the degree of phase coherence were calculated using the synchronization index “R” (see Supplemental

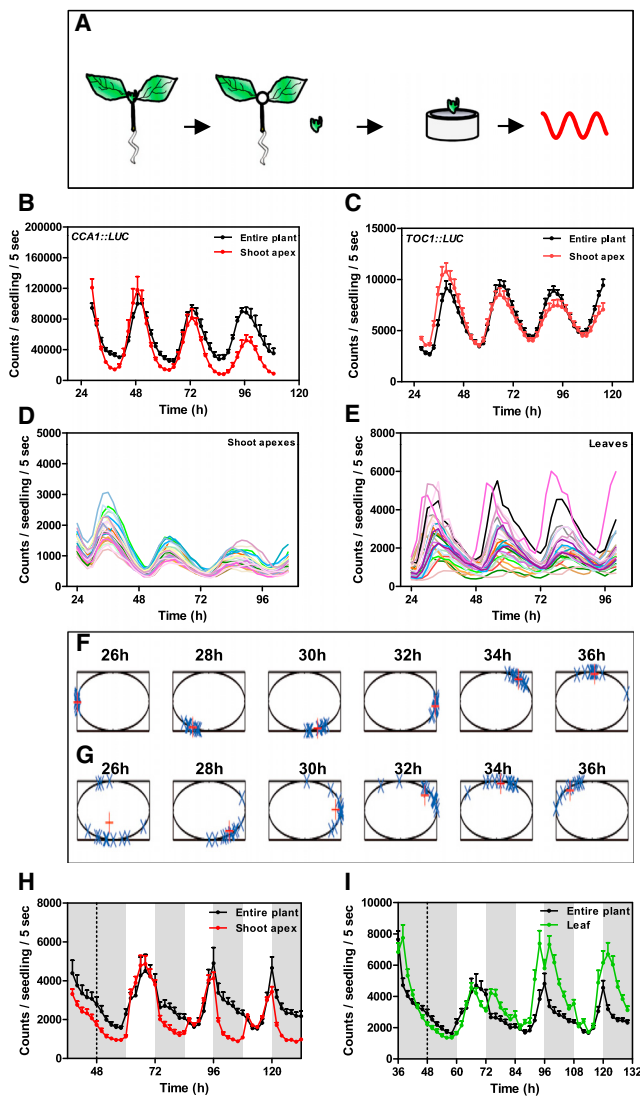


Figure 2. High Degree of Synchrony and Responsiveness to Environmental Changes of Shoot Apex Clocks

(A) Schematic drawing depicting the rhythmic analysis of excised shoot apices.

(B and C) In vivo circadian analysis of luminescent rhythms under LL from *CCA1::LUC* (B) and *TOC1::LUC* (C) in shoots apices.

(D and E) *TOC1::LUC* luminescence traces of individual excised shoot apices (D) and excised leaves (E).

(F and G) Analysis of the phase synchrony among the different samples (blue crosses) of individual shoot apices (F) and leaves (G) examined from 26 hr to 36 hr under LL. The red crosses indicate the means or circular variance (Mormann et al., 2000) at each time point.

(H and I) Average rhythms of *TOC1::LUC* luminescence in shoot apices (H) and leaves (I) subjected to a "jet-lag" experiment, with extended 12 hr darkness (extended night) at dawn.

Data are the means + SEM of the luminescence of 6–12 samples. White boxes: light; shaded boxes: dark. See also Figure S2.

Experimental Procedures. The analysis showed high R values, close to 1, for the shoot apices and lower values for leaves at all time points (Figure S2). Consistent with previous studies

(Wenden et al., 2012), the R values in leaves were well above 0, which suggests a certain degree of coherence. Rhythms in excised organs were highly reproducible in four different biological replicates (each one with 6–12 samples), which reduces the possibility that results were due to indirect effects of the excision procedure.

The circadian clock is not only a robust mechanism able to sustain rhythms in the absence of environmental transitions but also a flexible system that resynchronizes and properly adjusts to changes in the environmental cycle (Harrington, 2010). To explore whether the differences between shoot apices and leaves also extend to their capabilities for resynchronization and phase adjustment, we performed "jet-lag" experiments. In shoot apices, rhythms showed similar timing for resynchronization to that of entire plants (Figure 2H), although the shoot apex waveforms displayed very rapid declining at night for *TOC1::LUC* and an increased acute induction at dawn for *CCA1::LUC* (Figure S2). In leaves, rhythms showed a double peak for the first 2 days, reaching a stable phase at the third day after the extended night switch (Figure 2I). These results reveal different synchronizing behavior in leaves and shoot apices. The specific waveforms in shoot apices compared to the entire plant might also indicate a particular sensibility of shoot apices to dawn and dusk resetting signals.

Conserved Molecular Architecture of the Circadian Network at the Shoot Apex Clocks

To determine organ-specific differences in the clock molecular composition, we examined whether different clock outputs and mutations in core clock genes were distinctively regulated in shoot apices and leaves. Analysis of WT plants expressing the morning-phased clock output *CAB2* (*CHLOROPHYLL A/B-BINDING PROTEIN 2*) (Millar et al., 1995) showed that in shoot apices the phase was comparable to that in the entire plant, whereas increased heterogeneity and an average advanced phase were prevalent in leaves (Figure 3A). Similar to entire plants, the shoot apices and leaves of *cca1-11* mutants displayed persistent rhythms with shorter periods than WT shoot apices and WT leaves, respectively (Figures 3B–3D). Similarly, the short period of the evening-expressed clock output *CCR2* (*COLD, CIRCADIAN RHYTHM, AND RNA BINDING 2*) (Strayer et al., 2000) in *TOC1 RNAi* plants (Huang et al., 2012) was also observed in shoot apices and leaves (Figures 3E and 3F). Therefore, circadian gene expression in shoot apices and leaves with various reporter lines and clock mutant backgrounds did not render major differences between the two organs.

To profile the circadian transcriptional landscape at the shoot apex, we performed RNA sequencing (RNA-seq) analysis and used the JTK_CYCLE algorithm for precise definition of circadian expression (Hughes et al., 2010). After filtering out transcripts whose median expression across every sample was lower than 0.69 RPKM and those not differentially expressed, we identified over 1,400 genes with significant circadian fluctuations in mRNA abundance. Visual inspection of the data suggested that this may be a conservative estimation. However, the stringent analysis ensured the selection of the highest-confidence circadian hits. Rhythmic genes included all the

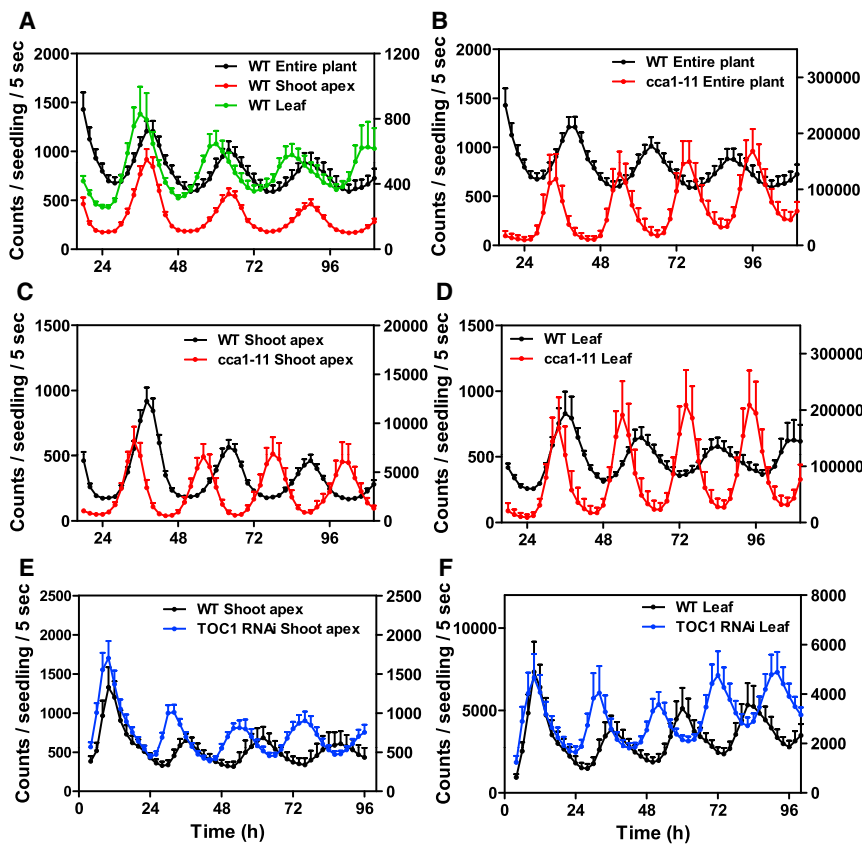


Figure 3. Phenotypes of Core Clock Mutations in Shoot Apices and Leaves

Average rhythms of *CAB2::LUC* (A–D) and *CCR2::LUC* (E and F) luminescence under LL in entire plants, shoot apices, and leaves of WT, *cca1-11* mutants (A–D) and *TOC1 RNAi* (E and F). Plants were entrained under LD cycles and processed as detailed in the [Supplemental Experimental Procedures](#). Data are the means + SEM of the luminescence signals of 6–12 samples. Values of luminescence signals from *cca1-11* mutant and *TOC1 RNAi* are represented on the right y axes.

previously described core clock components, genes involved in light signaling, and those involved in circadian outputs such as photosynthesis, photoperiodic flowering, and hormone signaling, among others (Figures 4A–4D and S3). The waveforms oscillated with similar phases and amplitudes to those previously reported in entire plants (Figures 4E–4G), which suggests no fundamental differences in the global transcriptional circadian networks in the shoot apex and entire plants. It is noteworthy that shoot apices display such strong and robust rhythms (both morning- and evening-expressed genes) as opposed to the uncoupled rhythms in roots (only morning) (James et al., 2008) and in veins (mainly evening) (Endo et al., 2014). Functional categorization of the rhythmic genes showed a wide range of biological functions, highlighting as most significantly enriched those genes involved in circadian rhythms and responses to environmental conditions, including different qualities of light, temperature, and radiation (Figure S3). This enrichment might explain the specific readjustment of shoot apices to environmental changes observed in our jet-lag experiments.

Differences in Synchrony of Clock Cells in Various Organs and Tissues

To understand the cellular basis of the circadian rhythmicity at the shoot apex, we examined rhythms from individual cells of plants expressing CCA1-HA-EYFP under its own promoter (Yakir et al., 2009). We performed *in vivo* time-course analysis by

confocal imaging of excised shoot apices embedded in agarose (Mas and Beachy, 1998). Fluorescent signals from individual nuclei of shoot apex cells sustained rhythmic oscillations. The circadian waveforms maintained good synchrony, manifested by similar timing in their rising and declining phases even after 3 days under LL (Figure 5A, left panel and Figure 5B). The results were also evident when the confocal imaging started at different time points (Figure S4). A similar pattern of highly synchronous waveforms was observed with single cells from shoot apices of FLAG-PRR7-EGFP-expressing plants (Nakamichi et al., 2010) (Figure S4). In contrast, and consistent

with previous data (Yakir et al., 2011), the variation in the rhythmic accumulation of CCA1-HA-EYFP in individual leaf cells significantly increased after 2 days under LL (Figure 5A, right panel and Figure 5C). Differences in phase and amplitude were also clearly observed when fluorescent signals were not relativized to the maximum (Figure S4). We also measured fluorescence from the leaf vasculature, as previous studies have shown that these cells are coupled (Endo et al., 2014). We observed two distinguishable populations with slightly different phases (Figure S4). Individual cell-to-cell comparisons showed that both populations maintain a certain degree of synchrony (Figures 5D and 5E). Synchrony appeared to be higher than that observed in leaf mesophyll cells but lower than in cells at the shoot apex. Quantitative analysis of the waveform correlation among individual cells confirmed that the correlation coefficient in shoot apex cells was higher than the one for vascular cells with the advanced (A) or delayed (D) phase (Figures 5F and 5G). The group of cells with a delayed phase appeared to be more synchronous than the group with an advanced phase. The waveforms in leaf mesophyll cells displayed lower correlation values and increased heterogeneity. A higher synchrony in shoot apices compared to vascular cells or the mesophyll cells adjacent to the leaf veins (Figure S4) was also observed when an evening-expressed gene was examined (ELF3-EYFP) (Dixon et al., 2011). In this case, the separation of cells with advanced and delayed phases was not so evident in veins (Figure S4). Together, the results confirmed at the level of single cells and with three different reporters our conclusions

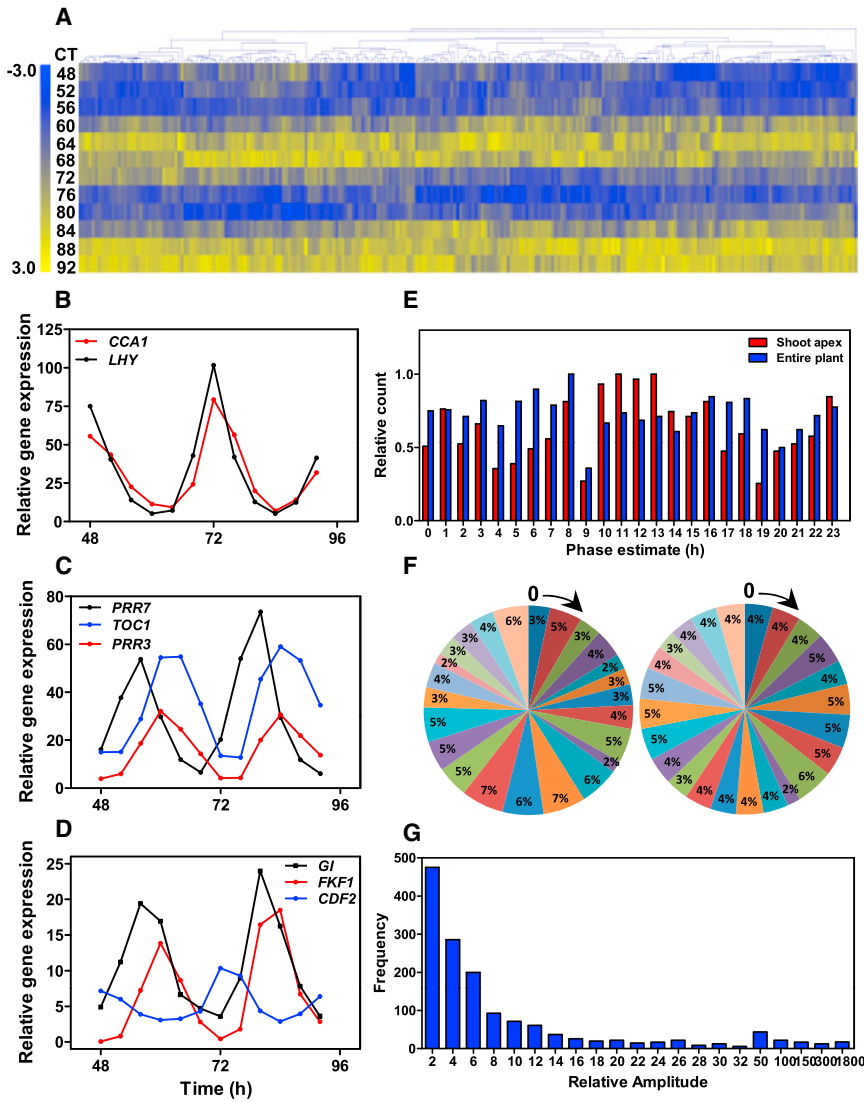


Figure 4. Transcriptional Profiling of the Circadian Program at the Shoot Apex

(A) Heatmap showing median-normalized gene expression at different circadian times (CT, vertical axis) for transcripts (horizontal axis) with a peak phase of expression at mid-late subjective night. Yellow indicates high expression and blue low expression.

(B–D) Gene-expression analysis of *CCA1*, *LHY* (B), *PRR3*, *PRR7*, *TOC1* (C), and *GI*, *FKF1*, *CDF2* (D) in shoot apices of WT plants grown under LD cycles followed by 2 days under LL.

(E and F) Phase distribution of rhythmic genes in shoot apices and entire plants. Phase enrichment was calculated using the web-based tool “Phaser.” The phase estimates were represented relative to their maximum (E) and in pie charts (F) displaying the contribution of each phase to the total. Left chart: shoot apex; right chart: entire plants.

(G) Distribution of amplitudes of cycling transcripts in shoot apices calculated by using the algorithm JTK_Cycle.

See also Figure S3.

ward (Figure 5J). As individual cells at the shoot apex are able to maintain rhythmic oscillations (Figure 5B), one plausible explanation to our results is that dispersed cells do not sustain rhythms due to reduced intercellular communication and subsequent desynchronization over time.

In the mammalian circadian system, the clock components PER1 and CRY1 are required for sustained rhythms in peripheral tissues and in neurons dissociated from the SCN (Welsh et al., 2010). However, cellular interactions at the SCN can compensate for *Per1* or *Cry1* deficiency (Evans et al., 2012; Liu et al., 2007). We

on the distinct degrees of synchrony in shoot apices, leaf mesophyll cells, and veins.

Intercellular Circadian Coupling among Clock Cells of the Shoot Apex

If coupling of shoot apex clocks is responsible for the waveform synchrony, then rhythms should be affected when the intercellular communication is disrupted. To explore this idea, we compared shoot apices from intact tissues and from dissociated and diluted protoplasts. Rhythms in excised shoot apices maintained good synchrony and were sustained for several days. However, in diluted shoot apex protoplasts, the oscillations persisted only for 2–3 days, increasing their heterogeneity over time (Figure 5H). Further dilution of protoplasts increasingly advanced the timing of rhythmic dampening (Figures 5I and S4). Analysis of the R values in shoot apices and in diluted protoplasts quantitatively confirmed that the phase coherence in protoplasts was only sustained for less than 2 days, reaching asynchrony after

found a similar scenario at the shoot apex of *lux* mutants. In contrast to the reported arrhythmia of *lux-2* plants, the *lux-2* shoot apices were able to sustain rhythms to a certain degree. Although the rhythms were clearly compromised, rhythmicity at the *lux-2* shoot apex was better than in leaves (Figures 5K, 5L, and S4). Thus, the absolute requirement of LUX function in leaves is not so apparent in shoot apices. The differences are not due to changes in the circadian expression of *LUX* or the other components of the EC, *ELF3*, and *ELF4*, as verified by our RNA-seq analysis and by qRT-PCR (Figure S4). If in analogy to the mammalian system, effective intercellular coupling among the shoot apex cells is responsible for the distinctive phenotype, then disruption of the cellular communication should affect the rhythms. Indeed, shoot apex protoplasts from *lux-2* mutants were arrhythmic throughout the time-course analysis (Figure 5M). We proposed that the arrhythmic phenotype in protoplasts is the result from the rapid desynchronization of the dispersed cells, each containing a semi-functional oscillator.

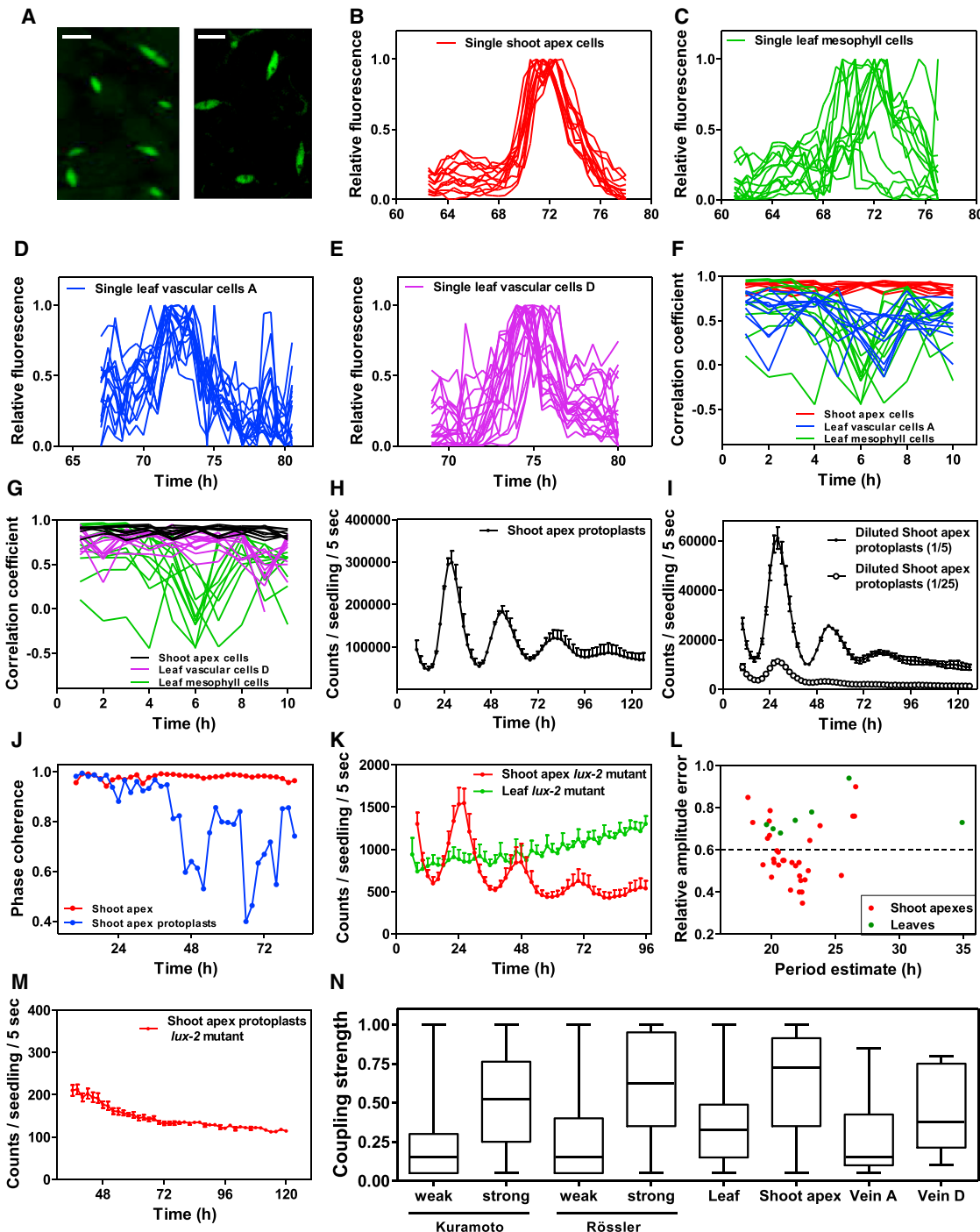


Figure 5. Circadian Coupling Defines the High Synchrony of Shoot Apex Clock Cells

(A) Representative fluorescent signals from CCA1-HA-EYFP accumulation in nuclei of shoot apex cells (left panel) and leaf cells (right panel). Panels show representative cells from a larger picture containing other cells out of the shown field (scale bar, 20 μm).

(B–E) In vivo time-course imaging of CCA1-HA-EYFP fluorescent signals quantified in individual nuclei from shoot apex (B), leaf mesophyll (C), and leaf vascular cells with advanced (D) and delayed (E) phases. Data are represented relative to the maximum value.

(F and G) Correlation coefficients among the waveforms of individual nuclei in shoot apex, leaf mesophyll cells, and leaf vascular cells with advanced (F) and delayed (G) phases.

(H and I) Luminescence analysis of CCA1::LUC activity in diluted (H) and further diluted series of protoplasts (I) from shoot apices. Protoplasts were synchronized for an additional day under LD before transferring to LL. Data are the means + SEM of the luminescence of 6–12 samples.

(J) Quantification of the phase coherence in intact shoot apices and in shoot apex protoplasts by calculating the synchronization index “R.”

(legend continued on next page)

Our results indicate that intercellular communication might be important for rhythms at the shoot apex. To mathematically explore the degree of intercellular coupling, we developed a predictive model by using barycentric coordinates for high-dimensional space (Hirata et al., 2015). The model involves the use of linear programming that assigns different weights to neighboring cells and identifies the strength of coupling based on the accuracy of the predictions given the weights. We first tested the performance of the proposed methods using the Kuramoto (Kuramoto, 1975) and the coupled Rössler (Rössler, 1976) toy models. The examples showed that the weights of neighboring oscillators are higher when the coupling is stronger (Figure 5N). When the model was used with the single-cell confocal data, we found that shoot apex clocks were highly coupled and had greater coupling strength than leaf vasculature or leaf mesophyll cells (Figure 5N). Together, the results confirmed a gradation or hierarchy in the strength of the circadian communication in different parts of the plant.

Relevance of the Shoot Apex Clocks in the Modulation of Circadian Oscillations in Roots

We next addressed the possible role of the shoot apex controlling the circadian function in roots. We adapted the luminescence assay protocol to examine rhythms in both shoots and roots of intact plants (Figure 6A). We also used laser microdissection (LMD) to excise shoot apices and examine rhythms in Δshoot apex plants (Figure 6B). Previous studies have reported that rhythms dampened low and waveforms broadened in entire plants after several days under free-running conditions (Yakir et al., 2011). We found that rhythms at the shoot apex were sustained for more than 7 days under LL (Figure 6C), which suggests that intercellular coupling at the shoot apex might contribute to the rhythmic robustness after extended periods under LL. When we examined rhythms in Δshoot apex plants, we observed an advanced average phase and increasing waveform variability, in a similar fashion to that of excised leaves (Figures 6D and S5). Application of auxin did not noticeably affect the rhythms in shoots of entire plants or Δshoot apex plants (Figure S5), which suggests that the Δshoot apex phenotypes are not due to changes in auxin flux. It is noteworthy that rhythms in plants that only lack the shoot apex are similar to the rhythms in leaves, whereas the small shoot apex is able to more precisely sustain rhythms. Unexpectedly, we also found that rhythms in plants without cotyledons or leaves were almost indistinguishable from the ones observed in intact plants (Figures 6E and 6F).

Photosynthetic sucrose has been shown to modulate clock function (Haydon et al., 2013; James et al., 2008). Our studies revealed an initial phase delay and period lengthening that led to damped rhythms in shoots from intact plants treated with the inhibitor of the photosynthetic electron transport [3-(3,4-di-

chlorophenyl)-1,1-dimethylurea, DCMU] (Figure S5). When we applied the drug only in shoots and checked the effects on roots, we found a phase delay and damped rhythms (Figure S5). These results confirmed that photosynthetic signals from shoots are important for the root clock. DCMU treatment in excised shoot apices also led to eventual dampening of rhythms, but the early phase delay observed in whole shoots and roots was not so evident (Figure S5). These results suggest increased robustness against pharmacological perturbation of photosynthesis at the shoot apex.

To further explore the importance of circadian communication, we used plants with reduced intercellular trafficking by means of *CALS3* gain-of-function mutations (*cals3-d*) that lead to reduced plasmodesmata aperture (Vatén et al., 2011). Our results showed that blocked trafficking clearly altered the rhythmic expression of core clock genes in roots, with no evident peak and trough expression as observed in WT roots (Figures 6G, 6H, and S5). We also examined rhythms in shoots and roots that were rapidly separated following 2 days of luminescence analysis of the intact plants (Figure 6I). The separation led to dampening of rhythms in roots, indicating that rhythms in roots are altered very rapidly after separation from shoots. To ascertain the role of the shoot apex on root synchronization, we then examined circadian rhythms in roots from intact plants in which the shoot apex was removed (Δshoot apex plants) (Figure 6B). Our results showed that rhythms were clearly affected, with an initial long-period phenotype that progressively led to arrhythmia (Figure 6J). Rhythms in roots from plants in which leaves and cotyledons were removed were not severely affected and showed a slightly advanced phase compared with the rhythms in roots from intact plants (Figure S5). Noteworthy are also the results of jet-jag experiments showing that roots from intact plants were able to resynchronize with a pattern that more closely resembled the one in shoot apices than the one in leaves (Figure S5).

A Hierarchical Structure at the Core of the *Arabidopsis* Clock

Efficient micrografting of *Arabidopsis* seedlings is a powerful tool for studying long-distance signaling (Bainbridge et al., 2014). To conclusively determine the possible hierarchical nature of the plant circadian system, we performed micrografting with young *Arabidopsis* seedlings using the shoot apex as scion (Figure 7A). We reasoned that grafting with different genotypes would provide definitive information on the role of shoot apices on the root oscillation.

Micrografting and luminescence analysis were first tested on WT self-grafts (WT Shoot Apex–WT Roots, WT SA-WT Rt). The analysis showed that *CCA1::LUC* and *TOC1::LUC* rhythms followed a similar trend to that observed in entire non-grafted

(K) Average luminescence of *CAB2::LUC* activity in shoot apices and leaves of *lux-2* mutant plants. Data are means + SEM of the luminescence of six samples.

(L) Period estimates of *CAB2::LUC* activity from individual traces analyzed as detailed in the [Supplemental Experimental Procedure](#).

(M) Luminescence analysis of *CAB2::LUC* activity in protoplasts from shoot apices of *lux-2* mutant plants. Data represent means + SEM of 6–12 samples. Protoplasts were synchronized for an additional day under LD before transferring to LL.

(N) Mathematical analysis of the coupling strength by barycentric coordinates for high-dimensional space using the Kuramoto and coupled Rössler toy models and the *in vivo* *CCA1*-EYFP imaging data. The line in the middle of the box is plotted at the median. The whiskers represent the minimum and maximum values. See also Figure S4.

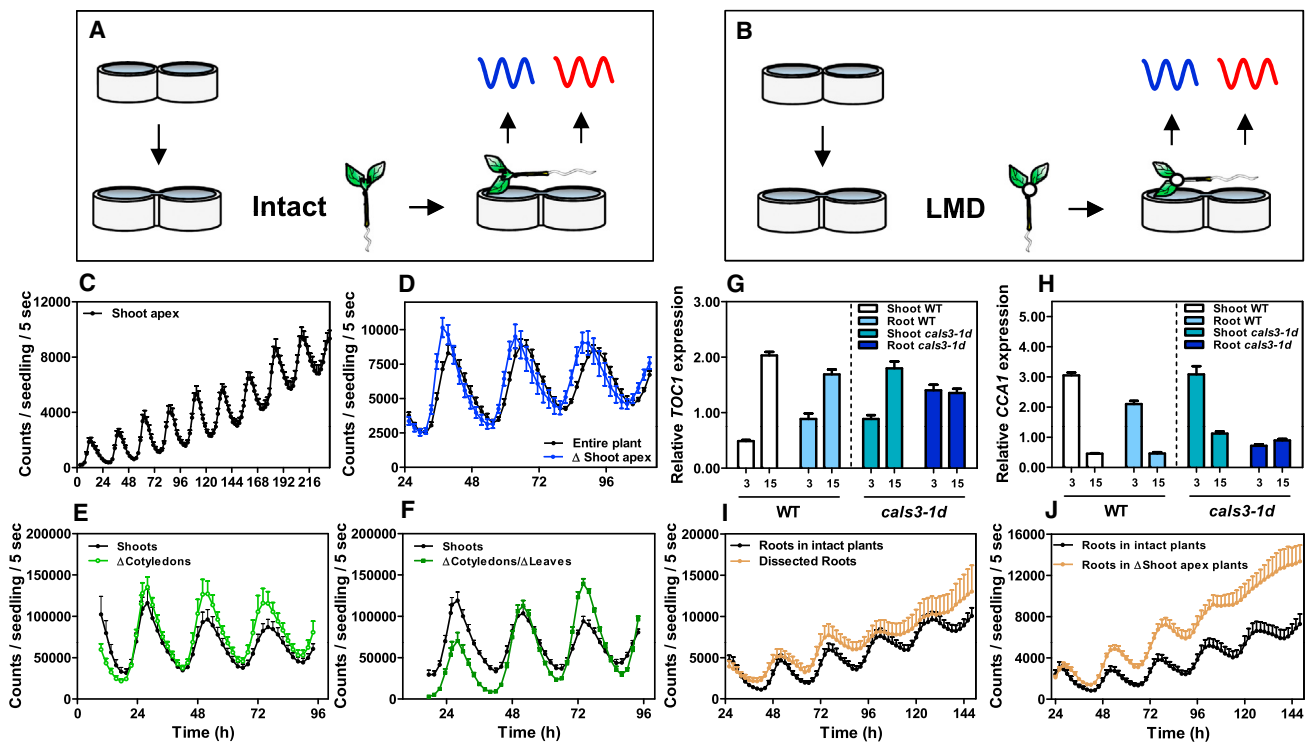


Figure 6. Rhythms at the Shoot Apex Influence the Circadian Activity in Roots

- (A) Schematic drawing depicting the rhythmic analysis of shoots and roots from intact plants.
- (B) LMD was used to obtain Δ shoot apex plants. Seedlings were horizontally positioned in serrated 96-well microplates so that rhythms could be examined in roots and shoots.
- (C) Average rhythms of TOC1::LUC luminescence in shoot apices for extended days under LL.
- (D) TOC1::LUC luminescence in plants in which the shoot apices were removed by LMD.
- (E and F) CCA1::LUC luminescence in plants in which the cotyledons (E) and leaves (F) were removed.
- (G and H) qRT-PCR analysis of TOC1 (G) and CCA1 (H) expression in shoots and roots of WT and cals3 mutant plants. Plants were synchronized under LD, and samples were taken after 2 days under LL at CT3 and CT15.
- (I) CCA1::LUC luminescence from roots after rapid dissection from shoots.
- (J) CCA1::LUC luminescence in roots from intact plants and Δ shoot apex plants. Luminescence was recorded under LL following synchronization under LD. Data are represented as the means + SEM. See also Figure S5.

plants (Figures 7B and 7C). Rhythms in roots exhibited a longer period compared to shoots, which also mirrored the observations in organs of non-grafted plants (Figure S1). As these results suggested that the grafting procedure did not manifestly alter the circadian oscillation, we next grafted the shoot apex of arrhythmic plants into a WT rootstock. We reasoned that the lack of a functional clock in the shoot apex should alter the rhythms in roots. Indeed, grafting the shoot apex of the arrhythmic *cca1-1/hy-11* plants (Mizoguchi et al., 2002; Portolés and Más, 2010) (Figure S6) disrupted the rhythms of WT roots (Figure 7D). A similar alteration of WT root rhythms was observed with the shoot apex of *elf3-2* mutants (Hicks et al., 1996) (Figure 7E). Although slight oscillations could be appreciated, the amplitude and robustness of the waveforms were clearly affected. These results confirmed that proper clock function in the shoot apex is important for the rhythmic activity in roots. We then performed the reverse experiment in which WT shoot apices were grafted into arrhythmic rootstocks to test the ability of shoot apex signals to reestablish the rhythms in roots.

Remarkably, the arrhythmia of *cca1-1/hy-11* or *elf3-2* roots could be partially restored by grafting the shoot apex of WT plants (Figures 7F and 7G). The oscillations were not very robust, but the patterns were not as arrhythmic as the roots of non-grafted plants (Figure S6). Although we observed variability in the degree of restored rhythms (Figure S6), the recovery was quite evident. Altogether, we conclude that signals from the shoot apex are important for circadian oscillations in roots.

DISCUSSION

A series of different protocols developed in this study has allowed us to follow the rhythmic expression in excised organs of the plant. Under sucrose, rhythms were sustained in all organs examined and the tissues continued growing normally after excision, which suggests that the excision did not manifestly affect the rhythms. The different excised organs displayed a wide range of circadian properties. Hypocotyls and roots lack precision and robustness, with long circadian periods and

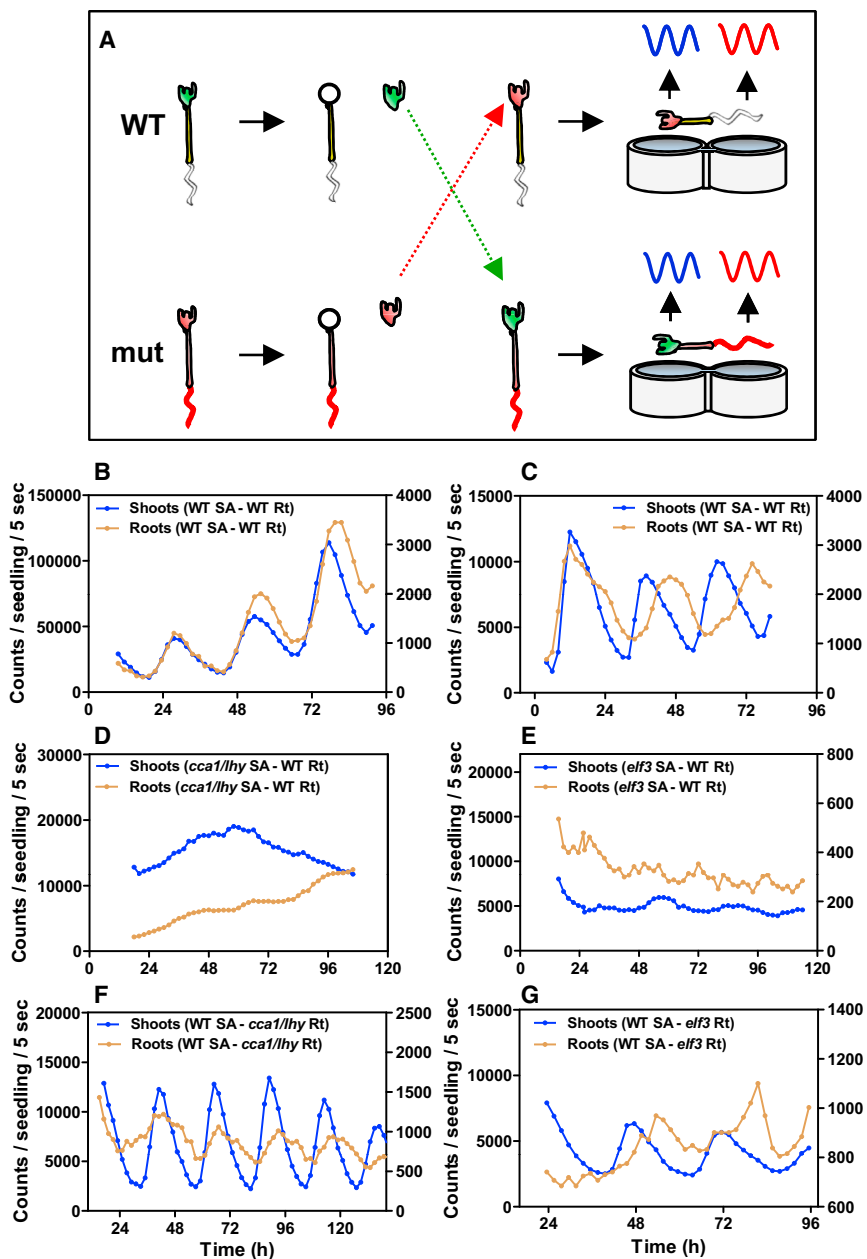


Figure 7. A Hierarchical Dominance of the Shoot Apex Clocks

(A) Schematic drawing depicting the rhythmic analysis of micrografted plants as detailed in [Experimental Procedures](#).

(B and C) Analysis of *CCA1::LUC* (B) and *TOC1::LUC* (C) luminescence in shoots and roots of WT scion and WT rootstocks.

(D–G) Luminescence in shoots and roots of *cca1/lhy* mutant scion and WT rootstocks (D), *elf3* mutant scion and WT rootstocks (E), WT scion and *cca1/lhy* mutant rootstocks (F), and WT scion and *elf3* mutant rootstocks (G). Luminescence was recorded under LL following synchronization under LD. Values of luminescence signals from roots are represented on the right y axes.

See also [Figure S6](#).

whereas the leaf vasculature synchronizes the neighboring mesophyll cells ([Endo et al., 2014](#)). This local synchronization raises the question about possible differences in rhythms of mesophyll cells close to the vasculature and those located far from the veins. Desynchronization between leaf stomatal and mesophyll cells ([Yakir et al., 2011](#)) could be another source of phase heterogeneity in leaves.

Shoot apices displayed remarkable homogeneous rhythmicity with highly synchronous waveforms. Among the tissues examined, different patterns of waveform synchrony could be distinguished: the cells from the shoot apex with the highest synchrony, the intermediate synchrony in the vascular cells, and the lowest synchrony observed in leaf mesophyll cells. The fact that the synchrony is lost in dispersed, diluted shoot apex protoplasts suggests that the phase coherence and synchrony might be due to high intercellular coupling among shoot apex clocks. The development of a tailor-designed mathematical model us-

ing barycentric coordinates for high-dimensional space confirmed this notion. The method has been proven successful for a wide range of uses, from weather forecasting to creation of musical instruments with natural sounds ([Hirata et al., 2015](#)). Our studies also revealed that the intercellular coupling or circadian communication among shoot apex clocks confer robustness against genetic mutations and pharmacological perturbations. These properties closely resemble those of the circadian system in mammals in which intercellular coupling among neurons at the SCN can compensate for the absence of functional key clock components ([Evans et al., 2012; Liu et al., 2007](#)).

The molecular circadian network and phenotypes of core clock mutants at the shoot apex appear to be similar to those

arrhythmia, whereas leaves lack synchrony among the different samples from plants similarly entrained. As roots are a sucrose sink, our results with excised roots (\pm sucrose) are consistent with previous studies ([Haydon et al., 2013; James et al., 2008](#)) and with the dampening of rhythms in roots when shoots are treated with DCMU. Analysis of root rhythms in Δ shoot apex plants rendered similar results to those of excised roots, which confirmed the dependency of roots on the circadian communication with shoot apices. The heterogeneity of circadian waveforms in leaves is also consistent with previous studies ([Wenden et al., 2012](#)). Phase heterogeneity might be due to differences in circadian coupling among various leaf cell types. Mesophyll cells in leaves are only weakly coupled,

described in the whole plant. However, prevalence for morning- or evening-expressed genes has been shown for the clocks of leaf mesophyll cells and leaf veins, respectively (Endo et al., 2014). Uncoupled morning and evening oscillators have been also previously reported for the clock in roots (James et al., 2008). Our full time-course analysis by RNA-seq showed robust rhythms of circadian genes with similar peak phases and relative amplitudes to those reported in entire plants. The particular properties that we observed at the shoot apex clocks might result from their strong intercellular coupling rather than from a distinctive molecular network. We also found a clear enrichment of genes involved in responses to environmental signals. This enrichment might be responsible for the distinctive waveforms in jet-lag experiments, as if the shoot apex clocks were highly sensible to perceive and respond to the changing environmental conditions. The enrichment might be particularly useful for the shoot apical cells that are buried and shielded from the environment. Intercellular coupling might also be an aid for circadian synchronization of cells with reduced light accessibility. The fact that genes responsible for perception of synchronizing signals such as light and temperature are enriched in our RNA-seq data is consistent with a main role of shoot apices as a synchronizing master clock.

Grafting has been used to study long-distance signaling in different processes, for instance shoot branching (Turnbull et al., 2002) or stress responses (Holbrook et al., 2002). The studies presented here demonstrate the long-distance circadian signaling by micrografting approaches. Our results have revealed the influence of shoot apices on the rhythmic activity of roots. A plausible idea is that changes in auxin flux could be responsible for synchronizing rhythms in roots. However, our results suggest that auxin signaling has a minor, if any, role in the long-distance circadian communication. The partial recovery of mutant rootstocks by grafting WT shoot apices and, conversely, the arrhythmia of WT roots grafted with arrhythmic shoot apices reflect the circadian hierarchy of shoot apices. This situation is reminiscent of the circadian system in mammals in which genetic defects in peripheral clocks are phenotypically rescued by the hierarchical dominance of the SCN (Pando et al., 2002). The micrografting results were consistent with the shoot apex role influencing rhythms in roots, which was observed by other approaches used in this study (rapid dissection of shoots and roots, delta shoot apex plants, pharmacological treatments, and genetic analysis). The similar phenotypes reinforce the validity of the different procedures and the consistency of our conclusions.

Based on the recently discovered role of the plant vasculature (Endo et al., 2014), a very interesting possibility is that veins are used as the circadian traveling “highway” in which the synchronizing signals circulate from shoot apices to roots. In analogy with the mammalian circadian system, the shoot apex clock cells might function as the SCN neurons, whereas the plant vasculature could be comparable to blood veins and arteries. Further studies of topographically defined areas of circadian coupling and elucidation of the signals and mechanisms contributing to the circadian communication will be central to fully define the spatio-temporal networks orchestrating plant physiology and development on each organ, tissue, and cell.

EXPERIMENTAL PROCEDURES

Organ Dissection and Micrografting Experiments

Organ dissection was performed as detailed in the [Supplemental Experimental Procedures](#). For micrografting experiments, *Arabidopsis* seedlings were grown vertically on half-strength Murashige and Skoog (MS) agar medium with 0.5% sucrose for 3–7 days. Seedlings were placed on wet filters under the dissecting microscope in a laminar flow cabinet as described (<http://www.bio-protocol.org/e1164>). Cotyledons were removed, and both scion and rootstock seedlings were horizontally cut with a razor blade just below the shoot apex. With forceps, and very gently, the scion and rootstock cut stumps were joined together, paying attention to match up the two phloem strands. When grafting was completed, plates were sealed with two layers of micropore tape and returned to the growth chamber for at least 4–6 more days. If present, adventitious roots on the scions were removed before luminescence analysis. The unsuccessful grafted seedlings were identified as the grafts failed to properly join together. In cases when the successful grafting was not clear, the resulting plants were discarded. A total of 120 grafting events were assayed for WT SA-*cca1/hy* Rt plants. The percentage of successfully micrografted plants was about 50% (possibly higher but only faultlessly grafted plants were examined). From the 59 successfully grafted WT SA - *cca1/hy* Rt plants, 50 (i.e., around 85%) showed different degrees of restored rhythms (p value = 3.77×10^{-12} by Fisher's exact test, considering that none of the 20 *cca1/hy* SA - *cca1/hy* Rt plants displayed rhythms in roots). For the control WT SA-WT Rt grafting, 22 out of 24 successfully grafted plants showed very robust rhythms.

RNA Extraction and RNA-Seq Analysis

RNA extraction and RNA-seq analysis were performed as detailed in the [Supplemental Experimental Procedures](#).

Single-Cell Confocal Microscopy Imaging

For *in vivo* confocal imaging at a single-cell resolution, excised shoot apices or leaves were embedded just after dissection in low-melting-point agarose dissolved in MS medium as previously described (Mas and Beachy, 1998). Further details are described in the [Supplemental Experimental Procedures](#).

Protoplast Preparation and Gene-Expression Analysis

Protoplast preparation (Yoo et al., 2007) and gene-expression analysis (Malapeira et al., 2012) were performed as described. Details are described in the [Supplemental Experimental Procedures](#).

Mathematical Analysis

Mathematical analysis was performed as described in Hirata et al. (2015). See further details in the [Supplemental Experimental Procedures](#).

SUPPLEMENTAL INFORMATION

Supplemental Information includes Supplemental Experimental Procedures and six figures and can be found with this article online at <http://dx.doi.org/10.1016/j.cell.2015.08.062>.

AUTHOR CONTRIBUTIONS

N.T. performed the biological experiments. Y.H. and K.A. designed and performed the mathematical analysis. P.M. designed the biological experiments and wrote the manuscript. All authors read, revised, and approved the manuscript.

ACKNOWLEDGMENTS

We thank Professor Y. Helariutta for the *ca/s3* seeds, Professor K. Kornacker for help with the JTK_CYCLE algorithm, Professor R. Green for CCA1-HA-EYP plants, and M. Amenós for help with the confocal microscope. This work was supported by research grants to P.M. from the Spanish Ministry of Economy and Competitiveness, from the Generalitat de Catalunya (AGAUR), from the

Global Research Network of the National Research Foundation of Korea, and from the European Commission Marie Curie Research Training Network (ChIP-ET). Y.H. and K.A. are supported by the Platform Project for Supporting in Drug Discovery and Life Science Research (Platform for Dynamic Approaches to Living System) from the Ministry of Education, Culture, Sports, Science (MEXT) and Japan Agency for Medical Research and development (AMED). K.A. is also partially supported by CREST, JST, Japan. N.T. is supported by a CRAG fellowship.

Received: March 13, 2015

Revised: July 1, 2015

Accepted: August 6, 2015

Published: September 24, 2015

REFERENCES

Alabadí, D., Oyama, T., Yanovsky, M.J., Harmon, F.G., Más, P., and Kay, S.A. (2001). Reciprocal regulation between TOC1 and LHY/CCA1 within the *Arabidopsis* circadian clock. *Science* 293, 880–883.

Aton, S.J., and Herzog, E.D. (2005). Come together, right...now: synchronization of rhythms in a mammalian circadian clock. *Neuron* 48, 531–534.

Bainbridge, K., Bennett, T., Crisp, P., Leyser, O., and Turnbull, C. (2014). Grafting in *Arabidopsis*. In *Arabidopsis Protocols*, J.J. Sanchez-Serrano and J. Salinas, eds. (New York: Humana Press), pp. 155–163.

de Montaigu, A., Tóth, R., and Coupland, G. (2010). Plant development goes like clockwork. *Trends Genet.* 26, 296–306.

Dixon, L.E., Knox, K., Kozma-Bognar, L., Southern, M.M., Pokhilko, A., and Millar, A.J. (2011). Temporal repression of core circadian genes is mediated through EARLY FLOWERING 3 in *Arabidopsis*. *Curr. Biol.* 21, 120–125.

Endo, M., Shimizu, H., Nohales, M.A., Araki, T., and Kay, S.A. (2014). Tissue-specific clocks in *Arabidopsis* show asymmetric coupling. *Nature* 515, 419–422.

Evans, J.A., Pan, H., Liu, A.C., and Welsh, D.K. (2012). Cry1^{-/-} circadian rhythmicity depends on SCN intercellular coupling. *J. Biol. Rhythms* 27, 443–452.

Fukuda, H., Nakamichi, N., Hisatsune, M., Murase, H., and Mizuno, T. (2007). Synchronization of plant circadian oscillators with a phase delay effect of the vein network. *Phys. Rev. Lett.* 99, 098102.

Gendron, J.M., Pruneda-Paz, J.L., Doherty, C.J., Gross, A.M., Kang, S.E., and Kay, S.A. (2012). *Arabidopsis* circadian clock protein, TOC1, is a DNA-binding transcription factor. *Proc. Natl. Acad. Sci. USA* 109, 3167–3172.

Harmer, S.L., Panda, S., and Kay, S.A. (2001). Molecular bases of circadian rhythms. *Annu. Rev. Cell Dev. Biol.* 17, 215–253.

Harrington, M. (2010). Location, location, location: important for jet-lagged circadian loops. *J. Clin. Invest.* 120, 2265–2267.

Haydon, M.J., Mielczarek, O., Robertson, F.C., Hubbard, K.E., and Webb, A.A.R. (2013). Photosynthetic entrainment of the *Arabidopsis thaliana* circadian clock. *Nature* 502, 689–692.

Helper, A., Nusinow, D.A., Chow, B.Y., Gehrke, A.R., Bulyk, M.L., and Kay, S.A. (2011). LUX ARRHYTHMO encodes a nighttime repressor of circadian gene expression in the *Arabidopsis* core clock. *Curr. Biol.* 21, 126–133.

Hicks, K.A., Millar, A.J., Carré, I.A., Somers, D.E., Straume, M., Meeks-Wagner, D.R., and Kay, S.A. (1996). Conditional circadian dysfunction of the *Arabidopsis* early-flowering 3 mutant. *Science* 274, 790–792.

Hirata, Y., Shiro, M., Takahashi, N., Aihara, K., Suzuki, H., and Mas, P. (2015). Approximating high-dimensional dynamics by barycentric coordinates with linear programming. *Chaos Interdisc. J. Nonlinear Sci.* 25, 013114.

Holbrook, N.M., Shashidhar, V.R., James, R.A., and Munns, R. (2002). Stomatal control in tomato with ABA-deficient roots: response of grafted plants to soil drying. *J. Exp. Bot.* 53, 1503–1514.

Huang, W., Pérez-García, P., Pokhilko, A., Millar, A.J., Antoshechkin, I., Riechmann, J.L., and Mas, P. (2012). Mapping the core of the *Arabidopsis* circadian clock defines the network structure of the oscillator. *Science* 336, 75–79.

Hughes, M.E., Hogenesch, J.B., and Kornacker, K. (2010). JTK_CYCLE: an efficient nonparametric algorithm for detecting rhythmic components in genome-scale data sets. *J. Biol. Rhythms* 25, 372–380.

James, A.B., Monreal, J.A., Nimmo, G.A., Kelly, C.L., Herzyk, P., Jenkins, G.I., and Nimmo, H.G. (2008). The circadian clock in *Arabidopsis* roots is a simplified slave version of the clock in shoots. *Science* 322, 1832–1835.

Katari, M.S., Nowicki, S.D., Aceituno, F.F., Nero, D., Kelfer, J., Thompson, L.P., Cabello, J.M., Davidson, R.S., Goldberg, A.P., Shasha, D.E., et al. (2010). VirtualPlant: A Software Platform to Support Systems Biology Research. *Plant Physiol.* 152, 500–515.

Kim, J., and Somers, D.E. (2010). Rapid assessment of gene function in the circadian clock using artificial microRNA in *Arabidopsis* mesophyll protoplasts. *Plant Physiol.* 154, 611–621.

Kinmonth-Schultz, H.A., Golembeski, G.S., and Imaizumi, T. (2013). Circadian clock-regulated physiological outputs: dynamic responses in nature. *Semin. Cell Dev. Biol.* 24, 407–413.

Kuramoto, Y. (1975). Self-entrainment of a population of coupled nonlinear oscillators. *Lect. N. Phys.* 39, 420–422.

Liu, A.C., Welsh, D.K., Ko, C.H., Tran, H.G., Zhang, E.E., Priest, A.A., Buhr, E.D., Singer, O., Meeker, K., Verma, I.M., et al. (2007). Intercellular coupling confers robustness against mutations in the SCN circadian clock network. *Cell* 129, 605–616.

Makino, S., Matsushika, A., Kojima, M., Yamashino, T., and Mizuno, T. (2002). The APRR1/TOC1 quintet implicated in circadian rhythms of *Arabidopsis thaliana*: I. Characterization with APRR1-overexpressing plants. *Plant Cell Physiol.* 43, 58–69.

Malapeira, J., Khaitova, L.C., and Mas, P. (2012). Ordered changes in histone modifications at the core of the *Arabidopsis* circadian clock. *Proc. Natl. Acad. Sci. USA* 109, 21540–21545.

Mas, P., and Beachy, R.N. (1998). Distribution of TMV movement protein in single living protoplasts immobilized in agarose. *Plant J.* 15, 835–842.

Millar, A.J., Carré, I.A., Strayer, C.A., Chua, N.H., and Kay, S.A. (1995). Circadian clock mutants in *Arabidopsis* identified by luciferase imaging. *Science* 267, 1161–1163.

Mizoguchi, T., Wheatley, K., Hanzawa, Y., Wright, L., Mizoguchi, M., Song, H.R., Carré, I.A., and Coupland, G. (2002). LHY and CCA1 are partially redundant genes required to maintain circadian rhythms in *Arabidopsis*. *Dev. Cell* 2, 629–641.

Mormann, F., Lehnertz, K., David, P., and Elger, C.E. (2000). Mean phase coherence as a measure for phase synchronization and its application to the EEG of epilepsy patients. *Physica D* 144, 358–369.

Nakahata, Y., Grimaldi, B., Sahar, S., Hirayama, J., and Sassone-Corsi, P. (2007). Signaling to the circadian clock: plasticity by chromatin remodeling. *Curr. Opin. Cell Biol.* 19, 230–237.

Nakamichi, N., Kiba, T., Henriques, R., Mizuno, T., Chua, N.-H., and Sakakibara, H. (2010). PSEUDO-RESPONSE REGULATORS 9, 7, and 5 are transcriptional repressors in the *Arabidopsis* circadian clock. *Plant Cell* 22, 594–605.

Nakamichi, N., Matsushika, A., Yamashino, T., and Mizuno, T. (2003). Cell autonomous circadian waves of the APRR1/TOC1 quintet in an established cell line of *Arabidopsis thaliana*. *Plant Cell Physiol.* 44, 360–365.

Nusinow, D.A., Helper, A., Hamilton, E.E., King, J.J., Imaizumi, T., Schultz, T.F., Farré, E.M., and Kay, S.A. (2011). The ELF4-ELF3-LUX complex links the circadian clock to diurnal control of hypocotyl growth. *Nature* 475, 398–402.

Pando, M.P., Morse, D., Cermakian, N., and Sassone-Corsi, P. (2002). Phenotypic rescue of a peripheral clock genetic defect via SCN hierarchical dominance. *Cell* 110, 107–117.

Portolés, S., and Más, P. (2010). The functional interplay between protein kinase CK2 and CCA1 transcriptional activity is essential for clock temperature compensation in *Arabidopsis*. *PLoS Genet.* 6, e1001201.

Rascher, U., Hütt, M.-T., Siebke, K., Osmond, B., Beck, F., and Lütge, U. (2001). Spatiotemporal variation of metabolism in a plant circadian rhythm: the biological clock as an assembly of coupled individual oscillators. *Proc. Natl. Acad. Sci. USA* 98, 11801–11805.

Ripperger, J.A., and Merrow, M. (2011). Perfect timing: epigenetic regulation of the circadian clock. *FEBS Lett.* **585**, 1406–1411.

Rössler, O.E. (1976). An equation for continuous chaos. *Phys. Lett. A* **57**, 397–398.

Sai, J., and Johnson, C.H. (1999). Different circadian oscillators control Ca(2+) fluxes and *lhc b* gene expression. *Proc. Natl. Acad. Sci. USA* **96**, 11659–11663.

Schaffer, R., Ramsay, N., Samach, A., Corden, S., Putterill, J., Carré, I.A., and Coupland, G. (1998). The late elongated hypocotyl mutation of *Arabidopsis* disrupts circadian rhythms and the photoperiodic control of flowering. *Cell* **93**, 1219–1229.

Stratmann, T., and Más, P. (2008). Chromatin, photoperiod and the *Arabidopsis* circadian clock: a question of time. *Semin. Cell Dev. Biol.* **19**, 554–559.

Strayer, C., Oyama, T., Schultz, T.F., Raman, R., Somers, D.E., Más, P., Panda, S., Kreps, J.A., and Kay, S.A. (2000). Cloning of the *Arabidopsis* clock gene *TOC1*, an autoregulatory response regulator homolog. *Science* **289**, 768–771.

Turnbull, C.G.N., Booker, J.P., and Leyser, H.M.O. (2002). Micrografting techniques for testing long-distance signalling in *Arabidopsis*. *Plant J.* **32**, 255–262.

Vatén, A., Dettmer, J., Wu, S., Stierhof, Y.-D., Miyashima, S., Yadav, S.R., Roberts, C.J., Campilho, A., Bulone, V., Lichtenberger, R., et al. (2011). Callose biosynthesis regulates symplastic trafficking during root development. *Dev. Cell* **21**, 1144–1155.

Wang, Z.Y., and Tobin, E.M. (1998). Constitutive expression of the *CIRCADIAN CLOCK ASSOCIATED 1* (*CCA1*) gene disrupts circadian rhythms and suppresses its own expression. *Cell* **93**, 1207–1217.

Welsh, D.K., Takahashi, J.S., and Kay, S.A. (2010). Suprachiasmatic nucleus: cell autonomy and network properties. *Annu. Rev. Physiol.* **72**, 551–577.

Wenden, B., Toner, D.L.K., Hodge, S.K., Grima, R., and Millar, A.J. (2012). Spontaneous spatiotemporal waves of gene expression from biological clocks in the leaf. *Proc. Natl. Acad. Sci. USA* **109**, 6757–6762.

Wijnen, H., and Young, M.W. (2006). Interplay of circadian clocks and metabolic rhythms. *Annu. Rev. Genet.* **40**, 409–448.

Yakir, E., Hilman, D., Harir, Y., and Green, R.M. (2007). Regulation of output from the plant circadian clock. *FEBS J.* **274**, 335–345.

Yakir, E., Hilman, D., Kron, I., Hassidim, M., Melamed-Book, N., and Green, R.M. (2009). Posttranslational regulation of *CIRCADIAN CLOCK ASSOCIATED1* in the circadian oscillator of *Arabidopsis*. *Plant Physiol.* **150**, 844–857.

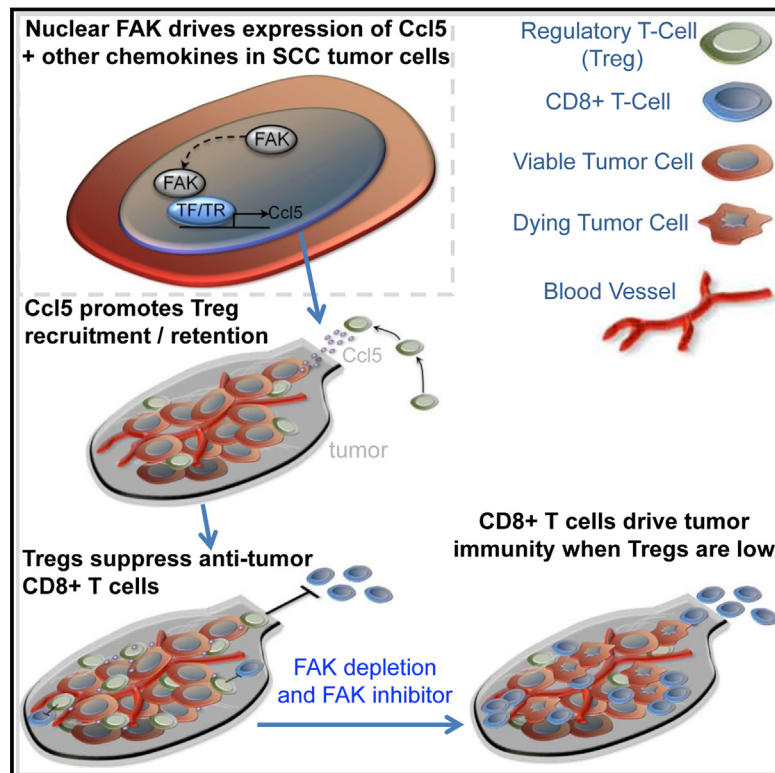
Yakir, E., Hassidim, M., Melamed-Book, N., Hilman, D., Kron, I., and Green, R.M. (2011). Cell autonomous and cell-type specific circadian rhythms in *Arabidopsis*. *Plant J.* **68**, 520–531.

Yoo, S.-D., Cho, Y.-H., and Sheen, J. (2007). *Arabidopsis* mesophyll protoplasts: a versatile cell system for transient gene expression analysis. *Nat. Protoc.* **2**, 1565–1572.

Young, M.W., and Kay, S.A. (2001). Time zones: a comparative genetics of circadian clocks. *Nat. Rev. Genet.* **2**, 702–715.

Nuclear FAK Controls Chemokine Transcription, Tregs, and Evasion of Anti-tumor Immunity

Graphical Abstract



Authors

Alan Serrels, Tom Lund, Bryan Serrels, ..., Stephen M. Anderton, Robert J.B. Nibbs, Margaret C. Frame

Correspondence

a.serrels@ed.ac.uk (A.S.), m.frame@ed.ac.uk (M.C.F.)

In Brief

Nuclear focal adhesion kinase (FAK) regulates transcription of chemokines that drive recruitment of tumor-associated regulatory T cells (Tregs), thereby creating a tumor suppressive microenvironment by inhibiting cytotoxic CD8+ T cell activity.

Highlights

- Depletion or kinase inhibition of FAK can cause squamous cell carcinoma regression
- FAK promotes tumor evasion by inducing an immuno-suppressive microenvironment
- Nuclear FAK promotes transcription of chemokines that drive recruitment of Tregs
- FAK-induced Tregs inhibit cytotoxic CD8+ T cells, allowing tumor tolerance and growth

Accession Numbers

GSE71662



Nuclear FAK Controls Chemokine Transcription, Tregs, and Evasion of Anti-tumor Immunity

Alan Serrels,^{1,7,*} Tom Lund,^{1,7} Bryan Serrels,¹ Adam Byron,¹ Rhoanne C. McPherson,² Alexander von Kriegsheim,¹ Laura Gómez-Cuadrado,¹ Marta Canel,¹ Morwenna Muir,¹ Jennifer E. Ring,³ Eleni Maniatı,⁴ Andrew H. Sims,¹ Jonathan A. Pachter,³ Valerie G. Brunton,¹ Nick Gilbert,⁵ Stephen M. Anderton,² Robert J.B. Nibbs,⁶ and Margaret C. Frame^{1,*}

¹Edinburgh Cancer Research UK Centre, Institute of Genetics and Molecular Medicine, University of Edinburgh, Edinburgh EH4 2XR, UK

²MRC Centre for Inflammation Research, The Queens Medical Research Institute, University of Edinburgh, Edinburgh EH16 4TJ, UK

³Verastem Inc., 117 Kendrick Street, Suite 500, Needham, MA 02494, USA

⁴Queen Mary, University of London, Centre for Cancer and Inflammation, Charterhouse Square, London EC1M 6BQ, UK

⁵MRC Human Genetics Unit, Institute of Genetics and Molecular Medicine, University of Edinburgh, Edinburgh EH4 2XU, UK

⁶Institute of Infection, Immunity, and Inflammation, University of Glasgow, Glasgow G12 8TA, UK

⁷Co-first author

*Correspondence: a.serrels@ed.ac.uk (A.S.), m.frame@ed.ac.uk (M.C.F.)

<http://dx.doi.org/10.1016/j.cell.2015.09.001>

This is an open access article under the CC BY license (<http://creativecommons.org/licenses/by/4.0/>).

SUMMARY

Focal adhesion kinase (FAK) promotes anti-tumor immune evasion. Specifically, the kinase activity of nuclear-targeted FAK in squamous cell carcinoma (SCC) cells drives exhaustion of CD8⁺ T cells and recruitment of regulatory T cells (Tregs) in the tumor microenvironment by regulating chemokine/cytokine and ligand-receptor networks, including via transcription of Ccl5, which is crucial. These changes inhibit antigen-primed cytotoxic CD8⁺ T cell activity, permitting growth of FAK-expressing tumors. Mechanistically, nuclear FAK is associated with chromatin and exists in complex with transcription factors and their upstream regulators that control Ccl5 expression. Furthermore, FAK's immuno-modulatory nuclear activities may be specific to cancerous squamous epithelial cells, as normal keratinocytes do not have nuclear FAK. Finally, we show that a small-molecule FAK kinase inhibitor, VS-4718, which is currently in clinical development, also drives depletion of Tregs and promotes a CD8⁺ T cell-mediated anti-tumor response. Therefore, FAK inhibitors may trigger immune-mediated tumor regression, providing previously unrecognized therapeutic opportunities.

INTRODUCTION

First described more than a decade ago (Onizuka et al., 1999; Shimizu et al., 1999), regulatory T cells (Tregs) have become recognized as a core component of the immuno-suppressive armory utilized by many tumors to keep the anti-tumor activity of antigen-primed CD8⁺ T cells at bay. Increased Treg numbers has been associated with poorer survival in ovarian (Curiel

et al., 2004), gastrointestinal (Sasada et al., 2003), and esophageal (Kono et al., 2006) cancer. Indeed, the ratio of CD8⁺ T cells/Tregs correlates with poor prognosis, shifting the balance from anti-tumor immunity toward tumor tolerance (Quezada et al., 2006; Sato et al., 2005; Shah et al., 2011). Through secreting a range of chemokines and cytokines, cancer cells can promote the recruitment of Tregs into tumors and can also facilitate their peripheral expansion and retention (Darrasse-Jéze and Podsypanina, 2013; Ondondo et al., 2013). Thus, Tregs can act as a barrier to effective immune-based therapy aimed at activation of a CD8⁺ T cell anti-tumor immune response. However, the specific signals within tumor cells that stimulate elevated intra-tumoral Tregs, giving rise to tumor tolerance, remain elusive.

FAK is a tyrosine kinase that regulates diverse cellular functions, including adhesion, migration, invasion, polarity, proliferation, and survival (Frame et al., 2010). Using targeted gene deletion in mouse skin, we have previously shown a requirement for *fak* in tumor initiation and progression to malignant disease (McLean et al., 2004). FAK is also required for mammary tumor progression, intestinal tumorigenesis, and the androgen-independent formation of neuroendocrine carcinoma in a mouse model of prostate cancer (Ashton et al., 2010; Lahliou et al., 2007; Luo et al., 2009a; Provenzano et al., 2008; Pylayeva et al., 2009; Slack-Davis et al., 2009). Expression of FAK is elevated in a number of tumor types (reviewed in McLean et al., 2005), and FAK inhibitors are being developed as potential cancer therapeutics (Roberts et al., 2008; Shapiro et al., 2014). Many of FAK's functions in cancer are via its role in signaling downstream of integrins and growth factor receptors at the plasma membrane. FAK also contains putative nuclear localization sequences (NLS) within the F2 lobe of its FERM domain and can localize to the nucleus upon receipt of cellular stress, where it binds to p53 (Lim et al., 2008). However, the extent of FAK's nuclear functions remains largely unknown. Here, we report a function for nuclear FAK in regulating transcription of inflammatory cytokines and chemokines, in turn promoting an immuno-suppressive, pro-tumorigenic microenvironment. This is mediated

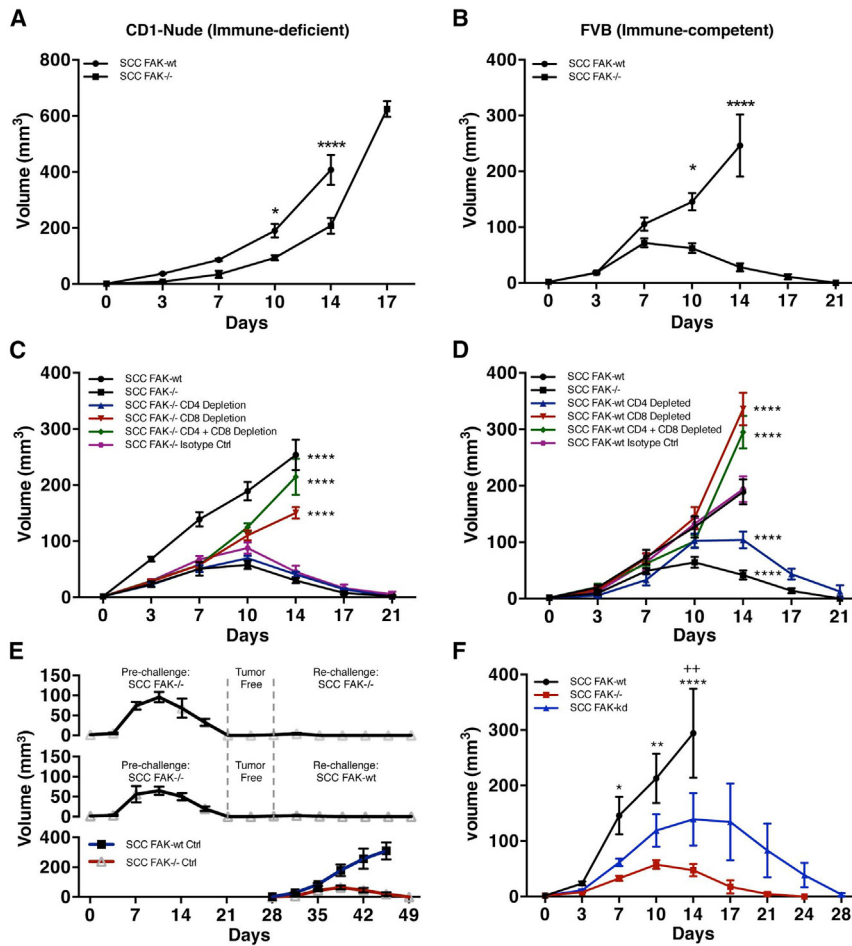


Figure 1. Loss of FAK or FAK Kinase Activity Results in CD8⁺ T Cell-Dependent SCC Tumor Clearance

(A and B) SCC FAK-WT and SCC FAK^{-/-} subcutaneous tumor growth in immune-deficient CD-1 nude mice (A) and immune-competent FVB mice (B).

(C and D) SCC FAK^{-/-} (C) and SCC FAK-WT (D) tumor growth in FVB mice treated with T-cell-depleting antibodies.

(E) Secondary tumor re-challenge with SCC FAK^{-/-} (top) and SCC FAK-WT (middle) cells following a pre-challenge with SCC FAK^{-/-} cells and a 7-day tumor-free period. Subcutaneous growth of SCC FAK-WT and SCC FAK^{-/-} tumors injected at day 28 without pre-challenge (bottom).

(F) Tumor growth in FVB mice following subcutaneous injection of SCC FAK-WT, SCC FAK^{-/-}, and SCC FAK-KD cells.

*p < 0.05, **p < 0.01, ***p < 0.0001; Sidak-corrected two-way ANOVA (A and B) or Tukey-corrected two-way ANOVA (C, versus SCC FAK^{-/-}; D, versus SCC FAK-WT; F, *, versus SCC FAK^{-/-} and +, versus SCC FAK-KD). Data are represented as mean ± SEM; n = 5–6 tumors.

growth of SCC tumors in FVB mice with a functional adaptive immune system.

SCC FAK^{-/-} Tumor Regression Is Dependent on CD8⁺ T Cells

To characterize the role of adaptive immunity in FAK^{-/-} SCC tumor regression, we used antibody-mediated T cell depletion in animals bearing FAK^{-/-} tumors

(Figures 1C and S1). Depletion of CD4⁺ T cells had no effect on tumor growth. In contrast, depletion of CD8⁺ T cells, either alone or in combination with CD4⁺ T cells, restored SCC FAK^{-/-} tumor growth. This implies that cytotoxic CD8⁺ T cells were responsible for regression of FAK^{-/-} tumors (Figure 1C) but does not exclude an accessory role for CD4⁺ T cells. T cell depletion in mice bearing SCC FAK-WT tumors (Figure 1D) revealed that: (1) depletion of CD8⁺ T cells, either alone or in combination with CD4⁺ T cells, caused a significant increase in tumor growth when compared to isotype-treated controls at day 14, and (2) depletion of CD4⁺ T cells alone caused regression of FAK-WT SCC tumors by day 21. This implied that FAK-expressing tumors were also under negative pressure from the immune system and that cells from the CD4⁺ T cell compartment play a role in protecting FAK-WT tumors from immune-mediated regression (reason discussed later; Figure 3).

Next, we re-challenged mice with 1 × 10⁶ SCC FAK-WT cells after regression of primary FAK^{-/-} SCC tumors, following 7 days of tumor-free survival after the tumors had regressed (Figure 1E, top and middle graphs). Neither FAK-deficient nor FAK-expressing SCC cells were able to grow after the mice had been pre-challenged with SCC FAK^{-/-} cells. As controls, SCC FAK-WT and FAK^{-/-} cells were injected at day 28 into mice with no pre-challenge, and these grew as expected (Figure 1E, bottom).

by recruitment and expansion of Tregs via FAK-regulated chemokine/cytokine networks, and we have found an important role for Ccl5 and TGF β 2. Therefore, FAK controls the tumor environment, and suppressing FAK activity, including via a clinically relevant FAK inhibitor, may be therapeutically beneficial by triggering immune-mediated tumor regression.

RESULTS

FAK-Deficient SCC Tumors Undergo Regression in an Immune-Competent Host

We used a syngeneic model of SCC in which the *fak* gene had been deleted by Cre-lox recombination (McLean et al., 2004; Serrels et al., 2012) and mutant tumor cell lines generated. We monitored tumor growth following injection of 1 × 10⁶ FAK-deficient cells (FAK^{-/-}) or FAK-deficient cells that re-expressed wild-type FAK (FAK-WT) at comparable levels to endogenous FAK in both CD-1 nude and FVB (syngeneic) host mouse strains. In CD-1 nude mice, SCC FAK^{-/-} tumor growth was characterized by a modest growth delay (Figure 1A) as reported previously (Serrels et al., 2012). By contrast, in FVB mice, SCC FAK^{-/-} tumor growth was characterized by an initial period of growth in the first 7 days followed by complete regression by day 21 (Figure 1B). Thus, FAK expression is required for the survival and

This implies that, following *FAK*^{-/-} SCC tumor regression, host mice remain immunized against further tumor challenge because immunological memory had been established. It is possible that either broad immunization against SCCs may have occurred or, more likely, that the *FAK*^{-/-} and FAK-WT SCCs shared common antigen(s) that are expressed irrespective of FAK status. We conclude that FAK enables SCC cancer cells to suppress an adaptive immune response rather than to circumvent it through evading recognition per se. SCC *FAK*^{-/-} cells in which a FAK kinase-deficient mutant was re-expressed (SCC FAK-KD) initially grew and then regressed with kinetics that were only modestly delayed when compared to *FAK*^{-/-} cells, indicating that immune suppression depends on FAK kinase activity (Figure 1F).

We next investigated the nature of the T cell response within tumors derived from all three SCC cell lines using FACS analysis on disaggregated tumor tissue taken at day 7. We did not observe a significant change in the percentage of total CD4⁺ T cells (Figures 2A and S2 and Table S2) or the percentage of CD4⁺ T cells that expressed the activation marker CD69 (Figure 2B). In contrast, we did observe a significant increase in the proportion of effector CD4⁺CD44^{hi}CD62L^{low} T cells in SCC *FAK*^{-/-} and FAK-KD tumors when compared to FAK-WT tumors (Figures 2C and S2 and Table S2). Analysis of tumor-infiltrating CD8⁺ T cells revealed a significant increase in SCC *FAK*^{-/-} and SCC FAK-KD tumors when compared to SCC FAK-WT tumors (Figures 2D and S2 and Table S2), indicative of a heightened cytotoxic anti-tumor immune response. Staining with the activation marker CD69 identified the presence of CD8⁺CD69⁺ T cells in all tumors (Figure 2E). Further analysis revealed an increase in percentage of effector CD8⁺CD44^{hi}CD62L^{low} T cells in SCC *FAK*^{-/-} and SCC FAK-KD tumors when compared to SCC FAK-WT tumors (Figures 2F and S2 and Table S2), especially when effector CD8⁺ T cell numbers were normalized to account for the observed changes in total CD8⁺ T cells and presented as a “fold change” (Figure 2G). However, while SCC *FAK*^{-/-} and SCC FAK-KD tumors had increased effector CD8⁺ T cells, there were activated CD8⁺ T cells present in all of the SCC tumors, raising the question of why SCC FAK-WT tumors do not succumb to the cytotoxic CD8⁺ T cell response.

It is now established that not only the quantity of tumor-infiltrating CD8⁺ T cells is important, but also their “quality.” Tumor-induced T cell exhaustion has been reported in a number of tumor types, including melanoma (Fourcade et al., 2010) and ovarian cancer (Matsuzaki et al., 2010), and is characterized by expression of co-inhibitory surface receptors, including programmed death receptor 1 (PD-1), lymphocyte-activation gene 3 (LAG-3), and T cell immunoglobulin mucin-3 (Tim-3), either alone or in combination (Fourcade et al., 2010; Sakuishi et al., 2010; Wherry, 2011). Analysis of these markers on antigen-primed CD8⁺CD44^{hi} T cells infiltrating SCC FAK-WT, *FAK*^{-/-}, and FAK-KD tumors revealed increased surface expression of PD-1, LAG-3, and Tim-3 in CD8⁺CD44^{hi} T cells present in SCC FAK-WT tumors (Figures 2H–2J). Together, our data imply that antigen-primed CD8⁺CD44^{hi} T cells infiltrating SCC FAK-WT tumors exhibit a heightened state of exhaustion indicative of a dysfunctional T cell response. Linked to their exhausted state, there was also evidence of decreased proliferation of CD8⁺

T cells isolated from SCC FAK-WT tumors (judged by Ki-67 staining in Figure 2K).

Histological staining of tumor sections taken at day 7 revealed that: (1) CD8⁺ T cells are present throughout all tumors, and (2) while CD8⁺ T cells infiltrating SCC FAK-WT tumors appear predominantly as individual cells, CD8⁺ T cells infiltrating SCC *FAK*^{-/-} and FAK-KD tumors are clustered (Figure 2L). Thus, the ability of SCC FAK-WT tumors to evade the anti-tumor immune response is not due to limited CD8⁺ T cell penetration into these tumors.

FAK Expression Drives Establishment of an Immuno-Suppressive Environment

Macrophages, myeloid-derived suppressor cells (MDSC), and Tregs with intrinsic immuno-suppressive capabilities can promote tumor development by inhibiting cytotoxic CD8⁺ T cell activity in mouse and humans (Beyer and Schultze, 2006; Biragyn and Longo, 2012; Marigo et al., 2008). Flow cytometric analysis revealed no differences in macrophage or MDSC populations that correlated with tumor regression (Figures 3A, 3B, S3, and S4 and Table S2), although this does not rule out an accessory role for these cells in eventual tumor clearance. However, we did find a significantly greater number of CD4⁺FoxP3⁺CD25⁺ Tregs in SCC FAK-WT tumors (Figures 3C and S4 and Table S2) when compared with *FAK*^{-/-} and FAK-KD tumors (Figure 3C). Tregs have been associated with the development of CD8⁺ T cell exhaustion (Sakuishi et al., 2013) and may therefore be linked to the CD8⁺ T cell exhaustion that we observed in SCC FAK-WT tumors (Figures 2H–2J). We next calculated the ratio of CD8⁺ T cells to Tregs (Figure 3D), as this has been reported to correlate with poor prognosis in a number of tumor types (Sato et al., 2005; Shah et al., 2011). We found a substantially lower CD8⁺ T cell to Treg ratio in SCC FAK-WT tumors when compared to SCC *FAK*^{-/-} and SCC FAK-KD tumors, which correlated with outcome in terms of tumor tolerance versus immune-mediated tumor regression.

Tregs Protect FAK-WT Tumors from Immune-Mediated Regression

We next examined SCC FAK-WT tumor growth in animals treated with an anti-CD25 antibody to deplete Tregs (Figure 3E). Depletion of CD25⁺ cells led to regression of SCC FAK-WT tumors. Therefore, FAK-dependent Tregs are required for the growth of FAK-WT-expressing tumors by creating an immuno-suppressive environment that impairs cytotoxic CD8⁺ T cell activity. This role of CD4⁺ Tregs is the likely reason for effects of the CD4-depleting antibody in promoting regression of SCC FAK-WT tumors (Figure 1D). We note that high Treg levels have been reported in a number of solid tumor types (Beyer and Schultze, 2006) and that elevated Tregs are linked to poor clinical outcome (Beyer and Schultze, 2006; Sato et al., 2005).

We demonstrated that Tregs derived from SCC FAK-WT tumors expressed the transcription factor (TF) Helios (Figure S5A), indicative of thymic origin (Thornton et al., 2010). Thus, we hypothesized that FAK may drive the recruitment and expansion of the intra-tumoral Tregs by influencing the availability of secreted factors.

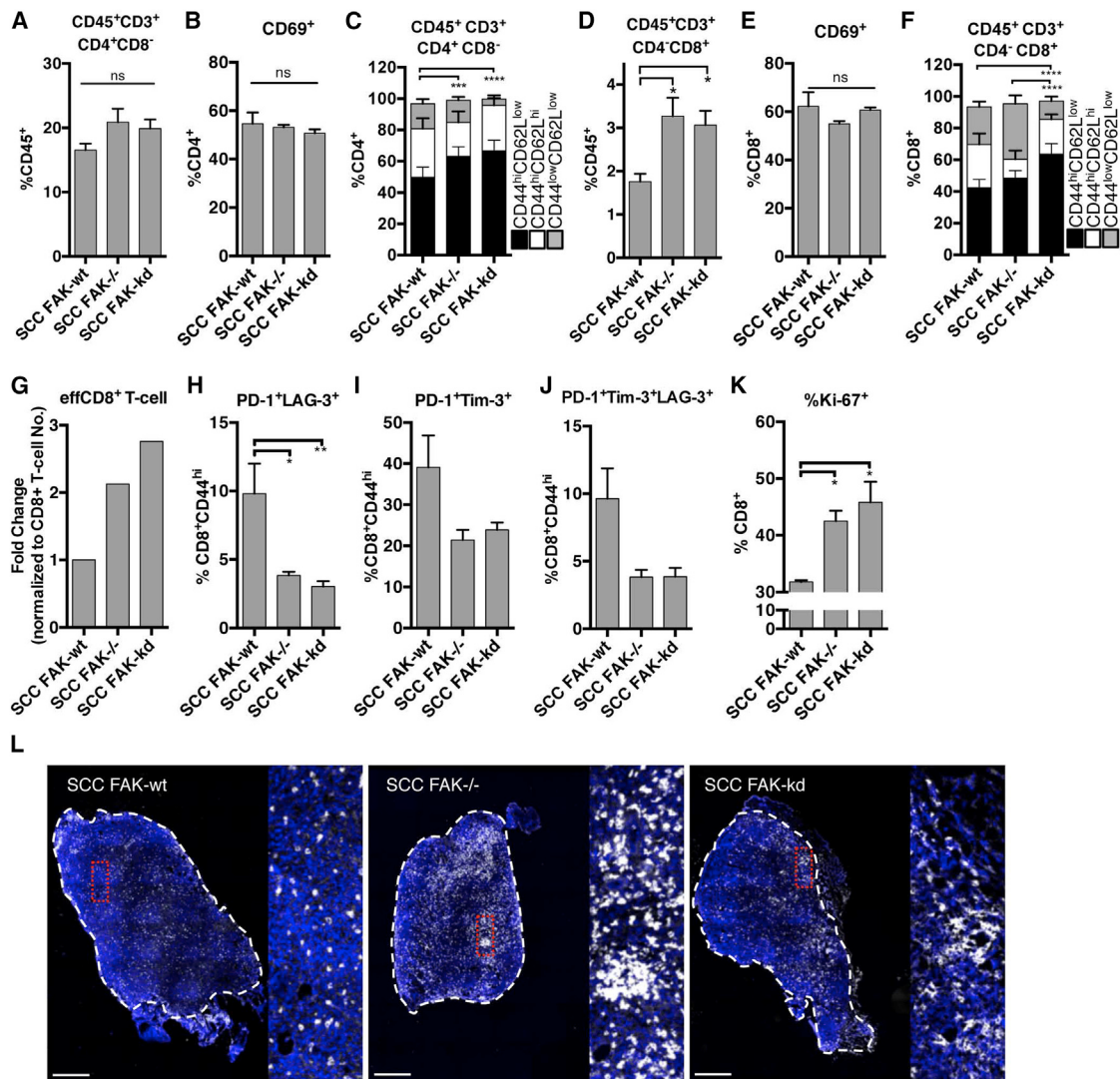


Figure 2. FAK-Depleted Tumors Exhibit a Heightened CD8⁺ T Cell Response

- (A) FACS quantification of total intra-tumoral CD4⁺ T cells.
- (B) FACS quantification of CD69⁺ cells as a percentage of CD4⁺ T cells.
- (C) FACS quantification of CD4⁺CD44^{hi}CD62L^{low}, CD4⁺CD44^{hi}CD62L^{hi}, CD4⁺CD44^{low}CD62L^{low} T cell subpopulations.
- (D) FACS quantification of total intra-tumoral CD8⁺ T cells.
- (E) FACS quantification of CD69⁺ cells as a percentage of CD8⁺ T cells.
- (F) Quantification of CD8⁺CD44^{hi}CD62L^{low}, CD8⁺CD44^{hi}CD62L^{hi}, CD8⁺CD44^{low}CD62L^{low} T cell subpopulations.
- (G) Changes in effector (CD8⁺CD44^{hi}CD62L^{low}) CD8⁺ T cells normalized to total CD8⁺ T cell proportions.
- (H) FACS quantification of PD-1⁺LAG-3⁺ T cells as a percentage of CD8⁺CD44^{hi} tumor-infiltrating T cells. n = 6 tumors.
- (I) FACS quantification of PD-1⁺Tim-3⁺ T cells as a percentage of CD8⁺CD44^{hi} tumor-infiltrating T cells. n = 3 tumors.
- (J) FACS quantification of PD-1⁺Tim-3⁺LAG-3⁺ T cells as a percentage of CD8⁺CD44^{hi} tumor-infiltrating T cells. n = 3 tumors.
- (K) FACS quantification of Ki-67⁺ cells as a percentage of tumor-infiltrating CD8⁺ T cells. n = 3 tumors.
- (L) Representative histological staining of CD8 in frozen sections from SCC FAK-WT, SCC FAK^{-/-}, and SCC FAK-KD tumors. Dashed white lines demarcate tumor boundary.

Scale bars, 500 μ m. *p < 0.05, **p < 0.01, ***p < 0.001, ****p < 0.0001; ns, not significant; Tukey-corrected one-way ANOVA (C and F, CD44^{hi}CD62L^{low} only). Data are represented as mean \pm SEM; n = 5 tumors unless stated.

FAK Regulates the Transcription of Chemokines and Cytokines to Control Tregs

To address how FAK activity in SCC cancer cells promotes elevated intra-tumoral Tregs, we next analyzed global transcript-

tional profiles of SCC FAK-WT and SCC FAK^{-/-} cells using Affymetrix GeneChip microarrays (Figure 4A). FAK expression resulted in the upregulation of 498 genes and the downregulation of 598 genes ($p < 0.01$). The upregulated transcript set in SCC

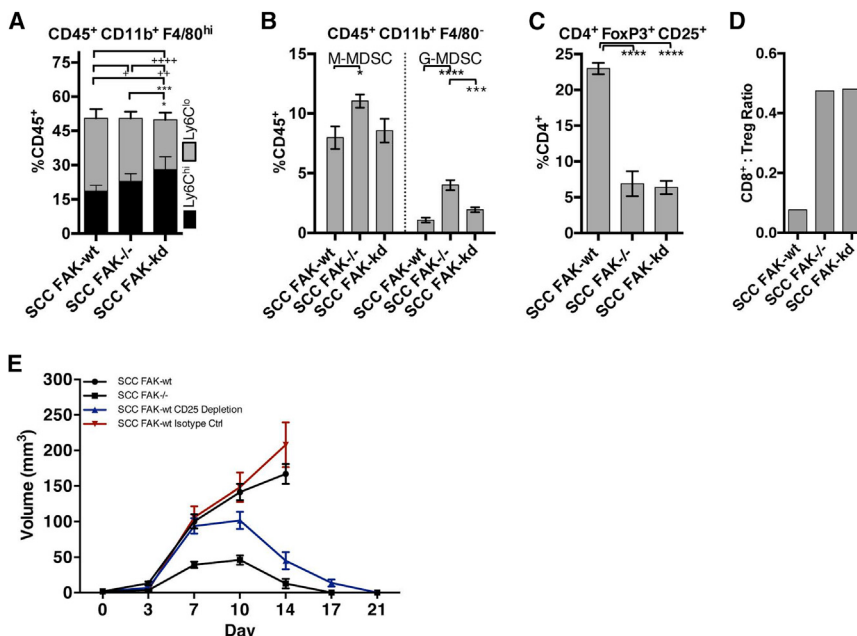


Figure 3. FAK Regulates the Immuno-Suppressive Microenvironment

(A) FACS quantification of Ly6C^{hi} and Ly6C^{low} macrophage populations expressed as a percentage of tumor-infiltrating CD45⁺ leukocytes. (B) FACS quantification of Ly6C^{hi}Gr1^{low} (M-MDSC) and Ly6C^{int}Gr1^{hi} (G-MDSC) populations expressed as a percentage of tumor-infiltrating CD45⁺ leukocytes. (C) Quantification of CD4⁺FoxP3⁺CD25⁺ Tregs expressed as a percentage of tumor-infiltrating CD4⁺ T cells. (D) CD8⁺ T cell-to-Treg ratio calculated using mean values from Figures 2D and 3C. (E) SCC FAK-WT tumor growth in FVB mice treated with anti-CD25 depleting antibody. n = 6 tumors. * or +p < 0.05, **p < 0.01, ***p < 0.001, ****p < 0.0001; Tukey-corrected one-way ANOVA (A, *, Ly6C^{hi}, +, Ly6C^{low}). Data are represented as mean ± SEM; n = 5 tumors unless stated.

FAK-WT cells was associated with a number of processes, including cell migration, receptor binding, secretion, wounding, and ovulation (Figure 4B, top). Analysis of this gene set revealed the chemokine ligand group of genes to be significantly overrepresented (Figure 4B, bottom), which is interesting given that a number of these chemokines and cytokines mediate both Treg recruitment to tumors and induction of peripheral Tregs within tumors (Goldstein et al., 2013; Ondondo et al., 2013).

To establish which chemokines and cytokines were regulated by FAK and to address whether the FAK-dependent transcriptional profile was linked to chemokine receptor expression on tumor-infiltrating Tregs, we performed quantitative (q)RT-PCR array analysis. Comparison of chemokine/cytokine transcript levels between SCC FAK-WT and SCC FAK^{-/-} cells revealed a subset of ligands increased >2-fold in SCC FAK-WT cells (Figure 4C). Several of these (*Ccl1*, *Ccl5*, *Ccl7*, *Cxcl10*) have roles in Treg recruitment (Ondondo et al., 2013) (green arrowheads, Figure 4C), while one (*Tgfb2*) has a reported role in peripheral induction and expansion of Tregs (Goldstein et al., 2013) (red arrowhead, Figure 4C). To complement this, comparison of Tregs isolated from the thymus of normal FVB mice with those isolated directly from SCC FAK-WT tumors revealed a chemokine receptor switch (Figure 4D). We found increased expression of the cognate receptors for five of the six chemokine ligands up-regulated in SCC FAK-WT cells (Figure 4C). These receptor changes may represent a switch from lymphoid homing receptors, including *Ccr7* and *Cxcr4*, toward expression of memory/effector-type chemokine receptors, including *Ccr2*, *Ccr5*, *Ccr8*, and *Cxcr6*, involved in recruitment to non-lymphoid tissues and sites of inflammation. Network analysis of the relationship between FAK-dependent chemokine ligand expression in SCC cells and tumor-infiltrating Treg chemokine receptor expression revealed the existence of a FAK-dependent paracrine signaling axis between cancer cells and intra-tumoral Tregs based on che-

mokine ligand-receptor interactions (Figure 4E). Furthermore, (q)RT-PCR analysis of *Ccl5*, *Cxcl10*, and *Tgfb2* demonstrated that their expression was dependent on FAK kinase activity (Figure 4F). We note that disruption of the *Ccl5/Ccr5* axis in a model of pancreatic adenocarcinoma results in reduced intra-tumoral Tregs and slows tumor growth (Tan et al., 2009), implying that FAK-dependent regulation of this paracrine signaling axis may be more generally important. Thus, FAK activity regulates the expression of a subset of chemokines that can specifically mediate crosstalk between tumor cells and tumor-infiltrating Tregs. This likely has importance in recruitment and retention of CD4⁺FoxP3⁺CD25⁺ Tregs into SCC FAK-WT tumors.

Nuclear FAK Regulates the Transcription of *Ccl5* and *TGFβ2* to Increase Tregs

The finding that the Tregs enriched in SCC FAK-WT tumors were likely recruited into SCC FAK-WT tumors led us to consider a potential role for *Ccl5* that has been implicated in the recruitment and expansion of CD4⁺FoxP3⁺CD25⁺ Tregs (Tan et al., 2009), via the paracrine signaling axis that we identified. We found that efficient knockdown of *Ccl5* using two independent shRNA hairpins (P1 and P2, Figure 5A) resulted in SCC FAK-WT shRNA-Ccl5 tumor regression by days 21–27 (Figure 5B). We measured the absolute number of Tregs in SCC FAK-WT shRNA-Ccl5 tumors at day 7 and found that there was a substantial reduction in both *Ccl5*-depleted tumors when compared with empty vector control SCC FAK-WT pLKO tumors (Figure 5C).

Expanding on these findings, shRNA-mediated knockdown of *Tgfb2* expression in SCC FAK-WT cells also influenced tumor growth (Figures S5B and S5C). Partial knockdown of TGFβ2 had complex effects, which resulted in one of two outcomes. One group (Figure S5C, dashed blue line), grew more rapidly and ulcerated, leading to removal from study at day 14. In the

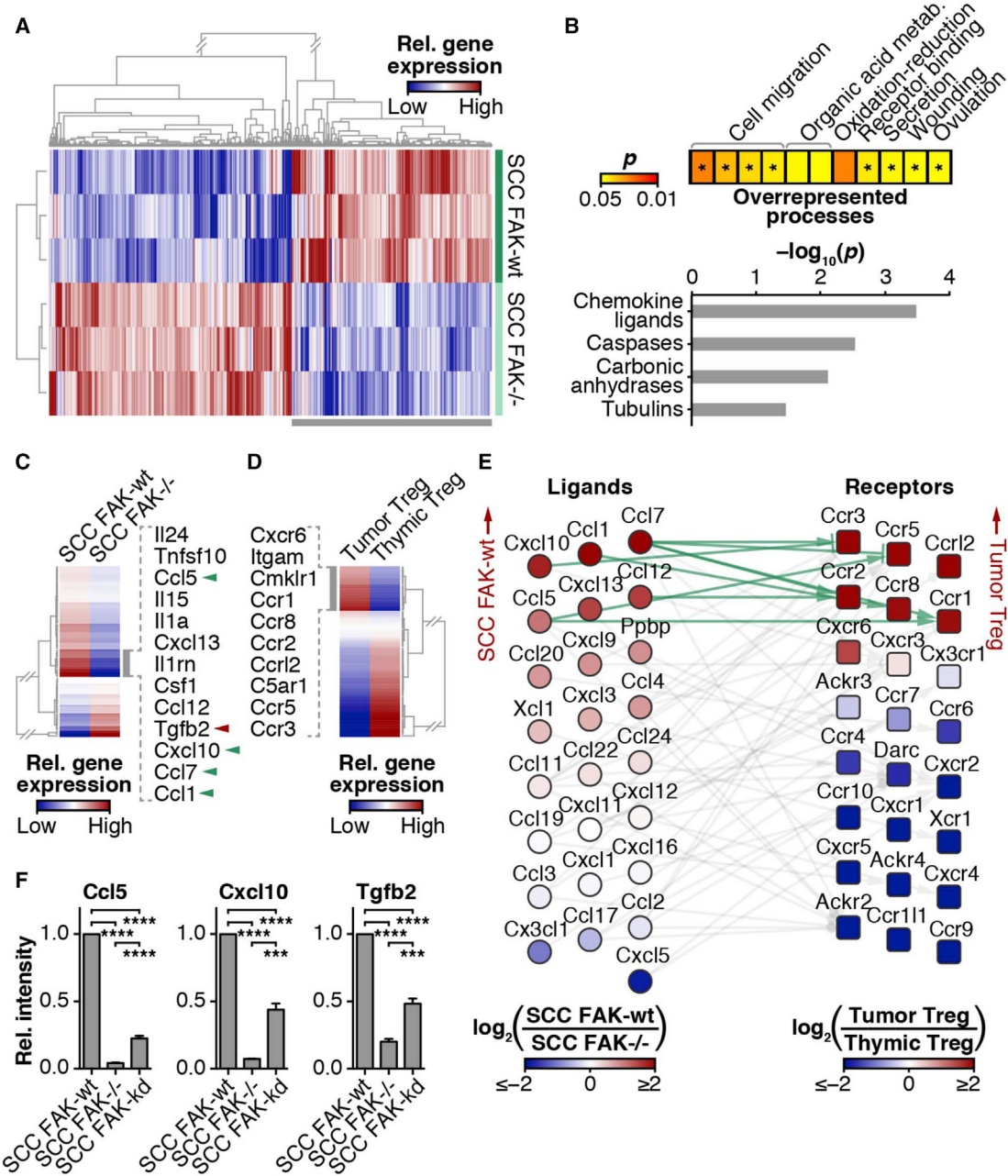


Figure 4. FAK Regulates Transcription of Cytokines Implicated in Treg Recruitment and Expansion

(A) Transcriptomic profiling of SCC FAK-WT and SCC FAK^{-/-} cells.

(B) Functional enrichment analysis of genes upregulated in SCC FAK-WT cells (bottom gray bar in A). Overrepresented biological processes are displayed as a heatmap (\log_{10} -transformed color scale) (top); asterisks indicate presence of cytokine-related genes. Overrepresented gene families are displayed as a bar chart (bottom), $p < 0.05$; Benjamini-Hochberg-corrected hypergeometric tests.

(C) qRT-PCR array analysis of cytokine and chemokine expression in SCC FAK-WT and SCC FAK^{-/-} cells. Gray bar indicates cluster of genes upregulated in SCC FAK-WT cells; cytokine and chemokine gene names are listed. Green arrowheads indicate reported roles in Treg recruitment; red arrowhead indicates reported role in peripheral Treg induction.

(D) qRT-PCR array analysis of chemokine and receptor expression in tumor- and thymus-derived Tregs. Gray bar indicates cluster of genes upregulated in tumor-derived Tregs; receptor gene names are listed.

(E) Interaction network analysis of chemokine ligand gene expression detected in SCC cells (circles, left) and corresponding receptor gene expression detected in Tregs (squares, right). Genes are ordered vertically by fold change. Light gray lines connect receptor-ligand pairs; green lines indicate pairs upregulated at least 2-fold in SCC FAK-WT cells and tumor-derived Tregs.

(F) qRT-PCR analysis of selected cytokine and chemokine gene expression in SCC cells. *** $p < 0.001$, **** $p < 0.0001$; Tukey-corrected one-way ANOVA. Data are represented as mean \pm SEM.

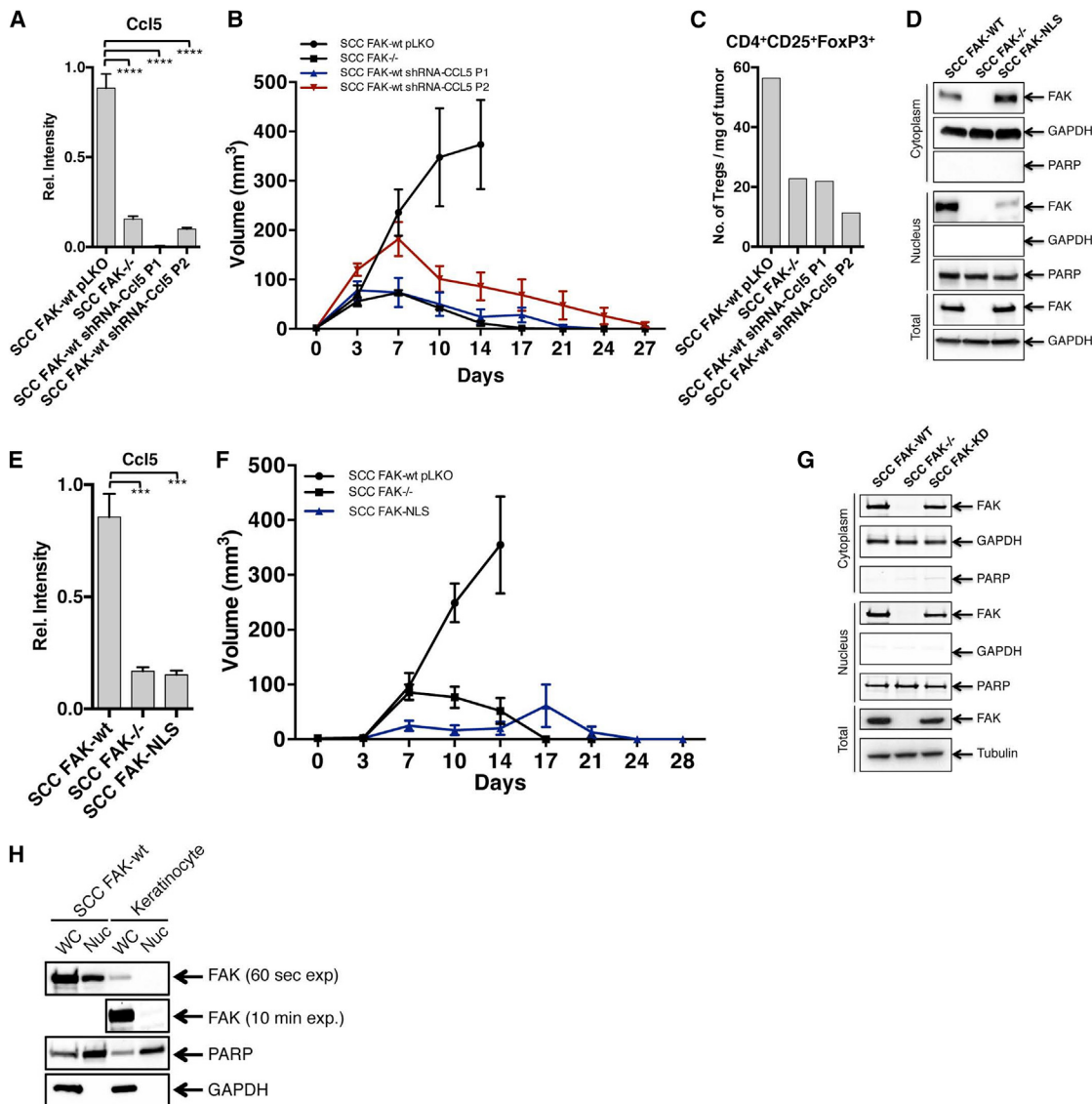


Figure 5. Nuclear FAK Regulates Transcription of Ccl5, which Is Required for Treg Recruitment and Tumor Growth

(A) qRT-PCR analysis of *Ccl5* gene expression knockdown in SCC FAK-WT cells stably expressing two independent shRNA constructs targeting *Ccl5* (P1 and P2).

(B) SCC FAK-WT shRNA-Ccl5 tumor growth in FVB mice. n = 6 tumors.

(C) FACS quantitation of tumor-infiltrating Treg numbers from SCC FAK-WT shRNA-Ccl5 tumors. Data represent a single value from six pooled tumors.

(D) Western blotting of cytoplasmic, nuclear, and total protein fractions from SCC FAK-WT, SCC FAK^{-/-}, and SCC FAK-NLS cells.

(E) qRT-PCR analysis of *Ccl5* gene expression in SCC FAK-NLS cells.

(F) Tumor growth of SCC FAK-NLS cells in FVB mice.

(G) Western blotting of cytoplasmic, nuclear, and total protein fractions from SCC FAK-WT, SCC FAK^{-/-}, and SCC FAK-KD cells.

(H) Western blotting of whole-cell (WC) and nuclear (Nuc) protein fractions from SCC FAK-WT cells and primary skin keratinocytes. 60 s exposure time is shown for all samples; additional 10 min exposure time is shown for FAK in keratinocyte samples. GAPDH, cytoplasmic; PARP, nuclear.

p < 0.001, *p < 0.0001; Tukey-corrected one-way ANOVA. Data are represented as mean ± SEM unless stated.

other group that did not display such frank ulceration, we observed tumor regression by day 27 (Figure S5C, dashed red line). Analysis of Treg levels in SCC FAK-WT shRNA-TGF β 2 tumors at day 7 (regardless of initial growth characteristics) revealed that TGF β 2 knockdown was also associated with a reduction in CD4 $^{+}$ FoxP3 $^{+}$ CD25 $^{+}$ Tregs (Figure S5D). Therefore,

while the effects of reducing TGF β 2 expression are more complicated than for *Ccl5*, FAK-dependent TGF β 2 expression does contribute to elevated CD4 $^{+}$ FoxP3 $^{+}$ CD25 $^{+}$ Tregs in SCC FAK-WT tumors; and in the subset of mice bearing tumors that were able to complete the study, TGF β 2 knockdown also caused tumor regression.

Our findings that FAK regulated the transcription of cytokines and chemokines (including *Ccl5* and *TGF β 2*) that were associated with elevated intra-tumoral Tregs and tumor tolerance led us to consider a possible role for nuclear FAK in regulating the transcription of these genes. Based on previous reports (Lim et al., 2008), which identified putative NLSs within the FERM domain of FAK, we constructed an optimally nuclear targeting-impaired mutant FAK by replacing two arginines (positions 177 and 178) and four lysines (positions 190, 191, 216, and 218) with alanines (termed FAK-NLS). Western blotting of cytoplasmic and nuclear fractions confirmed that the FAK-NLS mutant was indeed defective in nuclear localization (Figure 5D). Subsequent (q)RT-PCR analysis of *Ccl5* and *Tgfb2* expression in SCC cells expressing only FAK-NLS revealed that FAK nuclear localization was required for transcription of these genes (Figures 5E and S5E, respectively). Thus, nuclear FAK drives the transcription of *Ccl5* and *TGF β 2*, which are required for recruitment and expansion of immuno-suppressive Tregs into SCC tumors, altering the balance between CD8 $^{+}$ T cells and Tregs in favor of tumor tolerance. In support of this, growth of SCC FAK-NLS tumor cells was similar to that of SCC *FAK* $^{-/-}$, with ultimate tumor regression (Figure 5F). This confirmed that it was nuclear FAK that afforded protection from the anti-tumor immune response. Western blotting of cytoplasmic and nuclear fractions from SCC FAK-KD showed that the kinase-deficient mutant was able to localize to the nucleus, so we conclude that the immune modulatory effects of FAK are dependent on FAK kinase activity in the nucleus (Figure 5G).

We next examined nuclear FAK levels in primary skin keratinocytes, the normal cellular counterparts of the SCC cells used here, and did not find detectable nuclear FAK (Figure 5H). Thus, abundant nuclear localization, and therefore the capacity to exert regulatory control over chemokine and cytokine expression, is likely a feature of oncogenic transformation in skin keratinocytes. This suggests that the nuclear functions of FAK that we have identified—namely, regulating transcription of chemokine/cytokine networks—may be associated with the cancerous state when FAK is highly expressed.

Nuclear FAK Interacts with a Network of *Ccl5* Transcriptional Regulators

Having established an important role for the nuclear FAK-dependent transcription of *Ccl5* in mediating recruitment and expansion of intra-tumoral Tregs, we wanted to determine how nuclear FAK could exert control over *Ccl5* transcription. Using sucrose gradients, we fractionated the nuclei of SCC FAK-WT cells and demonstrated that nuclear FAK was present in the chromatin-containing fraction (Figure 6A). Transcriptional regulation of *Ccl5* is mediated predominantly through six short regulatory elements contained within a region of the *Ccl5* promoter spanning ~300 base pairs (Fessele et al., 2002). These regulatory elements contain binding sites for a number of TFs, including AP-1, C/EBP, IRF-1, NF- κ B, and TATA box-binding protein (TBP), which is part of the transcription factor IID complex (TFIID). Using FAK immunoprecipitation and quantitative label-free mass spectrometry, we identified FAK binding partners in purified nuclear extracts and contextualized these by mapping onto a network of proteins associated with pre-

dicted *Ccl5* TFs (constructed in silico; Figure 6B). This integrative approach identified a subset of *Ccl5* TFs and regulators of these that interact with FAK in SCC cell nuclei (Figures 6C, S6 and Table S1). Interaction network analysis of this protein subset revealed nuclear FAK binding partners with roles in multiple transcriptional pathways, including regulators of AP-1, C/EBP, IRF-1/7, NF- κ B/Rel, and TFIID. Thus, we identified nuclear FAK binding partners that can interact, directly or indirectly, with five of the six main regulatory elements reported to control transcription of *Ccl5* in multiple cell types (Fessele et al., 2002). Given that our interaction network was somewhat dominated by proteins associated with the TFIID pathway, including three TBP-associated factors (TAFs) (Figures 6C and S6), we used co-immunoprecipitation to confirm the interaction of nuclear FAK with one of these, TAF9, a core component of the TFIID complex (D'Alessio et al., 2009) (Figure 6D). Our data show that FAK binds to core components of the transcriptional machinery, many of which are known to be located on the promoter of genes undergoing active transcription and that are known or predicted to regulate *Ccl5*. Therefore, in SCC cells, nuclear FAK associates with chromatin and is physically linked to a network of TFs and their regulators known to modulate *Ccl5* expression.

Small-Molecule FAK Kinase Inhibitor Promotes Immune-Mediated Tumor Clearance

Therapeutic targeting of FAK kinase activity using small-molecule inhibitors will inhibit FAK signaling not only in tumor cells, but also potentially in multiple host cell types. To complement expression of the FAK-KD mutant protein in the cancer cells and investigate whether a FAK inhibitor could induce immune-mediated regression of SCC tumors, we used the FAK/Pyk2 kinase inhibitor VS-4718 (Shapiro et al., 2014), which is currently in clinical development. Mice were treated with VS-4718 at 75 mg/kg for 24 hr prior to injection of 1×10^6 FAK-WT or *FAK* $^{-/-}$ SCC tumor cells and twice daily thereafter. This resulted in VS-4718-induced regression of SCC FAK-WT tumors by day 24 (Figure 7A). Following cessation of VS-4718 treatment, no tumor regrowth was observed (data not shown). SCC *FAK* $^{-/-}$ tumor growth and clearance was not greatly affected by VS-4718 treatment, suggesting that the anti-tumor effects of VS-4718 can be explained by FAK inhibition in tumor cells. Activity of VS-4718 was confirmed using an ELISA to measure FAK autophosphorylation on tyrosine-397 in tumor lysates from mice treated with 75 mg/kg VS-4718 (Figure S7). Regression of VS-4718-treated SCC tumors was not accompanied by loss of cell viability at day 7, as measured by FACS using a viability stain following tumor disaggregation (Figure 7B). There was a significant but small increase in leukocytes in VS-4718-treated SCC FAK-WT tumors (Figure 7C) and a significant increase in total CD4 $^{+}$ T cells (Figures 7D and S2 and Table S2) and effector CD4 $^{+}$ CD44 $^{\text{hi}}$ CD62L $^{\text{low}}$ T cells (Figures 7E and S2 and Table S2). A significant increase in CD8 $^{+}$ T cells was also evident in SCC FAK-WT VS-4718-treated tumors (Figures 7F and S2 and Table S2), although there was no change in effector CD8 $^{+}$ CD44 $^{\text{hi}}$ CD62L $^{\text{low}}$ T cells (Figures 7G and S2 and Table S2). Crucially, there was a significant reduction in CD4 $^{+}$ CD25 $^{+}$ FoxP3 $^{+}$ Treg cells in VS-4718-treated SCC FAK-WT tumors, which was similar to that observed in vehicle and

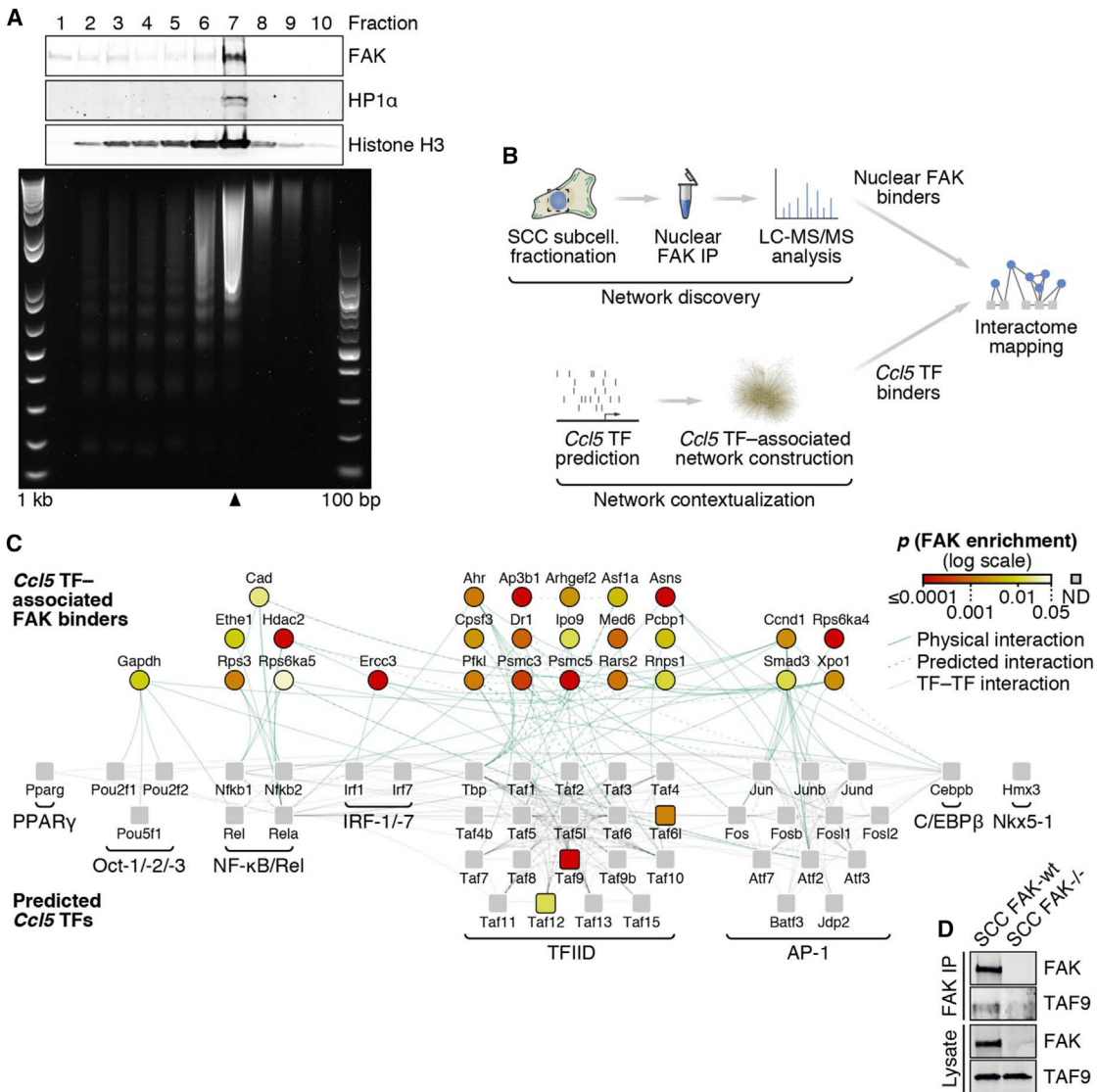


Figure 6. Nuclear FAK Interacts with Regulators of Ccl5 Transcription

(A) Sucrose fractionation of soluble chromatin prepared from SCC FAK-WT cell nuclei. Protein preparations recovered from each fraction were analyzed by western blotting (top). DNA recovered from each fraction was analyzed by agarose gel electrophoresis (bottom, 1 kilobase [kb] and 100 base pair [bp] ladders shown). Fraction 7 (black arrowhead) represents the chromatin-containing fraction.

(B) Schematic detailing the workflow used for proteomic analysis of the nuclear FAK interactome in the context of Ccl5 transcription factors (TFs).

(C) Interaction network analysis of proteins that bind FAK in the nucleus of SCC cells. Predicted Ccl5 TFs (squares, bottom) and respective TF binders (circles, top) enriched by at least 4-fold in nuclear FAK immunoprecipitations (SCC FAK-WT over SCC FAK $^{-/-}$ controls; $p < 0.05$) are shown (stringent network). Ccl5 TFs not detected (ND) are shown as gray squares. TF complexes or groups are indicated; proteins are labeled with gene names for clarity. TF binders are aligned above TF groups with which there are the greatest number of reported interactions. For full network, see Figure S6; for protein interaction list, see Table S1.

(D) Isolation of the TFIID component TAF9 by FAK immunoprecipitation (IP) from SCC FAK-WT cell nuclear extracts.

VS-4718-treated SCC FAK $^{-/-}$ tumors (Figures 7H and S4 and Table S2).

Thus, VS-4718 promoted robust anti-tumor activity, with similar immune cell changes to that observed upon FAK deletion or expression of a kinase-deficient form of FAK. Furthermore, anti-tumor efficacy of VS-4718 was also dependent on CD8 $^{+}$ T cells, and SCC FAK-WT tumors treated with VS-4718 on a CD8 $^{+}$ T cell-depleted background exhibited a growth delay but

did not undergo tumor regression (Figure 7I). We conclude that the FAK kinase inhibitor targets mechanisms of immune suppression and may therefore represent a form of effective “immuno-modulatory” therapy that reduces Tregs in the tumor environment. Importantly, the FAK kinase inhibitor does not affect the cytotoxic function of antigen-primed CD8 $^{+}$ T cells. We also found that VS-4718 treatment that was initiated 5 days post-inoculation of 1×10^6 SCC FAK-WT cells, when these had

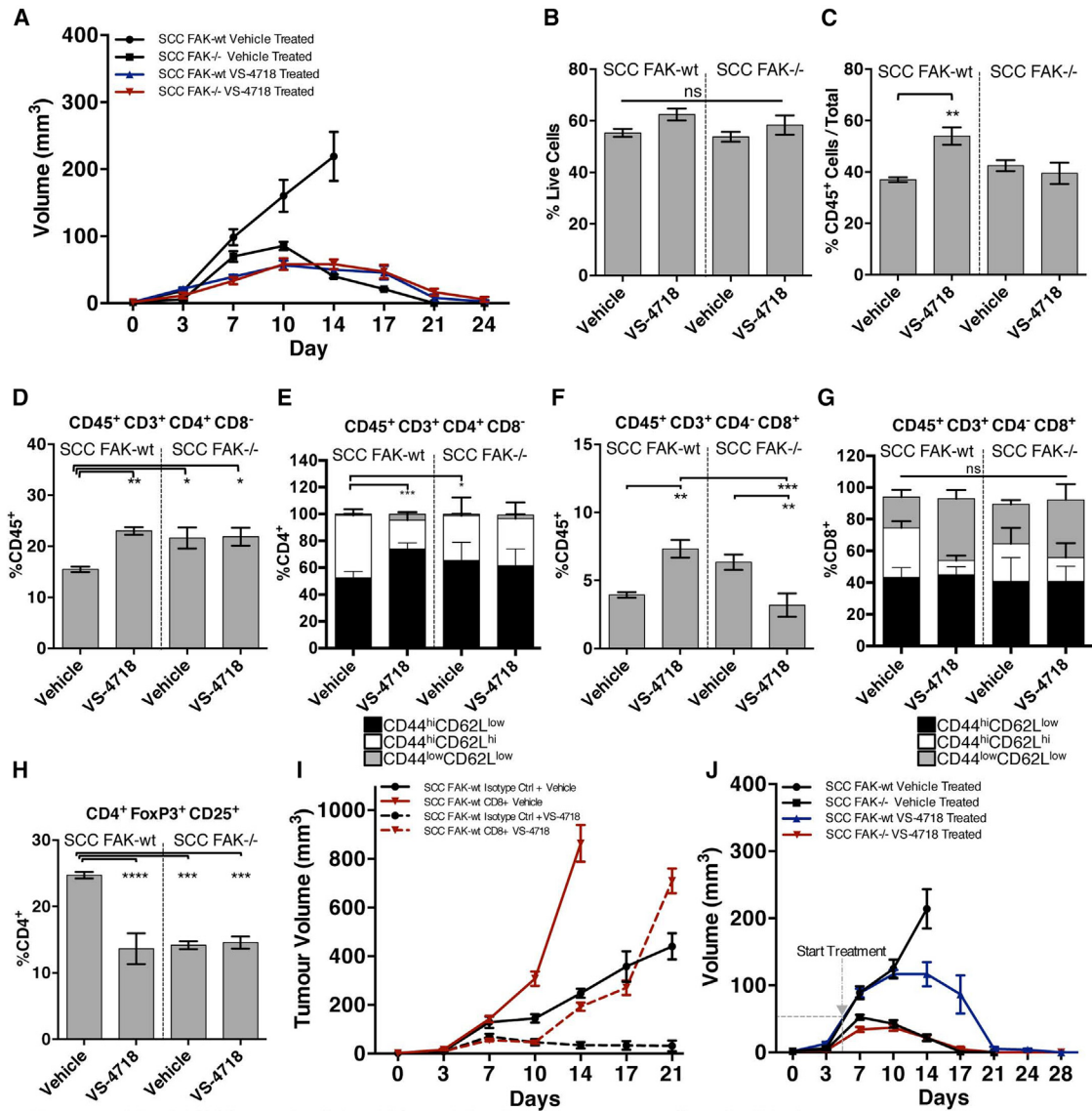


Figure 7. The FAK Kinase Inhibitor VS-4718 Leads to Immune-Mediated SCC Clearance

(A) SCC FAK-WT and SCC FAK^{-/-} tumor growth in FVB mice treated with either vehicle or VS-4718. Treatment started 24 hr pre-tumor cell inoculation and continued for the duration of the experiment.

(B) FACS analysis of cell viability from disaggregated tumors treated with either vehicle or VS-4718.

(C) FACS analysis of vehicle- or VS-4718-treated tumor-infiltrating leukocytes expressed as a percentage of viable CD45⁺ cells relative to the total number of single cells.

(D) FACS analysis of tumor-infiltrating CD4⁺ T cells from vehicle- or VS-4718-treated tumors.

(E) FACS sub-categorization of tumor-infiltrating CD4⁺ T cells into CD45⁺CD3⁺CD4⁺CD8⁻CD44^{hi}CD62L^{low}, CD45⁺CD3⁺CD4⁺CD8⁻CD44^{hi}CD62L^{hi}, and CD45⁺CD3⁺CD4⁺CD8⁻CD44^{low}CD62L^{low} populations.

(F) FACS analysis of tumor-infiltrating CD8⁺ T cells from vehicle- or VS-4718-treated tumors.

(G) FACS sub-categorization of tumor-infiltrating CD8⁺ T cells into CD45⁺CD3⁺CD4⁻CD8⁺CD44^{hi}CD62L^{low}, CD45⁺CD3⁺CD4⁻CD8⁺CD44^{hi}CD62L^{hi}, and CD45⁺CD3⁺CD4⁻CD8⁺CD44^{low}CD62L^{low} populations.

(H) FACS analysis of tumor-infiltrating CD4⁺CD25⁺FoxP3⁺ Tregs expressed as a percentage of tumor-infiltrating CD4⁺ T cells.

(I) SCC FAK-WT tumor growth in FVB mice treated with either vehicle or VS-4718 and either isotype control or CD8-depleting antibodies.

(J) SCC FAK-WT and SCC FAK^{-/-} tumor growth in FVB mice treated with either vehicle or VS-4718. Treatment started 5 days post-tumor cell inoculation (gray dashed line) and continued for the duration of the experiment.

*p < 0.05, **p < 0.01, ***p < 0.001, ****p < 0.0001; ns, not significant; Tukey-corrected one-way ANOVA (E and G, CD44^{hi}CD62L^{low} only). Data are represented as mean ± SEM; n = 6 tumors.

already formed palpable tumors of $\sim 50 \text{ mm}^3$, led to complete tumor regression (Figure 7J).

DISCUSSION

We show that nuclear FAK in SCC cancer cells drives the transcription of chemokines and cytokines, including *Ccl5* and *TGF β 2*, which promote the formation of an immuno-suppressive, pro-tumorigenic microenvironment. This is dependent on FAK kinase activity, and expression of a catalytically inactive mutant FAK protein (FAK-KD) or treatment with a small-molecule inhibitor causes tumor regression. This is effective even when tumors are already established, raising the exciting possibility that targeting of FAK kinase activity may have immune-mediated anti-tumor efficacy in patients. We established that nuclear FAK is associated with chromatin and interacts with a number of TFs and transcriptional regulators, including components of the TFIID complex, that are linked to regulation of *Ccl5* expression. Our data imply that FAK interacts with core transcriptional machinery to influence gene transcription and promote tumor immune escape.

Historically, FAK has been recognized as an adhesion-related non-receptor protein tyrosine kinase that clusters at focal adhesion (FA) structures and regulates cancer-associated processes, including adhesion, migration, invasion, survival, and proliferation (reviewed in Frame et al., 2010). FAK was also found to translocate to the nucleus (Lim et al., 2008; Luo et al., 2009b), leading to the idea of nuclear functions for FAK within the nucleus. Our data show that, at least in cancer cells, FAK regulates inflammatory transcriptional programs associated with generation and maintenance of a pro-tumorigenic and immuno-suppressive microenvironment. FAK associates with chromatin, and in the context of *Ccl5* expression, it interacts with a number of TFs, and regulators of TFs, that bind regulatory elements in the *Ccl5* promoter (Feselle et al., 2002). Our data imply that FAK exists in complexes with a number of TAF proteins, including TAF9 and TAF12, key components of the core promoter complex TFIID that serves to initiate transcription by driving recruitment of chromatin remodeling complexes, coactivators, and RNA polymerase II to the promoter (D'Alessio et al., 2009). Therefore, FAK interacts with components of the core transcriptional machinery in order to drive transcription of chemokines and cytokines that contribute to recruitment of Tregs into the tumor environment, promoting immunological tolerance and permitting tumor growth.

Recently, nuclear accumulation of active FAK (phosphorylated on Tyr-397) within tumor cells of patients with colorectal cancer was reported to correlate with poor prognosis (Albasri et al., 2014), highlighting the need to understand the nature of FAK's role within the nucleus. Studies using endothelial cells, muscle cells, and fibroblasts have previously reported low steady-state levels of nuclear FAK that are substantially increased in response to cellular stress (Lim, 2013; Lim et al., 2008; Luo et al., 2009b). Our work implies that oncogenic stress is another route to inducing high levels of nuclear FAK and that this, in turn, can influence transcriptional programs, such as the chemokine and cytokine networks that control the tumor microenvironment.

A number of therapeutic strategies targeting components of the immuno-suppressive tumor microenvironment are currently being tested, with the aim of restoring anti-tumor immunity by releasing the break on CD8 $^+$ T cell cytotoxic activity. In pre-clinical models of cancer, targeting Tregs (Ali et al., 2014; Bos et al., 2013) has shown anti-tumor efficacy, either alone or when used in combination with agents that enhance CD8 $^+$ T cell activation. A clinical study combining agents targeting cytotoxic-T-lymphocyte-associated antigen 4 (CTLA-4), which is thought to influence Treg function (Peggs et al., 2009; Quezada et al., 2006; Simpson et al., 2013; Wing et al., 2008), and PD-1, which blocks signals that inhibit T cell function, has reported impressive responses in patients with advanced melanoma (Wolchok et al., 2013). However, this combination of checkpoint blockade antibodies elicits substantial side effects in >50% of patients, highlighting the need to find alternative combinations with improved tolerability. We have shown that targeting FAK kinase activity has the potential to modulate intra-tumoral Treg levels, resulting in robust CD8 $^+$ T cell anti-tumor immunity, while others have reported previously that FAK kinase inhibitors block monocyte/macrophage and cancer-associated fibroblast recruitment into tumors by virtue of FAK's role in regulating their migration (Stokes et al., 2011). Taken together, these findings suggest that targeting the pleiotropic cellular functions of FAK may have a broad impact on the immuno-suppressive tumor microenvironment, differentiating these agents from many therapeutic approaches that target single immune cell populations.

Targeting a molecular pathway that is upregulated in cancer cells may provide tumor specificity and help to overcome some of the potential issues with severe autoimmunity when modulating immune cell populations. FAK inhibitors, such as VS-4718, are in clinical development. VS-4718 is currently in a phase I dose escalation clinical trial in patients with solid tumors (www.clinicaltrials.gov NCT01849744). Our findings provide good rationale for pre-clinical and clinical testing of FAK kinase inhibitors alongside agents that stimulate CD8 $^+$ T cell activity, such as the checkpoint blockade therapies that target PD-1 and CTLA-4, which are both in clinical development (Pardoll, 2012).

EXPERIMENTAL PROCEDURES

Experiments involving animals were carried out in accordance with the UKCCCR guidelines by approved protocol (HO PL 60/4248). Brief experimental procedures are listed here. For details, please see the *Supplemental Experimental Procedures*.

Generation of FAK Nuclear Localization Mutant

Mutations were introduced into FAK-WT at R177A, R178A, K190A, K191A, K216A, and K218A using PCR-based site-directed mutagenesis.

Cell Lines

Isolation and generation of the FAK SCC cell model is described in Serrels et al. (2012). Keratinocyte cultures were prepared as detailed in McLean et al. (2004).

Western Blot Analysis

To prepare whole-cell lysates, cells were washed in cold PBS and lysed in RIPA buffer. Cytoplasmic and nuclear extracts were prepared as described in Lim et al. (2008). Lysates were resolved by gel electrophoresis, transferred to nitrocellulose, and probed with respective antibodies.

Subcutaneous Tumor Growth

Cells were injected into both flanks of either CD-1 nude mice or FVB mice and tumor growth measured twice-weekly. Animals were sacrificed when tumors reached maximum allowed size or when signs of ulceration were evident. For treatment with VS-4718, drug was prepared in 0.5% carboxymethyl cellulose + 0.1% Tween 80 and mice treated at 75 mg/kg BID by gavage. No signs of toxicity were observed.

Tumor Growth following Re-Challenge

SCC $FAK^{-/-}$ cells were injected into the left flank of FVB mice. Following tumor regression, mice were left for 7 days before being challenged with SCC FAK-WT or $FAK^{-/-}$ cells injected into the right flank. Tumor growth was measured twice-weekly. Control groups were injected into both flanks at day 28 using mice that had not been pre-challenged with SCC $FAK^{-/-}$ cells.

CD4⁺, CD8⁺, and CD25⁺ T Cell Depletion

T cell depletion was achieved following IP injection of 150 µg of depleting antibody into female age-matched FVB mice for 3 consecutive days and was maintained by further IP injection at 3 day intervals until the study was terminated. SCC FAK-WT or $FAK^{-/-}$ cells were injected into both flanks 6 days after initial antibody treatment and tumor growth measured. The extent of T cell depletion was determined at the end of the study using FACS (Figure S1).

FACS Analysis of Immune Cell Populations

Tumors established following injection of SCC cells into both flanks of an FVB mouse were removed at day 7. Tumor tissue was processed to obtain single cell suspension for staining and subsequent FACS analysis (antibodies listed in Table S2).

Gene Expression Profiling

RNA was analyzed using the GeneChip Mouse Genome 430 2.0 Array. Normalized data for differentially expressed genes were median centered and clustered using Cluster 3.0 and Java TreeView. Functional enrichment analysis was performed using ToppGene.

Quantitative RT²-PCR Array Analysis of Cytokine, Chemokine, and Chemokine Receptor Expression

RNA prepared from SCC cells was analyzed using the mouse cytokine and chemokine RT² Profiler PCR Array and that from isolated Tregs was analyzed using the mouse chemokine and receptor array. Relative gene expression ($2^{-\Delta\Delta Ct}$) values were log transformed, median centered, and subjected to hierarchical clustering as for microarray analysis. An interactome of chemokine ligands and receptors was constructed using the IUPHAR/BPS Guide to Pharmacology database and curated from the literature, onto which expression data for detected genes were mapped and visualized using Cytoscape. Expression of selected cytokine and chemokine genes was assessed by standard quantitative RT-PCR.

shRNA-Mediated TGF β 2 and Ccl5 Knockdown

Cells were subject to two rounds of lentiviral infection prior to selection with puromycin. shRNA constructs used were part of the pLKO lentiviral TRC library.

Preparation and Fractionation of Nuclei and Chromatin

Nuclei were prepared as described (Gilbert et al., 2003) but with a reduced concentration (0.05%) of NP-40 in nuclei buffer B. Soluble chromatin was prepared as described (Gilbert et al., 2004) and fractionated on a sucrose step gradient to separate soluble and chromatin-associated nuclear proteins. DNA was recovered from fractions and subjected to agarose gel electrophoresis. Protein was purified using TCA precipitation. Samples were analyzed by SDS-PAGE and blotted using anti FAK, HP1 α , and histone H3 antibodies.

Proteomic Analysis of Nuclear FAK Protein Complexes

FAK nuclear protein complexes were subjected to on-bead proteolytic digestion, desalting, and liquid chromatography-tandem mass spectrometry, as described (Turziani et al., 2014). For interaction network analysis, Ccl5 transcription factors were extracted from the DECODE database and used to seed

a network of 1,000 transcription factor-related proteins using the GeneMANIA plugin in Cytoscape. Proteins specifically isolated in nuclear FAK protein complexes were mapped onto the interactome, and those with physical or predicted direct or indirect interactions with Ccl5 transcription factors were analyzed using the NetworkAnalyzer plugin in Cytoscape.

CD8 T Cell Fluorescent Immunohistochemistry

Tumors were removed 7 days post-implantation and frozen by submerging in liquid nitrogen. Tumor sections were cut, processed and stained. They were imaged using an Olympus FV1000 confocal microscope.

ACCESSION NUMBERS

The microarray data discussed in this manuscript has been deposited in NCBI's Gene Expression Omnibus and is accessible through GEO series accession number GEO: GSE71662.

SUPPLEMENTAL INFORMATION

Supplemental Information includes Supplemental Experimental Procedures, seven figures, and two tables and can be found with this article online at <http://dx.doi.org/10.1016/j.cell.2015.09.001>.

AUTHOR CONTRIBUTIONS

A.S. and M.C.F. devised and oversaw the project. A.S., T.L., B.S., A.B., S.M.A., R.J.B.N., and M.C.F. designed the experiments with contributions from E.M., J.A.P., V.G.B., and N.G. A.S., T.L., B.S., A.B., R.C.M., and A.v.K. performed experiments with contributions from L.G.-C., M.C., M.M., and J.E.R. A.S., T.L., B.S., A.B., R.C.M., A.v.K., and A.H.S. analyzed the data. A.B. and A.H.S. performed bioinformatic analysis. A.S. and M.C.F. wrote the manuscript with contributions from T.L., B.S., and A.B.; all authors commented on and approved the final version. We consider that A.S. and T.L. made equal contributions and that B.S. and A.B. made equal contributions.

ACKNOWLEDGMENTS

This work was supported by Cancer Research UK (Grant no. C157/A15703 to M.C.F.), European Research Council (Grant no. 29440 Cancer Innovation to M.C.F.) and Medical Research Council (Grant no. G1100084 to S.M.A.). We thank Frederic Li Mow Chee for help with transcriptomic analysis, Amaya García-Muñoz for help with mass spectrometry, Elisabeth Freyer for help with FACS, and Arkadiusz Welman for help with manuscript preparation. J.E.R. and J.A.P. are employees of Verastem Inc.

Received: March 6, 2015

Revised: July 17, 2015

Accepted: August 27, 2015

Published: September 24, 2015

REFERENCES

- Albasri, A., Fadhl, W., Scholefield, J.H., Durrant, L.G., and Ilyas, M. (2014). Nuclear expression of phosphorylated focal adhesion kinase is associated with poor prognosis in human colorectal cancer. *Anticancer Res.* 34, 3969–3974.
- Ali, K., Soond, D.R., Piñeiro, R., Hagemann, T., Pearce, W., Lim, E.L., Bouabe, H., Scudamore, C.L., Hancox, T., Maecker, H., et al. (2014). Inactivation of PI(3)K p110δ breaks regulatory T-cell-mediated immune tolerance to cancer. *Nature* 510, 407–411.
- Ashton, G.H., Morton, J.P., Myant, K., Phesse, T.J., Ridgway, R.A., Marsh, V., Wilkins, J.A., Athineos, D., Muncan, V., Kemp, R., et al. (2010). Focal adhesion kinase is required for intestinal regeneration and tumorigenesis downstream of Wnt/c-Myc signaling. *Dev. Cell* 19, 259–269.
- Beyer, M., and Schultze, J.L. (2006). Regulatory T cells in cancer. *Blood* 108, 804–811.

Biragyn, A., and Longo, D.L. (2012). Neoplastic "Black Ops": cancer's subversive tactics in overcoming host defenses. *Semin. Cancer Biol.* 22, 50–59.

Bos, P.D., Plitas, G., Rudra, D., Lee, S.Y., and Rudensky, A.Y. (2013). Transient regulatory T cell ablation deters oncogene-driven breast cancer and enhances radiotherapy. *J. Exp. Med.* 210, 2435–2466.

Curiel, T.J., Coukos, G., Zou, L., Alvarez, X., Cheng, P., Mottram, P., Evdemon-Hogan, M., Conejo-Garcia, J.R., Zhang, L., Burow, M., et al. (2004). Specific recruitment of regulatory T cells in ovarian carcinoma fosters immune privilege and predicts reduced survival. *Nat. Med.* 10, 942–949.

D'Alessio, J.A., Wright, K.J., and Tjian, R. (2009). Shifting players and paradigms in cell-specific transcription. *Mol. Cell* 36, 924–931.

Darrasse-Jeze, G., and Podsypanina, K. (2013). How numbers, nature, and immune status of foxp3(+) regulatory T-cells shape the early immunological events in tumor development. *Front. Immunol.* 4, 292.

Fessele, S., Maier, H., Zischek, C., Nelson, P.J., and Werner, T. (2002). Regulatory context is a crucial part of gene function. *Trends Genet.* 18, 60–63.

Fourcade, J., Sun, Z., Benallaoua, M., Guillaume, P., Luescher, I.F., Sander, C., Kirkwood, J.M., Kuchroo, V., and Zarour, H.M. (2010). Upregulation of Tim-3 and PD-1 expression is associated with tumor antigen-specific CD8+ T cell dysfunction in melanoma patients. *J. Exp. Med.* 207, 2175–2186.

Frame, M.C., Patel, H., Serrels, B., Lietha, D., and Eck, M.J. (2010). The FERM domain: organizing the structure and function of FAK. *Nat. Rev. Mol. Cell Biol.* 11, 802–814.

Gilbert, N., Boyle, S., Sutherland, H., de Las Heras, J., Allan, J., Jenuwein, T., and Bickmore, W.A. (2003). Formation of facultative heterochromatin in the absence of HP1. *EMBO J.* 22, 5540–5550.

Gilbert, N., Boyle, S., Fiegler, H., Woodfine, K., Carter, N.P., and Bickmore, W.A. (2004). Chromatin architecture of the human genome: gene-rich domains are enriched in open chromatin fibers. *Cell* 118, 555–566.

Goldstein, J.D., Pérol, L., Zaragoza, B., Baeyens, A., Marodon, G., and Piaggio, E. (2013). Role of cytokines in thymus- versus peripherally derived-regulatory T cell differentiation and function. *Front. Immunol.* 4, 155.

Kono, K., Kawaida, H., Takahashi, A., Sugai, H., Mimura, K., Miyagawa, N., Omata, H., and Fujii, H. (2006). CD4(+)CD25high regulatory T cells increase with tumor stage in patients with gastric and esophageal cancers. *Cancer Immunol. Immunother.* 55, 1064–1071.

Lahlou, H., Sanguin-Gendreau, V., Zuo, D., Cardiff, R.D., McLean, G.W., Frame, M.C., and Muller, W.J. (2007). Mammary epithelial-specific disruption of the focal adhesion kinase blocks mammary tumor progression. *Proc. Natl. Acad. Sci. USA* 104, 20302–20307.

Lim, S.T. (2013). Nuclear FAK: a new mode of gene regulation from cellular adhesions. *Mol. Cells* 36, 1–6.

Lim, S.T., Chen, X.L., Lim, Y., Hanson, D.A., Vo, T.T., Howerton, K., Larocque, N., Fisher, S.J., Schlaepfer, D.D., and Illic, D. (2008). Nuclear FAK promotes cell proliferation and survival through FERM-enhanced p53 degradation. *Mol. Cell* 29, 9–22.

Luo, M., Fan, H., Nagy, T., Wei, H., Wang, C., Liu, S., Wicha, M.S., and Guan, J.L. (2009a). Mammary epithelial-specific ablation of the focal adhesion kinase suppresses mammary tumorigenesis by affecting mammary cancer stem/progenitor cells. *Cancer Res.* 69, 466–474.

Luo, S.W., Zhang, C., Zhang, B., Kim, C.H., Qiu, Y.Z., Du, Q.S., Mei, L., and Xiong, W.C. (2009b). Regulation of heterochromatin remodelling and myogenin expression during muscle differentiation by FAK interaction with MBD2. *EMBO J.* 28, 2568–2582.

Marigo, I., Dolcetti, L., Serafini, P., Zanovello, P., and Bronte, V. (2008). Tumor-induced tolerance and immune suppression by myeloid derived suppressor cells. *Immunol. Rev.* 222, 162–179.

Matsuzaki, J., Gnjatic, S., Mhawech-Fauceglia, P., Beck, A., Miller, A., Tsuji, T., Eppolito, C., Qian, F., Lele, S., Shrikant, P., et al. (2010). Tumor-infiltrating NY-ESO-1-specific CD8+ T cells are negatively regulated by LAG-3 and PD-1 in human ovarian cancer. *Proc. Natl. Acad. Sci. USA* 107, 7875–7880.

McLean, G.W., Komiyama, N.H., Serrels, B., Asano, H., Reynolds, L., Conti, F., Hodivala-Dilke, K., Metzger, D., Chambon, P., Grant, S.G., and Frame, M.C. (2004). Specific deletion of focal adhesion kinase suppresses tumor formation and blocks malignant progression. *Genes Dev.* 18, 2998–3003.

McLean, G.W., Carragher, N.O., Avizienyte, E., Evans, J., Brunton, V.G., and Frame, M.C. (2005). The role of focal-adhesion kinase in cancer - a new therapeutic opportunity. *Nat. Rev. Cancer* 5, 505–515.

Ondondo, B., Jones, E., Godkin, A., and Gallimore, A. (2013). Home sweet home: the tumor microenvironment as a haven for regulatory T cells. *Front. Immunol.* 4, 197.

Onizuka, S., Tawara, I., Shimizu, J., Sakaguchi, S., Fujita, T., and Nakayama, E. (1999). Tumor rejection by in vivo administration of anti-CD25 (interleukin-2 receptor alpha) monoclonal antibody. *Cancer Res.* 59, 3128–3133.

Pardoll, D.M. (2012). The blockade of immune checkpoints in cancer immunotherapy. *Nat. Rev. Cancer* 12, 252–264.

Peggs, K.S., Quezada, S.A., Chambers, C.A., Korman, A.J., and Allison, J.P. (2009). Blockade of CTLA-4 on both effector and regulatory T cell compartments contributes to the antitumor activity of anti-CTLA-4 antibodies. *J. Exp. Med.* 206, 1717–1725.

Provenzano, P.P., Inman, D.R., Eliceiri, K.W., Beggs, H.E., and Keely, P.J. (2008). Mammary epithelial-specific disruption of focal adhesion kinase retards tumor formation and metastasis in a transgenic mouse model of human breast cancer. *Am. J. Pathol.* 173, 1551–1565.

Pylayeva, Y., Gillen, K.M., Gerald, W., Beggs, H.E., Reichardt, L.F., and Giaccio, F.G. (2009). Ras- and PI3K-dependent breast tumorigenesis in mice and humans requires focal adhesion kinase signaling. *J. Clin. Invest.* 119, 252–266.

Quezada, S.A., Peggs, K.S., Curran, M.A., and Allison, J.P. (2006). CTLA4 blockade and GM-CSF combination immunotherapy alters the intratumor balance of effector and regulatory T cells. *J. Clin. Invest.* 116, 1935–1945.

Roberts, W.G., Ung, E., Whalen, P., Cooper, B., Hulford, C., Autry, C., Richter, D., Emerson, E., Lin, J., Kath, J., et al. (2008). Antitumor activity and pharmacology of a selective focal adhesion kinase inhibitor, PF-562,271. *Cancer Res.* 68, 1935–1944.

Sakuishi, K., Apetoh, L., Sullivan, J.M., Blazar, B.R., Kuchroo, V.K., and Anderson, A.C. (2010). Targeting Tim-3 and PD-1 pathways to reverse T cell exhaustion and restore anti-tumor immunity. *J. Exp. Med.* 207, 2187–2194.

Sakuishi, K., Ngiow, S.F., Sullivan, J.M., Teng, M.W., Kuchroo, V.K., Smyth, M.J., and Anderson, A.C. (2013). TIM3(+)FOXP3(+) regulatory T cells are tissue-specific promoters of T-cell dysfunction in cancer. *Oncolmmonology* 2, e23849.

Sasada, T., Kimura, M., Yoshida, Y., Kanai, M., and Takabayashi, A. (2003). CD4+CD25+ regulatory T cells in patients with gastrointestinal malignancies: possible involvement of regulatory T cells in disease progression. *Cancer* 98, 1089–1099.

Sato, E., Olson, S.H., Ahn, J., Bundy, B., Nishikawa, H., Qian, F., Jungbluth, A.A., Frosina, D., Gnjatic, S., Ambrosone, C., et al. (2005). Intraepithelial CD8+ tumor-infiltrating lymphocytes and a high CD8+/regulatory T cell ratio are associated with favorable prognosis in ovarian cancer. *Proc. Natl. Acad. Sci. USA* 102, 18538–18543.

Serrels, A., McLeod, K., Canel, M., Kinnaird, A., Graham, K., Frame, M.C., and Brunton, V.G. (2012). The role of focal adhesion kinase catalytic activity on the proliferation and migration of squamous cell carcinoma cells. *Int. J. Cancer* 131, 287–297.

Shah, W., Yan, X., Jing, L., Zhou, Y., Chen, H., and Wang, Y. (2011). A reversed CD4/CD8 ratio of tumor-infiltrating lymphocytes and a high percentage of CD4(+)FOXP3(+) regulatory T cells are significantly associated with clinical outcome in squamous cell carcinoma of the cervix. *Cell. Mol. Immunol.* 8, 59–66.

Shapiro, I.M., Kolev, V.N., Vidal, C.M., Kadariya, Y., Ring, J.E., Wright, Q., Weaver, D.T., Menges, C., Padval, M., McClatchey, A.I., et al. (2014). Merlin deficiency predicts FAK inhibitor sensitivity: a synthetic lethal relationship. *Sci. Transl. Med.* 6, 237ra68.

Shimizu, J., Yamazaki, S., and Sakaguchi, S. (1999). Induction of tumor immunity by removing CD25+CD4+ T cells: a common basis between tumor immunity and autoimmunity. *J. Immunol.* 163, 5211–5218.

Simpson, T.R., Li, F., Montalvo-Ortiz, W., Sepulveda, M.A., Bergerhoff, K., Arce, F., Roddie, C., Henry, J.Y., Yagita, H., Wolchok, J.D., et al. (2013). Fc-dependent depletion of tumor-infiltrating regulatory T cells co-defines the efficacy of anti-CTLA-4 therapy against melanoma. *J. Exp. Med.* 210, 1695–1710.

Slack-Davis, J.K., Hershey, E.D., Theodorescu, D., Frierson, H.F., and Parsons, J.T. (2009). Differential requirement for focal adhesion kinase signaling in cancer progression in the transgenic adenocarcinoma of mouse prostate model. *Mol. Cancer Ther.* 8, 2470–2477.

Stokes, J.B., Adair, S.J., Slack-Davis, J.K., Walters, D.M., Tilghman, R.W., Hershey, E.D., Lowrey, B., Thomas, K.S., Bouton, A.H., Hwang, R.F., et al. (2011). Inhibition of focal adhesion kinase by PF-562,271 inhibits the growth and metastasis of pancreatic cancer concomitant with altering the tumor microenvironment. *Mol. Cancer Ther.* 10, 2135–2145.

Tan, M.C., Goedebure, P.S., Belt, B.A., Flaherty, B., Sankpal, N., Gillanders, W.E., Eberlein, T.J., Hsieh, C.S., and Linehan, D.C. (2009). Disruption of CCR5-dependent homing of regulatory T cells inhibits tumor growth in a murine model of pancreatic cancer. *J. Immunol.* 182, 1746–1755.

Thornton, A.M., Korty, P.E., Tran, D.Q., Wohlfert, E.A., Murray, P.E., Belkaid, Y., and Shevach, E.M. (2010). Expression of Helios, an Ikaros transcription factor family member, differentiates thymic-derived from peripherally induced Foxp3+ T regulatory cells. *J. Immunol.* 184, 3433–3441.

Turriani, B., Garcia-Munoz, A., Pilkington, R., Raso, C., Kolch, W., and von Kriegsheim, A. (2014). On-beads digestion in conjunction with data-dependent mass spectrometry: a shortcut to quantitative and dynamic interaction proteomics. *Biology (Basel)* 3, 320–332.

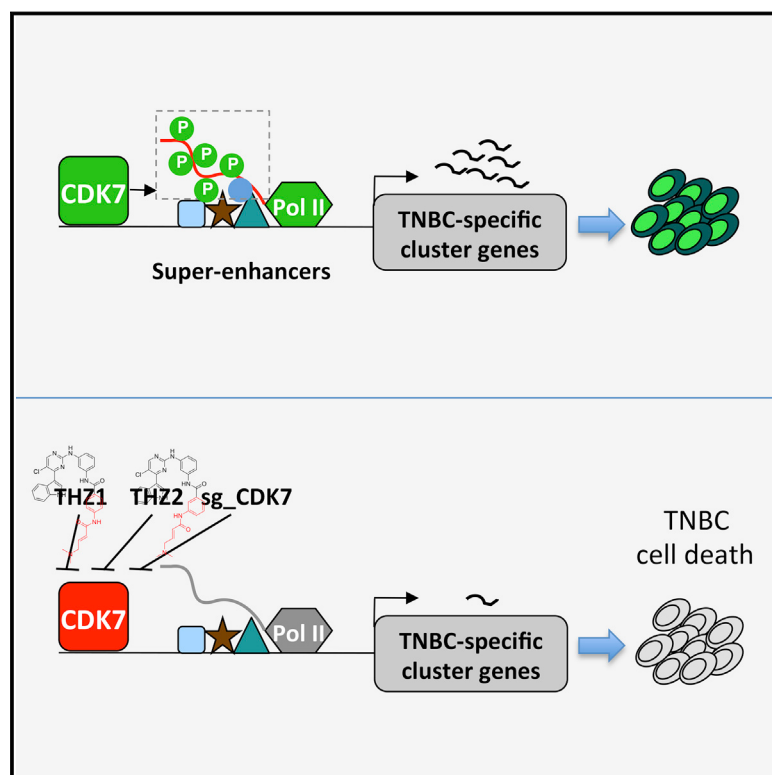
Wherry, E.J. (2011). T cell exhaustion. *Nat. Immunol.* 12, 492–499.

Wing, K., Onishi, Y., Prieto-Martin, P., Yamaguchi, T., Miyara, M., Fehervari, Z., Nomura, T., and Sakaguchi, S. (2008). CTLA-4 control over Foxp3+ regulatory T cell function. *Science* 322, 271–275.

Wolchok, J.D., Kluger, H., Callahan, M.K., Postow, M.A., Rizvi, N.A., Lesokhin, A.M., Segal, N.H., Ariyan, C.E., Gordon, R.A., Reed, K., et al. (2013). Nivolumab plus ipilimumab in advanced melanoma. *N. Engl. J. Med.* 369, 122–133.

CDK7-Dependent Transcriptional Addiction in Triple-Negative Breast Cancer

Graphical Abstract



Highlights

- Triple-negative breast cancer (TNBC) cells are highly dependent on CDK7
- CRISPR/Cas9-mediated gene editing shows selective dependency of TNBC on CDK7
- CDK7 activity is critical for the expression of a set of genes essential for TNBC
- A covalent CDK7 inhibitor blocks tumor growth in patient-derived xenografts of TNBC

Authors

Yubao Wang, Tinghu Zhang,
Nicholas Kwiatkowski, ...,
Richard A. Young, Nathanael S. Gray,
Jean J. Zhao

Correspondence

nathanael_gray@dfci.harvard.edu
(N.S.G.),
jean_zhao@dfci.harvard.edu (J.J.Z.)

In Brief

A potential therapy for triple-negative breast cancer is suggested by its strong dependence on the transcriptional kinase CDK7 and the cluster of genes the kinase regulates.

Accession Numbers

GSE69107

CDK7-Dependent Transcriptional Addiction in Triple-Negative Breast Cancer

Yubao Wang,^{1,2,7} Tinghu Zhang,^{1,2,7} Nicholas Kwiatkowski,^{3,7} Brian J. Abraham,³ Tong Ihn Lee,³ Shaozhen Xie,^{1,2} Haluk Yuzugullu,^{1,2} Thanh Von,^{1,2} Heyuan Li,¹ Ziao Lin,¹ Daniel G. Stover,⁴ Elgene Lim,⁴ Zhigang C. Wang,^{1,5} J. Dirk Iglehart,^{1,5} Richard A. Young,^{3,6,8} Nathanael S. Gray,^{1,2,8,*} and Jean J. Zhao^{1,2,8,*}

¹Department of Cancer Biology, Dana-Farber Cancer Institute, Boston, MA 02115, USA

²Department of Biological Chemistry and Molecular Pharmacology, Harvard Medical School, Boston, MA 02115, USA

³Whitehead Institute for Biomedical Research, 9 Cambridge Center, Cambridge, MA 02142, USA

⁴Department of Medical Oncology, Dana-Farber Cancer Institute, Boston, MA 02115, USA

⁵Department of Surgery, Brigham and Women's Hospital, Boston, MA 02115, USA

⁶Department of Biology, Massachusetts Institute of Technology, Cambridge, MA 02139, USA

⁷Co-first author

⁸Co-senior author

*Correspondence: nathanael_gray@dfci.harvard.edu (N.S.G.), jean_zhao@dfci.harvard.edu (J.J.Z.)

<http://dx.doi.org/10.1016/j.cell.2015.08.063>

SUMMARY

Triple-negative breast cancer (TNBC) is a highly aggressive form of breast cancer that exhibits extremely high levels of genetic complexity and yet a relatively uniform transcriptional program. We postulate that TNBC might be highly dependent on uninterrupted transcription of a key set of genes within this gene expression program and might therefore be exceptionally sensitive to inhibitors of transcription. Utilizing kinase inhibitors and CRISPR/Cas9-mediated gene editing, we show here that triple-negative but not hormone receptor-positive breast cancer cells are exceptionally dependent on CDK7, a transcriptional cyclin-dependent kinase. TNBC cells are unique in their dependence on this transcriptional CDK and suffer apoptotic cell death upon CDK7 inhibition. An “Achilles cluster” of TNBC-specific genes is especially sensitive to CDK7 inhibition and frequently associated with super-enhancers. We conclude that CDK7 mediates transcriptional addiction to a vital cluster of genes in TNBC and CDK7 inhibition may be a useful therapy for this challenging cancer.

INTRODUCTION

Recent advances in genomic sequencing have led to an unprecedented understanding of the genetics of tumor heterogeneity (Fisher et al., 2013). For a number of cancers, this has led to the discovery of “driver” oncogenes such as mutant BRAF, EGFR, and EML4-ALK, which has informed rational drug development strategies (Chin et al., 2011). For other tumors, however, sequencing has only revealed a striking level of heterogeneity and has not resulted in the identification of clear driver mutations (Cancer Genome Atlas Research Network, 2011, 2012). Despite this genetic heterogeneity, a number of these tumors can be readily identified based upon their gene expression programs

(Hoadley et al., 2014). We hypothesized that, despite the genetic heterogeneity, maintenance of these uniform gene expression programs might require continuous active transcription and therefore be more sensitive to drugs that target transcription.

We evaluated this hypothesis in the context of triple-negative breast cancer (TNBC) because this subtype is characterized by high genetic complexity (Abramson et al., 2015; Cancer Genome Atlas Network, 2012) and has a characteristic gene expression program (Parker et al., 2009; Perou et al., 2000). Compared to hormone receptor (estrogen and/or progesterone receptor)-positive (ER/PR+) breast cancer, TNBC demonstrates a higher level of genetic complexity, as indicated by a higher rate of point mutation, gene amplification, and deletion (Cancer Genome Atlas Network, 2012). Notably, TNBC lacks a common genetic alteration except mutations of tumor suppressor genes such as INPP4B, PTEN, and TP53 (Abramson et al., 2015; Andre et al., 2009; Cancer Genome Atlas Network, 2012; Gewinner et al., 2009; Shah et al., 2012), a situation that has limited the development of “targeted” therapies. The highly aggressive nature of TNBC and the lack of effective therapeutics make this disease a high priority for discovery biology efforts.

Targeting gene transcription for cancer therapy has long been considered difficult, due to a presumably universal role of transcription in non-malignant cells or tissues, and consequently, pharmacologic inhibition of general transcriptional machinery might lack selectivity for cancer cells and cause intolerable toxicity. Recent studies, however, have challenged this paradigm and found that transcription of certain genes is disproportionately sensitive to inhibition of transcription (Dawson et al., 2011; Delmore et al., 2011; Chapuy et al.; 2013; Chipumuro et al., 2014; Christensen et al., 2014; Kwiatkowski et al., 2014; Zuber et al., 2011). Those genes, often encoding oncogenic drivers with short mRNA and protein half-lives (e.g., MYC, MYCN, and RUNX1), have a striking dependence on continuous active transcription, thereby allowing for highly selective effects before “global” downregulation of transcription is achieved. The continuous active transcription of these genes in cancer cells is often driven by exceptionally large clustered enhancer regions, called super-enhancers, that are densely occupied by

transcription factors and co-factors (Hnisz et al., 2013, 2015; Lovén et al., 2013).

The control of gene transcription involves a set of cyclin-dependent kinases (CDKs), including CDK7, CDK8, CDK9, CDK12, and CDK13, that play essential roles in transcription initiation and elongation by phosphorylating RNA polymerase II (RNAPII) and other components of the transcription apparatus (Akhtar et al., 2009; Laroche et al., 2012; Zhou et al., 2012). We recently discovered a selective CDK7 inhibitor, THZ1, that covalently binds to CDK7 and suppresses its kinase activity with an unanticipated level of selectivity based upon modification of a unique cysteine residue (Kwiatkowski et al., 2014). We further identified a therapeutic effect of CDK7 inhibition in several types of cancer, including MYCN-amplified neuroblastoma, small-cell lung cancer, and T cell acute lymphoblastic leukemia (Chipumuro et al., 2014; Christensen et al., 2014; Kwiatkowski et al., 2014). Here, we report that TNBC demonstrates a profound dependence on CDK7. We further identified an “Achilles cluster” of TNBC genes that require CDK7 to maintain expression and that apparently mediate the extreme sensitivity of TNBC to CDK7 inhibition.

RESULTS

Exceptional Sensitivity of TNBC Cells to Covalent Inhibition of CDK7

To investigate whether the proliferation of TNBC cells is sensitive to CDK7 inhibition, we treated triple-negative or ER/PR+ breast cancer cell lines with increasing concentrations of THZ1. While ER/PR+ cells were largely unaffected by treatment of THZ1 at micromolar doses, triple-negative breast cancer cells were highly sensitive to CDK7 inhibition, with cell proliferation effectively suppressed by low nanomolar concentrations of THZ1 ($IC_{50} < 70$ nM) (Figures 1A and 1B). In contrast to the extreme sensitivity to THZ1, TNBC cells were more resistant to a non-cysteine reactive analog of THZ1 (THZ1-R) (Kwiatkowski et al., 2014) (Figure S1A), suggesting that the unique characteristic of THZ1 in covalently binding to its target determines its antiproliferative potency.

To understand the mechanism underlying the highly selective effect of THZ1, we next proceeded to test whether CDK7 is equally inhibited in both triple-negative and ER/PR+ breast cancer cells. CDK7 is implicated in regulating the phosphorylation of the carboxyl-terminal domain (CTD) of RNAPII at multiple sites (Ser 2, 5, and 7) either directly or via phosphorylating and activating other CDKs (Akhtar et al., 2009; Glover-Cutter et al., 2009; Laroche et al., 2012; Zhou et al., 2012). We exposed cells to increasing doses of THZ1 or THZ1-R and found that, in both triple-negative and ER/PR+ breast cancer cells, CTD phosphorylation at S2, S5, and S7 was effectively suppressed by THZ1 but not the inactive THZ1-R (Figures 1C and S1B). The similar effects on CTD phosphorylation by THZ1 indicates that CDK7 is similarly targeted in both drug-sensitive and -resistant cells; thus, TNBC cells appear to be far more dependent on the activity of CDK7 than ER/PR+ breast cancer cells.

We further found that CDK7 inhibition efficiently induced apoptotic cell death in TNBC cells, indicated by the induced cleavage of PARP and Caspase 3 (Figure 1D). In line with the differential response to CDK7 inhibition, cell death was not observed in ER/PR+ breast cancer cells treated with THZ1 (Figure 1D).

Consistent with previous studies, THZ1 treatment also failed to induce cell death in non-transformed human cell lines (BJ fibroblasts and retinal pigment epithelial cells, RPE-1) (Figure 1D) (Kwiatkowski et al., 2014). Notably, RNAPII CTD phosphorylation was suppressed by THZ1 in all of these cell lines (Figure 1D) and thus did not correlate with the cell fate, again indicating an exceptional dependence on CDK7-regulated pathways in TNBC cells.

In addition to regulating RNAPII CTD phosphorylation, CDK7 is a component of CDK-activating kinase (CAK), which is thought to phosphorylate and activate all CDKs, including cell-cycle CDKs (Schachter and Fisher, 2013). Indeed, CDK7 has been implicated in phosphorylating CDK1 and regulating mitosis (Laroche et al., 2007), and THZ1 treatment has been shown to induce a G2/M arrest in neuroblastoma cells with MYCN amplification (Chipumuro et al., 2014). Surprisingly, THZ1 treatment did not alter the cell cycle in TNBC cells (Figure S1C). To further investigate whether mitosis is impaired by CDK7 inhibition, we utilized live-cell imaging to observe the progression of mitosis. We found that mitosis of TNBC cells (MDA-MB-468) progressed normally in the presence of THZ1 (Figure S1D and Movie S1 and S2). The duration of time from nuclear envelope breakdown (NEBD) to anaphase onset was not significantly changed by THZ1 treatment (Figure S1E). Despite a lack of mitotic arrest by THZ1, cell death was efficiently induced (Figures S1D and S1F and Movie S1). Therefore, the sensitivity of TNBC cells to CDK7 inhibition is likely not derived from a role of CDK7 in directly regulating cell-cycle-related CDKs.

Next, we investigated whether the anti-proliferative effects displayed by THZ1 in established TNBC cell lines would translate to primary TNBC samples. To address this, we performed primary culture of tumor cells from patient-derived xenografts (PDX) of TNBC and treated these cells with THZ1. In three independent patient-derived TNBC cultures, THZ1 effectively reduced cell viability ($IC_{50} < 100$ nM) (Figure 1E). Consistent with our findings obtained from established cancer cell lines, we observed that two ER/PR+ primary cultures were largely insensitive to THZ1 (Figures 1E and 1F). Furthermore, treatment of primary TNBC cells with THZ1 led to suppressed RNAPII CTD phosphorylation and induction of apoptotic cell death (Figure 1G). Given that the primary samples were derived from patients with TNBC who had progressed on multiple lines of chemotherapies, our data indicate that CDK7 inhibition may provide an effective therapeutic option for patients with this aggressive disease.

An Analog of THZ1 with Improved Pharmacokinetics

Despite the high anti-proliferative potency of THZ1 in primary TNBC cells, the stability of THZ1 in vivo ($T_{1/2}$ of 45 min in mouse plasma) limits its utility for in vivo investigations. We therefore modified the structure of THZ1 by altering the regiochemistry of the acrylamide on THZ1 from 4-acrylamide-benzamide to 3-acrylamide-benzamide, giving rise to an analog THZ2 (Figure 2A). THZ2 had significantly improved pharmacokinetic features, with a 5-fold improved half-life in vivo (Figure 2B). Similar to THZ1, THZ2 selectively targeted CDK7 (Figure 2C and Table S1) and potently inhibited the growth of triple-negative, but not ER/PR+, breast cancer cells (Figures 2D and 2E). THZ2 at low

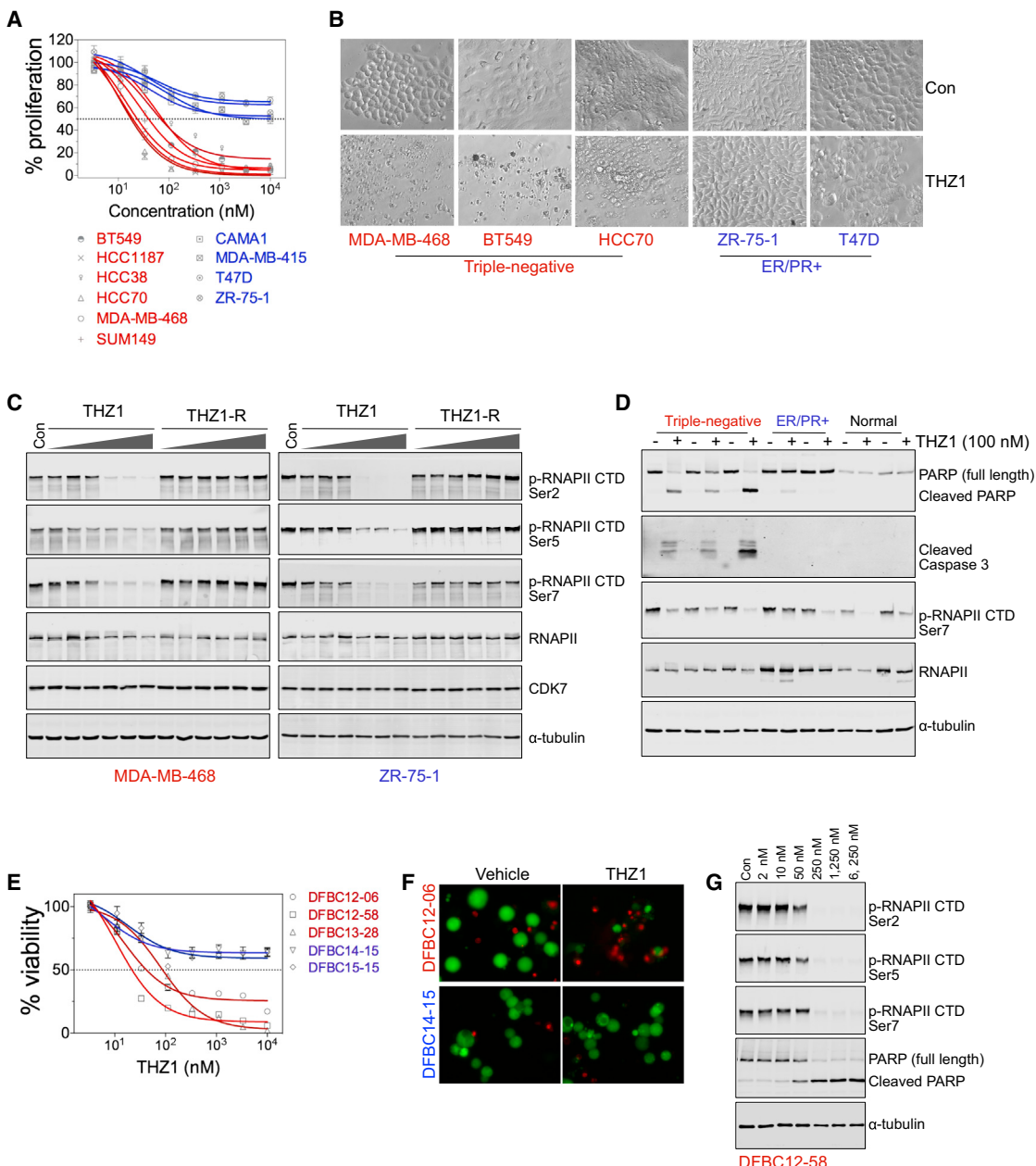


Figure 1. CDK7 Inhibition Selectively Targets TNBC Cells

(A) Cell growth curves of triple-negative (red) and ER/PR+ (blue) breast cancer cell lines. Cells were treated with increasing concentrations of THZ1 for 48 hr. Cells were then fixed and stained for the quantification of cell growth. Data are presented as means \pm SD.

(B) Bright-field images of cells that were treated with vehicle control or THZ1 (40 nM) for 7 days. Note that THZ1 induced cell death in triple-negative, but not ER/PR+ breast cancer cells.

(C) THZ1 inhibits RNAPII CTD phosphorylation in both triple-negative (MDA-MB-468) and ER/PR+ (ZR-75-1) breast cancer cells. Cells were treated with vehicle control (first lane) or increasing concentrations of indicated drug (2, 10, 50, 250, 1,250, and 6,250 nM) for 4 hr before lysates were prepared for immunoblotting. (D) Immunoblotting analysis of lysates harvested from cells treated for 24 hr with vehicle control or THZ1 (100 nM). Samples in the order of loading were triple

(E) Indicated TNBC (red) or ER/PR+ (blue) primary cultures were treated with increasing concentrations of THZ1. Cells were subjected to CellTiter-Glow

(F) Triple-negative (DFBC12-06) or ER/PR+ (DFBC14-15) primary culture was treated with vehicle control or THZ1 (250 nM) for 24 hr. Cells were subjected to LIVE/

(G) THZ1 inhibits RNAPII CTD phosphorylation and induces apoptosis in primary TNBC cells. Primary TNBC culture (DFBC12-58) was treated with vehicle control

(first lane) or indicated concentrations of Th

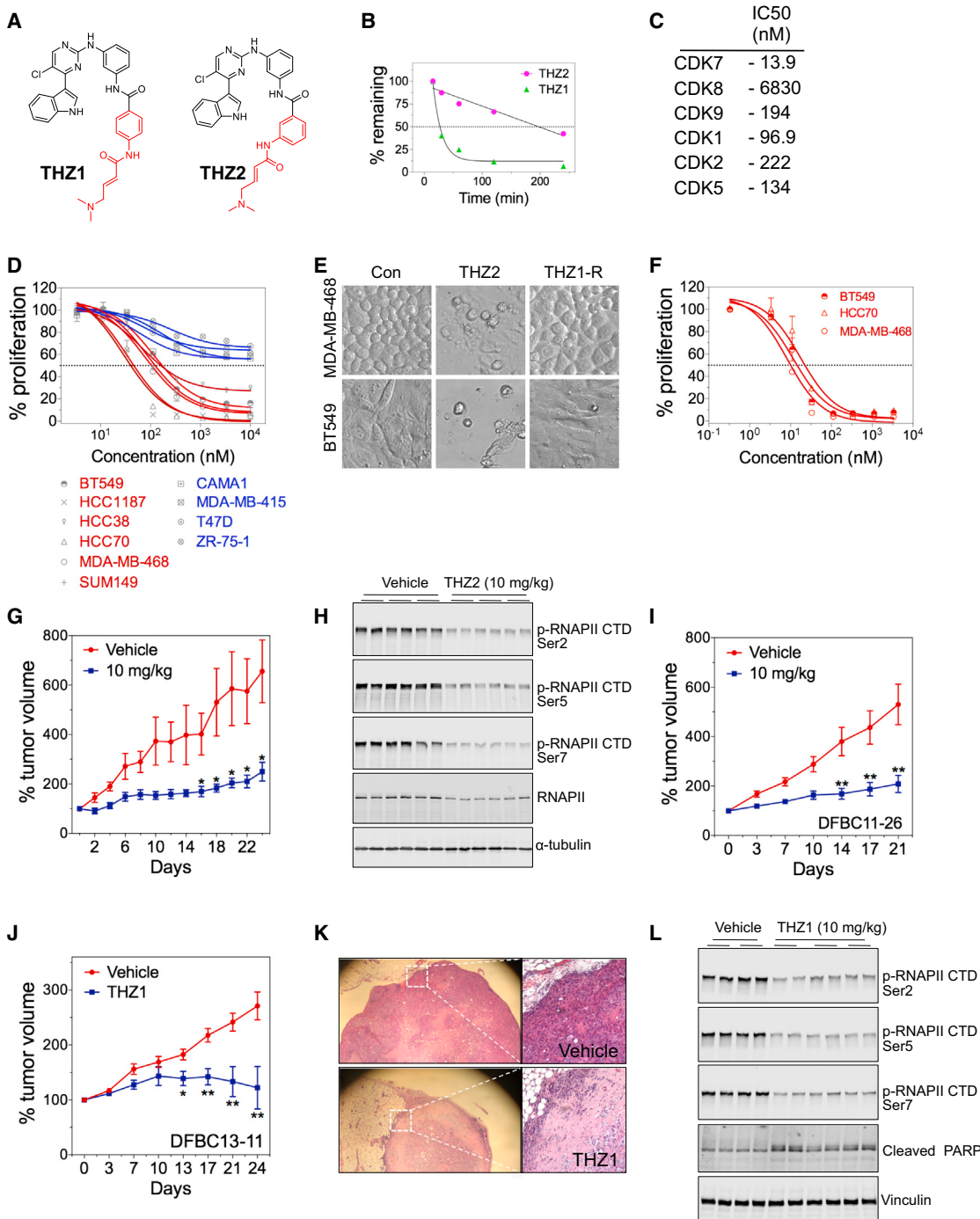


Figure 2. An Analog of THZ1 and the Effect of CDK7 Inhibition on the Growth of Triple-Negative Breast Tumors

(A) Structure of THZ1 and THZ2. The groups of 4-acrylamide-benzamide in THZ1 and 3-acrylamide-benzamide in THZ2 are colored red.

(B) Stability of THZ1 and THZ2 in vivo. Mice were administered by tail vein injection a single dose of THZ1 or THZ2, and blood samples were collected at different time points. Concentrations of THZ1 and THZ2 in plasma samples were determined by liquid chromatography-tandem mass spectrometry (LC-MS/MS) approach.

(C) In vitro IC₅₀ for THZ2's potency in binding to indicated CDK. The Lanthascreen Eu Kinase Binding assay (Invitrogen) was performed with indicated CDKs and their associated cyclins in the presence of different concentration of THZ2. The IC₅₀ values indicate the affinity of THZ2 toward the ATP binding pocket of CDK.

(D) Cell growth curve of breast cancer cells treated with increasing concentrations of THZ2 for 48 hr. Data are presented as mean ± SD.

(E) Bright-field images of cells treated with vehicle control, THZ2 (370 nM), or THZ1-R (370 nM) for 2 days.

(F) Cell growth curve of indicated TNBC cell lines that were treated with increasing concentrations of THZ2 for 7 days. Upon harvest, cells were fixed and stained with crystal violet, followed by extraction of the staining for the quantification of proliferation. Data are presented as mean ± SD.

(legend continued on next page)

nanomolar doses also efficiently suppressed the clonogenic growth of TNBC cells (IC_{50} of ~10 nM; Figure 2F and S2B). Like THZ1, THZ2 induced apoptotic cell death in triple-negative, but not ER/PR+, breast cancer cells or normal human cells (Figure S2A) and did not cause an obvious alteration in cell cycle (Figure S2C). Therefore, we have identified an analog of THZ2 with improved pharmacokinetic properties and comparable potency that we elected to use for further investigations.

CDK7 Inhibition Suppresses the Growth of Triple-Negative Breast Tumors

We proceeded to investigate whether CDK7 inhibitors would exhibit efficacy *in vivo*. Treating mice intraperitoneally with THZ2 twice daily at the dose of 10 mg/kg did not give rise to overt toxicity, such as a loss of body weight or behavioral changes (data not shown). To test whether THZ2 has any therapeutic effect on triple-negative breast tumors in an orthotopic xenograft model, we transplanted triple-negative breast tumor cells (MDA-MB-231) into the mammary fat pads of nude mice. When tumors reached ~200 mm³, mice were treated with vehicle or THZ2 (10 mg/kg). Continuous treatment of THZ2 for 25 days did not affect body weight (Figure S2D), indicating that THZ2 is well tolerated in nude mice. The growth rate of tumors in mice treated with THZ2 was markedly reduced as compared to that of control tumors (Figure 2G), demonstrating an anti-tumor activity of THZ2. We also harvested tumors following short-term (50 hr) or long-term (25 days) treatment and found that both acute and chronic exposure to THZ2 significantly reduced CTD phosphorylation of RNAPII at all three phosphorylation sites (S2, S5, and S7; Figures 2H and S2E), indicating that CDK7 was efficiently targeted in the tumor cells. Compared to vehicle-treated tumors, tumor tissues isolated from mice treated with THZ2 had reduced proliferation and increased apoptosis, as indicated by immunostaining against Ki67 and cleaved Caspase 3, respectively (Figure S2F). Together, these findings indicate that the CDK7 inhibitor was able to efficiently reduce tumor cell proliferation and induce cell death *in vivo*.

We further evaluated the anti-tumor effect of CDK7 inhibition in two independent PDX models of triple-negative breast tumors, DFBC11-26 and DFBC13-11. Both PDX models were established from patients with metastatic TNBC, who had progressed on multiple lines of chemotherapy. Tumor fragments were transplanted into the mammary fat pads of NOD-SCID mice. Our first experiment with THZ2 in NOD-SCID mice led to reduced body weight, suggesting that THZ2 might be less well-tolerated in

this particular mouse strain. We therefore proceeded with using THZ1 in the PDX model of TNBC. When tumors grew to an average size of ~80 mm³, mice were treated with THZ1. Although THZ1 has poor pharmacokinetic properties, treating mice with this drug led to a substantial blockage of tumor growth in both patient-derived tumor models (Figures 2I and 2J). Notably, THZ1 treatment resulted in a loss of tumor cellularity and disease regression (Figures 2J and 2K). Analysis of tumor tissues also demonstrated markedly decreased CTD phosphorylation of RNAPII and induced PARP cleavage, an indicator of apoptotic cell death (Figure 2L). These results indicate that CDK7 inhibition has potent anti-tumor activity in patient-derived TNBC *in vivo*.

TNBC Cells Are Highly Dependent on CDK7

To complement the pharmacological studies, which have the potential for unanticipated “off-target” effects, we first used short hairpin RNA (shRNA) to decrease expression of CDK7 in a variety of breast cancer cell lines. Using doxycycline-inducible shRNA vectors targeting multiple independent sequences of CDK7, we were able to reduce the abundance of CDK7 protein by ~20%–50% (Figure S3A). This modest reduction in CDK7 abundance was sufficient to inhibit the growth of triple-negative, but not ER/PR+, breast cancer cells (Figure S3B).

To further corroborate these results, we used the CRISPR/Cas9 technique to genetically edit the CDK7 gene in five TNBC cell lines. Treating cells with constructs encoding two independent small guiding RNA targeting CDK7 (sg_CDK7) led to a substantial reduction of CDK7 protein (Figure S3C) and suppression of cell growth preferentially in triple-negative, but not ER/PR+, breast cancer cells (Figure 3A). Notably, introducing sg_CDK7 strongly impaired tumor formation from orthotopically transplanted TNBC cells (Figure 3B). As observed with the CDK7 inhibitor, sg_CDK7 also induced apoptotic cell death in TNBC cells (Figure 3C) and had little effect on cell-cycle distribution (Figures 3D and S3D). Thus, both shRNA-mediated knockdown of CDK7 and CRISPR/Cas9-mediated CDK7 gene editing produce effects on TNBC cells that phenocopy pharmacologic inhibition of CDK7. These results support the view that CDK7 is the pharmacologically relevant target of the inhibitor and that CDK7 represents a bona fide target for TNBC.

CDK7 Is a Uniquely Important Transcriptional CDK for TNBC

CDK7 is one of the transcriptional CDKs that regulate the initiation or elongation of RNAPII-mediated transcription (Zhou

(G) Growth of triple-negative breast tumors (MDA-MB-231) in nude mice treated with vehicle (n = 8) or THZ2 (n = 7; 10 mg/kg intraperitoneal). Mean ± SEM values are presented; *p < 0.05 (Student's t test).

(H) Immunoblotting of tumor lysates harvested from nude mice treated with vehicle or THZ2 (10 mg/kg intraperitoneal) for 2 days. Tumors were isolated 3 hr after last treatment and subjected to the preparation of RIPA lysates. Three independent samples from each treatment were loaded in duplicates.

(I) Growth of patient-derived triple-negative breast tumors (DFBC11-26) in NOD-SCID mice treated with vehicle (n = 4) or THZ1 (n = 6; 10 mg/kg intraperitoneal). Mean ± SEM values are presented; **p < 0.01 (Student's t test).

(J) Growth of patient-derived triple-negative breast tumors (DFBC13-11) in NOD-SCID mice treated with vehicle (n = 6) or THZ1 (n = 5; 10 mg/kg intraperitoneal). Mean ± SEM values are presented; *p < 0.05 and **p < 0.01 (Student's t test).

(K) H&E staining of tissue sections (DFBC13-11) indicating tumor regression after THZ1 treatment. Note that THZ1-treated tumor shows a loss of cellularity compared to control. Images on the left and right were captured using 4× and 10× object lens, respectively.

(L) Immunoblotting of tumor lysates (DFBC11-26) harvested from mice treated with vehicle or THZ1 (10 mg/kg intraperitoneal) for 21 days. Samples (two and three for vehicle and THZ1 treated groups, respectively) were loaded in duplicates.

See also Figure S2 and Table S1.

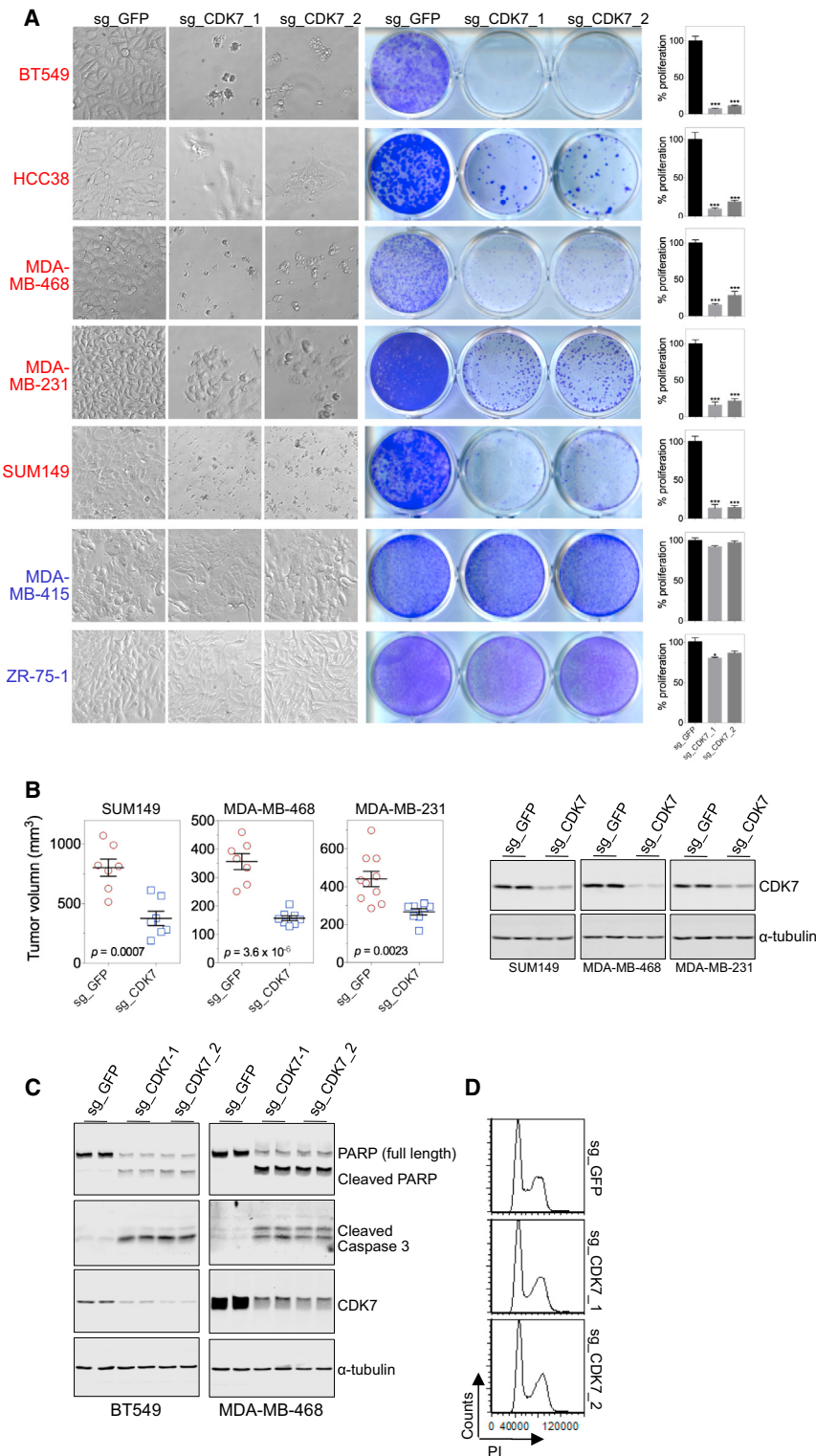


Figure 3. Loss of CDK7 Impairs TNBC Cell Growth and Tumorigenesis

(A) Loss of CDK7 in TNBC cells impairs cell viability and proliferation. The left, middle, and right panels show the bright-field images, the crystal violet staining of cells, and the quantification of cell growth, respectively. Data in the right panel are presented as mean \pm SD; * $p < 0.01$ and *** $p < 0.0001$ (Student's t test).

(B) Tumor volume of xenografts derived from cells infected with sg_GFP or sg_CDK7 (sg_CDK7_2 in Figure 3A). Cells were infected with lentivirus, selected with puromycin for 2 days, and then harvested for transplantation. Two million MDA-MB-468 or MDA-MB-231 or 4 million SUM149 cells (viability > 94% for all groups, assayed by trypan blue exclusion) were transplanted into mammary fat pads of nude mice. Tumor volume was measured 4 weeks after transplantation for the lines of SUM149 and MDA-MB-231 and 5 weeks for MDA-MB-468. Data were represented as mean \pm SEM, with p value indicated. The right panel shows immunoblotting from cultured cells that were used for transplantation. Note that the protein abundance of CDK7 was efficiently decreased by sg_CDK7.

(C) Immunoblotting of lysates from cells introduced with CRISPR constructs. Lentivirus-infected and puromycin-selected cells were seeded in 6-well plate (20,000 cells per well) and harvested in 4 days. RIPA lysates were subjected to the analysis of apoptotic cell death (indicated by PARP and Caspase 3 cleavage).

(D) Cell-cycle analysis of cells infected with lentivirus encoding sg_GFP, two independent sgRNA targeting CDK7. Cells were prepared as in (C) and then fixed for cell-cycle assay.

See also Figure S3.

regulation, including CDK7, 8, 9, 12, 13, and 19 (Figures 4A and S4). These studies demonstrated that, like CDK7, CDK9 was also required for clonogenic growth of TNBC cells (MDA-MB-231, MDA-MB-468, and BT549) (Figures 4B and 4C). CDK9 has been implicated in regulating transcriptional elongation, and physiologically, in the differentiation of multiple cell types (Shapiro, 2006). To determine whether CDK9 can also be targeted for TNBC in a selective manner, we further ablated transcriptional CDKs in ER/PR+ breast cancer line (ZR-75-1) (Figure S4). Notably, ER/PR+ breast cancer cells were also sensitive to sg_CDK9 but were largely unaffected by sg_CDK7 (Figures 4C and 4D). Together, these data suggest that, among these transcriptional CDKs, CDK7 is uniquely required for the survival and proliferation of TNBC cells.

et al., 2012). The demonstration of CDK7 as a selective target for TNBC led us to ask if other transcriptional CDKs might also serve as therapeutic targets. We used CRISPR/Cas9 to ablate six known CDKs that are implicated in transcriptional

unaffected by sg_CDK7 (Figures 4C and 4D). Together, these data suggest that, among these transcriptional CDKs, CDK7 is uniquely required for the survival and proliferation of TNBC cells.

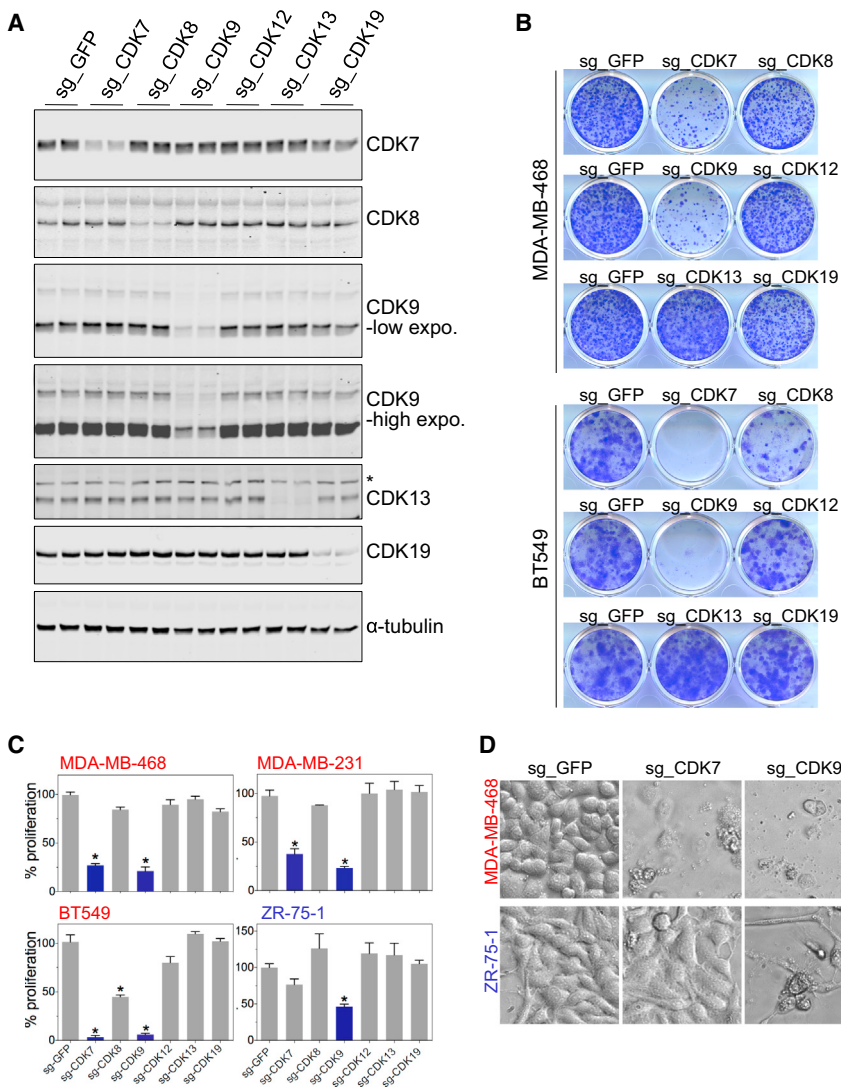


Figure 4. Unique Dependence of TNBC Cells on CDK7

(A) Immunoblotting of lysates from MDA-MB-468 cells that were infected with lentivirus encoding Cas9 and sgRNA targeting GFP or individual transcriptional CDK. The asterisk (*) denotes a non-specific signal for anti-CDK13.

(B) Role of transcriptional CDK for the indicated TNBC cells. After infection and selection with puromycin (1.5 μ g/ml, 48 hr), cells were seeded in 12-well plate (5000 per well for MDA-MB-468, 10,000 per well for BT549). Cells were fixed after 11 days and stained with crystal violet.

(C) Quantification of cell proliferation. Cells were treated as in (B). The staining was subsequently extracted for measurement of absorbance to quantify cell growth. Data are presented as mean \pm SD; * p < 0.0001 (Student's t test).

(D) Bright-field images of cells infected with virus encoding sg_GFP, sg_CDK7 or sg_CDK9. Cells were assayed as in (B) and imaged with an inverted microscope.

See also Figure S4.

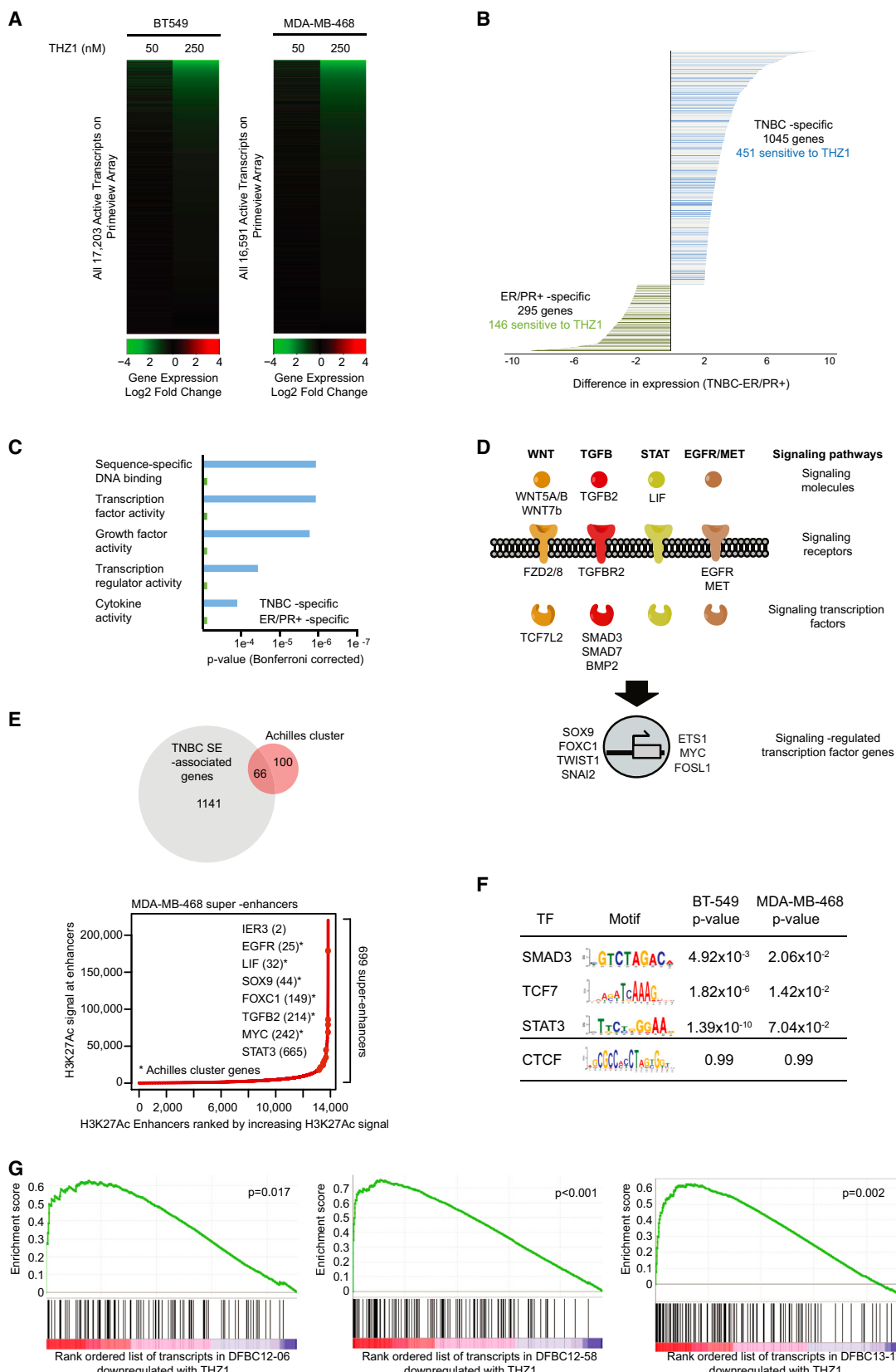
pressed in TNBC compared to ER/PR+ breast cancer lines. Genome-wide expression data were generated from two TNBC and two ER/PR+ cell lines over a THZ1 concentration course, and genes were identified that were overexpressed in either TNBC line relative to the ER/PR+ lines. Approximately 1,000 genes were overexpressed in TNBC lines relative to ER/PR+ lines; 451 of these were found to be especially sensitive to treatment with THZ1 (greater than 1.5-fold loss of expression) (Figure 5B).

Gene ontology analysis of the TNBC-specific and THZ1-sensitive genes showed that they were significantly enriched for factors involved in signaling and transcription regulation (Figure 5C). Notably, the genes within these categories included a substantial number of signaling molecules and transcription factors with established roles in breast cancer, including TGF β , STAT, WNT, and EGFR/MET-mediated signaling (Bafico et al., 2004; Brand et al., 2014; Knight et al., 2013; Lu et al., 2014; Pukrop et al., 2006; Truong et al., 2014; Yang et al., 2011) (Figure 5D). Additionally, genes encoding transcription factors whose transcription is regulated by these signaling pathways in breast cancer, including MYC, ETS1, and the epithelial-to-mesenchymal transition-related transcription factors SOX9, TWIST1, and FOXC1, were enriched in this gene set (Guo et al., 2012; Lu et al., 2014; Scheel et al., 2011; Taube et al., 2010; Watabe et al., 1998; Xu et al., 2010; Yang et al., 2004). The majority of these signaling components and transcription factors were commonly expressed in both TNBC cell lines and patient-derived primary cells (Tables S2 and S3A). We thus identified genes showing TNBC-specific expression and sensitivity to THZ1 that encode transcriptional

CDK7-Dependent Transcription of an “Achilles Cluster” of TNBC Genes

Given the role of CDK7 in phosphorylating the RNAPII CTD and CDK9 at active genes (Drapkin et al., 1996; Glover-Cutter et al., 2009; Akhtar et al., 2009; Larochelle et al., 2012; Kwiatkowski et al., 2014), we expected that CDK7 inhibition would disrupt gene expression. Indeed, THZ1 treatment led to a dose-dependent reduction in steady-state mRNA levels for the tested breast cancer cell lines (Figures 5A and S5A). However, THZ1 treatment affected the proliferation of triple-negative, but not ER/PR+, breast cancer cells. Previous studies with other cancer cell types have shown that THZ1 treatment can cause selective loss of cancer-specific oncogene expression with concurrent loss of tumor cell viability (Kwiatkowski et al., 2014; Chippumuro et al., 2014; Christensen et al., 2014). We therefore hypothesized that a critical set of TNBC genes that are differentially expressed between TNBC and ER/PR+ cells may confer the special sensitivity of TNBC cells to CDK7 inhibition. To test this hypothesis, we first identified genes that are overex-

riched for factors involved in signaling and transcription regulation (Figure 5C). Notably, the genes within these categories included a substantial number of signaling molecules and transcription factors with established roles in breast cancer, including TGF β , STAT, WNT, and EGFR/MET-mediated signaling (Bafico et al., 2004; Brand et al., 2014; Knight et al., 2013; Lu et al., 2014; Pukrop et al., 2006; Truong et al., 2014; Yang et al., 2011) (Figure 5D). Additionally, genes encoding transcription factors whose transcription is regulated by these signaling pathways in breast cancer, including MYC, ETS1, and the epithelial-to-mesenchymal transition-related transcription factors SOX9, TWIST1, and FOXC1, were enriched in this gene set (Guo et al., 2012; Lu et al., 2014; Scheel et al., 2011; Taube et al., 2010; Watabe et al., 1998; Xu et al., 2010; Yang et al., 2004). The majority of these signaling components and transcription factors were commonly expressed in both TNBC cell lines and patient-derived primary cells (Tables S2 and S3A). We thus identified genes showing TNBC-specific expression and sensitivity to THZ1 that encode transcriptional



(legend on next page)

regulators and signaling factors, which are candidate mediators of the response to THZ1. This cluster of vital genes encoding transcriptional regulators and signaling factors in TNBC cells may thus collectively represent a TNBC-specific vulnerability—an “Achilles cluster”—for TNBC (Table S3B).

We next sought a mechanistic explanation for the particular sensitivity of Achilles cluster genes to THZ1 treatment and first noticed that 40% of the genes in the Achilles cluster were associated with super-enhancers in TNBC cells. In comparison, only 11% of all expressed genes are associated with super-enhancers in TNBC cells ($p = 8.18 \times 10^{-20}$, chi-square test), and the majority of Achilles cluster genes (83%) are not associated with super-enhancers in ER/PR+ breast cancer cells (Figures 5E, S5B, and S5C and Table S4). Previous work has shown that super-enhancers concentrate components of the transcriptional apparatus to drive high-level expression of their target genes (Hnisz et al., 2013; Lovén et al., 2013; Whyte et al., 2013). Their extraordinary reliance on transcription regulators, including CDK7, may confer special sensitivity to transcriptional inhibitors like THZ1 (Kwiatkowski et al., 2014; Lovén et al., 2013; Chapuy et al., 2013; Chipumuro et al., 2014). Therefore, we hypothesized that the expression of these super-enhancer-associated Achilles cluster genes might be more sensitive to THZ1 than other TNBC genes. Indeed, analysis by microarray expression confirmed that expression of genes associated with super-enhancers in TNBC is particularly sensitive to THZ1 treatment (Figure S5D). Super-enhancers also serve as a platform for regulation by multiple signaling pathways, and perturbation of signaling pathway components can have a profound effect on super-enhancer-associated genes (Hnisz et al., 2015). The super-enhancers associated with genes in the Achilles cluster show a significant enrichment in DNA-binding motifs for terminal effector transcription factors of signaling pathways (Figure 5F). Taken together, these results suggest that the super-enhancer-driven Achilles cluster genes may be sensitive to

THZ1 as a result of their dependency on CDK7 and their interconnected regulation by signaling pathways whose components are encoded by genes that are themselves sensitive to THZ1.

We next asked whether THZ1 would induce similar gene expression changes in primary TNBC cells. Gene set enrichment analysis indicated that the genes most sensitive to THZ1 in primary TNBC cells are enriched for the TNBC-specific Achilles cluster genes (Figure 5G). Indeed, quantitative PCR (qPCR) confirmed that, in primary TNBC cultures, the expression of selected TNBC cluster genes was particularly vulnerable to CDK7 inhibition (Figure S5E).

TNBC Cells Are Addicted to the Expression of Achilles Cluster Genes

Next, we sought to confirm that components of the Achilles cluster are essential for TNBC cells and are thus likely to contribute to the cellular response of TNBC cells to CDK7 inhibition. To reflect the composition of the Achilles cluster, we chose eight candidate Achilles cluster genes that encode for super-enhancer-associated transcriptional regulators and signaling factors for this analysis. We used CRISPR/Cas9-mediated gene editing to knock out these candidate genes and assessed how the functional loss of these genes impacts TNBC proliferation and viability. We found that triple-negative (MDA-MB-468, BT549) breast cancer cells were more dependent for proliferation on EGFR, FOSL1, FOXC1, MYC, and SOX9 than ER/PR+ (ZR-75-1) breast cancer cells, while proliferation of the TNBC and ER/PR+ cell lines was similarly sensitive to loss of EN1, ETS1, and TWIST1 (Figures 6A and S6A). Using additional CRISPR vectors that target independent sequences of EGFR or SOX9, we confirmed that gene editing of these two genes suppressed cell growth and induced apoptotic cell death (Figures 6B, 6C, S6B, and S6C).

EGFR has been pursued as a therapeutic target for TNBC (Corkery et al., 2009; Ueno and Zhang, 2011). However, kinase inhibitors of EGFR have not produced satisfactory results in

Figure 5. Genes Expressed Differentially in TNBC versus ER/PR+ Breast Cancer Cells and Sensitive to CDK7 Inhibition Indicate Critical Cellular Functions for TNBC Survival

- (A) THZ1 treatment globally affects steady-state mRNA levels. BT549 and MDA-MB-468 TNBC cells were treated with THZ1 at the indicated concentrations for 6 hr. Heatmaps display the Log2 fold change in gene expression versus vehicle control for the set of expressed transcripts.
- (B) Genes differentially expressed between TNBC and ER/PR+ breast cancer lines. Individual bars represent the difference in expression in TNBC cells versus ER/PR+ cells for a gene. Genes that were differentially expressed in either of two TNBC cell lines (BT549 and MDA-MB-468) relative to two ER/PR+ lines (ZR-75-1 and T47D) were identified as TNBC specific (right side of y axis). Genes that were differentially expressed in either of two ER/PR+ lines relative to two TNBC breast cancer lines were identified as ER/PR+ specific (left side of y axis). Genes whose expression decreased by 1.5-fold or greater upon treatment with THZ1 were colored (blue for TNBC specific; green for ER/PR+ specific). Log2 fold change between TNBC and ER/PR+ expression is shown along the x axis at the bottom of the image.
- (C) Enriched Gene Ontology functional categories of TNBC-specific genes sensitive to THZ1 treatment. The top enriched molecular function GO categories are shown. Individual bars represent the Bonferroni-corrected p value for enrichment of specific gene ontology categories. Values for TNBC-specific, THZ1-sensitive genes are shown in blue. Values for ER/PR+-specific, THZ1-sensitive genes are shown in green.
- (D) Depiction of signaling pathways and transcription factors that comprise Achilles cluster genes. Highlighted genes are found in the Achilles cluster.
- (E) Achilles cluster genes are enriched in super-enhancers-associated genes. Venn diagram showing the overlap (66) between the genes that comprise the Achilles cluster (166) and genes that have TNBC super-enhancers (SE) in either MDA-MB-468 or BT549 (1207) (top). Total H3K27Ac ChIP-seq signal (length * density) in enhancer regions for all stitched enhancers in MDA-MB-468 TNBC cell line. Enhancers are ranked by increasing H3K27Ac ChIP-seq signal (bottom). Highlighted super-enhancers are associated with selected members of the Achilles cluster. Shown are top super-enhancers for each SE-associated gene.
- (F) Enrichment of DNA-binding motifs targeted by signaling transcription factors in constituent enhancers of super-enhancers regulating Achilles cluster genes in TNBC cells. The motif bound by the CTCF transcription factor is not enriched in the super-enhancers associated with Achilles cluster genes and is used as a negative control.
- (G) Genes most strongly downregulated by THZ1 treatment in patient-derived TNBC primary cells are enriched for Achilles cluster genes. Gene set enrichment analysis of Achilles cluster genes in comparison to genes downregulated in TNBC primary cultures (DFBC12-06, DFBC12-58, DFBC13-11) following treatment with THZ1 (250 nM) for 6 hr. GSEA-supplied p values are given.

See also Figure S5 and Tables S2, S3, and S4.

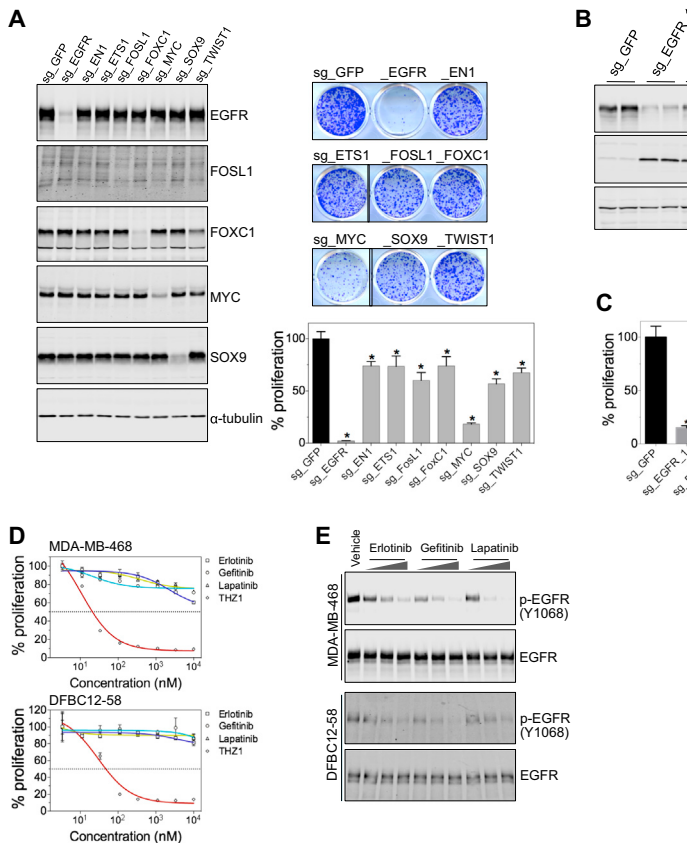


Figure 6. Functions of Achilles Cluster Genes in TNBC Cells

(A) CRISPR/Cas9-mediated editing of selected TNBC Achilles cluster genes in TNBC cell line. MDA-MB-468 cells were infected with lentivirus encoding indicated sgRNA, selected with puromycin. (Left) Immunoblotting for the expression of indicated genes. (Right, top) Cells were seeded in 12-well plates (5,000 cells per well), harvested in 10 days, and stained with crystal violet; the staining was extracted for the quantification of cell growth (right bottom). Data were represented as mean \pm SD; * $p < 0.001$.

(B) Additional CRISPR vectors decrease the protein abundance of EGFR. Vectors encoding sg_EGFR_2 and sg_EGFR_3 were tested along with sg_EGFR_1 (sg_EGFR in Figure 6A). Protein lysates were harvested for immunoblotting. Cleaved PARP was used as a marker for apoptotic cell death and Vinculin as a loading control.

(C) CRISPR/Cas9-mediated gene editing of EGFR impairs cell proliferation. MDA-MB-468 cells were treated as in (A) for measurement of cell proliferation, * $p < 0.001$.

(D) Proliferation of TNBC cells (top, MDA-MB-468; bottom, DFBC12-58) treated with increasing concentrations of EGFR inhibitors or THZ1. Cells were harvested in 3 days for measurement of cell proliferation.

(E) TNBC cells (top, MDA-MB-468; bottom, DFBC12-58) were treated with vehicle control or indicated EGFR inhibitors for 30 min. Cell lysates were harvested for immunoblotting.

See also Figure S6.

TNBC clinical trials (Carey et al., 2012). We used three independent kinase inhibitors that are known to target EGFR (erlotinib, gefitinib, and lapatinib) and found that EGFR kinase inhibition largely spared TNBC cells (Figures 6D and S6D), despite evident suppression of EGFR autophosphorylation and downstream MAPK phosphorylation by these inhibitors (Figures 6E and S6E). These data indicate the existence of kinase-independent functions of EGFR that are essential for TNBC cell growth and survival (Weihua et al., 2008) and further suggest that targeting the transcription of EGFR, as achieved by CDK7 inhibition, provides a unique advantage that cannot be achieved by inhibitors of EGFR kinase activity. Together, these data show that targeting CDK7-dependent transcription represents an effective means to collectively suppress the expression of multiple oncogenes that are critical for the proliferation and viability of TNBC cells.

DISCUSSION

Triple-negative breast cancer is a highly aggressive subtype of breast cancer that lacks effective therapeutics, due in part to the genetic complexity that has limited the development of “targeted” therapies. Despite its heterogeneous nature, TNBC cells share a similar transcriptional program, suggesting that tumors of this subtype may be highly dependent on expression of at least a subset of the active genes in these cells. We found that TNBC cells are exceptionally dependent on the transcriptional cyclin-dependent

kinase CDK7 and that a cluster of TNBC-specific genes is especially sensitive to CDK7 inhibition. Our results thus indicate that CDK7 mediates transcriptional addiction to this vital cluster of genes in TNBC and that CDK7 inhibition represents a highly promising therapy for this subtype of breast cancer.

CDK7 inhibition revealed an “Achilles cluster” of genes in the TNBC transcriptional program that are likely to be responsible, at least in part, for rendering these cells selectively sensitive to THZ1 treatment. These genes were identified by their overexpression in TNBC cells relative to ER/PR+ cells, their sensitivity to THZ1, and their involvement in transcriptional regulation and in signaling. This group contains putative oncogenes that are misregulated in the triple-negative disease state and essential for TNBC tumorigenicity. For example, loss of transcription factors FOSL1 or SOX9 dramatically impairs the tumorigenic potency of TNBC cells (Tam et al., 2013; Wang et al., 2013) (Figures 6 and S6). Similarly, perturbation of MET- and EGFR-mediated signaling reduces TNBC cell proliferation (Brand et al., 2014; Hsu et al., 2014; Sohn et al., 2014; Figures 6 and S6).

A striking number of genes in the TNBC “Achilles cluster” were associated with super-enhancers in triple-negative, but not in ER/PR+, breast cancer cells, suggesting a mechanism that may contribute to their sensitivity to CDK7 inhibition (Chipumuro et al., 2014; Christensen et al., 2014; Kwiatkowski et al., 2014). Transcription of many of these genes is known to be regulated by signaling pathways whose members are represented in the cluster, and super-enhancers are thought to serve as a platform

for regulation of transcription by signaling pathways. Thus, super-enhancers associated with genes in the Achilles cluster may confer sensitivity to THZ1 by two means: (1) dependency on high levels of transcription apparatus that includes the immediate target of the drug and (2) dependency on a functionally interconnected network of transcription factors and signaling components. Other genes in the cluster do not appear to be associated with super-enhancers, however, so there are likely to be other reasons for their sensitivity to CDK7 inhibition. For example, these genes may depend on continuous expression of some of the super-enhancer-driven transcription factors and may thus be affected secondarily. It is also possible that transcriptional control of this group is more dependent on CDK7 function than others (Kanin et al., 2007), perhaps because they cannot utilize alternative pathways of RNA Pol II CTD phosphorylation, such as that enabled by Erk1/2 (Tee et al., 2014).

The “Achilles cluster” of TNBC genes described here represents a collection of genes encoding transcriptional regulators and signaling components that are overexpressed in multiple TNBC cells and sensitive to CDK7 inhibition, which differs from the well-established approach of seeking a signature for a cancer subtype. Signatures typically include genes that are commonly expressed in cancer subtypes; such signatures are especially valuable when it is likely that a common gene or set of genes must be responsible for a phenotype. In contrast, when the subtype is genetically heterogeneous, we suggest that it is valuable to compile a larger collection of genes (the union of genes in multiple samples, rather than the intersection) that are affected by transcriptional inhibition in multiple cell lines or patient samples concurrent with a cellular phenotype because disregulation of different subsets of the genes in the cluster may produce the same phenotype in a cancer subtype with a complex genotype. The benefit of this approach is the potential to explain how tumor cells that are genetically heterogeneous may be dependent on diverse, yet overlapping, sets of genes.

The strategy of targeting transcription of a cluster of cancer-specific genes, as described here for TNBC, may be applicable to other difficult-to-treat cancers. Recent large-scale efforts have found that TNBC gene expression patterns are highly correlated with aggressive ovarian cancer and lung squamous carcinomas (Cancer Genome Atlas Network, 2012; Hoadley et al., 2014). As with TNBC, these cancers have a high mutation rate, an extremely high prevalence of p53 mutations, and lack a commonly altered genetic event that can be targeted for therapeutic intervention (Cancer Genome Research Network, 2011, 2012). Thus, it is possible that various aggressive tumors develop transcriptional addictions to clusters of genes that are misregulated and dependent on CDK7, and if so, CDK7 inhibition might be useful therapy for such cancers.

In summary, we have discovered a CDK7-dependent transcriptional addiction in triple-negative breast cancer and identified CDK7 inhibition as a highly selective and potent means to disrupt expression of a key cluster of genes. Our study demonstrates that inhibition of transcription is an effective strategy to target highly aggressive breast cancers with high genetic heterogeneity and lacking obvious “driver” oncogenes. Further studies will be required to determine whether these observations will translate to clinical treatment of human breast cancer.

EXPERIMENTAL PROCEDURES

Cell Culture

Human breast cancer cell lines were grown in RPMI-1640, 10% fetal bovine serum, and 1% penicillin/streptomycin. For gene knockdown assays, cells were infected with lentivirus encoding sgRNA or tetracycline-inducible shRNA. Details of cell culture, construction of plasmids, and viral infection are described in the [Supplemental Experimental Procedures](#).

Animal Studies

All animal experiments were conducted in accordance with the animal use guidelines from the NIH and with protocols approved by the Dana-Farber Cancer Institute Animal Care and Use Committee. Full details are described in the [Supplemental Experimental Procedures](#).

ChIP-Seq and Data Analysis

ChIP was performed as previously described (Lee et al., 2006), using anti-H3K27ac (Abcam, AB4729A). Details of ChIP-seq and data analysis are described in the [Supplemental Experimental Procedures](#). ChIP-Seq and gene expression microarray data are deposited in GEO: GSE69107.

Data Analysis of Gene Expression

To calculate differential expression, Log2 signal intensities were used. For each transcript, the maximum Log2 signal intensity from either of the two ER/PR+ breast cancer cell lines was subtracted from the maximum Log2 signal intensity for that transcript in either of the two TNBC cell lines. Transcripts with a difference of +2 or greater were classified as more expressed in TNBC cells. Transcripts with a difference of -2 or less were classified as more expressed in ER/PR+ breast cancer cells. For sensitivity to THZ1 treatment, transcripts were considered sensitive if the expression level declined greater than 1.5-fold upon treatment with 250 nM THZ1. Any gene with one or more transcripts that passed the two criteria described above was considered for further analysis. For gene ontology analysis, the DAVID suite of online tools (<http://david.abcc.ncifcrf.gov/tools.jsp>) was used to interrogate the molecular function ontology defined by the Gene Ontology Consortium.

ACCESSION NUMBERS

ChIP-seq and gene expression microarray data are deposited in GEO: GSE69107.

SUPPLEMENTAL INFORMATION

Supplemental Information includes Supplemental Experimental Procedures, six figures, four tables, and two movies and can be found with this article online at <http://dx.doi.org/10.1016/j.cell.2015.08.063>.

AUTHOR CONTRIBUTIONS

Y.W., T.Z., N.K., R.A.Y., N.S.G., and J.J.Z. conceived the studies. Y.W. and N.K. designed and performed the majority of experiments. T.Z. developed THZ2. B.J.A., N.K., and T.I.L. performed computational analyses. Patient-derived TNBC mouse models were developed by E.L., D.G.S., H.Y., T.V., Z.C.W., and J.D.I. Additional experiments were performed by S.X. (Ion Torrent sequencing), Z.L. (time-lapse image of cells treated with THZ1), and H.L. (cloning of CRISPR-Cas9 constructs targeting CDK7). Y.W., T.Z., N.K., R.A.Y., N.S.G., and J.J.Z. wrote the manuscript with input from all co-authors.

ACKNOWLEDGMENTS

We thank D. Wiederschain and F. Zhang for sharing the plasmids. We thank the Nikon Imaging Center at Harvard Medical School, DFCI Flow Cytometry Core Facility, and Dana-Farber/Harvard Cancer Center Rodent Histopathology Core for technical assistance and the use of instruments. This study was supported by NIH R01CA179483-01 (N.S.G.), a MIT-DFCI Bridge grant (N.S.G. and R.A.Y.), and NIH/NCI P50 CA168504 (J.Z.). N.S.G., T.Z., and

N.K. are inventors on a patent application covering THZ1 and THZ2. N.S.G. and R.A.Y. are scientific founders of Syros Pharmaceuticals, a company that has licensed THZ1 and THZ2 from the Dana-Farber Cancer Institute.

Received: January 22, 2015

Revised: May 27, 2015

Accepted: August 12, 2015

Published: September 24, 2015

REFERENCES

Abramson, V.G., Lehmann, B.D., Ballinger, T.J., and Pietenpol, J.A. (2015). Subtyping of triple-negative breast cancer: implications for therapy. *Cancer* **121**, 8–16.

Akhtar, M.S., Heidemann, M., Tietjen, J.R., Zhang, D.W., Chapman, R.D., Eick, D., and Ansari, A.Z. (2009). TFIID kinase places bivalent marks on the carboxy-terminal domain of RNA polymerase II. *Mol. Cell* **34**, 387–393.

Andre, F., Job, B., Dessen, P., Tordai, A., Michiels, S., Liedtke, C., Richon, C., Yan, K., Wang, B., Vassal, G., et al. (2009). Molecular characterization of breast cancer with high-resolution oligonucleotide comparative genomic hybridization array. *Clin. Cancer Res.* **15**, 441–451.

Bafico, A., Liu, G., Goldin, L., Harris, V., and Aaronson, S.A. (2004). An autocrine mechanism for constitutive Wnt pathway activation in human cancer cells. *Cancer Cell* **6**, 497–506.

Brand, T.M., Iida, M., Dunn, E.F., Luthar, N., Kostopoulos, K.T., Corrigan, K.L., Wleklinski, M.J., Yang, D., Wisinski, K.B., Salgia, R., and Wheeler, D.L. (2014). Nuclear epidermal growth factor receptor is a functional molecular target in triple-negative breast cancer. *Mol. Cancer Ther.* **13**, 1356–1368.

Cancer Genome Atlas Network (2012). Comprehensive molecular portraits of human breast tumours. *Nature* **490**, 61–70.

Cancer Genome Atlas Research Network (2011). Integrated genomic analyses of ovarian carcinoma. *Nature* **474**, 609–615.

Cancer Genome Atlas Research Network (2012). Comprehensive genomic characterization of squamous cell lung cancers. *Nature* **489**, 519–525.

Carey, L.A., Rugo, H.S., Marcom, P.K., Mayer, E.L., Esteva, F.J., Ma, C.X., Liu, M.C., Storniolo, A.M., Rimawi, M.F., Forero-Torres, A., et al. (2012). TBCRC 001: randomized phase II study of cetuximab in combination with carboplatin in stage IV triple-negative breast cancer. *J. Clin. Oncol.* **30**, 2615–2623.

Chapuy, B., McKeown, M.R., Lin, C.Y., Monti, S., Roemer, M.G., Qi, J., Rahl, P.B., Sun, H.H., Yeda, K.T., Doench, J.G., et al. (2013). Discovery and characterization of super-enhancer-associated dependencies in diffuse large B cell lymphoma. *Cancer Cell* **24**, 777–790.

Chin, L., Andersen, J.N., and Futreal, P.A. (2011). Cancer genomics: from discovery science to personalized medicine. *Nat. Med.* **17**, 297–303.

Chipumuro, E., Marco, E., Christensen, C.L., Kwiatkowski, N., Zhang, T., Hatheway, C.M., Abraham, B.J., Sharma, B., Yeung, C., Altabef, A., et al. (2014). CDK7 inhibition suppresses super-enhancer-linked oncogenic transcription in MYCN-driven cancer. *Cell* **159**, 1126–1139.

Christensen, C.L., Kwiatkowski, N., Abraham, B.J., Carretero, J., Al-Shahrour, F., Zhang, T., Chipumuro, E., Herter-Spriole, G.S., Akbay, E.A., Altabef, A., et al. (2014). Targeting transcriptional addictions in small cell lung cancer with a covalent CDK7 inhibitor. *Cancer Cell* **26**, 909–922.

Corkery, B., Crown, J., Clynes, M., and O'Donovan, N. (2009). Epidermal growth factor receptor as a potential therapeutic target in triple-negative breast cancer. *Ann. Oncol.* **20**, 862–867.

Dawson, M.A., Prinjha, R.K., Dittmann, A., Giopoulos, G., Bantscheff, M., Chan, W.I., Robson, S.C., Chung, C.W., Hopf, C., Savitski, M.M., et al. (2011). Inhibition of BET recruitment to chromatin as an effective treatment for MLL-fusion leukaemia. *Nature* **478**, 529–533.

Delmore, J.E., Issa, G.C., Lemieux, M.E., Rahl, P.B., Shi, J., Jacobs, H.M., Kastritis, E., Gilpatrick, T., Paranjal, R.M., Qi, J., et al. (2011). BET bromodomain inhibition as a therapeutic strategy to target c-Myc. *Cell* **146**, 904–917.

Drapkin, R., Le Roy, G., Cho, H., Akoulitchev, S., and Reinberg, D. (1996). Human cyclin-dependent kinase-activating kinase exists in three distinct complexes. *Proc. Natl. Acad. Sci. USA* **93**, 6488–6493.

Fisher, R., Pusztai, L., and Swanton, C. (2013). Cancer heterogeneity: implications for targeted therapeutics. *Br. J. Cancer* **108**, 479–485.

Gewinner, C., Wang, Z.C., Richardson, A., Teruya-Feldstein, J., Etemadmoghadam, D., Bowtell, D., Barretina, J., Lin, W.M., Rameh, L., Salmena, L., et al. (2009). Evidence that inositol polyphosphate 4-phosphatase type II is a tumor suppressor that inhibits PI3K signaling. *Cancer Cell* **16**, 115–125.

Glover-Cutter, K., Larochelle, S., Erickson, B., Zhang, C., Shokat, K., Fisher, R.P., and Bentley, D.L. (2009). TFIID-associated Cdk7 kinase functions in phosphorylation of C-terminal domain Ser7 residues, promoter-proximal pausing, and termination by RNA polymerase II. *Mol. Cell. Biol.* **29**, 5455–5464.

Guo, W., Keckesova, Z., Donaher, J.L., Shibue, T., Tischler, V., Reinhardt, F., Itzkovitz, S., Noske, A., Zurrer-Hardi, U., Bell, G., et al. (2012). Slug and Sox9 cooperatively determine the mammary stem cell state. *Cell* **148**, 1015–1028.

Hnisz, D., Abraham, B.J., Lee, T.I., Lau, A., Saint-André, V., Sigova, A.A., Hoke, H.A., and Young, R.A. (2013). Super-enhancers in the control of cell identity and disease. *Cell* **155**, 934–947.

Hnisz, D., Schijpers, J., Lin, C.Y., Weintraub, A.S., Abraham, B.J., Lee, T.I., Bradner, J.E., and Young, R.A. (2015). Convergence of developmental and oncogenic signaling pathways at transcriptional super-enhancers. *Mol. Cell* **58**, 362–370.

Hadley, K.A., Yau, C., Wolf, D.M., Cherniack, A.D., Tamborero, D., Ng, S., Leiserson, M.D., Niu, B., McLellan, M.D., Uzunangelov, V., et al.; Cancer Genome Atlas Research Network (2014). Multiplatform analysis of 12 cancer types reveals molecular classification within and across tissues of origin. *Cell* **158**, 929–944.

Hsu, Y.H., Yao, J., Chan, L.C., Wu, T.J., Hsu, J.L., Fang, Y.F., Wei, Y., Wu, Y., Huang, W.C., Liu, C.L., et al. (2014). Definition of PKC- α , CDK6, and MET as therapeutic targets in triple-negative breast cancer. *Cancer Res.* **74**, 4822–4835.

Kanin, E.I., Kipp, R.T., Kung, C., Slattery, M., Viale, A., Hahn, S., Shokat, K.M., and Ansari, A.Z. (2007). Chemical inhibition of the TFIID-associated kinase Cdk7/Kin28 does not impair global mRNA synthesis. *Proc. Natl. Acad. Sci. USA* **104**, 5812–5817.

Knight, J.F., Lesurf, R., Zhao, H., Pinnaduwage, D., Davis, R.R., Saleh, S.M., Zuo, D., Naujokas, M.A., Chughtai, N., Herschkowitz, J.I., et al. (2013). Met synergizes with p53 loss to induce mammary tumors that possess features of claudin-low breast cancer. *Proc. Natl. Acad. Sci. USA* **110**, E1301–E1310.

Kwiatkowski, N., Zhang, T., Rahl, P.B., Abraham, B.J., Reddy, J., Ficarro, S.B., Dastur, A., Amzallag, A., Ramaswamy, S., Tesar, B., et al. (2014). Targeting transcription regulation in cancer with a covalent CDK7 inhibitor. *Nature* **511**, 616–620.

Larochelle, S., Merrick, K.A., Terret, M.E., Wohlbond, L., Barboza, N.M., Zhang, C., Shokat, K.M., Jallepalli, P.V., and Fisher, R.P. (2007). Requirements for Cdk7 in the assembly of Cdk1/cyclin B and activation of Cdk2 revealed by chemical genetics in human cells. *Mol. Cell* **25**, 839–850.

Larochelle, S., Amat, R., Glover-Cutter, K., Sansó, M., Zhang, C., Allen, J.J., Shokat, K.M., Bentley, D.L., and Fisher, R.P. (2012). Cyclin-dependent kinase control of the initiation-to-elongation switch of RNA polymerase II. *Nat. Struct. Mol. Biol.* **19**, 1108–1115.

Lee, T.I., Johnstone, S.E., and Young, R.A. (2006). Chromatin immunoprecipitation and microarray-based analysis of protein location. *Nat. Protoc.* **1**, 729–748.

Lovén, J., Hoke, H.A., Lin, C.Y., Lau, A., Orlando, D.A., Vakoc, C.R., Bradner, J.E., Lee, T.I., and Young, R.A. (2013). Selective inhibition of tumor oncogenes by disruption of super-enhancers. *Cell* **153**, 320–334.

Lu, G., Zhang, Q., Huang, Y., Song, J., Tomaino, R., Ehrenberger, T., Lim, E., Liu, W., Bronson, R.T., Bowden, M., et al. (2014a). Phosphorylation of ETS1 by Src family kinases prevents its recognition by the COP1 tumor suppressor. *Cancer Cell* **26**, 222–234.

Parker, J.S., Mullins, M., Cheang, M.C., Leung, S., Voduc, D., Vickery, T., Davies, S., Fauron, C., He, X., Hu, Z., et al. (2009). Supervised risk predictor of breast cancer based on intrinsic subtypes. *J. Clin. Oncol.* 27, 1160–1167.

Perou, C.M., Sørlie, T., Eisen, M.B., van de Rijn, M., Jeffrey, S.S., Rees, C.A., Pollack, J.R., Ross, D.T., Johnsen, H., Akslen, L.A., et al. (2000). Molecular portraits of human breast tumours. *Nature* 406, 747–752.

Pukrop, T., Klemm, F., Hagemann, T., Grädl, D., Schulz, M., Siemes, S., Trümper, L., and Binder, C. (2006). Wnt 5a signaling is critical for macrophage-induced invasion of breast cancer cell lines. *Proc. Natl. Acad. Sci. USA* 103, 5454–5459.

Schachter, M.M., and Fisher, R.P. (2013). The CDK-activating kinase Cdk7: taking yes for an answer. *Cell Cycle* 12, 3239–3240.

Scheel, C., Eaton, E.N., Li, S.H., Chaffer, C.L., Reinhardt, F., Kah, K.J., Bell, G., Guo, W., Rubin, J., Richardson, A.L., and Weinberg, R.A. (2011). Paracrine and autocrine signals induce and maintain mesenchymal and stem cell states in the breast. *Cell* 145, 926–940.

Shah, S.P., Roth, A., Goya, R., Oloumi, A., Ha, G., Zhao, Y., Turashvili, G., Ding, J., Tse, K., Haffari, G., et al. (2012). The clonal and mutational evolution spectrum of primary triple-negative breast cancers. *Nature* 486, 395–399.

Shapiro, G.I. (2006). Cyclin-dependent kinase pathways as targets for cancer treatment. *J. Clin. Oncol.* 24, 1770–1783.

Sohn, J., Liu, S., Parinyanitkul, N., Lee, J., Hortobagyi, G.N., Mills, G.B., Ueno, N.T., and Gonzalez-Angulo, A.M. (2014). cMET Activation and EGFR-Directed Therapy Resistance in Triple-Negative Breast Cancer. *J. Cancer* 5, 745–753.

Tam, W.L., Lu, H., Buikhuisen, J., Soh, B.S., Lim, E., Reinhardt, F., Wu, Z.J., Krall, J.A., Bierie, B., Guo, W., et al. (2013). Protein kinase C α is a central signaling node and therapeutic target for breast cancer stem cells. *Cancer Cell* 24, 347–364.

Taube, J.H., Herschkowitz, J.I., Komurov, K., Zhou, A.Y., Gupta, S., Yang, J., Hartwell, K., Onder, T.T., Gupta, P.B., Evans, K.W., et al. (2010). Core epithelial-to-mesenchymal transition interactome gene-expression signature is associated with claudin-low and metaplastic breast cancer subtypes. *Proc. Natl. Acad. Sci. USA* 107, 15449–15454.

Tee, W.W., Shen, S.S., Oksuz, O., Narendra, V., and Reinberg, D. (2014). Erk1/2 activity promotes chromatin features and RNAPII phosphorylation at developmental promoters in mouse ESCs. *Cell* 156, 678–690.

Truong, H.H., Xiong, J., Ghotra, V.P., Nirmala, E., Haazen, L., Le Dévédec, S.E., Balcioğlu, H.E., He, S., Snaar-Jagalska, B.E., Vreugdenhil, E., et al. (2014). β 1 integrin inhibition elicits a prometastatic switch through the TGF β -miR-200-ZEB network in E-cadherin-positive triple-negative breast cancer. *Sci. Signal.* 7, ra15.

Ueno, N.T., and Zhang, D. (2011). Targeting EGFR in triple negative breast cancer. *J. Cancer* 2, 324–328.

Wang, H., He, L., Ma, F., Regan, M.M., Balk, S.P., Richardson, A.L., and Yuan, X. (2013). SOX9 regulates low density lipoprotein receptor-related protein 6 (LRP6) and T-cell factor 4 (TCF4) expression and Wnt/ β -catenin activation in breast cancer. *J. Biol. Chem.* 288, 6478–6487.

Watabe, T., Yoshida, K., Shindoh, M., Kaya, M., Fujikawa, K., Sato, H., Seiki, M., Ishii, S., and Fujinaga, K. (1998). The Ets-1 and Ets-2 transcription factors activate the promoters for invasion-associated urokinase and collagenase genes in response to epidermal growth factor. *Int. J. Cancer* 77, 128–137.

Weihua, Z., Tsan, R., Huang, W.C., Wu, Q., Chiu, C.H., Fidler, I.J., and Hung, M.C. (2008). Survival of cancer cells is maintained by EGFR independent of its kinase activity. *Cancer Cell* 13, 385–393.

Whyte, W.A., Orlando, D.A., Hnisz, D., Abraham, B.J., Lin, C.Y., Kagey, M.H., Rahl, P.B., Lee, T.I., and Young, R.A. (2013). Master transcription factors and mediator establish super-enhancers at key cell identity genes. *Cell* 153, 307–319.

Xu, J., Chen, Y., and Olopade, O.I. (2010). MYC and Breast Cancer. *Genes Cancer* 1, 629–640.

Yang, J., Mani, S.A., Donaher, J.L., Ramaswamy, S., Itzykson, R.A., Come, C., Savagner, P., Gitelman, I., Richardson, A., and Weinberg, R.A. (2004). Twist, a master regulator of morphogenesis, plays an essential role in tumor metastasis. *Cell* 117, 927–939.

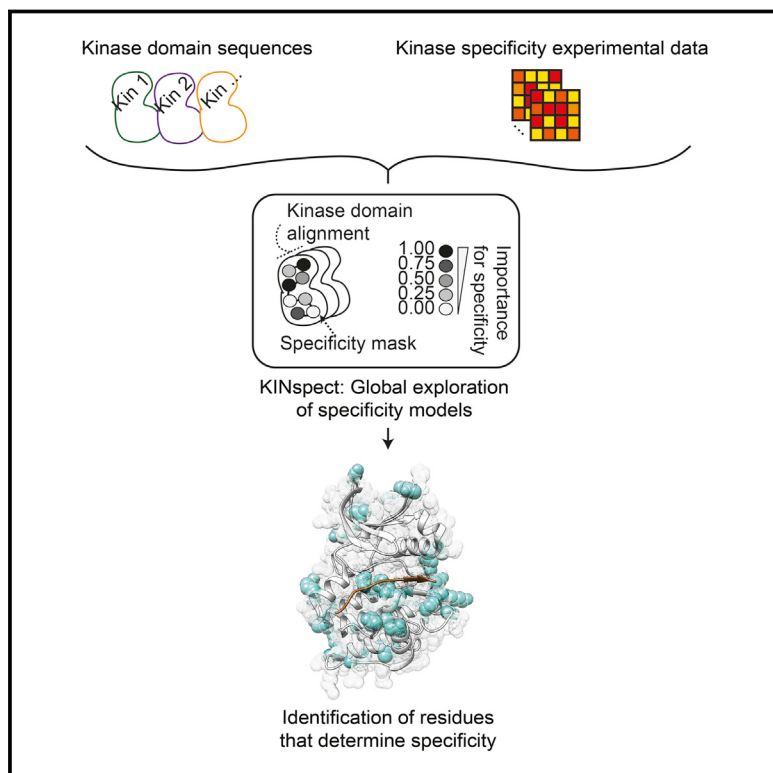
Yang, L., Wu, X., Wang, Y., Zhang, K., Wu, J., Yuan, Y.C., Deng, X., Chen, L., Kim, C.C., Lau, S., et al. (2011). FZD7 has a critical role in cell proliferation in triple negative breast cancer. *Oncogene* 30, 4437–4446.

Zhou, Q., Li, T., and Price, D.H. (2012). RNA polymerase II elongation control. *Annu. Rev. Biochem.* 81, 119–143.

Zuber, J., Shi, J., Wang, E., Rappaport, A.R., Herrmann, H., Sison, E.A., Magooon, D., Qi, J., Blatt, K., Wunderlich, M., et al. (2011). RNAi screen identifies Brd4 as a therapeutic target in acute myeloid leukaemia. *Nature* 478, 524–528.

Unmasking Determinants of Specificity in the Human Kinome

Graphical Abstract



Authors

Pau Creixell, Antonio Palmeri,
Chad J. Miller, ..., Morten Nielsen,
Benjamin E. Turk, Rune Linding

Correspondence

creixell@mit.edu (P.C.),
linding@lindinglab.org (R.L.)

In Brief

Determining the residues that drive the specificity of kinases and of SH2 domains that bind phosphorylation sites paves the way for a systematic interpretation of mutations on signaling networks.

Highlights

- Residues driving specificity in the kinase and SH2 domains are globally identified
- Three new such residues, termed α C1, α C3, and APE-7, are experimentally validated
- Specificity and catalytic activity appear to be encoded in distinct sets of residues
- The global identification of determinants allows the modeling of rewiring mutations



Unmasking Determinants of Specificity in the Human Kinome

Pau Creixell,^{1,5,*} Antonio Palmeri,² Chad J. Miller,³ Hua Jane Lou,³ Cristina C. Santini,^{1,4} Morten Nielsen,¹ Benjamin E. Turk,³ and Rune Linding^{1,4,*}

¹Department of Systems Biology, Technical University of Denmark, 2800 Lyngby, Denmark

²Centre for Molecular Bioinformatics, University of Rome Tor Vergata, 00133 Rome, Italy

³Department of Pharmacology, Yale University School of Medicine, New Haven, CT 06520, USA

⁴Biotech Research & Innovation Centre (BRIC), University of Copenhagen (UCPH), 2200 Copenhagen, Denmark

⁵Present address: Koch Institute for Integrative Cancer Research, Massachusetts Institute of Technology (MIT), Cambridge, MA 02139, USA

*Correspondence: creixell@mit.edu (P.C.), linding@lindinglab.org (R.L.)

<http://dx.doi.org/10.1016/j.cell.2015.08.057>

This is an open access article under the CC BY license (<http://creativecommons.org/licenses/by/4.0/>).

SUMMARY

Protein kinases control cellular responses to environmental cues by swift and accurate signal processing. Breakdowns in this high-fidelity capability are a driving force in cancer and other diseases. Thus, our limited understanding of which amino acids in the kinase domain encode substrate specificity, the so-called determinants of specificity (DoS), constitutes a major obstacle in cancer signaling. Here, we systematically discover several DoS and experimentally validate three of them, named the α C1, α C3, and APE-7 residues. We demonstrate that DoS form sparse networks of non-conserved residues spanning distant regions. Our results reveal a likely role for inter-residue allosteric coupling in specificity and an evolutionary decoupling of kinase activity and specificity, which appear loaded on independent groups of residues. Finally, we uncover similar properties driving SH2 domain specificity and demonstrate how the identification of DoS can be utilized to elucidate a greater understanding of the role of signaling networks in cancer (Creixell et al., 2015 [this issue of Cell]).

INTRODUCTION

Cellular organization and response to external and internal cues relies on swift and precise processing of information through cell signaling networks. High fidelity in these circuits depends critically on the recognition and phosphorylation of specific substrates by protein kinases, and perturbations of this cellular system have been linked to significant evolutionary transitions (Capra et al., 2012; Skerker et al., 2008; Tan et al., 2009; Zarrinpar et al., 2003), as well as to disease progression, in particular, in cancer (Borrello et al., 1995; Creixell et al., 2012; Marengere et al., 1994; Santoro et al., 1995; Songyang et al., 1995).

Cellular signaling fidelity is maintained essentially through two coupled mechanisms. At a macro-molecular level, protein spec-

ificity ensures that each protein kinase will reach and interact with its protein substrates. At a micro-molecular or atomic level, peptide specificity defines the ability of a given kinase domain present in all active protein kinases to recognize and phosphorylate a specific peptide within the protein substrate (Turk, 2008) (Figure 1A). A variety of experimental techniques have been developed to elucidate the peptide specificity for many modular signaling domains and obtain specificity profiles (e.g., the so-called Position-Specific Scoring Matrices, PSSMs), as a quantitative measure of the preference of each kinase domain for each amino acid residue at every peptide substrate position (Figure S1). While other factors contributing to protein interaction specificity at a macro-molecular level (such as co-localization, co-expression, docking motifs, and scaffold or adaptor proteins) have been described (Bhattacharyya et al., 2006; Linding et al., 2007; Reményi et al., 2005; Scott and Pawson, 2009), the combination of residues in the kinase domain that encode peptide substrate specificity, the so-called determinants of specificity (DoS), have remained largely elusive (Figure 1B). Even though some structural studies have helped identify residues that are in close contact with the substrate peptide which likely influence specificity (Brinkworth et al., 2003; Ellis and Kobe, 2011; Hanks and Hunter, 1995; Mok et al., 2010; Nolen et al., 2004), these studies were largely focused on specific kinase families and/or non-human species as well as limited in scope by the small number of kinase-peptide structures currently available and an inability to capture potentially long-range DoS.

Here, we present a computational approach that aims to overcome these limitations and address the following open questions. Which residues within the kinase domain contribute to peptide specificity (constituting the so-called DoS)? Are these determinants just a small group of residues localized in close proximity to the substrate as currently thought, or do they form a sparse network of residues instead (Figure 1C)? Are such principles of domain-peptide specificity conserved in other domains? Finally, how do these DoS relate, spatially and functionally, to those residues known to be involved in the regulation and catalytic activity of the kinase domain? In other words, are these different functionalities loaded onto the same residues or on independent groups of residues, and how did they evolve?

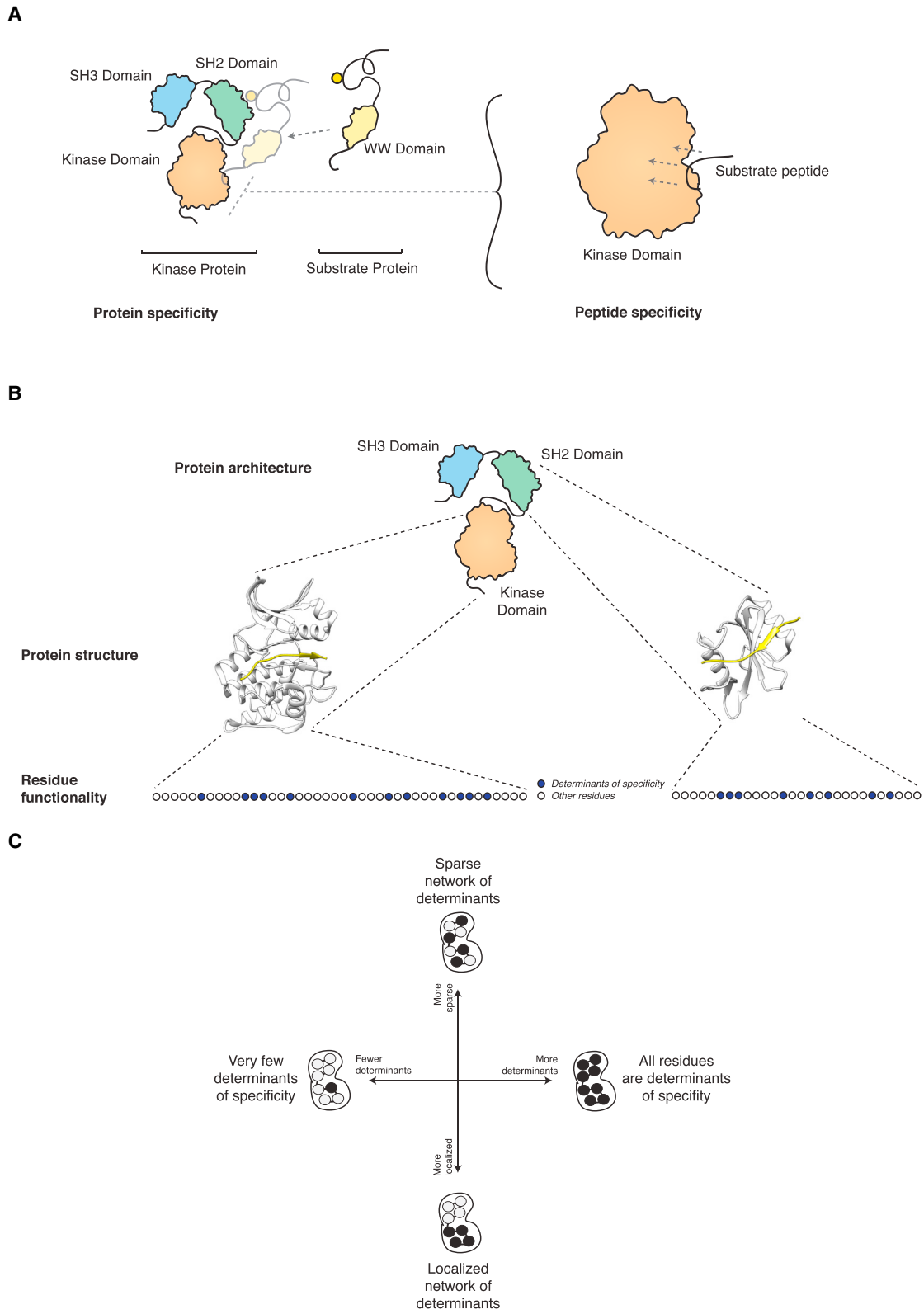


Figure 1. Open Questions in Protein Domain-Peptide Specificity

(A) Protein specificity determines the interaction between the whole kinase protein and its substrates and is driven by processes such as interactions between other domains and motifs (e.g., SH2 and phospho-tyrosine in this figure), co-expression of the two proteins, cellular localization, scaffold proteins, etc.

(legend continued on next page)

As we demonstrate in our accompanying article (Creixell et al., 2015 [this issue of *Cell*]), which explores how cancer mutations affect domain specificity by integrating the DoS identified here, resolving these questions could represent a valuable contribution not only for basic signaling biology but also for cancer research.

RESULTS

Learning about Residue Contributions to Specificity by Sampling over Different Specificity Masks

When investigating the relationship between kinases at the domain primary sequence similarity level and at the substrate sequence motif similarity level (using specificity profiles or PSSMs derived from Positional Scanning Peptide Library or PSPL experiments, see [Experimental Procedures](#) and [Figure S1](#)), it is apparent that, when considering the domain in its entirety, no strong linear correlation between these exists ([Figure S1](#)). We hypothesized that this lack of correlation could indicate that substrate specificity is not encoded by the domain as a whole. Instead, we hypothesized that a limited number of residues contribute to specificity, and that those that do contribute, are likely to do so to different degrees. In order to capture this principle, we introduced the specificity mask as a fundamental entity in our approach. As depicted in [Figures 1B](#) and [2](#) (small box), a specificity mask is defined as a particular combination of contributions to specificity from the different residues in the kinase domain. For example, an extreme hypothesis where all residues within the kinase domain contribute equally to specificity would be represented by all entries in a mask with the same score (e.g., 0.5). Instead, a situation where a single residue, X, would drive specificity would be represented by all entries scoring 0.0 except position X scoring 1.0.

Our approach (described below) explores the possibility that within a large ensemble of specificity masks, certain masks can discriminate between kinases with dissimilar substrate specificities better than others. These masks will range from those capturing very few and localized DoS (reminiscent of models explored in the structural studies; Brinkworth et al., 2003; Ellis and Kobe, 2011; Hanks and Hunter, 1995; Mok et al., 2010; Nolen et al., 2004) to those capturing a larger number of determinants distributed more sparsely across the kinase domain ([Figure 1C](#)). As further detailed in the next section, since our aim was to identify new DoS following an unbiased data-driven systematic approach, we did not impose any restrictions in the set of specificity masks that can be found; instead, we explore a large set of possible specificity masks and let the system evolve and find those showing the best discriminatory capabilities.

The KINspect Methodology

In order to identify which residues contribute to specificity, we developed a computational framework named KINspect, which explores a very large number of combinations of residues, and their contribution toward specificity, and subsequently identifies those featuring the best predictive capability ([Figure 2](#)). This type of approach, known in machine learning as learning classifier systems (Lanzi et al., 2000), enables the selection of the best-performing set of specificity masks starting from a large initial set of random masks by following three consecutive steps ([Figure 2](#)).

First, for each specificity mask, the specificity profiles (PSSMs) for each kinase are predicted by comparing all kinases across the human kinome at each amino acid position within the kinase domain (amino acid similarity) and by incorporating a weighting factor (from 0 to 1; 0 being not important, 1 being critical) of the “specificity importance” of each position as determined by the given specificity mask. A PSSM for each kinase is then predicted by integrating the PSSMs for the other kinases using the mask-dependent similarity as a weighting factor. Naturally, the majority of masks within the original set of random masks will predict specificity poorly, but, as the system evolves, the masks will improve their predictive power, i.e., become more fit.

Second, masks are ranked according to their predictive performance (i.e., their ability to predict PSSMs that are similar to the experimentally determined PSSMs). In essence, masks that more closely capture the true contribution of each position within the kinase domain (i.e., those scoring higher at kinase domain positions that truly contribute to specificity) will result in a better prediction of the specificity profiles, thus ranking higher.

Third, the worst-performing masks are filtered out and new masks, representing both subtle (mutation) but also more abrupt (cross-over) variations of the best-performing masks, will be added.

These three steps are initially started with random specificity masks and repeated until convergence is reached and fitness cannot be optimized further. Residues consistently scoring higher in the specificity masks following the optimization procedure will be considered candidate DoS. For a more technical description of the algorithm, please refer to [Figure 2](#) and [Extended Experimental Procedures](#).

Model Robustness, Validation, and Coverage

Since our method contains stochastic aspects (such as the starting set of random masks and the generation of new masks by mutation and cross-over), one initial question that must be addressed is whether the method is robust to this initial stochasticity, i.e., whether one would obtain similar results if the process was started with arbitrary initial conditions and evaluated independently several times. To this end, we compared the fitness evolution of ten independent KINspect evaluations and found

(Bhattacharyya et al., 2006; Linding et al., 2007; Reményi et al., 2005; Scott and Pawson, 2009). Peptide specificity, in contrast, is solely driven by the sequence and structure of the kinase domain and drives the phosphorylation of specific linear motifs within the substrate protein.

(B) The so-called determinants of specificity (DoS) are those residues within a protein domain that together drive and determine the peptide specificity of the domain.

(C) While relatively few localized DoS have been described in the kinase domain, this study explores the existence of more determinants and their relative domain positions.

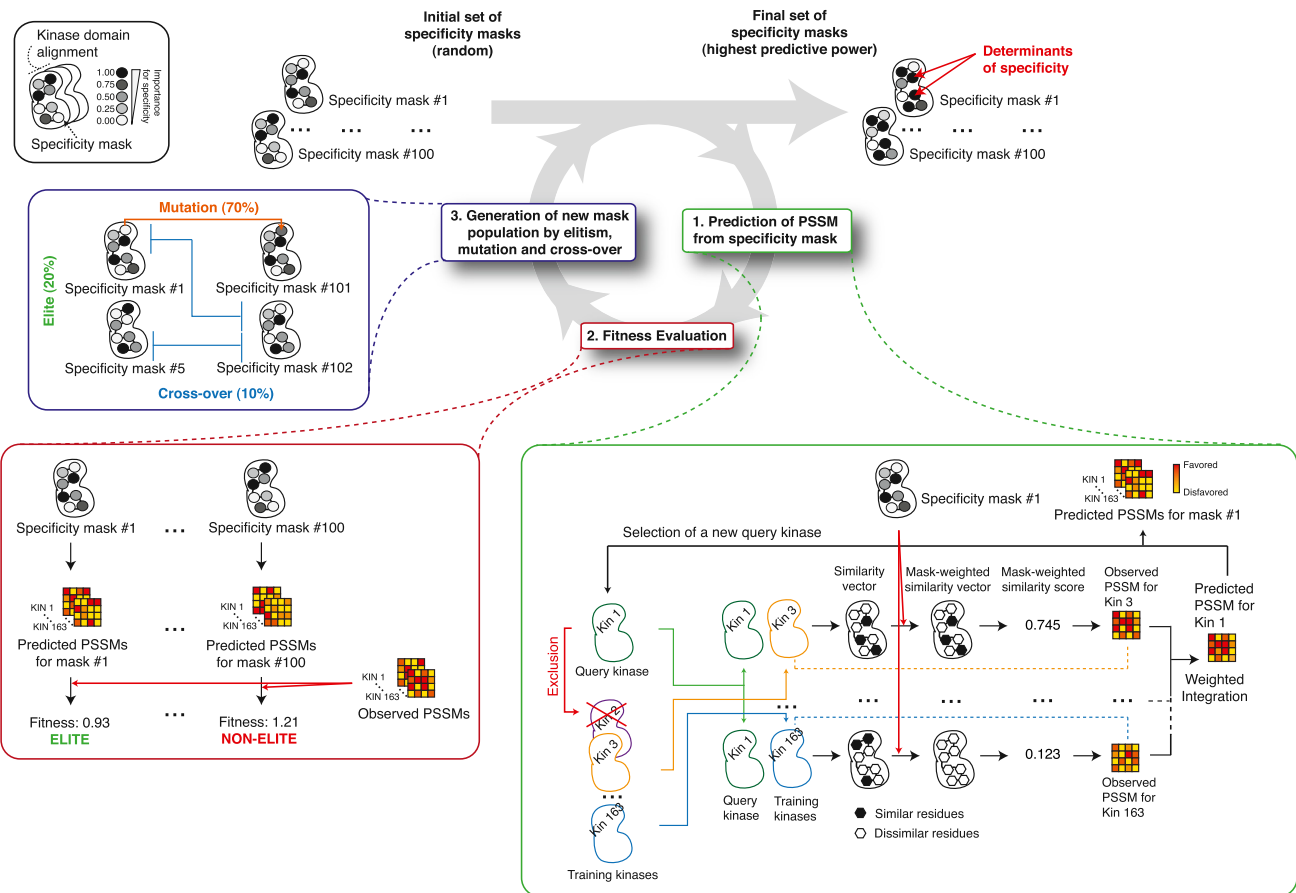


Figure 2. Overview of the KINspect Algorithm

The KINspect workflow is designed to identify the specificity mask that best describes the importance of the different residues for specificity. Different combinations of contributions to specificity by different kinase domain residues are collected as specificity masks (top left), where a score between 0 and 1 is given to each position within the kinase domain. Originally, the specificity masks are initialized with random values to then follow a machine-learning procedure that will ensure the masks with the highest predictive power toward specificity are selected for and optimized. This procedure, known as a learning classifier system, is divided into three separate steps.

In step 1, for each specificity mask the system loops over all query kinases and, using a kinase domain alignment, compares the query kinase to all other kinases (except those belonging to the same kinase family, which are excluded only at this stage to avoid over-fitting) at the sequence level, generating a similarity vector. This vector is combined with the specificity mask, so that similarity in high-scoring positions of the mask is reinforced and similarity in low-scoring position of the mask is silenced, effectively producing a mask-weighted similarity vector and sum score for each kinase. These values are subsequently used to integrate the different observed PSSMs into a combined predicted PSSM for the query kinase (as further explained by the equations and text in *Supplemental Experimental Procedures* section and in Zhang et al., 2009).

In step 2, after a predicted kinase has been generated for all the kinases in our set, fitness is computed as the median of all the differences between the predicted and the experimentally determined PSSM for all the kinases obtained from the NetPhorest repository (Miller et al., 2008).

In step 3, the best-performing specificity masks are kept ("elite"), and new ones are generated by mutation (changing the value of a given position in the mask) and cross-over of the elite sequences (combining two segments of two other masks), as typically done in genetic algorithms. Once a new set of masks has been generated, the whole procedure (prediction, fitness evaluation, and generation of new masks) is repeated iteratively until fitness (defined as median error between predicted and observed specificity profiles) cannot be improved any further (i.e., convergence is reached).

Residues scoring high in the optimized specificity masks will be considered candidate DoS. For further details on this procedure, please refer to *Supplemental Experimental Procedures*.

highly comparable fitness trajectories, as well as increasing similarity between the best-performing masks at each generation (Figure S2; Data S1, S2, and S3). Moreover, we confirmed that the results are not simply due to trivial technical factors, such as residue conservation or alignment gaps (Figure S3), and that similar results could not be obtained using uniform or randomized sets (Figure S3). Taken together, these results

demonstrate that KINspect is robust to arbitrary initial conditions and converges to a limited set of highly similar solutions (specificity masks, Figure S3).

Moreover, we also explored a vast number of possible combinations of residues and specificity models. Since convergence in the model requires approximately 2,500 cycles of the above three steps (in the case of the human kinase domain) and 100

specificity masks are used at every generation, 250,000 models were explored in the kinase-wide search for the most informative masks. By repeating this algorithmic deployment independently ten times with arbitrary initial conditions, 2,500,000 models were explored in total. The high number of models explored and the fact that the independent evaluations converge on their solutions imparted confidence that the results obtained could be close to the “true mask” of specificity.

In order to further benchmark our approach, we collected an inclusive “golden list” of residues that had been suggested or predicted as DoS (Table S1) in the literature covering a variety of methods and species (Brinkworth et al., 2003; Hanks and Hunter, 1995; Johnson et al., 1998; Mok et al., 2010; Nolen et al., 2004) and explored the possibility that the best masks would be enriched in this set of “golden” determinants. Indeed, Figure S3 shows that, while the distributions over specificity scores of previously reported DoS and other residues are probabilistically equivalent at the start of the optimization process, they are remarkably different at the end of it, supporting the aforementioned enrichment (Fisher’s exact test one sided, $p = 8.4 \times 10^{-7}$).

In addition to identifying candidate DoS, our approach can predict the domain specificity (PSSM) of every kinase in the human kinase from sequence alone. Therefore, we could compare these to those kinases where the specificity profile has previously been experimentally determined (Miller et al., 2008) and assess the algorithm’s predictive accuracy (Figure S2). As shown in Figure S2, KINspect presents better sequence-specificity predictive capabilities for some families (e.g., CK1 group) than others (e.g., STE group), likely reflecting both biological differences and algorithmic preferences (for instance, particular family differences in specificity that could not be captured by our kinase-wide specificity masks). Finally, for a small set of kinases used as a “gold standard” in the DREAM challenge (Ellis and Kobe, 2011) and that, importantly, were not part of our training set, we could confirm that overall KINspect performed better than other methods (Figure S3).

While the results in Figure S3E confirm enrichment in previously reported DoS, it is also important to note that KINspect identified a large number of additional DoS that had not been reported in the literature (e.g., 82 alignment positions above the arbitrary threshold of having a KINspect score above 0.8). Thus, we set out to evaluate the likelihood that these newly identified residues would be true DoS. Following up on our initial reasoning, we hypothesized that by identifying true DoS (the kinase domain residues that truly encode for the domain’s specificity) one should be able to observe better correlations between kinase sequence and kinase specificity, by limiting the comparison to this specific set of residues. Indeed, Figure 3A illustrates how limiting the comparison to those residues that obtained higher KINspect scores not only maintains, but, in fact, improves the sequence-to-specificity correlation by approximately 20% (as compared to the Spearman correlation obtained by considering the entire domain). Furthermore, we could confirm that other similarly small groups of residues, such as the set of previously reported DoS, or other selection strategies, such as residues close to the substrate, do not lead to similar improvements of the sequence-to-specificity correlation (Figure 3A; Figure S4).

We next selected a group of residues predicted by KINspect to be DoS and devised PSPL experiments to experimentally validate their involvement in specificity. In particular, as shown in Figure 3B, for our first experiment we selected two of the candidate DoS predicted by KINspect (named α C1 and α C3 as they are located on the first and third residues of the α C helix of the kinase domain) with scores of 1.0 and 0.95 that are in close proximity to residue P+2 in the peptide substrate. Next, since PKC γ has a strong preference for Arg and Lys at P+2 that had so far defied structural analysis, we mutated the α C1 and α C3 residues on PKC γ from the wild-type aspartates to alanines. As shown in Figure 3C (and Figure S4), the mutant form maintained the Arg preference but lost its Lys preference at this particular position, at the same time gaining preference for aromatic residues, thereby validating the specificity determining nature of these DoS predicted by KINspect.

For our second experiment, we selected a position (named APE-7 as it is located seven residues before the APE motif delimiting the activation segment) with a score of 0.75 in close proximity to residue P+1 (Figure 3B). Similar to the case of PKC γ in the α C1 and α C3 residues, Pim1 features an unexplained strong preference for Gly on position P+1, which is unusual for a kinase belonging to the CAMK family. Thus, we mutated Pim1 from its wild-type Asp to Cys, a residue more typically seen in other CAMK kinases, hypothesizing that if this single substitution could abrogate this Gly preference on position P+1, it would prove the specificity driving nature of the APE-7 residue. As shown in Figure 3C (and Figure S4), indeed this single-point mutation on Pim1 leads to a shift away from P+1 Gly preference to a non-specific profile similar to that of other CAMKs.

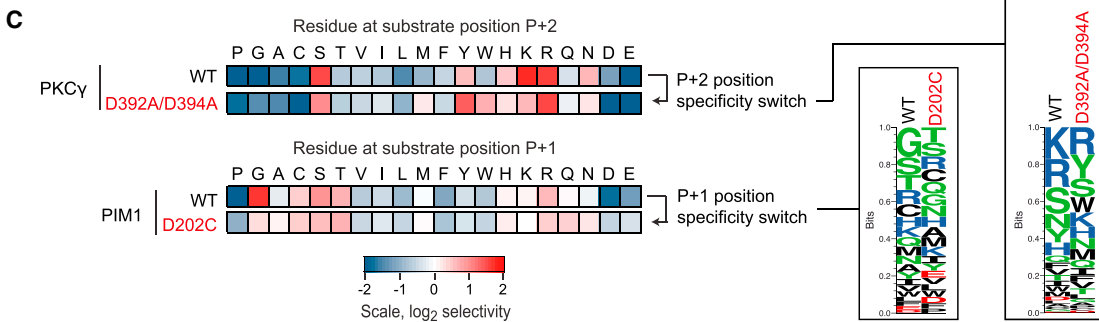
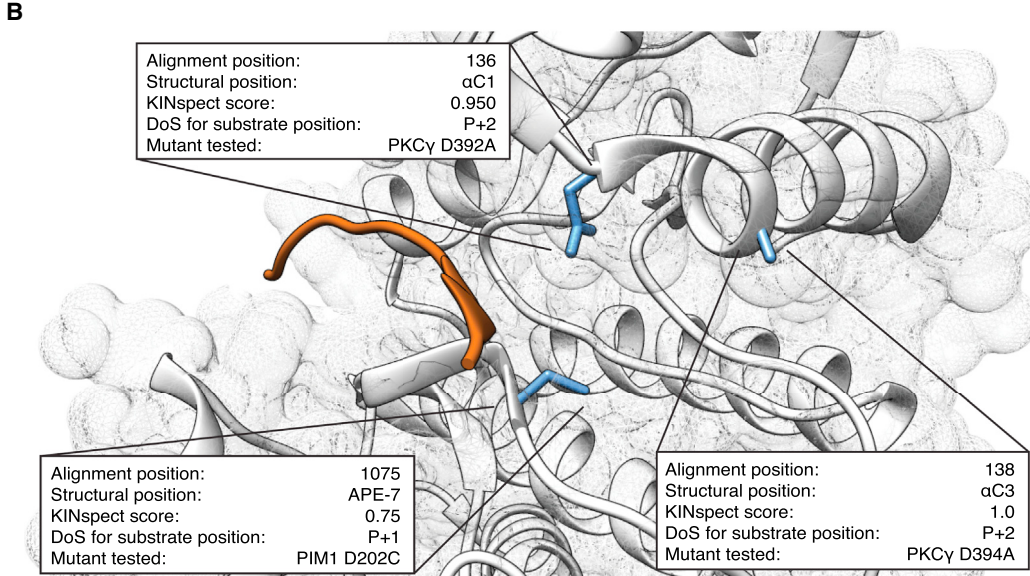
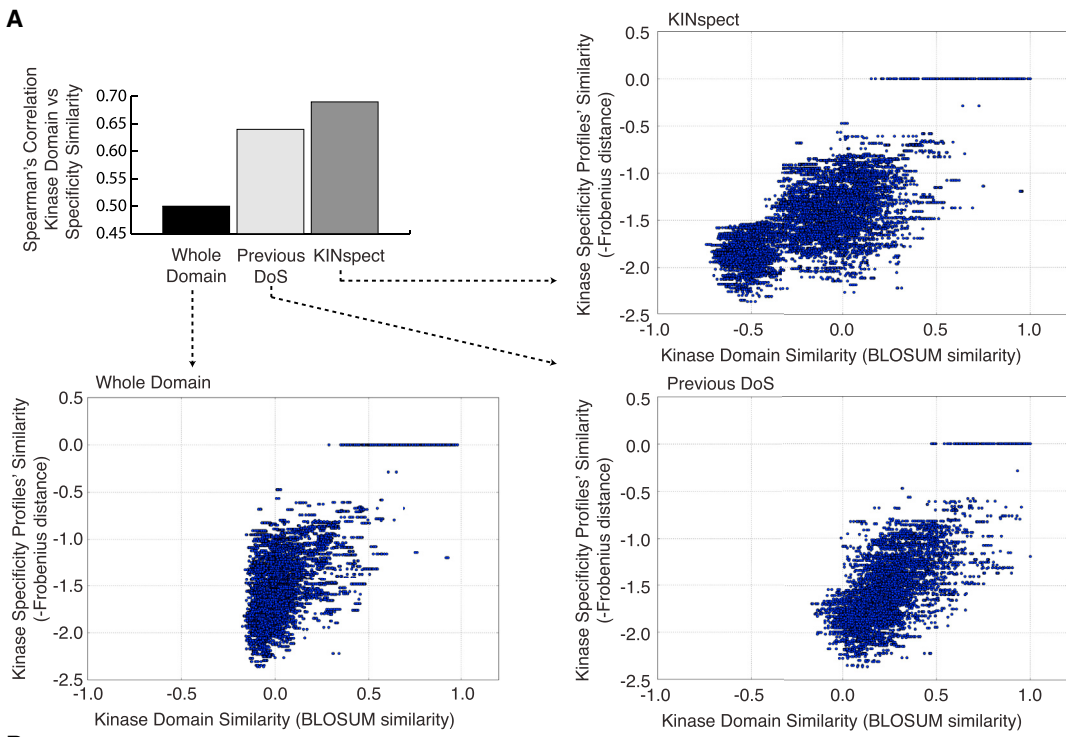
Taken together, these results demonstrate that KINspect successfully identified a set of residues on which the specificity of the entire domain is encoded.

The Determinants Form Sparse Networks of Residues that Together Encode Specificity

In order to evaluate the relationship between the different DoS, as well as between the DoS and the peptide substrate, we investigated their spatial distribution in the kinase domain. Figure 4 and Movie S1 show the tertiary structure of the DoS identified by KINspect (alignment positions above the arbitrary threshold of having a KINspect score above 0.9 across ten independent deployments of KINspect) and offers two interesting observations:

First, we note that several of the determinants localize relatively far from the peptide substrate. However, most of these distant DoS seem coupled to other DoS through “canals” (i.e., existing structural paths connecting the different DoS among each other and ultimately with the substrate) that eventually contact the substrate peptide, as shown, for instance, in Figures 4B, 4C, or 4J. Such distribution of residues in networks spanning different domain sites and the presence of these “canals” suggest that specificity could possibly be encoded by groups of residues that communicate from different parts of the domain, perhaps in a similar manner to which other domains are regulated allosterically through protein sectors (Reynolds et al., 2011).

Second, closer inspection of the results (Figure 4; Movie S1) suggests the presence of three clusters of DoS that, while



(legend on next page)

connected by other residues that (to a lesser extent) are also likely to contribute to specificity, are located on different patches of the kinase domain: cluster 1, while mainly containing residues from the bigger C-lobe (the lobe best described in terms of its importance for kinase specificity), also spans residues from the N-lobe and contacts directly with, and to a large degree encapsulates, the substrate peptide. This could be considered the main cluster directly driving specificity and includes several of the residues and structural features previously linked to specificity (e.g., the activation segment or the P+1 loop; Nolen et al., 2004), as well as new ones, such as the residues in the α C helix that we experimentally validated to encode specificity. Cluster 2, on the other hand, is comparably smaller and contains exclusively residues belonging to the big C-lobe of the domain. Given its position, we suggest that this cluster of residues could affect specificity by closing (or opening) the domain inward (or outward), effectively modifying the size and shape of the binding pocket, especially on the region that contacts the N-terminal section of the substrate peptide. Finally, cluster 3, containing very few residues of the small N-lobe, seems to contribute to specificity by causing subtle structural re-arrangements leading to differences in the opening and closing of the lobe onto the peptide. Overall, while all three clusters simultaneously encode specificity on different parts of the substrate peptide, by shaping the active site in a cumulative and non-linear fashion, cluster 1 appears to be the main driver of specificity (Figure S4).

Domain and Specificity Evolution

We next set out to explore whether evolutionary insights could be derived from these results. It has previously been observed that the evolution of the kinase domain as a whole is not an accurate reflection of how different kinases have evolved different peptide specificities (Miller et al., 2008; Rausell et al., 2010). Thus, we speculated that a Dendrogram based solely on residues identified as DoS by KINspect could carry significant differences compared to a domain-wide phylogenetic tree. Indeed, Figure 5A (and Figure S5) illustrates how the relationships between kinases (and even between kinase families) appear to deviate when addressed from the DoS' perspective. This DoS-based tree (Figures 5A and S5) illustrates interesting differences including: (1) the embedding of kinase families within other families, such as in the case of the PKN family, embedded within the PKC family, (2) clustering of seemingly unrelated families, such as the Yank and GRK families, or (3) the splitting

of families in two sets displaying marked amino acid differences on their DoS, such as in the case of the Ste20 family.

Thus, this analysis provides further proof and explanation as to how and why the evolution of the entire domain does not always parallel specificity evolution (Capra et al., 2012). Using the DoS-based Dendrogram (based on the DoS residues predicted by KINspect), we have provided an alternative evolutionary explanation of the human kinome, which we argue, more accurately reflects functional diversity and specificity evolution. Such a view, of proteins evolving new specificities by diverging at specific sites within protein domains, is supported by other recent studies conducted on bacterial signaling networks (Capra et al., 2012; Skerker et al., 2008).

Kinase Specificity, Regulation, and Activity Are Loaded onto Different Residues

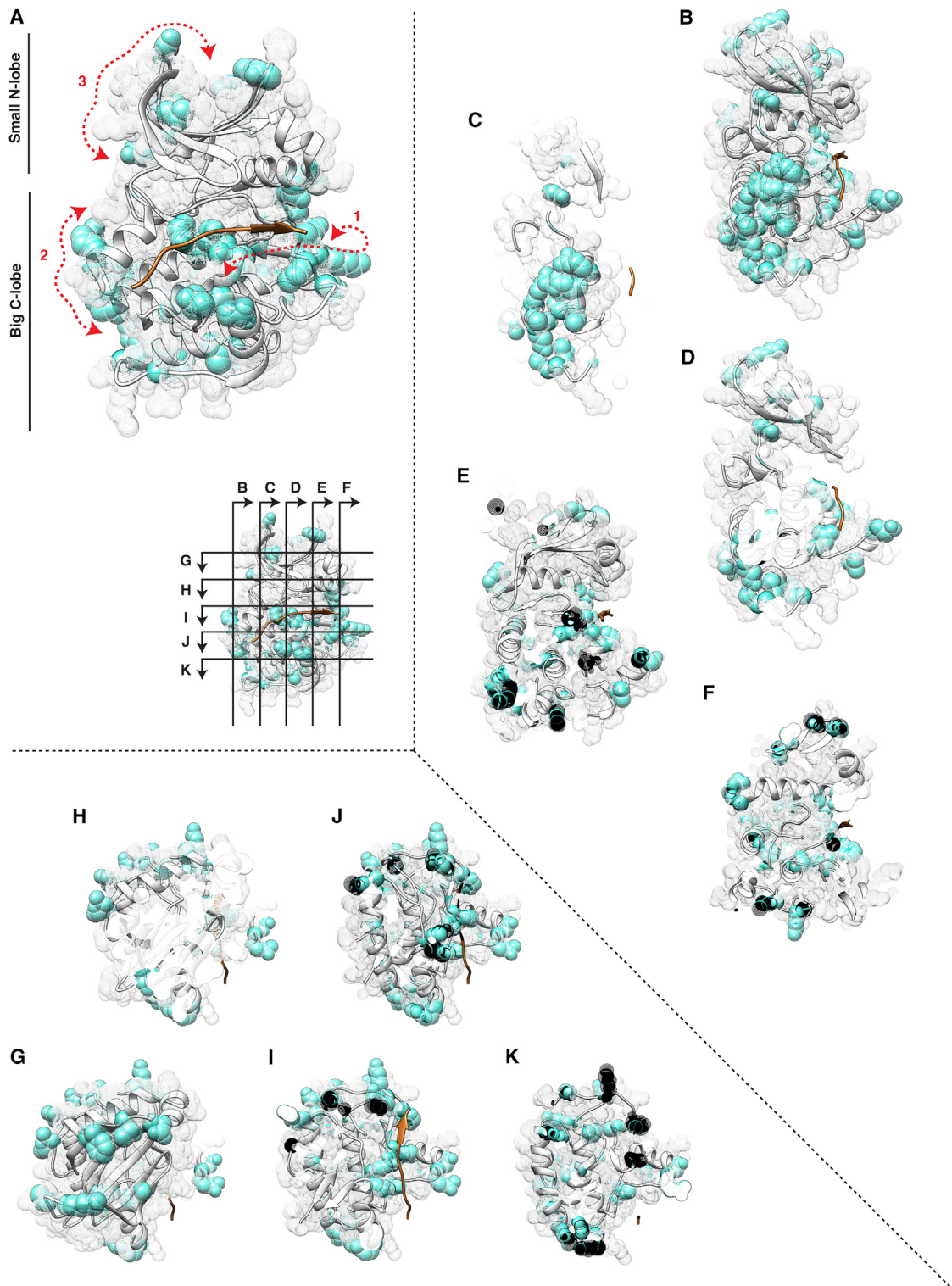
With the aim of interpreting our results from a more global perspective, we investigated to what extent the DoS residues identified by KINspect can interplay with residues known to be involved in the catalytic activation and regulation of the kinase domain.

Two independent sets of residues playing such crucial roles have been identified forming hydrophobic interactions at the core of the domain and stabilizing the active conformation of the domain (Kornev et al., 2006, 2008). These two networks of residues, critical for activation and regulation, are named the catalytic and regulatory spines, respectively. In order to examine how the DoS interact with the two spines (Figure 5B), we visualized the residues forming the catalytic and regulatory spines as well as those identified as DoS in the same kinase structure (Figure 5C). This representation shows that both groups are virtually mutually exclusive, with kinase domain residues belonging to either spines or the DoS set (mostly localized on the surface of the domain), but rarely both.

Despite this apparent separation of biological functions in the kinase domain, it is at the same time equally important to highlight that KINspect, in agreement with previous observations (Nolen et al., 2004), identifies the activation segment as playing a critical role in specificity. Since this segment also plays a crucial role in regulation and catalysis by stabilizing the R-spine (Kornev et al., 2006, 2008), in spite of the apparent general decoupling of these different functions, on this particular segment, they still appear to be partially intertwined (Figure 5C). Moreover, highlighting the distinct evolutionary and functional paths of these sets of residues, we could quantify their differences in

Figure 3. Computational and Experimental Validation of the DoS Identified by KINspect

- (A) Scatterplots comparing pairwise relationships between kinases' domain sequences, and their specificity profiles can illustrate the lack or existence of correlation between sequence and specificity. By limiting the comparison to specific sets, one can investigate whether such sets encode for specificity (i.e., maintain or increase the correlation), as measured by Spearman's correlation coefficients. By comparing the correlations obtained from different sets of residues, the whole domain on the left, previously reported determinants of specificity in the middle and KINspect scores on the right, we confirm that residues with a high KINspect score encode for specificity (e.g., residues scoring above 0.9 lead to very high sequence-to-specificity correlation, with a Spearman's correlation coefficient of 0.69, despite representing only 5.73% of the residues in the kinase domain alignment). Further comparisons with other sets of residues can be found in Figure S4.
- (B) Three new candidate determinants of specificity predicted by KINspect, positioned in the first and third residues of the α C helix and seven residues before the APE motif delimiting the activation segment, are experimentally verified to encode specificity by PSPL as described in [Experimental Procedures](#).
- (C) Experimental results for the PKC γ and PIM1 mutants showing a specificity switch for P+2 and P+1 substrate positions, as shown in matrix and logo form (logos generated using Seq2Logo; Thomsen and Nielsen, 2012). Complete PSSMs describing the PSPL results for wild-type and mutant kinases can be found in Figure S4.

**Figure 4. Determinants of Specificity in the Human Kinase Domain**

(A) Mesh representation of the kinase domain, including its secondary structure in cartoon representation and a bound peptide substrate colored in orange. Positions predicted as DoS by KINspect (i.e., residues with a KINspect specificity importance score higher than 0.9) are highlighted in cyan and the three “canals” formed by these determinants are outlined by red arrows.

(legend continued on next page)

sequence conservation and conclude that DoS are typically residues with considerably lower conservation than the highly conserved spines and many other residues in the domain (Figure 5D).

Similarly Sparse Networks of Determinants Drive Specificity in the SH2 Domain

To investigate the generality of these observations, we explored DoS patterns in another signaling modular protein domain, namely, the SH2 domain. Following a very similar approach as described for the kinase domain, and after identifying the required parameters (Figure S6) appropriately, KINspect identified several SH2 residues that are likely involved in peptide specificity (Figure 6; Movie S2).

Being a smaller domain of typically approximately 100 residues (as can be appreciated in the SH2 domain alignment in Data S4) and generally showing less variability in peptide specificity, it is perhaps not surprising that KINspect converged considerably faster for the SH2 domain (Figure S6) than in the case of the kinase domain.

Despite this difference, as with the kinase domain, independent deployments of KINspect led to the highly reproducible results (Figure S6), and the general model of peptide specificity observed in the kinase domain, where a sparse network of DoS involving a relatively larger number of residues, was also observed in the case of the SH2 domain (Figure 6; Data S5). Similarly, whereas some DoS were close to the peptide (e.g., Figures 6C, 6D, and 6G), others were relatively far away from it (e.g., Figures 6E and 6I), though often connected by inter-residue “canals.” The aforementioned control experiments, where uniform and randomized domain-specificity sets were used (Figure S3), exclude the possibility that the similarities between these results for the kinase and SH2 domains emanate from some intrinsic bias in our computational approach. The spatial representation for several of our DoS is also supported by previous studies of SH2 domains (Halabi et al., 2009; Lenaerts et al., 2008). All in all, this suggests that our findings, with a high number of DoS residues located away from the substrate, far from being unique to kinase specificity could be a more general trend applicable to other modular protein domains (Tompa et al., 2014).

DISCUSSION

Despite the crucial importance of signaling fidelity in biological organization and cellular responses to environmental cues, our perception of how peptide specificity is encoded in the kinase domain has been highly fragmented and biased toward certain kinase families, non-human species, or a subset of kinase domain residues (e.g., those close to the peptide substrate). Here, we developed a data-driven systematic approach to investigate the presence of DoS residues throughout the human kinaseome, experimentally validated several of these DoS, which

together with those shown in the accompanying article (Creixell et al., 2015) encode specificity for the five residue positions most critical for specificity in the peptide substrate (P-3, P-2, P0, P+1, P+2), and identified a distributed, but interconnected, network of DoS in different parts of the kinase domain. In contrast to previous studies, our results suggest specificity is driven by a larger number of residues and a more distributed network of typically non-conserved sets of residues than previously appreciated (Figures 7A and 7B).

Determinants in the Context of Spines and Sectors

The sparse networks of DoS also present interesting implications when compared and contrasted with previous work.

First, as mentioned earlier and illustrated in Figure 5, we note an apparent discrepancy between the residues we identify as DoS, mostly localized on the surface of the domain, and the core residues that form the catalytic and regulatory spines (Kornet et al., 2006, 2008). Whereas this suggests some degree of functional and evolutionary separation between catalytic activity (and regulation thereof) and peptide specificity, a separation of functions that is similar to those employed in other signaling systems (Goldman et al., 2014), our results also indicate that the activation segment provides a link between these biological functions. The fact that different functions seem to be “co-loaded” on this segment could explain why a large fraction of cancer mutations perturb this critical part of the kinase domain (Dixit et al., 2009; Creixell et al., 2015).

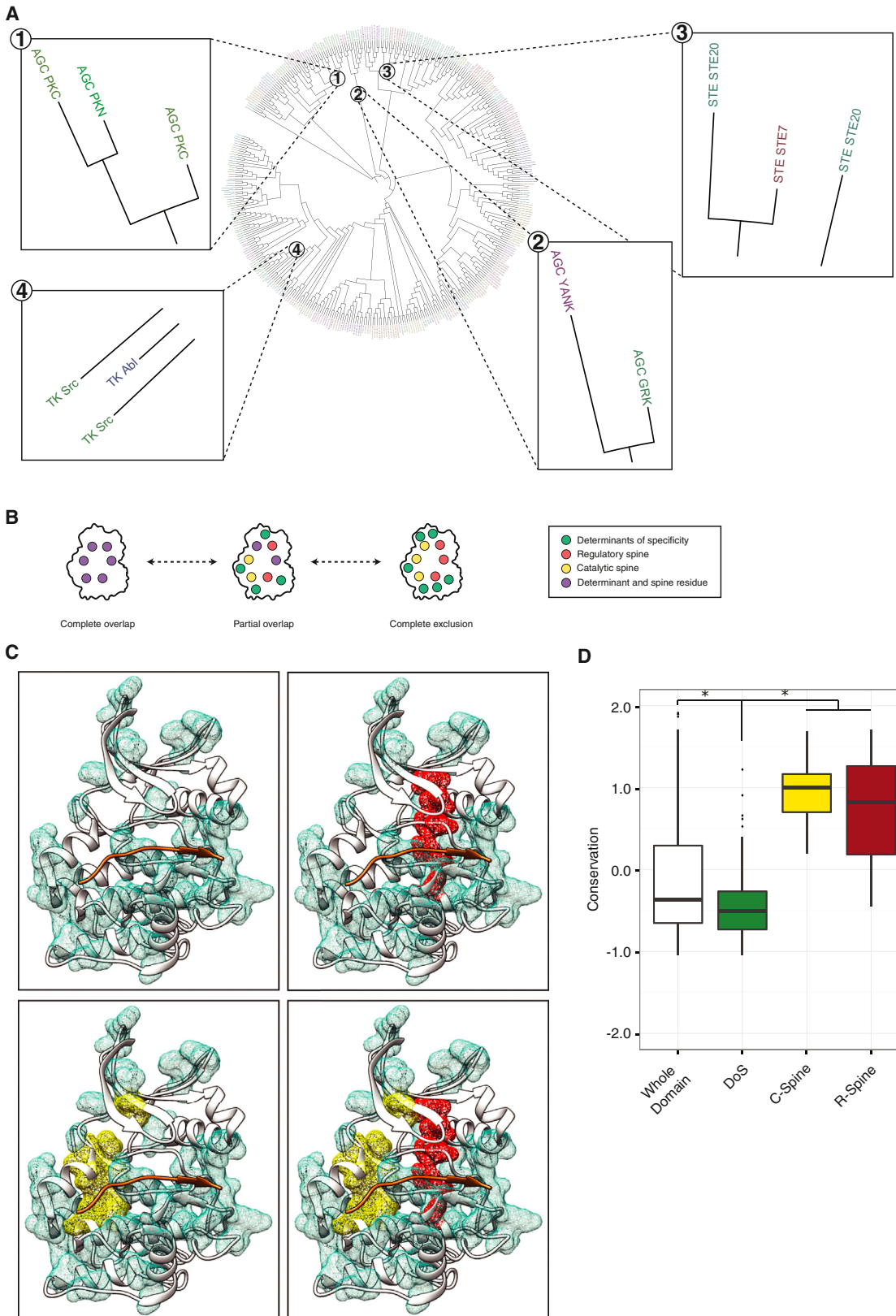
Moreover, this separation of function, together with our finding of very different evolutionary speeds and trajectories for spines and DoS, makes us speculate that kinases have evolved within tight constraints around spines, where maintaining spine integrity was critical to retain kinase activity. On the other hand, the more loose constraints on DoS have facilitated the evolution of new kinases with distinct specificities, a view that is consistent with the current understanding of the evolution of signaling systems (Lim and Pawson, 2010).

Furthermore, the picture portrayed by our results of sparse networks of multiple residues driving specificity together would fit within the scope of more recent theories on protein function, namely, the so-called protein sector model. According to this model, protein function is often encoded in protein sectors, defined as subsets of co-evolving residues (Halabi et al., 2009; Lockless and Ranganathan, 1999) identified in different protein domains, which often also include long-range interactions between distant residues by allosteric regulation (Reynolds et al., 2011). Our results suggest that similar mechanisms could be at work determining specificity in both the kinase and SH2 domains.

Perspectives

Despite the significant conceptual and analytical leap forward provided by KINspect in terms of capability and coverage, continued experimental and computational advances will make it even more precise and accurate in the future.

(B–K) For a more clear representation of different parts of the structure, longitudinal (B–F) and transversal (H–K) slices were taken through the kinase domain at the planes indicated in the inset of (A). A dynamic visualization of this structure can be found in Movie S1. The structure used is that of Akt/PKB in complex with GSK3 peptide (PDB ID: 1O6K; Yang et al., 2002), and the structural visualization on this and other subsequent figures was generated using Chimera (Petersen et al., 2004).



(legend on next page)

From an experimental perspective, it is clear that obtaining peptide specificity profiles for a larger number of kinases (currently, the percentage of kinases for which their specificity has been profiled is only about 30% of the whole human kinome) will only improve our method's results.

In terms of extending to other applications and expanding our current approach, KINspect's methodology could potentially be applied to several other fundamental biological questions such as the identification of residues driving kinase inhibitor binding and specificity. Naturally, we also plan to expand KINspect to add new peptide-recognizing modular domains other than the already-included kinase and SH2 domains (e.g., SH3 or WW domains) or even include inter-positional dependencies within the substrate peptide in the future when data become available.

Implications for Evolution and Disease

As introduced earlier, peptide specificity is a crucial component of a wider cellular requirement, signal fidelity, which ensures that cells will correctly decode input cues and respond accordingly. Changes in this system have been identified as playing a critical role in multicellular metazoan evolution (Tan et al., 2009, 2011), but also, at the domain level, in how proteins evolve new specificities allowing cells to start responding to new cues or unfold new responses to them (Capra et al., 2012; Marengere et al., 1994; Skerker et al., 2008; Zarrinpar et al., 2003). While this has perhaps been less studied in a disease context, it has been suggested that the same process occurs in cancer (Borrello et al., 1995; Santoro et al., 1995; Songyang et al., 1995). In the accompanying article (Creixell et al., 2015), we utilize the bona fide DoS described here to identify cancer mutations perturbing them and experimentally validate their role in causing signaling rewiring (Creixell et al., 2012) and thus contributing to oncogenesis by affecting kinase specificity. We are optimistic these mutations, and new ones that will be identified in the future, will constitute a novel and solid foundation for enhanced appreciation of how signaling networks are perturbed in cancer and other diseases.

EXPERIMENTAL PROCEDURES

Learning Classifier System

The learning classifier system briefly described in the main text that constitutes the computational engine behind KINspect is illustrated in Figure 2. Further

algorithmic and mathematical details can be found in [Supplemental Experimental Procedures](#).

Frobenius Distance between Matrices or Vectors

As a measure of dissimilarity between matrices or vectors, the Frobenius distance or norm can be simply calculated as the square root of the difference between every value in the two matrices or vectors squared (Ellis and Kobe, 2011).

Domain Information and Alignments

Domain sequences for all human kinase domains and additional information on the human kinome were obtained from the <http://kinase.com/> repository, with more recent and up-to-date unpublished data kindly provided by Dr. Gerard Manning (G. Manning, personal communication; Manning et al., 2002). Similar sequence and domain information was obtained for all the human SH2 domains from the SH2 domain site (Liu et al., 2006). Sequences were aligned using ClustalW2 (Larkin et al., 2007), and alignments were further refined manually with help from Dr. Toby Gibson (EMBL).

Dendrogram Construction

Distance matrices between kinases were computed using BLOSUM62 substitution matrix (Henikoff and Henikoff, 1992). The distances in the kinome tree are based on all the columns in the alignment, while the distances in the specificity tree only consider the selected DoS columns in the alignment. We used neighbor joining to build both trees.

Computing Minimum Distance to Substrate from PDB Files

In a similar manner as described in the accompanying article (Creixell et al., 2015), we computed a measure of the minimum distance between any position in our alignment and the substrate peptide. This distance was obtained by extracting distance information from ten representative kinase-substrate structures deposited in PDB (AKT2 [PDB ID: 1O6K]; Yang et al., 2002, PIM1 [PDB ID: 2BZK]; Bullock et al., 2005, DYRK1A [PDB ID: 2WO6]; Soundararajan et al., 2013, CDK2 [PDB ID: 2CC1]; Cheng et al., 2006, PAK4 [PDB ID: 2Q0N]; Chen et al., 2014, EPHA3 [PDB ID: 3FXX]; Davis et al., 2009, FES [PDB ID: 3CD3]; Filippakopoulos et al., 2008, EGFR [PDB ID: 2GS6]; Zhang et al., 2006, IGF1R [PDB ID: 1K3A]; Favelyukis et al., 2001, INSR [PDB ID: 3BU3]; Wu et al., 2008). By developing and deploying in-house python scripts that utilize the biopython package Bio.PDB, we could extract distance features between every residue of these kinase-substrate pairs. Subsequently, this information was collected and, by using the alignment to track the same position on different kinase-substrate structures, the minimum distance for each alignment position was obtained. Additional information on substrate peptide distance for the different mask positions can be found in [Data S3](#).

PSPL Analysis

PKC γ (WT and mutant) was produced in HEK293T cells with a 3 × FLAG epitope tag at the C terminus and isolated by affinity purification on M2 FLAG antibody resin (Sigma-Aldrich) as described (Mok et al., 2010). Pim1 (WT and mutant) was expressed as an N-terminally hexahistidine-tagged

Figure 5. Evolutionary Aspects of DoS and Their Co-existence with Kinase Spines

(A) As can be observed from the different panels on this DoS-based Dendrogram, where several kinases are localized discordantly with whole-domain evolution, peptide specificity evolution cannot be directly inferred from whole-domain specificity. These differences highlight how kinases have accumulated mutations on these specific residues, i.e., DoS, in order to evolve different specificities. For further explanation and information, please refer to [Experimental Procedures](#) and [Figures S5](#).

(B) We next investigated how DoS co-evolved with residues involved in structural changes related to catalysis (kinase spines). As can be seen here, there are different possible degrees to which DoS and spines could co-exist, ranging from complete overlap (left) to complete exclusion (right). In (C), we investigate which of these models is more supported by our data.

(C) By comparing the relative localization of the DoS (top-left structure) together with the residues belonging to the catalytic spine (in yellow, bottom-left structure), the regulatory spine (in red, top-right structure) or all residues together (bottom-right structure), our data suggest that the subgroups of residues that are DoS or spines are mutually exclusive or, in other words, that residues classified as DoS are not part of the catalytic or regulatory spines. Like in Figure 4A, the structure used is that of Akt/PKB in complex with GSK3 peptide (PDB ID: 1O6K; Yang et al., 2002).

(D) Evolutionary conservation for the different subsets of residues (whole domain, DoS, C-spine, and R-spine) was computed as the negative of entropy, using AL2CO algorithm with its default parameters (50), and shown to be significantly lower in DoS compared to the whole domain and the spines ($p = 0.014$ and $p = 1.4 \times 10^{-6}$ using Wilcoxon test, respectively).

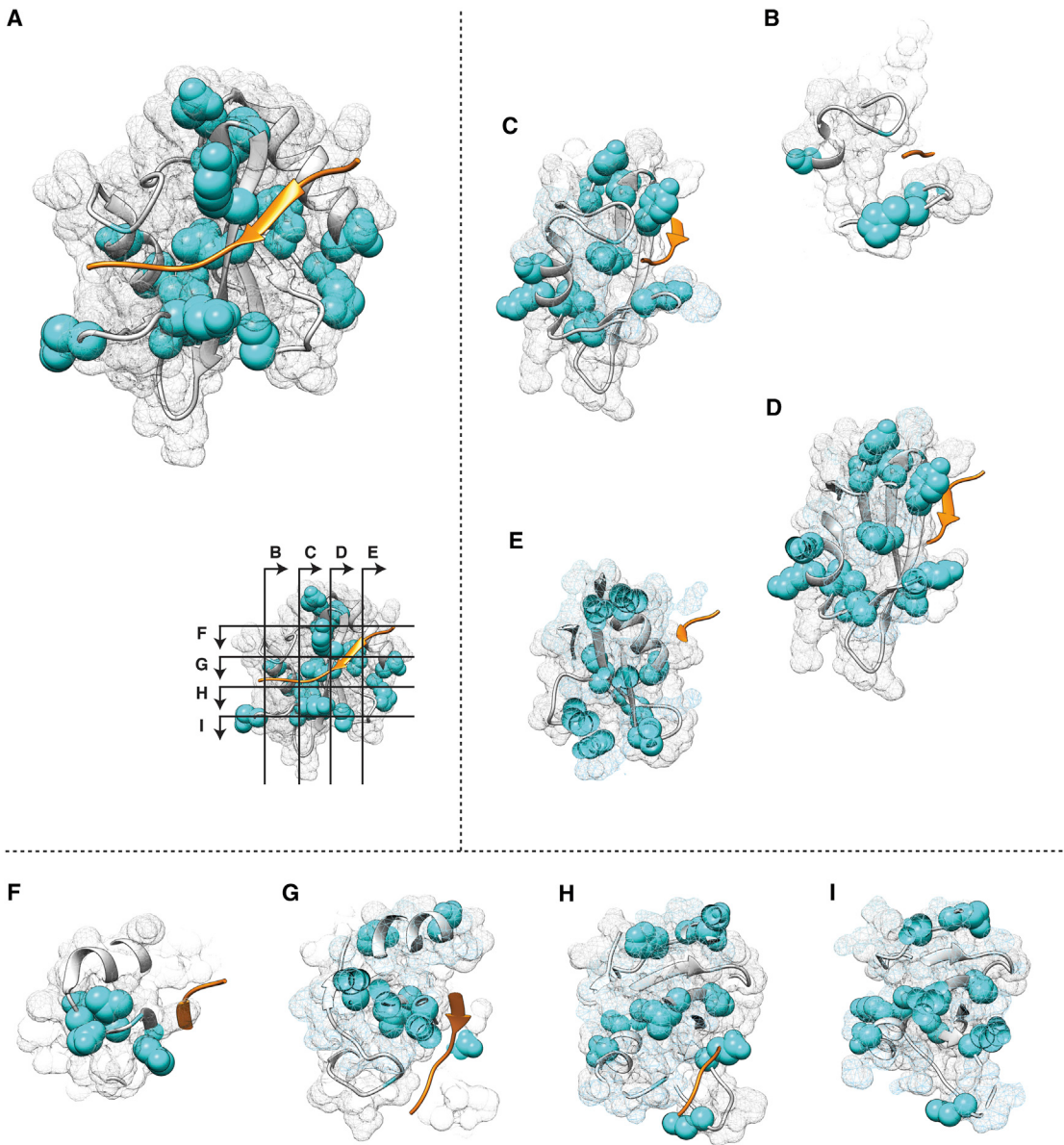


Figure 6. Determinants of Specificity in the Human SH2 Domain

(A) Mesh representation of the SH2 domain, including its secondary structure in cartoon representation and a bound peptide substrate colored in orange.

Positions predicted as DoS by KINspect (i.e., residues with a KINspect score higher than 0.9) are highlighted in cyan.

(B–I) As in the case of the kinase domain, longitudinal (B–E) and transversal (F–I) slices were taken through the SH2 domain at the planes indicated in the inset in (A). For a dynamic visualization of this structure, please refer to [Movie S2](#). The structure used is that of SAP in complex with SLAM peptide (PDB ID: 1D4T; [Poy et al., 1999](#)).

fusion protein in *E. coli* and purified from lysates using TALON resin (Clontech). Peptide library analysis was performed by arraying a set of 182 peptide mixtures (50 μ M) in a 1,536-well plate in kinase reaction buffer (2 μ l/well). Buffer for Pim1 reactions was 50 mM HEPES (pH 7.4), 10 mM MgCl₂, 0.1% Tween 20, and buffer for PKC γ reactions was 50 mM Tris-HCl (pH 7.5), 10 mM MgCl₂, 1 mM DTT, 0.1% Tween 20 containing a 5-fold dilution of lipid activator (EMD Millipore). Peptides had the sequence Y-A-X-X-X-X-S/T-X-X-X-A-G-K-K-biotin, in which X positions were generally an equimolar mixture of the 17 amino acids excluding Ser, Thr, and Cys, and S/T is an even mixture of Ser and Thr. In each well of the array, the peptide had one of the 20 amino acids fixed at one of the nine X positions. In addition, two peptides were

included that fixed either Ser or Thr at the phosphoacceptor position. Reactions were initiated by adding kinase (to 8 μ g/ml) and [γ -³³P]ATP (50 μ M at 0.03 μ Ci/ μ l), incubated 2 hr at 30°C, and then 200-nl aliquots were transferred to a streptavidin membrane (Promega). Membranes were washed and dried as described and exposed to a phosphor screen. Radiolabel incorporation into each peptide mixture was quantified by phosphor imaging using QuantityOne software (Bio-Rad). Following background subtraction, data were normalized so that the average value for a given position within the peptide was equal to 1. Normalized data from two (PKC γ) or three (Pim1) separate runs were averaged, log₂ transformed, and converted to heatmaps in Microsoft Excel.

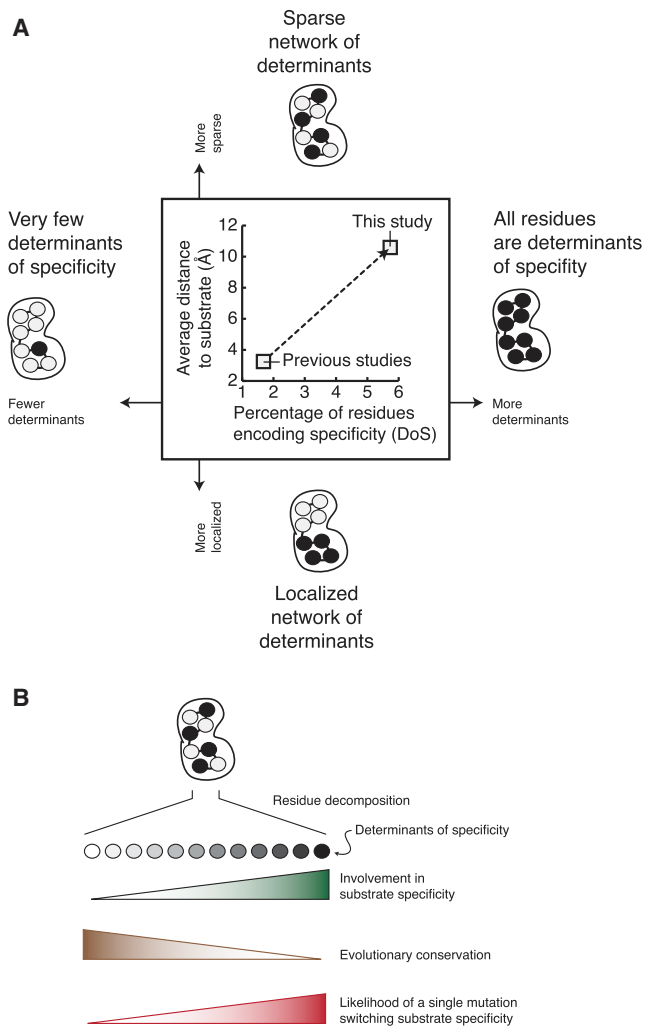


Figure 7. Model for DoS Encoding Specificity and Mutations on DoS Perturbing Substrate Specificity

(A) By computing the percentage of residues encoding specificity (DoS) and their average distance to the substrate, we conclude that the set of DoS uncovered by KINspect represent a larger and more sparse group of residues and that residues can contribute to peptide specificity even if they are not located in close proximity to the substrate.

(B) In this article, we have described the degree to which each residue contribute to specificity on a more quantitative scale and experimentally validated three novel determinants of specificity (Figure 3). Our results also indicate that specificity is loaded onto a set of residues that is less conserved than most others in the domain and where mutations, in cancer or evolution, can easily cause substrate specificity switches by single mutations. As shown in similar signaling systems (Skerker et al., 2008), such mutations represent key turns in how different kinases evolve and occupy separate and sometimes overlapping substrate subspaces. Similar mutations have been seen in cancer (Borrello et al., 1995; Creixell et al., 2012; Santoro et al., 1995; Songyang et al., 1995), despite the fact that this type of mutations has been largely understudied, and their role in the disease remains largely unknown (see Creixell et al., 2015).

SUPPLEMENTAL INFORMATION

Supplemental Information includes Supplemental Experimental Procedures, six figures, one table, five data files, and two movies and can be found with this article online at <http://dx.doi.org/10.1016/j.cell.2015.08.057>.

AUTHOR CONTRIBUTIONS

P.C. and R.L. conceived the project. P.C., A.P., C.C.S., and M.N. developed and implemented the computational framework. P.C., C.J.M., H.J.L., and B.E.T. devised and/or performed experiments. P.C. and A.P. generated the structural visualizations with Chimera and performed the evolutionary analysis of DoS. R.L. oversaw the project. P.C. and R.L. wrote the article assisted by the other authors. All the authors read and approved the final manuscript.

ACKNOWLEDGMENTS

We thank G. Manning for providing access to unpublished data, T. Gibson for critical assistance in the generation of the kinase domain alignment, and J. Erler, M. Sommer, and J. Saez-Rodriguez for helpful discussions in preparation of this manuscript. We thank members of R.L.'s laboratory and the Erler laboratory for advice and critical review of the manuscript, in particular, J. Longden, T. Cox, and J. Erler for assistance with the figures and text of this manuscript and J. Ferkinghoff-Borg for fruitful discussions and computational advice. We are especially indebted to J.D. Sørensen for technical assistance when deploying supercomputing infrastructures (SGI UV 2000). This work has received funding from the European Research Council under the European Union's Seventh Framework Programme (FP/2007-2013)/ERC Grant (KINOMEDRIFT). R.L. is funded as a Lundbeck Foundation Fellow. This work has also been supported by a Career Development Award from the Human Frontier Science Program to R.L. P.C. is currently funded by a Ludwig Fund Postdoctoral Fellowship. The algorithms and software developed in this work will be released under the Creative Commons licensing schemes at the websites <http://KinomeXplorer.science> and <http://KINspect.science>. For further information, see also <http://lindinglab.science>.

Received: August 2, 2014

Revised: April 9, 2015

Accepted: August 12, 2015

Published: September 17, 2015

REFERENCES

- Bhattacharyya, R.P., Reményi, A., Good, M.C., Bashor, C.J., Falick, A.M., and Lim, W.A. (2006). The Ste5 scaffold allosterically modulates signaling output of the yeast mating pathway. *Science* 311, 822–826.
- Borrello, M.G., Smith, D.P., Pasini, B., Bongarzone, I., Greco, A., Lorenzo, M.J., Arighi, E., Miranda, C., Eng, C., Alberti, L., et al. (1995). RET activation by germline MEN2A and MEN2B mutations. *Oncogene* 11, 2419–2427.
- Brinkworth, R.I., Breinl, R.A., and Kobe, B. (2003). Structural basis and prediction of substrate specificity in protein serine/threonine kinases. *Proc. Natl. Acad. Sci. USA* 100, 74–79.
- Bullock, A.N., Debreczeni, J., Amos, A.L., Knapp, S., and Turk, B.E. (2005). Structure and substrate specificity of the Pim-1 kinase. *J. Biol. Chem.* 280, 41675–41682.
- Capra, E.J., Perchuk, B.S., Skerker, J.M., and Laub, M.T. (2012). Adaptive mutations that prevent crosstalk enable the expansion of paralogous signaling protein families. *Cell* 150, 222–232.
- Chen, C., Ha, B.H., Thévenin, A.F., Lou, H.J., Zhang, R., Yip, K.Y., Peterson, J.R., Gerstein, M., Kim, P.M., Filippakopoulos, P., et al. (2014). Identification of a major determinant for serine-threonine kinase phosphoacceptor specificity. *Mol. Cell* 53, 140–147.
- Cheng, K.Y., Noble, M.E., Skamnaki, V., Brown, N.R., Lowe, E.D., Kontogianis, L., Shen, K., Cole, P.A., Siligardi, G., and Johnson, L.N. (2006). The role of the phospho-CDK2/cyclin A recruitment site in substrate recognition. *J. Biol. Chem.* 281, 23167–23179.
- Creixell, P., Schoof, E.M., Erler, J.T., and Linding, R. (2012). Navigating cancer network attractors for tumor-specific therapy. *Nat. Biotechnol.* 30, 842–848.
- Creixell, P., Schoof, E.M., Simpson, C.D., Longden, J., Miller, C.J., Lou, H.J., Perryman, L., Cox, T.R., Zivanovic, N., Palmeri, A., et al. (2015). Kinome-wide

decoding of network-attacking mutations rewiring cancer signaling. *Cell* 163, this issue, 202–217.

Davis, T.L., Walker, J.R., Allali-Hassani, A., Parker, S.A., Turk, B.E., and Dhe-Paganon, S. (2009). Structural recognition of an optimized substrate for the ephrin family of receptor tyrosine kinases. *FEBS J.* 276, 4395–4404.

Dixit, A., Yi, L., Gowthaman, R., Torkamani, A., Schork, N.J., and Verkhivker, G.M. (2009). Sequence and structure signatures of cancer mutation hotspots in protein kinases. *PLoS ONE* 4, e7485.

Ellis, J.J., and Kobe, B. (2011). Predicting protein kinase specificity: Predikin update and performance in the DREAM4 challenge. *PLoS ONE* 6, e21169.

Favelyukis, S., Till, J.H., Hubbard, S.R., and Miller, W.T. (2001). Structure and autoregulation of the insulin-like growth factor 1 receptor kinase. *Nat. Struct. Biol.* 8, 1058–1063.

Filippakopoulos, P., Kofler, M., Hantschel, O., Gish, G.D., Grebien, F., Salah, E., Neudecker, P., Kay, L.E., Turk, B.E., Superti-Furga, G., et al. (2008). Structural coupling of SH2-kinase domains links Fes and Abl substrate recognition and kinase activation. *Cell* 134, 793–803.

Goldman, A., Roy, J., Bodenmiller, B., Wanka, S., Landry, C.R., Aebersold, R., and Cyert, M.S. (2014). The calcineurin signaling network evolves via conserved kinase-phosphatase modules that transcend substrate identity. *Mol. Cell* 55, 422–435.

Halabi, N., Rivoire, O., Leibler, S., and Ranganathan, R. (2009). Protein sectors: evolutionary units of three-dimensional structure. *Cell* 138, 774–786.

Hanks, S.K., and Hunter, T. (1995). Protein kinases 6. The eukaryotic protein kinase superfamily: kinase (catalytic) domain structure and classification. *FASEB J.* 9, 576–596.

Henikoff, S., and Henikoff, J.G. (1992). Amino acid substitution matrices from protein blocks. *Proc. Natl. Acad. Sci. USA* 89, 10915–10919.

Johnson, L.N., Lowe, E.D., Noble, M.E., and Owen, D.J. (1998). The Eleventh Datta Lecture. The structural basis for substrate recognition and control by protein kinases. *FEBS Lett.* 430, 1–11.

Kornev, A.P., Haste, N.M., Taylor, S.S., and Eyck, L.F. (2006). Surface comparison of active and inactive protein kinases identifies a conserved activation mechanism. *Proc. Natl. Acad. Sci. USA* 103, 17783–17788.

Kornev, A.P., Taylor, S.S., and Ten Eyck, L.F. (2008). A helix scaffold for the assembly of active protein kinases. *Proc. Natl. Acad. Sci. USA* 105, 14377–14382.

Lanzi, P.L., Stolzmann, W., and Wilson, S.W. (2000). Learning classifier systems: from foundations to applications. (1813).

Larkin, M.A., Blackshields, G., Brown, N.P., Chenna, R., McGettigan, P.A., McWilliam, H., Valentin, F., Wallace, I.M., Wilm, A., Lopez, R., et al. (2007). Clustal W and Clustal X version 2.0. *Bioinformatics* 23, 2947–2948.

Lenaerts, T., Ferkinghoff-Borg, J., Stricher, F., Serrano, L., Schymkowitz, J.W., and Rousseau, F. (2008). Quantifying information transfer by protein domains: analysis of the Fyn SH2 domain structure. *BMC Struct. Biol.* 8, 43.

Lim, W.A., and Pawson, T. (2010). Phosphotyrosine signaling: evolving a new cellular communication system. *Cell* 142, 661–667.

Linding, R., Jensen, L.J., Ostheimer, G.J., van Vugt, M.A.T.M., Jørgensen, C., Miron, I.M., Diella, F., Colwill, K., Taylor, L., Elder, K., et al. (2007). Systematic discovery of *in vivo* phosphorylation networks. *Cell* 129, 1415–1426.

Liu, B.A., Jablonowski, K., Raina, M., Arcé, M., Pawson, T., and Nash, P.D. (2006). The human and mouse complement of SH2 domain proteins—establishing the boundaries of phosphotyrosine signaling. *Mol. Cell* 22, 851–868.

Lockless, S.W., and Ranganathan, R. (1999). Evolutionarily conserved pathways of energetic connectivity in protein families. *Science* 286, 295–299.

Manning, G., Whyte, D.B., Martinez, R., Hunter, T., and Sudarsanam, S. (2002). The protein kinase complement of the human genome. *Science* 298, 1912–1934.

Marengere, L.E., Songyang, Z., Gish, G.D., Schaller, M.D., Parsons, J.T., Stern, M.J., Cantley, L.C., and Pawson, T. (1994). SH2 domain specificity and activity modified by a single residue. *Nature* 369, 502–505.

Miller, M.L., Jensen, L.J., Diella, F., Jørgensen, C., Tinti, M., Li, L., Hsiung, M., Parker, S.A., Bordeaux, J., Sicheritz-Ponten, T., et al. (2008). Linear motif atlas for phosphorylation-dependent signaling. *Sci. Signal.* 1, ra2.

Mok, J., Kim, P.M., Lam, H.Y.K., Piccirillo, S., Zhou, X., Jeschke, G.R., Sheridan, D.L., Parker, S.A., Desai, V., Jwa, M., et al. (2010). Deciphering protein kinase specificity through large-scale analysis of yeast phosphorylation site motifs. *Sci. Signal.* 3, ra12.

Nolen, B., Taylor, S., and Ghosh, G. (2004). Regulation of protein kinases: controlling activity through activation segment conformation. *Mol. Cell* 15, 661–675.

Pettersen, E.F., Goddard, T.D., Huang, C.C., Couch, G.S., Greenblatt, D.M., Meng, E.C., and Ferrin, T.E. (2004). UCSF Chimera—a visualization system for exploratory research and analysis. *J. Comput. Chem.* 25, 1605–1612.

Poy, F., Yaffe, M.B., Sayos, J., Saxena, K., Morra, M., Sumegi, J., Cantley, L.C., Terhorst, C., and Eck, M.J. (1999). Crystal structures of the XLP protein SAP reveal a class of SH2 domains with extended, phosphotyrosine-independent sequence recognition. *Mol. Cell* 4, 555–561.

Rausell, A., Juan, D., Pazos, F., and Valencia, A. (2010). Protein interactions and ligand binding: from protein subfamilies to functional specificity. *Proc. Natl. Acad. Sci. USA* 107, 1995–2000.

Reményi, A., Good, M.C., Bhattacharyya, R.P., and Lim, W.A. (2005). The role of docking interactions in mediating signaling input, output, and discrimination in the yeast MAPK network. *Mol. Cell* 20, 951–962.

Reynolds, K.A., McLaughlin, R.N., and Ranganathan, R. (2011). Hot spots for allosteric regulation on protein surfaces. *Cell* 147, 1564–1575.

Santoro, M., Carluomagno, F., Romano, A., Bottaro, D.P., Dathan, N.A., Grieco, M., Fusco, A., Vecchio, G., Matoskova, B., Kraus, M.H., et al. (1995). Activation of RET as a dominant transforming gene by germline mutations of MEN2A and MEN2B. *Science* 267, 381–383.

Scott, J.D., and Pawson, T. (2009). Cell signaling in space and time: where proteins come together and when they are apart. *Science* 326, 1220–1224.

Skerker, J.M., Perchuk, B.S., Siriyaporn, A., Lubin, E.A., Ashenberg, O., Goulian, M., and Laub, M.T. (2008). Rewiring the specificity of two-component signal transduction systems. *Cell* 133, 1043–1054.

Songyang, Z., Caraway, K.L., 3rd, Eck, M.J., Harrison, S.C., Feldman, R.A., Mohammadi, M., Schlessinger, J., Hubbard, S.R., Smith, D.P., Eng, C., et al. (1995). Catalytic specificity of protein-tyrosine kinases is critical for selective signalling. *Nature* 373, 536–539.

Soundararajan, M., Roos, A.K., Savitsky, P., Filippakopoulos, P., Kettenbach, A.N., Olsen, J.V., Gerber, S.A., Eswaran, J., Knapp, S., and Elkins, J.M. (2013). Structures of Down syndrome kinases, DYRKs, reveal mechanisms of kinase activation and substrate recognition. *Structure* 21, 986–996.

Tan, C.S.H., Pascalescu, A., Lim, W.A., Pawson, T., Bader, G.D., and Linding, R. (2009). Positive selection of tyrosine loss in metazoan evolution. *Science* 325, 1686–1688.

Tan, C.S.H., Schoof, E., Creixell, P., Pascalescu, A., Lim, W., Pawson, T., Bader, G., and Linding, R. (2011). Response to comment on “Positive Selection of Tyrosine Loss in Metazoan Evolution.” *Science* 332, 917.

Thomsen, M.C.F., and Nielsen, M. (2012). Seq2Logo: a method for construction and visualization of amino acid binding motifs and sequence profiles including sequence weighting, pseudo counts and two-sided representation of amino acid enrichment and depletion. *Nucleic Acids Res.* 40, W281–W287.

Tompa, P., Davey, N., Gibson, T., and Babu, M. (2014). A million peptide motifs for the molecular biologist. *Mol. Cell* 55, 161–169.

Turk, B.E. (2008). Understanding and exploiting substrate recognition by protein kinases. *Curr. Opin. Chem. Biol.* 12, 4–10.

Wu, J., Tseng, Y.D., Xu, C.F., Neubert, T.A., White, M.F., and Hubbard, S.R. (2008). Structural and biochemical characterization of the KRLB region in insulin receptor substrate-2. *Nat. Struct. Mol. Biol.* 15, 251–258.

Yang, J., Cron, P., Good, V.M., Thompson, V., Hemmings, B.A., and Barford, D. (2002). Crystal structure of an activated Akt/protein kinase B ternary complex with GSK3-peptide and AMP-PNP. *Nat. Struct. Biol.* 9, 940–944.

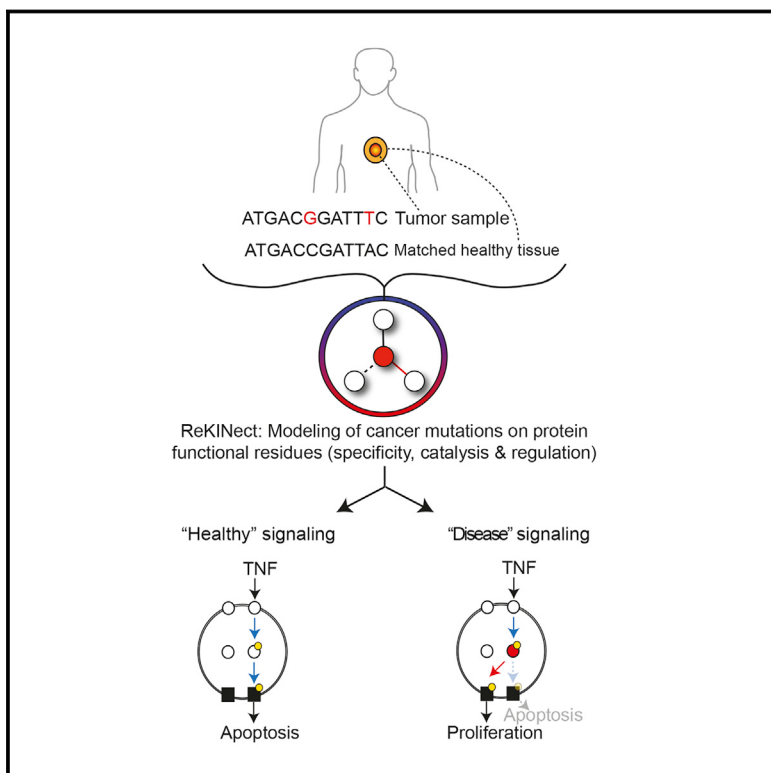
Zarrinpar, A., Park, S.H., and Lim, W.A. (2003). Optimization of specificity in a cellular protein interaction network by negative selection. *Nature* 426, 676–680.

Zhang, X., Gureasko, J., Shen, K., Cole, P.A., and Kuriyan, J. (2006). An allosteric mechanism for activation of the kinase domain of epidermal growth factor receptor. *Cell* 125, 1137–1149.

Zhang, H., Lundegaard, C., and Nielsen, M. (2009). Pan-specific MHC class I predictors: a benchmark of HLA class I pan-specific prediction methods. *Bioinformatics* 25, 83–89.

Kinome-wide Decoding of Network-Attacking Mutations Rewiring Cancer Signaling

Graphical Abstract



Authors

Pau Creixell, Erwin M. Schoof,
Craig D. Simpson, ..., Janine T. Erler,
Benjamin E. Turk, Rune Linding

Correspondence

linding@lindinglab.org

In Brief

A systematic classification of genomic variants in cancer reveals the many ways in which signaling networks can be perturbed, including rewiring and the creation or destruction of phosphorylation sites.

Highlights

- Mutations perturbing signaling networks are systematically classified and interpreted
- Several such functional mutations are identified in cancer and experimentally validated
- The results suggest that a single point mutant can have profound signaling effects
- Systematic interpretation of genomic data may assist future precision-medicine efforts

Kinome-wide Decoding of Network-Attacking Mutations Rewiring Cancer Signaling

Pau Creixell,^{1,7} Erwin M. Schoof,¹ Craig D. Simpson,² James Longden,² Chad J. Miller,³ Hua Jane Lou,³ Lara Perryman,² Thomas R. Cox,² Nevena Zivanovic,⁴ Antonio Palmeri,⁵ Agata Wesolowska-Andersen,¹ Manuela Helmer-Citterich,⁵ Jesper Ferkinghoff-Borg,² Hiroaki Itamochi,⁶ Bernd Bodenmiller,⁴ Janine T. Erler,² Benjamin E. Turk,³ and Rune Linding^{1,2,*}

¹Department of Systems Biology, Technical University of Denmark, 2800 Lyngby, Denmark

²Biotech Research and Innovation Centre (BRIC), University of Copenhagen (UCPH), 2200 Copenhagen, Denmark

³Department of Pharmacology, Yale University School of Medicine, New Haven, CT 06520, USA

⁴Institute of Molecular Life Sciences, University of Zurich, 8057 Zurich, Switzerland

⁵Centre for Molecular Bioinformatics, University of Rome Tor Vergata, 00133 Rome, Italy

⁶Tottori University School of Medicine, Yonago 683-8504, Japan

⁷Present address: Koch Institute for Integrative Cancer Research, Massachusetts Institute of Technology (MIT), Cambridge, MA 02139, USA

*Correspondence: linding@lindinglab.org

<http://dx.doi.org/10.1016/j.cell.2015.08.056>

This is an open access article under the CC BY license (<http://creativecommons.org/licenses/by/4.0/>).

SUMMARY

Cancer cells acquire pathological phenotypes through accumulation of mutations that perturb signaling networks. However, global analysis of these events is currently limited. Here, we identify six types of network-attacking mutations (NAMs), including changes in kinase and SH2 modulation, network rewiring, and the genesis and extinction of phosphorylation sites. We developed a computational platform (ReKINect) to identify NAMs and systematically interpreted the exomes and quantitative (phospho-)proteomes of five ovarian cancer cell lines and the global cancer genome repository. We identified and experimentally validated several NAMs, including PKC γ M501I and PKD1 D665N, which encode specificity switches analogous to the appearance of kinases *de novo* within the kinase. We discover mutant molecular logic gates, a drift toward phospho-threonine signaling, weakening of phosphorylation motifs, and kinase-inactivating hotspots in cancer. Our method pinpoints functional NAMs, scales with the complexity of cancer genomes and cell signaling, and may enhance our capability to therapeutically target tumor-specific networks.

INTRODUCTION

Since the discovery of the first oncogene, Src (Stehelin et al., 1976), and tumor suppressor, Rb (Friend et al., 1986), more than three decades ago, our understanding of some of the specific genetic aberrations supporting cancer progression has steadily risen. Recent advances in next-generation sequencing technologies have led to the identification of large numbers of

somatic cancer mutations through whole genome and exome sequencing of tumors. Given how complex it is to assess the relevance of this enormous repertoire of reported somatic cancer mutations (currently running in excess of 1 million variants) (Forbes et al., 2011), the discovery of new somatic mutations has vastly outpaced our ability to unravel their functional roles (Figure S1A).

Despite the fact that alterations to the physiological cellular responses to environmental cues are fundamental hallmarks of cancer cells (Hanahan and Weinberg, 2000) and that cellular responses to input cues are driven by signaling networks, a comprehensive understanding of how mutations perturb these networks is still missing. In fact, new conceptual paradigms and computational strategies allowing better assessment of the intrinsic complexities of cancer cells, such as the integration of cancer genomic and proteomic data, have been recently pinpointed as key requirements in the field of cancer research (Weinberg, 2014; Yaffe, 2013). Specifically, new approaches for decoding mutations that perturb signaling networks (or as we term them, “network-attacking” mutations [NAMs]) (Creixell et al., 2012a) and the mechanisms by which they may statically or dynamically alter these networks will be fundamental in closing this gap (Figure S1B) (Yaffe, 2013). Here, we describe and validate such a conceptual and computational framework capable of identifying, classifying and unraveling the impact of numerous predicted NAMs.

RESULTS

Classifying Mutations Affecting Signaling Networks

In order to evaluate whether cancer mutations perturb signaling networks, we initially developed a classification system with concrete types of NAMs. We divide NAMs into three fundamental classes.

The first and relatively well-described type of NAM is one that disrupts signaling network dynamics by constitutively activating or inactivating a protein kinase, thereby maintaining the

information flow either “on” or “off” uninterrupted over time. Examples of such “on” mutations are those substitutions that mimic activation loop phosphorylations, whereas examples of “off” mutations include those that alter catalytically essential residues of kinases, or residues in SH2 domains that are critical for phospho-tyrosine binding. Since the timely activation and termination of signals is critical for the proper cellular homeostasis as well as phenotypic responses to environmental stimuli, such mutations lead to aberrant information processing (Figure 1A).

A second, largely undescribed type of NAMs are those mutations that shift the signaling network structure by “rewiring” upstream or downstream interactions (of the mutated protein or node). Upstream rewiring can be caused by mutations in a kinase substrate that disrupt the linear motif around a phosphorylation site, thus causing a new upstream kinase to phosphorylate the mutant substrate. Downstream rewiring, in contrast, can be caused by drifts in the peptide specificity upon mutation of the determinants of specificity (DoS) in kinase (or SH2) domains (Creixell et al., 2015 [this issue of Cell]) (Figure 1A).

Finally, we hypothesized that a third type of NAMs could exist where mutations would generate or destroy phosphorylation sites, effectively generating new molecular logic gates in cancer cells (Figure 1A).

Node inactivation and node activation would fall within the categories of what is traditionally referred to as loss-of-function and gain-of-function hypermorphic mutations, while the other mutations would fit best within a gain-of-function neomorphic classification.

The ReKINect Methodology

With the aim of systematically identifying NAMs in phosphorylation-based signaling networks, we developed a computational approach, ReKINect, capable of predicting these defined functional mutations (Figures 1A and 1B; <http://ReKINect.science>). We began by assembling comprehensive sequence and positional information covering all known 538 kinase domains, 111 SH2 domains, and 149,838 phosphorylation sites in the human proteome (refer to the Experimental Procedures for further information). This information facilitated the mapping of NAMs onto these domains and the modeling of the likely functional effect of mutations (Figure 1B). Mutations in established or predicted functional residues (essential residues on the different domains, determinants of specificity identified in our accompanying paper [Creixell et al., 2015] as well as phosphorylation sites) would then be predicted to lead to the dysregulation of network dynamics, network rewiring, and gain or loss of phosphorylation sites (Figure 1B).

Below, we provide an overview, further details, and experimental evidence using a wide range of techniques (including genome-specific global phospho-proteomics, peptide specificity, or phenotypic data) for the different predictions generated by the ReKINect algorithm and explore the impact on signaling networks of the NAMs we identify.

Quantifying NAMs in Cancer Repositories and Cell Lines

Having defined the different NAMs, we next intended to assess their existence and abundance in cancer. We thus collected

a set of 678,050 unique missense somatic cancer variants from COSMIC (version 67) (Forbes et al., 2011) and deployed ReKINect on this set to predict a large number of instances across the NAM classes (Figure 2).

In order to experimentally investigate NAMs, we performed a global integrative analysis by combining exome next-generation sequencing (NGS) and quantitative mass spectrometry (MS)-based (phospho-)proteomics on a set of five ovarian cancer cell lines (ES2, OVAs, OVISE, TOV-21, and KOC-7C; Figures S1 and S2) and conducted genome-specific proteomics analyses (Experimental Procedures). By following a Spike-in SILAC-based labeling strategy (Geiger et al., 2011) (Figures S1 and S2; Experimental Procedures), we could identify and accurately quantify on average more than 6,000 unique phosphorylation sites across over 2,000 proteins in each of the five cell lines. Furthermore, NGS identified close to 9,000 unique missense variants per cell line (including SNPs and germline mutations as well as somatic mutations) that were subsequently interpreted by ReKINect (Figure 2).

As shown in Figure 2 (and Data S1–S6) ReKINect could identify functional mutations covering each class of NAM included in our model as well as enrichments in these functional mutations (Figure S1). In addition, we computed the frequency at which different protein domains are affected by cancer mutations in the global repository of somatic cancer mutations as a means to provide general estimations of the likelihood of finding perturbations in different modular protein domains in cancer (Figure S1).

Given our currently limited knowledge about the different processes that can lead to the different NAMs (e.g., phosphomimicking mutations are the only case currently covered by ReKINect that result in kinase activation) the number of functional mutations presented in Figure 2 is most likely a significant underestimation. Nevertheless, in the following sections we provide further details and evidence supporting the existence of these predicted NAMs in cancer signaling networks.

Genesis and Extinction of Phosphorylation Sites and Circuitry

Having collected both exome sequencing and proteomic data on the same set of cancer cell lines, we were able to address the question of whether mutations could create new phosphorylation sites or destroy existing ones, thereby generating new cancer-associated molecular logic gates within a cancer cell signaling circuitry. To identify such events, we specifically inquired the global sequencing data for the appearance of phosphorylatable residues resulting from mutations, some of which could be experimentally verified to be bona fide sites by mass spectrometry. Strikingly, this approach uncovered several examples of mutations that lead to the genesis of new phosphorylatable sites, which become recognized and phosphorylated by kinases (Figures 3A and S2). Among the proteins harboring these neomorphic phosphorylation sites were TANC1 and HSF1 (Figure 3A). While little is known about TANC1, HSF1 is a heat-shock protein previously reported to be associated with carcinogenesis and poor prognosis, as well as supporting malignancy in a variety of cancers (Dai et al., 2007). Thus, further investigations of this new phosphorylation site on HSF1 and its

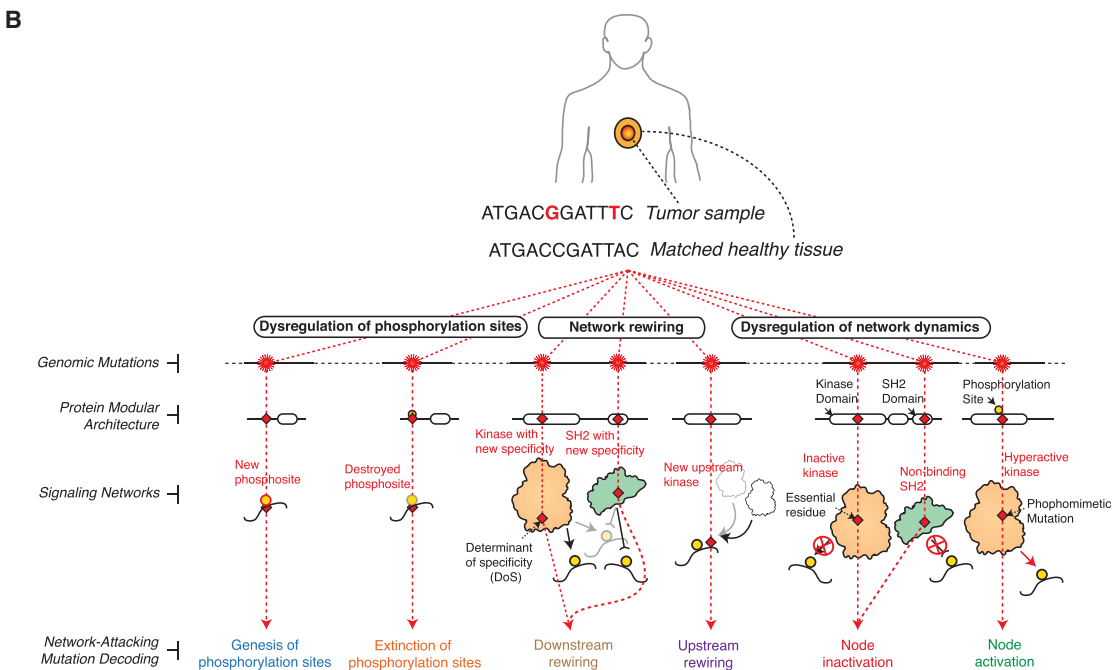
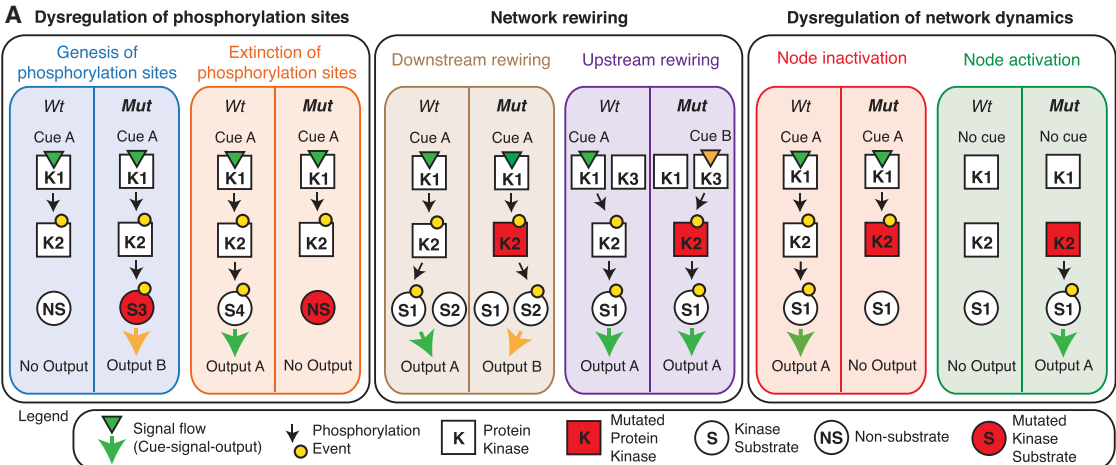


Figure 1. Network-Attacking Mutations

(A) Six distinct types of network-attacking mutations (NAMs) can be defined based on perturbations of signaling network dynamics, network structure, and dysregulation of phosphorylation sites. Cancer mutations could generate or destroy molecular logic gates, for example by creating new, or by removing existing, phosphorylation sites. Alternatively, mutant proteins could become activated by new upstream proteins (incoming edges) or start perturbing new downstream substrates (outgoing edges). Finally mutations could turn signaling proteins (e.g., protein kinases) constitutively “on” or “off.” The effect of these NAMs on the cue-signal-output flow of information is illustrated for each comparing the wild-type (WT) and mutant (Mut) cases.

(B) After mapping mutations at the genomic and proteomic level, every NAM class defined in (A) is modeled on the different protein domains and motifs currently included in ReKINect following a distinct procedure: mutations on the essential residues of the kinase and SH2 domains are classified as node inactivating. Acidic mutations mimicking the phosphorylated/active state of kinases are classified as node activating. Mutations perturbing phosphorylation motifs and causing changes in the upstream kinase phosphorylating the target protein are classified as upstream rewiring. On the other hand, mutations in residues that determine specificity of the kinase or SH2 domains (Creixell et al., 2015) perturb domain specificity and are classified as downstream rewiring. Finally, our genome-specific MS experiments enable the identification of mutations generating phosphorylatable residues or the extinction of phosphorylation sites by mutating away from phosphorylatable residues.

See also Supplemental Experimental Procedures.

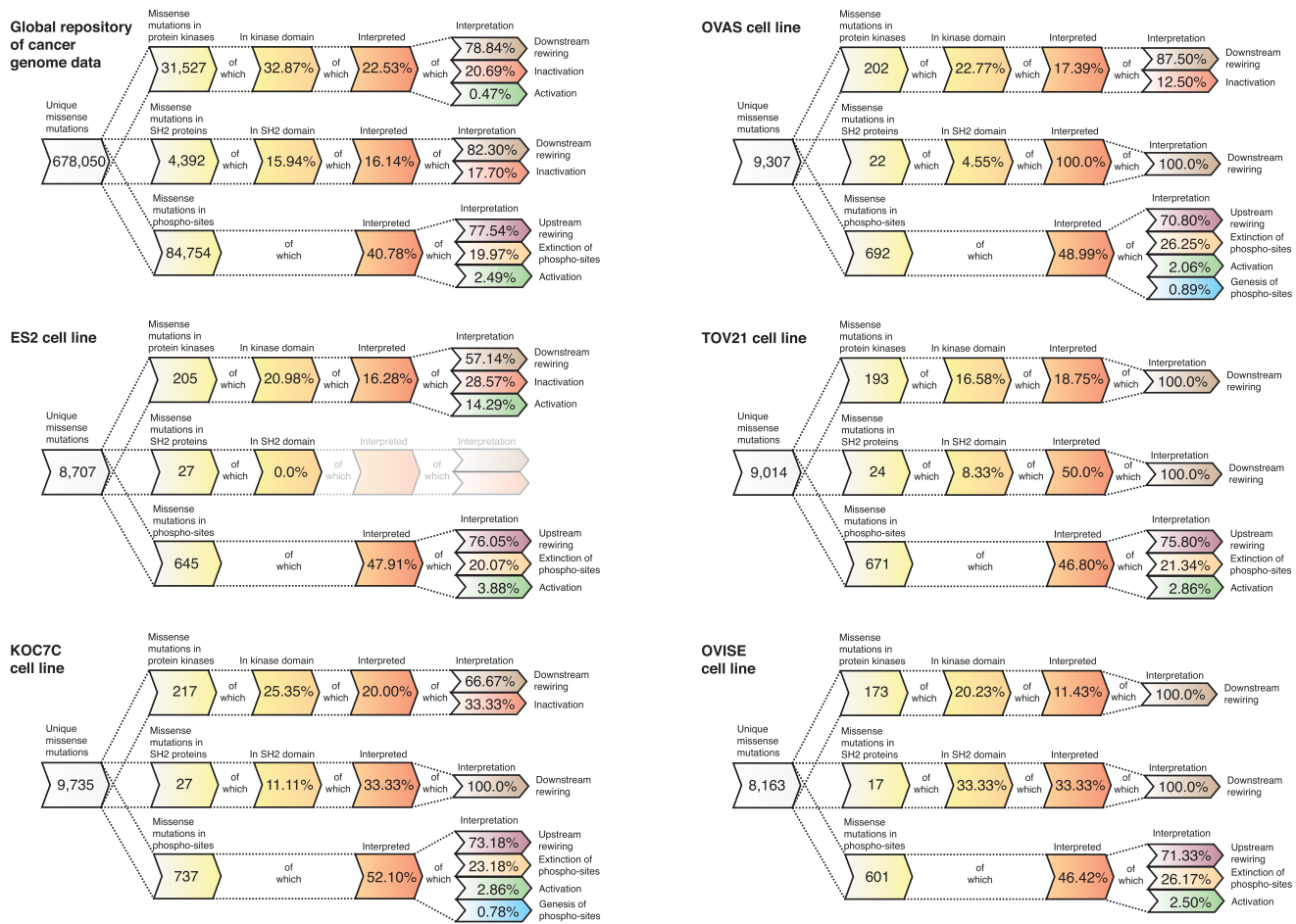


Figure 2. Overview of NAMs in Cancer Cell Lines and in the Global Repository of Cancer Somatic Mutations as Predicted by ReKINect

For each cell line and for the global repository of cancer somatic mutations we show the number of unique missense variants and how many of these variants fall within kinase proteins, SH2 proteins or phosphorylation sites (using a five-residue flanking region window surrounding the phosphorylation site). From these we then illustrate the fraction of variants falling within the respective domains and the fraction that can be interpreted by ReKINect. In the case of ES2, all of the 27 variants hitting an SH2 protein, hit outside SH2 domains, thus ReKINect could not make any predictions as to their effect (ghosted). It should be noted that the genesis of phosphorylation sites cannot be predicted from in silico analysis alone but require genome-specific-MS experiments. See also Figure S1.

predicted cell-cycle-dependent upstream kinase, CDK2, may lead to new insights on the role of this heat-shock protein in cancer (Figure 3A).

In order to discover NAMs destroying phosphorylation sites, we combined our exome sequencing data with those from the quantitative mass-spectrometry analysis of the phospho-proteomes of the five ovarian cancer cell lines. This enabled us to perform genome-specific searches of the mass-spectra, in order to identify direct proteomic evidence of the destruction of phosphorylation sites (Figure 3B) by identifying the mutated but unmodifiable peptides. This approach enabled us to identify 380 variants in our five cell lines and 6902 in the global repository of cancer mutations destroying phosphorylation sites (Experimental Procedures and Figure 2).

Two such events from the cell lines illustrated in Figure 3B, are RAB11FIP1 (T281M) and TNKS1BP1 (S1533G). Whereas the role of RAB11FIP1 in cancer is not as clear, Tankyrase-1-binding protein (TNKS1BP1) binds Tankyrase, which in turn, associates

with TRF1 protein at the telomeres. This complex is not only tightly regulated during cell-cycle progression but critically it regulates telomere length by binding on the double-stranded TTAGGG repeat of telomeres. This, together with the fact that Aurora Kinase B (AurKB), a key cell-cycle mitotic kinase (Alexander et al., 2011), is predicted by NetworKIN (Linding et al., 2007) to phosphorylate the wild-type form of TNKS1BP1, suggests a potential role in cell-cycle and telomere length dysregulation for this mutant variant.

In order to provide further characterization and assess the phenotypic impact of mutations resulting in genesis and destruction of phosphorylation respectively, we performed siRNA-based knockdown experiments of both TANC1 and RAB11FIP1 across the five cell lines. While knockdown effect could certainly be attributable to many other factors besides these specific mutations, surprisingly, as shown in Figure S3 and detailed in the *Supplemental Experimental Procedures*, we indeed observed phenotypic effects supporting

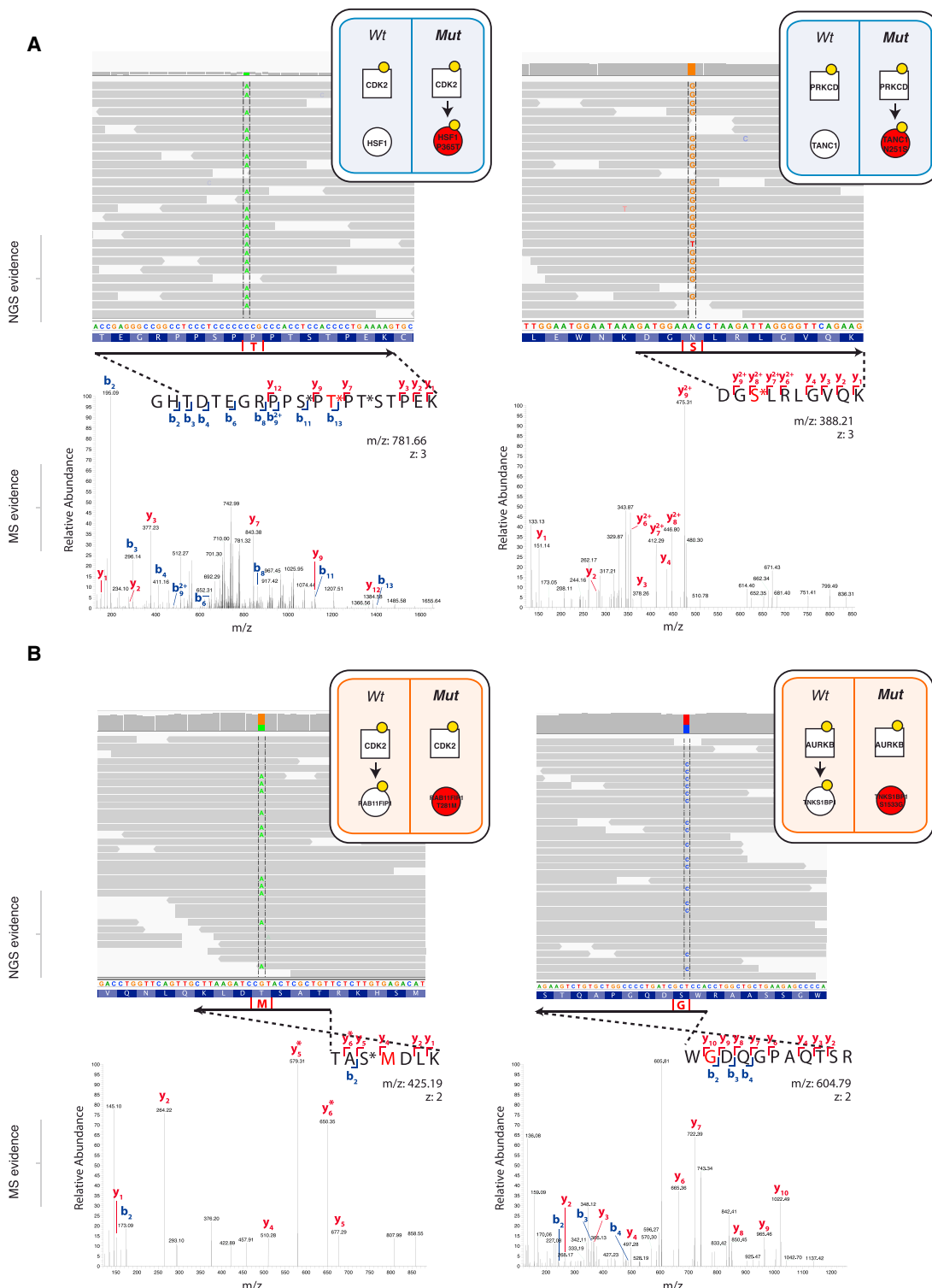
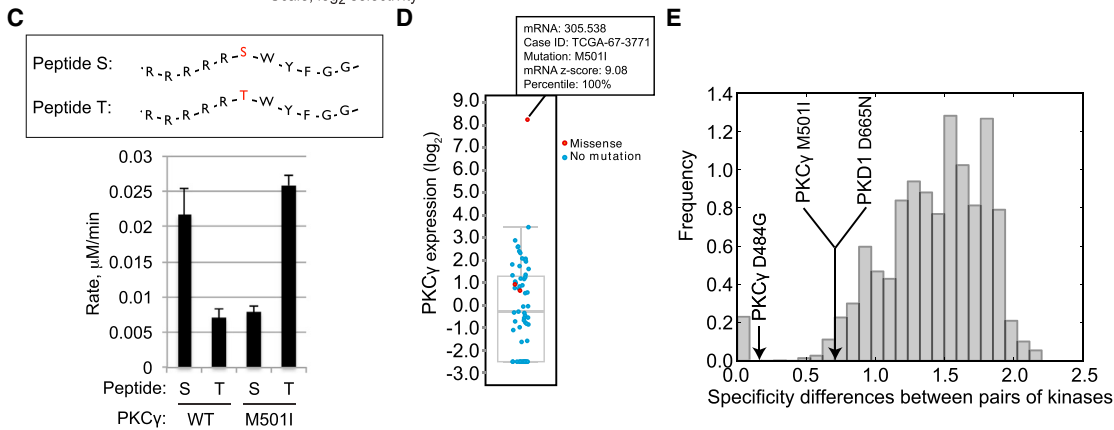
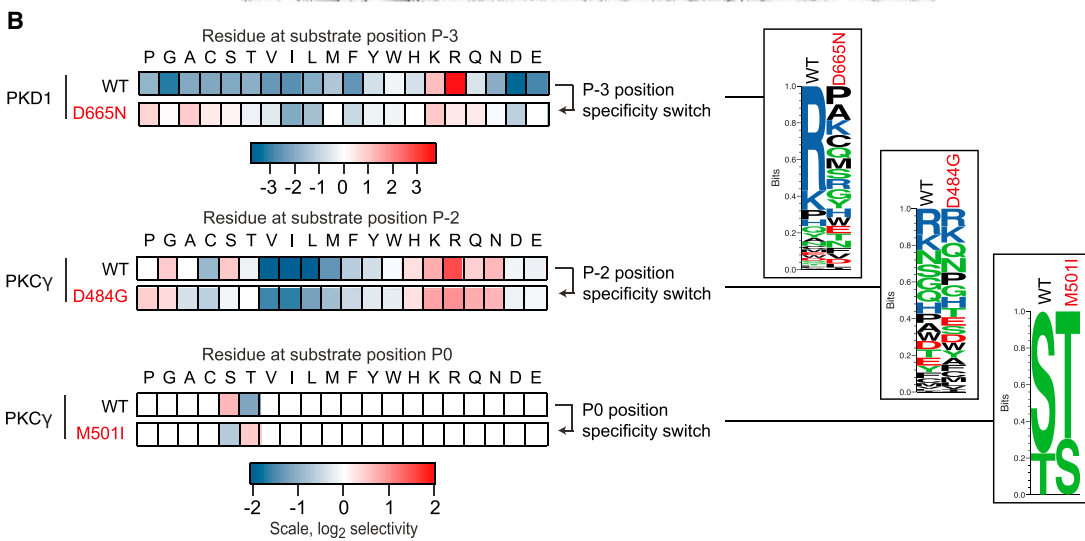
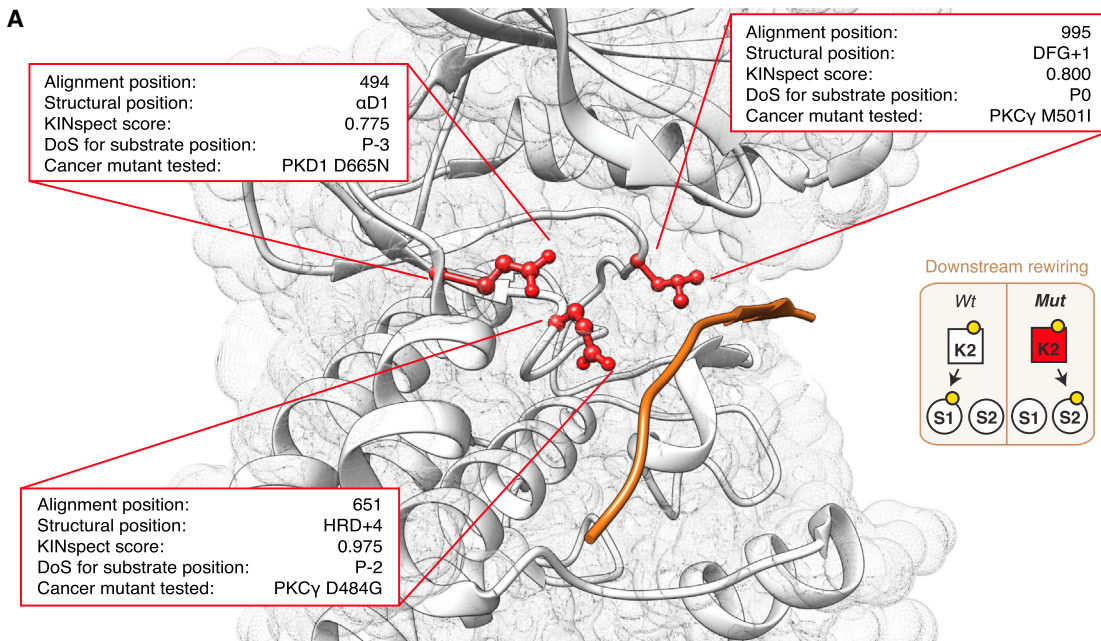


Figure 3. NAMs Leading to Genesis and Extinction of Phosphorylation Sites

(A) Two examples of network-attacking mutations generating new phosphorylation sites on HSF1 and TANC1, as evidenced by exome sequencing data and MS spectra matching the phosphorylated mutation.

(B) Two examples of network-attacking mutations causing the extinction of known phosphorylation sites on RAB11FIP1 and TNKS1BP1, supported by exome-sequencing data and MS spectra matching the unphosphorylatable mutated residue.

See also Figures S2 and S3.



(legend on next page)

the most parsimonious expectations arising from ReKINect's predictions.

Above, we aimed to provide the most accurate and evident instances of NAMs that generate and destroy phosphorylation sites and achieved this through integration of exome-sequencing and MS experimental data following stringent selection criteria ([Experimental Procedures](#)). Thus, we speculate that many more NAMs leading to the genesis and extinction of molecular logic gates will undoubtedly exist.

Kinase Downstream Rewiring

Next, in order to explore if cancer mutations can hit residues that determine kinase specificity (determinants of specificity [DoS]) and thereby impose downstream rewiring, we included the results from the KINspect algorithm, described in the accompanying article ([Creixell et al., 2015](#)), in the ReKINect platform. Sourcing from the global repository of cancer-associated somatic mutations we could predict a large set of putative NAMs leading to downstream rewiring ([Experimental Procedures; Table S1](#)).

Following a prioritization procedure described in the [Supplemental Experimental Procedures](#), we compiled a ranked list of cancer somatic mutations with the highest potential to cause downstream rewiring ([Table S1](#)). The list includes 1,871 unique missense mutations predicted to alter determinants of specificity by hitting the kinase domain residues most likely to play significant roles in specificity (specificity score higher than 0.9). Even with maximum stringency filters and focusing on the single kinase position most likely to drive specificity (highest specificity score of 1.0, previously reported by the literature as a determinant of specificity [[Brinkworth et al., 2003](#)]) and in direct physical contact with the substrate with a distance of <3 Å, we identified 42 unique missense mutations on this specific position covering all branches of the human kinome tree ([Table S1](#)).

As detailed in the [Supplemental Experimental Procedures](#), identifying the cases more suitable to experimental validation narrowed our candidates down to mutations on three positions in direct contact with the substrate and high KINspect score ([Creixell et al., 2015](#)) leading to the cloning, expression, and purification of these mutant kinases as well as their wild-type variants ([Figures 4A–4E](#)). First, we purified the two PKC γ mutants, D484G and M501I, predicted to perturb the determinants

of specificity in alignment positions 651 and 995, respectively ([Figures 4A and 4B](#)). Since the determinant of specificity perturbed by the mutant variant D484G was located four residues downstream of the conserved HRD motif on the kinase domain, we named this determinant as HRD+4 ([Figure 4A](#)). Given this spatial location and proximity to the P-2 position of the substrate peptide, we predicted this first mutant would affect P-2 specificity. In contrast, the mutant variant M501I was found immediately downstream of the conserved DFG motif within the kinase activation loop (DFG+1), a residue for which there is recent evidence for its role driving serine-threonine specificity at the phosphorylation site (P0 i.e., central S/T/Y residue) position ([Chen et al., 2014](#)). As shown in [Figures 4B and S4](#), experimental determination of the peptide specificity of both variants by positional scanning peptide library (PSPL) ([Hutti et al., 2004](#)) corroborated the specificity drift of both these mutants. In the case of the variant PKC γ D484G, our results uncovered a loss of Arg preference in position P-2 of the substrate peptide for the mutant variant ([Figures 4B and S4](#)). As predicted in the case of the variant M501I, PSPL results demonstrated a change in phosphoacceptor residue preference from Ser to Thr ([Figure 5B](#)). This specificity "switch" was further confirmed by performing phosphorylation assays on both the wild-type and mutant variants using a pair of matched peptide substrates of identical sequence save for having Ser or Thr in the P0 position ([Figure 4C](#)). As seen with PSPL analysis, WT PKC γ preferred Ser over Thr, while the M501I mutant by contrast phosphorylated the Thr peptide most efficiently. Given that PKC γ is a critical regulator of migration in development ([Kramer et al., 2002](#)), that it has been linked to metastasis ([Yang et al., 2014](#)), and that its overexpression in epithelial cells triggers a malignant phenotype and tumorigenic behavior *in vivo* ([Mazzoni et al., 2003](#)), we speculate that these specificity drifts ReKINect has predicted could provide tumorigenic, invasive, and metastatic capabilities to cancer cells. While these PKC γ mutants were identified in lung cancer samples ([Kan et al., 2010](#)) wild-type PKC γ is typically expressed only in the brain ([Sundram et al., 2011](#)). Interestingly, PKC γ was overexpressed in the tumor bearing the M501I mutation ([Figure 4D](#)) to levels substantially higher than in tumors where this genomic region had been amplified (as reported by cBioPortal [[Gao et al., 2013](#)]). A recent report highlighted loss-of-function mutations on PKC kinases

Figure 4. NAMs Causing Downstream Rewiring

(A) Three positions in direct contact with the substrate peptide, named α D1, HRD+4, and DFG+1, and likely involved in determining specificity for substrate positions P-3, P-2, and P0 (i.e., the phospho-acceptor site), respectively, harbor several cancer somatic mutations, three of which were selected for experimental validation.

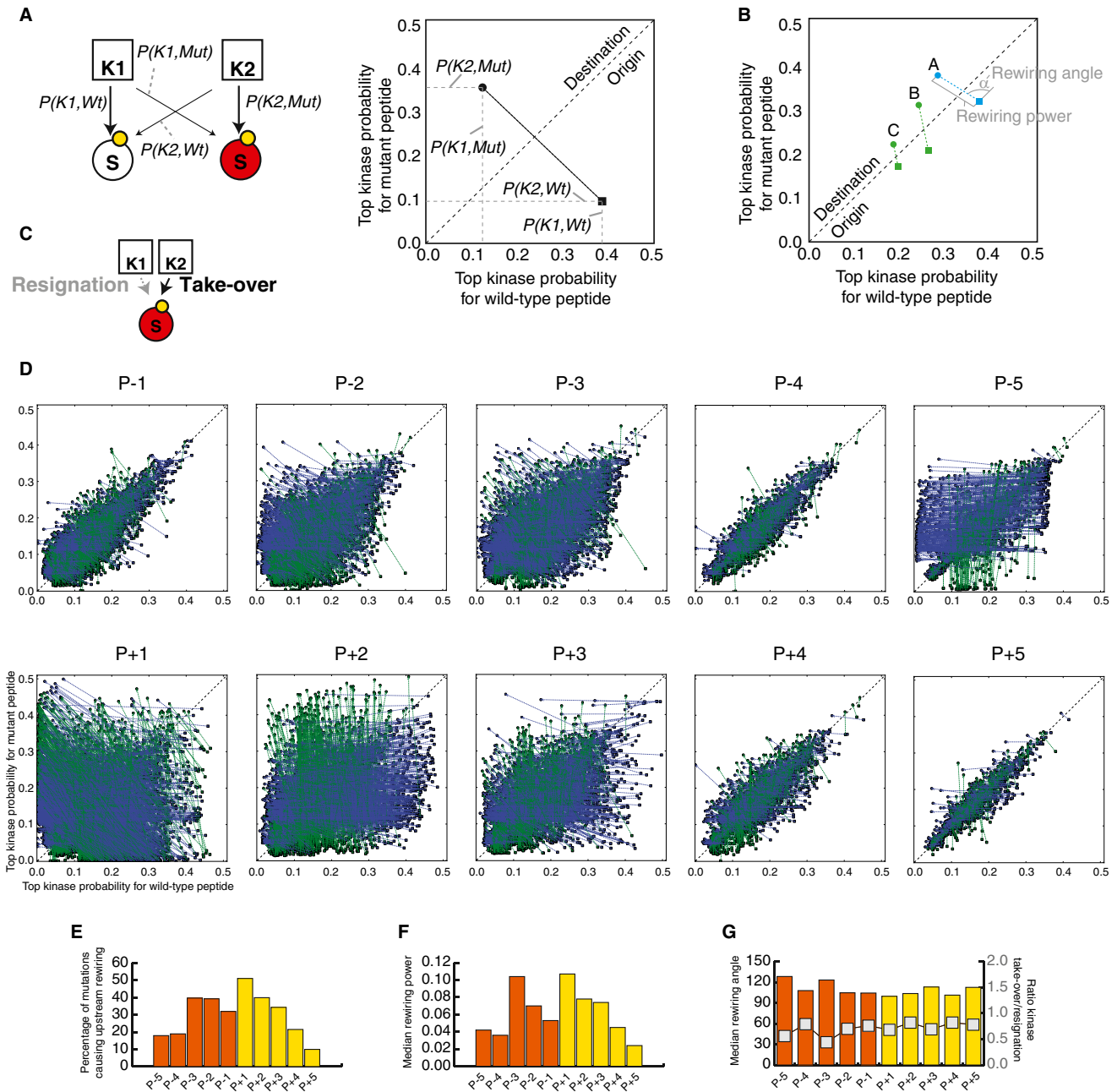
(B) Experimental validation by position scanning peptide library (PSPL) array of the specificity drift caused by downstream rewiring NAMs. Heat maps show normalized, averaged data from two independent experiments illustrating the specificity drift for the cancer variants PKD1 D665N and PKC γ D484G and M501I in substrate positions P-3, P-2, and P0, respectively. The results are also shown in logo form plotting the normalized information content in the wild-type and mutant specificity switch position (logos generated using Seq2Logo [[Thomsen and Nielsen, 2012](#)]).

(C) The P0 specificity switch of the PKC γ variant M501I was subsequently confirmed by quantifying the phosphorylation rate of identical peptide substrates containing either Ser or Thr at the phosphorylation site position (RRRRRSWYFGG and RRRRRRTWYFGG) by mutant and wild-type kinase variants. The graph shows the mean \pm SD (n = 4).

(D) PKC γ expression levels are markedly increased in the tumor sample harboring the PKC γ M501I downstream rewiring mutation.

(E) Comparison of the differences in substrate specificity typically observed between wild-type human kinases (gray histogram) and those mutant kinases reported here (black arrows). As evident from the plot, in two out of the three cases, the magnitude of the specificity drift caused by the cancer mutations is comparable to the specificity difference existing between different wild-type kinases.

See also [Figure S4](#).

**Figure 5. NAMs Causing Upstream Rewiring**

(A) Upstream rewiring mutations will cause a new kinase (from K1 to K2) to phosphorylate the mutant protein (S, red). By plotting the probability of both kinases to phosphorylate the wild-type and mutant variants of the protein, we can visualize, quantify, and compare different upstream rewiring mutations.

(B) The rewiring power and the rewiring angle can be computed by considering the necessary trajectory that the mutation causes (from the “origin” right-bottom triangle to the “destination” left-top triangle). The rewiring power is equivalent to the magnitude of the vector and measures the rewiring capacity of the mutation. The rewiring angle is the angle of the vector from the diagonal and distinguishes whether the rewiring effect is mainly driven by kinase resignation (i.e., a loss of phosphorylating ability of the wild-type kinase, angle >45°), depicted in blue, or by kinase take-over (i.e., an increase of phosphorylation ability of a new kinase, angle <45°), depicted in green. The three examples illustrate how three different mutations (A–C) can lead to different outcomes, such as the same rewiring power but different main driving force (A and B) or the same driving force but different magnitude (B and C).

(C) Illustration of the two main driving processes that cause upstream rewiring, namely the reduced ability of the original kinase to phosphorylate the new mutant substrate variant (resignation) and the increased ability of a second kinase to phosphorylate the mutant substrate protein (take-over).

(D) Representation of all the upstream rewiring mutations identified in the global repository of somatic mutations at different distances relative to the phosphorylation site (from five residues before a phosphorylation site, P-5, to five residues after a phosphorylation site, P+5). Rewiring events mainly driven by resignation are shown in blue and those mainly driven by take-over are shown in green.

(legend continued on next page)

(Antal et al., 2015), including PKC γ . By having altered substrate specificity, the two PKC γ mutants characterized here are likely to both lose the ability to phosphorylate some endogenous substrates while gaining the capacity to phosphorylate new de novo substrates.

Next, we purified the mutant variant of PKD1 predicted to perturb the determinant of specificity in alignment position 494 (Figures 4A and 4B) that we named α D1, given its location on the first residue of α helix D of the kinase domain. As with the PKC γ mutants, the PSPL experiments validated the specificity drift in PKD1 D665N (Figures 4B and S4). Specifically, this mutation causes loss of an essential feature of the WT kinase phosphorylation signature, namely selectivity for Arg at the P–3 position. An Arg residue is found at the P–3 position in critical targets of PKD1, including CREB, SSH1L, HDACs 5 and 7, HPK1, MARK2, and HSP27. This variant is therefore expected to perturb signaling downstream of PKD1, a kinase with roles in the development and metastatic progression of several cancers including prostate, breast, gastrointestinal, pancreatic, and skin cancers (Sundram et al., 2011). Having made this prediction for a mutation originating from a prostate cancer sample (Lindberg et al., 2013), potential deregulation between PKD1 and its substrate HSP27 is particularly notable, as its phosphorylation is closely related to androgen receptor function in prostate cancer (Hassan et al., 2009; Sundram et al., 2011). In addition to breaking these interactions in the signaling network, because the D665N mutation renders PKD1 a less specific kinase, we anticipate that the mutation will generate many new connections through phosphorylation of non-native substrates, some of which may contribute to the malignant phenotype.

We next assessed the magnitude of the specificity switches caused by these cancer mutations, by comparing the wild-type to mutant drift in specificity to the specificity differences observed between wild-type human kinases across the kinome. As shown in Figures 4E and S4, two out of the three downstream rewiring mutations cause a specificity drift of a magnitude comparable to the specificity difference that exists between different wild-type human kinases. Effectively, this implies that a single cancer mutation can lead to a specificity switch that is analogous to a new kinase appearing in the genome.

With these validated examples at hand, we set out to further investigate whether other cancer mutations could cause similar dramatic specificity drifts and switches in other human kinases. By analyzing predictions from ReKINect based on cancer mutations identified to hit validated DoS residues (Table S1), in many cases with amino acid substitutions analogous to the ones we experimentally tested above, we could indeed identify additional cancer mutations that with high likelihood cause downstream rewiring. In the case of the HRD+4 site, 41 additional cancer mutations were identified substituting this site to multiple other residues (Table S1).

Moreover, in addition to the PKC γ M501I mutant, we could identify 29 other cancer mutations hitting the DFG+1 site, eight of which with analogous substitutions of large hydrophobic residues with β -branched aliphatic residues (Haspin L669I, DDR1 M793I, ITK M503V, TRKA M671T, IRAK3 M314I/M341V/M341T, and BRAF L597V), the type of substitution that most likely leads to a specificity switch from a preference for phosphorylating Ser to Thr (Figure S4; Table S1). In contrast, no mutant was found that would perturb specificity in the opposite direction (from Thr to Ser phosphorylation preference; Figure S4). Thus, it appears there is a general trend toward increased phosphoThr-driven signaling in cancer.

Of these 29 mutants, the identification of a likely mechanism of action for BRAF L597V is of critical relevance as it is not only a germline mutation in Noonan syndrome and cardio-facio-cutaneous syndrome, but also plays a significant role in the development of cancer when acting in epistatic synergy with Ras G12V (Andreadi et al., 2012; Davies et al., 2002). While the molecular mechanisms of this epistatic interaction could potentially be linked to changes in BRAF dimerization, our results suggest that Ras G12V could ensure the hyperactivity of this signaling network, whereas BRAF L597V rewrites it by a drift in BRAF's kinase specificity. Such a scenario is reminiscent of previous interactions between different mutations promoting cancer development in a synergistic manner (Creixell et al., 2012a; Wu et al., 2010). Finally, we could identify 40 cancer mutations in addition to the PKD1 D665N mutation perturbing the α D1 site, eight of which containing the same amino acid substitution D to N (PKCb D427N, TSSK1 D97N, TTBK1 D116N, CDK11b D507N, CDK8 D103N, PFTAIRE1 D198N, PDGFRa D681N, and STYK1 D201N) and thereby constituting high-confidence downstream rewiring mutants (Figure S4; Table S1).

Altogether, these results represent the discovery of three new downstream rewiring mutations on three distinct determinants of specificity (HRD+4, DFG+1, and α D1) and show that single-point NAMs can drive downstream rewiring of a magnitude that is analogous to a new kinase suddenly appearing within the human kinome. They also suggest that the prioritized collection of mutations we provide is likely to contain even more cancer mutations causing rewiring (16 of which being clear high-confidence candidates, Figure S4).

Upstream Kinase Rewiring

Complementary to the downstream rewiring NAMs, we next investigated whether mutations could also cause upstream rewiring (i.e., when a substrate is, due to the impact of a mutation, being phosphorylated by different upstream kinases) by perturbing phosphorylation motifs on the substrate (Figure 1). By analyzing mutations that fall within 5 flanking residues of known phosphorylation sites (see Experimental Procedures) with the NetPhorest (Miller et al., 2008) and NetworKIN (Lindberg et al., 2007) algorithms on the wild-type and mutant variants of the

(E) Quantification of the percentage of mutations leading to upstream rewiring depending on their position relative to the phosphorylation site.

(F) Assessment of the median magnitude of rewiring for mutations based on their position relative to the phosphorylation site.

(G) The median rewiring angle (orange and yellow bars) and the ratio of take-over over resignation rewiring mutations (gray line) conditioned on the position of the mutation relative to the phosphorylation site.

See also Figure S5.

same protein, we could predict the likely upstream rewiring effects of mutations on substrates. As detailed in [Figure 5](#) (see also [Figure S5](#) and [Tables S2](#) and [S3](#)), for a given predicted rewiring event (i.e., where the upstream kinase predicted for the wild-type and mutant variants of the substrate is non-identical) we defined two variables termed “rewiring power” and “rewiring angle” based on the predicted probability for the most likely upstream kinase in the wild-type and mutant substrate variants ([Figures 5A](#) and [5B](#)).

The rewiring power measures the magnitude of the rewiring event, by accounting for the loss of phosphorylation potential of the old upstream kinase as well as the gain in phosphorylation potential of the new upstream kinase. The number of rewiring events and their rewiring power showed a non-uniform distribution where, generally, mutations closer to a phosphorylation site have a higher chance of causing upstream rewiring and the rewiring event itself will be of higher magnitude (rewiring power) ([Figures 5D–5F](#)). This global trend is observed for all positions except for the position just before the phosphorylation site, P–1, where mutations are less likely to lead to rewiring events and will most often be of lower magnitude. In fact, such distribution with the singularity of P–1 resembles the positional distribution of information content of kinase substrate specificity ([Figure S5](#)), underlining a fundamental link between the criticality of a given position for substrate recognition by upstream kinases and the disruptive potential of cancer somatic mutations hitting those positions. In other words, positions critical to and in direct close contact with the phosphorylating kinase (e.g., P+1, P+2, P–2, or P–3, as opposed to P–1 that makes very few contacts with the kinase) ([Brinkworth et al., 2003](#)) are far more likely to harbor strongly rewiring mutations.

The repertoire of potential upstream rewiring events allowed us to address the central question of whether rewiring is most often driven by an increased phosphorylation propensity for the mutant substrate variant by a new kinase (which we term “kinase take-over”) or, inversely, if caused by a reduced propensity for the original kinase upon mutation (which we term “kinase resignation”) ([Figure 5C](#)). The rewiring angle does, in effect, measure which of the two forces is stronger, with rewiring events mainly driven by kinase take-over leading to a rewiring angle $<45^\circ$ from the diagonal in [Figure 5B](#), while rewiring events mainly driven by kinase resignation would be associated with rewiring angles $>45^\circ$. As shown in [Figure 5G](#), our results based on the median rewiring angle as well as the ratio of take-over/resignation events measured at different positions relative to the phosphorylation site show that, regardless of the position, upstream rewiring events are predominantly driven by kinase resignation forces. Illustrative examples of this can be found in [Tables S2](#) and [S3](#), where many of the most strongly rewiring events are caused by cancer mutations disrupting, for instance, proline residues in P+1 positions of CDK substrates. For example, a mutation juxtaposed to a phosphorylation site on position 721 of damage-specific DNA binding protein 1 (DDB1 P721Q) is predicted to cause an upstream shift from CDK1 to ATM and a similar mutation on CCP110 (CCP110 P171L) leads to a predicted upstream rewiring from CDK1 to PLK1 ([Table S3](#)). Finally, mutations on ORC1 (P312S), CDC23 (P583T), and NUMA1 (P113H) illustrate how disruption of pleio-

tropic recognition motifs, such as the one for CDK1 kinase, can lead to upstream rewiring events.

Overall, these results suggest that cancer mutations may rewire upstream signaling typically by worsening an optimal substrate site for a given upstream kinase and not by generating a more optimal substrate better matching another upstream kinase. Considering the fact that it has taken millions of years to evolve exquisitely fine-tuned motifs around phosphorylation sites that would confer signaling specificity and fidelity ([Tan et al., 2009](#); [Zarrinpar et al., 2003](#)), it is not so surprising that cancer mutations most often perturb this finely evolved system by generating weaker phosphorylation motifs.

Constitutive Activation and Inactivation of Kinases

As a final group of NAMs on protein kinases, we also analyzed the presence of mutations that would lead to the constitutive activation and inactivation of protein kinases ([Figure 1](#)).

Starting from the former case, we used the so-called phospho-mimicking effect of acidic mutations in close proximity to (just before, P–1, or after, P+1) activating phosphorylation sites on the activation segments of kinase domains ([Davies et al., 2002](#)) to identify in silico missense mutations that can result in a constitutively active kinase.

Taking the well-characterized case of BRAF V600E, a phospho-mimicking activating mutation, as a positive test case, we confirmed that ReKINect could identify this mutation in one of the ovarian cell lines (ES2) and predict it as kinase activation. We subsequently experimentally confirmed the hyper-phosphorylated state of the BRAF substrate, MEK by immuno-blot in the ES2 line ([Figures 6A](#) and [6B](#)).

In addition to this well-known case, ReKINect predicted 23 other instances of potential constitutively activating kinase mutations ([Table S4](#)). Although some of these mutations fall nearby or on phosphorylation sites that have not yet been shown to regulate enzymatic activity, for a considerable fraction of them there is substantial evidence they could lead to kinase activation ([Table S4](#)). One exciting example of a predicted phospho-mimicking mutation was identified on the hematopoietic progenitor kinase 1 (HPK1), namely the mutant variant HPK1 A164D. Alanine 164 is immediately adjacent to the activating phosphorylation site T165 on the activation segment of HPK1, and mutation to Asp is predicted to confer constitutive activation of HPK1 and the likely engagement of its downstream JNK and NF- κ B signaling ([Arnold et al., 2005](#)). Thus, the ReKINect predictions suggest a role for cellular stress response and potentially hematopoietic involvement in lung cancer, the cancer type in which this mutation was identified.

To model kinase inactivating mutations, we hypothesized that mutations that alter catalytically essential residues (e.g., residues mediating ATP binding, Mg²⁺ coordination or phosphotransfer, as defined in [Zeqiraj and van Aalten, 2010](#) and [Table S5](#)) could lead to kinase inactivation. The high number of instances identified by ReKINect and detailed in [Table S6](#) (427 unique kinase inactivation events) suggests that a large number of kinases become inactivated during cancer development. While it has previously been shown that inactivating mutations on kinases could lead to Peutz-Jeghers syndrome ([Mehenni et al., 1998](#)) or to pseudo-kinases throughout natural

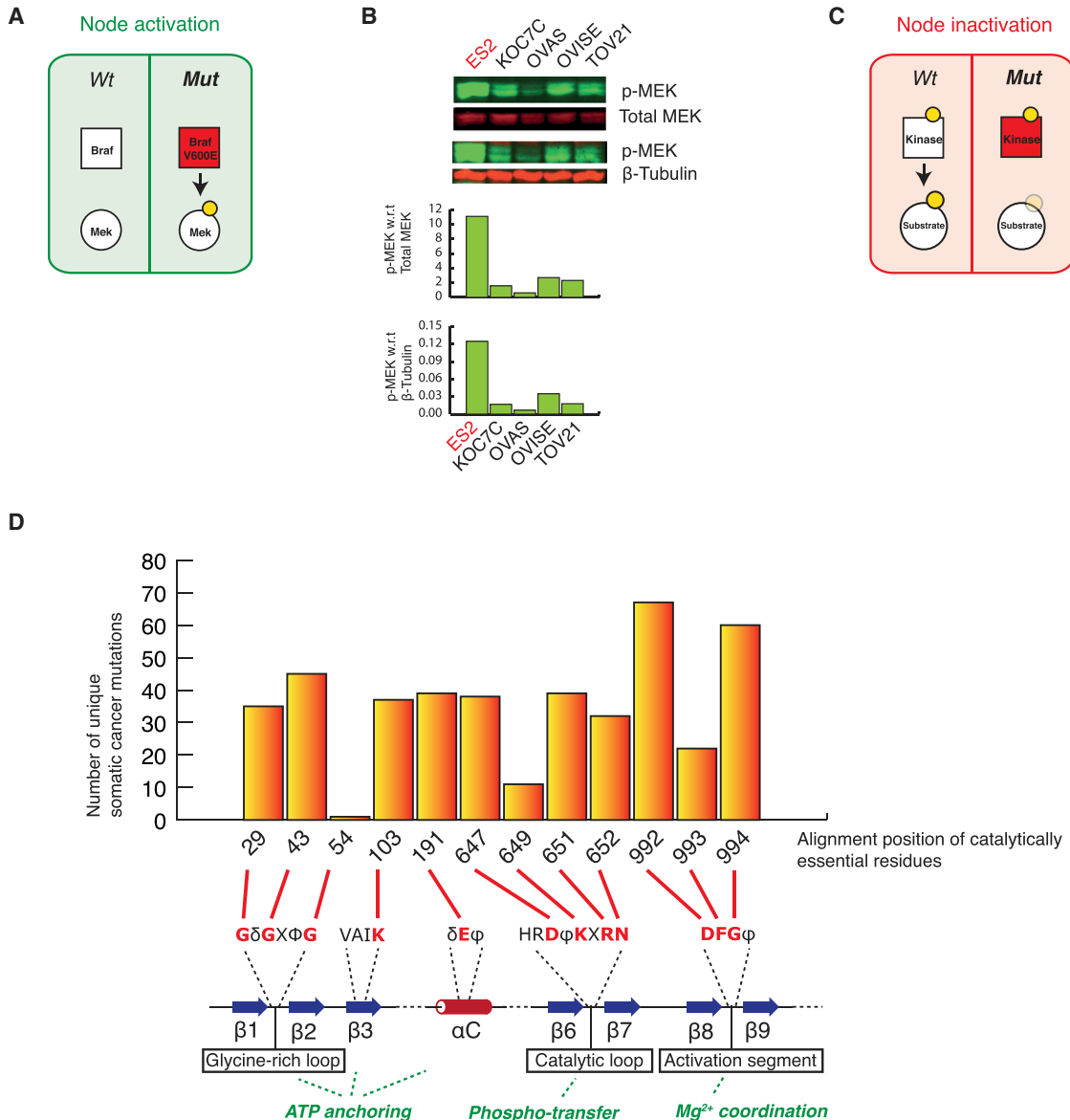


Figure 6. Constitutive Activation and Inactivation of Kinases by NAMs

- (A) ReKINect identified ES2 cells as containing the constitutively activating BRAF V600E mutation.
- (B) An immunoblot and associated quantification, illustrating the phosphorylation of BRAF substrate MEK in the mutant cell line ES2 (in red) compared to the wild-type cell lines (in black), using total MEK and β-tubulin for normalization.
- (C) ReKINect identified several cancer mutations in catalytically essential residues of kinase domains.
- (D) A quantification of all mutations from the global repository of cancer somatic mutations predicted to inactivate kinases and the catalytically essential positions they hit. Mutations leading to kinase domain catalytic inactivation are enriched (χ^2 test, $p = 1.69 \times 10^{-16}$) in cancer somatic mutations (with particular preference for the aspartate, D, and glycine, G, in the DFG motif).

evolution (Zeqiraj and van Aalten, 2010), our results indicate that kinase inactivation may hitherto have been largely under-appreciated in the interpretation of cancer genomes.

A closer inspection of these predicted inactivating mutations reveals a bias toward specific critical residues. In particular the first and third residues of the DFG motif (i.e., the glutamate and glycine, respectively) that defines the start of the activation segment, harbors approximately one-third of all inactivating

mutations (Figures 6C and 6D). While mutations in other essential residues are likely to equally lead to kinase inactivation (see Table S5 for further information on the kinase catalytically essential residues included as part of ReKINect), our results suggest a significant preference for these two residues being mutated in the context of kinase inactivating mutations in cancer (χ^2 test, $p = 2.2 \times 10^{-16}$). Thus, these two positions of the DFG motif are predicted to constitute structural and

biochemical hotspots for NAMs leading to inactivation of protein kinases in cancer.

Overall, these results suggest that ReKINect is capable of predicting NAMs that constitutively activate or inactivate protein kinases and that, in addition to BRAF V600E, numerous other similar mutations are likely to exist that directly affect the catalytic activity of kinases in cancer signaling.

Functional Mutations in SH2 Domains and Global Phenotypic Impact of NAMs

The SH2 domain is of seminal importance to signaling fidelity, cellular organization, and function across Metazoan species and is often part of protein kinases and perturbed in human disease (Bibbins et al., 1993; Manning et al., 2002; Marengere et al., 1994; Pawson et al., 2001). Thus, we reasoned that the inclusion of the SH2 domain as part of ReKINect would enable us to make integrated predictions of higher accuracy and relevance from a signaling perspective. SH2 domains possess an essential Arg residue found within a highly conserved sequence motif (FLVRES) that makes direct contact with phosphoTyr residues in its binding partners (Bibbins et al., 1993). By incorporating this critical residue for the phospho-tyrosine binding function of SH2 domains into ReKINect, we could predict 20 distinct instances (including mutations on ABL, SYK, and GRB10) where cancer mutations disrupt a critical functional residue, thus impairing the ability of the mutant SH2 domains to bind their substrates (Table S7).

As with the mutations causing kinase downstream rewiring, by mapping cancer mutations onto the determinants of specificity of the SH2 domain identified by our algorithm KINspect (Creixell et al., 2015), ReKINect predicted 93 NAMs causing SH2 downstream rewiring (Table S8) by changing positions within the domain that show a high likelihood of playing a critical role in substrate specificity (specificity score higher than 0.9). The comparably lower number of inactivating and downstream rewiring mutations in SH2 domains compared with kinase domains, is attributable at least in part to the smaller number and size of SH2 domains in comparison with kinase domains (Figure S1).

Finally, to systematically explore the potential functional or phenotypic impact of the NAMs described above, we performed RNAi knockdown of kinase and SH2 domain containing proteins across the ovarian cancer cell lines. The effect of these perturbations on nuclear number was then determined using a regressor network model of protein-protein interactions and NAMs (Figure S3; Experimental Procedures). We found that if ReKINect classified NAMs were present in the network vicinity of the RNAi target gene a significant impact on the phenotypic response, either pro- or anti-proliferative, was observed ($p = 7.1 \times 10^{-13}$). These results would suggest that network attacking mutations, predicted by ReKINect, are not only biochemically functional but also lead to significant phenotypic changes in cancer cell models, on a global scale.

DISCUSSION

Given that protein kinases are one of the protein classes most frequently encoded by cancer genes (Futreal et al., 2004) and

mutated in cancer (Figure S1) as well as a major molecular target of therapeutic drugs (Anastassiadis et al., 2011; Davis et al., 2011), it is essential to identify how phosphorylation-based signaling networks drive cancer. Thus, the number of distinct NAMs cataloged by ReKINect represents promising new leads for future studies. Serving as a systematic complement to previous efforts identifying the function that individual cancer mutations may play (Davies et al., 2002; Friend et al., 1986; Stehelin et al., 1976), ReKINect is designed to predict the underlying signaling mechanisms and perturbations caused by mutations in cancer, or other complex diseases, using first principles governing protein function from evolution, protein chemistry, and protein structure and architecture.

Evidence for NAMs and Signaling Trends in Cancer

Through integration of low and high-throughput computational and experimental technologies, we have discovered the existence of the NAMs described in Figure 1. Having analyzed the data generated here and in global genome sequencing efforts, we conclude that there is ample evidence supporting the hypothesis that all the different types of NAMs described do indeed occur in cancer.

In addition, our results also uncovered a variety of interesting signaling trends resulting from cancer mutations: first, our results demonstrate the existence of new molecular logic gates in cancer. The genesis of new phosphorylation sites by mutations as uncovered here illustrate how cancer cells can acquire novel and prominent signaling flows and altered information processing that may result in new phenotypic states to be reached.

We identified and experimentally confirmed three striking examples of cancer mutations directly leading to a catalytic specificity drift, PKD1 D665N, PKC γ D484N, and M501I. Downstream rewiring had until now been the most elusive type of NAMs, as reflected by the fact that only a single instance of this type of mutation, where a kinase is altered in specificity through mutation, RET M918T, had been reported in the literature (Borrello et al., 1995; Santoro et al., 1995; Songyang et al., 1995). The discovery of these three new NAMs, using a global yet selective and sensitive approach, would suggest that many more such events could exist in cancer.

Supporting this, we could pinpoint 16 additional cancer mutations that, given that they harbor identical amino acid substitutions to the ones we tested, are most likely to also encode downstream rewiring events. Next, when studying NAMs that would lead to downstream rewiring on a position that was recently confirmed to drive peptide specificity on the phospho-acceptor of phosphorylation sites (Chen et al., 2014), we could identify nine cancer mutations that are predicted to steer signaling toward phosphorylation of Thr, whereas no mutants were found in the opposite direction (Figure S4). Despite the fact that these numbers are not sufficiently high to enable robust statistics and that a large number of wild-type kinases originally encode Ser-directing residues in the DFG+1 position (thereby partially explaining the lack of Thr-to-Ser mutants), this bias suggests that specific cancers may harbor increased Thr-based signaling. Given that, due to its unique mutational and physico-chemical properties, serine has been identified as a mutational hub (Creixell et al., 2012b) and thereby a likely result of cancer

mutations, we speculate that through such Ser-to-Thr signaling rewiring cancer cells might evolve less dependency on serine signaling.

Furthermore, if by affecting a large number of substrates, downstream rewiring NAMs are likely to have a broader impact at the network level, the fact that two of the downstream rewiring mutants described here lead to a less specific kinase and are thus likely to phosphorylate more substrates, highlights even further the potential impact of these NAMs. These results significantly extend our previous observations that less-specific kinases tend to be cancer mutation targets (Miller et al., 2008) and serve as a critical resource that we hope will start paving a new avenue on signaling specificity in cancer research.

Similar to the case of kinase downstream rewiring, relatively few mutations on SH2 domains had been reported to obliterate tyrosine-binding or shift their specificity (Marengere et al., 1994; Pawson et al., 2001), highlighting that this might also be a hitherto hidden and yet perhaps a fundamental signaling trend in cancer.

Finally, an over-representation of kinase-resignation upstream rewiring events suggests that cancer mutations most often lead to upstream rewiring by worsening existing optimal substrates rather than generating super-optimal new substrates for other upstream kinases. Given the amount of fine-tuning achieved over millions of years of evolution at the substrate level (Tan et al., 2009; Zarrinpar et al., 2003), it is perhaps to be expected that mutations in substrates will most often lead to poorer phosphorylation motifs.

Finally, our results suggest both the existence of previously unknown constitutively activating mutations in kinases as well as the presence of mutational hotspots on two specific positions leading to the inactivation of protein kinases, namely the Asp and Gly within the DFG motif at the beginning of the activation segment. It could be the aim of future studies to elucidate why these spots are preferred by cancer mutations when inactivating kinases.

Non-Recurrent yet Functional NAMs

While a large fraction of recurrent and/or conserved mutations can directly or indirectly be considered NAMs as they typically perturb signaling networks (as exemplified here with BRAF V600E) and they typically operate as functional driver mutations, in this study we have demonstrated that non-recurrent and non-conserved mutations also can be functional NAMs (Figure 7B). This may be most evident from the observation that downstream rewiring mutations can lead to a switch of specificity of a comparable magnitude to the specificity difference between two distinct kinases in the human kinome. Thus, despite the fact that previous studies of cancer mutations, including some on kinase domains, have disregarded non-recurrent variants as being non-functional passenger mutations (Greenman et al., 2007), our results suggest that many of these do indeed have a functional role. Still, pinning down the actual contribution of these less frequent yet functional mutations, or combinations thereof, and under which context they drive oncogenesis will require a concerted research effort by both the genomics and signaling communities. If we move from a perception of oncogenes and tumor-suppressors operating in isolation to drive oncogenesis,

toward a new paradigm, where numerous mutations play a driving role under specific cellular contexts (e.g., when appearing in combination with other mutations) (Creixell et al., 2012a; Wu et al., 2010), it will be important to acknowledge that it is likely that several of these functional NAMs drive cancer in a concerted fashion.

As shown in Figure 7A, some of the NAMs we have identified here are likely to impose dramatic alterations in signaling networks, such as specificity switches that are analogous to introducing a new kinase and thus may play a driving role in oncogenesis.

The fact that there are multiple strategies in which the same signaling output can be achieved by distinct cancer mutations (as shown for instance by inactivating mutations in Figure 6D) and that we have identified overexpression of an instance of one of these functional NAMs, further supports the importance of such less frequent functional mutations (Figure 7B).

Perspectives

Our results suggest that signaling networks are both dynamically and structurally rewired in cancer cells to an extent far beyond what was previously anticipated. Such rewiring includes constitutive activation and inactivation of kinase and SH2 domains, upstream and downstream rewiring of phosphorylation-based signaling, and the extinction and genesis of phosphorylation sites. These findings will be critical for network medicine efforts where drug targets for complex diseases are defined at the network level and for the individual patient or tumor.

Here, we demonstrated six distinct NAMs as proof-of-principle and verified all the NAMs described in Figure 1A are present in cancer. Future expansions of the KINspect (Creixell et al., 2015) and ReKINect algorithms to include other protein domains, PTMs, and linear motifs, more complex genetic perturbations (such as copy-number variations or genomic re-arrangements leading to protein fusions) and the advancement of sequencing and MS technologies, will likely facilitate the discovery of many additional NAMs. Such advancements to link cancer genomic and proteomic data will become valuable resources for dealing with the intrinsic complexities of tumors (Weinberg, 2014; Yaffe, 2013).

In the last century, Schechter et al. (1984) and Ullrich et al. (1984) connected the discovery of the oncogene Her-2/neu to its hyperactivity in a fraction of breast cancers (Slamon et al., 1987) and the development of targeted therapies such as Trastuzumab (Carter et al., 1992). Others linked the discovery of the BCR-ABL fusion protein (Rowley, 1973) to CML leading to the development of Imatinib (Druker et al., 1996) and newer generation inhibitors. Similarly, we hope that ReKINect, and similar tools, can be utilized to close the cancer mutation interpretation gap. Boosting genomic interpretation capacity should ideally parallel the rate at which next generation technologies identify new mutations in order to help meet the bench-to-bedside challenge (Figure 7C), assist clinicians in making better treatment decisions for those patients carrying infrequent yet functional cancer mutations and facilitate the development of novel “magic bullets” (Strebhardt and Ullrich, 2008) and precision medicines (Creixell et al., 2012a).

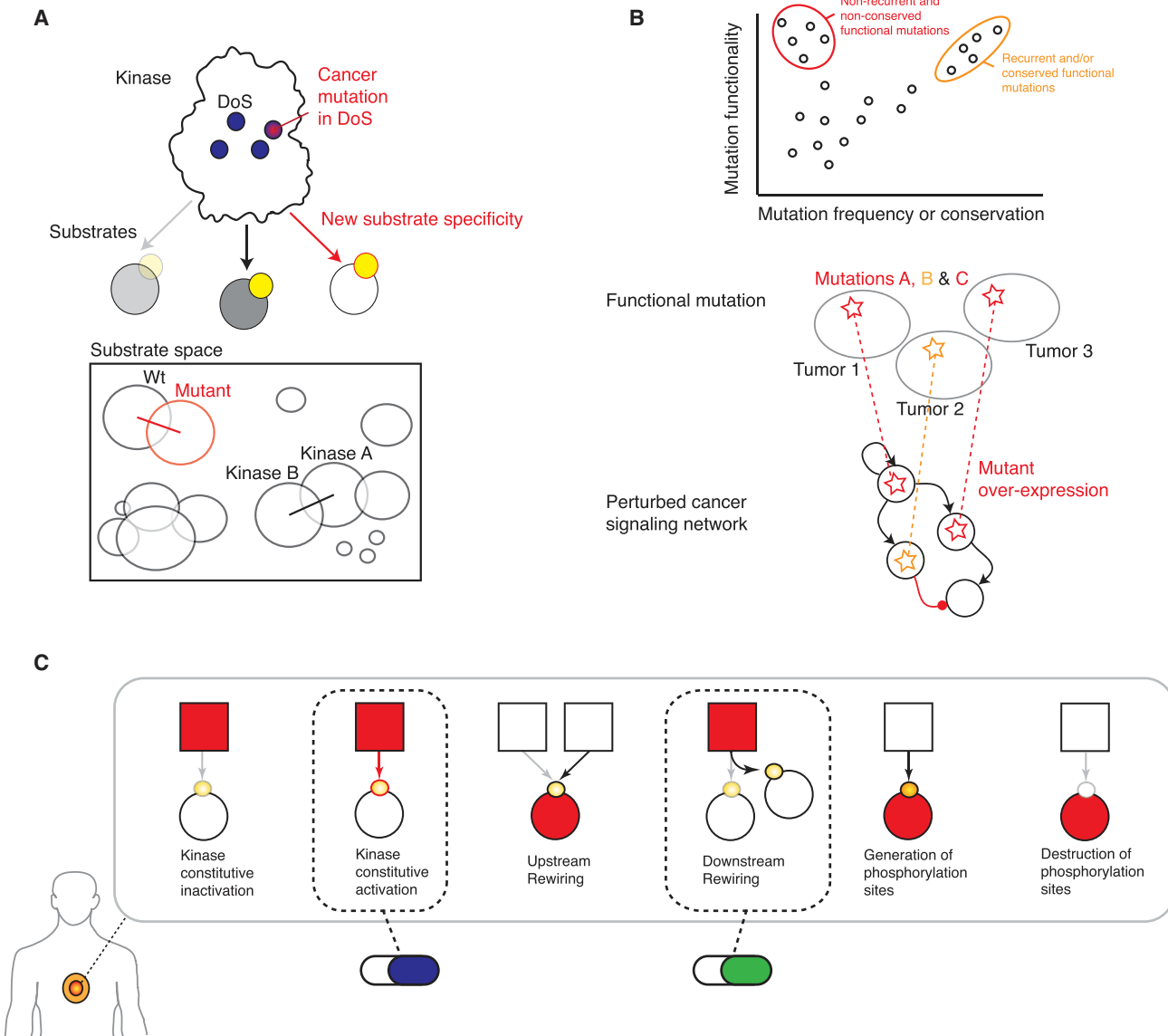


Figure 7. Evidence and Model for Functional Mutations and Tumor-Specific Network Medicine

(A) The functional mutations found in this study are clear examples of single amino acid mutations that can severely perturb signaling networks.

(B) Our study shows how non-recurrent cancer mutations on non-conserved residues can be functionally important and that functional recurrent (orange) and non-recurrent (red) NAMs can converge at the signaling network level. We also identified a case where a functional mutation in a low-abundant protein is accompanied by its overexpression.

(C) The deployment of tools like ReKINect should enable the proposition of more refined signaling mechanisms underlying cellular cancer phenotypes and identification of driver and therapeutically relevant mutations.

EXPERIMENTAL PROCEDURES

Building Comprehensive Sets of Sequences: Kinome, SH2ome, and Phosphorylation Sites

We built comprehensive sets of sequences covering all human kinase proteins (Manning et al., 2002), 120 SH2 domains (Liu et al., 2006), and a broad set of known human phosphorylation sites (Hornbeck et al., 2004). With these sets, we performed domain-centered sequence alignments using ClustalW and Omega (Sievers et al., 2011) followed by subsequent manual refinement. These alignments were then deployed by identifying functional residues on them and mapping these residues back to the wild-type version of the mutant

sequences analyzed with ReKINect. Similarly, phosphorylation site peptides were matched to the wild-type variants of all mutations, so that the distance between each mutation and its closest phosphorylation sites could be determined.

Collecting a Global Repository of Somatic Cancer Mutations

We compiled a global set of publicly available somatic cancer mutations from COSMIC v67 (Forbes et al., 2011) and generated the FASTA files required by ReKINect containing both the wild-type and mutant versions of all coding missense variants, using purpose-made Python scripts and ENSEMBL's VEP resource (Flicek et al., 2014).

Computing Minimum Distance to Substrate from PDB Files

Minimum distances to substrates were computed as described in the accompanying article (Creixell et al., 2015) and further detailed in the *Supplemental Experimental Procedures*.

Protein Kinase Specificity Assays

Kinases and mutants were expressed by transient transfection of encoding plasmids in HEK293T cells, purified by FLAG affinity purification, and PSPL experiments were performed as described (Mok et al., 2010). Further details can be found in the *Supplemental Experimental Procedures*.

Further details about the maintenance of cell lines, preparation of sequencing, mass spectrometry, and RNAi screening samples and their computational analysis can similarly be found in the *Supplemental Experimental Procedures*.

SUPPLEMENTAL INFORMATION

Supplemental Information includes Supplemental Experimental Procedures, five figures, eight tables, and six data files and can be found with this article online at <http://dx.doi.org/10.1016/j.cell.2015.08.056>.

AUTHOR CONTRIBUTIONS

P.C. and R.L. conceived the project. P.C., E.M.S., C.D.S., J.L., C.J.M., H.J.L., L.P., T.R.C., N.Z., and B.B. performed wet-lab experiments. P.C., E.M.S., A.P., A.W., and J.F.-B. performed computational experiments. P.C. generated the lists of NAMs assisted by A.P. P.C. and B.E.T. prioritized the list of NAMs likely to drive downstream rewiring. H.I. provided cell lines. All authors analyzed different parts of the data generated. P.C. and R.L. wrote the article with help from the other authors.

ACKNOWLEDGMENTS

This article is dedicated to the memory of late Tony Pawson, whose groundbreaking research represented a fundamental foundation to this work. We thank T. Gibson for technical assistance with sequence alignments, S. Knapp's group and the Structural Genomics Consortium for providing plasmids, G. Manning for sharing unpublished data, and members of the R.L. laboratory for critical reading of this manuscript, particularly C. Santini. We are further indebted to J. Kim for assistance with NetworkKIN, NetPhorest, and KinomeXplorer and X. Robin for assisting in developing and maintaining the ReKINect website. We are also indebted to several members of the Pawson laboratory, especially A. Pasculescu for his assistance in collecting phosphorylation site information, G. Gish for discussions on potentially essential SH2 residues, and B. Larsen for his suggestions on MS spectra annotation. Similarly, we thank members of the Yaffe laboratory for discussions on critical parts of this manuscript. This work was funded by The Lundbeck Foundation and the European Research Council under the European Union's Seventh Framework Programme (FP/2007–2013)/ERC grant (KINOMEDRIFT) and was conducted using the VKR funded Instrument Center for Systems Proteomics (VKR 022758). J.T.E. and L.P. are supported by a Hallas Møller Stipend from the Novo Nordisk Foundation. Work in the B.E.T. laboratory was partly supported by NIH grant R01 GM104047, and C.J.M. was supported by NIH training grant T32 GM007324. P.C. is currently funded by a Ludwig Fund Postdoctoral Fellowship. The algorithms and software developed in this work will be released under the Creative Commons licensing schemes at the websites <http://KinomeXplorer.science>, <http://ReKINect.science>, and <http://KINspect.science>. For further information see also <http://lindinglab.science>.

Received: August 25, 2014

Revised: April 9, 2015

Accepted: August 12, 2015

Published: September 17, 2015

REFERENCES

Alexander, J., Lim, D., Joughin, B.A., Hegemann, B., Hutchins, J.R.A., Ehrenberger, T., Ivins, F., Sessa, F., Hudecz, O., Nigg, E.A., et al. (2011). Spatial exclusivity combined with positive and negative selection of phosphorylation motifs is the basis for context-dependent mitotic signaling. *Sci. Signal.* 4, ra42.

Anastassiadis, T., Deacon, S.W., Devarajan, K., Ma, H., and Peterson, J.R. (2011). Comprehensive assay of kinase catalytic activity reveals features of kinase inhibitor selectivity. *Nat. Biotechnol.* 29, 1039–1045.

Andreadi, C., Cheung, L.K., Giblett, S., Patel, B., Jin, H., Mercer, K., Kamata, T., Lee, P., Williams, A., McMahon, M., et al. (2012). The intermediate-activity (L597V)*BRAF* mutant acts as an epistatic modifier of oncogenic RAS by enhancing signaling through the RAF/MEK/ERK pathway. *Genes Dev.* 26, 1945–1958.

Antal, C.E., Hudson, A.M., Kang, E., Zanca, C., Wirth, C., Stephenson, N.L., Trotter, E.W., Gallegos, L.L., Miller, C.J., Furnari, F.B., et al. (2015). Cancer-associated protein kinase C mutations reveal kinase's role as tumor suppressor. *Cell* 160, 489–502.

Arnold, R., Patzak, I.M., Neuhaus, B., Vancauwenbergh, S., Veillette, A., Van Lint, J., and Kiefer, F. (2005). Activation of hematopoietic progenitor kinase 1 involves relocation, autophosphorylation, and transphosphorylation by protein kinase D1. *Mol. Cell. Biol.* 25, 2364–2383.

Bibbins, K.B., Boeuf, H., and Varmus, H.E. (1993). Binding of the Src SH2 domain to phosphopeptides is determined by residues in both the SH2 domain and the phosphopeptides. *Mol. Cell. Biol.* 13, 7278–7287.

Borrello, M.G., Smith, D.P., Pasini, B., Bongarzone, I., Greco, A., Lorenzo, M.J., Arighi, E., Miranda, C., Eng, C., Alberti, L., et al. (1995). RET activation by germline MEN2A and MEN2B mutations. *Oncogene* 11, 2419–2427.

Brinkworth, R.I., Breinl, R.A., and Kobe, B. (2003). Structural basis and prediction of substrate specificity in protein serine/threonine kinases. *Proc. Natl. Acad. Sci. USA* 100, 74–79.

Carter, P., Presta, L., Gorman, C.M., Ridgway, J.B., Henner, D., Wong, W.L., Rowland, A.M., Kotts, C., Carver, M.E., and Shepard, H.M. (1992). Humanization of an anti-p185HER2 antibody for human cancer therapy. *Proc. Natl. Acad. Sci. USA* 89, 4285–4289.

Chen, C., Ha, B.H., Thévenin, A.F., Lou, H.J., Zhang, R., Yip, K.Y., Peterson, J.R., Gerstein, M., Kim, P.M., Filippakopoulos, P., et al. (2014). Identification of a major determinant for serine-threonine kinase phosphoacceptor specificity. *Mol. Cell* 53, 140–147.

Creixell, P., Schoof, E.M., Erler, J.T., and Linding, R. (2012a). Navigating cancer network attractors for tumor-specific therapy. *Nat. Biotechnol.* 30, 842–848.

Creixell, P., Schoof, E.M., Tan, C.S.H., and Linding, R. (2012b). Mutational properties of amino acid residues: implications for evolvability of phosphorylatable residues. *Philos. Trans. R. Soc. Lond. B Biol. Sci.* 367, 2584–2593.

Creixell, P., Palmeri, A., Miller, C.J., Lou, H.J., Santini, C.C., Nielsen, M., Turk, B.E., and Lining, R. (2015). Unmasking determinants of specificity in the human kinome. *Cell* 163, this issue, 187–201.

Dai, C., Whitesell, L., Rogers, A.B., and Lindquist, S. (2007). Heat shock factor 1 is a powerful multifaceted modifier of carcinogenesis. *Cell* 130, 1005–1018.

Davies, H., Bignell, G.R., Cox, C., Stephens, P., Edkins, S., Clegg, S., Teague, J., Woffendin, H., Garnett, M.J., Bottomley, W., et al. (2002). Mutations of the *BRAF* gene in human cancer. *Nature* 417, 949–954.

Davis, M.I., Hunt, J.P., Herrgard, S., Ciceri, P., Wodicka, L.M., Pallares, G., Hocker, M., Treiber, D.K., and Zarinkar, P.P. (2011). Comprehensive analysis of kinase inhibitor selectivity. *Nat. Biotechnol.* 29, 1046–1051.

Druker, B.J., Tamura, S., Buchdunger, E., Ohno, S., Segal, G.M., Fanning, S., Zimmermann, J., and Lydon, N.B. (1996). Effects of a selective inhibitor of the Abl tyrosine kinase on the growth of Bcr-Abl positive cells. *Nat. Med.* 2, 561–566.

Fliceck, P., Amode, M.R., Barrell, D., Beal, K., Billis, K., Brent, S., Carvalho-Silva, D., Clapham, P., Coates, G., Fitzgerald, S., et al. (2014). Ensembl 2014. *Nucleic Acids Res.* 42, D749–D755.

Forbes, S.A., Bindal, N., Bamford, S., Cole, C., Kok, C.Y., Beare, D., Jia, M., Shepherd, R., Leung, K., Menzies, A., et al. (2011). COSMIC: mining complete cancer genomes in the Catalogue of Somatic Mutations in Cancer. *Nucleic Acids Res.* 39, D945–D950.

Friend, S.H., Bernards, R., Rogelj, S., Weinberg, R.A., Rapaport, J.M., Albert, D.M., and Dryja, T.P. (1986). A human DNA segment with properties of the gene that predisposes to retinoblastoma and osteosarcoma. *Nature* 323, 643–646.

Futreal, P.A., Coin, L., Marshall, M., Down, T., Hubbard, T., Wooster, R., Rahman, N., and Stratton, M.R. (2004). A census of human cancer genes. *Nat. Rev. Cancer* 4, 177–183.

Gao, J., Aksoy, B.A., Dogrusoz, U., Dresdner, G., Gross, B., Sumer, S.O., Sun, Y., Jacobsen, A., Sinha, R., Larsson, E., et al. (2013). Integrative analysis of complex cancer genomics and clinical profiles using the cBioPortal. *Sci. Signal.* 6, pl1.

Geiger, T., Wisniewski, J.R., Cox, J., Zanivan, S., Kruger, M., Ishihama, Y., and Mann, M. (2011). Use of stable isotope labeling by amino acids in cell culture as a spike-in standard in quantitative proteomics. *Nat. Protoc.* 6, 147–157.

Greenman, C., Stephens, P., Smith, R., Dalgleish, G.L., Hunter, C., Bignell, G., Davies, H., Teague, J., Butler, A., Stevens, C., et al. (2007). Patterns of somatic mutation in human cancer genomes. *Nature* 446, 153–158.

Hanahan, D., and Weinberg, R.A. (2000). The hallmarks of cancer. *Cell* 100, 57–70.

Hassan, S., Biswas, M.H.U., Zhang, C., Du, C., and Balaji, K.C. (2009). Heat shock protein 27 mediates repression of androgen receptor function by protein kinase D1 in prostate cancer cells. *Oncogene* 28, 4386–4396.

Hornbeck, P.V., Chabra, I., Kornhauser, J.M., Skrzypek, E., and Zhang, B. (2004). PhosphoSite: a bioinformatics resource dedicated to physiological protein phosphorylation. *Proteomics* 4, 1551–1561.

Hutti, J.E., Jarrell, E.T., Chang, J.D., Abbott, D.W., Storz, P., Toker, A., Cantley, L.C., and Turk, B.E. (2004). A rapid method for determining protein kinase phosphorylation specificity. *Nat. Methods* 1, 27–29.

Kan, Z., Jaiswal, B.S., Stinson, J., Janakiraman, V., Bhatt, D., Stern, H.M., Yue, P., Haverty, P.M., Bourgon, R., Zheng, J., et al. (2010). Diverse somatic mutation patterns and pathway alterations in human cancers. *Nature* 466, 869–873.

Kramer, K.L., Barnette, J.E., and Yost, H.J. (2002). PKC γ regulates syndecan-2 inside-out signaling during *xenopus* left-right development. *Cell* 111, 981–990.

Lindberg, J., Mills, I.G., Klevebring, D., Liu, W., Neiman, M., Xu, J., Wikström, P., Wiklund, P., Wiklund, F., Egevad, L., and Grönberg, H. (2013). The mitochondrial and autosomal mutation landscapes of prostate cancer. *Eur. Urol.* 63, 702–708.

Linding, R., Jensen, L.J., Ostheimer, G.J., van Vugt, M.A.T.M., Jørgensen, C., Miron, I.M., Diella, F., Colwill, K., Taylor, L., Elder, K., et al. (2007). Systematic discovery of *in vivo* phosphorylation networks. *Cell* 129, 1415–1426.

Liu, B.A., Jablonowski, K., Raina, M., Arcé, M., Pawson, T., and Nash, P.D. (2006). The human and mouse complement of SH2 domain proteins—establishing the boundaries of phosphotyrosine signaling. *Mol. Cell* 22, 851–868.

Manning, G., Whyte, D.B., Martinez, R., Hunter, T., and Sudarsanam, S. (2002). The protein kinase complement of the human genome. *Science* 298, 1912–1934.

Marengere, L.E., Songyang, Z., Gish, G.D., Schaller, M.D., Parsons, J.T., Stern, M.J., Cantley, L.C., and Pawson, T. (1994). SH2 domain specificity and activity modified by a single residue. *Nature* 369, 502–505.

Mazzoni, E., Adam, A., Bal de Kier Joffe, E., and Aguirre-Ghiso, J.A. (2003). Immortalized mammary epithelial cells overexpressing protein kinase C gamma acquire a malignant phenotype and become tumorigenic *in vivo*. *Mol. Cancer Res.* 1, 776–787.

Mehenni, H., Gehrig, C., Nezu, J., Oku, A., Shimane, M., Rossier, C., Guex, N., Blouin, J.-L., Scott, H.S., and Antonarakis, S.E. (1998). Loss of LKB1 kinase activity in Peutz-Jeghers syndrome, and evidence for allelic and locus heterogeneity. *Am. J. Hum. Genet.* 63, 1641–1650.

Miller, M.L., Jensen, L.J., Diella, F., Jørgensen, C., Tinti, M., Li, L., Hsiung, M., Parker, S.A., Bordeaux, J., Sicheritz-Ponten, T., et al. (2008). Linear motif atlas for phosphorylation-dependent signaling. *Sci. Signal.* 1, ra2.

Mok, J., Kim, P.M., Lam, H.Y.K., Piccirillo, S., Zhou, X., Jeschke, G.R., Sheridan, D.L., Parker, S.A., Desai, V., Jwa, M., et al. (2010). Deciphering protein kinase specificity through large-scale analysis of yeast phosphorylation site motifs. *Sci. Signal.* 3, ra12.

Pawson, T., Gish, G.D., and Nash, P. (2001). SH2 domains, interaction modules and cellular wiring. *Trends Cell Biol.* 11, 504–511.

Rowley, J.D. (1973). Letter: A new consistent chromosomal abnormality in chronic myelogenous leukaemia identified by quinacrine fluorescence and Giemsa staining. *Nature* 243, 290–293.

Santoro, M., Carluomagno, F., Romano, A., Bottaro, D.P., Dathan, N.A., Grieco, M., Fusco, A., Vecchio, G., Matoskova, B., Kraus, M.H., et al. (1995). Activation of RET as a dominant transforming gene by germline mutations of MEN2A and MEN2B. *Science* 267, 381–383.

Schechter, A.L., Stern, D.F., Vaidyanathan, L., Decker, S.J., Drebin, J.A., Greene, M.I., and Weinberg, R.A. (1984). The neu oncogene: an erb-B-related gene encoding a 185,000-Mr tumour antigen. *Nature* 312, 513–516.

Sievers, F., Wilm, A., Dineen, D., Gibson, T.J., Karplus, K., Li, W., Lopez, R., McWilliam, H., Remmert, M., Söding, J., et al. (2011). Fast, scalable generation of high-quality protein multiple sequence alignments using Clustal Omega. *Mol. Syst. Biol.* 7, 539.

Slamon, D.J., Clark, G.M., Wong, S.G., Levin, W.J., Ullrich, A., and McGuire, W.L. (1987). Human breast cancer: correlation of relapse and survival with amplification of the HER-2/neu oncogene. *Science* 235, 177–182.

Songyang, Z., Caraway, K.L., 3rd, Eck, M.J., Harrison, S.C., Feldman, R.A., Mohammadi, M., Schlessinger, J., Hubbard, S.R., Smith, D.P., Eng, C., et al. (1995). Catalytic specificity of protein-tyrosine kinases is critical for selective signalling. *Nature* 373, 536–539.

Stehelin, D., Varmus, H.E., Bishop, J.M., and Vogt, P.K. (1976). DNA related to the transforming gene(s) of avian sarcoma viruses is present in normal avian DNA. *Nature* 260, 170–173.

Strebhardt, K., and Ullrich, A. (2008). Paul Ehrlich's magic bullet concept: 100 years of progress. *Nat. Rev. Cancer* 8, 473–480.

Sundram, V., Chauhan, S.C., and Jaggi, M. (2011). Emerging roles of protein kinase D1 in cancer. *Mol. Cancer Res.* 9, 985–996.

Tan, C.S.H., Pascalescu, A., Lim, W.A., Pawson, T., Bader, G.D., and Linding, R. (2009). Positive selection of tyrosine loss in metazoan evolution. *Science* 325, 1686–1688.

Thomsen, M.C.F., and Nielsen, M. (2012). Seq2Logo: a method for construction and visualization of amino acid binding motifs and sequence profiles including sequence weighting, pseudo counts and two-sided representation of amino acid enrichment and depletion. *Nucleic Acids Res.* 40, W281–W287.

Ullrich, A., Coussens, L., Hayflick, J.S., Dull, T.J., Gray, A., Tam, A.W., Lee, J., Yarden, Y., Libermann, T.A., Schlessinger, J., et al. (1984). Human epidermal growth factor receptor cDNA sequence and aberrant expression of the amplified gene in A431 epidermoid carcinoma cells. *Nature* 309, 418–425.

Weinberg, R.A. (2014). Coming full circle—from endless complexity to simplicity and back again. *Cell* 157, 267–271.

Wu, M., Pastor-Pareja, J.C., and Xu, T. (2010). Interaction between Ras(V12) and scribbled clones induces tumour growth and invasion. *Nature* 463, 545–548.

Yaffe, M.B. (2013). The scientific drunk and the lamppost: massive sequencing efforts in cancer discovery and treatment. *Sci. Signal.* 6, pe13.

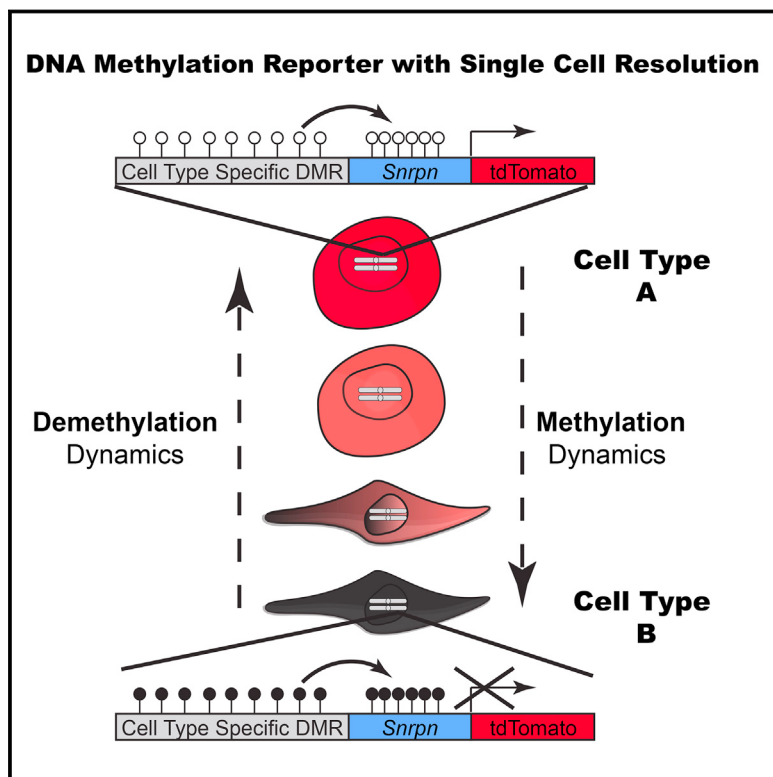
Yang, J., Song, X., Chen, Y., Lu, X., Fu, Y., and Luo, Y. (2014). PLC γ 1-PKC γ signaling-mediated Hsp90 α plasma membrane translocation facilitates tumor metastasis. *Traffic* 15, 861–878.

Zarrinpar, A., Park, S.H., and Lim, W.A. (2003). Optimization of specificity in a cellular protein interaction network by negative selection. *Nature* 426, 676–680.

Zeqiraj, E., and van Aalten, D.M. (2010). Pseudokinases—remnants of evolution or key allosteric regulators? *Curr. Opin. Struct. Biol.* 20, 772–781.

Tracing Dynamic Changes of DNA Methylation at Single-Cell Resolution

Graphical Abstract



Authors

Yonatan Stelzer, Chikdu Shakti Shivalila,
Frank Soldner, Styliani Markoulaki, Rudolf
Jaenisch

Correspondence

jaenisch@wi.mit.edu

In Brief

A clever reporter system indicates DNA methylation status and how it changes over time *in vivo* at single-cell resolution.

Highlights

- A reporter for endogenous genomic DNA methylation (RGM) is established
- RGM can capture endogenous methylation state of promoters and non-coding regions
- RGM allows tracing of methylation changes both *in vitro* and *in vivo*
- RGM allows monitoring dynamics at single-cell resolution during cell-fate changes



Tracing Dynamic Changes of DNA Methylation at Single-Cell Resolution

Yonatan Stelzer,^{1,3} Chikdu Shakti Shivalila,^{1,2,3} Frank Soldner,¹ Styliani Markoulaki,¹ and Rudolf Jaenisch^{1,2,*}

¹Whitehead Institute for Biomedical Research, Cambridge, MA 02142, USA

²Department of Biology, Massachusetts Institute of Technology, Cambridge, MA 02142, USA

³Co-first author

*Correspondence: jaenisch@wi.mit.edu

<http://dx.doi.org/10.1016/j.cell.2015.08.046>

SUMMARY

Mammalian DNA methylation plays an essential role in development. To date, only snapshots of different mouse and human cell types have been generated, providing a static view on DNA methylation. To enable monitoring of methylation status as it changes over time, we establish a reporter of genomic methylation (RGM) that relies on a minimal imprinted gene promoter driving a fluorescent protein. We show that insertion of RGM proximal to promoter-associated CpG islands reports the gain or loss of DNA methylation. We further utilized RGM to report endogenous methylation dynamics of non-coding regulatory elements, such as the pluripotency-specific super enhancers of *Sox2* and *miR290*. Loci-specific DNA methylation changes and their correlation with transcription were visualized during cell-state transition following differentiation of mouse embryonic stem cells and during reprogramming of somatic cells to pluripotency. RGM will allow the investigation of dynamic methylation changes during development and disease at single-cell resolution.

INTRODUCTION

DNA methylation is recognized as a principal contributor to the stability and regulation of gene expression in development and maintenance of cellular identity (Bird, 2002; Cedar and Bergman, 2012; Jaenisch and Bird, 2003; Reik et al., 2001). Changes in DNA methylation are dynamic and it is still largely unknown how they dictate spatial and temporal gene expression programs (Smith and Meissner, 2013). Recent advancements in sequencing technologies enabled the establishment of methylation maps for multiple cell types in both human (Kundaje et al., 2015; Schultz et al., 2015; Smith et al., 2014; Ziller et al., 2013) and mouse (Hon et al., 2013), thus providing a framework for identifying key lineage-specific regulators (Rivera and Ren, 2013). DNA methylation is a dynamic process and current methods are only bulk and provide a static “snapshot” view of the methylation state during cell-state transitions. The difficulty in translating real-time epigenetic changes into a traceable readout is, to date, a limiting factor in our ability to follow the dy-

namics of DNA methylation. Therefore, a key challenge in the field is to generate tools that allow tracing changes in DNA methylation over time.

Here, we set out to generate a DNA methylation reporter system that is capable of visualizing genomic methylation states at single-cell resolution. The design of the reporter was based on two premises: (1) previous observations suggesting that CpG sites can serve as *cis*-acting signals, affecting the methylation state of adjacent CpGs (Brandeis et al., 1994; Mummaneni et al., 1995; Turker, 2002), and (2) a methylation-sensitive promoter that, when introduced in proximity to a CpG region of choice, may be utilized to report on methylation changes of the adjacent sequences. Thus, a key issue in establishing a DNA methylation reporter was identifying a methylation-sensitive promoter, which is not independently regulated by the DNA methylation machinery, but can be affected by methylation changes of adjacent sequences. Constitutively active genes usually contain hypomethylated high density CpG islands (CGIs) in their promoter regions and are not regulated by DNA methylation (Deaton and Bird, 2011) whereas gene promoters associated with low-density CGIs are activated and repressed in a tissue-specific manner. Because methylation of both classes of promoters is either not regulated by the DNA methylation machinery in all tissues or regulated in a tissue-dependent manner, these promoters cannot be utilized as DNA methylation reporters. In contrast, imprinted gene promoters exhibit inherent sensitivity to DNA methylation of adjacent genomic regions resulting in transcriptional activation or silencing. This mechanism has been established for a subgroup of germline-derived differentially methylated regions (DMRs) that affect in *cis* the methylation state of secondary regulatory promoter elements, which in turn control imprinted gene activity. Importantly, following their establishment, promoter-associated imprinted DMRs are not regulated by the DNA methylation machinery in a tissue-specific manner (Ferguson-Smith, 2011). We hypothesized that these intrinsic characteristics of imprinted gene promoters make them attractive candidates for methylation sensors. Perhaps one of the best-studied examples is the Prader-Willi Angelman region, in which an imprinted DMR resides at the small nuclear ribonucleoprotein polypeptide N (*SnRNP*) gene promoter region controlling its parent-of-origin monoallelic expression (Buiting et al., 1995; Kantor et al., 2004). Furthermore, *SnRNP* is expressed in most of the tissues and thus serves as an attractive candidate to generate a DNA methylation reporter.

Changes in DNA methylation occur mostly at non-CGIs, some of which are associated with tissue-specific gene promoters (Jones, 2012). Nevertheless, a growing body of evidence suggests that the bulk of tissue-specific changes in DNA methylation is associated with non-coding sequences (Iribarry et al., 2009) such as distal regulatory elements, which include enhancers and transcription factor binding sites (Hon et al., 2013; Stadler et al., 2011; Ziller et al., 2013). Recent reports identified super-enhancers (SE) as clusters of TF and mediator-binding sites associated with bona fide enhancer chromatin marks to control the expression of key cell identity genes (Dowen et al., 2014; Hnisz et al., 2013; Whyte et al., 2013). Global genomic comparisons of tissue-specific DNA methylation and transcription factor (TF) chromatin immunoprecipitation sequencing (ChIP-seq) data correlated the chromatin with the methylation state (Xie et al., 2013). Thus, many tissue-specific enhancers are hypomethylated in tissues where the target genes are expressed, but are hypermethylated in tissues where the target genes are silent (Hon et al., 2013).

In this paper, we establish a reporter of genomic methylation (RGM) that enables the visualization of changes in DNA methylation in live cells. We show that a minimal *Snrpn* promoter can report on the DNA methylation state of endogenous gene promoters. We also generated reporter cell lines for the pluripotency-specific *miR290* and *Sox2* SEs and demonstrate that RGM can be used to capture dynamic DNA methylation changes in distal non-coding regulatory regions. An attractive aspect of RGM is its utility to visualize DNA methylation changes in development and disease at single-cell resolution in the same sample.

RESULTS

A Methylation-Sensitive Reporter System Based on a Minimal Imprinted Promoter

To establish a methylation reporter, we generated a minimal *Snrpn* promoter that includes the conserved elements between human and mouse and contains the endogenous imprinted DMR region (Figure S1A). The minimal promoter region driving GFP was cloned into a sleeping beauty transposon vector (Ivics et al., 1997) to facilitate stable integration into the genome. Recent studies have demonstrated that different CGI vectors, when stably inserted into mouse embryonic stem cells (mESCs), adopt a methylation pattern that corresponds to the in vivo methylation pattern of the respective endogenous sequence (Sabag et al., 2014). To test whether DNA methylation can propagate into the *Snrpn* promoter region in vivo, we designed an experimental system in which the CGI regions of *Gapdh* and *Dazl* were cloned upstream of our reporter (Figure 1A). The promoter of *Gapdh* encompasses a hypomethylated CGI consistent with constitutive expression in all tissues. In contrast, the *Dazl* promoter-associated CGI is hypermethylated in all tissues excluding the germ cells (Hackett et al., 2013). Given the different expression and methylation patterns of both genes, upon stable integration of the two reporter vectors into mESCs the *Gapdh* CGI is expected to maintain its hypomethylated state, while the *Dazl* CGI would be subjected to de novo methylation (Sabag et al., 2014). Figure 1B shows that >95% of cells carrying the *Gapdh* reporter expressed GFP. In contrast, >30% of cells carrying the *Dazl* reporter were GFP-negative, corresponding

to reporter silencing. The effect of the *Dazl* reporter becomes more robust upon continued passage, with >80% of the cells silencing their reporter within 4 weeks (Figure 1B).

To assess the DNA methylation levels of the *Gapdh* and *Dazl* reporters following introduction into mESCs, we sorted *Gapdh* GFP-positive and *Dazl* GFP-negative cell populations (Figure 1C). The GFP expression state was stable upon continuous culture and passaging of the two sorted cell populations for over 7 weeks (Figure 1C). DNA was extracted from both *Gapdh* GFP-positive and *Dazl* GFP-negative cells and subjected to bisulfite conversion and PCR sequencing. Figure 1D shows that *Gapdh* GFP-positive cells maintained the hypomethylated state at both *Gapdh* CGI and the *Snrpn* promoter regions, whereas *Dazl* GFP-negative cells became highly de novo methylated at the *Dazl* CGI region and its corresponding downstream *Snrpn* promoter (Figure 1E). These results are consistent with the hypothesis that DNA methylation can be propagated from the CGI into the *Snrpn* promoter region resulting in repression of transcriptional activity.

RGM Is a Reporter for In Vivo Demethylation

The experiments described above showed that RGM reports on de novo methylation imposed in vivo on the unmethylated *Dazl* CGI donor test sequence. Conversely, we were interested to assess whether a methylated and silent donor *Snrpn* promoter can be reactivated by means of demethylation acquired in vivo. For this, we used the CpG methyltransferase M.SssI to in vitro methylate both *Gapdh* and *Dazl* reporter constructs. Treatment of the plasmids with M.SssI enzyme followed by bisulfite conversion, PCR amplification, and sequencing, confirmed the complete hypermethylation of both the CGI and *Snrpn* promoter regions (Figures 2A, S1B, and S1C). ESCs were transfected with either *Gapdh* or *Dazl* reporter and selected for cells carrying stably integrated vectors. Following 1 week of culture, we identified robust activation of GFP in virtually all cells carrying the integrated *Gapdh* reporter, whereas cells carrying the *Dazl* reporter remained GFP-negative (Figures 2B–2D). To assess the DNA methylation state of the *Gapdh* and *Dazl* CGI and the respective downstream *Snrpn* promoter regions, DNA was extracted from the two cell lines, subjected to bisulfite conversion, PCR amplification and sequencing. Figure 2E demonstrates that, consistent with high GFP expression, the *Gapdh* CGI and its downstream *Snrpn* promoter had become fully demethylated. In contrast, the *Dazl* CGI and its downstream *Snrpn* promoter sequences maintained the hypermethylated state in agreement with complete repression of the GFP signal (Figure 2F). Thus, our data support the hypothesis that a *Snrpn* promoter can report on in vivo demethylation of the CGI in its proximity.

Dnmt1, *Dnmt3a*, and *Dnmt3b* Mediate Methylation and Reporter Activity

We used ESCs deficient for the DNA methyltransferases *Dnmt1*, *Dnmt3a*, and *Dnmt3b* to gain mechanistic insights into demethylation and de novo methylation imposed on the *Snrpn* promoter in transfected ESCs. Figure 2G shows that introduction of an in vitro methylated *Dazl* *Snrpn* vector into *Dnmt1* mutant cells resulted in ~80% GFP-positive cells by passage five, in contrast to no GFP-positive cells when inserted into wild-type (WT) cells. In agreement with the role of *Dnmt1* as being the maintenance DNA

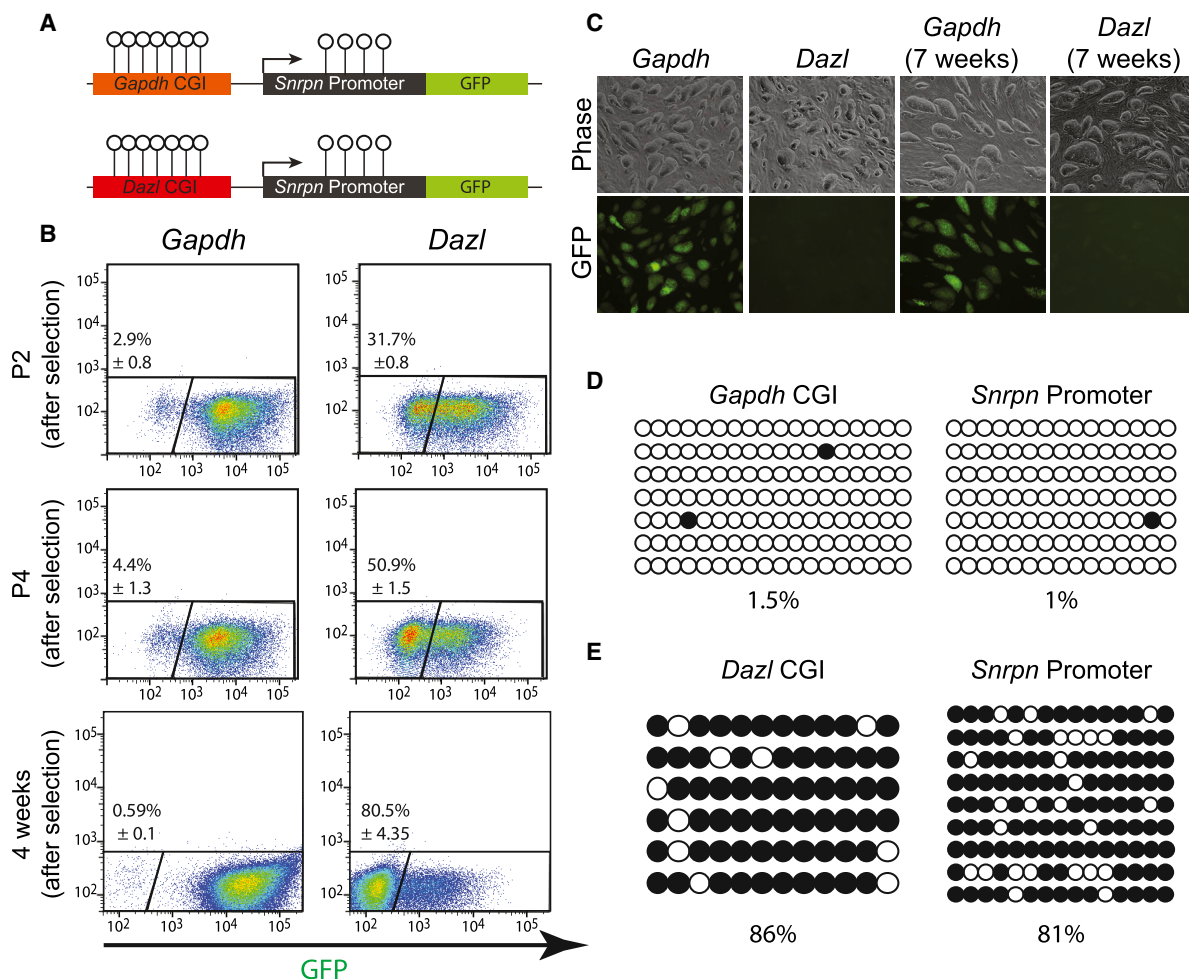


Figure 1. An Active Minimal *Snrpn* Promoter Can Be Repressed in *cis* by Means of Spreading of DNA Methylation into the Promoter Region

(A) Schematic representation of the sleeping-beauty-based vectors. Endogenous CpG Islands (CGI) of *Dazl* and *Gapdh* genes were cloned upstream of a minimal *Snrpn* promoter region-driving GFP. Open circle lollipops schematically represent individual unmethylated CpG.

(B) Flow cytometric analysis of V6.5 mESCs cultured in serum + LIF, following stable integration of unmethylated *Gapdh* and *Dazl* reporter vectors, demonstrating robust repression of GFP signal in the *Dazl* reporter cells over time. Shown are the mean percentages of GFP-negative cells ± STD of two biological replicates.

(C) Phase and fluorescence images of the sorted V6.5 mESCs, comprising stable integration of the *Gapdh* (left) and *Dazl* (right) vectors following prolonged culturing for 7 weeks.

(D and E) Bisulfite sequencing analysis of the stably transfected *Gapdh* (D) and *Dazl* (E) reporter cell lines was performed on the gene promoter-associated CGI (left) and the downstream *Snrpn* promoter region (right). Open circles represent unmethylated CpGs; Filled circles, methylated CpGs.

See also Figure S1.

methyltransferase (Li et al., 1992), bisulfite sequencing analysis on the sorted GFP-positive cells confirmed that reactivation of the methylated *Dazl* reporter occurred by passive demethylation (Figure 2H). To clarify the mechanism of de novo methylation, we introduced an unmethylated version of both vectors into mESCs deficient for both de novo DNA methyltransferases *Dnmt3a* and *Dnmt3b* (Pawlak and Jaenisch, 2011). Figure 2I shows that the vast majority of cells carrying the *Dazl* or the *Gapdh* reporters were positive for GFP unlike *Dazl* reporter expression in control V6.5 cells (Figure 2I), which is consistent with *Dnmt3a/b* mediating de novo methylation and reporter silencing.

Recent studies have shown that culturing mESCs in 2i medium (inhibitors of MEK and GSK3), and leukemia inhibitory factor (LIF)

results in downregulation of *Dnmt3a* and *Dnmt3b*, consequently leading to global hypomethylation (Lee et al., 2014). To assess whether these culture conditions affect reporter activity, we transfected the unmethylated *Gapdh* and *Dazl* reporters into WT mESCs cultured in 2i and LIF. Figure 2I shows that the great majority of the stably transfected cells were GFP-positive, consistent with 2i-mediated downregulation of the *Dnmt3a* and *Dnmt3b*.

RGM Can Report on Methylation Associated with Endogenous Gene Promoters

To test whether the *Snrpn* promoter could also report on DNA methylation levels associated with endogenous gene promoters, we utilized CRISPR/Cas-mediated gene editing to target the

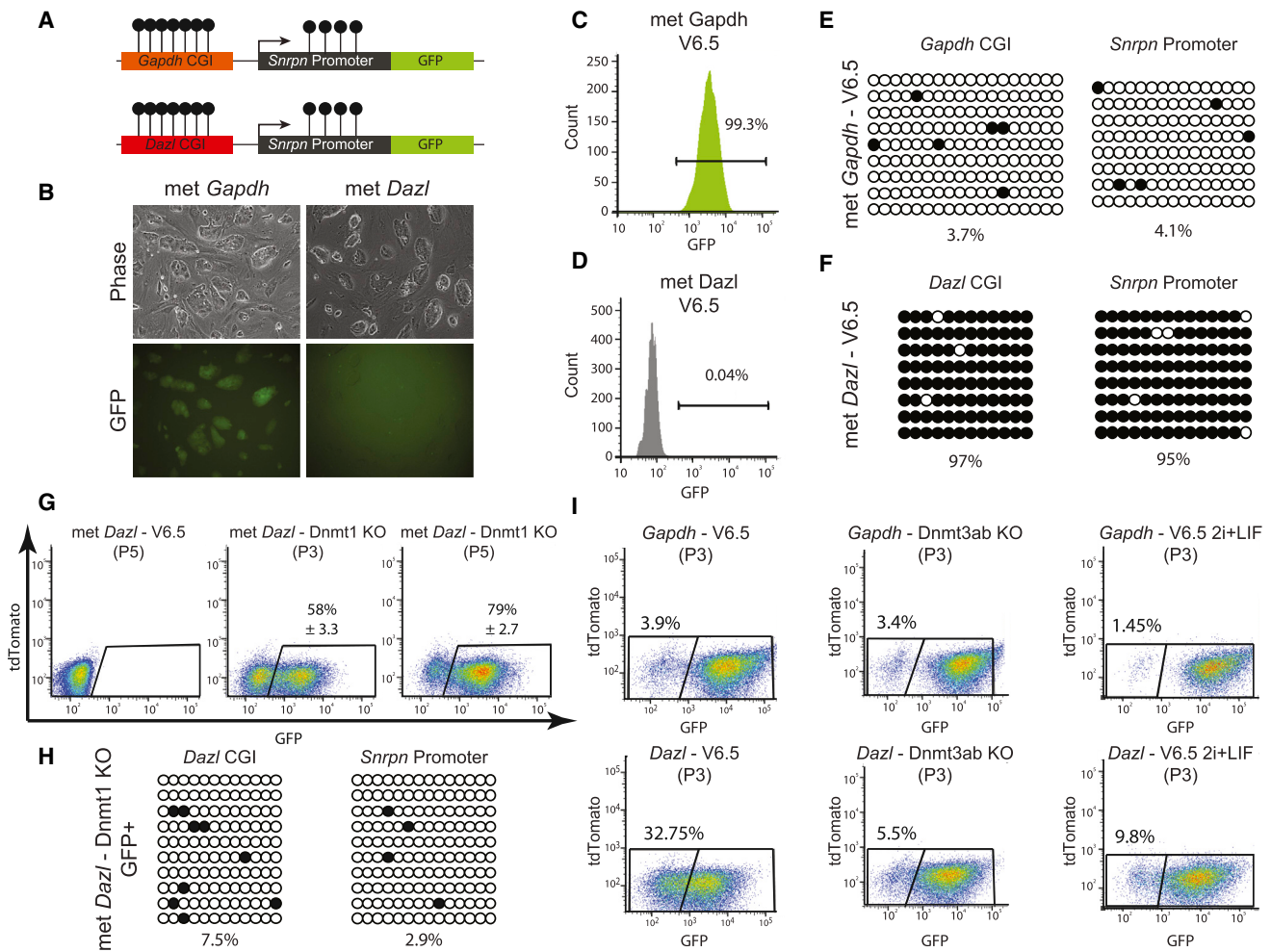


Figure 2. An In Vitro Repressed Snrpn Promoter Can Be Reactivated in cis by Means of Spreading of DNA Demethylation into the Promoter Region

(A) Schematic representation of in vitro methylated sleeping-beauty-based vectors. Closed circle lollipops schematically represent individual methylated CpG.

(B) Phase and fluorescence images of the stably integrated V6.5 mESCs harboring *Gapdh* (left) and *Dazl* (right) in vitro methylated vectors, following 1 week of antibiotics selection.

(C and D) Flow cytometric analysis of the proportion of GFP-positive cells in V6.5 mESCs, stably integrated with either *Gapdh* (C) or *Dazl* (D) in vitro methylated vectors, following 2 weeks in culture.

(E and F) Bisulfite sequencing analysis of the stably transfected *Gapdh* (E) and *Dazl* (F) reporter cell lines, was performed on the gene promoter-associated CGI (left) and the downstream *Snrpn* promoter region (right).

(G) Flow cytometric analysis of the proportion of GFP-positive cells in V6.5 mESCs and *Dnmt1* KO mESCs, stably integrated with in vitro methylated *Dazl* reporter vector.

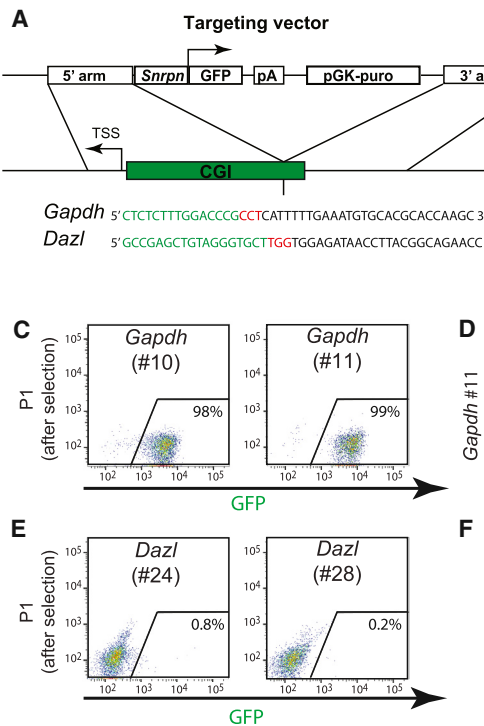
(H) Bisulfite sequencing analysis of sorted GFP-positive *Dnmt1* KO mESCs, stably integrated with in vitro methylated *Dazl* reporter vector.

(I) Flow cytometric analysis of the proportion of GFP-negative cells in control V6.5 mESCs, mESCs deficient for both *Dnmt3a* and *Dnmt3b* (*Dnmt3ab* KO) and V6.5 mESCs cultured in 2i + LIF, which were stably integrated with unmethylated *Gapdh* (top) and *Dazl* (bottom) reporter vectors.

See also Figure S1.

endogenous CGIs located at the promoter regions of *Gapdh* and *Dazl* (Figures 3A, S2A, and S2B). Figure 3B shows 35/36 *Dazl*-vector-transfected clones were GFP-negative indicating robust silencing of the *Dazl* reporter whereas 20/21 *Gapdh*-vector-transfected clones were GFP-positive (Figure 3B). FACS analysis of correctly targeted clones confirmed that *Gapdh* reporter cells were all GFP-positive with the CGI and *Snrpn* promoter unmethylated (Figures 3C and 3D) in contrast to *Dazl*

GFP-negative clones with the corresponding sequences methylated (Figures 3E and 3F). Our results demonstrate that *Snrpn* reporter activity reports on the methylation state of its surrounding sequences and does not alter their methylation state. Furthermore, the endogenous targeting results suggested that the partial repression of the *Dazl* reporter (Figure 1B), observed at early passages of the transgene experiment, may be due to multiple genome integration and position effects.



(F) Bisulfite sequencing analysis was performed on mESCs harboring the DNA methylation reporter in *Dazl* promoter region. For each cell line, the PCR amplicon (marked with dashed line) includes both the endogenous CGI (left) and the downstream integrated *Srnpn* promoter region (right). See also Figure S2.

RGM Can Report on Methylation of Pluripotency-Specific Super-Enhancers

Methylation of super enhancers (SEs) has been shown to change during differentiation. We tested whether RGM would report on the active and hypomethylated state of the pluripotency-specific SEs associated with the *miR290* and *Sox2* genes in mESCs and their methylated and inactive state in somatic cells (Figures 4A and S3A). In contrast to the CGIs located at gene promoters (*Gapdh* and *Dazl*), the SE regions of both *Sox2* and *miR290* represent low-density CpG sequences. Utilizing CRISP/Cas-mediated gene editing, we inserted a *Srnpn* tdTomato reporter into the endogenous *miR290* and *Sox2* enhancer (Figures 4B and S3B, respectively). As recipient cells, we used the previously established *Oct4*, *Sox2*, *Klf4*, and *c-Myc* (OSKM) polycistronic dox-inducible secondary reprogrammable mESCs (Carey et al., 2011), which also carried a GFP reporter knocked into the endogenous *Nanog* locus. Correct integration of the vector was validated by PCR and Southern analysis (Figure S3C). Figure 4C shows that both targeted ESC lines (*miR290* #21 and *Sox2* #2) expressed tdTomato as well as *Nanog*-GFP. To assess whether the tdTomato expression correlated with hypomethylation of the inserted RGM, DNA extracted from the bulk mESCs population was bisulfite converted, amplified by PCR, and sequenced with the PCR amplification including both the SE CpG region and the downstream *Srnpn* promoter. As predicted from the methylation maps (Figures 4A and S3A), both endogenous *miR290* and *Sox2* CpG regions were mostly hypomethylated (Figure 4D). Importantly, the *Srnpn* promoter was also hypomethylated consistent with reporter expression. Of note, a few highly methylated

alleles were detected (Figure 4D), possibly reflecting an inherent variation in the bulk population due to the presence of cells that carry an inactive reporter. To test this possibility, we analyzed the *Sox2* SE region in the untargeted parental cell, which identified the presence of both methylated and unmethylated alleles at the same frequency as the targeted reporter cell line (Figure S3D). We conclude that RGM can report on the methylation state of distal genomic regulatory regions.

Dynamic De Novo DNA Methylation during Differentiation

To monitor real-time changes in genomic DNA methylation during in vitro differentiation, mESCs carrying the tdTomato reporters reflecting DNA methylation levels at the SE regions, were exposed to retinoic acid (RA), which induces a rapid exit from pluripotency, and cellular differentiation (Rhinn and Dollé, 2012). The presence of the *Nanog*-GFP reporter allowed monitoring exit from pluripotency by loss of GFP expression. Sorted double-positive (tdTomato⁺/GFP⁺) *miR290* and *Sox2* cells were plated on feeder-free gelatin coated plates, treated with 0.25 μM RA the following day (Figure 5A) and analyzed at different times after addition of RA (Figures 5A and 5B). As expected, undifferentiated cells were double-positive (tdTomato⁺/GFP⁺). However, upon induction of differentiation a gradual reduction in the fraction of double-positive cells was observed with most disappearing over the time course of 7 days, resulting in a largely double-negative cell population (Figures 5B and 5C). This is in contrast to control *Gapdh* reporter cells that, as expected, appeared completely GFP-positive

Figure 3. Generation of DNA Methylation Reporter Cell Lines for Endogenous Gene Promoters

(A) CRISPR/Cas-based strategy used to integrate the DNA methylation reporter into the endogenous promoter region of *Gapdh* and *Dazl* genes. TSS, transcription start site; green sequence, endogenous CGI region; black sequence, targeting CRISPR; red sequence, PAM recognition site.

(B) Flow cytometric analysis depicting the mean GFP intensity of randomly picked clones following antibiotic selection of both (top) *Gapdh*- and (bottom) *Dazl*-reporter-transfected V6.5 mESCs.

(C) Flow cytometric analysis of the proportion of GFP-positive cells in two representative clones correctly targeted with the methylation reporter at the promoter region of *Gapdh*.

(D) Bisulfite sequencing analysis was performed on mESCs harboring the DNA methylation reporter in *Gapdh* promoter region. For each cell line, the PCR amplicon (marked with dashed line) includes both the endogenous CGI (left) and the downstream integrated *Srnpn* promoter region (right).

(E) Flow cytometric analysis of the proportion of GFP-positive cells in two representative clones correctly targeted with the methylation reporter at the promoter region of *Dazl*.

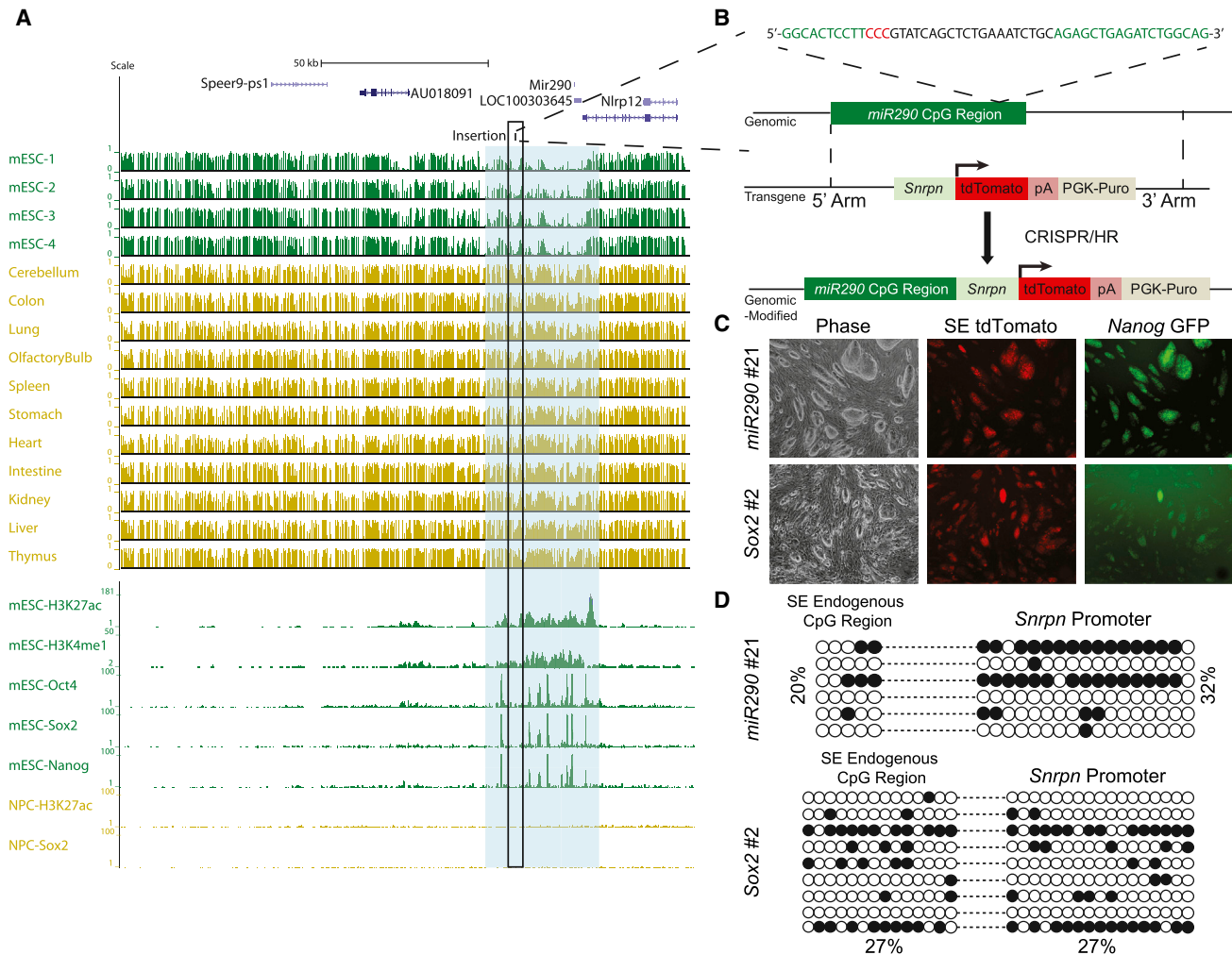


Figure 4. Generation of DNA Methylation Reporter Cell Lines for the Pluripotent-Specific *miR290* and *Sox2* SE Regions

(A) Regional view depicting the DNA methylation (top) and chromatin (bottom) landscape of *miR290* upstream pluripotent-specific SE. Shown are average methylation levels and enrichment of chromatin marks in mouse undifferentiated cells (green) and in adult tissues (gold), with respect to the genomic organization of the genes. DNA methylation varies from 1-hypermethylated to 0-hypomethylated. Characteristic clusters of typical enhancer marks and binding of tissue-specific TF determine the SE region (light blue).

(B) CRISPR/Cas-based strategy used to integrate the DNA methylation reporter into the endogenous SE region. HR, homologous recombination; green sequence, endogenous *miR290* CpG region; black sequence, targeting CRISPR; red sequence, PAM recognition site.

(C) Phase and fluorescence images of correctly integrated DNA methylation reporter cell lines for *miR290* (upper panel) and *Sox2* (lower panel) endogenous SE regions. GFP marks endogenous expression levels of *Nanog*, whereas tdTomato reflects the endogenous DNA methylation levels at both *miR290* and *Sox2* SE regions.

(D) Bisulfite sequencing analysis was performed on undifferentiated mESCs harboring the DNA methylation reporter in either *miR290* SE region (top) or *Sox2* SE region (bottom). For each cell line, the PCR amplicon (marked with dashed line) includes both the endogenous CGI (left) and the downstream integrated *Snrpn* promoter region (right).

See also Figure S3.

following 7 days of RA differentiation (Figure S4A). tdTomato and *Nanog*-GFP-positive cells disappeared with different kinetics: while singly tdTomato-positive cells (*tdTomato*⁺/*GFP*⁻) appeared after 2 days, only a few single *Nanog*-GFP-positive cells (*tdTomato*⁻/*GFP*⁺) were detected during differentiation (Figures 5B and 5C) suggesting that *Nanog* was silenced prior to methylation and silencing of the *miR290* and *Sox2* SEs.

To confirm that loss of the tdTomato signal correlated with accumulation of de novo methylation in both SE regions, we

sorted the main populations at different time points during RA differentiation (Figure 5C). DNA was extracted from the different cell populations and subjected to bisulfite sequencing, thus allowing a comprehensive analysis of the methylation state in both the endogenous *miR290* and *Sox2* SE and their respective *Snrpn* promoter regions (Figures 5D, 5E, S4B, and S4C). In contrast to the bulk population of mESCs (Figure 4D), the sorted double-positive cells did not harbor completely methylated alleles, consistent with the notion that methylated alleles in the

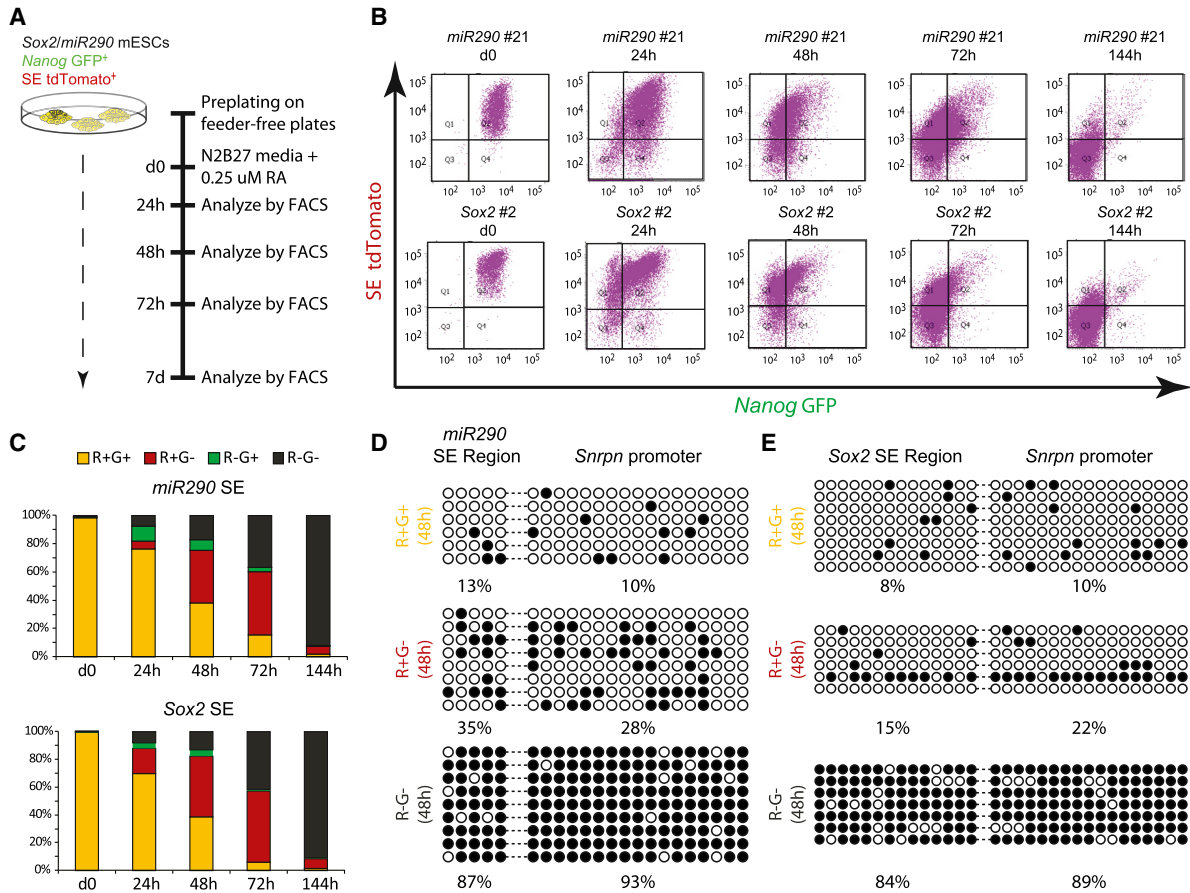


Figure 5. Dynamics of De Novo DNA Methylation of miR290 and Sox2 SE Regions upon In Vitro Differentiation

(A) Schematic representation of the RA-based differentiation protocol used on miR290 and Sox2 reporter cell lines. GFP marks endogenous expression levels of Nanog, whereas tdTomato reflects the endogenous DNA methylation levels at both miR290 and Sox2 SE regions.

(B) Flow cytometric analysis of the proportion of Nanog-GFP-positive cells (x axis) and tdTomato-positive cells (y axis) during 7 days of differentiation of miR290 #21 (top) and Sox2 #2 (bottom) reporter cell lines.

(C) Bar graph summarizing the proportion of the different cell populations during the course of 7 days RA differentiation for both miR290 #21 (top) and Sox2 #2 (bottom) reporter cell lines. Data represent two biological replicates. R, tdTomato; G, GFP.

(D and E) Bisulfite sequencing analysis on the three main cell populations sorted at 48 hr following initial treatment with RA. For both miR290 #21 (D) and Sox2 #2 (E) cell lines, the PCR amplicon (marked with dashed line) includes the endogenous CGI (left) and the downstream integrated Snrpn promoter region (right). R, tdTomato; G, GFP.

See also Figure S4.

bulk population represent intrinsic variation. The methylation of both miR290 and Sox2 in single-positive cells (tdTomato+/GFP-) was low, consistent with tdTomato expression. The overall increased de novo methylation in the single-positive cells, compared with the double-positive cells, may suggest that DNA methylation-mediated silencing was already initiated in this intermediate cell population. Notably, our analysis identified completely methylated genomes in the Sox2 single-positive (tdTomato+/GFP-) cell population (Figure 5E). This suggests that during rapid changes of de novo methylation, the half-life of the fluorescent protein (FP) may lead to an over-estimation of cells that are still hypomethylated during cell-state transitions. Finally, in agreement with the silencing of tdTomato expression, the double-negative cells (tdTomato-/GFP-) exhibited robust hypermethylation on both endogenous SE regions and their

respective Snrpn promoters (Figures 5D, 5E, S4B, and S4C). To test whether the targeted reporter allele correlated with the methylation levels of the untargeted allele (WT), we analyzed the WT allele in Sox2 reporter cells at different time points during differentiation. Figure S4D shows that similar to the reporter allele, the WT allele exhibited low levels of methylation in the sorted double-positive cells and high levels of methylation following 7 days of differentiation. We conclude that RGM allows dynamic monitoring de novo methylation events that are imposed on genomic sequences upon exiting from pluripotency. Our data suggest that the differentiation of ESCs induces silencing of Nanog prior to de novo methylation of the two miR290 and Sox2 SEs.

To test whether in vivo differentiation resulted in silencing of the tdTomato reporter in both miR290 and Sox2 SE regions,

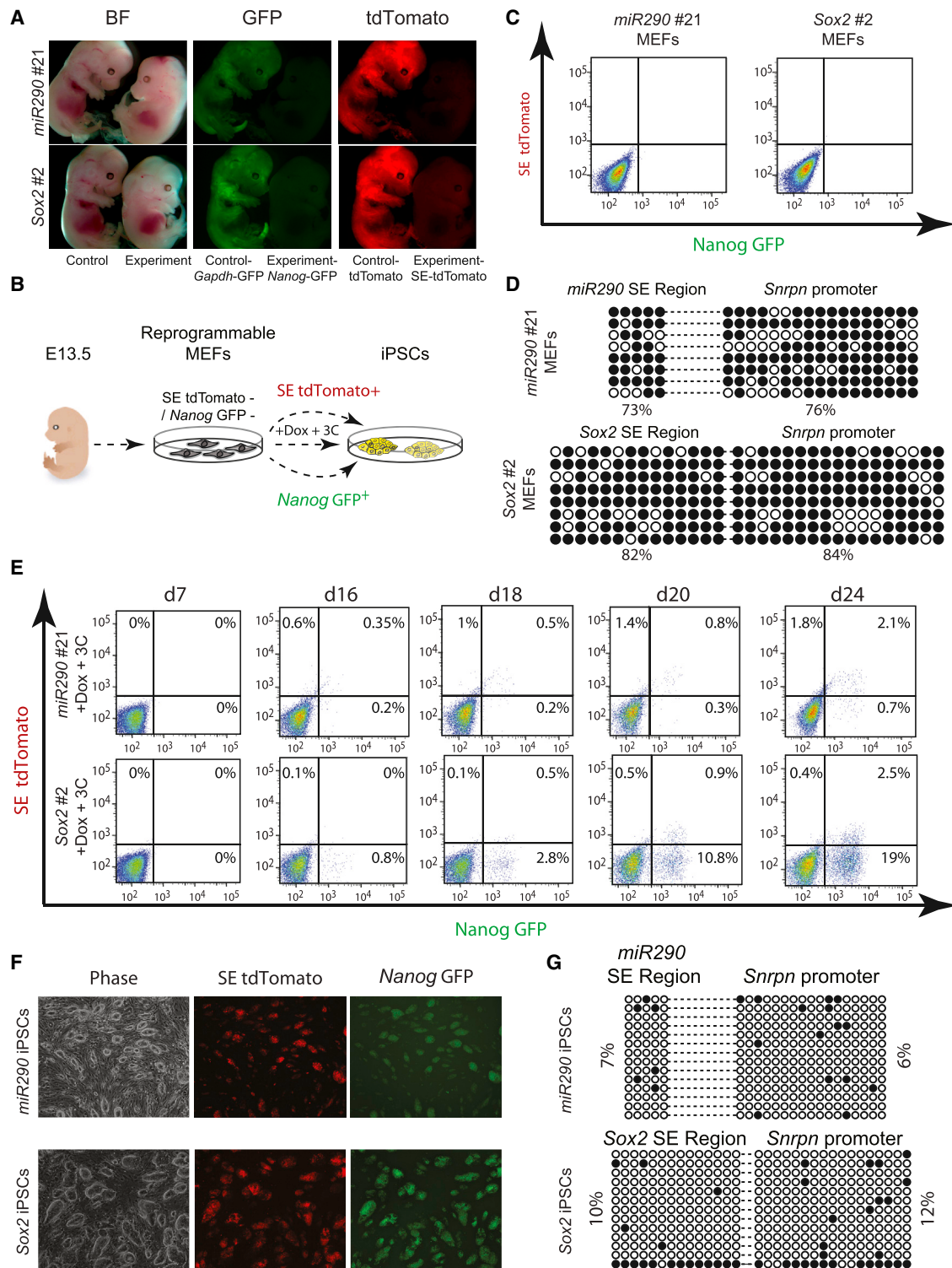


Figure 6. Dynamics of DNA Demethylation of miR290 and Sox2 SE Regions during Cellular Reprogramming

(A) miR290 (top) and Sox2 (bottom) reporter chimeric experimental embryos (right embryo in each panel). As controls, *Gapdh* CGI reporter mESCs driving GFP and constitutively expressing tdTomato (Control, *Gapdh*-GFP, and tdTomato, respectively) were injected into host blastocysts (left embryo in each panel).

(B) Schematic representation of the experimental procedure to monitor the dynamics of demethylation during reprogramming of miR290 and Sox2 reporter cell lines. GFP marks endogenous expression levels of Nanog, whereas tdTomato reflects the endogenous DNA methylation levels at both miR290 and Sox2 SE regions.

(legend continued on next page)

we analyzed 13.5 dpi chimeric embryos. As control, we injected ESCs harboring the *Gapdh* CGI reporter driving a GFP sequence, which had also been infected with lentiviruses resulting in constitutive expression of tdTomato. The robust expression of GFP in the *Gapdh* control embryos demonstrated the widespread expression signature of the *Snrpn* promoter throughout mouse tissues (Figure 6A). Unlike the *Gapdh* control, both *miR290* and *Sox2* embryos were completely negative for both GFP and tdTomato, demonstrating robust repression of *Nanog* and the *Snrpn* promoter during *in vivo* differentiation (Figure 6A).

DNA Demethylation during Cellular Reprogramming

Reprogramming of somatic cells to iPS cells involves demethylation and activation of the pluripotency SEs *Sox2* and *miR290* (see Figures 4A and S3A). We investigated whether RGM could be used to capture demethylation events that are gradually acquired during cellular reprogramming. For this, we used secondary Dox-inducible reprogrammable mouse embryonic fibroblasts (MEFs) isolated from 13.5 dpi chimeric embryos that had been injected at the blastocyst stage with the OSKM DOX-inducible ESCs (Carey et al., 2011) carrying *Nanog*-GFP and the tdTomato reporter reflecting DNA methylation levels at the *Sox2* or *miR290* SE alleles (see Figure 6B). Culture of these MEFs in DOX induces the reprogramming factors while *Nanog*-GFP activation allows monitoring the course of reprogramming in the bulk somatic cell population (Buganim et al., 2012). As expected, MEFs isolated from 13.5 dpi embryos were negative for both GFP and tdTomato expression, as measured by fluorescent microscopy and fluorescence-activated cell sorting (FACS) analysis (Figures 6C and S5A). Importantly, consistent with tdTomato repression, both endogenous *miR290* and *Sox2* SE regions as well as their corresponding downstream *Snrpn* promoter regions were hypermethylated (Figure 6D). Further analysis of the WT allele in *Sox2* MEF showed high correlation with the targeted reporter allele, demonstrating robust repression of the SE region *in vivo* (Figure S5B).

To test whether reprogramming-induced demethylation can be visualized by RGM, we treated the secondary MEFs with serum and LIF medium supplemented with 2 µg/ml doxycycline (Dox). Both *miR290* and *Sox2* MEFs were successfully reprogrammed, resulting in double-positive cells (tdTomato⁺/GFP⁺, data not shown). It was recently shown that a combination of three chemicals, TGF-β antagonist ALK5 inhibitor II, GSK3b antagonist CHIR99021, and ascorbic acid, an enzymatic cofactor (from here on referred to as 3C), results in more efficient and synchronous reprogramming (Vidal et al., 2014). To achieve more

synchronized and efficient reprogramming, both *miR290* and *Sox2* MEFs were subjected to 3C culture conditions and the dynamics of reporter activation was monitored by flow cytometry. While the first expression of tdTomato⁺ and GFP⁺ cells emerged at day 16 (Figure 6E), reporter activation of both *miR290* and *Sox2* occurred with different kinetics. Figure 6E shows accumulation of *miR290* reporter cells that activated both GFP and tdTomato (tdTomato⁺/GFP⁺) over time. A small population of single-positive GFP cells appeared in late stages of reprogramming consistent with a stochastic sequence of events in the reprogramming of the *miR290* SE region. Unlike *miR290* reporter cells, however, *Sox2* cells showed a more robust and defined dynamic of activation of both reporters. By day 16, a population of single-positive GFP cells (tdTomato⁻/GFP⁺) had accumulated, which gradually shifted to become double-positive (tdTomato⁺/GFP⁺) over time (Figures 6E and S5C). To test whether the single-positive GFP cells give rise to double-positive cells, we sorted the single-positive GFP cells and replated them on feeders using Dox independent culture conditions. Consistent with the repression of the tdTomato signal, bisulfite sequencing confirmed that the single-positive GFP cells exhibit high levels of methylation in the SE region, as well as in the downstream *Snrpn* promoter region (Figure S5D). Upon further culture, tdTomato-positive cells appeared demonstrating that single-positive GFP cells give rise to double-positive cells (Figure S5E).

Our results suggest that reprogramming of both *miR290* and *Sox2* SE regions are late events, with the *Sox2* SE region being reprogrammed subsequently to the activation of endogenous *Nanog*. *miR290* and *Sox2* double-positive (tdTomato⁺/GFP⁺) cells invariably proceed to a Dox-independent iPS cell state (Figure 6F). To assess the methylation state of the *Sox2* and *miR290* SEs, we performed bisulfite sequencing on DNA extracted from sorted double-positive (tdTomato⁺/GFP⁺) iPS cells. As shown in Figure 6G, both *miR290* and *Sox2* SE regions and their corresponding downstream *Snrpn* promoters were demethylated. These results confirmed that RGM can visualize demethylation of regulatory genomic regions during reprogramming with single-cell resolution.

DISCUSSION

In this work, we have generated a DNA methylation reporter (RGM) that allows imaging of DNA methylation with single-cell resolution. The design of the reporter system took advantage of the intrinsic characteristics of imprinted gene promoters, for which the transcriptional activity reflects the DNA methylation state of adjacent sequences. Importantly, imprinted promoters

(C) Flow cytometric analysis of the proportion of GFP-positive cells (x axis) and tdTomato-positive cells (y axis) in P0 MEFs derived from *miR290* #21 (left) and *Sox2* #2 (right) chimeric embryos.

(D) Bisulfite sequencing analysis was performed on P0 MEFs derived from *miR290* #21 (top) and *Sox2* #2 (bottom) chimeras. For each cell line, the PCR amplicon (marked with dashed line) includes both the endogenous CGI (left) and the downstream integrated *Snrpn* promoter region (right).

(E) Analysis of the proportion of GFP-positive cells (x axis) and tdTomato-positive cells (y axis) during the course of reprogramming of MEFs derived from *miR290* #21 (upper panel) and *Sox2* #2 (lower panel) chimeras. Shown are flow cytometric data from different time points following addition of dox supplemented with 3C culture condition.

(F) Representative images of established *miR290* and *Sox2* iPSC lines, derived from sorted double-positive (tdTomato⁺/GFP⁺) colonies.

(G) Bisulfite sequencing analysis was performed on P2 iPSCs derived from *miR290* #21 (top) and *Sox2* #2 (bottom) MEFs. For each cell line, the PCR amplicon (marked with dashed line) includes both the endogenous CGI (left) and the downstream integrated *Snrpn* promoter region (right).

See also Figure S5.

are neutral to developmental or tissue-specific DNA methylation changes, with their activity strictly dependent on the methylation state of the adjacent regulatory elements. This is in contrast to CGI sequences such as *Gapdh* or tissue-specific elements such as the *Dazl* promoter-associated sequences, which become demethylated or de novo methylated, respectively, when inserted into the genome of ESCs (Brandeis et al., 1994; Sabag et al., 2014). This indicates that methylation of these elements as opposed to imprinted promoters is sequence-dependent and subject to *trans*-acting signals and cell state-dependent regulation.

The RGM reporter system described here is based on the *Snrpn* minimal promoter that is not subjected to methylation changes by itself, and therefore GFP expression is solely dependent on the methylation state of surrounding sequences. Consistent with this premise, ES cells appeared GFP-positive when stably transfected with the methylated or unmethylated *Gapdh/Snrpn*-GFP vector, but were GFP-negative when transfected with the methylated or unmethylated *Dazl/Snrpn*-GFP reporter. This indicates that the *Snrpn* promoter region can be used as a faithful sensor for regional methylation changes of adjacent sequences.

To investigate whether RGM can report on the methylation state of endogenous loci, we targeted CGIs located at *Gapdh* and *Dazl* promoter regions, resulting in differential methylation and activity of the *Snrpn* reporter. Thus, the *Snrpn* promoter effectively reflects local methylation patterns without affecting the endogenous epigenetic state. As most of the tissue-specific DNA methylation changes occur in low-density CpG regulatory regions, we asked whether RGM could report on the methylation state of non-coding low-density CpG regions. We chose two pluripotency-specific SEs that are associated with the *miR290* and *Sox2* genes and are known to be active and unmethylated in ESCs but become methylated and inactive upon cellular differentiation. CRISPR/Cas-mediated insertion of the *Snrpn*-tdTomato reporter into ESCs resulted in tdTomato-positive clones but tdTomato expression was silenced in mid-gestation chimeric embryos, which reflects the demethylation state of the SEs in pluripotent cells and their de novo methylation upon induction of differentiation. Consistent with this, MEFs isolated from chimeric embryos were tdTomato-negative with both elements highly methylated. Upon conversion of the MEFs into induced pluripotent stem cells (iPSCs), however, the cells became tdTomato-positive reflecting demethylation of the SEs during reprogramming to pluripotency. Our results establish that RGM reporter activity mirrors the changes of DNA methylation imposed on endogenous CGI and low-density CpG genomic elements during development, upon cellular differentiation, and during reprogramming. Extensive epigenomic analyses of multiple tissues and cell types in both human and mice, suggest that embryonic development and cell-type specification are associated with massive epigenomic remodeling at discrete enhancers (Hon et al., 2013; Kundaje et al., 2015; Schultz et al., 2015; Ziller et al., 2013). It will thus be of interest to test whether RGM can be utilized to report on the DNA methylation state associated with more discrete regulatory regions. Implementing the methylation reporter to tissue-specific DMRs holds the promise to further elucidate the link between DNA methylation and other epigenetic mechanisms, with cell-fate regulation.

Reprogramming of somatic cells into iPSCs involves extensive resetting of the epigenome (Buganim et al., 2013; Hanna et al., 2010), and coinciding with this notion, recent studies identified a key role for epigenetic modifiers during this process (Mansour et al., 2012; Rais et al., 2013; Soufi et al., 2012). However, the exact kinetics of these epigenetic changes during the reprogramming process are difficult to define because of cell heterogeneity and the stochastic nature of the reprogramming process. Here, we followed the methylation changes of two SEs associated with *Sox2* and *miR290*, demonstrating that demethylation of both regions is a late event in the reprogramming process. Simultaneous activation of endogenous *Nanog* and *miR290* SE demethylation is consistent with *Nanog* directly regulating the expression of *miR290* cluster during reprogramming to iPS cells (Gingold et al., 2014). The gradual activation of the *Sox2* tdTomato reporter followed expression of endogenous *Nanog*, consistent with demethylation of *Sox2* SE being a late event in the process (Buganim et al., 2012). Systematic deletion of the *Sox2* upstream SE region was recently shown to dramatically affect *Sox2* expression in ESCs (Li et al., 2014; Zhou et al., 2014). Thus, the *Sox2* SE methylation reporter cells provide a rigorous experimental system to investigate how DNA methylation changes at distal regulatory region influence the expression of downstream target genes.

Changes in DNA methylation during development, lineage commitment, and disease are dynamic, and studies of epigenetic changes are hampered by two experimental constraints that limit mechanistic studies of methylation and gene regulation: (1) current methodology provides only a static "snapshot" view of the methylation state during cell state transitions, and (2) current methylation analyses require the examination of multiple cells precluding assessment of epigenetic changes in single cells. Given the overwhelming evidence of cell-cell heterogeneity in embryos, cultured cells, or disease states such as cancer (Junker and van Oudenaarden, 2014), this is a serious limitation for a mechanistic understanding of the epigenetic state and gene expression during these complex processes. For example, monitoring the course of differentiation in both *miR290* and *Sox2* reporter cells confirmed the co-existence of cell populations that harbor distinct epigenetic states. In contrast, commonly used bulk methodologies would not allow isolating and distinguishing the different cell populations. Thus, sorting and isolating different cell types according to their methylation states can be achieved only by using readout for methylation state at single-cell resolution. The RGM reporter system overcomes some of the limitations of conventional methylation analyses by providing real-time visualization of DNA methylation at single-cell resolution. As with any fluorescent protein-based reporter system, the accuracy to trace real-time changes depends on the half-life of the respective FP. Because the current version of the methylation reporter does not use a destabilized FP, silencing of the reporter after de novo methylation-induced repression of the *Snrpn* promoter is likely delayed. To generate a reporter that more rapidly responds to DNA methylation, changes would require the use of a destabilized FP. Targeting additional loci in future studies will allow us to further elucidate other possible limitations of the RGM reporter system, such as inhibition of the *Snrpn* transcriptional activity by chromatin conformation.

As RGM allows measuring dynamics of DNA methylation at single-cell resolution, it provides a framework for understanding epigenetic changes during cell state transition in heterogeneous cell populations. For example, replacing the fluorescent-based reporter system with Cre-Lox will enable the generation of epigenetic lineage tracing maps. Furthermore, utilizing RGM together with conventional gene expression reporters may offer detailed insights into the interplay between epigenetic cues and the execution of tissue-specific gene expression programs. The use of fluorescent reporters as readout for locus-specific methylation changes may also provide an effective screening platform for the isolation of small molecule compounds that affect the methylation state of specific genomic regions.

EXPERIMENTAL PROCEDURES

mESCs Cell Culture

V6.5 mouse embryonic stem cells (mESCs) were cultured on irradiated mouse embryonic fibroblasts (MEFs) with standard ESCs medium: (500 ml) DMEM supplemented with 10% FBS (Hyclone), 10 µg recombinant leukemia inhibitory factor (LIF), 0.1 mM beta-mercaptoethanol (Sigma-Aldrich), penicillin/streptomycin, 1 mM L-glutamine, and 1% nonessential amino acids (all from Invitrogen). For experiments in 2i culture conditions, mESCs were cultured on gelatin-coated plates with N2B27 + 2i + LIF medium containing: (500 ml), 240 ml DMEM/F12 (Invitrogen; 11320), 240 ml Neurobasal media (Invitrogen; 21103), 5 ml N2 supplement (Invitrogen; 17502048), 10 ml B27 supplement (Invitrogen; 17504044), 10 µg recombinant LIF, 0.1 mM beta-mercaptoethanol (Sigma-Aldrich), penicillin/streptomycin, 1 mM L-glutamine, and 1% nonessential amino acids (all from Invitrogen), 50 µg/ml BSA (Sigma), PD0325901 (Stemgent, 1 µM), and CHIR99021 (Stemgent, 3 µM).

Reporter Cell Lines

To generate stably integrated *Gapdh* and *Dazl* transgene reporter cell lines, either *Gapdh*- or *Dazl*-modified PiggyBac transposon (see [Supplemental Experimental Procedures](#)), and a helper plasmid expressing transposase, were transfected into mESCs cells using Xfect mESC Transfection Reagent (Clontech), according to the provider's protocol. Stably integrated reporter cells were selected with puromycin (2 mg/ml) for 4 days.

To generate *Dazl*, *Gapdh*, *miR290*, and *Sox2* SE reporter cell lines, targeting vectors, and CRISPR/Cas9 were transfected into mESCs using Xfect mESC Transfection Reagent (Clontech), according to the provider's protocol. Forty-eight hours following transfection, cells were FACS-sorted for GFP or tdTomato expression (respectively) and plated on MEF feeder plates. Single colonies were further analyzed for proper and single integration by Southern blot and PCR analysis.

Flow Cytometry

To assess the proportion of GFP and tdTomato in the established reporter cell lines, a single-cell suspension was filtered and assessed on the LSR II SORP, LSRFortessa SORP, or FACSCanto II.

Retinoic Acid-Induced Differentiation

mESCs carrying the reporter for both *miR290* and *Sox2* SE regions were sorted for double-positive GFP and tdTomato expression and plated on gelatin-coated plates in ES cell medium (+LIF). The next day, cells were washed with PBS, resuspended in basal N2B27 medium (2i medium without LIF, insulin, and the two inhibitors), and supplemented with 0.25 µM RA. Medium was replaced every other day.

Blastocyst Injections for the Generation of Chimeras and Secondary MEFs

Blastocyst injections were performed using (C57Bl/6xDBA) B6D2F2 host embryos. In brief, B6D2F1 females were hormone primed by an intraperitoneal (i.p.) injection of pregnant mare serum gonadotropin (PMS, EMD Millipore) fol-

lowed 46 hr later by an injection of human chorionic gonadotropin (hCG, VWR). Embryos were harvested at the morula stage and cultured in a CO₂ incubator overnight. On the day of the injection, groups of embryos were placed in drops of M2 medium using a 16-µm diameter injection pipet (Origio). Approximately ten cells were injected into the blastocoel cavity of each embryo using a Piezo micromanipulator (Prime Tech). Approximately 20 blastocysts were subsequently transferred to each recipient female; the day of injection was considered as 2.5 days postcoitum (DPC). Fetuses were collected at 13.5 DPC for the extraction of embryonic fibroblasts as described before ([Buganim et al., 2012](#)).

Southern Blots

Genomic DNA (10–15 µg) was digested with appropriate restriction enzymes overnight. Subsequently, genomic DNA was separated on a 0.7% agarose gel, transferred to a nylon membrane (Amersham) and hybridized with 32P random primer (Stratagene)-labeled probes.

Reprogramming to iPSCs

MEFs isolated from *miR290* and *Sox2* fetuses were plated at density of 50,000 cells per 6-well in gelatin-coated plates with standard MEF medium (mESCs media without LIF). The following day MEF medium was replaced with mESCs medium containing 2 mg/ml doxycycline (Sigma). Alternatively, cells were grown in mESCs medium containing 2 mg/ml doxycycline and a combination of three compounds (TGF-β antagonist ALK5 inhibitor II, GSK3b antagonist CHIR99021, ascorbic acid) as described before ([Vidal et al., 2014](#)). Medium was replaced every other day during the course of reprogramming.

SUPPLEMENTAL INFORMATION

Supplemental Information includes Supplemental Experimental Procedures and five figures and can be found with this article online at <http://dx.doi.org/10.1016/j.cell.2015.08.046>.

AUTHOR CONTRIBUTIONS

Y.S. and R.J. conceived the idea for this project. Y.S. and C.S.S. designed and conducted experiments and interpreted the data. F.S. assisted with targeting of mESCs. S.M. conducted blastocyst injections. Y.S. and R.J. wrote the manuscript with input from all other authors.

ACKNOWLEDGMENTS

We thank Thorold W. Theunissen, Patti Wisniewski, and Colin Zollo for FACS analyses and cell sorting, Denes Hnisz for providing ChIP-seq tracks, Kibibi Ganz for mouse injections, Huijing Yu for help in cloning, and Stefan Semrau for help with the RA differentiation and comments on the manuscript. This study was supported by NIH grant HD 045022. Y.S. is supported by a Human Frontier Postdoctoral Fellowship and. R.J. is co-founder of Fate Therapeutics and an adviser to Stemgent.

Received: February 6, 2015

Revised: June 21, 2015

Accepted: August 5, 2015

Published: September 24, 2015

REFERENCES

- Bird, A. (2002). DNA methylation patterns and epigenetic memory. *Genes Dev.* *16*, 6–21.
- Brandeis, M., Frank, D., Keshet, I., Siegfried, Z., Mendelsohn, M., Nemes, A., Temper, V., Razin, A., and Cedar, H. (1994). Sp1 elements protect a CpG island from de novo methylation. *Nature* *371*, 435–438.
- Buganim, Y., Faddah, D.A., Cheng, A.W., Itsikovich, E., Markoulaki, S., Ganz, K., Klemm, S.L., van Oudenaarden, A., and Jaenisch, R. (2012). Single-cell expression analyses during cellular reprogramming reveal an early stochastic and a late hierachic phase. *Cell* *150*, 1209–1222.

Buganim, Y., Faddah, D.A., and Jaenisch, R. (2013). Mechanisms and models of somatic cell reprogramming. *Nat. Rev. Genet.* 14, 427–439.

Buiting, K., Saitoh, S., Gross, S., Dittrich, B., Schwartz, S., Nicholls, R.D., and Horsthemke, B. (1995). Inherited microdeletions in the Angelman and Prader-Willi syndromes define an imprinting centre on human chromosome 15. *Nat. Genet.* 9, 395–400.

Carey, B.W., Markoulaki, S., Hanna, J.H., Faddah, D.A., Buganim, Y., Kim, J., Ganz, K., Steine, E.J., Cassady, J.P., Creyghton, M.P., et al. (2011). Reprogramming factor stoichiometry influences the epigenetic state and biological properties of induced pluripotent stem cells. *Cell Stem Cell* 9, 588–598.

Cedar, H., and Bergman, Y. (2012). Programming of DNA methylation patterns. *Annu. Rev. Biochem.* 81, 97–117.

Deaton, A.M., and Bird, A. (2011). CpG islands and the regulation of transcription. *Genes Dev.* 25, 1010–1022.

Dowen, J.M., Fan, Z.P., Hnisz, D., Ren, G., Abraham, B.J., Zhang, L.N., Weintraub, A.S., Schuijers, J., Lee, T.I., Zhao, K., and Young, R.A. (2014). Control of cell identity genes occurs in insulated neighborhoods in mammalian chromosomes. *Cell* 159, 374–387.

Ferguson-Smith, A.C. (2011). Genomic imprinting: the emergence of an epigenetic paradigm. *Nat. Rev. Genet.* 12, 565–575.

Gingold, J.A., Fidalgo, M., Guallar, D., Lau, Z., Sun, Z., Zhou, H., Faiola, F., Huang, X., Lee, D.F., Waghray, A., et al. (2014). A genome-wide RNAi screen identifies opposing functions of Snai1 and Snai2 on the Nanog dependency in reprogramming. *Mol. Cell* 56, 140–152.

Hackett, J.A., Sengupta, R., Zlylich, J.J., Murakami, K., Lee, C., Down, T.A., and Surani, M.A. (2013). Germline DNA demethylation dynamics and imprint erasure through 5-hydroxymethylcytosine. *Science* 339, 448–452.

Hanna, J.H., Saha, K., and Jaenisch, R. (2010). Pluripotency and cellular reprogramming: facts, hypotheses, unresolved issues. *Cell* 143, 508–525.

Hnisz, D., Abraham, B.J., Lee, T.I., Lau, A., Saint-André, V., Sigova, A.A., Hoke, H.A., and Young, R.A. (2013). Super-enhancers in the control of cell identity and disease. *Cell* 155, 934–947.

Hon, G.C., Rajagopal, N., Shen, Y., McCleary, D.F., Yue, F., Dang, M.D., and Ren, B. (2013). Epigenetic memory at embryonic enhancers identified in DNA methylation maps from adult mouse tissues. *Nat. Genet.* 45, 1198–1206.

Irizarry, R.A., Ladd-Acosta, C., Wen, B., Wu, Z., Montano, C., Onyango, P., Cui, H., Gabo, K., Rongione, M., Webster, M., et al. (2009). The human colon cancer methylome shows similar hypo- and hypermethylation at conserved tissue-specific CpG island shores. *Nat. Genet.* 41, 178–186.

Ivics, Z., Hackett, P.B., Plasterk, R.H., and Izsvák, Z. (1997). Molecular reconstruction of Sleeping Beauty, a Tc1-like transposon from fish, and its transposition in human cells. *Cell* 91, 501–510.

Jaenisch, R., and Bird, A. (2003). Epigenetic regulation of gene expression: how the genome integrates intrinsic and environmental signals. *Nat. Genet.* 33 (Suppl), 245–254.

Jones, P.A. (2012). Functions of DNA methylation: islands, start sites, gene bodies and beyond. *Nat. Rev. Genet.* 13, 484–492.

Junker, J.P., and van Oudenaarden, A. (2014). Every cell is special: genome-wide studies add a new dimension to single-cell biology. *Cell* 157, 8–11.

Kantor, B., Kaufman, Y., Makedonski, K., Razin, A., and Shemer, R. (2004). Establishing the epigenetic status of the Prader-Willi/Angelman imprinting center in the gametes and embryo. *Hum. Mol. Genet.* 13, 2767–2779.

Kundaje, A., Meuleman, W., Ernst, J., Bilenky, M., Yen, A., Heravi-Moussavi, A., Kheradpour, P., Zhang, Z., Wang, J., Ziller, M.J., et al.; Roadmap Epigenomics Consortium (2015). Integrative analysis of 111 reference human epigenomes. *Nature* 518, 317–330.

Lee, H.J., Hore, T.A., and Reik, W. (2014). Reprogramming the methylome: erasing memory and creating diversity. *Cell Stem Cell* 14, 710–719.

Li, E., Bestor, T.H., and Jaenisch, R. (1992). Targeted mutation of the DNA methyltransferase gene results in embryonic lethality. *Cell* 69, 915–926.

Li, Y., Rivera, C.M., Ishii, H., Jin, F., Selvaraj, S., Lee, A.Y., Dixon, J.R., and Ren, B. (2014). CRISPR reveals a distal super-enhancer required for Sox2 expression in mouse embryonic stem cells. *PLoS ONE* 9, e114485.

Mansour, A.A., Gafni, O., Weinberger, L., Zviran, A., Ayyash, M., Rais, Y., Krupnik, V., Zerbib, M., Armann-Zalcenstein, D., Maza, I., et al. (2012). The H3K27 demethylase Utx regulates somatic and germ cell epigenetic reprogramming. *Nature* 488, 409–413.

Mummaneni, P., Walker, K.A., Bishop, P.L., and Turker, M.S. (1995). Epigenetic gene inactivation induced by a cis-acting methylation center. *J. Biol. Chem.* 270, 788–792.

Pawlak, M., and Jaenisch, R. (2011). De novo DNA methylation by Dnmt3a and Dnmt3b is dispensable for nuclear reprogramming of somatic cells to a pluripotent state. *Genes Dev.* 25, 1035–1040.

Rais, Y., Zviran, A., Geula, S., Gafni, O., Chomsky, E., Viukov, S., Mansour, A.A., Caspi, I., Krupnik, V., Zerbib, M., et al. (2013). Deterministic direct reprogramming of somatic cells to pluripotency. *Nature* 502, 65–70.

Reik, W., Dean, W., and Walter, J. (2001). Epigenetic reprogramming in mammalian development. *Science* 293, 1089–1093.

Rhinn, M., and Dollé, P. (2012). Retinoic acid signalling during development. *Development* 139, 843–858.

Rivera, C.M., and Ren, B. (2013). Mapping human epigenomes. *Cell* 155, 39–55.

Sabag, O., Zamir, A., Keshet, I., Hecht, M., Ludwig, G., Tabib, A., Moss, J., and Cedar, H. (2014). Establishment of methylation patterns in ES cells. *Nat. Struct. Mol. Biol.* 21, 110–112.

Schultz, M.D., He, Y., Whitaker, J.W., Hariharan, M., Mukamel, E.A., Leung, D., Rajagopal, N., Nery, J.R., Urich, M.A., Chen, H., et al. (2015). Human body epigenome maps reveal noncanonical DNA methylation variation. *Nature* 523, 212–216.

Smith, Z.D., and Meissner, A. (2013). DNA methylation: roles in mammalian development. *Nat. Rev. Genet.* 14, 204–220.

Smith, Z.D., Chan, M.M., Humm, K.C., Karnik, R., Mekhoubad, S., Regev, A., Eggan, K., and Meissner, A. (2014). DNA methylation dynamics of the human preimplantation embryo. *Nature* 511, 611–615.

Soufi, A., Donahue, G., and Zaret, K.S. (2012). Facilitators and impediments of the pluripotency reprogramming factors' initial engagement with the genome. *Cell* 151, 994–1004.

Stadler, M.B., Murr, R., Burger, L., Ivanek, R., Lienert, F., Schöler, A., van Nimwegen, E., Wirbelauer, C., Oakeley, E.J., Gaidatzis, D., et al. (2011). DNA-binding factors shape the mouse methylome at distal regulatory regions. *Nature* 480, 490–495.

Turker, M.S. (2002). Gene silencing in mammalian cells and the spread of DNA methylation. *Oncogene* 21, 5388–5393.

Vidal, S.E., Amlani, B., Chen, T., Tsirigos, A., and Stadtfeld, M. (2014). Combinatorial modulation of signaling pathways reveals cell-type-specific requirements for highly efficient and synchronous iPSC reprogramming. *Stem Cell Reports* 3, 574–584.

Whyte, W.A., Orlando, D.A., Hnisz, D., Abraham, B.J., Lin, C.Y., Kagey, M.H., Rahl, P.B., Lee, T.I., and Young, R.A. (2013). Master transcription factors and mediator establish super-enhancers at key cell identity genes. *Cell* 153, 307–319.

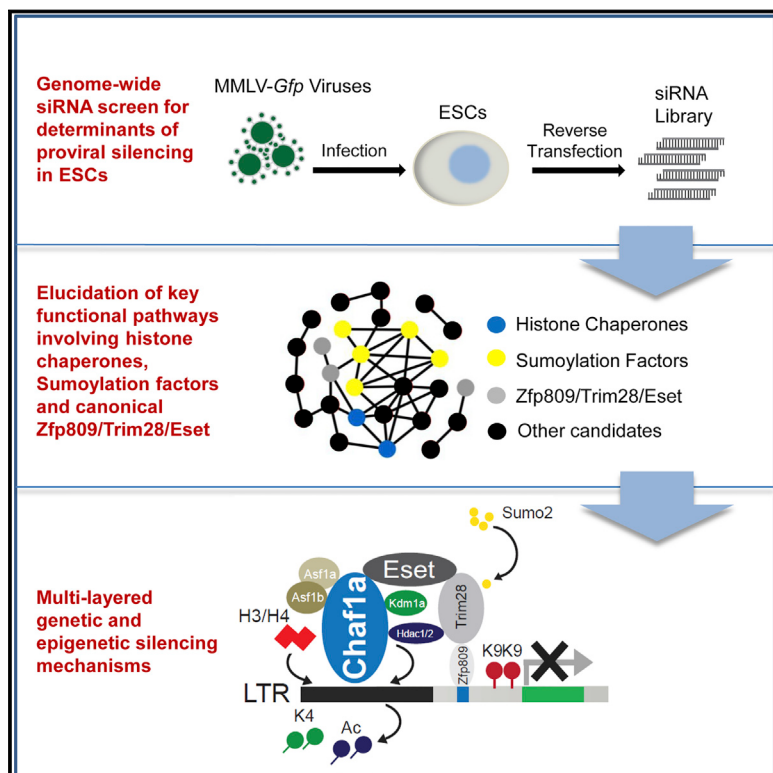
Xie, W., Schultz, M.D., Lister, R., Hou, Z., Rajagopal, N., Ray, P., Whitaker, J.W., Tian, S., Hawkins, R.D., Leung, D., et al. (2013). Epigenomic analysis of multilineage differentiation of human embryonic stem cells. *Cell* 153, 1134–1148.

Zhou, H.Y., Katsman, Y., Dhaliwal, N.K., Davidson, S., Macpherson, N.N., Sakthidevi, M., Collura, F., and Mitchell, J.A. (2014). A Sox2 distal enhancer cluster regulates embryonic stem cell differentiation potential. *Genes Dev.* 28, 2699–2711.

Ziller, M.J., Gu, H., Müller, F., Donaghey, J., Tsai, L.T., Kohlbacher, O., De Jager, P.L., Rosen, E.D., Bennett, D.A., Bernstein, B.E., et al. (2013). Charting a dynamic DNA methylation landscape of the human genome. *Nature* 500, 477–481.

Systematic Identification of Factors for Provirus Silencing in Embryonic Stem Cells

Graphical Abstract



Highlights

- Genome-wide siRNA screen identifies key determinants for proviral silencing in ESCs
- Histone chaperones, sumoylation factors, and chromatin modifiers can repress ERVs
- Sumo2 orchestrates viral silencing through sumoylation modification of Trim28
- Chaf1a regulates provirus and ERVs via its interaction with Eset, Kdm1a, and Hdac1/2

Authors

Bin Xia Yang, Chadi A. EL Farran,
Hong Chao Guo, ..., Hu Li,
Frederic A. Bard, Yuin-Han Loh

Correspondence

yhloh@imcb.a-star.edu.sg

In Brief

Proviral silencing is a characteristic of the pluripotent state, and the precise expression of endogenous retrovirus is critical for embryogenesis and development. In this study, a genome-wide siRNA screen identifies new cellular factors and new mechanisms involved in retroviral repression in embryonic stem cells.

Accession Numbers

GSE70865

Systematic Identification of Factors for Proivirus Silencing in Embryonic Stem Cells

Bin Xia Yang,^{1,22} Chadi A. EL Farran,^{1,2,22} Hong Chao Guo,^{3,22} Tao Yu,^{1,2,22} Hai Tong Fang,¹ Hao Fei Wang,^{1,2} Sharon Schlesinger,^{4,5} Yu Fen Samantha Seah,¹ Germaine Yen Lin Goh,⁶ Suat Peng Neo,⁷ Yinghui Li,⁹ Matthew C. Lorincz,¹⁰ Vinay Tergaonkar,^{9,21} Tit-Meng Lim,² Lingyi Chen,³ Jayantha Gunaratne,^{7,8} James J. Collins,^{11,12,13,14} Stephen P. Goff,^{4,5,15} George Q. Daley,^{14,16,17,18,19} Hu Li,²⁰ Frederic A. Bard,^{6,21} and Yuin-Han Loh^{1,2,*}

¹Epigenetics and Cell Fates Laboratory, A*STAR Institute of Molecular and Cell Biology, 61 Biopolis Drive Proteos, Singapore 138673, Singapore

²Department of Biological Sciences, National University of Singapore, Singapore 117543, Singapore

³College of Life Sciences, Nankai University, Tianjin 300071, China

⁴Department of Biochemistry and Molecular Biophysics, Columbia University, New York, NY 10032, USA

⁵Department of Microbiology and Immunology, Columbia University, New York, NY 10032, USA

⁶Membrane Traffic Laboratory, A*STAR Institute of Molecular and Cell Biology, 61 Biopolis Drive Proteos, Singapore 138673, Singapore

⁷Quantitative Proteomics Group, A*STAR Institute of Molecular and Cell Biology, 61 Biopolis Drive Proteos, Singapore 138673, Singapore

⁸Department of Anatomy, Yong Loo Lin School of Medicine, National University of Singapore, Singapore 117597, Singapore

⁹Division of Cancer Genetics and Therapeutics, Laboratory of NF-κB Signaling, A*STAR Institute of Molecular and Cell Biology, 61 Biopolis Drive Proteos, Singapore 138673, Singapore

¹⁰Department of Medical Genetics, Life Sciences Institute, University of British Columbia, Vancouver, BC V6T 1Z3, Canada

¹¹Department of Biological Engineering, Synthetic Biology Center, Institute for Medical Engineering and Science, Massachusetts Institute of Technology, Cambridge, MA 02139, USA

¹²Broad Institute of MIT and Harvard, Cambridge, MA 02139, USA

¹³Wyss Institute for Biologically Inspired Engineering, Harvard University, Boston, MA 02115, USA

¹⁴Howard Hughes Medical Institute, Boston, MA 02115, USA

¹⁵Howard Hughes Medical Institute, New York, NY 10032, USA

¹⁶Stem Cell Transplantation Program, Division of Pediatric Hematology/Oncology, Boston Children's Hospital and Dana-Farber Cancer Institute, Boston, MA 02115, USA

¹⁷Department of Biological Chemistry and Molecular Pharmacology, Harvard Medical School, Boston, MA 02115, USA

¹⁸Harvard Stem Cell Institute, Boston, MA 02115, USA

¹⁹Manton Center for Orphan Disease Research, Boston, MA 02115, USA

²⁰Center for Individualized Medicine, Department of Molecular Pharmacology & Experimental Therapeutics, Mayo Clinic, Rochester, MN 55905, USA

²¹Department of Biochemistry, Yong Loo Lin School of Medicine, National University of Singapore, Singapore 119077, Singapore

²²Co-first author

*Correspondence: yhloh@imcb.a-star.edu.sg

<http://dx.doi.org/10.1016/j.cell.2015.08.037>

SUMMARY

Embryonic stem cells (ESCs) repress the expression of exogenous proviruses and endogenous retroviruses (ERVs). Here, we systematically dissected the cellular factors involved in provirus repression in embryonic carcinomas (ECs) and ESCs by a genome-wide siRNA screen. Histone chaperones (Chaf1a/b), sumoylation factors (Sumo2/Ube2i/Sae1/Uba2/Senp6), and chromatin modifiers (Trim28/Eset/Atf7ip) are key determinants that establish provirus silencing. RNA-seq analysis uncovered the roles of Chaf1a/b and sumoylation modifiers in the repression of ERVs. ChIP-seq analysis demonstrates direct recruitment of Chaf1a and Sumo2 to ERVs. Chaf1a reinforces transcriptional repression via its interaction with members of the NuRD complex (Kdm1a, Hdac1/2) and Eset, while Sumo2 orches-

trates the provirus repressive function of the canonical Zfp809/Trim28/Eset machinery by sumoylation of Trim28. Our study reports a genome-wide atlas of functional nodes that mediate proviral silencing in ESCs and illuminates the comprehensive, interconnected, and multi-layered genetic and epigenetic mechanisms by which ESCs repress retroviruses within the genome.

INTRODUCTION

The expression of proviruses and endogenous retroviruses (ERVs) is restricted in pluripotent stem cells (Feuer et al., 1989; Niwa et al., 1983; Teich et al., 1977). This silencing has likely evolved for the protection of germline cells from insertional mutagenesis (Gaudet et al., 2004; Walsh et al., 1998). The expression and DNA methylation profiles of the Moloney murine leukemia virus (MMLV) have been investigated in embryonic carcinoma

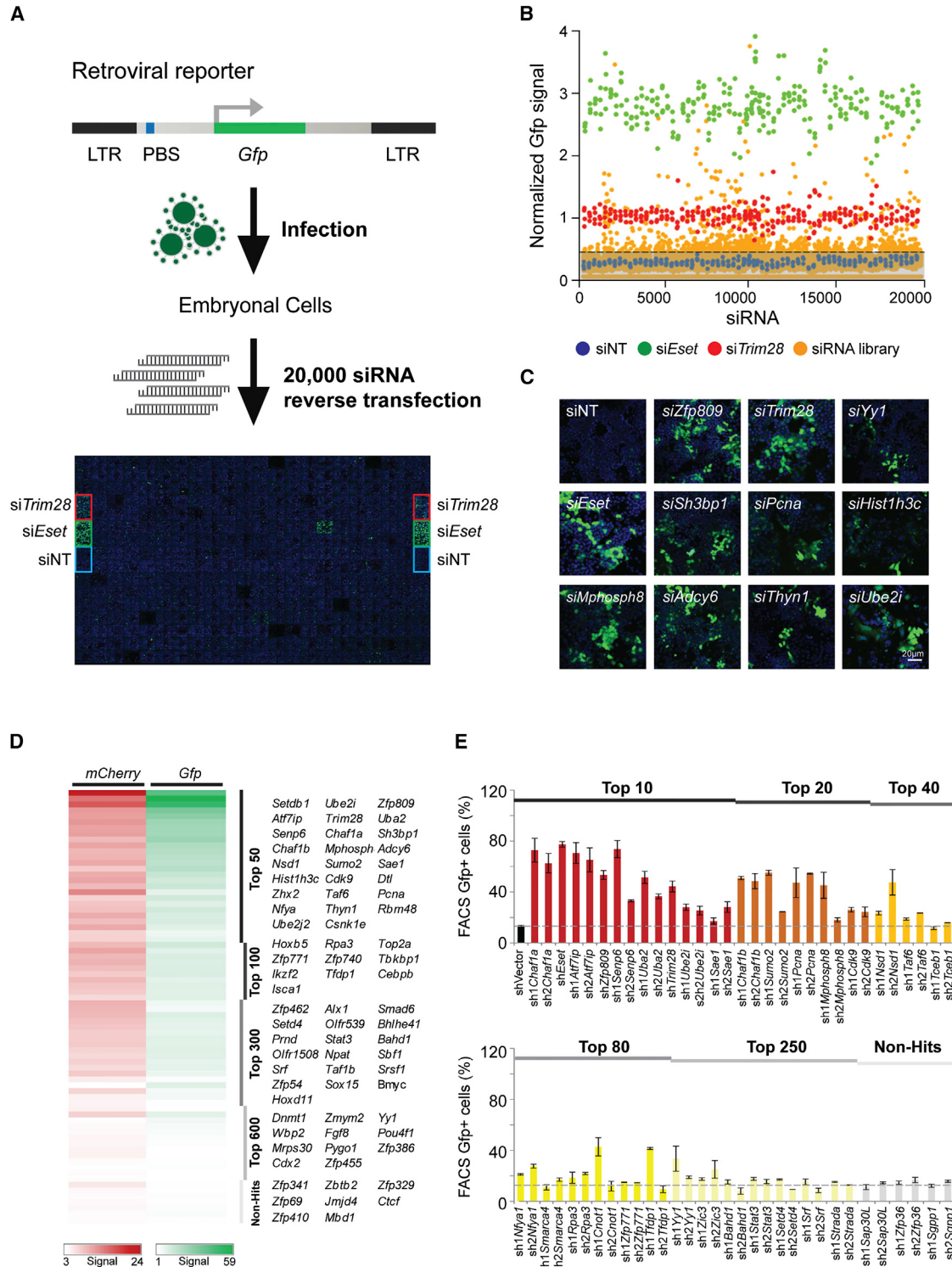


Figure 1. Genome-wide siRNA Screen for Regulators of Proviral Silencing in Mouse F9 ECs

(A) Schematic of the proviral MMLV-Gfp reporter assay. The map of the proviral reporter is shown (upper panel). LTR (black) indicates the long terminal repeats, while PBS (blue) represents the primer binding site. F9 cells were infected with the reporter virus and subjected to reverse transfection with the siRNA library in 384-well plates. A representative image for Gfp fluorescence (green) and nuclear Hoechst 33342 staining (blue) in a 384-well plate is shown. In each 384-well plate, non-targeting siRNA control (siNT) and positive control siRNA against *Trim28* and *Eset* (si*Trim28* and si*Eset*) were added.

(legend continued on next page)

cells (ECs) and embryonic stem cells (ESCs) (Niwa et al., 1983). DNA methylation is thought to repress the expression of viral genes in differentiated cells, while repression in pluripotent cells is mediated by both *cis*-acting de novo methylation of the integrated proviruses (Gaudet et al., 2004; Walsh et al., 1998) and *trans*-acting transcriptional repressors (Petersen et al., 1991; Stewart et al., 1982; Walsh et al., 1998; Wolf et al., 2008a; Wolf and Goff, 2007).

It has been reported that many ERVs affect cellular gene activity by acting as alternative promoters or enhancers (Peaston et al., 2004). For example, MERV1 is transiently activated during the mouse two-cell (2C) stage, regulating the expression of 2C-specific genes (Macfarlan et al., 2012). ERVs may also function in the reprogramming of somatic cells into induced pluripotent stem cells (iPSCs). Specific ERVs are re-activated during the reprogramming process, while other classes of ERVs have to be silenced to attain complete reprogramming (Friedli et al., 2014; Wissing et al., 2012). Together, these studies suggest that proviral silencing is a characteristic of the pluripotent state, and the precise expression of ERVs have critical roles during embryogenesis and development.

Various studies have implicated diverse epigenetic mechanisms in the silencing of retroviruses and ERVs. Repression is thought to be dependent on a conserved sequence element termed the primer binding site (PBS). Factors such as Zfp809, Trim28, and Eset are responsible for mediating the H3K9me3 repressive silencing mechanism (Friedli et al., 2014; Rowe et al., 2010; Wolf and Goff, 2007, 2009; Wolf et al., 2008b). Eset was shown to be involved in the repression of retroviruses and subfamilies of ERVs, predominantly of class I and II ERVs (Karimi et al., 2011; Matsui et al., 2010). More recently, viral-silencing factors such as the zinc finger protein Yin yang 1 (Yy1), Erb3 binding protein 1 (Ebp1), and the polycomb repressive complex 2 (PRC2) catalytic subunit Ezh2 (Schlesinger et al., 2013; Schlesinger and Goff, 2013; Wang et al., 2014) have been described. Other studies reporting the role of host factors governing ERVs in model organisms, such as *Saccharomyces cerevisiae* (Maxwell and Curcio, 2007) have also provided critical evolutionary insight into the dynamics of retroviral regulation.

Despite many efforts to identify the factors involved, many components of the epigenetic machinery required for stable silencing of proviruses and ERVs remains poorly characterized. To advance our understanding, we developed a powerful high-throughput screening approach based on a provirus MMLV-Gfp reporter (Schlesinger et al., 2013) and genome-wide small interfering RNA (siRNA) knockdown. Our screen identified 303 determinants of viral silencing in mouse ESCs with high confi-

dence and provides a genome-wide functional interrogation of determinants mediating proviral silencing in pluripotent embryonic stem cells.

RESULTS

Unbiased Genome-wide siRNA Screen for Determinants of Proviral Silencing in Embryonic Carcinoma Cells

To define the factors involved in the silencing process, we developed a high-throughput screening approach based on a provirus MMLV-Gfp reporter and siRNA knockdown in F9 ECs (Figure 1A). F9 cells were infected with the MMLV-Gfp virus and then reverse transfected with siRNA in 384-well plates. Expression of Gfp on day 4 post-infection indicated retrovirus activation.

We first confirmed the sensitivity of the reporter assay via knockdown of canonical repressive genes *Trim28* and *Eset*. Consistently, imaging, and fluorescence-activated cell sorting (FACS) analysis showed that knockdown of both factors dramatically relieved the repression of retroviral Gfp (Figures S1A and S1B). We next carried out a pilot screen on the kinome siRNA library in F9 cells, using non-targeting (siNT) *Trim28* and *Eset* siRNAs as controls. The kinome library screen was analyzed by Z-prime score (Figures S1C–S1F). From the screen, we identified both known (*Trim28* and *Cdk9*) and undetermined factors (*Chuk*, *Epha4*, *Csnk1e*, *Sgpp1*, and *Npp4a*) responsible for retrovirus silencing (Figure S1G). *Cdk9* was previously reported to interact with HIV-1 Tat protein and regulate HIV-1 transcription (Kao et al., 1987).

Next, we carried out a whole genome siRNA screen targeting 20,000 genes in F9 cells (Figure 1A). Candidates that caused excessive cell death upon siRNA knockdown were excluded using a stringent nuclei number cut-off threshold. Based on the normalized Gfp signal cut-off value, which short-listed factors that had values larger than 2 SDs from the mean of the negative controls (Figure 1B), 650 factors were short-listed (Table S1). Among the hits are factors previously implicated in retroviral silencing process, such as *Eset*, *Zfp809*, *Yy1*, and *Trim28*. In addition, new candidates identified include *Ube2i*, *Pcna*, *Hist1h3c*, *Mphosph8*, *Adcy6*, *Sh3bp1*, and *Thyn1* (Figure 1C).

To validate the genome-wide siRNA screen, we performed secondary siRNA screens utilizing the MMLV-Gfp reporter and an independent MMLV-mCherry reporter. We observed strong correlation between the two reporters (Figure 1D). To minimize possible non-specific effects from the pooled siRNA, we designed two pairs of short hairpin RNAs (shRNAs) for 31 candidate genes and three non-candidate genes. shRNA validation was performed in F9 cells, followed by FACS analysis of Gfp

(B) Dot plot for genome-wide siRNA screen. A cut-off threshold was set at 0.37 (dotted line). Candidate genes above the threshold showed significant Gfp reactivation.

(C) Representative images of Gfp rescue for selected hits from the genome-wide screen. Gfp (green) and Hoechst 33342 staining of the nucleus (blue) are shown.

(D) Secondary siRNA screen for 74 genes. Results for reactivation of proviral Gfp or mCherry reporters are shown as heatmaps. Intensity of green or red color represents the level of reactivation of Gfp and mCherry reporters respectively. See *Supplemental Experimental Procedures* for details on the gene selection criteria and experimental design.

(E) Validation of candidate genes using shRNA knockdown. Gfp signal was detected by FACS. The percentage of Gfp activation is shown on the y axis. Values are mean \pm SEM from independent replicate experiments.

See also Figure S1 and Table S1.

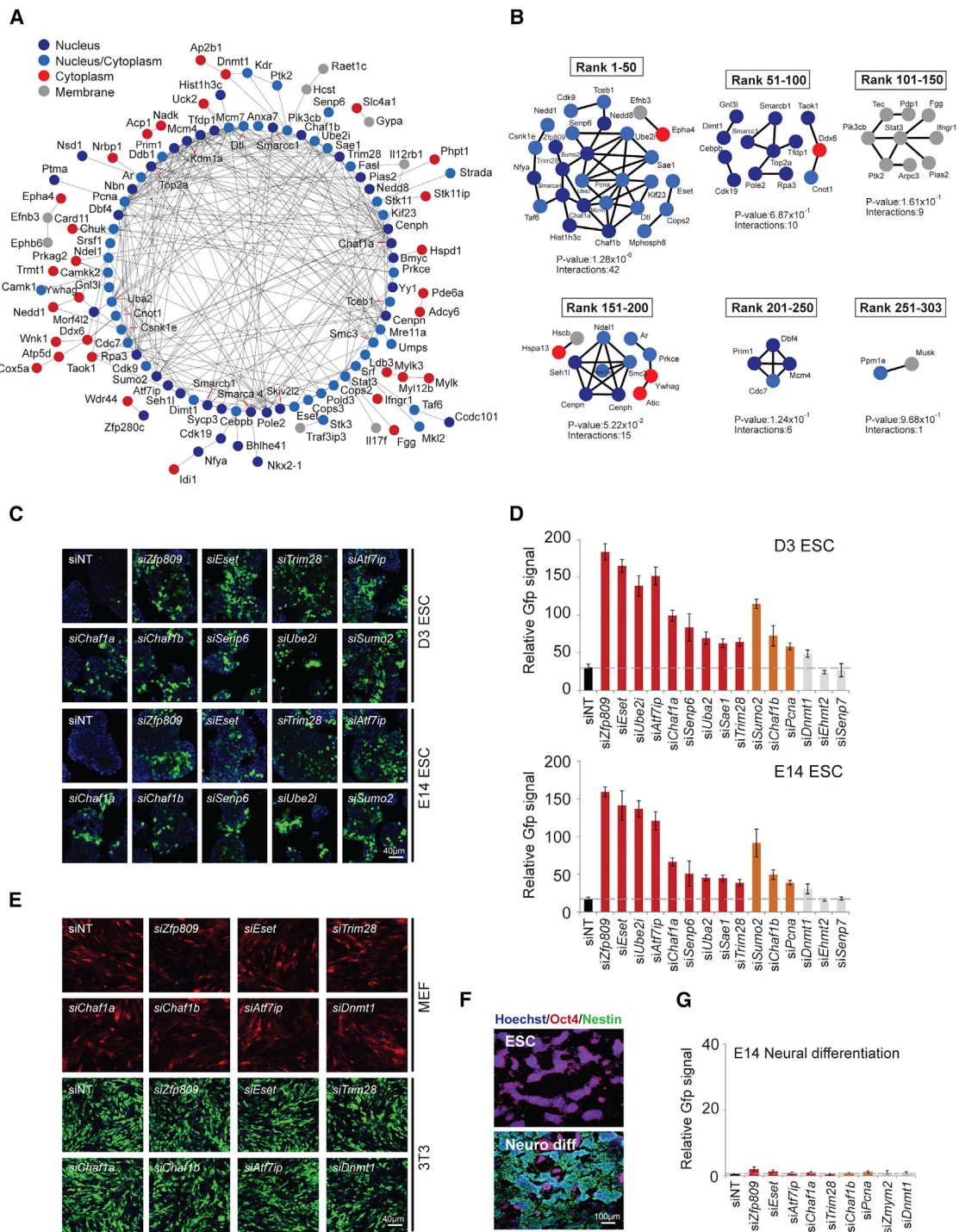


Figure 2. Bioinformatics Analyses for the Genome-wide siRNA Screen and the ESC Specificity of the Candidate Genes

(A) Interactome analysis. Cellular localization of the hits is indicated.

(B) Interactions observed in hits of different ranking tiers. Localization of hits is indicated as in (A). P values and number of interactions are indicated.

(C and D) Validation of MMLV-Gfp rescue by siRNA knockdown of the top candidates in D3 and E14 ESCs. Non-targeting siRNA (siNT) and siRNA targeting non-hits (*Dmmt1*, *Ehm2*, *Senp7*) were selected as controls. (C) Representative images of Gfp rescue by siRNA knockdown of the indicated hits. Gfp (green) and Hoechst 33342 nucleus staining (blue) are shown. (D) Bar chart graphs for Gfp activation. Relative Gfp signal is shown on the y axis. Values are mean \pm SEM from independent replicate experiments.

(E) Representative images of MMLV-mCherry and MMLV-Gfp rescue by siRNA knockdown of selected top hits in MEF and 3T3 cells. mCherry (red), Gfp (green) and Hoechst 33342 nucleus staining (blue) are shown.

(legend continued on next page)

expression. shRNA knockdown efficiencies were confirmed by qPCR (Figure S1H) and western blot analysis for selected genes (Figure S1). Notably, we observed robust Gfp reactivation for the majority of top hits (Figure 1E). From the results of secondary siRNA and shRNA screens, we focused on the top 303 hits that were highly corroborative with the primary screen and are considered high confidence candidates.

Network Analysis of the Candidates Reveals Multiple Interacting Pathways Involved in Proviral Silencing

We performed Gene Ontology (GO), KEGG, and Interpro analysis (Huang et al., 2009) on the top 303 hits and elucidated 148 statistically enriched biological processes and pathways, including chromatin modification and organization, protein sumoylation and phosphorylation, regulation of transcription, DNA replication, DNA repair, and methylation (Figure S2A; Table S2). Protein-protein interaction analysis of the high confidence hits demonstrates tight and dense interaction between the candidate proteins (Figure 2A). In addition, cellular component analysis revealed that the candidates were widely distributed in different sub-cellular fractions (Figures 2A and S2B). These suggest that proviral silencing is controlled by multilayered machineries involving components of different cellular pathways and with varied cellular localization.

Candidate Genes Are Potent Repressors of Provirus Expression in Embryonic Stem Cells

We analyzed the expression profiles of the candidate genes in over 100 cell lines using the cTen database (Shoemaker et al., 2012). The majority of candidate genes are highly expressed in embryonic stem cell lines and are low in other tissue-specific cell lines (Figure S2C). The expression of selected candidates was further tested in the mouse ESC lines E14 and D3, mouse EC lines F9 and P19, as well as in differentiated mouse embryo fibroblasts (MEFs). Consistent with cTen enrichment scores, qPCR analyses showed embryonal and stem cell-specific expression of the candidates (Figure S2D).

To further interrogate the function of our candidate hits, we performed network analysis of the hits based on their tiered ranking. We observed greater interactions among our top 50 candidates, although the lower ranked hits also exhibited specific interactions indicative of their biological significances (Figure 2B). Among the top 20 hits are the histone chaperones (Chaf1a/b), sumoylation modification genes (Ube2i, Sumo2, Uba2, Sae1, and Senp6), and chromatin-bound factors (Eset, Atf7ip, Zfp809, Trim28). To test the functional specificity of these strong candidates in mESCs, we conducted siRNA and shRNA knockdowns in two mESC lines E14 and D3 and in two differentiated cell types, 3T3 and MEFs. The results of the Gfp reporter rescue assay from mESC lines corroborate well with the primary screen done in F9 cells (Figures 2C, 2D, and S2E). In contrast, MMLV-driven expression of Gfp or mCherry was high in 3T3 and MEFs at the outset and knockdown of candidate genes

did not result in perturbations of the reporter signal in these cell lines (Figures 2E and S2F).

To further assess the ESC specificity of our candidates, we differentiated E14 and D3 cells via embryoid body (EB) formation and neural differentiation (Ying et al., 2003). The differentiated cells lost their ESC-specific morphologies and pluripotency markers and expressed high levels of differentiation genes (Figures 2F and S2G). Consistent with a previous report, the MMLV virus remain silenced in differentiated ESCs (Niwa et al., 1983). None of the candidate gene knockdowns in the differentiated cells could rescue MMLV-Gfp reporter expression (Figures 2G and S2H), suggesting that alternative or additional silencing pathways are active in these cells. Relative copy number of integrated reporters in E14 and the differentiated cells was indistinguishable, ruling out the possibility of reduced viral integration in the latter (Figures S2I and S2J). In addition, knockdown of the top hits did not reduce provirus integration efficiency in E14 cells (Figure S2K). Of note, we observed no significant change in Gfp signal driven by an integrated non-LTR reporter (PiggyBac-CAG-Gfp) upon knockdown of the top hits (Figures S2L and S2M). This strongly suggests that the mode of proviral regulation by the factors is transcriptional or epigenetic.

Chaf1a/b and Sumoylation Modification Complex Play Critical Roles in Regulating ERVs

To evaluate the roles of Chaf1a/b and the sumoylation factors in ERV regulation, we measured ERV expression by qPCR upon depletion of the candidates. Consistent with a previous study, Trim28 knockdown elicited reactivation of IAP elements in ESCs (Figure S3A) (Rowe et al., 2010). Intriguingly, we found up-regulation of class I (GLN), class II (MMERVK10c), and class III (MERVL) elements following depletion of the factors from the Caf1 complex, sumoylation complex, and Atf7ip (Figure S3A). Notably, Northern blot assays confirmed increased transcription of MERVL, but not of IAP and MusD elements in Chaf1a/b depleted E14 cells (Figure S3C). Meanwhile, knockdown of selected weaker candidates also showed consistent de-repression of MERVL but not of the other ERVs (Figure S3B).

To further delineate the regulatory roles of the candidates on ERVs, we performed genome-wide RNA sequencing (RNA-seq) of Chaf1a/b-, Sumo2-, Sae1-, Ube2i-, Ube2-, Senp6-, Trim28-, Eset-, and Atf7ip-depleted cells. Transcriptomic analyses revealed significant de-repression of several families of ERVs upon depletion of each factor (Figure 3A; Table S3). In contrast to their effects on global gene expression (Figure S3D), the majority of the ERV targets are upregulated upon shRNA knockdown (Figure 3B). Together, these suggest an ERV-specific repressive function of the candidates.

Next, we evaluated the ERV classes regulated by the candidates. Chaf1a/b depletion resulted in the de-repression of large numbers of Class III ERVs, while the sumoylation and canonical factors regulated more Class II ERVs (Figure 3C). Cluster analysis detected strong correlation of ERV regulation within the

(F) Representative images for Oct4 and Nestin staining on E14 cells (upper panel) and E14 ESCs derived differentiated neural cells (lower panel).

(G) MMLV-Gfp rescue in E14-derived neural cells by siRNA knockdown of selected top hits. Relative Gfp signal is shown on the y axis. Values are mean ± SEM from independent replicate experiments.

See also Figure S2 and Table S2.

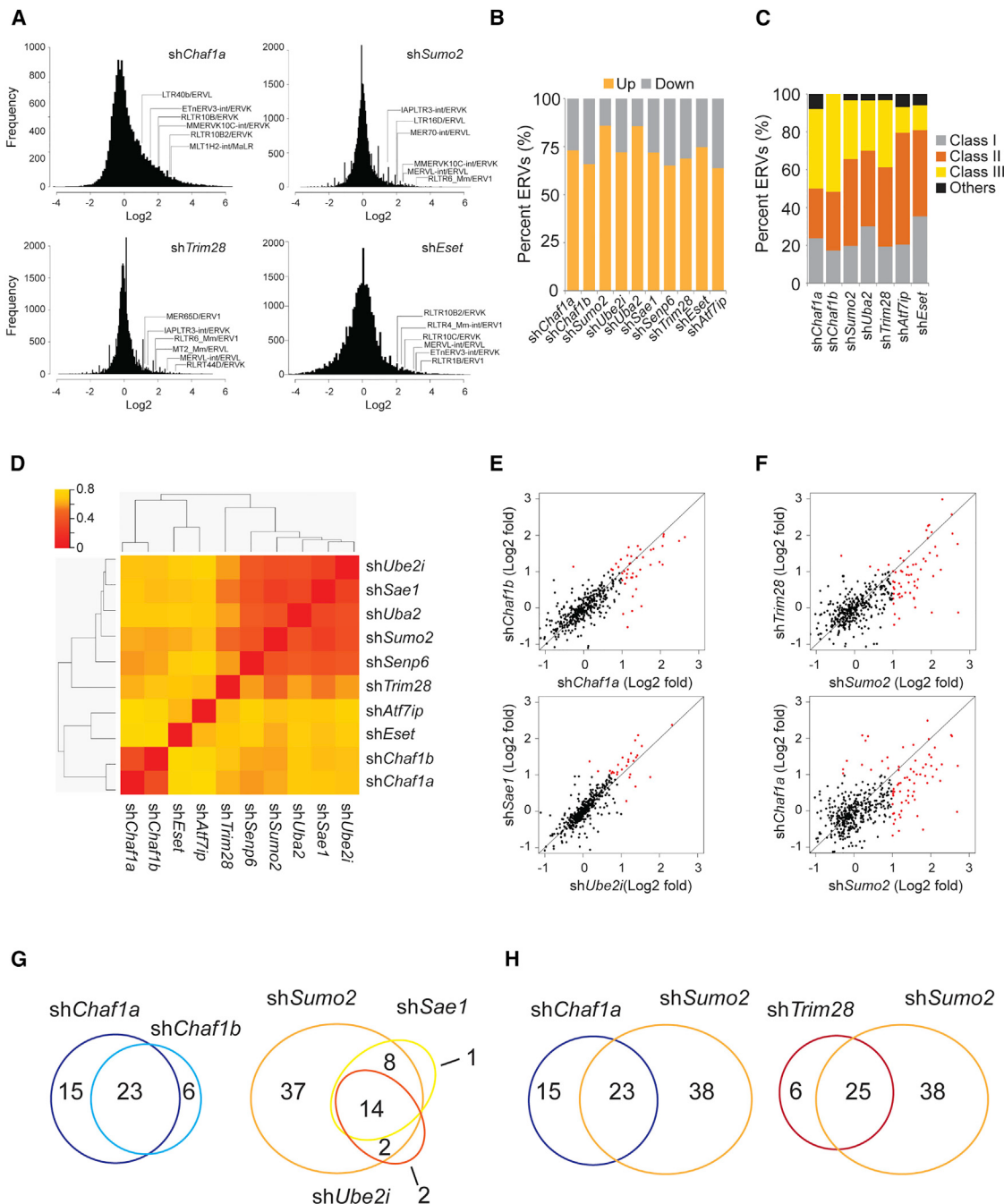


Figure 3. Histone Modifiers and Sumoylation Factors Regulate ERVs in Mouse Embryonic Stem Cells

(A) Frequency histogram of gene expression from RNA-seq data after *Chaf1a*, *Sumo2*, *Trim28*, or *Eset* depletion in E14 cells. Log₂ fold change of expression levels is shown on the x axis. The number of genes at a given expression level is shown on the y axis.

(B) Percentage stacked columns indicating the up or downregulation of ERVs upon the depletion of the indicated factors.

(C) Percentage stacked columns indicating the classes of upregulated ERVs upon the depletion of the indicated factors.

(D) Clustering analysis of the indicated RNA-Seq libraries based on differential ERV expression. Heatmap color intensity signifies the correlation strength between 0 (red-high similarity) to 0.8 (yellow-high difference).

(E and F) Genome-wide de-regulation of ERVs in E14 cells after depletion of the indicated genes. RNA-seq data for RNAi samples and the shVector control were used to calculate the Log₂ fold change values. Red dots indicate the elements with significantly increased expression.

(G and H) Venn diagrams demonstrating the number of commonly and differentially upregulated ERVs among the depletion of indicated factors.

See also Figure S3 and Table S3.

Chaf1a/b, sumoylation factors, and the chromatin binding factors Trim28, Atf7ip, and Eset (Figure 3D), whereas the analysis of global gene expression displayed a different pattern (Figure S3E).

Remarkably, Trim28 shares significant similarity with both the Chaf1a/b and sumoylation factors in their ERV regulation (Figure 3D), suggesting overlapping mechanisms. ERVs controlled by Atf7ip overlapped extensively with the ones regulated by Trim28 or Eset (Figure S3F), indicating that Atf7ip may be integral to the canonical Krab-Zfp/Trim28/Eset machinery. Atf7ip was shown to be a co-factor of Eset that helps in facilitating the conversion of H3K9me2 to H3K9me3 (De Graeve et al., 2000; Wang et al., 2003). Furthermore, the ERVs regulated by Chaf1a overlaps significantly with the ones regulated by Chaf1b (Figures 3D, 3E and 3G), but differ significantly from those controlled by Sumo2 (Figures 3F and 3H). One key feature of the cluster of sumoylation genes is the strong correlation between the factors in the specific control of their ERV targets as shown by the tight pairwise correlation (Figure 3E). This suggests a coordinated mechanism involving multiple members of the same sumoylation pathway. Interestingly, most ERVs regulated by Sae1 and Ube2i are part of the larger number of ERVs governed by Sumo2, suggesting a central role for Sumo2 in this sumoylation process (Figure 3G). It is noteworthy that many ERVs regulated by Sumo2 are similarly governed by Trim28 (Figures 3F and 3H).

To validate the RNA-seq data, we performed qPCR on each class of ERVs (Figure S3G). Consistently, RLTR6_Mm/ERV1 was specifically regulated by the sumoylation factors, while ET-nERV3-int/ERVK was regulated by Atf7ip, Eset, and Chaf1a, but not by the sumoylation factors. MT2_Mm/ERVL was sharply up-regulated upon the depletion of Chaf1a/b, while expression was less perturbed with depletion of factors from the other two clusters. Finally, LTR16D was upregulated upon depletion of genes from all the clusters.

Chaf1a and Sumo2 Are Directly Recruited to ERVs

We wanted to determine whether Chaf1a and Sumo2 are enriched on genomic ERVs. First, we introduced 3xHA tags at the 3'end of the endogenous *Chaf1a* locus in F9 cells using CRISPR/Cas technology (Figure S4A). The Chaf1a-3xHA cell line was characterized by shRNA knockdown, which led to the specific reduction of Chaf1a-3xHA as measured by western blot and immunostaining (Figure S4B). In addition, a Zfp809-3xHA overexpression D3 cell line was also established and similarly characterized (Figure S4C). The reliability of the Sumo2 antibodies used for chromatin immunoprecipitation (ChIP) was confirmed with knockdown of *Sumo2* followed by western blot analysis (Figure S4D). To survey the global binding profiles of Chaf1a, Sumo2, Trim28, and Zfp809 on genomic ERV loci, we performed ChIP sequencing (ChIP-seq). The quality of the ChIP DNA was determined by qPCR and motif analysis. Zfp809-3xHA ChIP-qPCR yielded high enrichment at proline PBS site (Figures S4E and S4F), and Trim28 ChIP-qPCR showed strong binding at a previously reported target gene *Ptpn18* (Figure S4G) (Hu et al., 2009).

ChIP-seq analysis revealed that both Chaf1a and Sumo2 are recruited to loci of members of several classes of ERVs (Figures 4A and 4B; Table S4). We next asked if the bound ERV

loci are enriched for any histone modifications. We compared the Chaf1a, Sumo2, Trim28, and Zfp809 ChIP-seq data with publicly available datasets of histone marks and Eset ChIP-seq. Although the majority of ERVs bound by Chaf1a are enriched with H3K9me3 (Figure 4C), the H3K9me3 is of lower intensity compared to that of Trim28, Zfp809, and Sumo2 bound ERVs (Figure 4C). Intriguingly, considerable proportions (15%) of Chaf1a bound ERVs are also enriched for the active H3K4me3 modification (Figure 4C). Furthermore, Chaf1a-bound ERVs exhibit higher levels of H3K4me2 and H3K9Ac (Figure S4H). This raises the possibility that additional accessory proteins may be required for Chaf1a to exert the silencing effects. Notably, Sumo2-targeted ERV loci are associated with elevated H3K9me3 levels and reduced levels of H3K4me3 modification. This binding pattern strongly resembles that of Zfp809 and Trim28 (Figure 4C). In contrast, the non-ERV loci bound by Chaf1a were enriched with abundant H3K4me3 marks and had no trace of H3K9me3 modifications. On the other hand, Sumo2/Trim28/Zfp809-bound loci exhibit detectable but low levels of H3K9me3 (Figure 4D). Collectively, this indicates differing modes of regulation by which individual factors control ERVs and non-ERV targets (Figures 4C, 4D, and S3C).

To determine the action of Chaf1a and Sumo2, we represented ERV loci bound by these factors in Venn diagrams. We found that Trim28 binds 56% of Chaf1a-bound sites, while 57% of Chaf1a ERVs are also targets of Sumo2 (Figure 4E). Moreover, only 31% of Chaf1a ERV loci are enriched for Zfp809 (Figure S4I). In contrast, 77% of Trim28 targets and 73% of Eset-bound ERVs are accompanied by enrichment of Sumo2 (Figures 4E and S4I). When we extend the analysis to three factors, we observed that more than 80% of Chaf1a/Trim28 and Chaf1a/Eset common targets have Sumo2 binding (Figure 4F). These observations strongly suggest a possible role of Sumo2 in Trim28/Eset ERV regulation. The co-regulation of Chaf1a and Sumo2 with the canonical Zfp809/Trim28/Eset machinery seems to be ERV-specific as very little overlap was observed between the factors on non-ERV loci (Figure S4J). Collectively, in terms of ERV regulation, Chaf1a binding is clustered away from the Sumo/Zfp809/Trim28/Eset axis (Figures 4G, 4H, and S4K). This is remarkably similar to the pattern observed from the RNA-seq data (Figure 3D). Overall, our ChIP data provides the first biochemical demonstration that a histone chaperone and a sumoylation modification protein can exert direct regulation of genomic ERVs.

Sumo2 Orchestrates the Viral Silencing Activities of Trim28 through Its Sumoylation Modification

Our genome-wide siRNA screen identified Sumo2, and not Sumo1 or Sumo3, to have a distinct role in proviral silencing (Figures S5A–S5C). The global RNA-seq and ChIP-seq data further suggest that Sumo2 may repress proviruses and ERVs through modulation of the Trim28/Eset machinery (Figure 5A). To test this possibility, we first performed Sumo2 ChIP-qPCR and identified its binding on the proviral LTR. Importantly, when *Trim28* was knocked-down, the level of Sumo2 binding on both proviral elements and most of the ERVs tested was drastically reduced (Figures 5B and 5C). In contrast, enrichment of Sumo2 was not

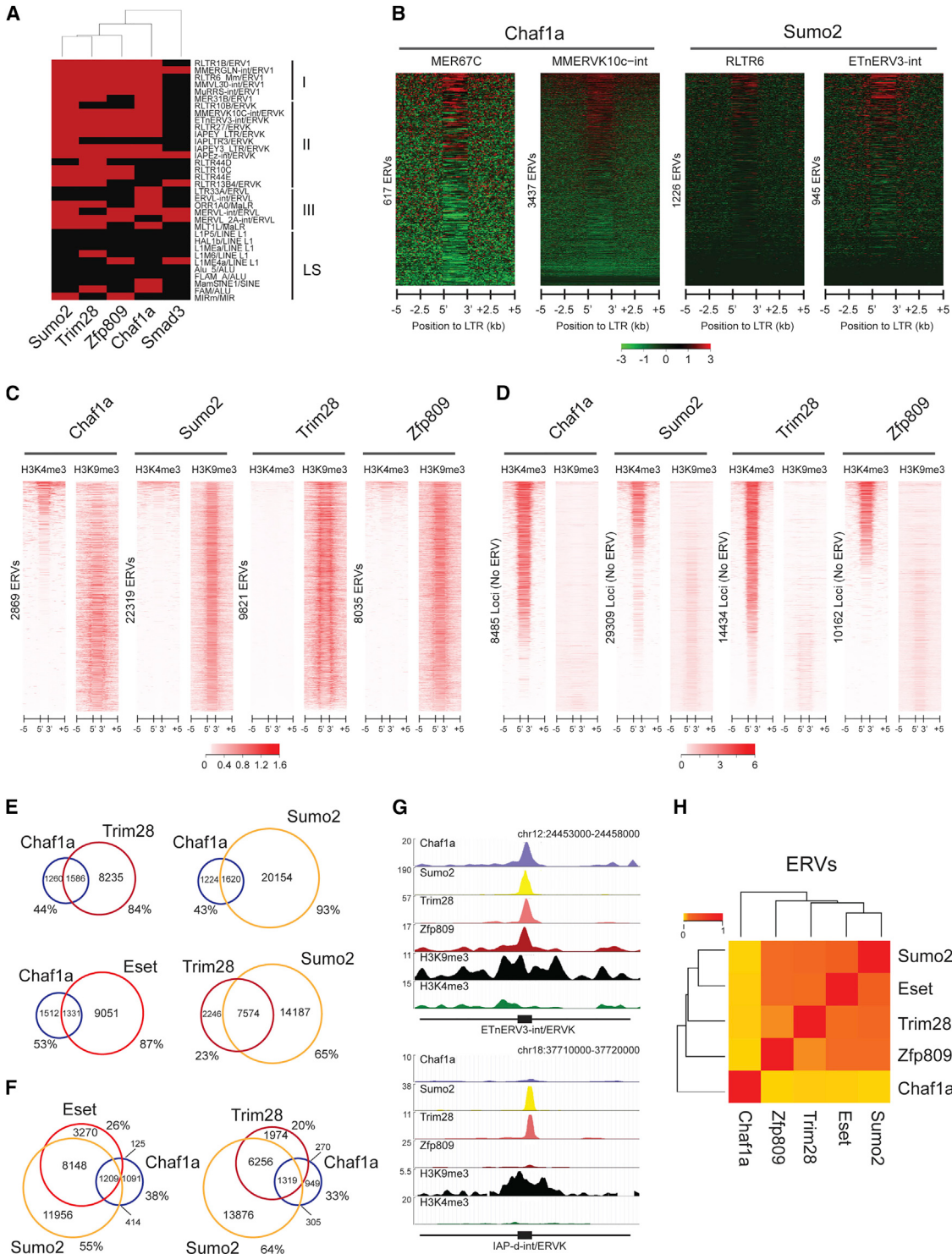


Figure 4. Direct Recruitment of Chaf1a and Sumo2 to Genomic ERVs

(A) Heatmap indicating the recruitment of Sumo2, Trim28, Zfp809, and Chaf1a on the indicated ERVs of different classes (I-III) and Line/Sine elements (LS). ChIP-seq was performed for the indicated factors, Smad3 is used as a control. Red indicates binding whereas black indicates the absence of binding.

(B) Heatmaps of Chaf1a enrichment at the genomic regions flanking MER67C and MMERVK10c-int (left panels) and Sumo2 enrichment at the genomic regions flanking RLTR6 and ETnERV3-int (right panels).

(C) Heatmaps of histone modifications at the genomic regions of the ERV loci bound by Chaf1a, Sumo2, Trim28, and Zfp809. The heatmaps are clustered according to the enrichment profile of H3K4me3.

(legend continued on next page)

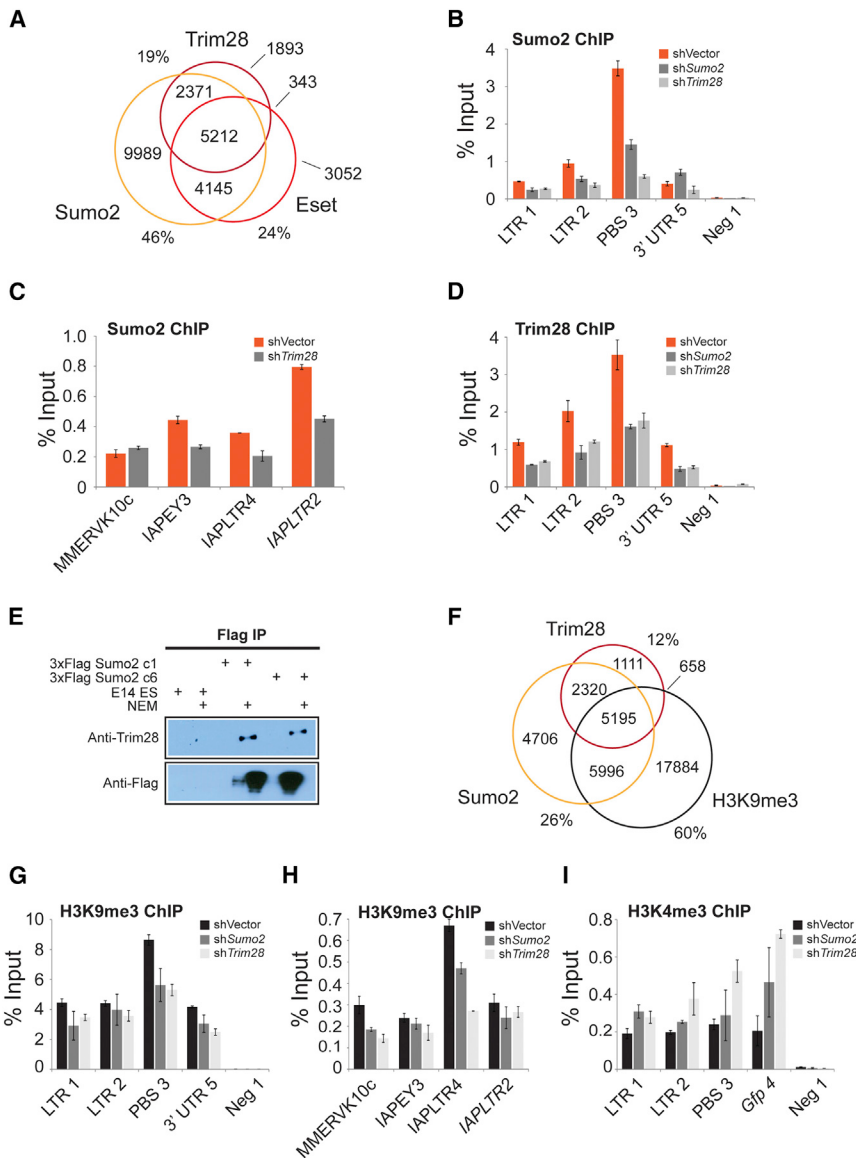


Figure 5. Sumo2 Regulates Proviruses by Post-translational Modification of Trim28

(A) Venn diagrams demonstrating the number of common and uniquely-bound ERV loci among the indicated factors. Sumo2 interacts extensively with the factors from the canonical pathway. Percentage values indicate uniquely bound sites.

(B–D) Sumo2 functions through Trim28 in proviral silencing. Sumo2 and Trim28 ChIP experiments were conducted on the samples with depletion of *Sumo2* or *Trim28*. The enrichment was measured by qPCR. Data is presented as mean ± SEM from independent replicate experiments.

(E) Trim28 is modified by Sumo2 in vivo. A 3xFlag tag was added to the 5' end of *Sumo2* genomic region using CRISPR/Cas in E14 cells. Two homozygous lines were selected for the immunoprecipitation assays. NEM was added to protect the sumoylated proteins from desumoylation by SENPs in the cell lysates.

(F) Venn diagrams demonstrating the number of common and uniquely-bound ERV loci among indicated factors. The majority of the Trim28/H3K9me3 enriched ERVs are also bound by Sumo2. Percentage values indicate uniquely-bound sites.

(G and H) Knockdown of *Sumo2* and *Trim28* significantly reduced the H3K9me3 enrichment on proviral PBS and ERVs. H3K9me3 ChIP was performed on the samples with depletion of *Sumo2* or *Trim28*. Data is presented as mean ± SEM from independent replicate experiments.

(I) Knockdown of *Trim28* and *Sumo2* increased the active H3K4me3 mark on proviral elements. H3K4me3 ChIP was performed on samples with depleted *Sumo2* or *Trim28*. Data is presented as mean ± SEM from independent replicate experiments.

See also Figure S5.

affected by *Chaf1a* knockdown (Figures S5D and S5E). Furthermore, the removal of Sumo2 abolished the binding of Trim28 at the LTR (Figure 5D).

To interrogate whether Sumo2 directly targets Trim28 for sumoylation, we studied well characterized 3xFlag-Sumo2 E14 cells generated using CRISPR/Cas technology (Figures S5F–

G). Notably, we identified Trim28 in the pull-down of sumoylated proteins (Figure 5E).

Venn diagram analysis of ChIP-seq data indicates that ~90% of Sumo2/

Trim28-bound ERV sites are marked with H3K9me3 modifications (Figure 5F). Trim28 is known to mediate the recruitment of Eset, which in turn deposits the repressive H3K9me3 mark at the proviral LTR (Matsui et al., 2010). Consistently, *Sumo2* knockdown resulted in concomitant reduction in H3K9me3 marks and elevation of H3K4me3 modifications at the proviral

(D) Enrichment of several histone marks at the genomic regions of the non-ERV loci that are bound by indicated factors. The reads in the heatmaps are clustered according to the enrichment profile of H3K4me3.

(E and F) Venn diagrams demonstrating the number of commonly and uniquely-bound ERV loci among the indicated factors. Percentage values indicate uniquely bound sites.

(G) UCSC genome browser screenshots. *Chaf1a*, *Sumo2*, *Trim28*, and *Zfp809* bind ETnERV3-int-ERVK, while IAP-d-int/ERVK is bound specifically by *Sumo2* and *Trim28*. Both ERVs are enriched with H3K9me3.

(H) Clustering analysis of the ERVs bound by the indicated factors. The color intensity signifies strength of correlation. Red indicates strong correlation, whereas yellow indicates weak correlation.

See also Figure S4 and Table S4.

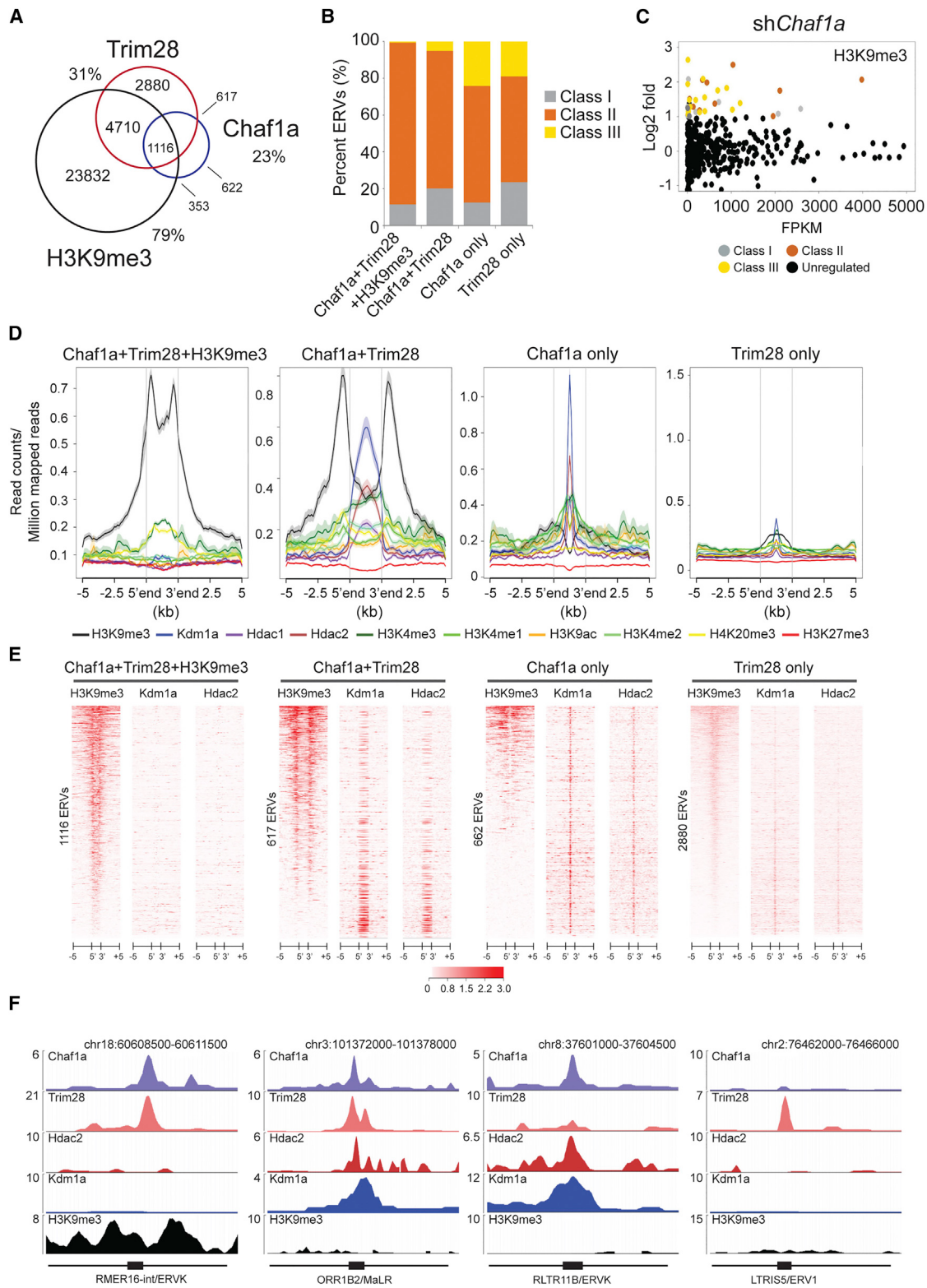


Figure 6. Differential Regulation of Class I, II, and III ERVs by Chaf1a

(A) Venn diagrams demonstrating the number of common and uniquely-bound ERV loci among Chaf1a, Trim28, and H3K9me3. Percentage values indicate uniquely-bound ERVs.

(legend continued on next page)

elements and ERVs to levels that are comparable with that seen upon Trim28 knockdown (Figures 5G–5I).

Chaf1a Has Differential Regulatory Roles on Class I, II, and III ERVs

Venn diagram analysis on ERVs bound by Chaf1a, Trim28, and those associated with the H3K9me3 modification revealed that about 64% of ERVs co-bound by Chaf1a and Trim28 are enriched with H3K9me3 (Figure 6A). In comparison, only 23% of Chaf1a/Trim28 bound non-ERV loci are marked with H3K9me3 (Figure S6A). This concurs with the notion that Chaf1a and Trim28 exert ERV-specific repressive functions. In particular, there are significant numbers of ERVs co-bound by Chaf1a and Trim28, or exclusively bound by Chaf1a that are not marked with H3K9me3, suggesting that Chaf1a may adopt alternative repressive mechanisms on these ERVs. To this end, we classified the ERVs into four categories, namely, those bound by Chaf1a+Trim28+H3K9me3, Chaf1a+Trim28, Chaf1a only, and Trim28 only (Table S5). Interestingly, the Chaf1a only category has the highest percentage of class III ERVs (Figure 6B), while the Chaf1a+Trim28+H3K9me3 category primarily belong to class I and class II ERVs (Figure 6B). Consequentially, the dot plots (Figures 6C and S6B) correlating ERV upregulation and the enrichment of histone marks further highlighted the low levels of H3K9me3 on Chaf1a-regulated class III ERVs.

Specific class III ERVs are highly expressed in early embryonic development and downregulated at the morula and blastula stages. Histone demethylase Kdm1a (Macfarlan et al., 2012) and H3K9 dimethyl transferase G9a are the key epigenetic regulators of these ERVs (Leung et al., 2011; Maksakova et al., 2013). It was found that Kdm1a and histone deacetylase Hdac1/2 cooperatively contribute to transcriptional silencing (Shi et al., 2004). Hdacs have been shown to repress MERVL in concert with Kdm1a in pluripotent stem cells (Macfarlan et al., 2011; Reichmann et al., 2012). Interestingly, Kdm1a is one of the candidate hits in our siRNA screen (Table S1). To further dissect the mode of ERV regulation within each of the four categories, we integrated our Chaf1a and Trim28 ChIP-seq data with datasets for epigenetic factors, such as Kdm1a and Hdac1/2. Surprisingly, the ERVs from the Chaf1a only category display the highest enrichment of Kdm1a and Hdac1/2 in comparison to the other categories (Figures 6D and 6E). In contrast, the ERVs bound by Chaf1a+Trim28+H3K9me3 exhibit low levels of Kdm1a and Hdac1/2 binding (Figures 6D–6F and S6D). Consistently, the Chaf1a only category is characterized by significantly higher levels of H3K4me2, H3K9Ac, and H3K27Ac marks, which

are the substrates of Kdm1a and Hdacs, respectively (Figures 6D and S6C). We further performed ERV expression analysis using a published mESC *Kdm1a* knockdown RNA-seq dataset (Agarwal et al., 2015). *Kdm1a* knockdown resulted in mostly class I and III ERV upregulation, in a manner similar to *Chaf1a* knockdown (Figure S6E). In terms of ERVs regulated, *Kdm1a/Chaf1a* knockdown has 80% more overlap than *Kdm1a/Trim28* knockdown (Figures S6F and S6G). Overall, our data indicates that Chaf1a regulates class I, II, and III ERVs through vastly different mechanisms, which may depend on the co-regulators.

Chaf1a Represses Proviruses through Epigenetic Co-factors

Chaf1a is the core component of the chromatin assembling factor complex (Caf1) that also includes Rbbp4. Interestingly, only Chaf1a/b exhibited a proviral silencing function, while the knockdown of *Rbbp4* had no effect (Figures S7A and S7B). Moreover, our siRNA screen did not uncover other histone chaperones necessary for retroviral silencing, further highlighting the specificity of Chaf1a/b in this process (Figure S7B). To further delineate the function of Chaf1a, we performed a pull-down of Flag-tagged Chaf1a followed by stable isotope labeling using amino acids (SILAC)-based quantitative mass spectrometry (MS) analysis (Figure 7A). The complete list of Chaf1a-interacting proteins includes several known and unknown factors (Figure 7A; Table S6). Chaf1a has previously been shown to interact with chromatin modifying factors (Quivy et al., 2004; Sarraf and Stancheva, 2004). Indeed, we identified several epigenetic modifiers that appeared in both the Chaf1a MS and genome-wide siRNA screen list, such as Kdm1a, Smarcc1, and Eset. Using co-immunoprecipitation (coIP), we confirmed the interaction of Chaf1a with histone methyltransferase Eset, histone demethylase Kdm1a, deacetylase Hdac2, and histone chaperones Chaf1b (Figures 7B–7D, S7C, and S7D).

To investigate the direct effects of Chaf1a at provirus loci, we used the Chaf1a-3xHA CRISPR F9 cell line for ChIP-qPCR analysis. We observed direct localization of Chaf1a to the proviral LTR elements (Figure 7E), which was further confirmed by Chaf1a-V5 ChIP (Figure S7E). To address the relationship between Chaf1a and Trim28, we performed ChIP on Trim28 upon *Chaf1a* knockdown. The binding of Trim28 was significantly abolished by the knockdown of *Trim28* itself, whereas Chaf1a-knockdown elicited no effect (Figure S7F). This suggests that Trim28 recruitment to the provirus is independent of Chaf1a. Moreover, we did not detect any change in Chaf1a enrichment upon *Sumo2* depletion (Figure S7G).

(B) Percentage stacked columns demonstrating the classes of ERVs bound by the indicated categories on the x axis.

(C) The correlation between the upregulation of the different classes of ERVs upon *Chaf1a* depletion and the enrichment of H3K9me3 mark. The data is plotted using sh*Chaf1a* RNA-seq and H3K9me3 ChIP-seq. Grey, orange, and yellow dots represent ERVs with significantly increased expression in class I, II, and III, respectively. Black dots indicate the non-regulated ERVs.

(D) Average binding profiles of the individual categories shows that ERVs belonging to the Chaf1a only and Chaf1a+Trim28 categories are highly enriched with Kdm1a and Hdac2 in comparison to the other categories.

(E) Enrichment of H3K9me3, Kdm1a, and Hdac2 in the genomic regions of the indicated categories. The reads in the heatmaps are clustered according to the enrichment profile of H3K9me3.

(F) UCSC genome browser screenshots of representative repeat elements. RMER16-int bound by Chaf1a and Trim28 is highly enriched with H3K9me3. In contrast, ORR1B2 is bound by Chaf1a, Trim28, Hdac2, and Kdm1a with very low H3K9me3 enrichment. Chaf1a, Hdac2, and Kdm1a bind RLTR11B with the absence of Trim28 and H3K9me3, while LTRIS5 is bound exclusively by Trim28.

See also Figure S6 and Table S5.

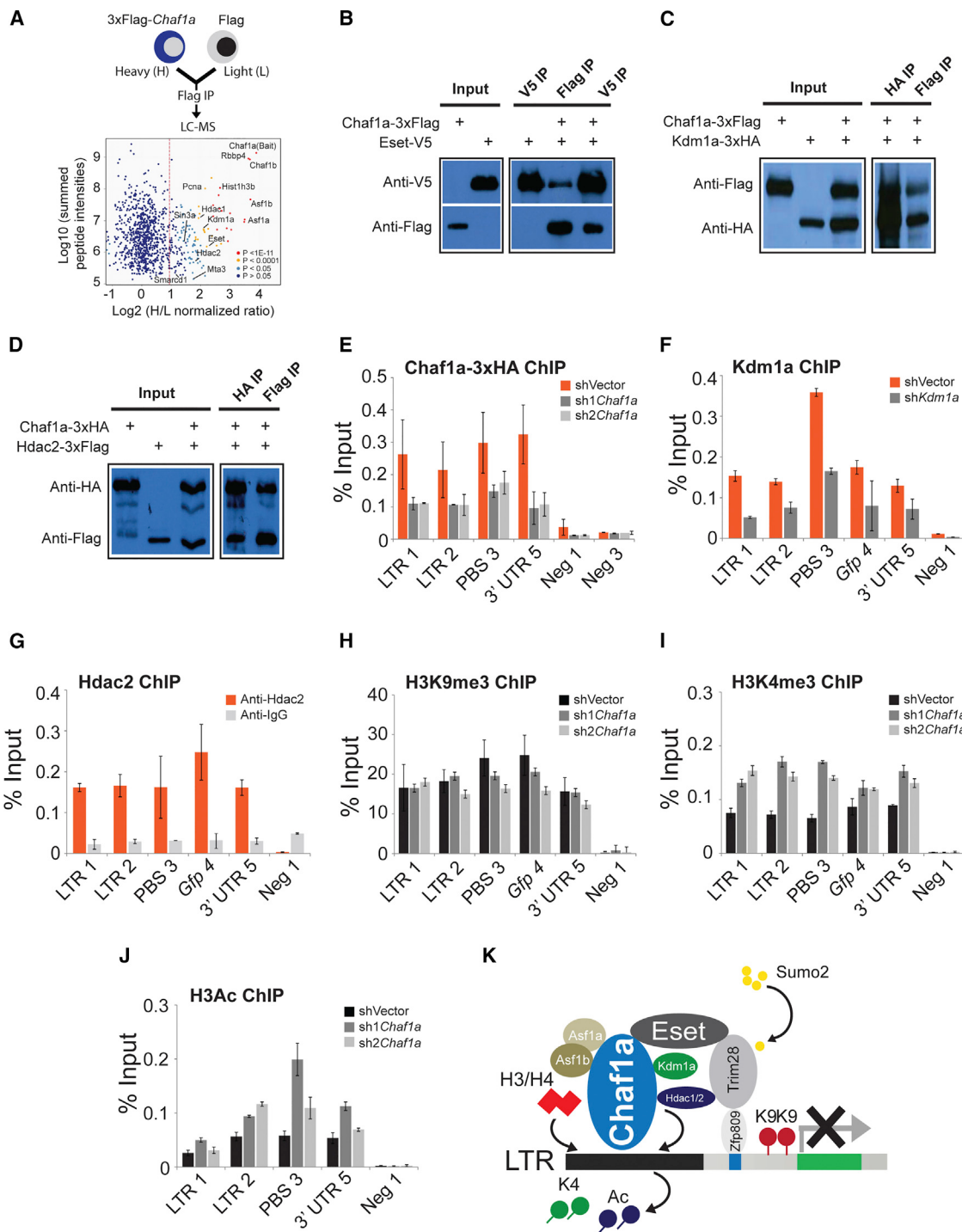


Figure 7. Chaf1a Are Enriched at Proviruses and Regulates Their Expression through Its Interacting Epigenetic Co-factors

(A) SILAC mass spectrometry (MS) analysis uncovers the Chaf1a interactome network. Upper panel: schematic representation of the SILAC MS work-flow as described in the supplemental procedures. Lower panel: differential protein identification in Flag-tagged Chaf1a immunoprecipitation. Several epigenetic and chromatin regulators are indicated.

(B-D) Western blots confirm the interacting proteins identified by MS. Western blots showing co-immunoprecipitation (coIP) of Chaf1a with Eset, Kdm1a, and Hdac2.

(E) Chaf1a is enriched at the proviral elements. Chaf1a-3xHA ChIP was carried out in F9 Chaf1a-3xHA cell line using a HA antibody. The enrichment was analyzed by qPCR. Data are presented as mean \pm SEM from independent replicate experiments.

(legend continued on next page)

To understand the mechanisms by which Chaf1a silences the newly introduced proviruses, we performed ChIP on the Chaf1a interacting histone modifiers Kdm1a and Hdac2. To our surprise, both Kdm1a and Hdac2 were enriched at the proviral LTR (Figures 7F and 7G). In addition, consistent with the siRNA screen, shRNA knockdown of *Kdm1a* was able to rescue the expression of MMLV-*Gfp* reporter (Figure S7H). Treatment of E14 cells using the Hdac inhibitor TSA also relieved silencing of the MMLV-*Gfp* reporter (Figure S7I). Next, we tested the dynamic changes of the histone marks on the provirus LTR and ERVs upon the depletion of *Chaf1a*. The enrichment of H3K9me3 on provirus LTR was slightly reduced (Figure 7H), while the active H3K4me3 and total H3Ac marks were significantly increased (Figures 7I, 7J, and S7J–S7L). Together, our data shows that the repressive function of Chaf1a on proviruses is reinforced by the presence of its interacting partners, Kdm1a, Hdac2, and Eset.

To test whether Chaf1a can directly bind the viral DNA, we performed electrophoretic mobility shift assays (EMSA). We did not observe a specific EMSA band for the Chaf1a protein, indicating that Chaf1a does not bind directly to the viral DNA (Figures S7M–S7O). The Caf1 complex is thought to assemble histones H3/H4 during DNA replication and repair (Gaillard et al., 1996; Kaufman et al., 1995). Other studies have indicated that histone chaperones Asf1a/b work synergistically with Caf1 (Tyler et al., 1999). Our proteomics data also identified Asf1a/b as components of the Chaf1a interactome (Figure 7A), and the interaction between Chaf1a and Asf1a/b was confirmed by coIP (Figure S7P). To further test the function of histone assembly on proviral silencing, we performed single and combinatorial shRNA knockdown of *Asf1a/b*. Surprisingly, combinatorial depletion of *Asf1a/b* induced strong *Gfp* reactivation to a level comparable to that observed following *Chaf1a* depletion (Figure S7Q), indicating functional redundancy between Asf1a and Asf1b. This data substantiates a possible role of histone assembly in the silencing of proviral elements and ERVs.

DISCUSSION

Mammalian genomes are cluttered with endogenous viral elements, vestiges of the long history of coevolution with retrotransposons that have shaped the genome. Complex mechanisms have evolved to manage these elements, restricting their expression and reactivation. Silencing of retroviruses also played a fortuitous role in the development of somatic cell reprogramming by transcription factors, as extinction of the reprogramming transgenes that occurs when fibroblasts revert to a pluripotent state is essential for the induced pluripotent stem cells to avoid

oncogenic transformation and manifest their multi-lineage differentiation potential (Takahashi and Yamanaka, 2006). Our work provides insights into the role of the histone chaperone Chaf1a and sumoylation factor Sumo2 in the silencing of exogenous proviruses and ERVs. It supports a model where Chaf1a promotes the deposition of histone H3/H4, thus marking the integrated proviral DNA for silencing, helping to localize the Chaf1a protein to the viral LTR region (Figure 7K). The binding and transcriptional repression of the proviral chromatin by Chaf1a is further reinforced via the enzymatic activities of Chaf1a-interacting proteins Eset, Kdm1a, and Hdac1/2, which modify proviral chromatin with the repressive histone mark H3K9me3 and reduce the acquisition of activating H3K4me3 and H3Ac marks (Figure 7K). In parallel, Sumo2 is required to play critical roles in the canonical Zfp809/Trim28/Eset complex via post-translational sumoylation of Trim28. Sumoylation enhances the recruitment of Trim28 to the proviral DNA, which in turn results in the modification of proviral chromatin with repressive histone H3K9me3 marks (Figure 7K). Our unbiased screen for factors involved in proviral silencing has thus revealed a complex set of genetic and epigenetic mechanisms by which exogenous proviruses and ERVs are transcriptionally silenced in pluripotent stem cells.

Cross-Talk between the Sumoylation Pathway and the Canonical Complex

Among the Sumo2-related candidates, Senp6 deconjugates Sumo2 from targeted proteins (Mukhopadhyay and Dasso, 2007), while the other factors are involved in covalent attachment of Sumo2 to the targeted proteins (Desterro et al., 1999; Geiss-Friedlander and Melchior, 2007; Gong et al., 1999; Hay, 2005; Johnson, 2004; Zhao, 2007). As such, it is tempting to speculate that the modification of key determinants by sumoylation or de-sumoylation may affect their capacity to silent the proviruses and ERVs. The cross-talk between chromatin modifying complex subunits (such as Trim28, Atf7ip, and Eset) and sumoylation factors can be inferred from the overlap of target ERVs observed, as well as their close protein-protein interactions. Importantly, our study clarifies the mechanism by which Sumo2 targets the proviral elements and ERVs—through the sumoylation of Trim28. Furthermore, Sumo modification on other epigenetic factors may potentially help mediate heterochromatin formation. It will be of great interest to determine the proteome-wide set of sumoylated proteins in ESCs.

Regulation of Different Classes of ERVs

Our RNA-seq analysis indicates that Chaf1a/b and sumoylation factors regulate different families of ERVs. Localization of Chaf1a

(F and G) Localization of Kdm1a and Hdac2 on proviral DNA. ChIP was performed using antibodies against Kdm1a or Hdac2 and the enrichment was tested by qPCR.

(H–J) The perturbation of histone mark enrichment on proviral elements upon the depletion of *Chaf1a* in F9 cells. H3K9me3, H3K4me3, and H3Ac ChIP were performed on the samples upon depletion of *Chaf1a*. Data are presented as mean ± SEM from independent replicate experiments.

(K) Schematic model for the silencing mechanism of the proviruses in mESCs involving Chaf1a, Sumo2, and the canonical Zfp809/Trim28/Eset pathway. Chaf1a and its upstream histone chaperones Asf1a/b promote the deposition of histone H3/H4 to mark the integrated proviral DNA. Transcriptional repression of the proviral chromatin is reinforced by the enzymatic activities of Chaf1a-interacting proteins, including the members of the NuRD complex (Kdm1a, Hdac1/2) and Eset. This results in reduced acquisition of activating H3K4me3 and H3Ac marks. In parallel, Sumo2 sumoylates Trim28, which is necessary for recruiting Trim28 onto the proviral DNA, in turn resulting in the deposition of the repressive H3K9me3 mark.

See also Figure S7 and Table S6.

and Sumo2 at ERV loci was confirmed by ChIP-seq analysis. It is noteworthy that the pattern of the ERVs regulated by Chaf1a is distinct from that of the sumoylation machinery or chromatin-modifying factors (Trim28, Eset, and Zfp809). Interestingly, Chaf1a regulates a significant number of ERVs from class III that are not marked with H3K9me3, but instead are enriched for H3K4me2 and H3K27Ac. Moreover, Chaf1a works with the enzymatic epigenetic modifiers, including Kdm1a and Hdac2 at these class III ERVs. In addition, Chaf1a also cooperates with Trim28 to repress the ERVs by reinforcing high levels of the H3K9me3 on class I and II ERVs. Thus, our study highlights how a chaperone like Chaf1a regulates different classes of ERVs through distinct interacting co-factors.

Suppressive Function of Histone Chaperone Chaf1a/b on Newly Integrated Proviruses

Caf1 has been reported to have diverse functions, including epigenetic regulation, DNA damage repair, and DNA replication (Green and Almouzni, 2003; Kaufman et al., 1995; Poleshko et al., 2010; Shibahara and Stillman, 1999). More recently, Chaf1a was shown to be critical for maintaining the heterochromatin state through its interaction with HP1, MBD1, and Eset (Murzina et al., 1999; Reese et al., 2003; Sarraf and Stancheva, 2004). In fact, protein structure analysis of Chaf1a indicates a PXVXL pentapeptide motif at the N terminus, which allows Chaf1a to specifically interact with the HP1 chromo shadow domain (Thiru et al., 2004). Stable association of Chaf1a with HP1 proteins may lead to its retention in heterochromatin (Murzina et al., 1999). HP1 proteins are “readers” of repressive H3K9me3 marks and interact extensively with Eset. Intriguingly, our proteomics identified Eset, HP1 α , HP1 β , and HP1 γ among the Chaf1a interactome. Remarkably, only the knockdown of Chaf1a/b was capable of rescuing the viral reporter, but not the knockdown of Rbbp4 (Figures S7A and S7B). Previous studies suggest that Rbbp4 complexes with Chaf1a/b in G1 phase. Notably, the epigenetic modification brought about by Chaf1a through HP1 or Caf1/Mbd1/Eset is S-phase-specific (Quivy et al., 2004; Sarraf and Stancheva, 2004).

How does a histone chaperone like Chaf1a localize to the proviral LTR and ERVs? Previous work has localized histone chaperones such as Hira and Daxx to the genomic sites where histones are deposited (Banaszynski et al., 2013; Elsässer et al., 2012). A recent publication also described the role of histone variants H3.3 in regulating ERVs (Elsässer et al., 2015). Indeed, our Chaf1a ChIP-seq shows the enrichment of Chaf1a at the genomic sites of downstream ERV targets. When we knockdown the upstream histone chaperones of Chaf1a (Asf1a/b), we observed the abolishment of the viral silencing effect of Chaf1a. Thus, we speculate that its nucleosome assembly function may play a role in localizing Chaf1a to the integrated proviruses.

In conclusion, our work reveals the genome-wide compendium of players that mediate proviral silencing in mouse ESCs. Multiple pathways and multi-layered machineries are employed by pluripotent embryonic stem cells to maintain the silencing of proviruses and ERVs. Further studies aimed at dissecting the intricate mechanisms by which the various factors act will help fill the remaining gap in our understanding of proviral repression.

EXPERIMENTAL PROCEDURES

Genome-wide siRNA Screen

F9 cells were seeded at 6×10^5 /well in 6-well tissue culture plates. Twelve hours later, MMLV virus was added into the wells with 8 $\mu\text{g}/\text{ml}$ polybrene (107689, Sigma). Eight hours later, F9 cells were trypsinized into single cells and seeded onto individual well of 384-well plates (REF 781091, Greiner) that were pre-printed with Mouse siGENOME SMARTpool library (G-015000, Thermo Scientific Dharmacon) and contain DharmaFECT 1 (Thermo Scientific). Four days later, cells were fixed with 4% paraformaldehyde and cell nuclei were stained with Hoechst 33342 (Invitrogen). Images were acquired using the ImageXpress Ultra Confocal High Content Screening System (Molecular Devices). *Gfp* signal was quantified by the MetaXpress software (Molecular Devices). Both the siRNA screens were carried out in duplicates. The average of the duplicate *Gfp* signal was calculated by normalizing to both positive and negative controls using ScreenSifter software (Kumar et al., 2013). A cut-off threshold was set at value >2 SD from mean of negative controls, above which siRNA of 650 candidate genes significantly increase *Gfp* expression level. Based on the secondary screening, 303 high-confidence hits with *Gfp* signal (CtrlNorm value = $(X - \text{Avg}(x_{cn})) / (\text{Avg}(x_{cp}) - \text{Avg}(x_{cn}))$) cut off above 0.45 were selected.

RNA-Sequencing

Total RNA was extracted as described in the [Supplemental Experimental Procedures](#). DNA contamination was removed using a QIAGEN RNeasy Kit. The RNA samples were subject to mRNA selection, fragmentation, cDNA synthesis, and library preparation using a TruSeq RNA Sample Prep Kit (RS-122-2001, Illumina). Library quality was analyzed on a Bioanalyzer. High-throughput sequencing was performed on the Genome Analyzer IIx (Illumina).

ChIP and ChIP-Seq Assay

Chromatin was prepared according to the methods provided in the [Supplemental Experimental Procedures](#). Chromatin extracts were immunoprecipitated using H3K4me3 (Abcam), H3Ac (Abcam), H3K9me3 (Abcam), Eset (Abcam), Trim28 (Bethyl), Sumo2 (Abcam), and HA (Santa Cruz) antibodies. Input and immunoprecipitation samples were analyzed by qPCR. All primers used are listed in [Table S7](#). ChIP-seq libraries were prepared according to manufacturer’s instructions (Illumina). High-throughput sequencing was performed on a Genome Analyzer IIx (Illumina).

Bioinformatics Analysis

See detailed information in the [Supplemental Experimental Procedures](#).

ACCESSION NUMBERS

The accession number for all sequencing samples reported is GEO: GSE70865.

SUPPLEMENTAL INFORMATION

Supplemental Information includes Supplemental Experimental Procedures, seven figures, and seven tables and can be found with this article online at <http://dx.doi.org/10.1016/j.cell.2015.08.037>.

AUTHOR CONTRIBUTIONS

B.X.Y. and C.A.E.F. designed and performed research, analyzed data, and wrote the paper. H.C.G., T.Y., H.T.F., H.F.W., Y.F.S.S., Y.L.G.G., S.P.N., and Y.-H.L. designed and conducted research. S.S., M.C.L., V.T., T.-M.L., L.Y.C., J.G., J.J.C., S.P.G., G.Q.D., H.L., and F.A.B. analyzed data. Y.-H.L. designed research, analyzed data, and wrote the paper.

ACKNOWLEDGMENTS

We are grateful to Yang Lin for helpful discussion. We thank Wong Chee Wai for technical assistance. H.L. is supported by Mayo Clinic Center for Individualized Medicine. S.P.G. is supported by NIH grant R01 CA30488. Y.-H.L. is

supported by the A*Star Investigatorship research award. We are grateful to the Biomedical Research Council, Agency for Science, Technology and Research, Singapore for research funding.

Received: November 26, 2014

Revised: July 7, 2015

Accepted: August 13, 2015

Published: September 10, 2015

REFERENCES

Agarwal, S., Macfarlan, T.S., Sartor, M.A., and Iwase, S. (2015). Sequencing of first-strand cDNA library reveals full-length transcriptomes. *Nat. Commun.* 6, 6002.

Banaszynski, L.A., Wen, D., Dewell, S., Whitcomb, S.J., Lin, M., Diaz, N., Elsässer, S.J., Chagpier, A., Goldberg, A.D., Canaan, E., et al. (2013). Hira-dependent histone H3.3 deposition facilitates PRC2 recruitment at developmental loci in ES cells. *Cell* 155, 107–120.

De Graeve, F., Bahr, A., Chatton, B., and Kedinger, C. (2000). A murine ATFa-associated factor with transcriptional repressing activity. *Oncogene* 19, 1807–1819.

Desterro, J.M., Rodriguez, M.S., Kemp, G.D., and Hay, R.T. (1999). Identification of the enzyme required for activation of the small ubiquitin-like protein SUMO-1. *J. Biol. Chem.* 274, 10618–10624.

Elsässer, S.J., Huang, H., Lewis, P.W., Chin, J.W., Allis, C.D., and Patel, D.J. (2012). DAXX envelops a histone H3.3-H4 dimer for H3.3-specific recognition. *Nature* 491, 560–565.

Elsässer, S.J., Noh, K.M., Diaz, N., Allis, C.D., and Banaszynski, L.A. (2015). Histone H3.3 is required for endogenous retroviral element silencing in embryonic stem cells. *Nature* 522, 240–244.

Feuer, G., Taketo, M., Hanecak, R.C., and Fan, H. (1989). Two blocks in Moloney murine leukemia virus expression in undifferentiated F9 embryonal carcinoma cells as determined by transient expression assays. *J. Virol.* 63, 2317–2324.

Friedli, M., Turelli, P., Kapopoulou, A., Rauwel, B., Castro-Díaz, N., Rowe, H.M., Ecco, G., Unzu, C., Planet, E., Lombardo, A., et al. (2014). Loss of transcriptional control over endogenous retroelements during reprogramming to pluripotency. *Genome Res.* 24, 1251–1259.

Gaillard, P.H., Martini, E.M., Kaufman, P.D., Stillman, B., Moustacchi, E., and Almouzni, G. (1996). Chromatin assembly coupled to DNA repair: a new role for chromatin assembly factor I. *Cell* 86, 887–896.

Gaudet, F., Rideout, W.M., 3rd, Meissner, A., Dausman, J., Leonhardt, H., and Jaenisch, R. (2004). Dnmt1 expression in pre- and postimplantation embryogenesis and the maintenance of IAP silencing. *Mol. Cell. Biol.* 24, 1640–1648.

Geiss-Friedlander, R., and Melchior, F. (2007). Concepts in sumoylation: a decade on. *Nat. Rev. Mol. Cell Biol.* 8, 947–956.

Gong, L., Li, B., Millas, S., and Yeh, E.T. (1999). Molecular cloning and characterization of human AOS1 and UBA2, components of the sentrin-activating enzyme complex. *FEBS Lett.* 448, 185–189.

Green, C.M., and Almouzni, G. (2003). Local action of the chromatin assembly factor CAF-1 at sites of nucleotide excision repair in vivo. *EMBO J.* 22, 5163–5174.

Hay, R.T. (2005). SUMO: a history of modification. *Mol. Cell* 18, 1–12.

Hu, G., Kim, J., Xu, Q., Leng, Y., Orkin, S.H., and Elledge, S.J. (2009). A genome-wide RNAi screen identifies a new transcriptional module required for self-renewal. *Genes Dev.* 23, 837–848.

Huang, da W., Sherman, B.T., and Lempicki, R.A. (2009). Bioinformatics enrichment tools: paths toward the comprehensive functional analysis of large gene lists. *Nucleic Acids Res.* 37, 1–13.

Johnson, E.S. (2004). Protein modification by SUMO. *Annu. Rev. Biochem.* 73, 355–382.

Kao, S.Y., Calman, A.F., Luciw, P.A., and Peterlin, B.M. (1987). Anti-termination of transcription within the long terminal repeat of HIV-1 by tat gene product. *Nature* 330, 489–493.

Karimi, M.M., Goyal, P., Maksakova, I.A., Bilenky, M., Leung, D., Tang, J.X., Shinkai, Y., Mager, D.L., Jones, S., Hirst, M., and Lorincz, M.C. (2011). DNA methylation and SETDB1/H3K9me3 regulate predominantly distinct sets of genes, retroelements, and chimeric transcripts in mESCs. *Cell Stem Cell* 8, 676–687.

Kaufman, P.D., Kobayashi, R., Kessler, N., and Stillman, B. (1995). The p150 and p60 subunits of chromatin assembly factor I: a molecular link between newly synthesized histones and DNA replication. *Cell* 81, 1105–1114.

Kumar, P., Goh, G., Wongphayak, S., Moreau, D., and Bard, F. (2013). Screen-Sifter: analysis and visualization of RNAi screening data. *BMC Bioinformatics* 14, 290.

Leung, D.C., Dong, K.B., Maksakova, I.A., Goyal, P., Appanah, R., Lee, S., Tachibana, M., Shinkai, Y., Lehnertz, B., Mager, D.L., et al. (2011). Lysine methyltransferase G9a is required for de novo DNA methylation and the establishment, but not the maintenance, of proviral silencing. *Proc. Natl. Acad. Sci. USA* 108, 5718–5723.

Macfarlan, T.S., Gifford, W.D., Agarwal, S., Driscoll, S., Lettieri, K., Wang, J., Andrews, S.E., Franco, L., Rosenfeld, M.G., Ren, B., and Pfaff, S.L. (2011). Endogenous retroviruses and neighboring genes are coordinately repressed by LSD1/KDM1A. *Genes Dev.* 25, 594–607.

Macfarlan, T.S., Gifford, W.D., Driscoll, S., Lettieri, K., Rowe, H.M., Bonanomi, D., Firth, A., Singer, O., Trono, D., and Pfaff, S.L. (2012). Embryonic stem cell potency fluctuates with endogenous retrovirus activity. *Nature* 487, 57–63.

Maksakova, I.A., Thompson, P.J., Goyal, P., Jones, S.J., Singh, P.B., Karimi, M.M., and Lorincz, M.C. (2013). Distinct roles of KAP1, HP1 and G9a/GLP in silencing of the two-cell-specific retrotransposon MERVL in mouse ES cells. *Epigenetics Chromatin* 6, 15.

Matsui, T., Leung, D., Miyashita, H., Maksakova, I.A., Miyachi, H., Kimura, H., Tachibana, M., Lorincz, M.C., and Shinkai, Y. (2010). Proviral silencing in embryonic stem cells requires the histone methyltransferase ESET. *Nature* 464, 927–931.

Maxwell, P.H., and Curcio, M.J. (2007). Host factors that control long terminal repeat retrotransposons in *Saccharomyces cerevisiae*: implications for regulation of mammalian retroviruses. *Eukaryot. Cell* 6, 1069–1080.

Mukhopadhyay, D., and Dasso, M. (2007). Modification in reverse: the SUMO proteases. *Trends Biochem. Sci.* 32, 286–295.

Murzina, N., Verreault, A., Laue, E., and Stillman, B. (1999). Heterochromatin dynamics in mouse cells: interaction between chromatin assembly factor 1 and HP1 proteins. *Mol. Cell* 4, 529–540.

Niwa, O., Yokota, Y., Ishida, H., and Sugahara, T. (1983). Independent mechanisms involved in suppression of the Moloney leukemia virus genome during differentiation of murine teratocarcinoma cells. *Cell* 32, 1105–1113.

Pearson, A.E., Esvikov, A.V., Gruber, J.H., de Vries, W.N., Holbrook, A.E., Solter, D., and Knowles, B.B. (2004). Retrotransposons regulate host genes in mouse oocytes and preimplantation embryos. *Dev. Cell* 7, 597–606.

Petersen, R., Kempler, G., and Barklis, E. (1991). A stem cell-specific silencer in the primer-binding site of a retrovirus. *Mol. Cell. Biol.* 11, 1214–1221.

Poleshko, A., Einarsen, M.B., Shalginskikh, N., Zhang, R., Adams, P.D., Skalka, A.M., and Katz, R.A. (2010). Identification of a functional network of human epigenetic silencing factors. *J. Biol. Chem.* 285, 422–433.

Quivy, J.P., Roche, D., Kirschner, D., Tagami, H., Nakatani, Y., and Almouzni, G. (2004). A CAF-1 dependent pool of HP1 during heterochromatin duplication. *EMBO J.* 23, 3516–3526.

Reese, B.E., Bachman, K.E., Baylin, S.B., and Rountree, M.R. (2003). The methyl-CpG binding protein MBD1 interacts with the p150 subunit of chromatin assembly factor 1. *Mol. Cell. Biol.* 23, 3226–3236.

Reichmann, J., Crichton, J.H., Madej, M.J., Taggart, M., Gautier, P., Garcia-Perez, J.L., Meehan, R.R., and Adams, I.R. (2012). Microarray analysis of LTR retrotransposon silencing identifies Hdac1 as a regulator of retrotransposon expression in mouse embryonic stem cells. *PLoS Comput. Biol.* 8, e1002486.

Rowe, H.M., Jakobsson, J., Mesnard, D., Rougemont, J., Reynard, S., Aktas, T., Maillard, P.V., Layard-Liesching, H., Verp, S., Marquis, J., et al. (2010). KAP1 controls endogenous retroviruses in embryonic stem cells. *Nature* 463, 237–240.

Sarraf, S.A., and Stancheva, I. (2004). Methyl-CpG binding protein MBD1 couples histone H3 methylation at lysine 9 by SETDB1 to DNA replication and chromatin assembly. *Mol. Cell* 15, 595–605.

Schlesinger, S., and Goff, S.P. (2013). Silencing of proviruses in embryonic cells: efficiency, stability and chromatin modifications. *EMBO Rep.* 14, 73–79.

Schlesinger, S., Lee, A.H., Wang, G.Z., Green, L., and Goff, S.P. (2013). Pro-viral silencing in embryonic cells is regulated by Yin Yang 1. *Cell Rep.* 4, 50–58.

Shi, Y., Lan, F., Matson, C., Mulligan, P., Whetstine, J.R., Cole, P.A., Casero, R.A., and Shi, Y. (2004). Histone demethylation mediated by the nuclear amine oxidase homolog LSD1. *Cell* 119, 941–953.

Shibahara, K., and Stillman, B. (1999). Replication-dependent marking of DNA by PCNA facilitates CAF-1-coupled inheritance of chromatin. *Cell* 96, 575–585.

Shoemaker, J.E., Lopes, T.J., Ghosh, S., Matsuoka, Y., Kawaoka, Y., and Kitano, H. (2012). CTen: a web-based platform for identifying enriched cell types from heterogeneous microarray data. *BMC Genomics* 13, 460.

Stewart, C.L., Stuhlmann, H., Jähner, D., and Jaenisch, R. (1982). De novo methylation, expression, and infectivity of retroviral genomes introduced into embryonal carcinoma cells. *Proc. Natl. Acad. Sci. USA* 79, 4098–4102.

Takahashi, K., and Yamanaka, S. (2006). Induction of pluripotent stem cells from mouse embryonic and adult fibroblast cultures by defined factors. *Cell* 126, 663–676.

Teich, N.M., Weiss, R.A., Martin, G.R., and Lowy, D.R. (1977). Virus infection of murine teratocarcinoma stem cell lines. *Cell* 12, 973–982.

Thiru, A., Nietlispach, D., Mott, H.R., Okuwaki, M., Lyon, D., Nielsen, P.R., Hirshberg, M., Verreault, A., Murzina, N.V., and Laue, E.D. (2004). Structural basis of HP1/PXVXL motif peptide interactions and HP1 localisation to heterochromatin. *EMBO J.* 23, 489–499.

Tyler, J.K., Adams, C.R., Chen, S.R., Kobayashi, R., Kamakaka, R.T., and Kadonaga, J.T. (1999). The RCAF complex mediates chromatin assembly during DNA replication and repair. *Nature* 402, 555–560.

Walsh, C.P., Chaillet, J.R., and Bestor, T.H. (1998). Transcription of IAP endogenous retroviruses is constrained by cytosine methylation. *Nat. Genet.* 20, 116–117.

Wang, H., An, W., Cao, R., Xia, L., Erdjument-Bromage, H., Chatton, B., Tempst, P., Roeder, R.G., and Zhang, Y. (2003). mAM facilitates conversion by ESET of dimethyl to trimethyl lysine 9 of histone H3 to cause transcriptional repression. *Mol. Cell* 12, 475–487.

Wang, G.Z., Wolf, D., and Goff, S.P. (2014). EBP1, a novel host factor involved in primer binding site-dependent restriction of moloney murine leukemia virus in embryonic cells. *J. Virol.* 88, 1825–1829.

Wissing, S., Muñoz-Lopez, M., Macia, A., Yang, Z., Montano, M., Collins, W., Garcia-Perez, J.L., Moran, J.V., and Greene, W.C. (2012). Reprogramming somatic cells into iPS cells activates LINE-1 retroelement mobility. *Hum. Mol. Genet.* 21, 208–218.

Wolf, D., and Goff, S.P. (2007). TRIM28 mediates primer binding site-targeted silencing of murine leukemia virus in embryonic cells. *Cell* 131, 46–57.

Wolf, D., and Goff, S.P. (2009). Embryonic stem cells use ZFP809 to silence retroviral DNAs. *Nature* 458, 1201–1204.

Wolf, D., Cammas, F., Looson, R., and Goff, S.P. (2008a). Primer binding site-dependent restriction of murine leukemia virus requires HP1 binding by TRIM28. *J. Virol.* 82, 4675–4679.

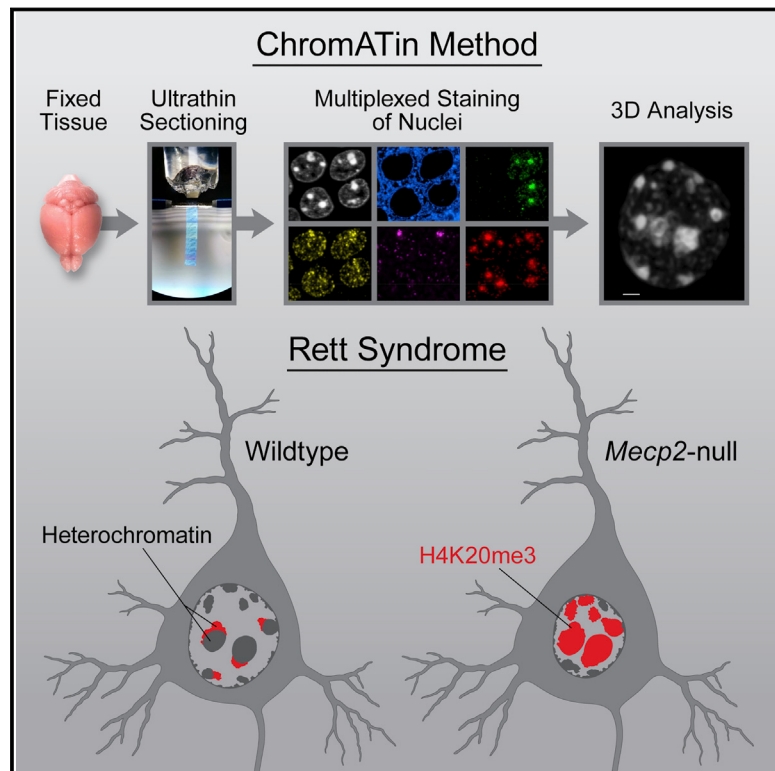
Wolf, D., Hug, K., and Goff, S.P. (2008b). TRIM28 mediates primer binding site-targeted silencing of Lys1,2 tRNA-utilizing retroviruses in embryonic cells. *Proc. Natl. Acad. Sci. USA* 105, 12521–12526.

Ying, Q.L., Stavridis, M., Griffiths, D., Li, M., and Smith, A. (2003). Conversion of embryonic stem cells into neuroectodermal precursors in adherent monoculture. *Nat. Biotechnol.* 21, 183–186.

Zhao, J. (2007). Sumoylation regulates diverse biological processes. *Cell. Mol. Life Sci.* 64, 3017–3033.

A High-Resolution Imaging Approach to Investigate Chromatin Architecture in Complex Tissues

Graphical Abstract



Authors

Michael W. Linhoff, Saurabh K. Garg, Gail Mandel

Correspondence

mandelg@ohsu.edu

In Brief

The ChromATin approach combines analysis of epigenetic modifications by immunostaining, localization of specific DNA sequences by FISH, and high-resolution segregation of nuclear compartments using advanced array tomography (AT) imaging, producing a high-resolution picture of chromatin architecture in complex tissues such as the brain.

Highlights

- ChromATin allows for 3D analysis of chromatin architecture in complex tissues
- Low-temperature FISH allows for array tomography localization of nucleic acids
- Cell-type-specific increase in chromatin compaction is seen in *Mecp2*-null neurons
- Spatial reorganization of the H4K20me3 modification accompanies chromatin compaction

A High-Resolution Imaging Approach to Investigate Chromatin Architecture in Complex Tissues

Michael W. Linhoff,¹ Saurabh K. Garg,^{1,2} and Gail Mandel^{1,2,*}

¹Vollum Institute, Oregon Health and Science University, 3181 SW Sam Jackson Park Road, Portland, OR 97239, USA

²Howard Hughes Medical Institute, Oregon Health and Science University, 3181 SW Sam Jackson Park Road, Portland, OR 97239, USA

*Correspondence: mandelg@ohsu.edu

<http://dx.doi.org/10.1016/j.cell.2015.09.002>

SUMMARY

We present ChromATin, a quantitative high-resolution imaging approach for investigating chromatin organization in complex tissues. This method combines analysis of epigenetic modifications by immunostaining, localization of specific DNA sequences by FISH, and high-resolution segregation of nuclear compartments using array tomography (AT) imaging. We then apply this approach to examine how the genome is organized in the mammalian brain using female Rett syndrome mice, which are a mosaic of normal and *Mecp2*-null cells. Side-by-side comparisons within the same field reveal distinct heterochromatin territories in wild-type neurons that are altered in *Mecp2*-null nuclei. Mutant neurons exhibit increased chromatin compaction and a striking redistribution of the H4K20me3 histone modification into pericentromeric heterochromatin, a territory occupied normally by MeCP2. These events are not observed in every neuronal cell type, highlighting ChromATin as a powerful *in situ* method for examining cell-type-specific differences in chromatin architecture in complex tissues.

INTRODUCTION

The organization of chromatin within the nucleus plays an important role in the regulation of gene expression (Bickmore and van Steensel, 2013; Politz et al., 2013). Although high-throughput sequencing strategies have revolutionized chromatin research by enabling genome-wide analysis of chromatin interactions (Dixon et al., 2012; Lieberman-Aiden et al., 2009), fluorescent *in situ* hybridization (FISH) remains a powerful tool in studying the organization of chromosomal territories (Cremer and Cremer, 2010). New high-resolution imaging technologies promise to advance our understanding of how chromatin is packaged in the nucleus for appropriate gene expression (Ricci et al., 2015; Smeets et al., 2014).

New methods for examining chromatin architecture are needed. The two most widely used strategies, chromosome conformation capture (C-method) and FISH, each have their own strengths and weaknesses. Although C-methods offer base pair resolution and, in the case of HiC, genome-wide anal-

ysis of chromatin, this method is most often performed on pooled cell populations, which might obscure cell-type-specific differences that exist in complex tissues. On the other hand, FISH is an ideal method for analysis of different cell types in tissue, but probes are typically limited to a small number of genetic loci. Interestingly, these methods are not always in agreement with regard to chromatin organization. For example, analysis of the *HoxD* locus in mutant embryonic stem cells shows an open chromatin structure using FISH and a closed structure using 5C (Williamson et al., 2014). A potential source of these differences is that C-methods may involve fixation of relatively large, cross-linked chromatin domains, detecting cytological co-localization rather than direct molecular interaction (Belmont, 2014; Gavrilov et al., 2013). Also, to associate C-method and FISH results with chromatin modifications requires a separate analysis using different experimental conditions. For these reasons, we sought to develop a quantitative, high-resolution imaging method for investigating chromatin organization in complex tissues. This method would combine analysis of epigenetic modifications by immunostaining, localization of specific DNA sequences by FISH, and high-resolution segregation of nuclear compartments using an advanced imaging technique. We have adapted the array tomography (AT) imaging method for this purpose.

AT is a high-resolution imaging method developed for the reconstruction and analysis of neuronal circuitry in the brain (Micheva and Smith, 2007). The enhanced resolution is achieved by generating ultrathin serial sections of the specimen, followed by image acquisition and alignment. Acrylic sections can be stripped repeatedly, allowing for multiple rounds of imaging. This multiplexed staining approach increases the amount of molecular information that can be derived from a tissue volume (Micheva et al., 2010). FISH methods have not been reported for AT, and developing this capability would increase the utility of the approach for localizing DNA sequences or expressed RNAs. Our motivation in developing this method was to gain a deeper understanding of how the genome is organized in the mammalian brain, a tissue with an extreme variety of cell types. To this end, we tested AT for examining neuronal chromatin in mice lacking the DNA binding protein, MeCP2. Mutations in *MECP2* give rise to the neurological disorder, Rett syndrome (RTT) (Amir et al., 1999). MeCP2 is expressed to high levels in neurons and binds globally to methyl- and hydroxymethyl-cytosine within different dinucleotide contexts (Guo et al., 2014; Lewis et al., 1992; Mellén et al., 2012). *Mecp2* is an X-linked gene (Quaderi et al., 1994), and cells in female RTT patients and mouse models

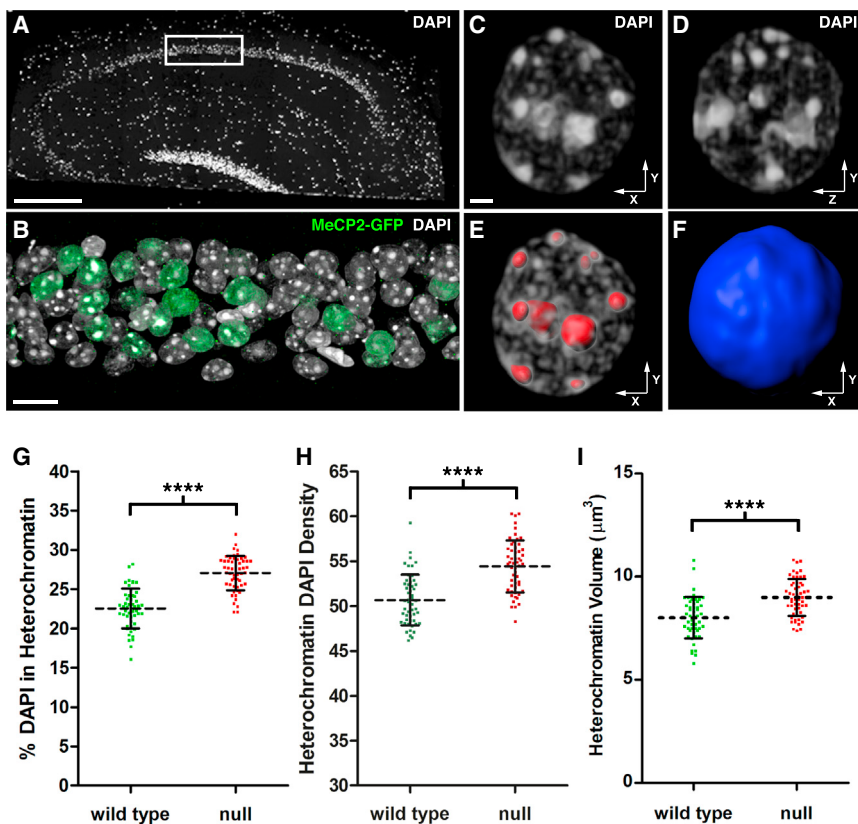


Figure 1. Quantitative Analysis of Chromatin Architecture in Hippocampal Pyramidal Neurons

(A) DAPI-stained nuclei in a 200 nm hippocampal section from a symptomatic female RTT mouse (*Mecp2-EGFP^{B/+}*). The image was stitched from multiple fields acquired using a 25× objective. Scale bar, 100 μm. The white rectangle encloses the portion of the CA1 pyramidal cell layer used for high-resolution imaging.

(B) Volume rendering of 59 serial sections (200 nm thick) through the hippocampal pyramidal cell layer. DAPI labels nuclei, and an antibody to GFP was used to identify cells expressing MeCP2-GFP. Note mosaic expression of *Mecp2-EGFP* gene due to random Xi. Scale bar, 10 μm.

(C–F) Nucleus from a WT pyramidal neuron. (C) Volume rendering of the nucleus viewed along the x-y axis. Scale bar, 1 μm. (D) Nucleus viewed along the y-z axis. (E) 3D surfaces (red) used to isolate heterochromatin for quantification. (F) A single 3D surface (blue) encloses the entire contents of the nucleus.

(G–I) Analysis of WT and *Mecp2*-null pyramidal neurons.

(G) Scatterplot showing the percentage of total nuclear DAPI pixel intensity located within the heterochromatin threshold (mean ± SD). (WT, 22.5 ± 2.5%, n = 51 nuclei from three mice), (null, 27.1 ± 2.2%, n = 55 nuclei from three mice). Unpaired t test, p < 0.0001. Xi chromosome values were subtracted from total heterochromatin.

(H) Scatterplot showing the density of DAPI pixel intensity within the heterochromatin threshold

(mean ± SD). Density is expressed as pixel intensity ($\times 10^3$) per μm^3 . WT, 50.7 ± 2.8 ; null, 54.4 ± 2.9 . Unpaired t test, p < 0.0001.

(I) Scatterplot showing heterochromatin volume (mean ± SD). WT, $8.0 \pm 1.0 \mu\text{m}^3$; null, $9.0 \pm 0.9 \mu\text{m}^3$. Unpaired t test, p < 0.0001.

See also Figure S1 and Movie S1.

are mosaic for loss of MeCP2 due to dosage compensation in mammals (Adler et al., 1995). This mosaicism provides an ideal experimental context wherein neurons with normal chromatin architecture are adjacent to *Mecp2*-null neurons. While in vitro studies suggest that MeCP2 may regulate higher-order chromatin structure, it is not known how these findings impact chromatin organization in vivo. Further, several additional models for its function, including gene repression and activation, have also been proposed (Lyst and Bird, 2015).

Using AT imaging, we quantify large-scale chromatin changes in symptomatic adult female RTT mouse brain. We detect a significant increase in chromatin compaction in two types of *Mecp2*-null hippocampal neurons together with a striking redistribution of the H4K20me3 histone modification into pericentromeric heterochromatin. In contrast, we do not detect these changes in cerebellar granule cells. We observe a spectrum of chromatin condensation states among cells in the nervous system providing a potential mechanism to explain cell-type-specific differences in gene expression upon loss of MeCP2.

In summary, we show that AT is an ideal tool for investigating chromatin architecture in complex tissues where cellular heterogeneity may confound methods that sample populations of cells. Multiplexed detection of epigenetic modifications and genomic sequences combines with the resolving power of the AT imaging

method to permit quantitative analysis within defined nuclear compartments.

RESULTS

Quantitative Analysis of Chromatin Organization in Neurons Using AT

We initially chose hippocampal CA1 pyramidal neurons for our investigation due to their location within a well-defined layer in the hippocampus (Figure 1A). Neuronal nuclei, as in other cell types, can be visualized using the fluorescent DNA intercalator, DAPI (Wilson et al., 1990). To determine the utility of AT for analyzing chromatin architecture, we exploited the mosaic nature of female RTT mouse brain expressing a knockin *Mecp2-EGFP* gene fusion (Lyst et al., 2013). Mosaicism is ideal for imaging comparisons because fixation, embedding, staining, and imaging steps are equivalent for the wild-type (WT) and mutant populations of neurons under investigation. As predicted, due to the X-linked nature of *Mecp2* and random X inactivation, the ratio of WT (GFP positive) to mutant cells was approximately 1:1 (Figure 1B).

We found that 200 nm sections allowed for full-volume reconstruction of an sufficient number of nuclei for analysis. Figure 1C shows 3D reconstruction for a WT nucleus visualized along the x-y axis, while Figure 1D shows equivalent resolution along

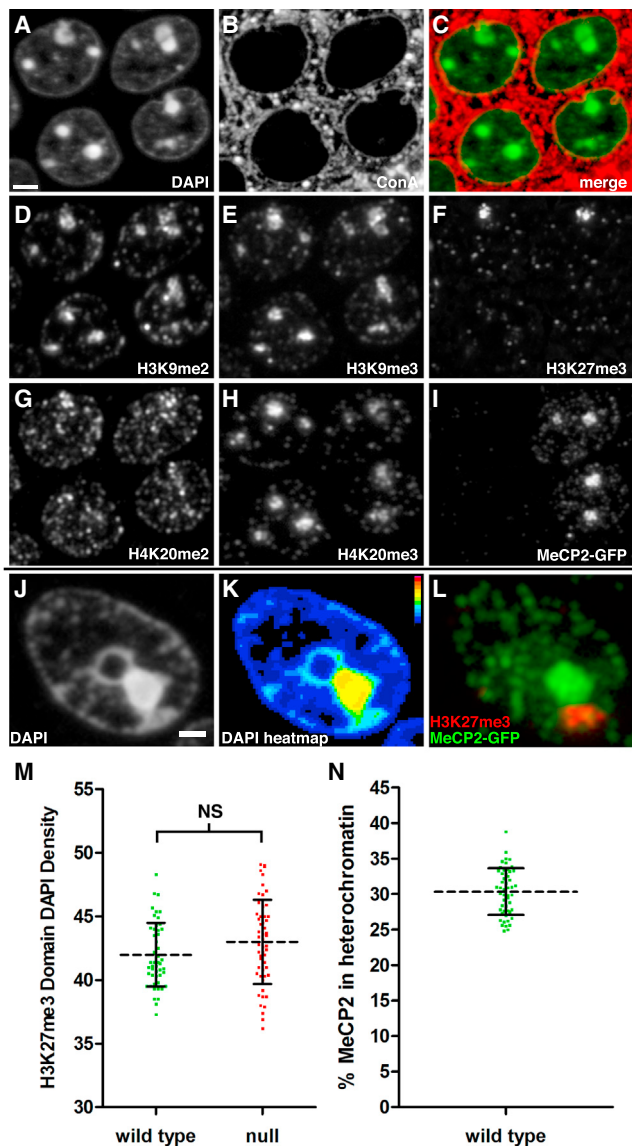


Figure 2. Multiplexed Immunostaining for Histone Modifications
 (A–I) Panels (A)–(I) represent fluorescence images acquired using the same 200 nm section through the hippocampal pyramidal cell layer.
 (A) DAPI staining of CA1 pyramidal neuron nuclei. Right, two WT nuclei (see I). Left, two mutant nuclei. Scale bar, 2 μ m.
 (B) Binding of the lectin Concanavalin A (ConA) to membrane glycoproteins.
 (C) Merge of ConA (red) with DAPI (green).
 (D) Immunostaining for H3K9me2.
 (E) Immunostaining for H3K9me3.
 (F) Immunostaining for H3K27me3. The two intense H3K27me3 clusters represent the Xi. These clusters are not visible in the two lower nuclei because this image is of a single 200 nm section.
 (G) Immunostaining for H4K20me2.
 (H) Immunostaining for H4K20me3.
 (I) Immunostaining for the MeCP2-GFP fusion protein.
 (J) DAPI staining of a nucleus from a WT neuron. Panels (J)–(L) represent fluorescence images acquired from the same 200 nm section from another mouse. Scale bar, 1 μ m.
 (K) Heatmap representation of DAPI pixel intensity for the section shown in Figure 2J. The two adjacent heterochromatin clusters exhibit different density profiles. Bar shows heatmap index.

the z axis. Heterochromatic foci in neuronal nuclei exhibit a wide range of sizes and numbers. We therefore established a threshold based upon pixel intensity to quantify heterochromatin intensity and volume. A representative surface rendering of the heterochromatic foci enclosed by our threshold is shown in Figure 1E. A second 3D surface enclosing the entire nucleus was used to determine total nuclear volume and DAPI pixel intensity (Figure 1F). The structures enclosed by these surfaces are best visualized in Movie S1.

Using AT, we found that the total amount of nuclear DAPI did not differ between WT and *Mecp2*-null neurons (Figure S1A). However, loss of MeCP2 resulted in a 20% increase in the amount of DNA packaged within the heterochromatin threshold (Figure 1G). The increase in chromatin compaction was detected as both an increase in DAPI density within heterochromatin (Figure 1H), as well as an increase in heterochromatin volume (Figure 1I). These results indicate that, in *Mecp2*-null neurons, there is a redistribution of DAPI-labeled DNA into more densely compact heterochromatin, and the increase in volume is not due to “unraveling” of chromatin within heterochromatic foci.

Previous studies found that nuclear diameters in RTT neurons were smaller than WT neurons (Li et al., 2013; Stuss et al., 2013; Yazdani et al., 2012). In agreement with these reports, AT analysis of nuclear volume revealed a modest (~5%) decrease in mutant neurons compared to WT (Figure S1B). Interestingly, we found a strong negative correlation when we plotted heterochromatin content versus nuclear volume for CA1 pyramidal neurons regardless of MeCP2 status (Figure S1C). This is consistent with previous reports that show an expansion of nuclear size when chromatin is decondensed (Mazumder et al., 2008; Shen et al., 1995).

Resolving Spatial Organization of Histone Modifications with Multiplexed Immunostaining

The other notable advantage of AT over other imaging methods is the ability to perform multiple rounds of imaging on the same sections using a variety of detection reagents. The observation of more compact chromatin in *Mecp2*-null neurons led us to examine whether we could detect any changes in heterochromatin-associated histone modifications. In Figure 2, we show the results of multiplexed immunostaining using antibodies against five different histone modifications, as well as for DAPI, MeCP2-GFP, and Concanavalin A (ConA). Immunostaining for H3K9me2, H3K9me3, H3K27me3, and H4K20me3 shows expected patterns in terms of their association with DAPI-labeled heterochromatin, indicating that our cytological criterion for heterochromatin is consistent with previously published studies (Figures 2D–2H).

(L) Merged immunostaining for MeCP2-GFP (green) and H3K27me3 (red). MeCP2-GFP is enriched in the heterochromatin cluster with higher DAPI pixel intensity in Figure 2K, while H3K27me3 enriched heterochromatin has lower DAPI pixel intensity.

(M) Scatterplot showing Xi DAPI pixel density (mean \pm SD). Density is expressed as pixel intensity ($\times 10^3$) per μm^3 . WT, 42.0 ± 2.5 , n = 51; null, 43.0 ± 3.3 , n = 55. Unpaired t test, p = 0.078.

(N) Scatterplot showing the percentage of MeCP2-GFP (mean \pm SD) localized within the heterochromatin threshold in WT neurons. $30.4 \pm 3.3\%$, n = 51. See also Movie S2.

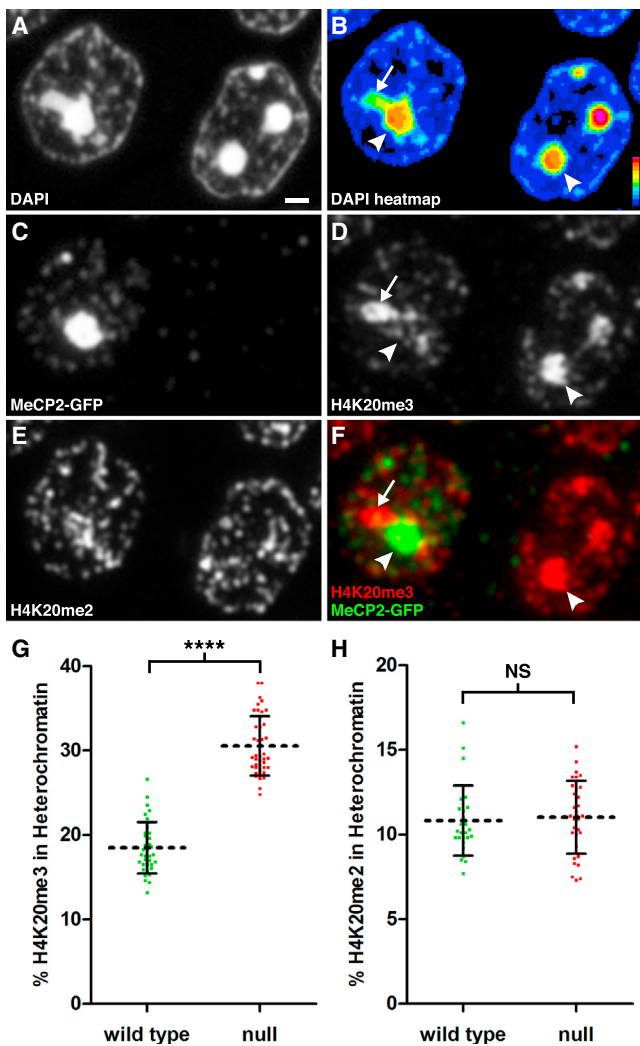


Figure 3. The H4K20me3 Modification Is Redistributed Spatially upon Loss of MeCP2

(A–F) Panels (A)–(F) represent fluorescence images acquired using the same 200 nm section through the hippocampal pyramidal cell layer.
 (A) DAPI staining. Scale bar, 1 μ m.
 (B) Relative pixel intensity of DAPI staining. Heat map index is located in the lower right corner. Arrow indicates lower intensity heterochromatin still within threshold level. Arrowhead points to high intensity heterochromatin.
 (C) Immunostaining for MeCP2-GFP. Left, WT nucleus; right, *Mcp2*-null nucleus.
 (D) Immunostaining for H4K20me3. Arrows and arrowhead as in Figure 3B.
 (E) Immunostaining for H4K20me2.
 (F) Merged image for MeCP2-GFP and H4K20me3. In the WT nucleus, MeCP2-GFP binding dominates in pericentromeric heterochromatin (arrowhead), while H4K20me3 localizes to the heterochromatin region with lower DAPI density (arrow).
 (G) Scatterplot showing percentage of total nuclear H4K20me3 within heterochromatin in pyramidal neurons (mean \pm SD). There is a significant redistribution of H4K20me3 into heterochromatin after loss of MeCP2 (WT, 18.5 \pm 3.0, n = 36 nuclei from three mice; null, 30.5 \pm 3.5, n = 41 nuclei from three mice). Unpaired t test, p < 0.0001.
 (H) Scatterplot showing the percentage of total nuclear H4K20me2 within heterochromatin (mean \pm SD) for pyramidal neurons. WT, 10.8 \pm 2.1, n = 27 nuclei from two mice; null, 11.0 \pm 2.2, n = 31 nuclei from two mice. Unpaired t test, p = 0.72. See also Figures S2 and S3 and Movie S3.

We always observed a single intense cluster of H3K27me3 in female cells that represents the Xi (Figure 2F), and MeCP2-GFP was generally excluded from this heterochromatin compartment (Figures 2J–L). These exclusive heterochromatin territories are best appreciated by viewing the full 3D reconstruction (Movie S2). Using H3K27me3 immunostaining as a guide, we isolated this compartment (green surface in Movie S1) from total heterochromatin. Consistent with the observation that MeCP2 is excluded from this territory, we did not observe a significant difference in DAPI density for the Xi chromosome between WT and mutant neurons (Figure 2M). Further, the density of DAPI within the Xi was less than the density within other heterochromatin compartments (~80%, compare with Figure 1H). This less condensed heterochromatin state for Xi has been described previously by light and electron microscopy (Rego et al., 2008).

In addition to quantifying DAPI intensity, the established heterochromatin threshold can be applied to all the imaging channels acquired in an experiment. For example, although it appears upon visual examination that most of the MeCP2 is localized to heterochromatic foci, low-intensity clusters are highly abundant in euchromatin and nucleoplasm, resulting in heterochromatin MeCP2 content being ~30% of total MeCP2 in a pyramidal cell nucleus (Figure 2N).

The H4K20me3 Modification Defines a Unique Heterochromatin Territory

AT imaging revealed an unexpected alteration in the spatial organization of H4K20me3 when WT and *Mcp2*-null nuclei were compared. In neurons deficient for MeCP2, H4K20me3 displayed a staining pattern that was almost identical to that of DAPI (compare Figures 3A–3D, right nuclei), which is consistent with previous reports that H4K20me3 is associated with pericentromeric heterochromatin (Schotta et al., 2004). Strikingly, this extensive overlap with heterochromatic foci was not observed in WT neurons (Figures 3A–3D, left nuclei). In WT neurons, MeCP2 clustered intensely in heterochromatic foci, while the H4K20me3 intensity was reduced in these regions (arrowheads, compare Figures 3D and 3F left nuclei), instead occupying a territory peripheral to the dense heterochromatic foci (arrows, Figures 3D and 3F). These H4K20me3-rich territories are well within the heterochromatin threshold, but they display reduced DAPI intensity when compared to pericentromeric heterochromatin (arrow, Figure 3B). The segregation of H4K20me3, H3K27me3, and MeCP2 enriched heterochromatin territories is easily observed using AT (Movie S3). We performed confocal microscopy on brain sections to confirm that the H4K20me3 territories were not an artifact of the AT procedure. Examination of CA1 pyramidal neurons from female heterozygotes or wild-type (WT) male mice shows that the H4K20me3 territories can be detected using standard microscopy methods albeit at lower resolution (Figure S2).

We used the heterochromatin threshold to quantify the extent of this altered localization and detected a robust (65%) redistribution of H4K20me3 into dense heterochromatin upon loss of MeCP2 (Figure 3G). This spatial redistribution occurred in conjunction with a modest (11%) increase in the total nuclear amount of H4K20me3 (see Figure 4F). In contrast to

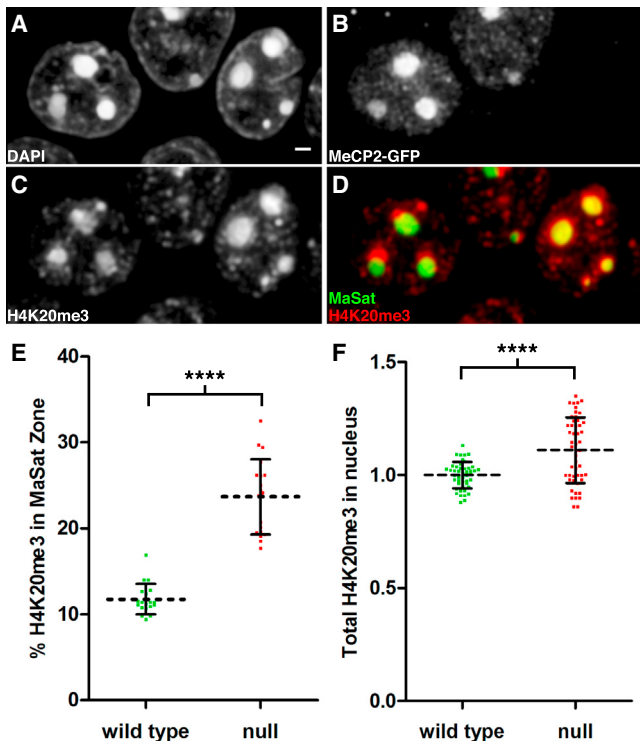


Figure 4. The H4K20me3 Modification Expands into Pericentromeric Heterochromatin in *Mecp2*-Null Nuclei

(A–D) Panels (A)–(D) represent fluorescence images taken from a volume rendering through the hippocampal pyramidal cell layer.

(A) DAPI staining. Scale bar, 1 μ m.

(B) Immunostaining for MeCP2-GFP identifies left neuron as WT and right neuron as *Mecp2* null.

(C) Immunostaining for H4K20me3.

(D) Merged image showing H4K20me3 distribution (red) relative to major satellite FISH signal (green). In the WT neuron, H4K20me3-enriched regions are peripheral to the major satellite heterochromatin territory.

(E) Scatterplot showing the percentage of total nuclear H4K20me3 within the major satellite threshold (mean \pm SD). There is a significant redistribution of H4K20me3 into pericentromeric heterochromatin after loss of MeCP2 (WT, 11.8 \pm 1.8, n = 19 nuclei from 3 mice; null, 23.7 \pm 4.4, n = 19 nuclei from three mice). Unpaired t test, p < 0.0001.

(F) The relative amount of H4K20me3 within the nucleus (mean \pm SD) is compared between WT and null neurons. Intensity units represent total integrated intensity ($\times 10^6$) with mean intensity normalized for WT pyramidal neurons. (WT, 1.00 \pm 0.01, n = 46 nuclei from three mice; null, 1.11 \pm 0.02, n = 50 nuclei from three mice. Unpaired t test, p < 0.0001.

See also Movie S4.

H4K20me3, we did not observe a significant change in the spatial organization of H4K20me2 with loss of MeCP2 (Figure 3H), indicating specificity in spatial organization of different histone marks in mutant nuclei.

We also examined the spatial distribution of H3K9me3, another heterochromatin-associated histone modification. Unlike the case for H4K20me3, no heterochromatin territories were enriched exclusively for this modification. In fact, H3K9me3 appeared to be present throughout all of the heterochromatin territories that we observed. Although it was difficult to detect by eye, AT analysis showed that there was still a signif-

icant (26%) redistribution of H3K9me3 into densely packed heterochromatin in *Mecp2*-null nuclei (Figure S3A). This occurred in conjunction with a 10% increase in total nuclear H3K9me3 levels (Figure S3C). We also detected a slight redistribution of H3K9me2 into dense heterochromatin (Figure S3B).

AT FISH Shows Expansion of the H4K20me3 Modification into Pericentromeric Heterochromatin in *Mecp2*-Null Nuclei

To map chromosomal territories more precisely in the nucleus, we used peptide nucleic acid probes specific for both major and minor satellite sequences to localize pericentromeric and centromeric heterochromatin, respectively (Movie S4). We performed one round of immunostaining followed by FISH on the same hippocampal sections to determine the relative positions of H4K20me3, MeCP2-GFP, and the major and minor satellite sequences. As expected, the major satellite probe localized with the most condensed heterochromatic foci (Figures 4A and 4D). As predicted on the basis of our DAPI staining, the H4K20me3-rich territory was adjacent to the major satellite territory in WT nuclei (Figure 4D, left nuclei). In neurons lacking MeCP2, this segregation was lost, and H4K20me3 was enriched significantly in the major satellite territory (Figure 4D, right nuclei). We created a 3D threshold surrounding the major satellite FISH signal and measured the intensity of H4K20me3 immunostaining within the major satellite zone relative to the total nuclear intensity. We detected a robust (100%) redistribution of H4K20me3 into pericentromeric heterochromatin upon loss of MeCP2 (Figure 4E). This spatial reorganization occurred in conjunction with a modest increase in the total nuclear amount of the modification (Figure 4F).

Changes in Chromatin Architecture upon Loss of MeCP2 Are Cell-Type Specific

To determine if the changes in chromatin architecture we observed for CA1 pyramidal neurons were occurring in other neuronal cell types, we performed a similar analysis for hippocampal dentate granule cells, as well as cerebellar granule cells. We performed two rounds of antibody staining to collect information for both H4K20me3 and H3K9me3 modifications, followed by FISH for major satellite sequences. MeCP2-GFP is abundant in dentate granule cell nuclei, with the typical strong localization in heterochromatic foci (Figure 5B). Similar to CA1 pyramidal neurons, we find that loss of MeCP2 results in a significant redistribution (93%) of H4K20me3 into the major satellite territory (Figures 5D and 5E). Analysis for H3K9me3 showed redistribution to a lesser extent (37%, Figures S4E and S4G), while H3K9me2 levels show a slight decrease in the major satellite territory (Figures S4F and S4H). The changes in H4K20me3 and H3K9me3 in dentate granule cells lacking MeCP2 are accompanied by a 15% increase in DAPI-labeled DNA packaged into densely packed heterochromatin (Figure 5F).

We next imaged chromatin organization in WT and *Mecp2*-null cerebellar granule cells, which have smaller nuclei and abundant heterochromatin. While we could easily identify MeCP2-positive granule cells (Figure 5H), the expression level of MeCP2-GFP and intensity in the major satellite territory was lower in these neurons compared to other neuronal cell types. We could not detect a change in the spatial distribution of H4K20me3 in

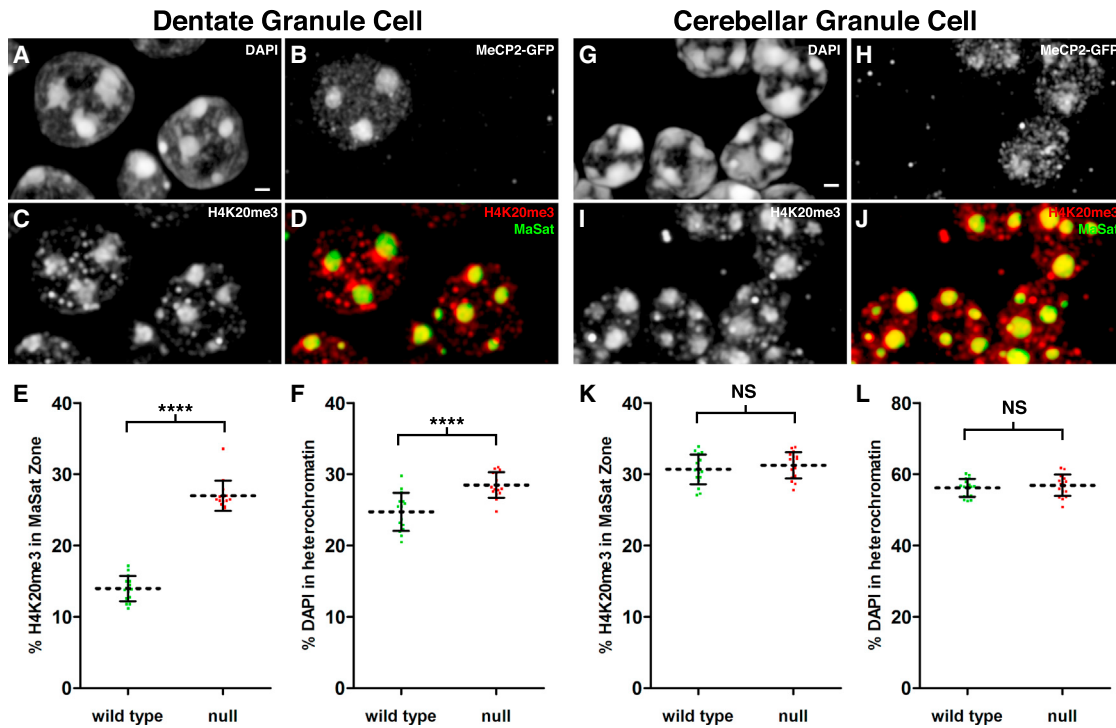


Figure 5. H4K20me3 Redistribution in *Mecp2*-Null Nuclei Is a Cell-Type-Specific Event

(A–D) Panels (A)–(D) represent fluorescence images taken from a volume rendering through the suprapyramidal dentate granule cell layer.
 (A) DAPI staining. Scale bar, 1 μ m.
 (B) Immunostaining for MeCP2-GFP identifies left neuron as WT and right neuron as *Mecp2*-null.
 (C) Immunostaining for H4K20me3.
 (D) Merged image showing H4K20me3 distribution (red) relative to major satellite FISH signal (green).
 (E) Scatterplot showing the percentage of total nuclear H4K20me3 within the major satellite threshold (mean \pm SD). There is a significant redistribution of H4K20me3 into pericentromeric heterochromatin after loss of MeCP2 (WT, 14.0 ± 1.8 , n = 15 nuclei from two mice; null, 27.0 ± 2.1 , n = 15 nuclei from two mice). Unpaired t test, p < 0.0001.
 (F) Scatterplot showing the percentage of total nuclear DAPI pixel intensity located within the heterochromatin threshold (mean \pm SD). WT, 24.7 ± 2.7 ; null, 28.5 ± 1.8 . Unpaired t test, p < 0.0001. Panels (G)–(J) represent fluorescence images taken from a volume rendering through the cerebellar granule cell layer.
 (G) DAPI staining. Scale bar, 1 μ m.
 (H) Immunostaining for MeCP2-GFP distinguishes between WT and *Mecp2*-null granule cells.
 (I) Immunostaining for H4K20me3.
 (J) Merged image showing H4K20me3 distribution (red) relative to major satellite FISH signal (green).
 (K) Scatterplot showing the percentage of total nuclear H4K20me3 within the major satellite threshold (mean \pm SD). WT, 30.7 ± 2.1 , n = 17 nuclei from two mice; null, 31.2 ± 1.8 , n = 17 nuclei from two mice. Unpaired t test, p = 0.4075.
 (L) Scatterplot showing the percentage of total nuclear DAPI pixel intensity located within the heterochromatin threshold (mean \pm SD). WT, 56.2 ± 2.5 ; null, 56.9 ± 3.0 . Unpaired t test, p = 0.4526.

See also Figures S4 and S5 and Movie S5.

cerebellar granule cells (Figure 5K). Consistent with their visible heterochromatic abundance, the amount of DAPI within heterochromatin was much greater for these neurons than for the hippocampal cell types we examined (Figure 5L). This was not a consequence of the brain region per se because neighboring cell types in the cerebellum expressed much higher levels of MeCP2-GFP than granule cells and exhibited the alterations in H4K20me3 organization that we observed for *Mecp2*-null hippocampal neurons. For example, cerebellar Purkinje neurons have extremely decondensed chromatin, and major satellite repeats are typically packaged in a massive heterochromatin cluster near the nucleolus (Figure S5A). In WT Purkinje neurons, MeCP2-GFP clusters intensely in the major satellite territory, and

H4K20me3 is predominantly localized to an adjacent heterochromatin territory (Figure S5B). In a Purkinje neuron that lacks MeCP2, H4K20me3 spreads into the major satellite territory (Figure S5C and Movie S5). Due to the large size of Purkinje nuclei, we have not acquired enough data from full Purkinje nuclei to quantify this change.

AT Analysis of Transcriptional Activity

We used antibodies against phosphorylated Serine5 on the carboxy terminal domain (CTD) of RNA polymerase II (RNAPII) to quantify transcriptional activity within single nuclei (Egloff and Murphy, 2008). As predicted, the signal for this antibody was excluded from highly condensed heterochromatin (Figures 6A–6C). Further,

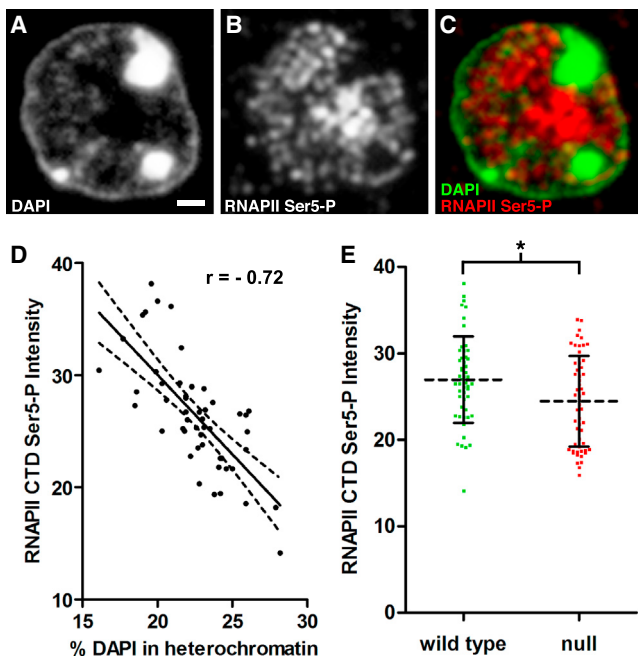


Figure 6. AT Analysis of Transcriptional Activity

(A–C) Panels (A)–(C) represent fluorescence images acquired using the same 200 nm section through a pyramidal neuron.
 (A) DAPI staining. Scale bar, 1 μ m.
 (B) Immunostaining with antibodies directed against the phosphorylated CTD (Ser5) of RNA polymerase II (RNAPII Ser5-P) to detect the active polymerase.
 (C) Merged image of DAPI and RNAPII Ser5-P. Note that RNAPII Ser5-P is excluded from heterochromatic foci.
 (D) Total integrated pixel intensity ($\times 10^5$) for RNAPII Ser5-P from WT nuclei was plotted versus heterochromatin content. RNAPII Ser5-P levels are negatively correlated with increasing heterochromatin content ($n = 51$ nuclei from three mice, Pearson $r = -0.72$, $p < 0.0001$).
 (E) Scatterplot comparing RNAPII Ser5-P levels in WT and *Mecp2*-null pyramidal neurons. Intensity units represent total integrated pixel intensity ($\times 10^5$) with mean intensity normalized for WT pyramidal neurons. WT, 27.0 ± 5.0 , $n = 51$ nuclei from 3 mice; null, 24.5 ± 5.2 , $n = 55$ nuclei from three mice). Unpaired t test, $p = 0.013$.

analysis of the reconstructed nuclei revealed a strong negative correlation between Phospho Ser5 CTD levels and nuclear heterochromatin content (Figure 6D). We also compared total nuclear levels of Phospho Ser5 CTD between WT and mutant neurons in female RTT hippocampus. This analysis showed a slight but significant reduction in Phospho Ser5 CTD in mutant neurons (Figure 6E). Antibodies against the N terminus of RNAPII did not work in AT, so we could not determine whether the reduction in Phospho Ser5 CTD was a result of lower total levels of RNAPII or is indeed a reflection of reduced transcriptional initiation in *Mecp2*-null nuclei. These experiments show that, upon the development of improved reagents, AT imaging can be effectively used to quantify transcriptional activity in different cell types.

DISCUSSION

Here, we describe an adaptation and expansion of AT for the investigation of chromatin organization. The advantages that

make AT a useful tool for resolving synaptic junctions in the brain also make it an ideal tool for resolving nuclear compartments. Ultrathin sectioning improves resolution along the z axis while also eliminating signal degradation due to poor depth penetrance of staining reagents (Micheva and Smith, 2007). We have generated high-resolution, three-dimensional reconstructions of nuclei to show how AT can be used to quantify a variety of parameters of nucleus and chromatin structure.

A powerful feature of AT is the ability to acquire multiple rounds of imaging information. This provides a way to survey the molecular composition of specific compartments within the nucleus. We performed up to five rounds of imaging on one set of serial sections, but up to nine rounds have been reported with AT (Micheva and Smith, 2007). Multiplexed immunostaining permits a candidate screening approach in addition to targeted studies. In our case, we did not initiate the experiments with a predetermined hypothesis about the spatial organization of H4K20me3 and how loss of MeCP2 may alter this organization. We performed an initial screen of antibodies for histone modifications, and the results led us to focus on modifications that mark distinct heterochromatin territories. For example, H4K20me3- and H3K27me3-rich regions in WT neurons were adjacent to, but clearly segregated from, MeCP2-bound heterochromatin (Movie S3). While we were able to detect the segregated distribution of H4K20me3 in CA1 pyramidal neurons by conventional confocal microscopy (Figure S2), AT imaging provided much greater resolution of these structures. The importance of examining chromatin organization in the brain is underscored by our finding that dissociated hippocampal neurons did not show distinct H4K20me3 territories adjacent to pericentromeric heterochromatin in culture (J. Sinnamon, personal communication).

By developing FISH conditions for AT, we have added another dimension to the method that considerably broadens its applications. There has recently been great interest in relating spatial organization of genes with chromatin modifications by combining HiC analysis with ChIP (Dixon et al., 2012; Rao et al., 2014). The development of an *in situ* detection method for chromatin organization fills a need for investigators who work in systems with extreme cellular diversity where anatomy is an integral part of the information desired.

We challenged the AT imaging method by using it on brains from symptomatic RTT female mice at 4–6 months of age. Not only does the mammalian brain contain a staggering variety of cell types, but the mosaic expression of MeCP2 provided a tightly controlled experimental system for comparing WT and *Mecp2*-null cells. Using these methods, AT has provided *in vivo* evidence supporting a role for MeCP2 in regulating chromatin architecture in neurons. We found that chromatin becomes more densely packed upon loss of MeCP2. Along with the compaction, we see a dramatic redistribution of H4K20me3 into pericentromeric heterochromatin. Consistent with the finding of more condensed chromatin, we observed a slight reduction of active RNAPII in mutant nuclei. The ability to assess large-scale chromatin organization, histone modifications, and transcriptional activity within the same nucleus in its native environment highlights the usefulness of AT as tool for chromatin research.

What could explain the increase in chromatin compaction when MeCP2 is absent in neurons? The redistribution of

H4K20me3 into pericentromeric chromatin accompanied the increased DNA compaction in *Mecp2*-null neurons. Given this result, it is of note that nucleosomal arrays reconstituted with H4K20me3 modified histones form locally condensed, oligomeric structures (Lu et al., 2008). Another potential mechanism is the interplay between MeCP2 and other chromatin architectural proteins, such as histone H1, which may promote higher-order aggregation of chromatin fibers when MeCP2 is absent. Previous studies have shown that MeCP2 competes with H1 for binding to nucleosomal DNA (Ghosh et al., 2010; Nan et al., 1997), and levels of H1 increase in the absence of MeCP2 (Skene et al., 2010). The presence of other chromatin architectural proteins in nuclei may explain why our results appear to be in opposition to *in vitro* studies that show nucleosome compaction in the presence of purified MeCP2 (Baker et al., 2013; Georgel et al., 2003). Structural studies need to be performed to compare how chromatin fibers with repressive histone modifications are packaged when bound by MeCP2 or H1. Finally, we cannot exclude the possibility that the chromatin changes are indirect and downstream effects of gene expression.

We observed similar alterations in chromatin for both hippocampal CA1 pyramidal neurons and dentate granule cells, but we did not detect changes for cerebellar granule cells. This difference between cell types is consistent with studies showing that loss of MeCP2 results in different gene expression profiles depending on neuronal type (Mellén et al., 2012; Sugino et al., 2014). It has also been shown that neurons differ with respect to levels of MeCP2 expression (Chao et al., 2010). Our general observation is that MeCP2 expression scales with nuclear size, and cerebellar granule cells express the lowest amount of MeCP2 of the cell types examined in this study (data not shown). The lack of changes in H4K20me3 distribution in cerebellar granule cells agrees with results from a previous study that did not find differences in histone modifications in *Mecp2*-null retinal neurons (Song et al., 2014). These results stress the importance of cell sorting or *in situ* approaches when studying gene expression in the brain.

Taken together with previous studies, our AT study suggests two levels of MeCP2 regulation of gene expression programs. At one level, MeCP2 prevents higher-order chromatin aggregation either by preventing H4K20me3 modification or by out-competing H1 binding at methylated nucleosomal linker DNA. At another level, MeCP2 functions as a transcriptional regulator, either through recruitment of co-repressors (Lyst et al., 2013; Nan et al., 1998) or via recruitment of co-activators (Chahrour et al., 2008). This second function may be more subject to regulation by signaling pathways, with the phosphorylation state of MeCP2 dynamically regulating association with its co-factors (Ebert et al., 2013; Lyst et al., 2013). This dual functionality would allow MeCP2 to maintain a segregated chromatin fiber that allows for long-lived neurons to adapt their gene expression programs to events, including synaptic activity or injury. In the absence of MeCP2, more compact packaging of these sequences may restrict such flexibility, and this would agree with a previous model suggesting that MeCP2 functions as a facilitator of transcriptional activation (Mellén et al., 2012).

The increase in DNA compaction in mutant nuclei raises the possibility that genes required for neuronal function may become

inappropriately relocated to a more repressive compartment and thus less subject to regulation by signaling pathways. In future studies, AT imaging can be combined with emerging FISH strategies (Beliveau et al., 2015; Boyle et al., 2011) to localize MeCP2-regulated genes in the RTT brain.

EXPERIMENTAL PROCEDURES

Experimental Animals

Animal procedures were approved by Oregon Health and Science University Institutional Animal Care and Use Committee regulations and licenses. Mice were housed with littermates on a 12:12 hr light/dark cycle. Both *Mecp2*^{tm3.1Bird} (catalog 014610; *Mecp2*^{EGFP}; Lyst et al., 2013) and *Mecp2*^{tm1.1Bird} (catalog 003890; *Mecp2*^{Bnull}; Guy et al., 2001) mice were obtained from Jackson Laboratory and were maintained on a C57BL/6 background. In order to yield heterozygote females carrying a germline *Mecp2*-null mutation and a *Mecp2*-*EGFP* allele (*Mecp2*^{Bnull/EGFP}), *Mecp2*^{EGFP/+} male mice were crossed to heterozygous *Mecp2*^{Bnull/+} mice. Genotyping for *Mecp2*^{Bnull} and *Mecp2*^{EGFP} alleles were conducted as described previously (Lioy et al., 2011; Lyst et al., 2013).

Tissue Preparation

The AT procedure was performed using the published protocol with modifications (Micheva and Smith, 2007). Five-month-old heterozygous RTT female mice were evaluated for symptoms using the observational scale (Guy et al., 2007). Mice were anaesthetized by intraperitoneal injection of Avertin (2,2,2-tribromoethanol) and perfused transcardially with 4% depolymerized paraformaldehyde in PBS. The hippocampus was dissected, and slices of hippocampus were fixed and embedded using microwave irradiation (PELCO BioWave with ColdSpot; Ted Pella). All sectioning was performed by the Array Tomography Core at the SOM Beckman Center's Cell Sciences Imaging Facility (Jon Mulholland, Director). Serial sections were cut to a thickness of 200 nm.

Immunofluorescence Procedure

Ribbons of sections were circled with an ImmEdge Pen (Vector Laboratories) to allow for small staining volumes. The sections were pretreated with 50 mM glycine in PBS + 0.05% Tween-20, washed with PBS, and blocked with 3% BSA in PBS (PBS-B) for 15 min prior to application of primary antibodies. Primary antibodies were incubated with the sections overnight at 4°C in PBS-B. Sections were washed with PBS, and secondary antibodies were incubated with sections at room temperature for 2 hr in PBS-B. The sections were washed with PBS and a water rinse before mounting with SlowFade Gold anti-fade with DAPI (Invitrogen).

To remove bound antibodies prior to a subsequent round of imaging, the ribbons were exposed to two rounds of stripping buffer. The first stripping buffer was 50 mM Tris (pH 6.8), 2% SDS, 50 mM DTT, and the second stripping buffer was Restore PLUS Western Blot Stripping Buffer (Thermo Scientific). Both buffers were incubated with sections for 10 min at 42°C with very mild agitation. Stripped sections were washed with water and PBS before initiating another round of immunostaining.

Antibodies

Histone antibodies were prescreened using the Antibody Validation Database to limit testing to antibodies that have proven specificity records (Egelhofer et al., 2011). Each antibody was tested independently for AT application, and we continued to use only those that localized exclusively to the nucleus. Commercially sourced primary antibodies used in this study include H4K20me3, clone 6F8-D9 (Abcam, ab78517), H3K9me2 (Abcam, ab1220), H3K9me3 (Diagenode, mAb-146-050), H3K27me3 (Cell Signaling, #9733), GFP (Abcam, ab13970), RNA polymerase II clone 4H8 (Abcam, ab5408), and MAP2 (Abcam, ab5392). Monoclonal antibody specific for H4K20me2 was a gift from Hiroshi Kimura. Secondary antibodies used in this study from Biotium: CF488A Goat Anti-Mouse IgG2a (20256), CF488A Goat Anti-Chicken IgY, CF647 Goat Anti-Mouse IgG. Secondary antibodies and lectins used from Life Technologies: Alexa Fluor 488 conjugated Concanavalin A (C11252), Alexa

Fluor 555 Goat Anti-Mouse IgG2a (A21137), Alexa Fluor 555 Goat Anti-Rabbit (A21429), and Alexa Fluor 647 Goat Anti-Chicken (A21449).

Fluorescent In Situ Hybridization

Standard protocols for FISH proved difficult to use with AT due to reduced adherence of the plastic sections to the coverslip when using formamide and elevated temperatures. We circumvented this problem by using ethylene carbonate as a solvent for melting DNA strands for hybridization (Matthiesen and Hansen, 2012), allowing for lower hybridization temperature. The following peptide nucleic acid (PNA) probes were used for FISH experiments: Cy3-labeled PNA probe against minor satellite sequence (CENPB-Cy3) (PNA Bio). The FITC labeled major satellite PNA probe was a kind gift from Peter Lansdorp (Falconer et al., 2010). After antibody stripping, the sections were washed with 1xSSC. Sections were incubated with 0.1 mg/ml pepsin in 10 mM HCl for 2 min at 37°C followed by washing with TE, pH 8.8. Sections were incubated with 200 µg/ml RNase A in 1xSSC for 30 min at 37°C and washed with 1xSSC. The hybridization buffer was similar to the previously described protocol with some modifications (15% ethylene carbonate, 10% dextran sulfate, 600 mM NaCl, 10 mM sodium citrate [pH 6.2], 1 × Denhardt's, and 0.1% Tween-20). After a 30 min prehybridization incubation at 50°C, the sections were incubated with PNA probes for 2 hr at 50°C. The samples were washed with 1× SSC at 50°C, with 0.2× SSC at 50°C, and rinsed with water before mounting in SlowFade Gold.

Fluorescence Microscopy and Image Processing

Sections were imaged on a Zeiss Axio Observer.Z1 inverted microscope with motorized stage. Fluorescence imaging was performed using custom filter sets and a Lumencor Spectra light engine. Images were acquired using a Zeiss 63×/1.4 NA Plan Apochromat objective and either AxioCam MRm or AxioCam 506 mono digital camera. Image stacks were created in Fiji, and the DAPI image stacks were aligned using the MultiStackReg plugin. The alignment transform for the DAPI alignment was applied to image stacks for other fluorescent channels imaged in the first round. A detailed manual describing the AT alignment procedure is provided here: http://nisms.stanford.edu/UsingOurServices/pdf/ArrayTomographyVolumeReconstruction_v1.4.pdf.

Three-Dimensional Analysis

Visualization and quantification of reconstructed nuclei was performed using Imaris software (Bitplane). A more detailed description of the analysis is included in the [Supplemental Experimental Procedures](#).

SUPPLEMENTAL INFORMATION

Supplemental Information includes Supplemental Experimental Procedures, five figures, and five movies and can be found with this article online at <http://dx.doi.org/10.1016/j.cell.2015.09.002>.

ACKNOWLEDGMENTS

We thank Ibanri Phanwar-Wood at the Stanford Cell Sciences Imaging Facility for exceptional sectioning, Peter Lansdorp at ERIBA for the major satellite PNA, Hiroshi Kimura at the Tokyo Institute of Technology for providing antibodies, Andrea Ansari for technical assistance, Lori Vaskalis for scientific illustration, and Aurelie Snyder in The Jungers Center Advanced Light Microscopy Core for Imaris instruction (P30 NS061800). M.W.L. thanks Kristina Micheva, Gordon Wang, Forrest Collman, and Brad Busse for advice on the array tomography procedure. Funding was provided generously by grants from Rett Syndrome Research Trust and NIH (HD056503 and NS022518) to G.M. M.W.L. received financial support from Fund for Science and MDA255543. G.M. is an Investigator of the Howard Hughes Medical Institute.

Received: December 2, 2014

Revised: May 22, 2015

Accepted: August 11, 2015

Published: September 24, 2015

REFERENCES

- Adler, D.A., Quaderi, N.A., Brown, S.D., Chapman, V.M., Moore, J., Tate, P., and Disteche, C.M. (1995). The X-linked methylated DNA binding protein, MeCP2, is subject to X inactivation in the mouse. *Mamm. Genome* 6, 491–492.
- Amir, R.E., Van den Veyver, I.B., Wan, M., Tran, C.Q., Francke, U., and Zoghbi, H.Y. (1999). Rett syndrome is caused by mutations in X-linked MeCP2, encoding methyl-CpG-binding protein 2. *Nat. Genet.* 23, 185–188.
- Baker, S.A., Chen, L., Wilkins, A.D., Yu, P., Lichtarge, O., and Zoghbi, H.Y. (2013). An AT-hook domain in MeCP2 determines the clinical course of Rett syndrome and related disorders. *Cell* 152, 984–996.
- Beliveau, B.J., Boettiger, A.N., Avendaño, M.S., Jungmann, R., McCole, R.B., Joyce, E.F., Kim-Kiselak, C., Bantignies, F., Fonseka, C.Y., Erceg, J., et al. (2015). Single-molecule super-resolution imaging of chromosomes and *in situ* haplotype visualization using Oligopaint FISH probes. *Nat. Commun.* 6, 7147.
- Belmont, A.S. (2014). Large-scale chromatin organization: the good, the surprising, and the still perplexing. *Curr. Opin. Cell Biol.* 26, 69–78.
- Bickmore, W.A., and van Steensel, B. (2013). Genome architecture: domain organization of interphase chromosomes. *Cell* 152, 1270–1284.
- Boyle, S., Rodesch, M.J., Halvorsleben, H.A., Jeddoh, J.A., and Bickmore, W.A. (2011). Fluorescence *in situ* hybridization with high-complexity repeat-free oligonucleotide probes generated by massively parallel synthesis. *Chromosome Res.* 19, 901–909.
- Chahrour, M., Jung, S.Y., Shaw, C., Zhou, X., Wong, S.T.C., Qin, J., and Zoghbi, H.Y. (2008). MeCP2, a key contributor to neurological disease, activates and represses transcription. *Science* 320, 1224–1229.
- Chao, H.-T., Chen, H., Samaco, R.C., Xue, M., Chahrour, M., Yoo, J., Neul, J.L., Gong, S., Lu, H.-C., Heintz, N., et al. (2010). Dysfunction in GABA signaling mediates autism-like stereotypies and Rett syndrome phenotypes. *Nature* 468, 263–269.
- Cremer, T., and Cremer, M. (2010). Chromosome territories. *Cold Spring Harb. Perspect. Biol.* 2, a003889.
- Dixon, J.R., Selvaraj, S., Yue, F., Kim, A., Li, Y., Shen, Y., Hu, M., Liu, J.S., and Ren, B. (2012). Topological domains in mammalian genomes identified by analysis of chromatin interactions. *Nature* 485, 376–380.
- Ebert, D.H., Gabel, H.W., Robinson, N.D., Kastan, N.R., Hu, L.S., Cohen, S., Navarro, A.J., Lyst, M.J., Ekiert, R., Bird, A.P., and Greenberg, M.E. (2013). Activity-dependent phosphorylation of MeCP2 threonine 308 regulates interaction with NCoR. *Nature* 499, 341–345.
- Egelhofer, T.A., Minoda, A., Klugman, S., Lee, K., Kolasinska-Zwierz, P., Alekseyenko, A.A., Cheung, M.-S., Day, D.S., Gadel, S., Gorchakov, A.A., et al. (2011). An assessment of histone-modification antibody quality. *Nat. Struct. Mol. Biol.* 18, 91–93.
- Egloff, S., and Murphy, S. (2008). Cracking the RNA polymerase II CTD code. *Trends Genet.* 24, 280–288.
- Falconer, E., Chavez, E.A., Henderson, A., Poon, S.S.S., McKinney, S., Brown, L., Huntsman, D.G., and Lansdorp, P.M. (2010). Identification of sister chromatids by DNA template strand sequences. *Nature* 463, 93–97.
- Gavrilov, A.A., Gushchanskaya, E.S., Strelkova, O., Zhironkina, O., Kireev, I.I., Iarovaia, O.V., and Razin, S.V. (2013). Disclosure of a structural milieu for the proximity ligation reveals the elusive nature of an active chromatin hub. *Nucleic Acids Res.* 41, 3563–3575.
- Georgel, P.T., Horowitz-Scherer, R.A., Adkins, N., Woodcock, C.L., Wade, P.A., and Hansen, J.C. (2003). Chromatin compaction by human MeCP2. Assembly of novel secondary chromatin structures in the absence of DNA methylation. *J. Biol. Chem.* 278, 32181–32188.
- Ghosh, R.P., Horowitz-Scherer, R.A., Nikitina, T., Shlyakhtenko, L.S., and Woodcock, C.L. (2010). MeCP2 binds cooperatively to its substrate and competes with histone H1 for chromatin binding sites. *Mol. Cell. Biol.* 30, 4656–4670.

Guo, J.U., Su, Y., Shin, J.H., Shin, J., Li, H., Xie, B., Zhong, C., Hu, S., Le, T., Fan, G., et al. (2014). Distribution, recognition and regulation of non-CpG methylation in the adult mammalian brain. *Nat. Neurosci.* 17, 215–222.

Guy, J., Hendrich, B., Holmes, M., Martin, J.E., and Bird, A. (2001). A mouse MeCP2-null mutation causes neurological symptoms that mimic Rett syndrome. *Nat. Genet.* 27, 322–326.

Guy, J., Gan, J., Selfridge, J., Cobb, S., and Bird, A. (2007). Reversal of neurological defects in a mouse model of Rett syndrome. *Science* 315, 1143–1147.

Lewis, J.D., Meehan, R.R., Henzel, W.J., Maurer-Fogy, I., Jeppesen, P., Klein, F., and Bird, A. (1992). Purification, sequence, and cellular localization of a novel chromosomal protein that binds to methylated DNA. *Cell* 69, 905–914.

Li, Y., Wang, H., Muffat, J., Cheng, A.W., Orlando, D.A., Lovén, J., Kwok, S.-M., Feldman, D.A., Bateup, H.S., Gao, Q., et al. (2013). Global transcriptional and translational repression in human-embryonic-stem-cell-derived Rett syndrome neurons. *Cell Stem Cell* 13, 446–458.

Lieberman-Aiden, E., van Berkum, N.L., Williams, L., Imakaev, M., Ragoczy, T., Telling, A., Amit, I., Lajoie, B.R., Sabo, P.J., Dorschner, M.O., et al. (2009). Comprehensive mapping of long-range interactions reveals folding principles of the human genome. *Science* 326, 289–293.

Lioy, D.T., Garg, S.K., Monaghan, C.E., Raber, J., Foust, K.D., Kaspar, B.K., Hirrlinger, P.G., Kirchhoff, F., Bissonnette, J.M., Ballas, N., and Mandel, G. (2011). A role for glia in the progression of Rett's syndrome. *Nature* 475, 497–500.

Lu, X., Simon, M.D., Chodaparambil, J.V., Hansen, J.C., Shokat, K.M., and Luger, K. (2008). The effect of H3K79 dimethylation and H4K20 trimethylation on nucleosome and chromatin structure. *Nat. Struct. Mol. Biol.* 15, 1122–1124.

Lyst, M.J., and Bird, A. (2015). Rett syndrome: a complex disorder with simple roots. *Nat. Rev. Genet.* 16, 261–275.

Lyst, M.J., Ekiert, R., Ebert, D.H., Merusi, C., Nowak, J., Selfridge, J., Guy, J., Kastan, N.R., Robinson, N.D., de Lima Alves, F., et al. (2013). Rett syndrome mutations abolish the interaction of MeCP2 with the NCoR/SMRT co-repressor. *Nat. Neurosci.* 16, 898–902.

Matthiesen, S.H., and Hansen, C.M. (2012). Fast and non-toxic *in situ* hybridization without blocking of repetitive sequences. *PLoS ONE* 7, e40675.

Mazumder, A., Roopa, T., Basu, A., Mahadevan, L., and Shivashankar, G.V. (2008). Dynamics of chromatin decondensation reveals the structural integrity of a mechanically prestressed nucleus. *Biophys. J.* 95, 3028–3035.

Mellén, M., Ayata, P., Dewell, S., Kriaucionis, S., and Heintz, N. (2012). MeCP2 binds to 5hmC enriched within active genes and accessible chromatin in the nervous system. *Cell* 151, 1417–1430.

Micheva, K.D., and Smith, S.J. (2007). Array tomography: a new tool for imaging the molecular architecture and ultrastructure of neural circuits. *Neuron* 55, 25–36.

Micheva, K.D., Busse, B., Weiler, N.C., O'Rourke, N., and Smith, S.J. (2010). Single-synapse analysis of a diverse synapse population: proteomic imaging methods and markers. *Neuron* 68, 639–653.

Nan, X., Campoy, F.J., and Bird, A. (1997). MeCP2 is a transcriptional repressor with abundant binding sites in genomic chromatin. *Cell* 88, 471–481.

Nan, X., Ng, H.H., Johnson, C.A., Laherty, C.D., Turner, B.M., Eisenman, R.N., and Bird, A. (1998). Transcriptional repression by the methyl-CpG-binding protein MeCP2 involves a histone deacetylase complex. *Nature* 393, 386–389.

Politz, J.C.R., Scalzo, D., and Groudine, M. (2013). Something silent this way forms: the functional organization of the repressive nuclear compartment. *Annu. Rev. Cell Dev. Biol.* 29, 241–270.

Quaderi, N.A., Meehan, R.R., Tate, P.H., Cross, S.H., Bird, A.P., Chatterjee, A., Herman, G.E., and Brown, S.D. (1994). Genetic and physical mapping of a gene encoding a methyl CpG binding protein, MeCP2, to the mouse X chromosome. *Genomics* 22, 648–651.

Rao, S.S.P., Huntley, M.H., Durand, N.C., Stamenova, E.K., Bochkov, I.D., Robinson, J.T., Sanborn, A.L., Machol, I., Omer, A.D., Lander, E.S., and Aiden, E.L. (2014). A 3D map of the human genome at kilobase resolution reveals principles of chromatin looping. *Cell* 159, 1665–1680.

Rego, A., Sinclair, P.B., Tao, W., Kireev, I., and Belmont, A.S. (2008). The facultative heterochromatin of the inactive X chromosome has a distinctive condensed ultrastructure. *J. Cell Sci.* 121, 1119–1127.

Ricci, M.A., Manzo, C., García-Parajo, M.F., Lakadamyali, M., and Cosma, M.P. (2015). Chromatin fibers are formed by heterogeneous groups of nucleosomes *in vivo*. *Cell* 160, 1145–1158.

Schotta, G., Lachner, M., Sarma, K., Ebert, A., Sengupta, R., Reuter, G., Reinberg, D., and Jenuwein, T. (2004). A silencing pathway to induce H3-K9 and H4-K20 trimethylation at constitutive heterochromatin. *Genes Dev.* 18, 1251–1262.

Shen, X., Yu, L., Weir, J.W., and Gorovsky, M.A. (1995). Linker histones are not essential and affect chromatin condensation *in vivo*. *Cell* 82, 47–56.

Skene, P.J., Illingworth, R.S., Webb, S., Kerr, A.R.W., James, K.D., Turner, D.J., Andrews, R., and Bird, A.P. (2010). Neuronal MeCP2 is expressed at near histone-octamer levels and globally alters the chromatin state. *Mol. Cell* 37, 457–468.

Smeets, D., Markaki, Y., Schmid, V.J., Kraus, F., Tattemusch, A., Cerase, A., Sterr, M., Fiedler, S., Demmerle, J., Popken, J., et al. (2014). Three-dimensional super-resolution microscopy of the inactive X chromosome territory reveals a collapse of its active nuclear compartment harboring distinct Xist RNA foci. *Epigenetics Chromatin* 7, 8.

Song, C., Feodorova, Y., Guy, J., Peichl, L., Jost, K.L., Kimura, H., Cardoso, M.C., Bird, A., Leonhardt, H., Joffe, B., and Solovei, I. (2014). DNA methylation reader MECP2: cell type- and differentiation stage-specific protein distribution. *Epigenetics Chromatin* 7, 17.

Stuss, D.P., Cheema, M., Ng, M.K., Martinez de Paz, A., Williamson, B., Misraien, K., Cosman, J.D., McPhee, D., Esteller, M., Hendzel, M., et al. (2013). Impaired *in vivo* binding of MeCP2 to chromatin in the absence of its DNA methyl-binding domain. *Nucleic Acids Res.* 41, 4888–4900.

Sugino, K., Hempel, C.M., Okaty, B.W., Arnon, H.A., Kato, S., Dani, V.S., and Nelson, S.B. (2014). Cell-type-specific repression by methyl-CpG-binding protein 2 is biased toward long genes. *J. Neurosci.* 34, 12877–12883.

Williamson, I., Berlivet, S., Eskeland, R., Boyle, S., Illingworth, R.S., Paquette, D., Dostie, J., and Bickmore, W.A. (2014). Spatial genome organization: contrasting views from chromosome conformation capture and fluorescence *in situ* hybridization. *Genes Dev.* 28, 2778–2791.

Wilson, W.D., Tanious, F.A., Barton, H.J., Jones, R.L., Fox, K., Wydra, R.L., and Strekowski, L. (1990). DNA sequence dependent binding modes of 4',6-diamidino-2-phenylindole (DAPI). *Biochemistry* 29, 8452–8461.

Yazdani, M., Deogracias, R., Guy, J., Poot, R.A., Bird, A., and Barde, Y.-A. (2012). Disease modeling using embryonic stem cells: MeCP2 regulates nuclear size and RNA synthesis in neurons. *Stem Cells* 30, 2128–2139.

Age-Associated Loss of Lamin-B Leads to Systemic Inflammation and Gut Hyperplasia

Haiyang Chen, Xiaobin Zheng, and Yixian Zheng*

*Correspondence: zheng@ciwemb.edu

<http://dx.doi.org/10.1016/j.cell.2015.08.043>

(Cell 159, 829–843; November 6, 2014)

When preparing Figure 6, we inadvertently assembled incorrect immunofluorescence images for Figures 6F, 6H, and 6J. The figure has been corrected online, and the corrected version appears below. The description of the results based on this figure in the text and in the figure legend is correct. The authors sincerely apologize for this mistake.

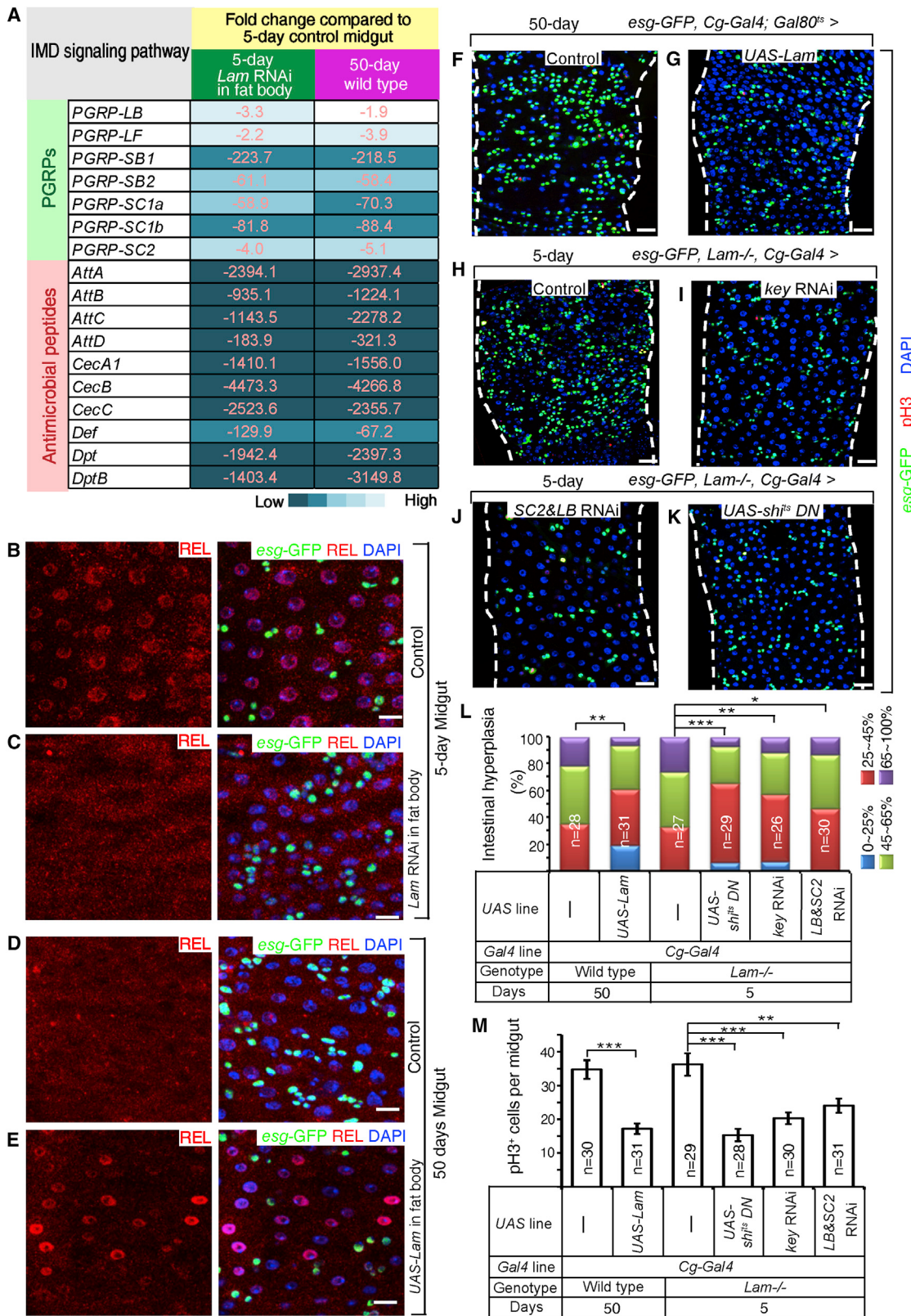


Figure 6. LAM Maintains Gut Homeostasis by Inhibiting Systemic Inflammation Caused by the Fat Body

Indigenous Bacteria from the Gut Microbiota Regulate Host Serotonin Biosynthesis

Jessica M. Yano, Kristie Yu, Gregory P. Donaldson, Gauri G. Shastri, Phoebe Ann, Liang Ma, Cathryn R. Nagler, Rustom F. Ismagilov, Sarkis K. Mazmanian, and Elaine Y. Hsiao*

*Correspondence: ehsiao@caltech.edu

<http://dx.doi.org/10.1016/j.cell.2015.09.017>

(Cell 161, 264–276; April 9, 2015)

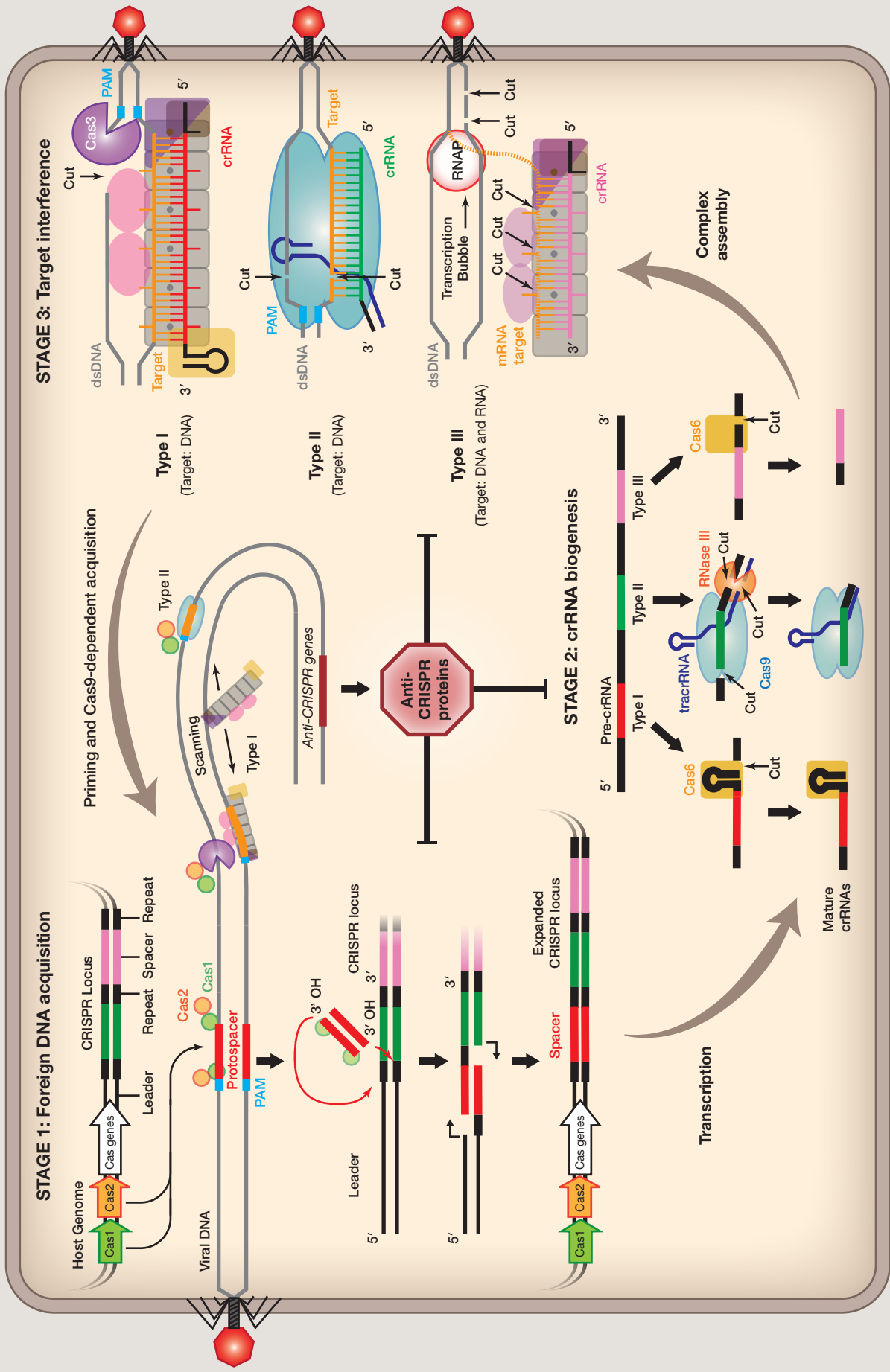
In Figure S5D of this article, the representative flow cytometry plot of forward versus side scatter for unstimulated platelets was incorrectly duplicated during the final formatting of the paper for SPF+PCPA and GF conditions. The figure has been corrected online, and the originally published descriptions of the results in the text and figure legend are accurate.

In Figure 3A, the “GF+conv” bar represents germ-free (GF) mice conventionalized with standard pathogen-free (SPF) microbiota on postnatal day 21 (P21). The published main text incorrectly referred to conventionalization on P42. Though we show in Figure 1B very similar levels of colonic serotonin after conventionalization on P21 versus P42, the “GF+conv” data in Figure 3A is specifically from GF mice conventionalized on P21. This error in the text has also been corrected online.

Overall, these changes have no bearing on the experimental results or conclusions presented in the manuscript. We apologize for any inconvenience that these errors have caused.

SnapShot: CRISPR-RNA-Guided Adaptive Immune Systems

Joshua Carter and Blake Wiedenheft
Montana State University, Department of Microbiology and Immunology, Bozeman, MT 59715, USA



SnapShot: CRISPR-RNA-Guided Adaptive Immune Systems

Cell

Joshua Carter and Blake Wiedenheft

Montana State University, Department of Microbiology and Immunology, Bozeman, MT 59715, USA

Bacteria and archaea have evolved sophisticated adaptive immune systems that rely on CRISPR (clustered regularly interspaced short palindromic repeat) loci and a diverse cassette of CRISPR-associated (*cas*) genes (Sorek et al., 2013). CRISPR systems are classified into three main types (I–III) and at least eleven different subtypes (I-A to I-F, II-A to II-C, and III-A to III-B) (Makarova et al., 2011). Despite this diversity, all CRISPR-Cas immune systems operate through three main stages: acquisition, CRISPR RNA (crRNA) biogenesis, and target interference.

Stage 1. Foreign DNA Acquisition

Foreign nucleic acids are recognized by Cas proteins, and short fragments (30–50 base pairs) of invading DNA, called protospacers, are inserted into the host's CRISPR locus as spacer sequences, separated by repeat sequences. In type I and II systems, protospacers are selected from regions of invading DNA that are flanked by a 2–5' nucleotide (nt) motif called a PAM (protospacer adjacent motif) (Sorek et al., 2013). Protospacers are generally incorporated at one end of the CRISPR locus, referred to as the leader, by a mechanism that involves Cas1, Cas2, and free 3' hydroxyls on the protospacer (Nuñez et al., 2015). Protospacer integration is accompanied by the duplication of the leader-terminal repeat sequence, which may involve host polymerases and DNA repair machinery.

Stage 2. crRNA Biogenesis

CRISPR RNA biogenesis starts with transcription, followed by nucleolytic processing of the primary transcript (pre-crRNA) into a library of short CRISPR-derived RNAs (crRNAs) that each contains a sequence complementary to a previously encountered foreign DNA. The crRNA-guide sequence is flanked by regions of the adjacent repeats. In type I and III systems, the primary CRISPR transcript is processed by CRISPR-specific endoribonucleases (Cas6 or Cas5d) that cleave within the repeat sequence (Sorek et al., 2013). In many type I systems, the repeat sequences are palindromic and Cas6 remains stably associated with a stem loop on the 3' end of the crRNA (Sorek et al., 2013). In type III systems, Cas6 transiently associates with the CRISPR RNA, and the 3' end of the crRNA is further trimmed by unknown nucleases. CRISPR RNA processing in type II systems relies on a *trans*-acting crRNA (tracrRNA), which contains a sequence that is complementary to the repeat sequences (Jackson and Wiedenheft, 2015; Sorek et al., 2013). These double-stranded regions are processed by RNase III while in the presence of Cas9 (Sorek et al., 2013). In type II systems, both the tracrRNA and the crRNA are required for target interference (Sorek et al., 2013). The two RNAs from this system have been fused into a single-guide RNA (sgRNA), and Cas9 has become a powerful tool for targeted genome engineering in a wide variety of cell types and multicellular organisms (Hsu et al., 2014).

Stage 3. Target Interference

The mature crRNAs guide Cas proteins to complementary targets. Target sequences are degraded by dedicated Cas nucleases, but the mechanisms of target degradation are diverse (Jackson and Wiedenheft, 2015; Sorek et al., 2013). Type I and II systems both target dsDNA substrates that contain a PAM and a complementary protospacer sequence. Target cleavage in type II systems is performed by a single protein (Cas9) and two RNAs, whereas type I systems rely on multi-subunit surveillance complexes that bind dsDNA substrates and then recruit Cas3, a *trans*-acting nuclease that is often fused to an ATP-dependent helicase (Sorek et al., 2013). Like type I systems, type III systems also rely on multi-subunit complexes for target detection, but unlike the type I systems, these complexes exhibit endogenous nuclease activity that degrades complementary RNA and target DNA in a transcription-dependent manner (Samai et al., 2015). Type III systems do not rely on a PAM for target recognition; rather, base pairing that extends beyond the guide sequence and into the 5' handle of the crRNA signals "self" (the CRISPR locus contains sequences that are complementary to the guide and the 5' handle) and prevents target cleavage (Samai et al., 2015).

Closing the Loop

In type I systems, target binding by the surveillance complex results in Cas3-mediated target degradation (direct interference) or primed acquisition, which involves crRNA-guided recruitment of Cas3, Cas1, and Cas2 to foreign DNA and results in rapid acquisition of new spacers into the CRISPR (Datsenko et al., 2012; Sorek et al., 2013). While primed acquisition has not yet been observed in type II systems, Cas9 is required for proper protospacer selection, suggesting a functional link between the target interference and foreign DNA acquisition (Heler et al., 2015; Wei et al., 2015). Recently, diverse viral-encoded genes that produce proteins known as anti-CRISPRs have been shown to subvert CRISPR systems by interfering with each of the different stages (Bondy-Denomy et al., 2015).

ACKNOWLEDGMENTS

J.C. is supported by a grant from the Howard Hughes Medical Institute (#52006931), IDeA Networks of Biomedical Research Excellence (INBRE, 5P20GM103474) and the Irving Weissman Scholarship. B.W. is the recipient of the Amgen Young Investigator award. Wiedenheft lab is supported by NIH P20GM103500 and R01GM108888, NSF EPSCoR (EPS-110134), the M.J. Murdock Charitable Trust, and the Montana State University Agricultural Experimental Station.

REFERENCES

Bondy-Denomy, J., Garcia, B., Strum, S., Du, M., Rollins, M.F., Wiedenheft, B., Maxwell, K.L., and Davidson, A.R. (2015). *Nature*. Published online September 23, 2015. <http://dx.doi.org/10.1038/nature15254>.

Datsenko, K.A., Pougach, K., Tikhonov, A., Wanner, B.L., Severinov, K., and Semenova, E. (2012). *Nat. Commun.* 3, 945.

Heler, R., Samai, P., Modell, J.W., Weiner, C., Goldberg, G.W., Bikard, D., and Marraffini, L.A. (2015). *Nature* 519, 199–202.

Hsu, P.D., Lander, E.S., and Zhang, F. (2014). *Cell* 157, 1262–1278.

Jackson, R.N., and Wiedenheft, B. (2015). *Mol. Cell* 58, 722–728.

Makarova, K.S., Haft, D.H., Barrangou, R., Brouns, S.J., Charpentier, E., Horvath, P., Moineau, S., Mojica, F.J., Wolf, Y.I., Yakunin, A.F., et al. (2011). *Nat. Rev. Microbiol.* 9, 467–477.

Nuñez, J.K., Lee, A.S., Engelman, A., and Doudna, J.A. (2015). *Nature* 519, 193–198.

Samai, P., Pyenson, N., Jiang, W., Goldberg, G.W., Hatoum-Aslan, A., and Marraffini, L.A. (2015). *Cell* 161, 1164–1174.

Sorek, R., Lawrence, C.M., and Wiedenheft, B. (2013). *Annu. Rev. Biochem.* 82, 237–266.

Wei, Y., Terns, R.M., and Terns, M.P. (2015). *Genes Dev.* 29, 356–361.